Geological Characteristics and Origin of the Watershed W deposit, North Queensland

Thesis submitted by

Jaime Andrés Poblete Alvarado

M.Sc. Geological Sciences, The University of British Columbia, 2011

B.Sc. Geological Sciences, Universidad de Chile, 2008

For the Degree of Doctor of Philosophy

College of Science and Engineering

James Cook University

(Townsville)

August 2019

Statement of Access

I, the undersigned author of this thesis, understand that James Cook University will make this thesis available for use within the university library and allow access in other approved libraries after its submission. All users consulting this thesis will have to sign the following statement:

In consulting this thesis, I agree not to copy or closely paraphrase it in whole or in part without the written consent of the author, and to make proper public written acknowledgement for any assistance that I have obtained from it.

Beyond this, I do not wish to place any restrictions on access to this thesis

Jaime Andrés Poblete Alvarado

August 2019

Declaration

I declare that this thesis is my own work and has not been submitted in any form for another degree or diploma at any university or other institute of tertiary education. Information derived from the published or unpublished work of others has been acknowledged in the text and a list of reference is given.

Jaime Andrés Poblete Alvarado

August 2019

Acknowledgements

I would like to thank all the people that have been involved in the thesis and in my life during the period that this work started in early 2015. Firstly, thank you very much to my former primary advisor Prof. Zhaoshan Chang for giving me the opportunity to work on this PhD project and also for sharing his knowledge in different geological aspects. I also want to thank my current primary advisor Prof. Paul Dirks, for the time invested during long discussions and brainstorming on the direct benefit of the final thesis product. Additionally I would like to thank my secondary advisor Dr. Jan-Marten Huizenga for all his help on fluid inclusions matters and technical assistance.

I am also extremely grateful to Vital Metals Inc., and its former CEO Mark Strizek, whom they allowed complete access to the Watershed deposit, drill core and geological records. Special thanks are extended to Dr. Martin Griessmann for his assistance during fieldwork and his time for geological discussion during fieldwork at the Watershed camp.

I would like to thank to the numerous EGRU friends and colleagues, including Isaac, Neus, Fredrik, Stephanie, Michael, Prince, Ashish, Sybille, Connor, Tiffany, Yanbo, Jelle, Chris, Paul, Robbie, Grace, Hannah, Judy, Kaylene, Bec and everyone I have forgotten to mention here. Great to meet you all guys and hope to see you again soon!

A big thank to my family in Chile who supported me and encouraged me at all times during this period of time in Townsville. It was great to perform the final writing of this thesis between the inspirational mountains around Santiago and the beach in Reñaca, combined with relaxing surf sessions.

Statement of the Contribution of Others

Nature of Assitance	Contribution	Name and affiliation of contributors
Intelectual support	Supervision	Prof. Paul Dirks, JCU Prof. Zhaoshan Chang, JCU and Colorado School of Mines Dr. Jan-Marten Huizenga, JCU
	Proposal writing	Prof. Zhaoshan Chang, JCU and Colorado School of Mines
	Data collection/analysis	Prof. Zhaoshan Chang, JCU and Colorado School of Mines Prof. Paul Dirks, JCU Dr. Jan-Marten Huizenga, JCU Dr. Martin Griessmann, Vital Metals Ltd. Dr. Kevin Blake, JCU/AAC Dr. Isaac Corral, JCU Dr. Yanbo Cheng, JCU Dr. Yi Hu, JCU/AAC Dr. Chris Hall, U Michigan Dr. Jen Whan, JCU/AAC Dr. Christian Dietz, U of Tasmania Dr. Huiqing (Jeffrey) Huang, JCU
	Editorial and writing assitance	Prof. Paul Dirks, JCU Prof. Zhaoshan Chang, JCU and Colorado School of Mines Dr. Jan-Marten Huizenga, JCU Prof. Bob Henderson, JCU
Financial support	Research funding	Geological Survey of Queensland Vital Metals Ltd. College of Science and Engineering, JCU
	Conference	College of Science and Engineering, JCU Society of Economic Geologists Geological Society of Australia Economic Geology Research Centre, JCU
	Scholarship	JCU Postgraduate Research Scholar Award
	Write-up grant	College of Science and Engineering, JCU
	Stipend	Prof. Zhaoshan Chang, JCU and Colorado School of Mines Prof. Paul Dirks, JCU

Abstract

Tungsten is considered a strategic metal by various countries, including Australia. Between 1998 and 2016 Australia has been steadily increasing its tungsten production, but it is still far smaller than those of the main producers (e.g., China, Russia). Watershed with its current resources of 49.2 Mt averaging 0.14% WO_3 is considered one of the biggest undeveloped tungsten deposits outside of China, and if developed would boost Australia's tungsten production. The main goal of this PhD thesis is to improve our understanding of the Watershed tungsten deposit and how to explore for similar deposits in northeast Queensland. This goal was approached by documenting the geological, geochemical and structural characteristics of the Watershed deposit, as well as the timing, mineral paragenesis and fluid characteristics of the mineralizing system.

The Watershed tungsten deposit lies within the Mossman Orogen, which comprises multiple deformed Silurian-Ordovician metasedimentary rocks of the Hodgkinson Formation intruded by Carboniferous-Permian granites of the Kennedy Igneous Association. The Hodgkinson Formation in the Watershed area comprises skarn-altered conglomerate, psammite and slate units, which record at least four deformation events ranging from early ductile folding and shearing events (D_1 to D_3) to the development of later brittle-ductile shear zones (D_4) associated with veining and four separate stages of retrograde metamorphism/alteration (Retrograde Stages 1 to 4). Peak metamorphic assemblages (garnet, actinolite, quartz, clinopyroxene, titanate) in the host rocks to mineralisation formed during D_{1-2}. Multiple felsic dykes intrude the metasedimentary rocks at Watershed and include: (a) Carboniferous, monzonite dykes (zircon U/Pb age of 350 ± 7 Ma) emplaced during D_{1-2}; and (b) Permian granite plutons and dykes (zircon U/Pb ages of 291 ± 6 Ma, 277 ± 6 Ma and 274 ± 6 Ma), and diorite (zircon U/Pb age of 281 ± 5 Ma) emplaced during D_4.

An early (syn-D_{1-2}) mineralization event involved the syn-tectonic growth of disseminated scheelite in monzonite dykes and adjacent skarn-altered conglomerate, and was associated with the emplacement of the monzonite, which appears to have enriched the Hodgkinson Formation in W-Be-B-Sc-Cu-Mo-Re. The bulk of the economic scheelite mineralization formed in syn-D_4 shear-related, quartz-oligoclase veins and associated vein haloes (with a muscovite Ar-Ar age of 276 ± 6 Ma). The veins developed preferentially in skarn-altered conglomerate and terminate abruptly when they encounter slate. Vein opening occurred synchronous with four retrograde alteration stages in skarn-altered conglomerate. The margins of the D_4 veins contain feldspar, scheelite and quartz, which represents Retrograde Stages 1 and 2. During Retrograde Stage 1 early sanidine (overgrown by plagioclase, An_{15-55}) formed with minor quartz. Retrograde Stage 2 is characterised by intergrown scheelite and plagioclase (An_{3-43}) overgrowing early plagioclase, phlogopite and trace apatite. Further vein opening during Retrograde Stage 3 infilled the central part of the vein with quartz, which is cross cut by muscovite, calcite and minor chlorite, tourmaline and fluorite. Fractures that formed during

Retrograde Stage 4 cut textures belonging to the previous stages and contain pyrrhotite, arsenopyrite with lesser pyrite, chalcopyrite, and sphalerite.

Scheelite can incorporate small amounts of REE, and the origin of the scheelite grains (i.e. intrusion-related vs metamorphic) has been investigated using the relative abundance of contained LREE, MREE and HREE. Using ternary REE plots, early D_{1-2} scheelite in monzonite coincides with the compositional field for scheelite that forms during magmatic-hydrothermal processes, whereas late D_4 vein-hosted scheelite is compositionally similar to pure hydrothermal scheelite. The Eu and Mo contents of scheelite, coupled with graphite inclusions in scheelite and the presence of pyrrhotite and arsenopyrite in scheelite-bearing veins, show that D_{1-2} scheelite precipitated from a relatively oxidized fluid, while vein-hosted D_4 scheelite record a shift to more reduced conditions as a result of fluid interaction with carbonaceous shale.

Whole rock geochemistry of the various rock types within the deposit indicates that the Watershed deposit is characterized by an enrichment of W-Be-B-Sc-Cu-Mo-Re. These elements were probably introduced by hydrothermal fluids during D_4 veining. The fluid interacted with the skarn-altered conglomerate to leach REE, Y and Nb plus skarn-related elements (i.e., Ca-F-P-Fe-Sr), and add Rb, Cs and Li in vein haloes. Whole rock geochemistry of psammite units along a 2 km transect north of the deposit shows a regional footprint that is characterised by enrichment in W-Cu-Mo-Ca-Fe-Mn-Li.

Fluid inclusions in D_4 vein scheelite and quartz from Retrograde Stage 2 preserve a low salinity H_2O-NaCl-CH_4 fluid ($XCH_4 < 0.01$). The fluid inclusions show evidence for fluid-fluid mixing between low- (close to 0 wt.% NaCl) and medium-salinity (< 8 wt.% NaCl) fluids. The *P-T* conditions during mineralisation were determined at ca. 300°C and 1-1.5 kbar (i.e. depths of 3.5-6 km) indicating a high geothermal gradient, linked to the emplacement of Permian granites. Those *P-T* conditions are similar to those recorded in lode-gold deposits in the Hodgkinson Gold Field and elsewhere. The oxygen fugacity was calculated at 0.6 to 0.8 $\log_{10}$ values below the FMQ buffer, consistent with the reduced mineralogy and geochemical signatures. $\delta^{18}O_{VSMOW}$ values obtained for scheelite (+3.4 to +7.3‰), plagioclase (+7.0 to +11.8‰) and quartz (+12.6 to +15.5‰), which formed during Retrograde Stage 2, and δD_{VSMOW} (−73.4 to −62.7‰) and $\delta^{18}O_{VSMOW}$ (+11.5 to +13.2‰) values for muscovite that formed during Retrograde Stage 3 are indicative of a metamorphic origin for the mineralising fluids, with a possible magmatic component. Sulphur isotope ($\delta^{34}S_{CDT}$) values for sulphides formed during Retrograde Stage 4 in veins are consistent with the presence of seawater sulphate (i.e. basinal brine) in the system. Metamorphic fluids probably originated from prograde devolatilization reactions during metamorphism of the Hodgkinson Formation.

Our findings indicate that tungsten was sourced from Carboniferous monzonite, which enriched the metasedimentary rock units of the Hodgkinson Formation during the early stages of deformation/

metamorphism. Continued ductile deformation and associated metamorphism during D_{1-3} caused devolatilization reactions in the host rocks and remobilisation of tungsten. Permian scheelite mineralisation during D_4 involved a metamorphic-hydrothermal fluid with minor magmatic input that deposited tungsten at 300°C and 1-1.5 kbar (<6 km depth). This tungsten was transported as $NaWO_4^-$, HWO_4^- and WO_4^{2-} complexes along extensional shear zones. Calcium was supplied by the skarn-altered conglomerate that hosts the scheelite-bearing veins. It is proposed that the precipitation of scheelite was promoted by the interaction between the relatively acidic hydrothermal fluids and the alkaline, carbonate-rich, skarn-altered conglomerate host rock, lowering the solubility of the tungsten complexes and co-precipitating scheelite and Na-rich plagioclase during Retrograde Stage 2. Considering a continuum model for this deposit type (i.e. mineralization could form between 2-20 km depth) it is feasible to consider the potential for mineralization at depth.

Table of Contents

List of Tables

List of Figures

Chapter 1 – Introduction

Tungsten is considered a strategic metal by various countries around the world. It has unique physical and chemical properties, such as the highest melting point of all metals (3422°C), a high density similar to Au (19.3 g/cm^3), and when combined with carbon it makes WC (tungsten carbide), which is nearly as hard as diamond (i.e. Mohr hardness scale of 9). Thus, tungsten cannot be easily substituted in many of its applications in modern technologies (e.g. cemented carbide, mill products, steel/alloy, lamp industry, electronic industries) and others such as sport and leisure (e.g. horse riding, biking or trekking). The total world production of tungsten for 2016 was 88,100t **(Table 1.1)**. China, which historically has been the primary tungsten producer **(Fig. 1.1)**, accounted for 82% of that total production (72,000t W), whilst Vietnam was the second-ranked producer with 7% (6,500t W), and Russia was ranked third with 4% (3,100t W). When considering total historical tungsten production, Russia is ranked second after China (Shedd, 2018) **(Table 1.1)**. Australia has been steadily increasing its tungsten production since the early 2000's with 348t of tungsten in 2016, but its production totals are still far smaller than those from the main producers **(Table 1.1, Fig. 1.1)**. Since Australia considers tungsten a highly ranked critical metal (Skirrow et al., 2013), it is desirable for Australia to increase its tungsten resources.

1.1 Tungsten budget in the Earth crust

The average tungsten (W) concentration in the Earth's crust is 1 ppm (Rudnick and Gao, 2014), however, W values vary with rock type and crustal depth; e.g. Rudnick and Gao (2014) suggest an average W value of 0.6 ppm in the middle crust affected by amphibolite to granulite facies metamorphism. In granite, a common rock type to the mid- to upper-crust, W values range from 1.2-3.1 ppm, however Li-F-rich granitoids show W background enrichment of at least two-fold compared to average granite values (Ivanova, 1986). Ongonites, which are the sub-volcanic analogues of rare-metal Li-F granites (Antipin et al., 2009), have W concentrations of up to 50 ppm, suggesting a possible release of W into the fluid phase during magma crystallization (Ivanova, 1986). Mineral chemistry in granitic rocks shows that W concentrations range from 0.2 to 4.8 ppm in quartz and from 0.4 to 4 ppm in K-feldspar; in contrast in ongonites, W is mainly concentrated in albite with around 20 ppm (Antipin et al., 1981). In addition, chemically analyzed phyllosilicates such as biotite from Li-F-rich, late phase granites record W concentrations between 10-40 ppm, with a progressive increase in W with increased Al values; i.e. relatively more felsic granites are more enriched in W than granites with a more mafic alkaline composition (Ivanova, 1986). In addition, muscovite is shown to be enriched in W (14-550 ppm) in greisen altered granites (Ivanova, 1986). Thus, different factors such as alkalinity and the presence of F are important in controlling the presence of W in granitoids and related sub-volcanic rocks.

Table 1.1. Tungsten production per country for the period 2010-2017 reported by the U.S. Geological Survey. Information is current as February, 2019. The production is reported in metric tons. of contained W. Note that some countries have not reported their production in 2017.

Country/Year	2010	2011	2012	2013	2014	2015	2016	2017
Australia	18	15	290	320	477	348	40	
Austria	977	861	706	850	819	861	954	950
Bolivia	1,204	1,124	1,247	1,253	1,252	1,461	1,110	1,100
Brazil	166	244	381	494	510	510	510	
Burma	163	140	131	140	143	140	90	
Burundi	100	200	270	6	23	20	10	
Canada	420	1,966	2,194	2,128	2,344	1,680		
China	59,000	61,800	64,400	71,100	71,000	73,000	72,000	79,000
Congo (Kinshasa)	25	41	35	55	12	21	53	
Korea, North	110	110	100	65	70	70	50	
Mongolia	20	13	66	274	479	600	753	150
Nigeria			40	380	290	70	50	
Peru	571	439	276	28	61	110		
Portugal	799	819	763	692	671	474	549	680
Russia	2,785	3,314	3,537	2,973	2,659	2,600	3,100	3,100
Rwanda	330	480	830	1,100	1,000	850	820	650
Spain	240	497	542	510	800	835	650	570
Thailand	300	160	80	140	100	30	30	
Uganda	44	8	34	57	63	60	40	
Vietnam	1,150	1,635	1,050	1,660	4,500	5,600	6,500	7,200
Total World	68,400	73,900	77,700	85,400	88,500	89,700	88,100	95,000

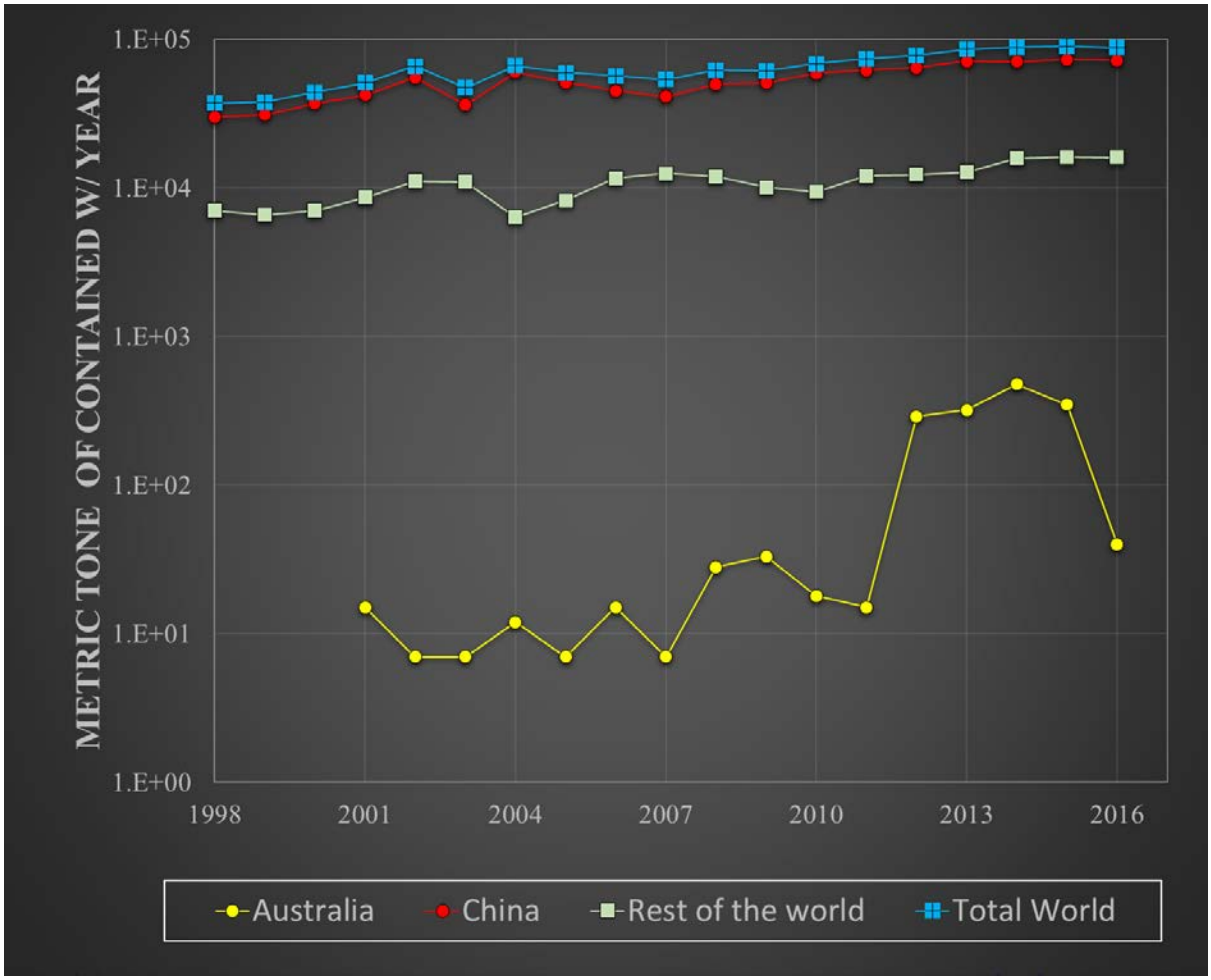

Figure 1.1 Graph that shows the tungsten production for the period 1998-2016 including Australia, China, rest of the world (excluding Australia and China) and the total of the world. Historically China has lead the W production. Source: U.S. Geological Survey (minerals.usgs.gov/minerals/pubs/commodity/tungsten)

In general, W in sedimentary rocks and sediments links to the average grain-size of the sediments. In upper crustal sedimentary rocks the average W concentration is 3.3 ppm (Rudnick and Gao, 2014), with W being enriched in finer-grained (mud-rich) rock types compared to coarser-grained siliciclastic rocks and limestone (0.3-0.4 ppm); a trend observed in various geological terrains and in recent sediments (Ivanova, 1986). In Quaternary pelagic sediments from non-volcanic settings, W concentrations vary from 1-10 ppm (Ivanova, 1986), whilst high W values (7-210 ppm) were found in marine nodules in the Pacific Ocean (Strekopytov, 1998). Tungsten accumulation in pelagic deposits have been linked to adsorption reactions (Ivanova, 1986; Strekopytov, 1998).

1.2 Tungsten deposits

Tungsten deposits can occur in different geodynamic settings and they can be of many types **(Fig. 1.2)**. They occur in practically all Phanerozoic fold belts, convergent plate margins zones, collision zones, as well as ancient structures and stable cratons (Rundquist and Denisenko, 1986). Tungsten deposits have been sub-divided into seven types (Werner et al., 2014): vein/stockwork, skarn, porphyry, strata-bound, disseminated, placer and brine/evaporate. Additional deposit types associated with pegmatite, breccia pipes and hot springs are relatively less important. The most common occurrences are vein/stockwork deposits (e.g. southern Jiangxi region, China, Bolivia, Peru, Portugal and Russia) and skarn deposits (e.g. Brazil, Canada, Russia, Australia, South Korea, Turkey and the United States) (Kim, 1971; Solomon, 1981; Murray, 1986; Newberry and Swanson, 1986; Yingjun and Dongsheng, 1993) in the contact aureoles of granitic intrusions. The style of mineralization at Watershed is disseminated in intrusive rock and in skarn-altered conglomerate and in veins, thus summaries of these types of mineralization style are provided here.

Tungsten deposits can have variable origins. Tungsten vein/stockwork deposits have generally been related to an intrusive precursor (Rundquist and Denisenko, 1986; Wood and Samson, 2000). This granitic body may or may not be associated with massive skarn and/or greisen alteration and high-grade tungsten mineralization, which will depend on the host-rock composition and the metal availability (Pirajno, 2009). Tungsten-rich vein deposits associated with granitic rocks usually have a consistent mineral paragenesis summarized by Wood and Samson (2000). Generally an ‘oxidized’ phase rich in wolframite and scheelite (generally wolframite >> scheelite) occurs early in the paragenesis and is followed by a later sulphide stage or stages. The W-rich stage is usually accompanied by quartz, cassiterite, muscovite, molybdenite, and tourmaline. The later sulphide stage or stages are characterized by base-metal sulphides, fluorite and carbonates. Usually the sulphides accompanying this stage are pyrrhotite, arsenopyrite and pyrite. Due to the generally multi-stage origin of these types of deposits it can be problematic to work out if these minerals are in equilibrium, as the textural relationships are in many cases inconclusive or undocumented. Moreover, because the veins have a multi-stage history, it may be hard to understand if the vein haloes are genetically related to the event that carried the W. Some notable examples of this type are the tungsten deposits of the Dahutang district in northern Jiangxi Province, China (Mao et al., 2013b; Jiang et al., 2015).

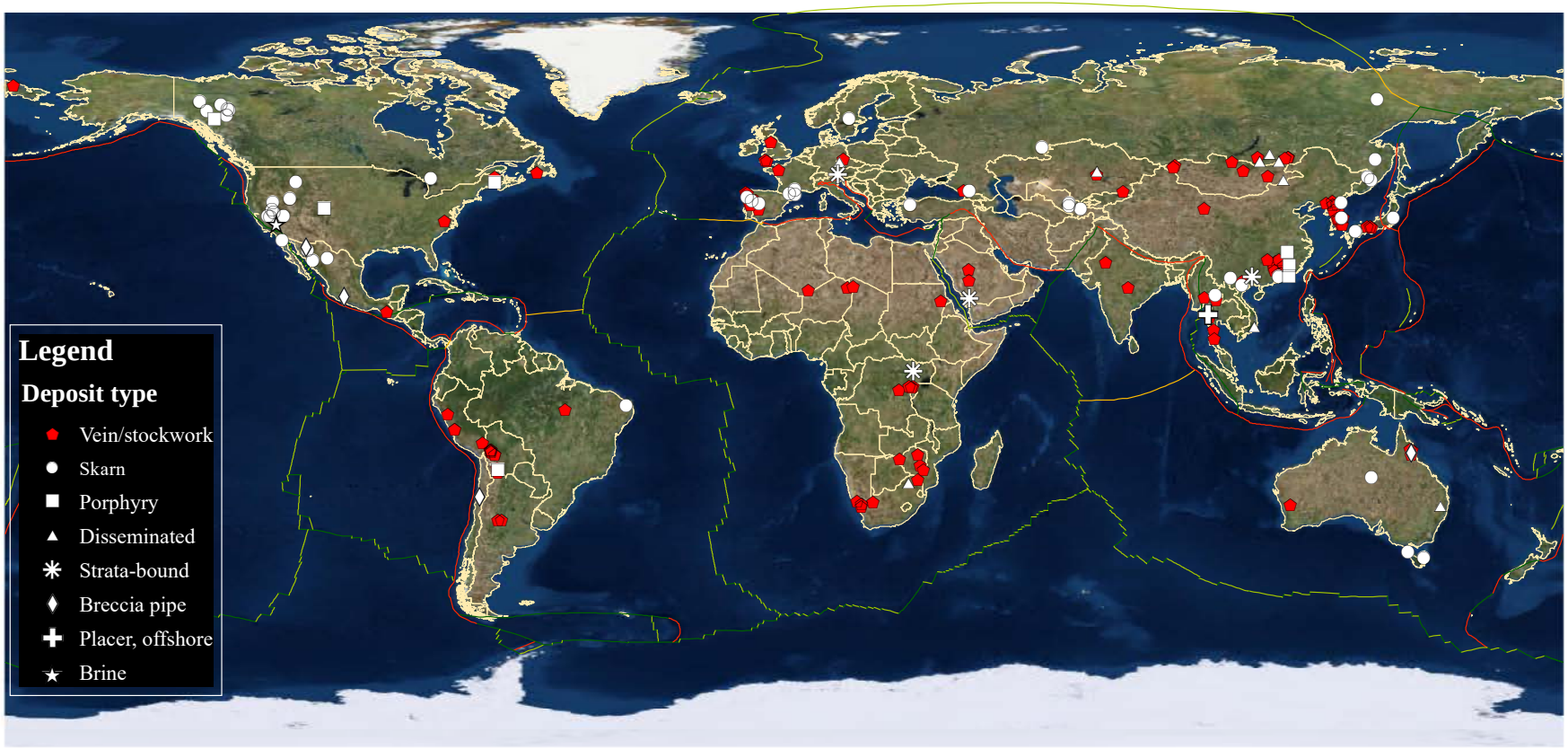

Figure 1.2 Location map that shows the tungsten deposits distribution around the world. Vein/stockwork, skarn and porphyry style of mineralization are the most common type. Note the high density of tungsten deposits in the east and southeast areas of China and adjacent countries. Tectonic boundaries are indicated for reference where red denotes convergence, light green denotes ridge, dark green denotes transform and orange is diffuse. **Source: U.S. Geological Survey (minerals.usgs.gov/minerals/pubs/commodity/tungsten).**

Tungsten skarn deposits are generally spatially and/or genetically associated with an intrusive precursor (Einaudi and Burt, 1982). Such intrusive rocks are typically derived from reduced ilmenite-series magmatism (Ishihara, 1977) with a lack of co-genetic volcanic rocks, and with compositions that vary from quartz diorite to quartz monzonite with rare alaskite in large plutons and batholiths that generally cut reduced pelitic and carbonaceous host-rocks (Einaudi and Burt, 1982). This interaction between granitoids and mainly marine rocks commonly form exoskarn in calcareous-rich levels or narrow zones of endoskarn on the flanks of the intrusive bodies that were emplaced between ~5-10 km depth (Meinert, 1992). The main ore mineral in tungsten skarn deposits is scheelite ($CaWO_4$) with significant amounts of Mo replacing W in its crystal structure, and associated molybdenite, chalcopyrite and minor sphalerite, pyrrhotite, magnetite, pyrite and bismuth. In all skarn deposits the ore mineralogy is accompanied by a complex paragenesis of gangue minerals exhibiting a wide range of mineral phases, however a common mineral sequence vectoring towards the fluid source has been observed, which from distal to proximal involves: biotite → amphibole → pyroxene → (garnet) (Einaudi and Burt, 1982). Even though the composition of the alteration mineralogy usually shows a systematic and symmetrical compositional variation towards the source of the granitic mineralizing fluids, compositions can vary depending on the oxygen fugacity of the system (Newberry, 1983). The gangue mineralogy is characterized by prograde spessartine (Mn), almandine (Fe^{2+}) and grossular (Ca) garnet with variable compositional zoning (Shimazaki, 1977; Newberry, 1983) and generally little andradite (Fe^{3+}); in addition to more hedenbergic pyroxene, wollastonite and titanite. The previous garnet and pyroxene compositions are indicative of the reduced nature of tungsten skarn systems (Shimazaki, 1980). However, W skarns can be slightly oxidized if associated with Mo mineralization (Meinert, 1995). The retrograde hydrous mineral phases are characterized by clinozoisite (Fe-poor epidote), amphibole (actinolite), chlorite, calcite, biotite, muscovite; and if the intrusive source was rich in fluorine or boron, greisenized skarn can be developed in the surroundings of the intrusive host-rock contact zone (Kwak, 1987). Scheelite is almost everywhere associated with the later retrograde stages, occurring as disseminations replacing prograde Ca-rich phases, as well as in minor veins cutting skarn. Some notable tungsten skarn examples are the Sangdong deposit in South Korea (John, 1963), the scheelite-bearing grossular-hedengbergite skarns in Japan (Sato, 1980; Shimazaki, 1980), the King Island occurrences in Tasmania (Kwak and Tan, 1981), the Pine Creek deposit in California (Newberry, 1982), and the MacTung W-Cu-(Zn) deposit in the Canadian Cordillera (Dick and Hodgson, 1982).

In contrast, some tungsten skarns were formed during greenschist and higher grade regional metamorphism (Tweto, 1960; Derre et al., 1986; Kwak, 1987) or a combination of early magmatism with later metamorphism (Fonteilles et al., 1989; Thalhammer et al., 1989). These tungsten skarns are unrelated to plutonic activity, nonetheless they contain a similar skarn mineralogy and paragenetic sequence to those skarns formed from a granitic source. However, they lack magnetite, they contain very little andraditic garnet and they display a poorly developed or absent metal or mineral zonation pattern (Kwak, 1987). The main ore mineral is Mo-poor scheelite (Kwak, 1987) with minor chalcopyrite, sphalerite, galena and molybdenite, and trace wolframite, covellite, associated with other sulphide assemblages such as pyrrhotite and arsenopyrite. Scheelite may occur in the

prograde and/or the retrograde stages (Barnes, 1983); and the style of mineralization is disseminated or vein-hosted (Skaarup, 1974). A positive correlation between disseminated scheelite and the oldest lithological units is found in several metamorphic terranes of the world (Tweto, 1960; Kantor, 1974). For instance, Tweto (1960) claims that W was already present in significant amounts in the pelitic host-rock facies with later W remobilization in response to deformation/metamorphism to be concentrated and precipitated in anomalous amounts to form W deposits. A similar mechanisms of enrichment has been proposed for some orogenic Au systems in the Otago schists (Pitcairn et al., 2006), however, in the latter area the strongly deformed rocks show a depletion in ore grades possibly as a result of remobilization of the ore elements to relatively more undeformed units. Well documented examples of this type of W skarns include the scheelite mineralization in the Precambrian gneisses in Colorado (Tweto, 1960), the Bindal Area, Norway (Skaarup, 1974), the Bohemian Massif and the Austroalpine Crystalline Complex in Austria (Beran et al., 1985; Raith, 1991), the Blacklite Prospect in New Mexico (Fulp and Renshaw, 1985), the Archean Malene belt in West Greenland (Appel, 1986) the Monumento/Cacaria area in Brazil (Alves Cruz et al., 2016) and the Corruga-type scheelite deposits in the Broken Hill Block, Australia (Barnes, 1983).

1.3 Regional geological context of the Watershed W deposit

The Watershed deposit is positioned within the central part of the Mossman Orogen, which is an extinct convergent margin system abutting the North Australia craton, from which it is separated by a major fault zone called the Palmerville Fault **(Fig. 1.3A-B)**. The Mossman Orogen comprises the Silurian and Devonian Hodgkinson and the Broken River provinces, which form a belt, 500 km long and up to 200 km wide **(Fig. 2.1)**. The Mossman Orogen largely consists of multiply deformed sedimentary successions interpreted as turbiditic sequences with minor intercalations of mafic volcanic rocks and chert, largely deposited in a deep-marine environment (Henderson et al., 2013). The Hodgkinson and Broken River provinces are intruded by Carboniferous to Permian granitoids of the Kennedy Igneous Association **(Fig. 1.3B)**. The Watershed deposit is located in the Hodgkinson Province within rocks of the Hodgkinson Formation, which has undergone intense deformation with associated regional metamorphism (Davis, 1993; Henderson et al., 2013), and hosts a large number of Au, W and Sn deposits **(Fig. 1.3)**. Detailed descriptions of the regional geological setting of the Watershed deposit are contained at the start of **Chapters 2-4**, and will not be discussed here.

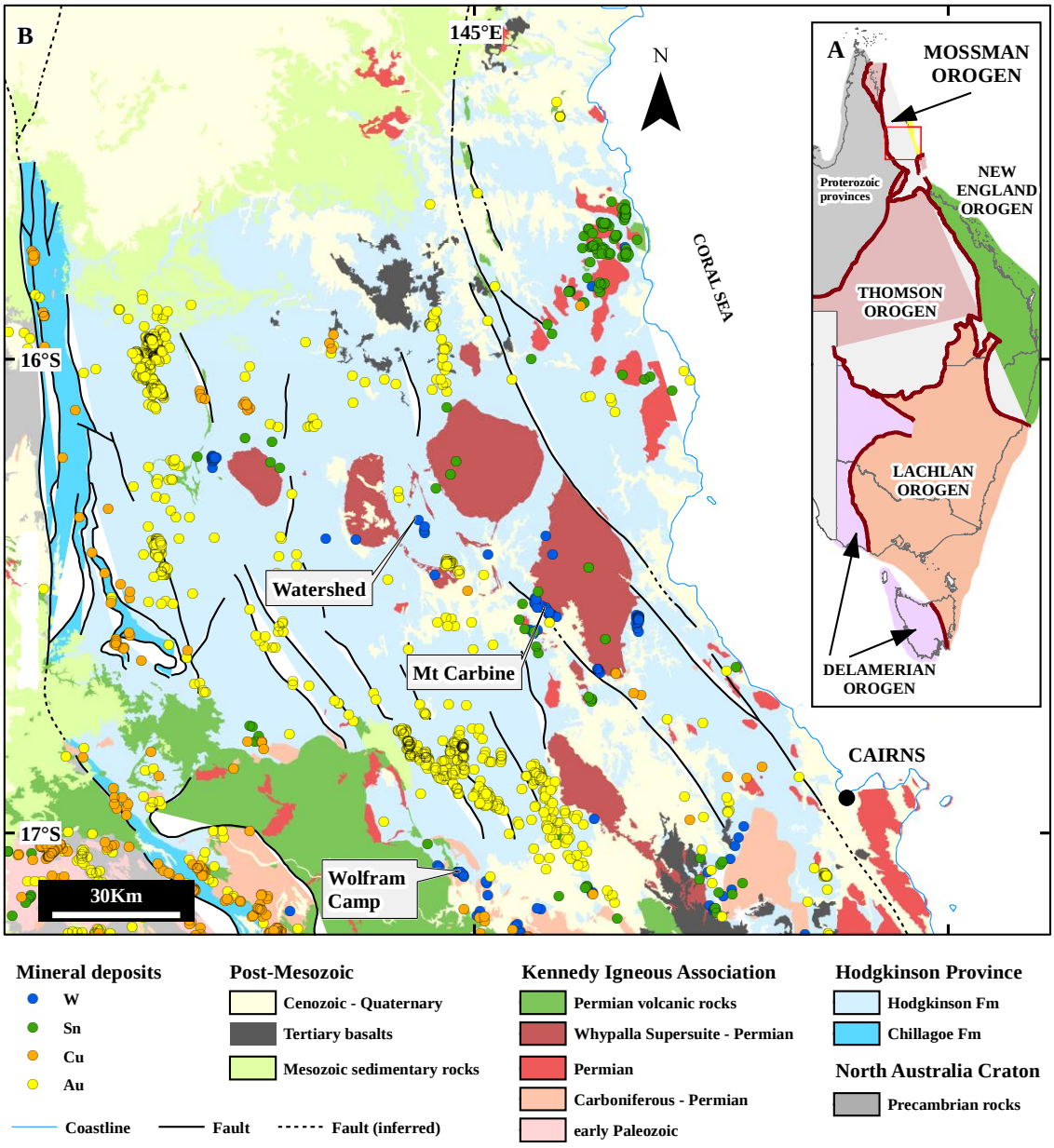

Palmerville Fault

Figure 1.3 Regional geological setting of the Watershed deposit in northeast Queensland. Also shown is the Whypalla Supersuite. The three largest W deposits are labelled: Mt Carbine (83,706 t WO_3), Watershed (70,400 t WO_3), and Wolfram Camp (12,260 t WO_3). Other W deposits are much smaller (Chang et al., 2017). Also Au, Cu and Sn deposits hosted in hard rock are shown in the map. Note the higher density of mineral occurrence in the Hodgkinson Formation compared with the rocks of the Kennedy Igneous Association. Mineral occurrences are those compiled by the Geological Survey of Queensland (Greenwood, 2017).

1.4 Watershed exploration history

Watershed has 40 years of exploration history since its discovery in 1979 by Utah Development Company (Utah), and four companies have worked on the property since. Watershed was a greenfields discovery following a regional stream sediment exploration program that started in 1977. Since then, extensive drilling and detailed geological and geochemical work has been performed at Watershed. During 1980-1984, Utah carried out more exploration work that involved diamond drilling (for a total of 61 holes at 13,526 meters), detailed mapping, structural studies and the definition of an initial resource. During this period, Utah discovered three more prospects south of Watershed (Watershed South, Desailly North and Desailly), which were subsequently explored in more detail. In 1984, BHP Billiton acquired Utah and entered into a joint venture agreement with Peko-Wallsend Operations Ltd (GeoPeko). They conducted exploration work at Watershed until 1985 (e.g. drilling of 26 holes with a total length of 2,127 meters, detailed mapping and stream sediment sampling), until the W price dropped during the second half of the 1980's, after which no significant additional work was carried out at Watershed for the next twenty years.

In 2005, Watershed was acquired from BHP by Vital Metals Limited (Vital). Aggressive exploration was carried out until 2009, when the impact of the global financial crisis stopped further exploration and the on-going feasibility study was abandoned. Exploration activities were resumed in 2011, and in 2012 Vital formed a joint venture with the Japan Oil, Gas and Mineral National Cooperation (JOGMEC), which earned a 30% share in the Watershed project. The feasibility study was completed in 2014, with the definition of a proposed 2.5 Mt per year open-pit operation. During the 2005-2014 period Vital placed 203 diamond drill holes (36,235 meters) and 77 reverse circulation holes (5,466 meters). All exploration information on the Watershed deposit was compiled by Vital Metals in an internal report in 2015, to serve as a reference for future geoscientists working at Watershed and surrounding areas.

In 2018 Vital and Tungsten Mining NL (TGN) reached an agreement for TGN to acquire a 100% interest in the Watershed tungsten deposit. The deposit is currently placed on care and maintenance awaiting an increase in the W price. Currently Watershed has a declared JORC mineral resource of 70,400t of WO_3 (49.32 Mt at 0.14% WO_3, Vital Metals Inc., ASX announcements, 2018).

1.5 Significance of Watershed

Northeast Queensland is well-endowed with mineral deposits that are enriched in a range of commodities including W, Sn, Au, Cu, and Ag **(Fig. 1.3B)**. Most of these deposits are associated with the regionally extensive Permian-Carboniferous Kennedy Igneous Association and were discovered decades ago. Exploration activity in this region, especially for W, has been very limited in more recent times.

This PhD research thesis forms part of a multidisciplinary research project ("Characterizing and assessing prospectivity of intrusion-related hydrothermal mineral systems in NE Queensland"), directed by the Geological Survey of Queensland, which was largely completed by the end of 2017. The main goal of this regional project was to improve the understanding of the Permian-Carboniferous metallogeny of northeast Queensland, and to identify new prospective exploration areas.

The northern portion of the Mossman Orogen contains clusters of W, Sn and Au-lode deposits **(Fig. 1.3B)**. These deposits are hosted within the strongly deformed Silurian-Devonian Hodgkinson Formation, and minor in Permian granitoids. The Watershed deposit, which is hosted in the Hodgkinson Formation and surrounded by Permian granitoids (Champion and Bultitude, 2013; Henderson et al., 2013), has a JORC resource of 49.2 Mt grading at 0.14% WO_3 totaling 70,400t of WO_3 with a cut-off of 0.05% WO_3 (Vital Metals Inc, ASX announcements, 2018). This resource makes Watershed one of the biggest undeveloped W deposits in the world, outside of China. Besides the presence of disseminated scheelite mineralization in dykes and skarn-altered conglomerate, the bulk of the scheelite mineralization is hosted in veins that crosscut the conglomerate units, and that do not have a clear relationship to the surrounding intrusive rocks. By studying the Watershed deposit, we aim to gain a comprehensive understanding of the geologic characteristics and origin of this deposit type as detailed below.

1.6 Rationale and thesis objectives

This PhD thesis investigates the Watershed W deposit, with the main goal of improving the understanding of Australian W deposits and how to explore for them in North Queensland. This goal was approached by addressing a series of research objectives, which form the basis of three data **chapters** presented in this thesis. The principle objectives of this study are:

- Document the geological characteristics of the Watershed W deposit by determining the spatial zoning patterns, paragenetic events, timing and structural controls of the mineralizing system **(Chapter 2)**
- Improve exploration methodologies by identifying geochemical footprints and fingerprints for the deposit **(Chapter 3)**
- Investigate the trace element and REE characteristics of scheelite and associated mineral assemblages to understand: (1) the mobility and source of W and associated pathfinder elements, and (2) the genesis of the alteration mineral assemblages **(Chapter 3)**
- Understand the physico-chemical evolution of mineralizing fluids, and the genesis, mobility and precipitation mechanisms of W to further understand how Watershed formed **(Chapter 4)**

1.7 Thesis organization

1.7.1 Thesis by papers and authorship

This thesis is presented as a series of manuscripts following the recommended structure by the Graduate Research School of James Cook University. At the time of thesis submission, the three principle data chapters in the thesis (i.e. **chapters 2, 3 and 4**) have been prepared for submission to relevant scientific journals in the field of economic geology. These chapters are formatted according to scientific journal requirements.

For the chapters that have been written as manuscripts for publication, there is some (unavoidable) repetition in the materials presented. These repetitions occur in the sections that deal with the regional geological setting and the deposit geology and their related figures. However each of the data chapters deals with different aspects of the Watershed deposits with different research questions, analytical approaches and conclusions, and in each of these chapters, the geological setting is introduced in a manner that supports the specific objectives at hand.

In summary, **Chapter 2** provides the geological context for Watershed. **Chapter 3** addresses the geochemical footprints, fingerprints and mineral characteristics of Watershed. **Chapter 4** explores the fluid characteristics, source and thermodynamic evolution of scheelite mineralization. **Chapter 5** summarises the main findings of the thesis and provides a proposed ore-forming model for Watershed.

1.7.1.1 Chapter 2

Chapter 2 is titled "Geological Controls on the formation of the Watershed Tungsten Deposit, Northeast Queensland, Australia" and has been prepared for submission to "Economic Geology". The first author is Jaime Poblete, and this chapter is co-authored with Paul Dirks, Zhaoshan Chang, Jan-Marten Huizenga, Martin Griessmann, Robert Skrzeczynsky and Chris Hall. Poblete was the main scientific investigator and author of the paper. Paul Dirks assisted with mapping, data collection during fieldwork and structural analysis, editorial assistance and assistance in writing of the structural geology analysis. Zhaoshan Chang contributed with mineral data discussions, editorial assistance and budget. Jan-Marten Huizenga helped with editorial assistance and discussions. Martin Griessmann assisted during fieldwork with samples collection and discussions about the geology of Watershed, and provided editorial assistance. Robert Skrzeczynsky helped with the geological map of the Watershed area. Chriss Hall assisted with $^{40}Ar/^{39}Ar$ muscovite dating.

1.7.1.2 Chapter 3

Chapter 3 is titled "Constraining scheelite mineralization with mineral chemistry: An example from the Watershed tungsten deposit, northeast Queensland, Australia" and has been prepared for submission to a

pertinent journal in the economic geology field (i.e. Mineralium Deposita). The first author is Jaime Poblete, and this chapter is co-authored with Paul Dirks and Zhaoshan Chang. Poblete was the main scientific investigator and author of the paper. Paul Dirks assisted with data discussions and provided editorial assistance. Zhaoshan Chang assisted with sampling strategy and budget.

1.7.1.3 Chapter 4

Chapter 4 is titled "The Permian Watershed tungsten deposit (northeast Queensland): fluid inclusion and stable isotope constraints" and has been prepared for submission to a pertinent journal in the economic geology field. The first author is Jaime Poblete, and this chapter is co-authored with Jan-Marten Huizenga, Paul Dirks and Zhaoshan Chang. Poblete was the main scientific investigator and author of the paper. Jan-Marten Huizenga assisted with fluid inclusions analysis and modelling, discussions and editorial assistance. Paul Dirks assisted with the discussion and provided editorial assistance. Zhaoshan Chang helped with sample selection and budget.

1.7.1.4 Chapter 5

In **Chapter 5**, the conclusion chapter, the main scientific outcomes of the previous three chapters are summarized and a mineralization model is proposed for Watershed. This model integrates the main conclusions from the previous data **Chapters** (i.e., **Chapters 2 to 4**).

1.7.2 Appendices

Supplementary materials linked to **Chapters 2 to 4 (Appendices 1-4)** have been included at the end of the thesis. **Appendix 1** provides general information related to the entire thesis. **Appendix 1.1** provides a list of samples with coordinates and the analytical method(s) that have been used for each sample.

Appendix 2 provides all supplementary materials that link to **Chapter 2,** and has been subdivided into six parts. **Appendix 2.1** includes all data underpinning the fault kinematics analysis that was performed after the 2016 and 2017 mapping campaigns. **Appendix 2.2** explains the methodology used in **Chapter 2**. **Appendices 2.3 to 2.6** provide the data tables for the microprobe mineral chemistry **(Appendix 2.3)**, and whole-rock geochemistry **(Appendix 2.4)** in support of the dated intrusive rocks using U-Pb dating of zircon by LA-ICP-MS **(Appendix 2.5)**, whereas **Appendix 2.6** provides the data tables and plateau graphs for the $^{40}Ar/^{39}Ar$ muscovite dating.

Appendix 3 provides all supplementary materials that link to **Chapter 3** and has been subdivided into two parts. **Appendix 3.1** provides the whole-rock geochemistry data for the sampled intrusive and metasedimentary rock units, and the mineralized veins. **Appendix 3.2** provides the mineral trace element chemistry data (i.e., scheelite and associated minerals). **Appendix 4** provides all supplementary materials that link to **Chapter 4**, and includes the raw data that supports the fluid inclusions micro-thermometry **(Appendix 4.1)**.

Additional work undertaken in the course of this PhD candidature are included in **Appendix 5**. **Appendices 5.1 to 5.5** are all abstracts first-authored by Poblete at various national and international conferences. **Appendix 5.1** is an abstract of a poster titled "Scheelite vein mineralization at the Watershed tungsten deposit, Northeast Queensland, Australia" presented at the Society of Economic Geologist Conference ("World-Class Ore Deposits: Discovery to Recovery") held in Hobart, Tasmania, Australia between September 27th -30th, 2015. This work deals with preliminary findings of the first and second field campaigns (February and August 2015), and a mineral paragenetic sequence is proposed based on core-logging and macroscopic observations. **Appendix 5.2** is an abstract of a talk presented at the Australian Earth Sciences Convention ("Uncover Earth's Past to Discover Our Future") held in Adelaide, South Australia, Australia between June 26th-30th, 2016. This abstract presents a refined version of the mineral paragenetic sequence using petrography, back scattered images and EPMA. Additionally new geochronology data of a granitic dyke and of muscovite from veins were presented. **Appendix 5.3** is an abstract of a talk presented at the FUTORES II Conference ("Future Understanding of Tectonics, Ores, Resources, Environment and Sustainability") held in Townsville, Queensland, Australia between June 4th-7th, 2017. In this abstract a new geochronology of scheelite-rich monzonite dykes age and REE trace elements in scheelite were presented, in addition to an updated version of the paragenetic mineral sequence. **Appendix 5.4** is an abstract of a talk presented at the Society of Economic Geologist Conference ("Ore Deposits of Asia; China and Beyond") held in Beijing, China between September 17th-20th, 2017. The main outcome was the metamorphic and magmatic origins for the scheelite from different textural positions based on a ternary REE diagram and various stable isotope systematics. **Appendix 5.5** is an abstract of a poster presented at the Society of Economic Geologist Conference ("Metals, Minerals, and Society") held in Keystone, Colorado, U.S., between September 22nd-25th, 2018. The abstract deals with the relation between scheelite mineralization and the timing of deformation at Watershed, in addition a set of geochronology data supporting the previous are also discussed. Additionally, the results of the fluid thermometry are presented coupled with stable isotope geochemistry data.

Additional publications on which Poblete is a co-author are presented in **Appendices 5.6 to 5.9**. These include a book chapter in the Australian Ore Deposits Monograph 32 (Chang et al., 2017) (**Appendix 5.9)**, which deals with the Sn-W-Mo mineralization in the region of northeast Queensland, Australia. Conference abstracts include Cheng et al. (2015, 2016) (**Appendices 5.6-5.7),** which deal with the Geology of the Mt. Carbine W deposit in north Queensland, Australia and Cheng et al. (2018) (**Appendix 5.8)**, which deals with the Sn and W prospectivity in northeast Queensland, Australia **(Fig. 1.3)**.

Chapter 2 – Geological Controls on the formation of the Watershed W Deposit, northeast Queensland, Australia

Abstract

The Watershed tungsten deposit (49.2 Mt averaging 0.14% WO_3) lies within the Mossman Orogen, which comprises deformed Silurian-Ordovician metasedimentary rocks of the Hodgkinson Formation intruded by Carboniferous-Permian granites of the Kennedy Igneous Association. The Hodgkinson Formation in the Watershed area comprises skarn altered conglomerate, psammite and slate units, which record at least four events of deformation evolving from ductile isoclinal co-linear folding and transposition (D_1 to D_3) to brittle ductile shear zones (D_4). Peak metamorphic mineralogy, formed during ductile deformation, comprises garnet ($grt_{40-87}alm_{0-35}sps_{1-25}adr_{0-16}$), actinolite, quartz, clinopyroxene ($di_{36-59}hd_{39-61}jhn_{1-5}$) and titanite. Multiple felsic dykes cut across the metasedimentary rocks at Watershed including: (a) Carboniferous, monzonite dykes (zircon U/Pb age of 350 ± 7 Ma) emplaced during D_{1-2}; and (b) Permian granite plutons and dykes (zircon U/Pb age of 291 ± 6 Ma, 277 ± 6 Ma and 274 ± 6 Ma) and diorite (zircon age U/Pb of 281 ± 5 Ma) emplaced during D_4. A first non-economic mineralization event corresponds to the crystallization of disseminated scheelite in monzonite dykes (pre-D_3) and adjacent units, with scheelite grains aligned in the S_{1-2} fabric affected by D_3 folding. This event enriched the Hodgkinson Formation in tungsten. The bulk of the scheelite mineralization formed during a second event in shear-related quartz oligoclase veins and vein haloes, which were emplaced during D_4 (muscovite ^{40}Ar-^{39}Ar 276 ± 6 Ma). The multi-staged vein systems developed preferentially in skarn-altered conglomerate units, mostly terminate abruptly when they encounter slate. The vein stages occurred synchronous with four retrograde stages in skarn-altered conglomerate during D_4. The retrograde skarn minerals in conglomerate comprise clinozoisite after garnet, quartz, plagioclase, scheelite and phlogopite with minor sodium-rich amphibole in Retrograde Stages 1 and 2 accompanied with later muscovite, calcite and chlorite from Retrograde Stage 3. The Retrograde Stage 4 is a non-economic sulphide stage. The principle controls on scheelite mineralization at Watershed are: (a) early monzonite dykes enriched in scheelite; (b) D_4 shear zones that acted as fluid conduits transporting tungsten from source areas to traps; (c) skarn-altered conglomerate lenses that provide a source for calcium to form scheelite; and (d) an extensional depositional environment characterized by vein formation and normal faulting, which provide trapping structures for fluids pregnant in tungsten, with fluid decompression being a likely control on scheelite deposition. Monzonitic and granitic dykes provide a source for sodium, and the coexistence of scheelite with oligoclase in monzonite and veins suggest that tungsten was transported as $NaHWO_4^0$. Exploration in the area should target Carboniferous monzonite, associated with later syn-D_4 shear-zones cutting skarn-altered conglomerate.

2.1 Introduction

The region of northeast Queensland is host to numerous tungsten, tin and lode-gold deposits. Most of these deposits occur in the Silurian-Devonian metasedimentary rock units of the extensively deformed Hodgkinson Formation, intruded by S-type, granitic bodies of the Permian Whypalla Supersuite. The Watershed scheelite deposit is located in northeast Queensland **(Fig. 2.1)** at 16.33°S latitude and 144.86°W longitude. It has a JORC resource of 49.2 Mt grading at 0.14% WO_3 totalling 70,400 t of WO_3 with a cut-off of 0.05% WO_3 (Vital Metals Inc., ASX announcements, 2018). This makes Watershed one of the biggest undeveloped tungsten deposits in the world outside of China. Scheelite mineralization at Watershed is largely hosted by vein systems that preferentially cut skarn-altered conglomerate of the Hodgkinson Formation (Garrad and Bultitude, 1999).

Scheelite tungsten deposits may be of metamorphic hydrothermal or magmatic hydrothermal origins. Some scheelite-dominant deposits were found genetically associated with intrusive rocks (Rundquist and Denisenko, 1986; Wood and Samson, 2000). Some examples are the Dae Hwa W-Mo deposit in Korea (So et al., 1983), the Yangjiashan W deposit and the Dahutang W-Cu-Mo deposit, both in southern China (Song et al., 2018; Xie et al., 2018). These deposits may or may not develop massive endo- or exo-skarn and/or greisen alteration (Kwak, 1987), depending on the host-rock composition and metal availability (Pirajno, 2009). Scheelite-rich skarns are associated with either a reduced environment (Ishihara, 1977; Shimazaki, 1980; Newberry, 1983), or else slightly oxidized when associated with Mo mineralization (Meinert, 1995). They are normally associated with reduced gangue mineralogy (Shimazaki, 1977; Newberry, 1983), characterized by low-andradite garnet and hedenbergic pyroxene (Meinert et al., 2005), which show a systematic mineral compositional change towards the source of the mineralizing fluids (Newberry, 1983). In contrast, metamorphic hydrothermal scheelite deposits, such as the Glenorchy W-Au deposit in New Zealand (Henley et al., 1976), the scheelite deposits in the Precambrian gneisses of Colorado (Tweto, 1960) and scheelite deposits in Portugal (Derre et al., 1986) are unrelated to plutonic activity and formed during regional metamorphism in mostly pelitic sedimentary rocks (Kwak, 1987). In such deposits the compositional zonation of metals and gangue minerals is poorly developed or absent (Kwak, 1987). For metamorphic scheelite deposits, Tweto (1960) claims that the sedimentary host rocks have to be enriched in tungsten prior to metamorphism to allow tungsten to be remobilized and redeposited in response to deformation, in a process similar to lode gold deposits (Pitcairn et al., 2006). Hybrid models have also been proposed, in which scheelite deposits may form through a combination of early magmatic tungsten emplacement and later metamorphic remobilization with localized enrichment (Fonteilles et al., 1989; Thalhammer et al., 1989).

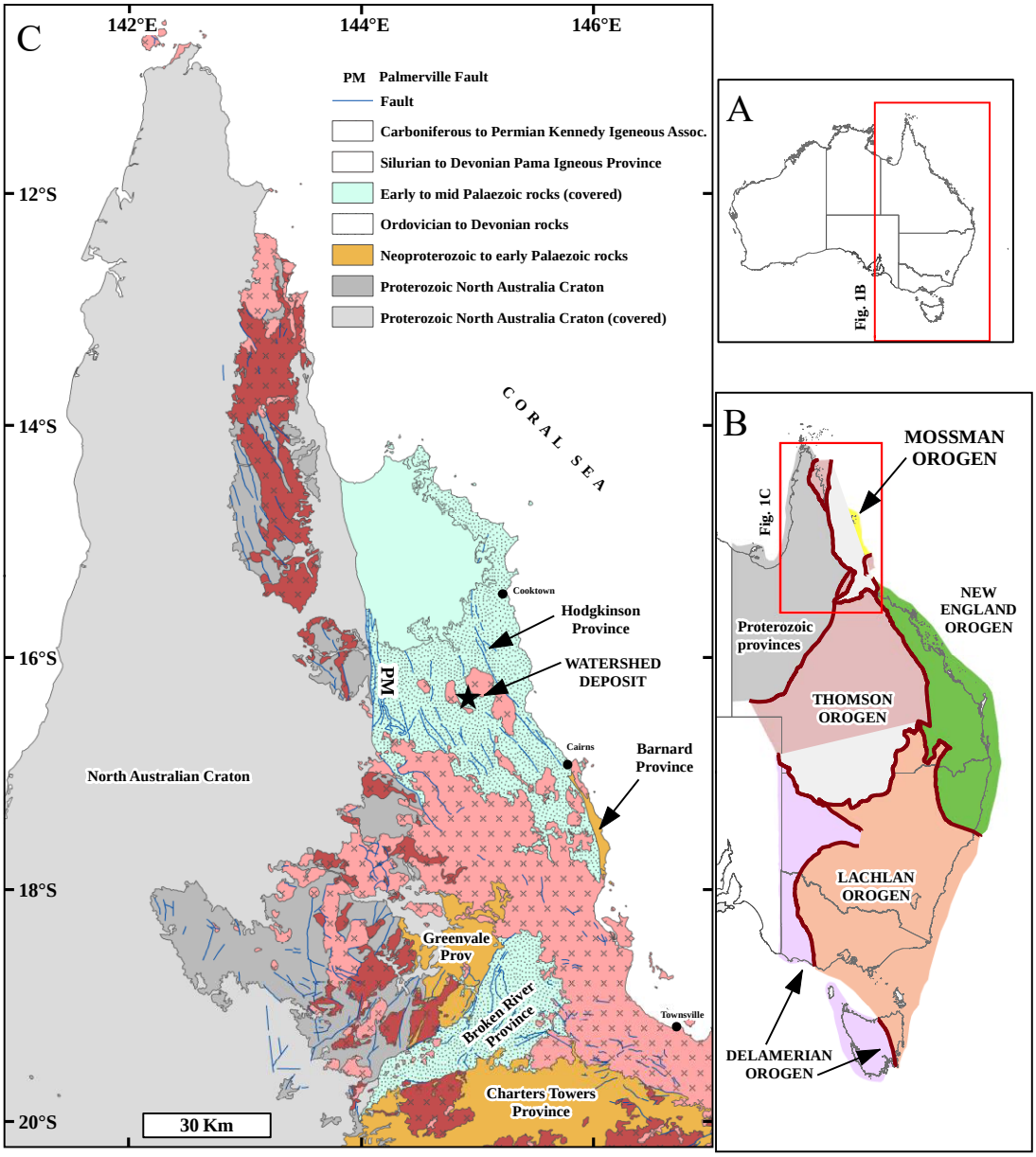

Figure 2.1 Regional geologic setting of the Watershed tungsten deposit in northeast Queensland (black star). **A.** Australia contour with state boundaries. **B.** Orogen map of eastern Australia. C. Geology of the region on northeast Queensland. See text for details. Geology from Geoscience Australia compilation (Raymond et al., 2018).

Many of the tungsten-rich deposits of northeast Queensland have been linked to intrusive rocks (Bateman, 1985; de Roo, 1988; Bain and Draper, 1997; Garrad and Bultitude, 1999). Considering the range of geological settings (i.e. igneous vs metamorphic) in which scheelite deposits can form it is important to develop a detailed understanding of the geological factors that constrain scheelite-rich vein formation at the Watershed deposit, and by extension, in the Hodgkinson Formation. In this paper we present: (a) detailed geological information to constrain the relationship between deformation events and scheelite mineralization; (b) mineral chemistry to understand the fluid evolution at Watershed and investigate if the skarn mineralogy exhibits compositional trends indicative of an intrusive source; and (c) ^{40}Ar-^{39}Ar muscovite geochronology from veins and vein haloes, and U-Pb zircon geochronology from intrusive rocks to constrain the age of deformation and mineralization in the Watershed area. This information is presented with the aim to develop a model for the origin and evolution of the Watershed tungsten deposit, and define the principal controls on mineralization.

2.2 Regional geological setting

The Watershed deposit is positioned within the central part of the Mossman Orogen, which is an extinct convergent margin system abutting the North Australia craton, from which it is separated by a major fault zone called the Palmerville Fault **(Fig. 2.1)**. The Mossman Orogen comprises the Silurian and Devonian Hodgkinson and the Broken River provinces, which form a belt, 500 km long and up to 200 km wide, and are fault-bounded by the Charter Towers and Barnard provinces of the Thomson Orogen to the south and southeast, respectively. The Mossman Orogen largely consists of multiply deformed sedimentary successions interpreted as turbiditic sequences with minor intercalations of mafic volcanic rocks and chert, largely deposited in a deep-marine environment (Henderson et al., 2013). The Hodgkinson and Broken River provinces are intruded by Carboniferous to Permian granitoids of the Kennedy Igneous Association (Champion and Bultitude, 2013). The exact boundary between the two provinces is believed to have been masked by the igneous rocks. The Watershed deposit is located in the Hodgkinson Province **(Fig. 2.1)**.

The Hodgkinson Province is composed of the Chillagoe Formation and the Hodgkinson Formation. The Chillagoe Formation occurs along the western edge of the Hodgkinson Province. It is composed of Silurian-Devonian sandstone, limestone, chert, and mafic volcanic rocks with minor mudstone, conglomerate and breccia, which were deposited in a shallow-water shelf environment (Fig. 2.1; Amos, 1968). These rocks occur in a narrow (2-5 km), north-south trending zone that runs parallel to the Palmerville Fault over a distance of ~250 km (Henderson et al., 2013). To the east of this marginal zone, the remainder of the Hodgkinson Province is composed of Silurian to early Carboniferous Hodgkinson Formation (Fig. 2.2; Adams et al., 2013; Kositcin et al., 2015). These rocks comprise alternating sandstone-mudstone beds with turbidite affinities that are locally interbedded with greywacke and quartz-greywacke units and rare intercalated beds of chert, volcanic rocks, limestone and polymictic conglomerate (Amos, 1968; de Keyser and Lucas, 1968). Field relations and sedimentary characteristics indicate that the rocks of the western and eastern Hodgkinson Formation represent the more proximal and distal facies on a sub-marine fan delta system (Amos, 1968), respectively. Rocks of the

Hodgkinson Province are interpreted to have formed in a fore-arc system with the intrusive rocks of the Pama Igneous Association to the west in the North Australian Craton **(Fig. 2.1A)** (Withnall and Hutton, 2013), representing a contemporary magmatic arc (Henderson et al., 2013).

The Hodgkinson Formation has undergone intense deformation with associated regional metamorphism. Whilst detailed deformation histories of rocks of the Hodgkinson Formation based on local studies vary (Bateman, 1985; Davis, 1993; Peters, 1993; Davis and Forde, 1994), there is consensus that, on a broad scale, at least four discrete regional deformation events (D_1 to D_4) occurred (Davis, 1993; Henderson et al., 2013). D_1 events are Devonian in age and coincide with peak-metamorphism at low- to mid-greenschist facies in the southwest, grading to upper-greenschist facies in the northeast of the Hodgkinson Formation. D_1 is commonly represented by a bedding-parallel slaty cleavage and variable plunging, mesoscale isoclinal folds. A rock type referred to as "broken formation" (Wood, 1982) or "melange" (Henderson et al., 2013) is widely developed in the Hodgkinson Formation, and occurs in up to 5 kilometer wide zones with gradational contacts to coherent strata. The formation of these deformational zones has been linked to D_1. D_2 is also regarded as province wide and related to large-scale folds with wavelengths of several kilometres, which formed during Devonian to early Carboniferous compressional events (Henderson et al., 2013). D_3 is represented by a penetrative crenulation cleavage best developed in aureole zones of early Permian granitoids, and considered to have formed as a sub-horizontal cleavage during early Permian extension (Davis and Henderson, 1999). Structures assigned to D_4 are more localized and variable in nature, and tend to be co-planar with D_2 structures making their recognition difficult. D_4 is linked to mesoscopic folds and an associated north-south trending crenulation cleavage best developed near Permian granitoid plutons (Davis et al., 2002), and linked to compressional events during the late-Permian. In addition, Davis (1993) describes two localized events (D_5 and D_6) from the metamorphic aureole around the Cannibal Creek pluton further west of Watershed **(Fig. 2.2)**.

Rocks of the Hodgkinson Formation were intruded by late Carboniferous to Permian (322 - 265 Ma) granites of the Kennedy Igneous Association (Champion and Bultitude, 2013) **(Figs. 2.1-2.2)**. In the northern part of the Hodkinson Province these intrusions are represented by ~4,000 km^2 of outcrop of mainly Permian S-type and minor I-type granites assigned to the Daintree Subprovince (Mackenzie and Wellman, 1997). The intrusive rocks were emplaced along a northwest trend in the central part of the Hodkinson Province, where it may coincide with a crustal-scale dislocation called the Desailly Structure (Davis et al., 1998). Intrusions follow a more northerly trend towards the east of the province. The Daintree Subprovince has been further sub-divided into different suites and supersuites on the basis of geochemistry (Bultitude and Champion, 1992). Thus, the Watershed deposit is surrounded by S-type syenogranites of the early Permian Whypalla Supersuite, which were emplaced during D_4 (Davis, 1993) between ca. 285 and 260 Ma (Champion and Bultitude, 2013). These granite plutons include the Mt. Windsor, Whypalla, Kelly St. George, Koobaba and Desailly granites **(Fig. 2.2)**. The granites of the Whypalla Supersuite exhibit variable textures, mineralogy and widespread but scarce enclaves. These rocks are porphyritic to equigranular, and mainly consist of muscovite-biotite syenogranite and monzogranite with rare granodiorite (Bultitude and Champion, 1992). Accessory minerals include widespread

garnet and tourmaline and rare sillimanite and orthopyroxene. Garnet is the main accessory phase forming early Fe-rich almandine and late Mn-rich spessartine (Bultitude and Champion, 1992). Plagioclase is more common than K-feldspar. Enclaves commonly include biotite-(garnet) gneiss, 'microdiorite', 'microgranite', quartz fragments and locally derived metasedimentary rocks such as shale.

2.2.1 Tungsten metallogeny of the Hodgkinson Formation

Numerous tungsten occurrences are present in the Hodgkinson Formation, the most significant of which are the Watershed and Mount Carbine (de Roo, 1988) deposits **(Fig. 2.2)**. Mount Carbine has a resource of 59.3 Mt averaging 0.12 percent WO_3, plus a past production of 12, 456 t WO_3; together the contained WO_3 is 83,706 t (Chang et al., 2017). Another significant tungsten deposit hosted in the Hodgkinson Formation, with similarities to Mt Carbine, is the abandoned Mt Perseverance mine which was mined in the 1960's (de Keyser, 1961). A further ~60 small tungsten-only mineral occurrences are found in the Hodgkinson Formation in the vicinity of the Permian S-type Whypalla Supersuite (Geological Survey of Queensland database, Greenwood, 2017). Mt Carbine shares some geological similarities with Watershed such as the vein style of mineralization in meta-sedimentary host rocks (de Roo, 1988). Differences between the two deposits include ore mineralogy (scheelite only at Watershed versus wolframite with less scheelite at Mount Carbine (Cheng et al., 2017)), and differences in alteration type (skarns at Watershed versus chlorite-illite alteration at Mt Carbine (Chang et al., 2017)).

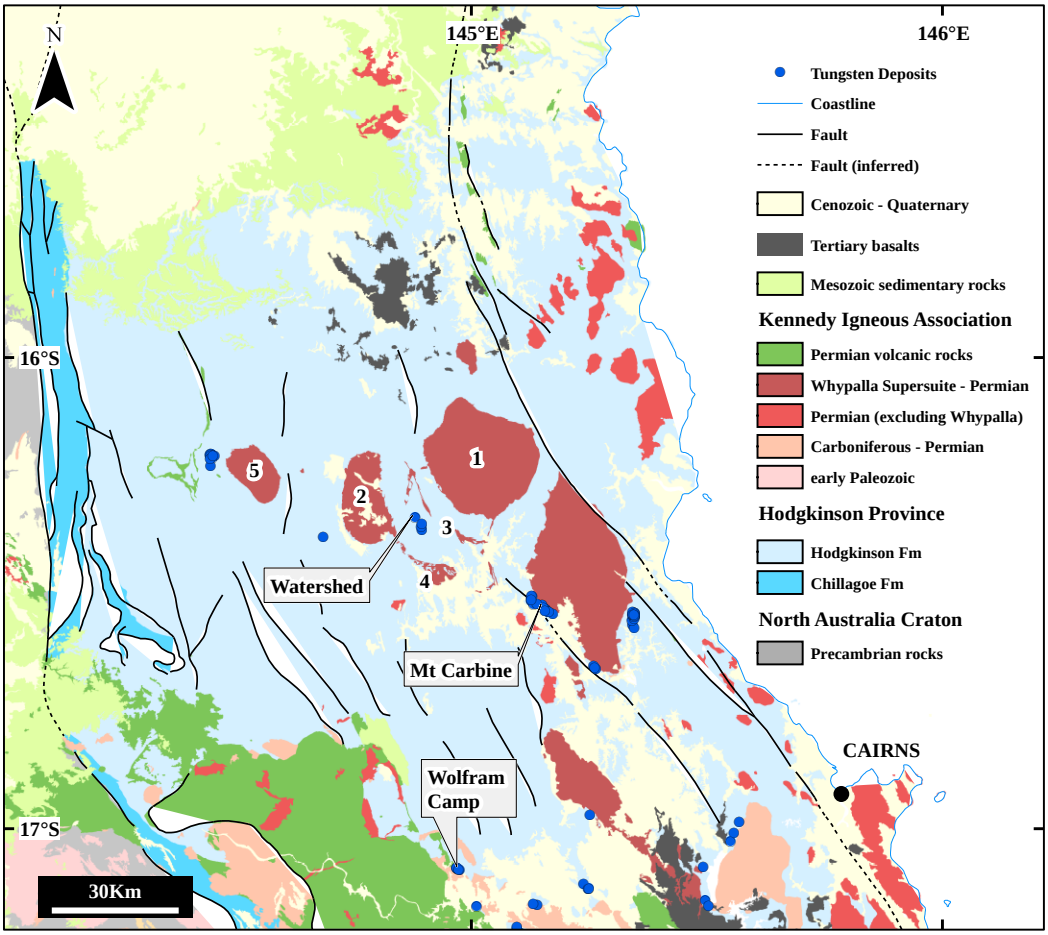

Figure 2.2 Regional geological setting of the Watershed deposit in the Hodgkinson Province. Also shown is the Whypalla Supersuite. Mentioned plutons in the text as follows: (1) Mt. Windsor and Whypalla; (2) Kelly St.George; (3) Koobaba, (4) Desailly and (5) Cannibal Creek. The three largest W deposits are labelled: Mt Carbine (83,706 t WO_3), Watershed (70,400 t WO_3), and Wolfram Camp (12,260 t WO_3). Other deposits are much smaller (Chang et al., 2017).

2.3 Geology and structure of the Watershed deposit

Similar to much of the Hodgkinson Province, the sedimentary units around the Watershed deposit have undergone complex deformation, and common disruption of bedding as explained below. The sequence of deformation events around the deposit have resulted in a transposition fabric characterized by a strongly developed linear fabric and several generations of overprinting folds. The intensity with which transposition fabrics have developed is variable, and changes from minor in psammite-dominated sequences where primary layering can be preserved along significant strike-lengths, to intense in slate-dominated sequences in which the primary layering is completely destroyed. Due to the pervasive occurrence of high strain fabrics and transposition, it is difficult to define a type stratigraphic column for the Watershed area; more so because sedimentary structures are normally not preserved. Instead, a description of the main sedimentary rock units found near the Watershed deposit has been provided below **(Figs. 2.3-2.4)**.

2.3.1 Meta-sedimentary rock units

2.3.1.1 Psammite

This unit is a common rock type in the Watershed area, and ranges from quartzo-feldspathic greywacke to arkose. Generally, psammite consists of fine- to coarse-grained sandstone with a fine-sand to mud matrix, which forms massive to poorly graded beds that preserve evidence for one or more foliations. In the field, the psammite units form monotonous sequences of sandstone beds with few internal structures and rare intercalations of shale. The psammite units are typically composed of angular to sub-rounded quartz (45 vol. %) and euhedral to subhedral plagioclase (40 vol. %; An_{16-34}) grains, < 2 mm, with minor (5 vol. %) fine-grained biotite. Matrix grains consist of fine-grained quartz, plagioclase, biotite and muscovite. In some areas this rock type is strongly fractured and deformed, with framework grains exhibiting dynamic recrystallization and extension along the regional elongation lineation direction, with muscovite aligned in foliation planes that formed during D_1 to D_3 events. **(Figs. 2.3A, 2.4, 2.5A; see below).**

2.3.1.2 Quartzite

This unit constitutes only a minor portion of the sedimentary rock suite, and occurs in isolated beds that are incorporated in psammite units. The quartzite consists of a medium-grained, dark grey rock, composed of >70 vol.% quartz grains that are typically 2-5 mm, with minor biotite and feldspar (**Figs. 2.4, 2.5B)**.

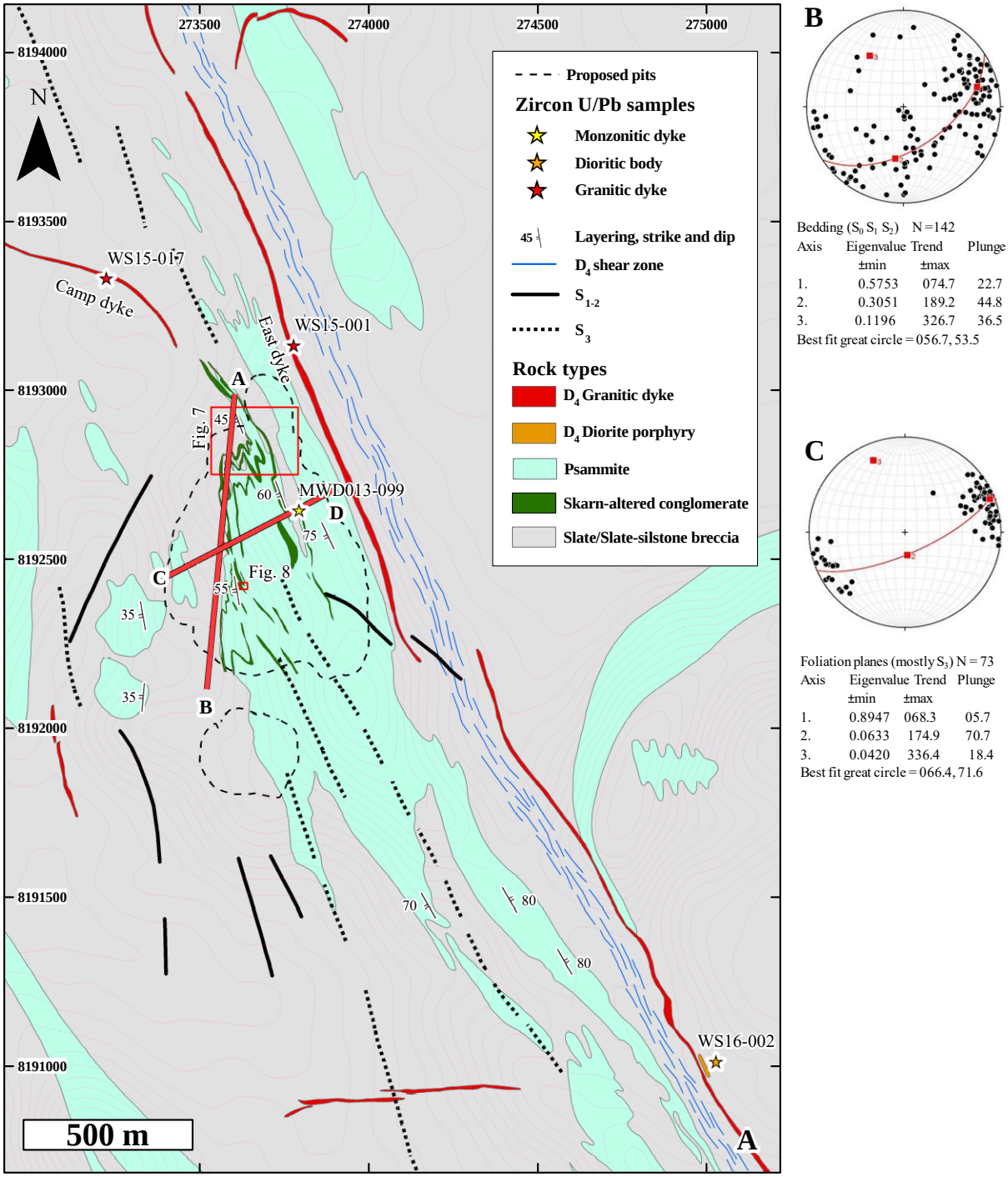

B

Bedding (S_0 S_1 S_2) N = 142

Axis	Eigenvalue	Trend ±min	Plunge ±max
1.	0.5753	074.7	22.7
2.	0.3051	189.2	44.8
3.	0.1196	326.7	36.5

Best fit great circle = 056.7, 53.5

C

Foliation planes (mostly S_3) N = 73

Axis	Eigenvalue	Trend ±min	Plunge ±max
1.	0.8947	068.3	05.7
2.	0.0633	174.9	70.7
3.	0.0420	336.4	18.4

Best fit great circle = 066.4, 71.6

Figure 2.3 **A.** Generalized geological map of the Watershed deposit where the green denotes the skarn-altered conglomerate following the regional fabric and showing transposition of these levels. The red thick lines denotes the long (A-B) and cross (C-D) sections traces in **Figure 2.4**. Surface U/Pb zircon dating samples are indicated. The grid system is Geocentric Datum of Australia 1994 (GDA94), zone 55. Base map from Skrzeczynski and Wood (1984). **B.** Poles to bedding $S_0/S_1/S_2$ (142 points) **C.** Poles to foliation planes mostly for S_3 (73 points).

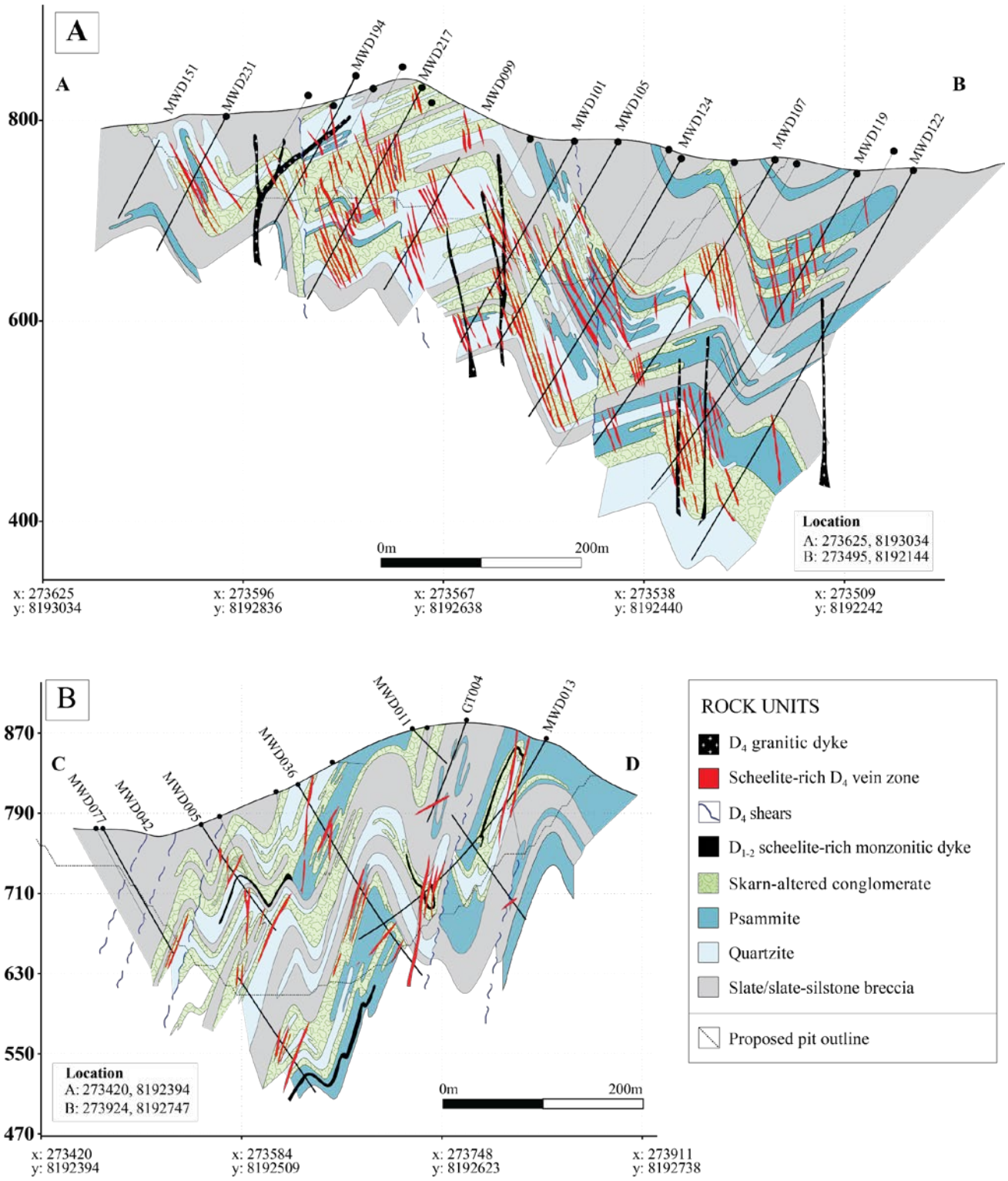

Figure 2.4 Generalized sections through the Watershed deposit. **A.** NNE (008°section orientation) long section looking east. In the long section D4 veins are better represented since the main orientation of these veins are east-west. **B.** Cross-section (055°section orientation) looking north. In the cross-section the early $D_{1\text{-}2}$ and D_3 deformation events and related transposition is better represented, since the σ_1 has a preferential east-west orientation. See **Figure 2.3A** for the section locations.

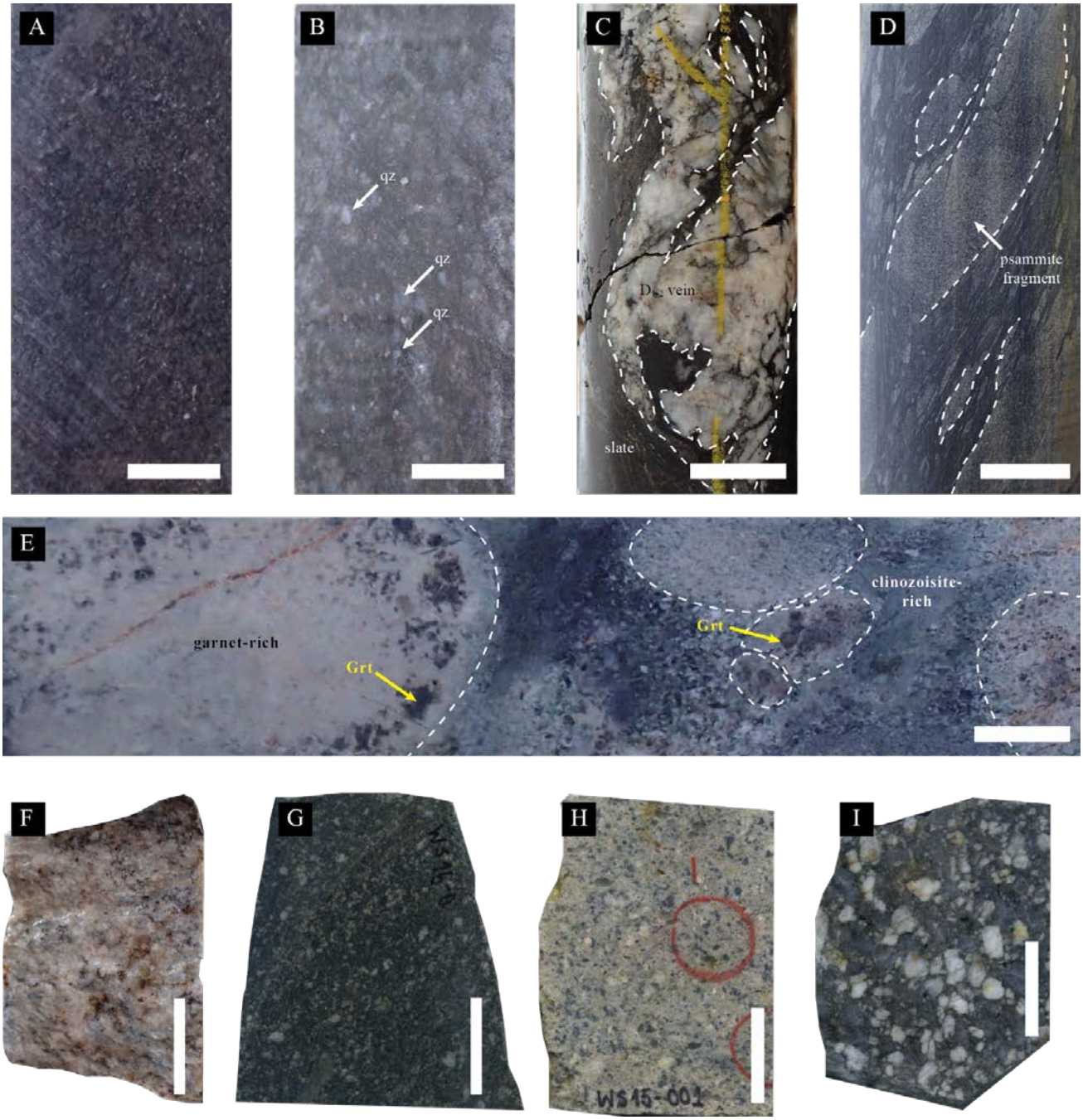

Figure 2.5 Photos of the metasedimentary units of the Hodgkinson Formation and the intrusive rocks at Watershed. White rectangles are 2 cm scale bars in each image. See **figures 2.3-2.4** for sample location. Mineral abbreviations after Whitney and Evans (2010). **A.** Psammite from hole **MWD124 at 216 m**. **B.** Quartzite from hole **MWD099 at 150 m**. **C.** Slate cross-cut by $D_{1\text{-}2}$ quartz vein from hole **MWD119 at 155 m**. **D.** Slate-siltstone breccia from hole **MWD119 at 20 m**. **E.** Skarn-altered conglomerate from hole **MWD101 at 159 m**. **F.** Monzonitic dyke from hole **MWD013 at 99 m**. **G.** Diorite porphyry (sample WS16-002). **H.** Granitic East dyke (sample WS15-001). **I.** Koobaba Granite (sample WS15-005).

2.3.1.3 Slate

This rock type incorporates massive shale units as well as interbedded shale-siltstone units in which individual siltstone layers vary in thickness from 0.5 to 20 cm. The shale is composed of dark-coloured carbonaceous (graphitic) mudstone **(Figs. 2.3A, 2.4, 2.5C)**, usually preserving at least one, well-developed penetrative foliation.

2.3.1.4 Slate-silstone breccia

This rock type represents the principle unit in the Watershed area and occurs along a 2 to 3 km wide zone that strikes north-northwest over a strike length of at least 20 km. The brecciation was structural rather than sedimentary. The slate-siltstone breccia is typically composed of isolated fragments of sandstone and siltstone (psammite) set in a strongly foliated, dark-grey matrix of mudstone (slate). Psammite fragments make up between 10 and 90 vol.% of the rock mass, and vary in width from 0.5 to 5 cm. They can be planar to linear in shape, and are locally strongly rodded to define an intense linear fabric. Some fragments preserve hook-like shapes resembling isolated fold hinges. The slate-siltstone breccia unit is generally homogenous in composition and represents the highly-deformed and transposed equivalent of the interlayered sandstone-siltstone-mudstone beds. Small (<0.5 mm) elongated aggregates of pyrrhotite crystals are common (<0.3 vol.%) along foliation planes **(Figs. 2.3A, 2.4, 2.5D)**.

2.3.1.5 Chert

This rock type occurs only within the slate-siltstone breccia zones as pods or layer-fragments of thinly-banded (0.5 to 30 cm), black to cream-grey siliceous rock with shale interlayers. The chert fragments are interpreted to represent disrupted layers that were locally interbedded with the slate-siltstone-sandstone sequence.

2.3.1.6 Skarn-altered conglomerate

This unit occurs as isolated pod-like bodies (i.e. boudins) and layer fragments, up to 15 m in width and tens of meters in length **(Fig. 2.3A, 2.4)** within psammite, generally close to the contact with slate-siltstone breccia. This rock type is typically altered to skarn and light green to cream in colour. Individual boudin segments range in size from a few centimetres to tens of meters, and may be layer-like, ovoid, irregular or wispy in shape. The unit is a clast-supported, polymictic conglomerate composed of rounded clasts that vary in size from 3 to 30 cm (average 6 cm) set in a matrix of coarse sand- to grit. Clasts typically are fine- to medium-grained rocks of calc-arenitic composition with variable amounts of carbonate vs quartz and feldspar, which have been altered to skarn minerals **(see below)**, and vary from pale pink (garnet-rich), pale-green (clinozoisite-rich), to pale grey (siliceous). The matrix is green-grey and consists of quartz, clinozoisite, garnet, feldspar, and muscovite with minor carbonate, biotite, titanite, scheelite and pyrrhotite **(Fig. 2.5E)**. The conglomerate unit is

the principle host for scheelite-rich vein mineralization, and its distribution **(Figs. 2.3A, 2.4A-B)** is of critical importance when defining the ore zones.

2.3.2 Deformation events

The (meta) sedimentary rock units of the Watershed area are strongly deformed with intense folding, and up to three penetrative foliations best developed in the slate/slate-siltstone breccia **(Fig. 2.6A)**. The psammite and conglomerate units occur as tectonic lenses in the form of boudins, boudin trails and layer segments enveloped by slate and slate-siltstone breccia units. These boudins are generally elongated with long axes plunging northwest at 20° to 50° (**Fig. 2.3**). Primary layering (S_0) is generally destroyed, but is locally preserved within boudins of psammite. The semi-continuous boudin trails of skarn-altered conglomerate **(Fig. 2.3A)** also provide evidence for early layering in the area. The principle characteristics of each of the deformation events is summarized below.

2.3.2.1 D_1 and D_2 events

The earliest deformation events, summarized as $D_{1\text{-}2}$ involved complete transposition of the primary layering as a result of at least two stages of upright isoclinal folding **(Figs. 2.4B, 2.6A)**. During $D_{1\text{-}2}$ pre-existing sequences of alternating mudstone, siltstone and sandstone together with the interbedded, chert and conglomerate units, were isoclinally folded and flattened to form the dominant, steeply southwest dipping foliation trend (**Fig. 2.6B**). The resultant fabric, S_1/S_2, is characterized by isolated, tight fold hinges, or fold limb segments defined by more competent lithologies (i.e. layer segments of siltstone and sandstone), enveloped in foliation domains dominated by slate, to form a typical high-strain transposition fabric (**Fig. 2.6C**).

Fabric transposition probably happened repeatedly, considering the complex, refolded fold shapes of some of the fold hinges, and the fact that early-layer-parallel fabrics (S_1) are seen folded around isolated fold hinges that are transposed within the composite S_1/S_2 fabric. D_1 and D_2, therefore, represent a progressive, composite set of events.

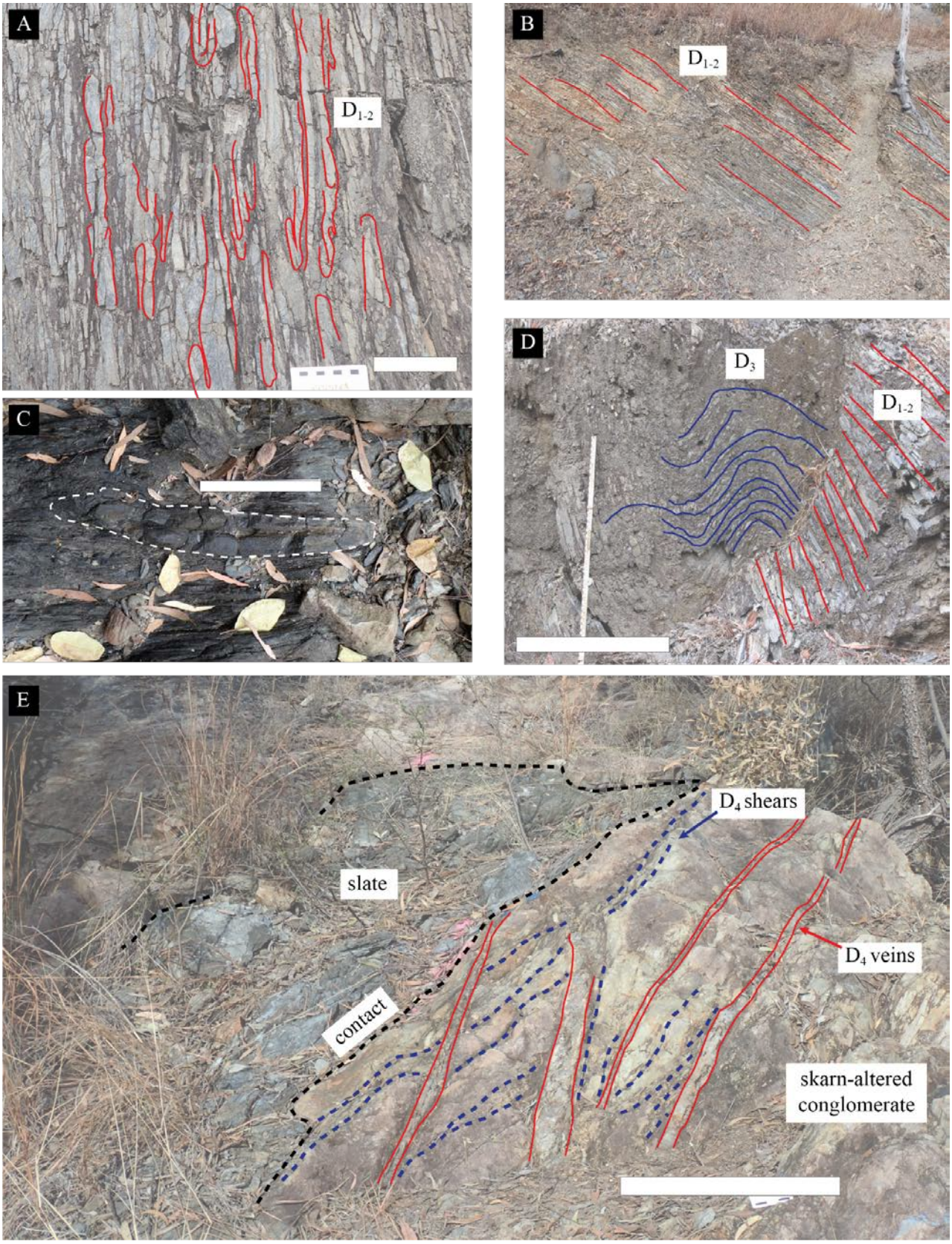

Figure 2.6 Outcrop images showing deformation events at Watershed. **A.** S_1/S_2 transposition fabric in slate/siltstone breccia after D_{1-2}. White scale bar is 10 cm. **B.** Linear trend of the S_{1-2} linear fabric after D_{1-2} showing southwest dipping foliation. **C.** Sheath folding (white dashed line). Isolated psammite enclosed by slate along north-northwest fabric. White scale bar is 25 cm. **D.** Open D_3 folds overprints D_{1-2} folds in slate-silstone breccia. White scale bar is 50 cm. **E.** Outcrop image showing the relationship between a D_{1-2} fold in slate and D_4 veins and shear zones. White scale bar is 50 cm.

During the D_{1-2} events, the primary layering was tightly folded and boudinaged, with the resultant fabric characterized by: (1) parallelism of mineral lineations, fold axes, long axes of boudins, intersection lineations, and rodding, resulting in an extremely well-developed linear fabric or L-tectonite (**Fig. 2.6B)**; (2) localized sheath folding (**Fig. 2.6C**); and (3) extreme transposition that resulted in the complete break-up of more competent siltstone and sandstone layers within the slate matrix (to result in the slate-siltstone breccia unit). The lensoidal nature of broadly cigar-shaped or strongly elongated lenses of more competent rock types within a matrix of slate can be observed on outcrop scale (e.g. **Fig. 2.6C**) as well as a regional scale (**Fig. 2.3A**); i.e. the competent psammite and conglomerate units that host mineralization and occur as 10-100 m scale lensoidal bodies, are also elongated parallel to the regional mineral lineation direction (~340/40 (DD/D); **Fig. 2.3B**).

Quartz veining accompanying D_{1-2} events are intensely folded and boudinaged, with vein fragments extended along the principle elongation direction (L_{1-2}). In slate, deformed D_{1-2}, quartz veins **(Fig. 2.5C)** can be up to 10 cm wide preserving sinuous, and locally ptygmatic shapes.

2.3.2.2 D_3 event

During D_3, deformation was partitioned in high- and low-strain zones. A major, planar D_3 high-strain zone bounds the Watershed deposit to the east **(Fig. 2.3A)**. In this zone, a planar transposition fabric is preserved as a composite $S_1/S_2/S_3$ fabric that bounds lower strain domains to the west and east, where D_3 is characterized by folding. Around the Watershed deposit the dominant D_3 structures are represented by cm- to km-scale (**Figs. 2.3C, 2.6D**) folds of the S_1/S_2 transposition fabric. In outcrop, D_3 folds are closed to tight, upright folds that locally preserve a near vertical, north-northwest-trending axial planar fabric, S_3 (a crenulation cleavage in slate; a spaced fracture cleavage in sandstone/psammite) **(Fig. 2.6D)**. Fold shapes are generally more open in psammite units than in the slate-siltstone breccia and F_3 fold axes plunge in a north-west direction, parallel to the penetrative L_{1-2} lineation. This parallelism in structural trends suggests that D_3 events represent a progressive continuation of D_{1-2} events, at waning metamorphic conditions as strain is being partitioned.

2.3.2.3 D_4 events

Shear zones that cut and displace the dominant ductile fabric elements are common in the Watershed area **(Figs. 2.6E, 2.7A)**. The shear zones are generally narrow (<10 cm), brittle-ductile fracture zones associated with minor veining along slickensided or striated fracture surfaces. Discrete shear zones occur along lithological contacts and may displace earlier structures including quartz veins. A major D_4 shear zone also occurs along the eastern margin of the D_3 high strain zone east of the Watershed deposit **(Fig. 2.3A)**, where it is associated with a steeply plunging, near down-dip lineation.

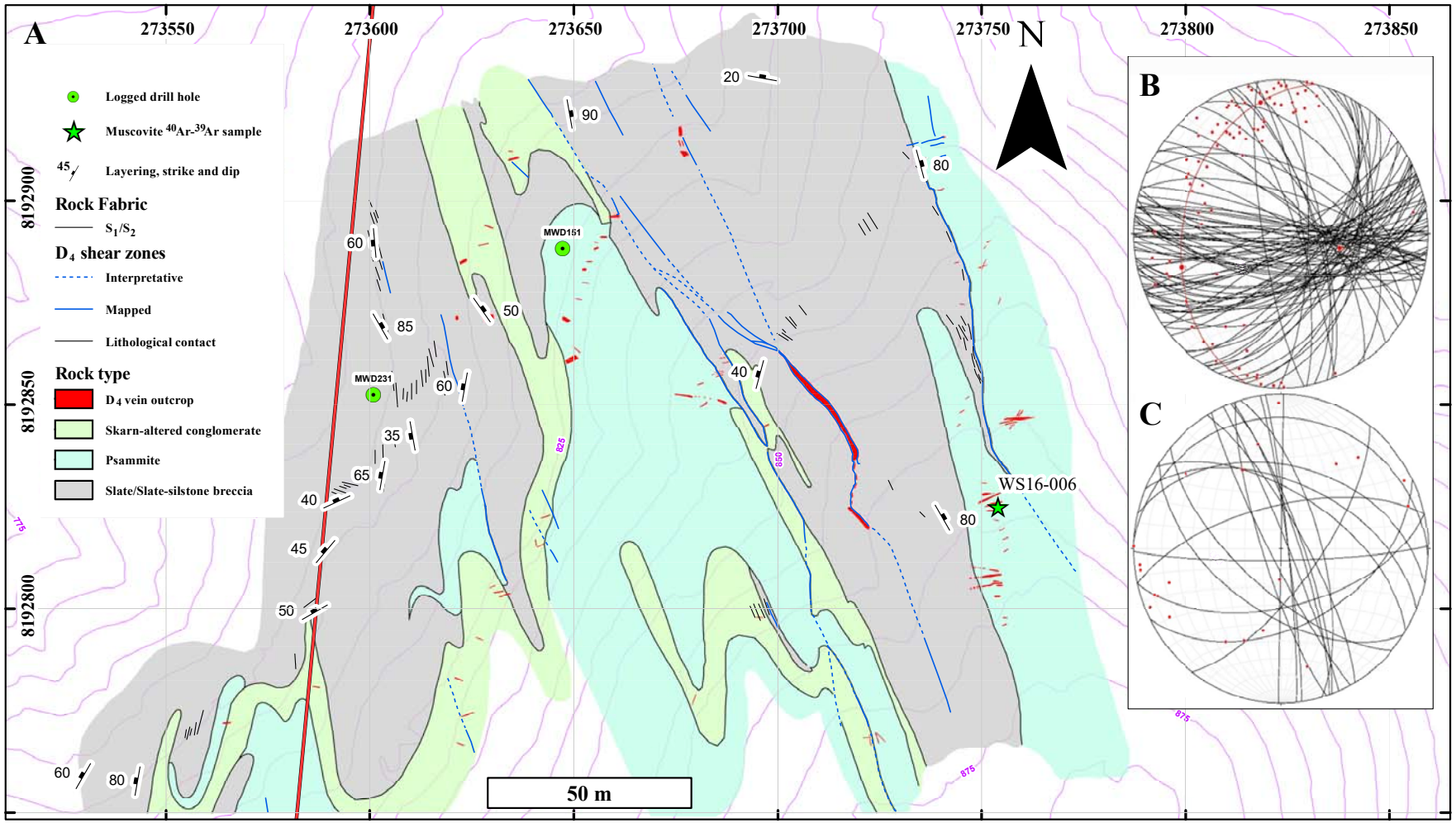

Figure 2.7 Lithological and structural mapping performed in the northern part of the Watershed deposit. For map location see **Figure 2.3A.** **A.** Map showing the relation between rock types, shear zones and vein development. **B.** Plot of veins (great circles) and poles to veins (red dots) in the mapping area. The poles show a well-developed great circle distribution. **C.** Plot of D_4 shear zones (great circles) and poles to shears (red dots) in the mapping area.

Around the Watershed deposit, D_4 shear zones display a wide variety of orientations **(Figs. 2.7A, 2.7C, 2.8A)**, with the dominant through-going structures being generally parallel to the main north-northwest to north trending ductile S_{1-2} fabric. The major shear zones are near vertical **(Fig. 2.7C)** with steeply north or south pitching lineations recording a west-up movement sense, generally associated with a dextral component of shear (i.e., they commonly offset veins in a dextral fashion) **(Fig. 2.8A)**. Numerous smaller fractures and shears in the vicinity of the major shears display a greater variation of orientations, and a normal movement sense is common. The shear zones are spatially associated with scheelite-bearing vein systems, with higher concentrations of veins apparent along the margins of the shears and near shear intersections (see detailed analysis of veins below).

A paleo-stress analysis using the Faultkin© software (Marrett and Allmendinger, 1990; Allmendinger et al., 2012; Dirks et al., 2013) for the D_4 shear zones was performed on fault planes obtained from the outcrop in **Figure 2.8A** and combined with additional fault planes from nearby outcrops. These shear zones are part of the interconnected network of fractures that control the distribution of scheelite-bearing veins **(Fig. 2.8A)**. In performing the analysis it is assumed that they formed simultaneously in response to the same far field stress (Dirks et al., 2013). In doing the analysis all shear planes were given the same weight; the methodology to conduct paleo-stress analysis has been explained in **Appendix 2.1**. Results are shown in **figures 2.8B-C**, and indicate that the D_4 shear zones associated with the Watershed deposit formed in response to horizontal, north-northeast extension (σ_3 towards ~020°), with a steep σ_1 direction.

2.3.3 Intrusive rocks

There are minor intrusions at Watershed, mostly occurring as dykes. The intrusions are monzonite, granite and diorite.

2.3.3.1 Granite plutons

Around the Watershed deposit and the surrounding areas several intrusive bodies crop out that have been assigned to the Whypalla Supersuite (**Fig. 2.2**). Unorientated porphyroblasts of andalusite, up to 8 cm in length are common, especially to the south of the Watershed deposit. The andalusite grains overgrow the D_1 to D_3 fabrics, but are cut by scheelite-bearing veins and associated D_4 fractures. The andalusite probably formed in a contact metamorphic aureole above a pluton that must be close to surface, but is not exposed in the immediate vicinity of the Watershed deposit.

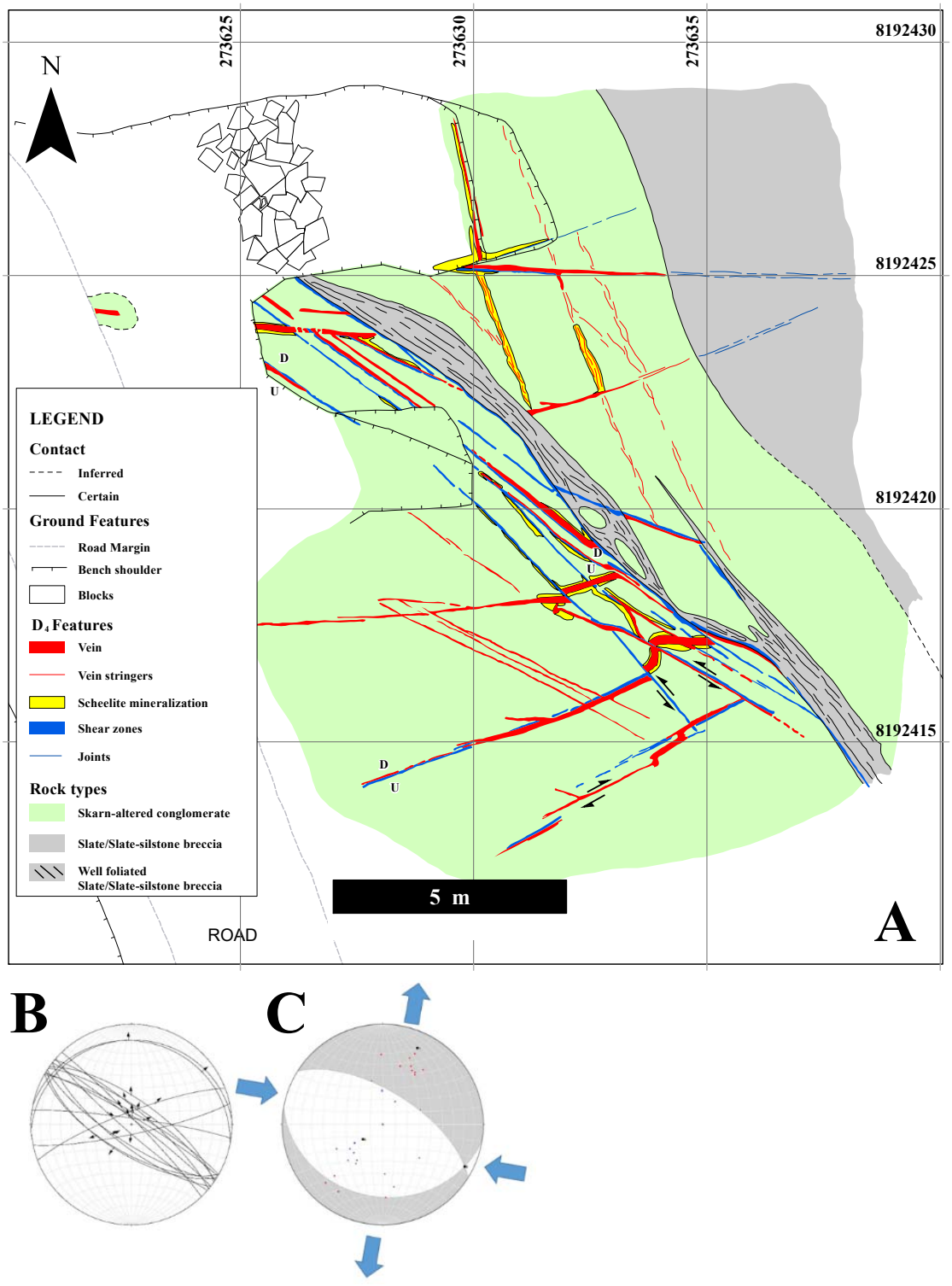

Figure 2.8 Mapping and paleo-stress analysis of an outcrop at Watershed. For map location see **Figure 2.3A. A.** Form surface map for platform outcrop. The map was constructed in WGS 84. D and U denote down and up block movement, respectively. **B.** Shear zones planes and lineation directions for faults and sheared vein margins in outcrop of **Figure 2.8A**. The arrows are the direction of movement of hanging wall. Note that most of the fractures and associated quartz veins were mineralized with scheelite. **C.** Fault plane solution for fractures shown on **B**; all fractures were given an equal weighting (even though the plot includes several 2 m wide shear zones next to mm-wide fractures). The fractures are consistent with north-south extension and the formation of east-west tension veins.

Outcrops of the Koobaba Granite occur 3 km to the northeast of the Watershed deposit (**Figs. 2.2, 2.5I)**. Outcrops of this granite are elongated, generally subparallel to the regional structural fabric, and have a porphyritic texture with euhedral feldspar phenocrysts up to 4 cm long; the groundmass is composed of quartz, feldspar and minor biotite, locally replaced by chlorite. The outcrops contain a north-south alignment of feldspar phenocrysts, which may suggest that the Koobaba granite was emplaced during D_4 (Davis, 1994; Davis and Forde, 1994).

2.3.3.2 Deformed monzonite dykes

Monzonite dykes were encountered only in drill cores, especially those orientated east-west **(Fig. 2.4B)**. The monzonite dykes are less than 40 cm wide, dark to light-grey, and contain a foliation (S_{1-2}) **(Fig. 2.9A)**, indicating that they were deformed and emplaced early in the deformational history of the area. Monzonite have a porphyritic texture, with mafic and felsic phenocrysts. Mafic phenocrysts comprise about 3 vol.% of the rock, and consist mostly of <0.5 mm, subhedral biotite, locally as fan-shaped aggregates. Felsic phenocrysts include 50 vol.% subhedral to euhedral plagioclase (<0.5 mm), 40 vol% subhedral k-feldspar (<0.5 mm) and ~5 vol% anhedral quartz. In addition the dykes contain ~ 5 vol.% primary muscovite (up to 3 mm). Groundmass consists of fine grained plagioclase and minor quartz. Accessory magmatic mineral include fluorite. Secondary interstitial calcite, chlorite after biotite and fine-grained muscovite (sericite) are also present. Locally, up to 10-15% of the rock consists of euhedral, deformed, partly resorbed and strongly fractured scheelite crystals, that occur in close association with oligoclase **(see below)**. The scheelite crystals are locally crenulated in open fold shapes **(Fig. 2.9A)**, which together with the internal foliation suggests that the dykes were emplaced during D_1 to D_3.

2.3.3.3 Granitic dykes

Granite dykes are common in the vicinity of the Watershed deposit **(Fig. 2.3A)**, and comprise dykes that are concordant and discordant with the main north-northwest trending S_{1-2} fabric. Dykes cut across D_1 to D_3 structures and generally show no evidence of internal ductile deformation, and they appear to mostly post-date the D_4 shear zones **(see below)**. Dykes vary in width from 0.5 m to several tens of meters, and can be traced over strike lengths of tens to hundreds of meters **(Fig. 2.3A)**. Textural variations occur both within dykes and between dykes, ranging from coarse porphyritic **(Fig. 2.5H)** to fine-grained. In porphyritic dykes, phenocrysts vary from 40 to 50 vol%, with 45 vol% K-feldspar, 45 vol% quartz and 10 vol% plagioclase (i.e. granite). Locally, K-feldspar is replaced by sericite and clay, and quartz exhibits minor recrystallization, due to post-emplacement deformation. The groundmass is composed of fine-grained quartz, K-feldspar and muscovite in equal amounts; with muscovite grains occurring along quartz and K-feldspar crystal boundaries. To the southeast of the Watershed deposit, biotite grains along the margin of a north-northwest trending granitic dyke (East Dyke) are oriented parallel to the mineral orientation (L_3 or L_4) in a nearby shear zone, suggesting that at least some of the granite dykes were emplaced late syn-tectonically (either late syn-D_3 or syn-D_4) **(Fig. 2.3A)**.

2.3.3.4 Diorite porphyry

A small diorite porphyry occurs about 2 km southeast of the Watershed deposit (**Fig. 2.3A**). In outcrop this body has a dyke-like appearance that parallels the East Dyke over a short distance. In hand specimen, the matrix is dark grey and accounts for ~50% of the total volume. White phenocrysts (~50 vol%) are euhedral plagioclase grains <2 mm in diameter **(Fig. 2.5G)**. Thin quartz veinlets with minor scheelite cross-cut this rock type.

2.4 Relationship between scheelite mineralization and deformation events

Tungsten mineralization in the Watershed deposit occurs in the form of pure scheelite ($CaWO_4$). Scheelite is found as disseminated crystals in monzonite dykes, and as stringers in skarn-altered conglomerate lenses, with the bulk of scheelite mineralization occurring along the margins and in alteration haloes of quartz-plagioclase veins that formed within lenses of skarn altered conglomerate.

2.4.1 Disseminated scheelite in deformed monzonite dykes

Scheelite crystals up to 2 mm in diameter occur as disseminations throughout the monzonite dykes where they are transected in drill core **(Figs. 2.4B, 2.9A)**. The scheelite crystals are subhedral to euhedral and are generally strongly fractured. They preserve complex growth zoning, dissolution lamellae and resorped boundaries suggesting partial recrystallization during metamorphism. Scheelite also preserves ductile deformational features such as sigmoidal shapes, boudinage, and (D_3) folding of trails of scheelite grains **(Fig. 2.9A)**. Taken together the textures have been interpreted to indicate that mineralization formed during D_1 or D_2, and pre-dated D_3.

2.4.2 Disseminated scheelite in skarn-altered conglomerate

Scheelite is common, but scarcely disseminated in skarn-altered conglomerate. The altered conglomerate units are generally massive, but preserve anastomosing fabrics, mainly defined by compositional bands of aligned clinozoizite and amphibole. Zoned, quartz-rich patches, with clinozoisite, garnet and feldspar, which formed within foliation domains at some time during D_1 or D_2 locally contain scheelite mineralization. These scheelite crystals are aligned along the deformational fabric (S_1 or S_2), and preserve sigmoidal grain shapes consistent with dynamic recrystallization and ductile deformation **(Fig. 2.9B)**.

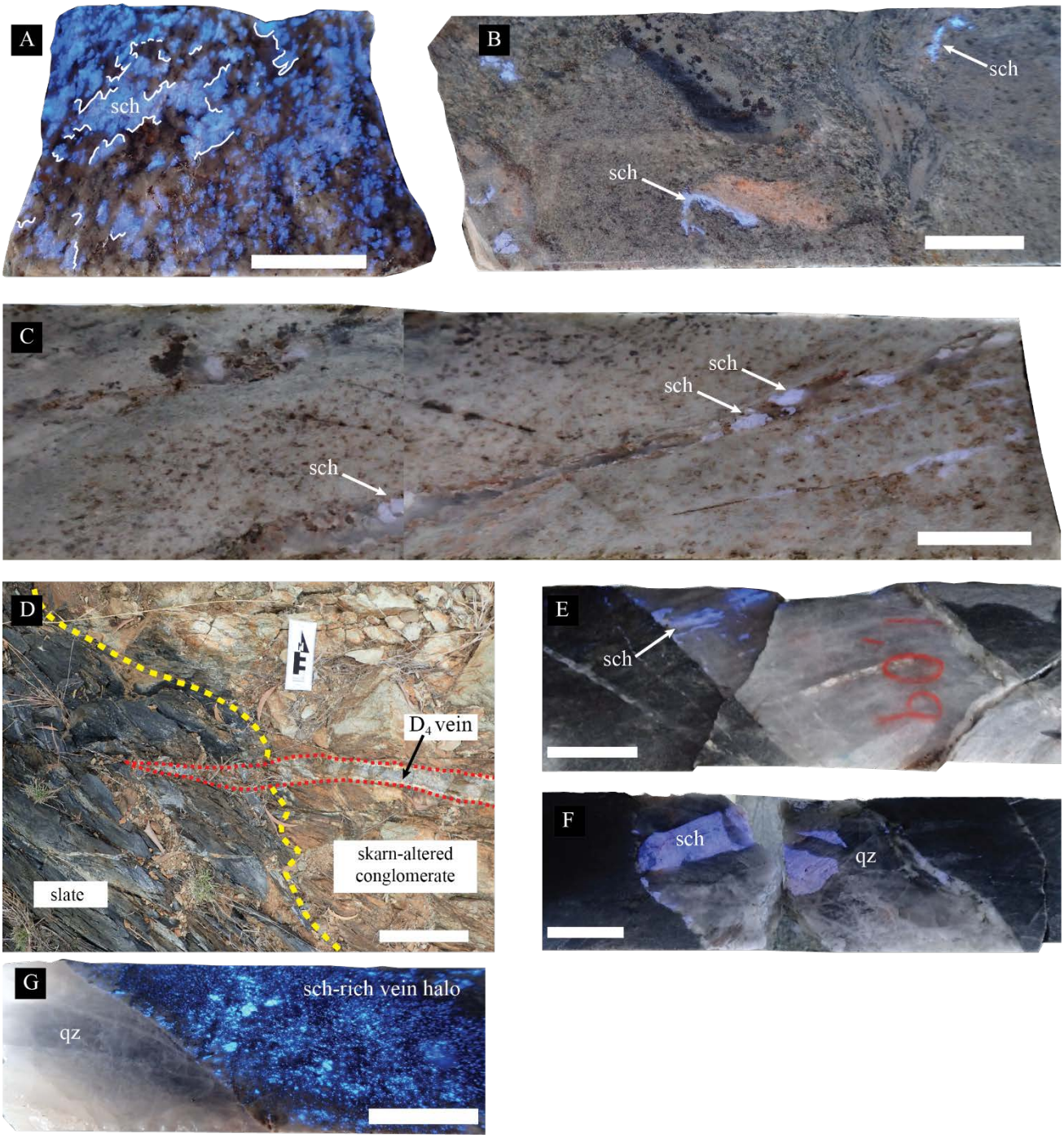

Figure 2.9 Images showing the scheelite relationship with deformation events. All the minerals abbreviations are from Whitney and Evans (2010). **A.** Scheelite mineralization (sch) affected by S_{1-2} fabric (few white traced lines for reference) in D_{1-2} monzonite (hole **MWD013 at 99 m**) under UV light. **Figure 2.5F** shows the same sample without UV light. White scale bar are 2 cm. **B.** Skarn-altered conglomerate (hole **MWD011 at 147.5 m**) under UV light showing syn-D_{1-2} sigmoidal scheelite (sch) mineralization along ductile S_{1-2} fabric. White scale bar are 2 cm. **C.** Skarn-altered conglomerate (hole **MWD217 at 114 m**) cut by D_4 quartz-scheelite (sch) stringers. White scale bar are 2 cm. **D.** Image showing scheelite-rich quartz-plagioclase D_4 vein, cutting skarn-altered conglomerate, pinching out when encounter slate. White scale bar are 20 cm. **E.** Scheelite-rich quartz-plagioclase D_4 vein (hole **MWD099 at 124 m**) with scheelite crystals (sch) growing at high angles from vein walls. White scale bar are 2 cm. **F.** Scheelite crystal (sch) in central part of D_4 vein (hole **MWD099 at 54 m**), cross-cut by quartz event (qz). White scale bar are 2 cm. **G.** Sheelite-rich D_4 vein halo of quartz (qz) vein (hole **MWD107 at 256 m**). White scale bar are 2 cm.

A second generation of disseminated scheelite mineralization associated with alteration zones near syn-D_4 shear zones and veins **(Fig. 2.9C)** occurs in skarn altered conglomerate, in which the amount of disseminated scheelite decreases away from the veins. This relationship is illustrated with a form surface map of a well-mineralized zone in skarn altered conglomerate **(Fig. 2.8A)**. In this outcrop the main shear zone is associated with interconnected secondary fractures and micro-fracturing of the host-lithology. Thin (<0.5 cm wide) quartz veinlets contain scheelite-quartz stringers, mainly where they cut garnet-rich clasts in the conglomerate **(Fig. 2.9C)**. Disseminated scheelite grains occur along micro-fracture planes in skarn altered conglomerate in the absence of quartz veins.

2.4.3 Scheelite in D_4 veins

D_4 shear zones are spatially associated with scheelite-bearing veins. Veins are distributed as sheeted swarms that occur mainly in skarn-altered conglomerate and minor psammite **(Figs. 2.4, 2.6E)**. The veins are generally of limited (<30m) strike length, and vary in widths from a few cm to 3m. Where they are developed in psammite and skarn altered conglomerate they generally terminate abruptly where they encounter slate units **(Fig. 2.9D)**, although there are places (e.g. GR 273710E-8192850N) where veins continue for several meters into slate **(Fig. 2.7A)**. Mineralized D_4 veins are largely restricted to skarn-altered conglomerate units, indicating that the host lithology asserts a critical control on the formation of scheelite in the syn-D_4 veins. The veins show a clear spatial association with D_4 shear zones, with the highest concentrations of veins occurring along shear planes and near shear intersections (**Figs. 2.7A, 2.8A**).

D_4 veins appear to vary in width and in the nature of internal deformation features as a function of orientation. The widest veins are tension veins with crystal growth at high angles to vein margins **(Fig. 2.9E)**. Such veins typically strike east-west and have a steep southerly dip **(Figs. 2.4A, 2.7-2.8)**. Veins in all other orientations are generally thinner (<10 cm), with crystal growth at lower angles or near-parallel to the vein walls, indicative of a shear component during vein opening and crystal growth. In some places along such veins, scheelite crystals have been broken and boudinaged along the long axis of the grains, i.e. parallel to the extension direction internal to the veins. Also, in some cases, scheelite crystals less than 3 cm in size occur in the central part of syn-D_4 veins cross-cut by quartz events **(Fig. 2.9F)**

Veins display a wide variety of orientations, with poles to veins, in the mineralized area in the centre of the Watershed deposit (**Fig. 2.7A**), distributed along a great circle with a pole to 103/57; i.e. the planar veins share a common intersection lineation around 103/57. The highest concentration of veins occurs around an orientation of 171/76 (**Fig. 2.7B**), however, vein orientations are fairly evenly distributed around the great circle and it would appear that all orientations could be associated with scheelite, even though they may differ in tungsten grades.

A more detailed analysis of scheelite growth in quartz veins near D_4 shear zones was undertaken in a high-grade zone in the centre of the deposit (**Fig. 2.8**). Here, mineralization is concentrated along the zone of

most intense fracturing and occurs along northwest trending fractures and veins; north-northwest-trending quartz stringer zones; east-west trending veins, and as disseminations in the skarn altered conglomerate (**Fig. 2.8**). The east-west veins are only mineralized near D_4 shear zone, with mineralized vein margins developed where the east-west veins occur within a several meter wide damage zone surrounding the D_4 shear zone.

2.5 Mineral composition and paragenesis in relation to deformational events

Scheelite mineralization is spatially and chemically linked to the skarn altered conglomerate lenses distributed across the Watershed area. In this section we will focus on the peak prograde and retrograde, hydrothermal mineral assemblages that formed in the skarn-altered conglomerate, and their association to scheelite mineralization. To investigate the effects of the complex deformation history on the distribution of scheelite in the Watershed deposit, minerals from monzonite, veins and skarn altered conglomerate were analyzed by EPMA techniques at the Advanced Analytical Centre at James Cook University. In addition, backscattered electron (BSE) images were taken during the procedure to investigate replacement textures and cross cutting relationships **(Figs. 2.10-2.12)**. This information helps to determine mineralogical and geochemical changes during the evolution of the Watershed deposit in relation to the deformation sequence **(Table 2.1)**, as well as to prove or disprove any mineral composition changes that may vector towards a possible intrusive source for the tungsten mineralization. For the methodology and full EPMA results refer to **appendices 2.2 and 2.3).**

2.5.1 Mineral assemblages formed during D_1 to D_3

Garnet and quartz formed in skarn altered conglomerate from D_1 to D_3. Garnet grains are euhedral and vary in size from fine- to coarse-grained. Using backscattered imaging, garnet can be texturally divided into un-rimmed and rimmed garnets **(Figs. 2.10A-B)**. Compositionally they comprise mainly grossular (Ca^{2+}), with lesser spessartine (Mn^{2+}) and almandine (Fe^{2+}), and rare andradite (Fe^{3+}) **(Fig. 2.10C)**. Rimmed garnets show complex textural and chemical zoning patterns with spessartine-almandine-rich cores and an increase in grossular towards the rims **(Fig. 2.10B)**. The core of rimmed garnets are interpreted to have formed during peak metamorphism (D_{1-2}), while the outer rims reflect initial retrograde conditions and probably formed during D_3 **(see below; Table 2.1)**. In contrast, un-rimmed garnets exhibit variable compositions in terms of mole % spessartine + almandine but display no zoning. Garnet compositions are plotted in terms of mole % grossular, almandine and spessartine in **Figure 2.10C**.

Table 2.1 Mineral paragenesis table for the Watershed tungsten deposit.

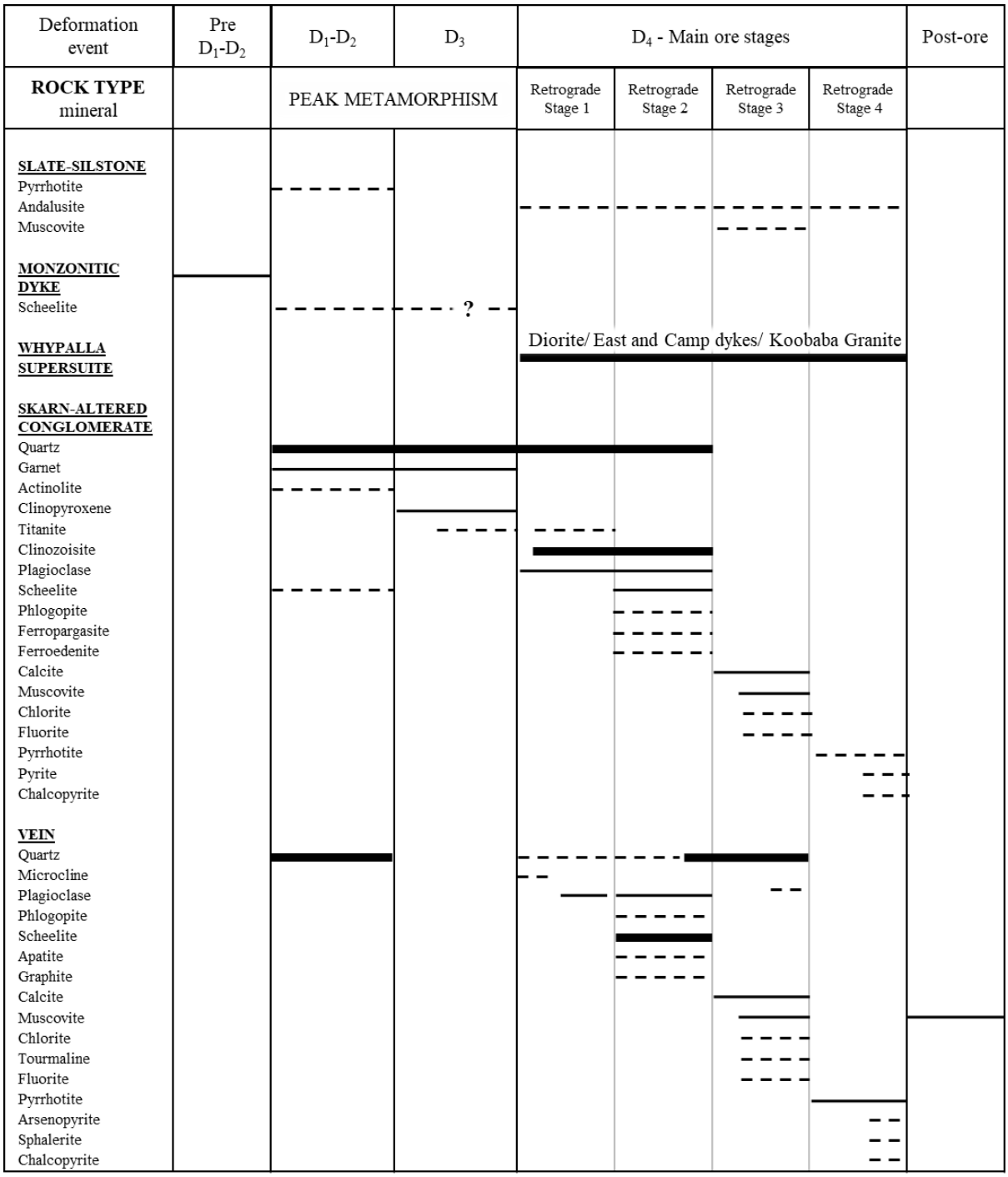

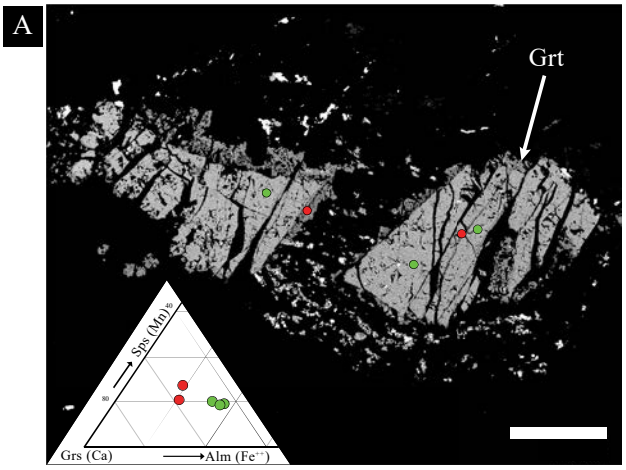
A
Grt
Sps (Mn)
Grs (Ca)
Alm (Fe++)

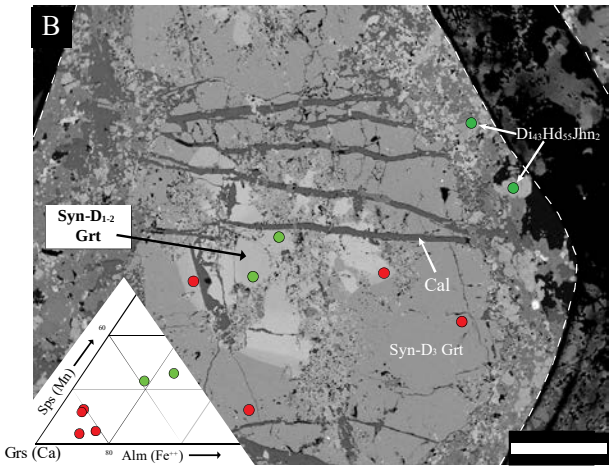
B
Di43Hd55Jhn2
Syn-D1-2 Grt
Cal
Syn-D3 Grt
Sps (Mn)
Grs (Ca)
Alm (Fe++)

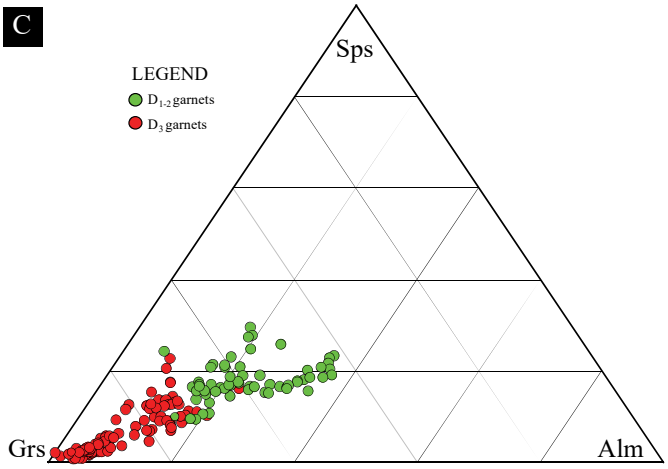
C
LEGEND
D1-2 garnets
D3 garnets
Sps
Grs
Alm

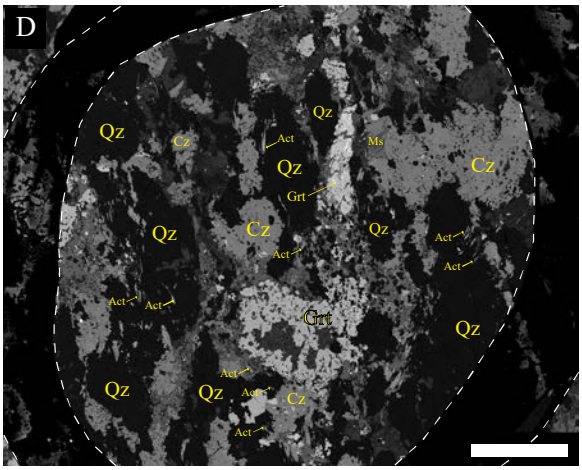
D
Qz
Cz
Act
Ms
Grt

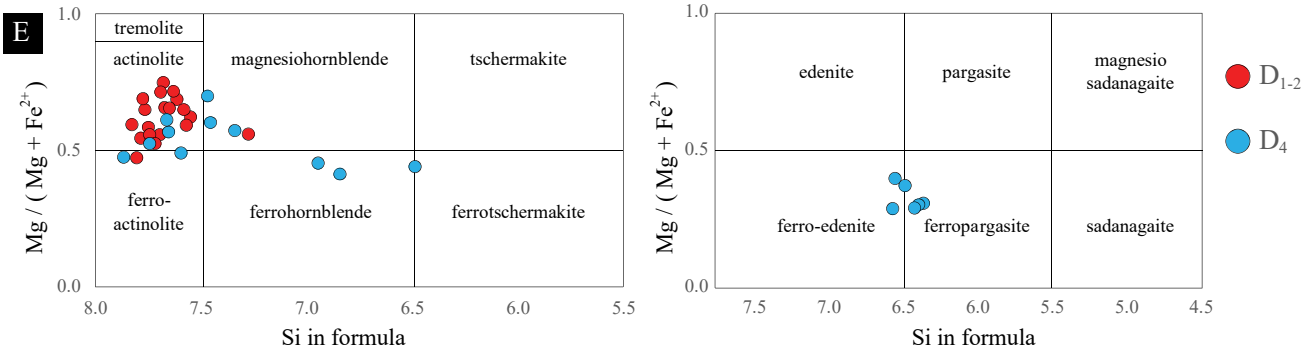
E
tremolite
actinolite
magnesiohornblende
tschermakite
ferro-
actinolite
ferrohornblende
ferrotschermakite
Mg / (Mg + Fe2+)
Si in formula
edenite
pargasite
magnesio
sadanagaite
ferro-edenite
ferropargasite
sadanagaite
D1-2
D4

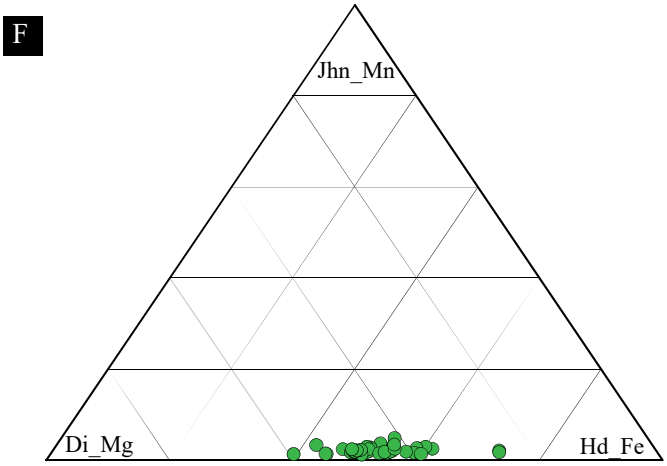
F
Jhn_Mn
Di_Mg
Hd_Fe

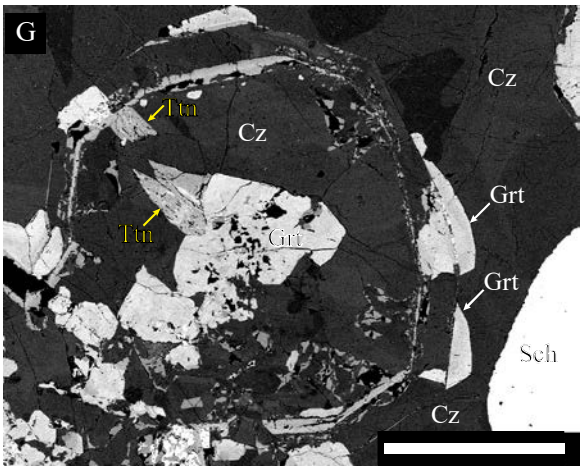
G
Cz
Ttn
Grt
Sch

Figure 2.10 Summary of microprobe results with back scattered electron (BSE) images to give textural context in skarn-altered conglomerate. All the minerals abbreviations are from Whitney and Evans (2010). **A.** BSE image of a boudin shape deformed D_{1-2} un-rimmed garnet (Grt; green spots), overgrown by a later D_3 garnet (red spots) (**hole MWD119 at 126 m**). **B.** BSE image (hole **MWD099 at 163.5 m**) of a rimmed garnet where the core represents D_{1-2} garnet (Grt; green spots) and the growing zones represents D_3 garnet (red spots). The garnet crystal is cross cut by calcite stringers. Synchronous D_3 pyroxene where also analysed (green spots on the right). White dashed lines denotes the limit of sharpie marker. White bar are 500 microns. **C.** Spessartine-grossular-almandine (Sps-Grs-Alm) triangular diagram for garnets from Watershed analysed in this study. Early D_{1-2} garnets have a more Mn and Fe^{2+} composition compared with more Ca-rich D_3 garnets. **D.** D_{1-2} garnet (Grt) deformed along the composite S_{1-2} foliation traces, marked by fine actinolite (Act) needles (hole **MWD099 at 81 m**). Quartz (Qz) grains are also elongated along the S_{1-2} foliations and garnet (Grt) is partly replaced by D_4 clinozoisite (Cz). Clinozoisite is also replaced by muscovite (Ms). White dashed lines denotes the limit of sharpie marker. White bar are 500 microns. **E.** Compositional diagrams for analysed prograde D_{1-2} (red dots) and retrograde D_4 (blue dots) amphiboles at Watershed. The left diagram is for amphiboles with $(Na + K)_A < 0.5$ and the right diagram for $(Na + K)_A \geq 0.5$. D_4 amphiboles contain an increasing Na content compared with early D_{1-2} amphiboles. **F.** Johanssenite-diopside-hedenbergite (Jhn-Di-Hd) triangular compositional diagram for analyzed D_3 clinopyroxene from Watershed. **G.** D_4 clinozoisite (Cz) pseudomorphing D_3 garnet (gt) during D_4 (hole **MWD011 at 147.5 m**). D_{1-2} scheelite (Sch) and D_3 titanite (Ttn) are observed as well. White bar are 500 microns.

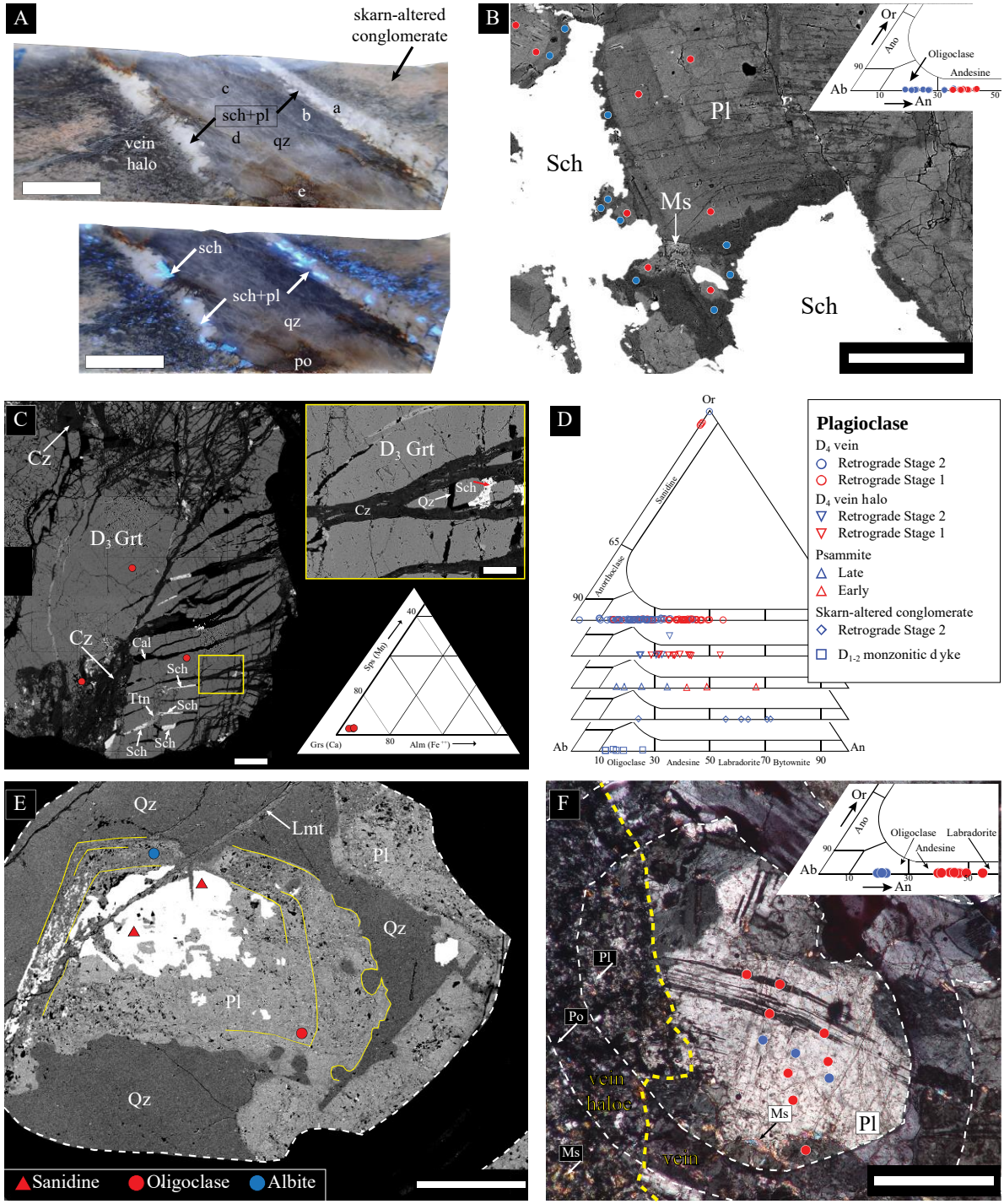

Figure 2.11 Summary of microprobe results accompanied by back scattered electron (BSE) and petrography images to give textural context in D_4 veins compared with D_4 mineralization in skarn-altered conglomerate . All the minerals abbreviations are from Whitney and Evans (2010). **A.** Detailed images of a multi-stage scheelite-rich quartz plagioclase D_4 vein from hole **MWD107 at 259 m** (note the blue color of scheelite under UV light in the bottom image). The white bar in both images are 2 cm scale. The letters on the top image denotes different stages within the veins: **(a)** early plagioclase + scheelite (sch + pl) - quartz assemblage as margins of veins (Retrograde Stages 1 and 2; **Table 2.1**); **(b)** grey quartz **(c)** white quartz veinlets **(d)** calcite stringers from Retrograde Stage 3 and **(e)** late pyrrhotite fracture filling from the late Retrograde Stage 4. Note the relation between the centimetric dark vein halo and the skarn-altered conglomerate on the top image. **B.** BSE image from hole **MWD 122 at 289 m** showing early andesine (Retrograde Stage

1; red spots) with late oligoclase (Retrograde Stage 2; blue spots) (Pl). Scheelite (Sch) is intergrown with oligoclase from Retrograde stage 2 **(Table 2.1)**. Late muscovite (Ms) from Retrograde Stage 3 is cutting plagioclase (Pl). **C.** Fractured D_3 garnet (Grt) cross-cut D_4 quartz (Qz), clinozoisite (Cz), scheelite (Sch), titanite (Ttn) and calcite (Cal) assemblage (scale bar are 500 microns). Detailed image on the top right corner (scale bar are 100 microns) corresponds to the yellow rectangle on the image on the left. This image illustrates the complex cross-cutting relationship in skarn altered conglomerate during D_4. **D.** Orthoclase-albite-anortite (Or-Ab-An) triangular compositional diagram for plagioclase from different rock-types at Watershed. **E.** BSE image from hole **MWD107 at 259 m** (**Fig. 2.11A**), showing the growing zone (yellow outlines) of a plagioclase (Pl) crystal from D_4 vein margin, shidting towards a more Na composition to the margin of the crystal. Early sanidine and oligoclase from Retrograde Stage 1 (red triangles and circle), and late albite from Retrograde Stage 2 (blue circle). Late quartz (Qz) is filling space between plagioclase (Pl) crystals and later laumontite stringer is cross-cutting all the later assemblages. **F.** Plagioclase microphotograph showing deformed twinning (pinch and swell), from a D_4 vein margin in hole **MWD119 at 128 m**. Early andesine from Retrograde stage 1 (red circles), overprinted by late oligoclase from Retrograde Stage 2 (blue circles). The plagioclase (Pl) crystals is cross-cut by a D_3 muscovite (Ms) stringer. The yellow dashed line denotes the vein and the vein halo limit. Vein halo assemblage is plagioclase (Pl), muscovite (Ms) and pyrrhotite (Po).

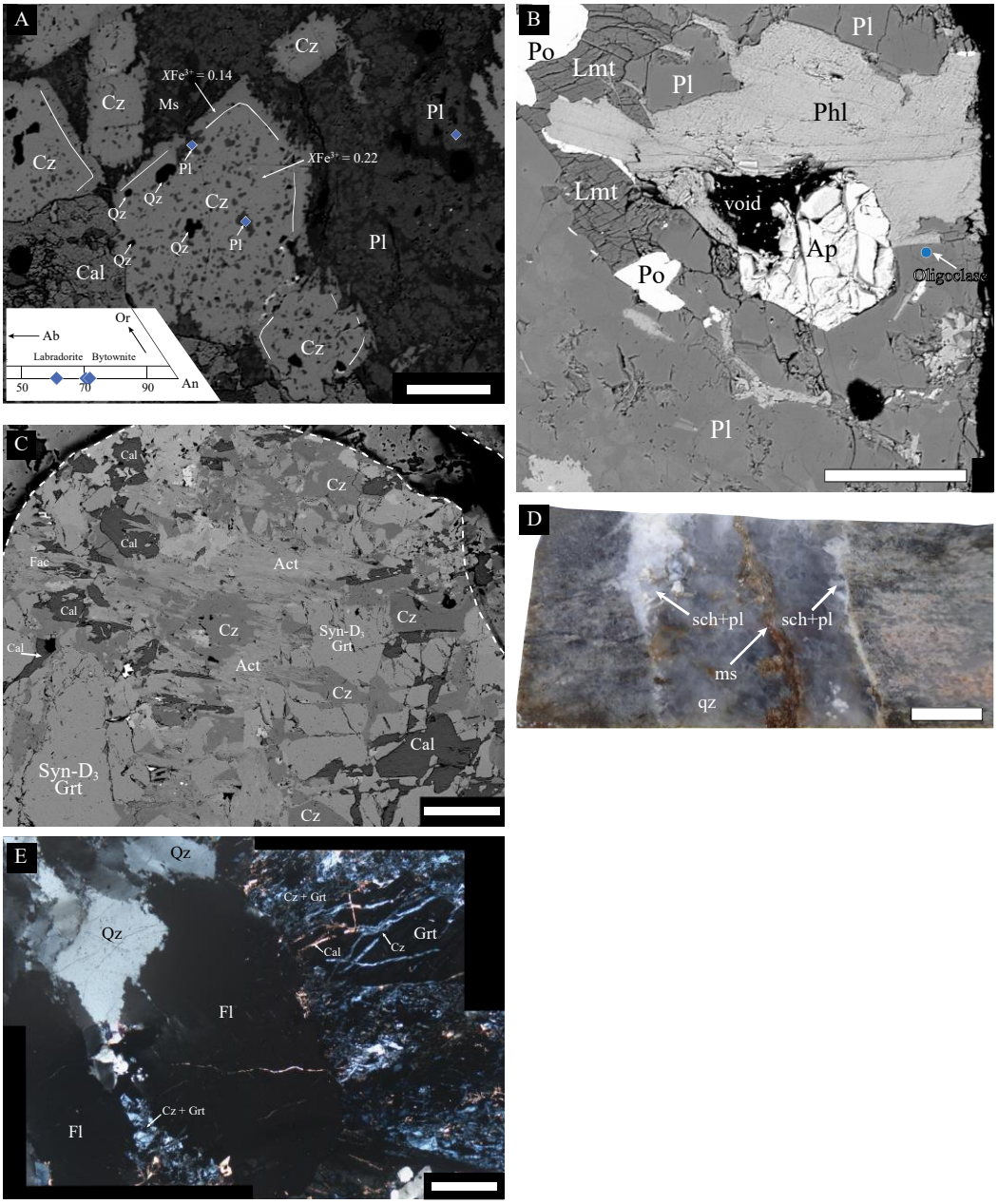

Figure 2.12 Back scattered electron (BSE) and petrography images to give textural context in D_4 veins compared with D_4 mineralization in skarn-altered conglomerate. All the minerals abbreviations are from Whitney and Evans (2010). **A.** Zoned D_4 clinozoisite (Cz) from Retrograde Stage 1 and plagioclase (Pl) from Retrograde Stage 2 in skarn-altered conglomerate (hole **MWD099 at 54 m**; 10 cm from a mineralized vein). Clinozoisite (Cz) is cut by Retrograde Stage 3 calcite (Cal). Clinozoisite (Cz) exhibits a compositional zonation with a diminish in Fe^{3+} content towards the margin. Clinozoisite (Cz) is also replaced by Ca-rich plagioclase (Pl) **(see inset)** and quartz (Qz). White scale bar are 100 microns. **B.** D_4 from Retrograde Stage 2 oligoclase (blue circle) intergrown with phlogopite (Phl) and apatite (Ap) in a mineralized D_4 vein in hole **MWD122 at 289 m (Fig. 2.11B; Table 2.1)**. Pyrrhotite (Po) from Retrograde Stage 4 is also observed. Lmt = laumontite. White scale bar are 100 microns. **C.** Strongly fractured D_3 garnet (Grt), replaced by D_4 clinozoisite (Cz) and subsequently replaced by amphibole (Act: actinolite; Fac: ferro-actinolite). Later fracture filling of calcite (Cal). Hole **MWD101 at 100** m. White scale bar are 200 microns. **D.** D_4 scheelite-plagioclase-quartz (sch-pl-qz) vein, cut by a Retrograde Stage 3 muscovite (ms) center line in hole **MWD217 at 80 m**. White scale bar are 2 cm. **E.** D_3 garnet (Grt) cross-cut by D_4 clinozoisite (Cz) and calcite (Cal) in clinozoisite + garnet (Cz+Grt)-rich skarn-altered conglomerate. The previous is cross-cut by a Retrograde Stage 3 quartz (qz) – fluorite (Fl) veinlet. White scale bar is 1 mm.

During D_{1-2} events both the core of rimmed garnets and un-rimmed garnets, quartz and actinolite formed along the composite S_{1-2} foliation traces **(Fig. 2.10D)**. The core of rimmed garnets and unrimmed garnets have a composition of grs_{40-65} $(alm\text{-}sps\text{-}prp)_{29-57}$ $adr_{<10}$. Un-rimmed garnets are generally fractured with fragments pulled-apart along the principle elongation direction (i.e. L_{1-3}) and interstitial spaces filled with quartz **(Figs. 2.10A, 2.10D)**. Actinolite is aligned in S_1 and S_2, in which S_1 foliation traces defined by the alignment of fine actinolite needles are crenulated on a sub-mm scale **(Fig. 2.10D-E)**. The limb regions of these asymmetric crenulations are aligned with S_2 foliation traces.

D_3 mineral growth in conglomerate skarn-altered conglomerate is characterized by garnet with compositions of $grs_{>65}$ $(alm\text{-}sps\text{-}prp)_{<38}$ $adr_{<16}$ **(Fig. 2.10C)**, clinopyroxene with compositions of Di_{25-59} Hd_{39-73} Jo_{1-5} **(Figs. 2.10B, 2.10F)**, quartz and minor titanite **(Fig. 2.10G; Table 2.1)**. The rims of rimmed garnets are interpreted to have formed during D_3, since they have a similar composition to garnet that overgrew boudinaged and broken up D_{1-2} garnets **(Figs. 2.10A-B)**. Later grown, D_3 garnets generally exhibit dissolution textures, and fracturing with calcite and/or quartz fracture fill and alignment along the L_{1-3} elongation lineation **(Fig. 2.10B)**. Garnet in skarn altered conglomerate is commonly replaced and pseudomorphed by retrograde mineral assemblages **(see below; Fig. 2.10G)**. Clinopyroxene occurs together with D_3 garnet and quartz **(Fig. 2.10B)**. Fine grained titanite occurs as an accessory phase, mostly spatially associated and intergrown with garnet **(Fig. 2.10G)**.

2.5.2 Retrograde alteration mineral assemblages formed during D_4

Peak-metamorphic mineral assemblages in skarn altered conglomerate that formed during D_{1-3} have been totally or partially replaced by hydrous retrograde mineral assemblages during D_4 **(Table 2.1)**. Four retrograde stages are recognized, which are interpreted to have formed during the shear related D_4 events and associated scheelite-rich veining. The retrograde events are, from early to late: "Retrograde Stage 1"; "Retrograde Stage 2"; "Retrograde Stage 3" and "Retrograde Stage 4" **(Table 2.1)**. The relative timing between the different retrograde stages have been defined based on cross-cutting and overgrowth relationships observed in drill core and in polished thin sections. It is important to define these retrograde stages because scheelite-rich veins opened in a multi-staged manner, with tungsten mineralization forming during the earlier stages of vein development in association with more sodic plagioclase **(Table 2.1; Figs. 2.11A-B; details below)**. Correlations between retrograde assemblages observed in veins and adjacent skarn altered conglomerate were based on key minerals that occur in both rock types (e.g. scheelite). By inference, it is assumed that the retrograde mineral assemblages observed in skarn-altered conglomerate formed during D_4, synchronous with the multi-staged emplacement of scheelite-rich quartz-feldspar veins. The Retrograde Stage 4 in vein corresponds to a sulphide stage, which developed in late fractures and veins **(Fig. 2.11A)**.

2.5.2.1 Retrograde Stage 1

The minerals that characterize the Retrograde Stage 1 assemblage replaced prograde skarn during the early stages of vein formation. Sanidine (Or_{93-94}) with minor quartz formed in vein margins **(Fig. 2.11D-E; Table 2.1)**, accompanied by quartz in the immediate vicinity of the veins. As feldspar crystals grew, early sanidine was overgrown by plagioclase (with An_{15-55}) **(Figs. 2.11D-E).** Outside the veins, quartz, clinozoisite and plagioclase replaced earlier phases in the adjacent wall rock **(Table 2.1; Figs. 2.10G, 2.12A)**. Vein plagioclase crystals are generally euhedral and between 0.1-1.5 mm in size with twinning, including deformation twinning **(Fig. 2.11F)**, and growth zoning. Plagioclase in vein haloes varies in composition from An_{29-54} with adjacent skarn altered conglomerate preserving plagioclase in the range of An_{56-72}, with more calcic compositions occurring away from the veins **(Figs. 2.11D, 2.12A)**.

Clinozosite that formed during Retrograde Stage 1 occurs preferentially in garnet-rich bands, and mostly replaces, and locally pseudomorphs, garnet that formed during D_{1-3} **(Figs. 2.10D, 2.10G)** and pyroxene that formed during D_3. In general, clinozoisite shows a homogeneous composition, with $X\mathrm{Fe}^{3+}$ (Fe^{3+}/ [Fe^{3+} + Al]) ranging from 0.12 to 0.31 (average of 0.23 ± 0.03; n=68). Clinozoisite that replaces pyroxene has $X\mathrm{Fe}^{3+}$ values of around 0.23, clinozoisite pseudomorphing garnet has $X\mathrm{Fe}^{3+}$ values of 0.20-0.25, and zoned clinozoisite crystals (most likely after garnet) have $X\mathrm{Fe}^{3+}$ values that vary from 0.22 to 0.24 in the core and 0.14 to 0.21 in the rim, which possibly inherits the Fe-poor nature of the original garnet rims **(Fig. 2.12A)**.

2.5.2.2 Retrograde Stage 2

This stage is associated with abundant scheelite growth and a shift in plagioclase composition **(Figs. 2.9E-G, 2.11B, 2.11D)**. The mineral assemblage in Retrograde Stage 2 is characterized by intergrown plagioclase (An_{3-43}) and scheelite **(Fig. 2.11B)**, as well as quartz **(Fig. 2.11E)** and phlogopite with trace apatite **(Fig. 2.12B)**, which formed near vein margins, and by clinozoisite, amphibole **(Fig. 2.12C)**, plagioclase (An_{16-34}), phlogopite and scheelite in skarn altered conglomerate **(Table 2.1)**. Clinozoisite and scheelite formed along fractures inside garnet **(Fig. 2.11C)**. Phlogopite is restricted to veins and to vein haloes, whilst plagioclase in vein haloes has a more sodic composition (An_{25-32}) when compared to plagioclase in skarn-altered conglomerate away from veins **(Fig. 2.11D)**.

Scheelite in D_4 veins that formed during Retrograde Stage 2 show variable textures and shapes **(Figs. 2.9E-F, 2.11B)**. Scheelite generally occurs in the margin of the veins **(Fig. 2.11A)**, with grains generally smaller than 2 cm, and formed in equilibrium with plagioclase (An_{3-43}) **(Fig. 2.11B)**. Plagioclase also forms more Na rich rims that overgrow more calcic plagioclase precipitated during Retrograde Stage 1 **(Fig. 2.11B, 2.11E)**. Larger scheelite crystals (up to 4 cm) locally occur in the central parts of veins and are commonly fractured and boudinaged with quartz veins filling the interstitial space between scheelite fragments; i.e. deformation of veins continued after scheelite growth **(Fig. 2.9F)**. In other places, scheelite remains intact and has grown as elongated crystals either perpendicular to the vein wall (e.g. in east-west striking veins, **Fig. 2.9E)** or at low angles to the

vein wall (e.g. in northwest and northeast striking veins). In the skarn altered conglomerate wall rock, relatively Na-rich amphibole (**Fig. 2.10E)** formed during Retrograde Stage 2 and replaced clinozoisite **(Fig. 2.12C)** and clinopyroxene.

2.5.2.3 Retrograde Stage 3

During Retrograde Stage 3 further vein opening occurred along the central parts of veins, where it is associated with the new-growth of quartz, in addition to calcite **(Fig. 2.11A)**, muscovite **(Fig. 2.11B, 2.11F, 2.12D)**, and minor chlorite, tourmaline and fluorite **(Fig. 2.12E)**; with the same assemblage minus tourmaline, also forming in skarn altered conglomerate **(Table 2.1)**. Irregular calcite stringers also cut earlier retrograde assemblages in veins **(Fig. 2.11A)**. Late during Retrograde Stage 3, muscovite formed along the centre line of veins, cutting all earlier assemblages **(Fig. 2.12D)**. Muscovite also occurs in the haloes of mineralized veins where it replaces earlier phlogopite, while minor chlorite replaces amphibole in the skarn-altered conglomerate.

2.5.2.4 Retrograde Stage 4

A late sulfide event affected all rock types in the Watershed area, and is expressed as pyrrhotite **(Fig. 2.11A, 2.11F, 2.12B)** and arsenopyrite with minor sphalerite and chalcopyrite occurring along fractures and in stringer veins **(Table 2.1)**. This event is not of economic significance.

2.6 Whole-rock geochemistry of intrusive rocks

Representative intrusive rock samples near the Watershed deposit were sampled for major and trace element geochemistry. The samples were analyzed at Bureau Veritas Canada Inc in Vancouver, British Columbia. The methodology and full results are presented in **Appendices 2.2 and 2.4**, respectively. Assessments of the rock composition and tectonic setting were performed by using high field strength elements (HFSE), since some rocks types are strongly mineralized and altered, which potentially affects major element compositions. This is particularly true for the monzonite dykes emplaced during $D_{1\text{-}2}$, which contain up to 30 vol% scheelite **(Fig. 2.9A)**.

A Y vs Nb tectonic discrimination plot (Pearce et al., 1984) shows that all of the intrusive rocks from Watershed have volcanic arc affinities (with Nb/Y between 0.2 and 1) **(Fig. 2.13A)**. The latter is in agreement with enriched Th, reduced Ti and P values, moderate LREE enrichments (La/Yb_N between 2.6 to 10.4) and relatively flat HREE patterns (Gd/Yb_N between 1.4 and 2.1) for this suite of rocks when compared with chondritic and MORB values (Bevins et al., 1984; McDonough and Sun, 1995) **(Figs. 2.13B-C)**. $D_{1\text{-}2}$ monzonite dykes and D_4 diorite and Koobaba granite show a distinct negative Eu anomaly (Eu/Eu^*_N between 0.6 and 0.8), in contrast to the D_4 granitic rocks (East and Camp dykes)with a weakly negative Eu anomaly (Eu/Eu^*_N of 0.1). This is consistent with their lower Sr anomalies and plagioclase content for the monzonite dyke and showing

that older intrusive rocks, diorite and Koobaba granite come from a relatively more oxidized source than the younger granitic dykes.

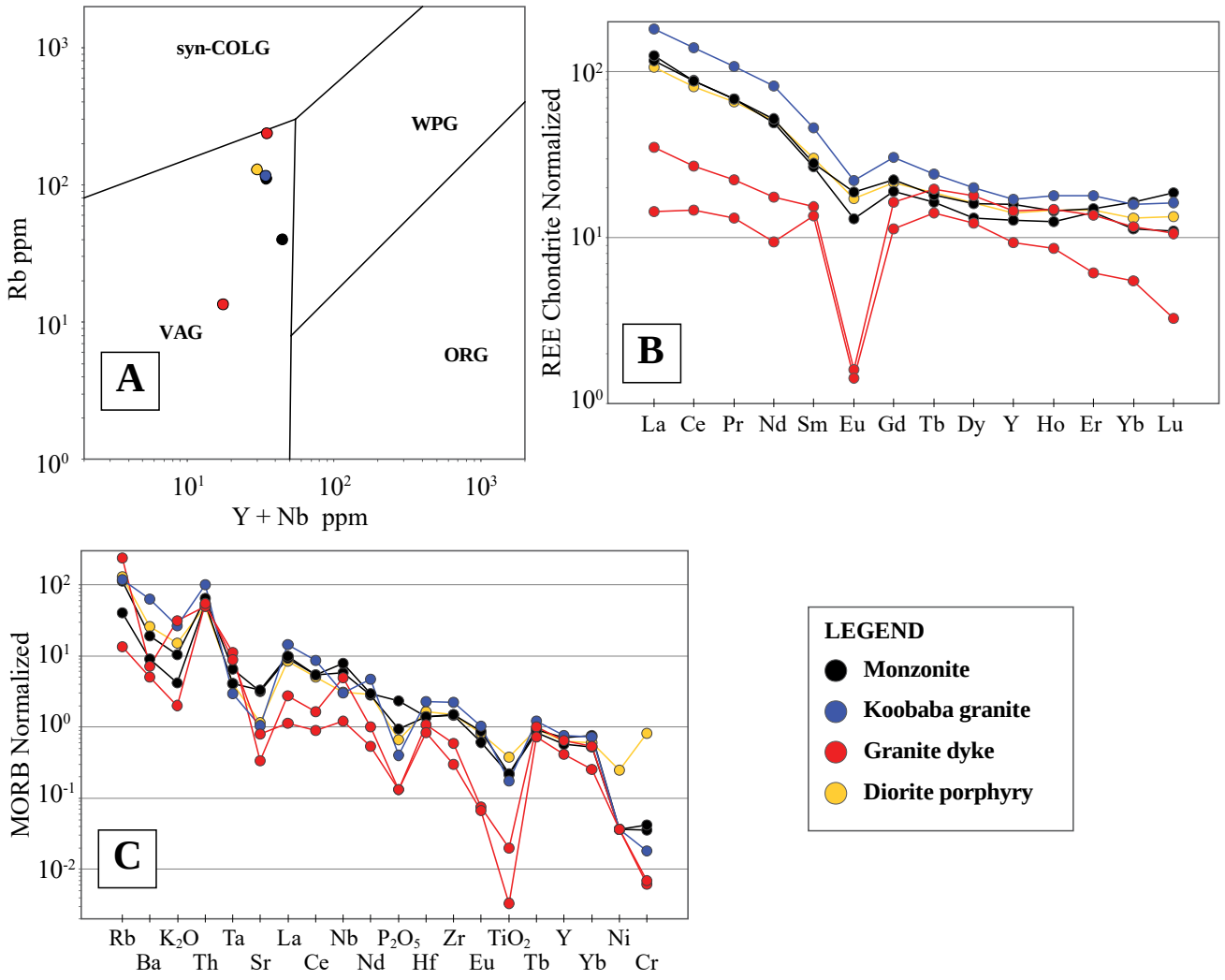

Figure 2.13 Trace element of dated igneous rocks at the Watershed deposit. **A.** Y + Nb vs Rb tectonic setting discrimination diagram. All of the analysed samples plot in the volcanic arc granite (VAG) field. Tectonic fields from (Pearce et al., 1984); **B.** Rare earth elements (REE) spider diagram normalized to C1 chondrite (McDonough and Sun, 1995); **C.** Trace element spider diagram normalized to MORB (Bevins et al., 1984).

2.7 Geochronology of igneous rocks and alteration

U/Pb dating was conducted to constrain the age of the intrusive rocks and indirectly, the age of alteration and mineralization. Muscovite ^{40}Ar-^{39}Ar dating was used to constrain the age of alteration and mineralization.

2.7.1 Sample descriptions

For zircon U/Pb dating, samples were taken from a D_{1-2} monzonite dyke (MWD013-099), granite dykes (WS15-001 and WS15-017) interpreted as early D_4, as well as from the largely undeformed diorite porphyry dyke (WS16-002) southeast of the Watershed deposit (**Figs. 2.3A, 2.5F-H**). In addition, zircon grains were separated from a sample of the late tectonic (D_4?) Koobaba Granite (WS15-005) north of the Watershed deposit **(Fig. 2.5I)**. Zircon separates were dated by in situ Laser Ablation Inductively Coupled Plasma Mass Spectrometry (LA-ICP-MS) in the Advanced Analytical Centre at James Cook University, Townsville. Sample locations, analytical techniques and data tables are presented in **appendices 1.1, 2.2 and 2.5**, and a summary of results is shown in **Table 2.2**.

In addition, muscovite was dated by ^{40}Ar-^{39}Ar geochronology at the Argon Geochronology Laboratory (AGL, University of Michigan, USA) to obtain a minimum age for the mineralization event. Muscovite ages were obtained by weighted average of two duplicate age runs performed at the AGL. One muscovite separate selected for dating was obtained from the halo of a D_4, mineralized vein (WS16-006; Retrograde stage 3; **Fig. 2.7A**). A second sample of late-stage muscovite was taken from the center line of a mineralized vein (MWD217-056; Retrograde Stage 3; **Figs. 2.4A, 2.12D**). Samples location, analytical methods and data tables are described in **appendices 1.1, 2.2 and 2.6**, and a summary of results is shown in **Table 2.2**.

2.7.2 Zircon U/Pb dating of intrusive rocks

To determining an emplacement age for the intrusive rocks at Watershed, the following procedure was followed. Once zircons for a particular sample were separated, mounted and dated, the distribution of $^{206}Pb/^{238}U$ ages for zircons were plotted on histograms binned at 10 Ma intervals. For each sample, the youngest distinct grouping of near-concordant (<10% discordant) zircons was identified for further age analysis on the assumption that this group of zircons is most likely to represent the crystallization age of the parent intrusion. Once the assemblage of zircons to be included in the final age analysis was identified, only zircons with less than 10% discordancy were chosen to calculate the average emplacement age. For one sample (WS15-017) there were insufficient near-concordant zircons, in which case zircons with less than 15% discordancy were chosen to calculate an emplacement age. The procedures followed for each sample are discussed in more detail below.

Five zircon grains in the youngest population group analysed from sample MWD013-099 **(Figs. 2.4B, 2.5F, 2.9A)** yielded analysis with <10% discordance. These zircon grains are euhedral, have low luminescence

and some grains contain relict core with a rim overgrowth **(Appendix 2.5)**. The $^{206}Pb/^{238}U$ ages vary from 360 ± 5 to 350 ± 5 Ma with a weighted average age of 355 ± 7 Ma (2% error, **Fig. 2.14A)**. The upper concordia age for these zircon grains is 359 ± 23 Ma **(Fig. 2.14B)**, which is similar within error to the weighted average $^{206}Pb/^{238}U$ age. The two youngest zircons in this population have near-identical concordant ages **(Fig. 2.14A-B)** that yield a weighted average age of 350 ± 7 Ma (2% error), which is the preferred crystallization age for this sample. This date provides a minimum age for the Hodgkinson Formation in the Watershed area, and constrains an early stage of igneous activity.

Five zircon grains in the youngest population group obtained from the granitic "East Dyke" (sample WS15-001; **Figs. 2.3, 2.5F)** yielded analysis with <10% discordance. The zircon grains are euhedral and contain concentric growth zones **(Appendix 2.5)**, with $^{206}Pb/^{238}U$ ages that vary from 293 ± 4 to 288 ± 5 Ma with a weighted average age of 291 ± 6 Ma (2% error, **Fig. 2.14B)**. These ages are similar within error and are considered to belong to the same age population. The upper concordia age for these zircon grains is 303 ± 140 Ma **(Fig. 2.14D)**. This age is interpreted as the onset of the second stage of intrusive activity at the Watershed area which coincides with the later stages of D_3 or D_4 tectonic activity.

The diorite sample (WS16-002; **Figs. 2.3A, 2.5G**) contains few zircons grains, however seven zircon grains within the youngest age population returned near-concordant analyses (<11% discordance). Several of these zircon grains are broken, some contain growth zones and all display low luminesce **(Appendix 2.5)**. The $^{206}Pb/^{238}U$ ages for the selected zircon grains vary from 284 ± 4 to 279 ± 4 Ma with a weighted average age of 281 ± 5 (2% error, **Fig. 2.14E)**. These ages are similar within error and are interpreted to belong to the same age population. The lower concordia age for these zircon grains is 272 ± 94 Ma **(Fig. 2.14F)**. This diorite is undeformed and contains scheelite-bearing veinlets. It provides a maximum age limit for the age of scheelite veins.

Five zircon grains from the youngest age group obtained from the post-tectonic granitic "Camp Dyke" (sample WS15-017, **Fig. 2.3)** yielded results with <15% discordance. These zircon grains are euhedral and contain concentric growth zones **(Appendix 2.5)** with $^{206}Pb/^{238}U$ ages that vary from 283 ± 6 to 274 ± 5 Ma with a weighted average age of 277 ± 6 Ma (2% error, **Fig. 2.14G)**. These ages are similar within error and are considered to belong to a single age population. The zircon grains did not yield a reliable concordia age **(Fig. 2.14H)**.

Nine zircon grains from the youngest age group obtained from the post-tectonic granitic Koobaba granite (WS15-005; **Figs. 2.3, 2.5I)** yielded analysis with <10% discordance. The zircon grains are euhedral and contain concentric growth zones **(Appendix 2.5)** with $^{206}Pb/^{238}U$ ages that vary from 278 ± 5 to 272 ± 5 Ma with a weighted average age of 274 ± 6 Ma (2% error, **Fig. 2.14I)**. These ages are similar within error and are considered to belong to the same age population. These zircon grains yielded a concordia age of 279 ± 15 Ma, within error of the weighted average age **(Fig. 2.14J)**.

2.7.3 Muscovite ^{40}Ar-^{39}Ar dating from vein and vein halo

The muscovite separate from the vein halo (WS16-006; **Fig. 2.7A**) provides a weighted average plateau age of 276 ± 6 Ma (2σ error) **(Table 2.2)**, i.e. within error of the granite dykes (Camp and East dykes), and consistent with mineralized vein emplacement (Retrograde Stage 3) during D_4. The late stage muscovite sample (MWD217-056) yields a weighted average plateau age of 253 ± 5 Ma (2σ error) **(Table 2.2)**, which suggests it formed during late-stage events possibly coincident with the Hunter-Bowen Orogeny (Davis et al., 2002; Henderson et al., 2013). It demonstrates that tectonism continued after the scheelite-rich veins were emplaced.

Table 2.2 Summary of geochronology undertaken in this work at the Watershed deposit

Sample	Lithology	Def event	UTM East[1]	UTM North[1]	Elevation m a.s.l.[2]	Method	Mineral	Age [Ma] ± 2% error
MWD013-099	Monzonitic dyke	D_{1-2}	273795	8192644	783	U/Pb	Zircon	350 ± 7
WS15-001	Granitic dyke	D_{3-4}	273779	8193133	800	U/Pb	Zircon	291 ± 6
WS16-002	Diorite	D_4	275029	8191013	790	U/Pb	Zircon	281 ± 6
WS15-017	Granitic dyke	D_4	273225	8193331	744	U/Pb	Zircon	277 ± 6
WS15-005	Koobaba granite	D_4	275604	8194873	662	U/Pb	Zircon	274 ± 6
WS16-006	Vein halo	D_4	273754	8192825	872	Ar-Ar	Muscovite	276 ± 6
MWD217-056	Vein	Post-D_4	273569	8192686	784	Ar-Ar	Muscovite	253 ± 5

[1]: GDA94 zone 55

[2]: m a.s.l.= metres above sea level

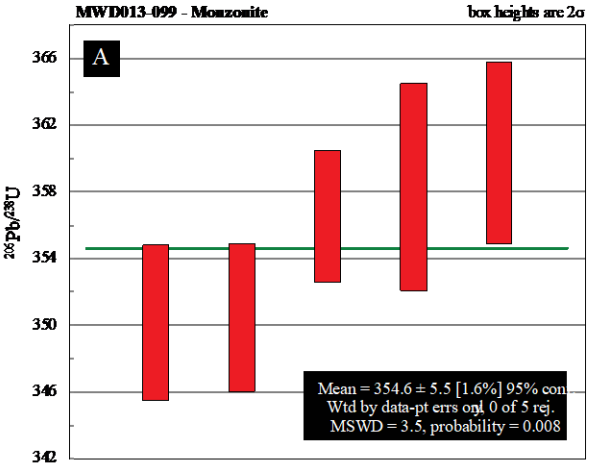
MWD013-099 - Monzonite
box heights are 2σ
A
Mean = 354.6 ± 5.5 [1.6%] 95% con
Wtd by data-pt errs only, 0 of 5 rej.
MSWD = 3.5, probability = 0.008

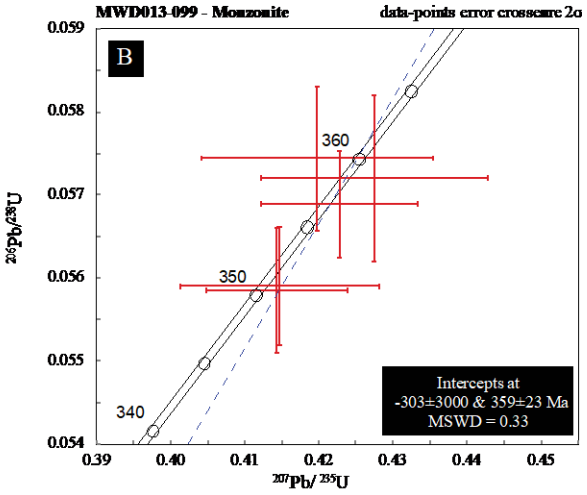
MWD013-099 - Monzonite
data-points error crosscure 2σ
B
360
350
340
Intercepts at
-303±3000 & 359±23 Ma
MSWD = 0.33

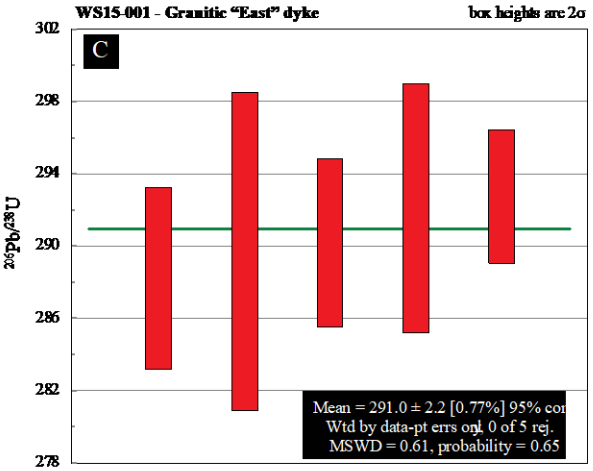
WS15-001 - Granitic "East" dyke
box heights are 2σ
C
Mean = 291.0 ± 2.2 [0.77%] 95% con
Wtd by data-pt errs only, 0 of 5 rej.
MSWD = 0.61, probability = 0.65

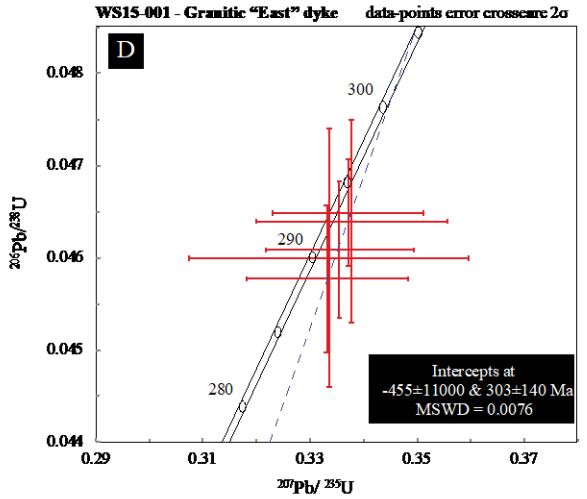
WS15-001 - Granitic "East" dyke
data-points error crosscure 2σ
D
300
290
280
Intercepts at
-455±11000 & 303±140 Ma
MSWD = 0.0076

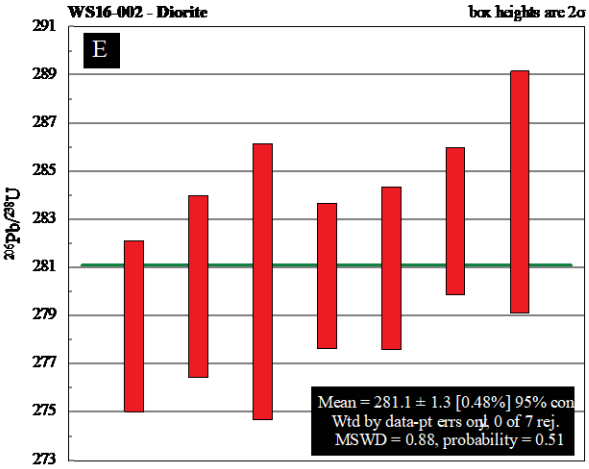
WS16-002 - Diorite
box heights are 2σ
E
Mean = 281.1 ± 1.3 [0.48%] 95% con
Wtd by data-pt errs only, 0 of 7 rej.
MSWD = 0.88, probability = 0.51

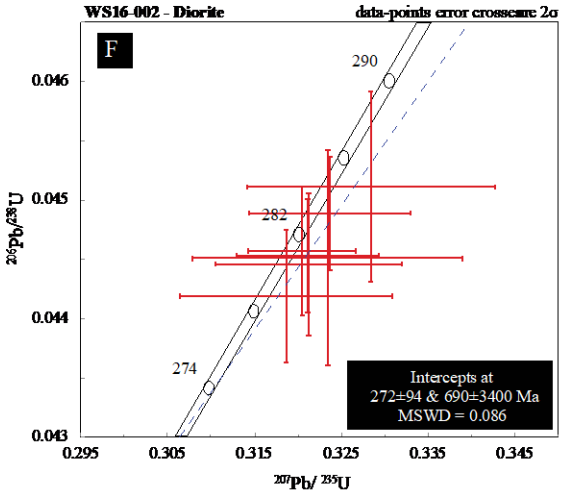
WS16-002 - Diorite
data-points error crosscure 2σ
F
290
282
274
Intercepts at
272±94 & 690±3400 Ma
MSWD = 0.086

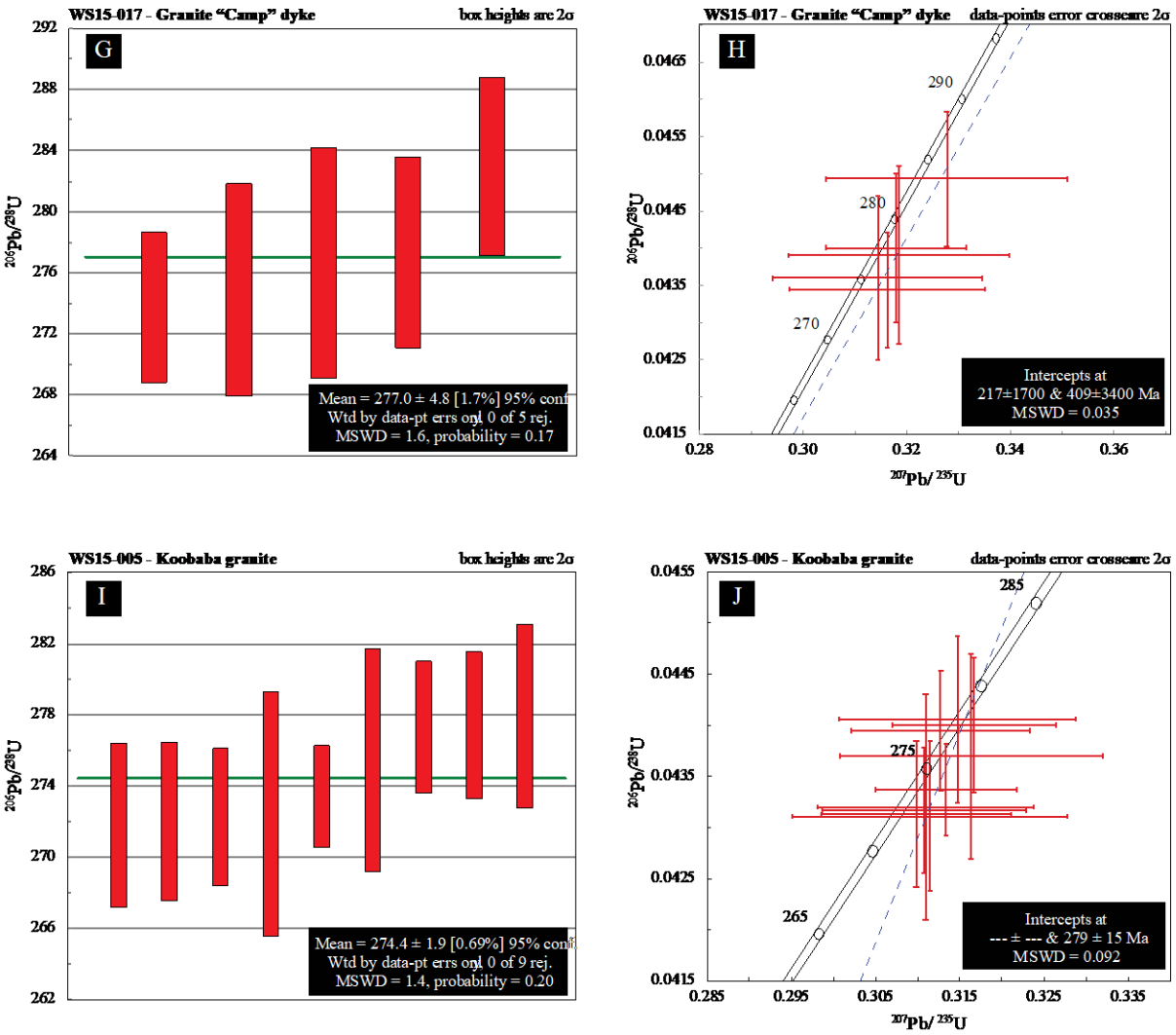

Figure 2.14 Weighted average bar charts and Concordia plots for U/Pb dating in zircons from intrusive rocks at the Watershed deposit. A and B. Carboniferous scheelite-rich monzonitic dyke; C and D. Permian granite "East" dyke; E and F. Permian diorite porphyry; G and H. Permian granite "Camp" dyke; and I and J. Permian Koobaba granite. See Appendix 1.1 for samples coordinates and Appendix 2.5 for full data set and CL images of analysed zircons.

2.8 Discussion

2.8.1 Timing of deformation events and mineralization

Deformation and metamorphic events in the Watershed area can be sub-divided into two groups that influence the distribution of scheelite mineralization at different scales in different ways. The first group involves progressive D_1 to D_3 events characterized by intense deformation and peak metamorphism, which resulted in at least one, if not two stage(s) of complete transposition, the destruction of primary bedding to form slate-siltstone breccia units, and the formation of an intense linear fabric. The second group of structures includes D_4 and later events, which are largely constrained to brittle-ductile shear zones, and associated with scheelite-bearing veins and retrograde alteration, or a regional metamorphic overprint at lower metamorphic grade. The early group of ductile, D_{1-3} structures resulted in an intense linear fabric in which the immediate host to scheelite mineralization, i.e. the skarn-altered conglomerate, was boudinaged and deformed into semi-continuous trails of elongated, cigar shaped bodies (**Figs. 2.3A, 2.6C, 2.7A**). The later group of D_4 shear-zones and veins, provides a second-order, more localized control on the distribution of scheelite mineralization, through the formation of mineralized shear zones and veins concentrated in the conglomerate altered to skarn-altered conglomerate lenses.

The D_1 to D_3 events in the Watershed area probably occurred shortly after deposition of the sediments of the Hodgkinson Formation and coincided with the emplacement of monzonite dykes at 350 ± 7 Ma. The monzonite dykes were emplaced in a volcanic arc setting **(Fig. 2.13A)**. These deformation events also coincide with the formation of the peak-metamorphic (garnet-clinopyroxene) mineral assemblage in the skarn-altered conglomerate unit. In comparison with previous studies, D_{1-2} events discussed here represent accretionary events of the Hodgkinson Formation along the northeast margin of the Australia Craton, and are the equivalent to D_1 of Davis (1993) and Henderson et al. (2013), whilst our D_3 is similar to D_2 of Henderson et al (2013). D_4 events are associated with extension **(Fig. 2.8)** and granite emplacement between 291-274 Ma **(Figs. 2.14C-J)**, and coincides with the main stage of tungsten mineralization. These events correlate with the regional D_3 events associated with Permian granite emplacement and extension of Davis and Henderson (1999), in a volcanic arc setting **(Fig. 2.13A).** They also coincide with the onset of opening of the Bowen Basin in a back-arc setting to the south of the study area, where similar events are associated with porphyry-style Cu-Au mineralization (Sahlström et al., 2018).

Based on textural evidence, the scheelite mineralization in the Watershed deposit can also be divided into two groups: (a) relatively early mineralization aligned in S_{1-2} and affected by F_3 folds; and (b) relatively late mineralization that is spatially associated with D_4 shear-zones and veins, and related alteration haloes in skarn-altered conglomerate.

Early scheelite mineralization is developed in skarn-altered conglomerate and monzonite dykes **(Figs. 2.9A-B)**, and can be recognized as trails of scheelite aligned in S_{1-2} foliation traces that are affected by open

folds interpreted as F_3 crenulations. The nature of F_3 folding in the skarn-altered conglomerate and monzonite dykes is less intense than in the surrounding slate and slate-siltstone breccia, and reflects the relative competency of these rock types. This generation of scheelite is spatially related to, and inter-grown with peak-metamorphic garnet, and commonly shows partly resorbed and irregular grain boundaries. The monzonite dykes were emplaced at 350 ± 7 Ma, and are strongly enriched in scheelite. Given that the scheelite grains are distributed along $S_{1\text{-}2}$ the most logical explanation would be that the scheelite crystallized within the monzonite dykes shortly after their emplacement, and were possibly part of the magmatic hydrothermal assemblage. In addition some disseminated scheelite growth occurred in nearby skarn-altered conglomerate. The texturally early scheelite mineralization may, therefore, have a magmatic hydrothermal origin related to the ~350 Ma igneous events affecting the Hodgkinson Formation (Zucchetto et al., 1999; Henderson et al., 2013).

The second generation of scheelite mineralization is more widespread and occurred at ~275 Ma in veins associated with shearing during D_4 **(Table 2.2)**. Synchronous to vein emplacement and D_4 shearing, intrusive events occurred at 281 ± 5 Ma with the emplacement of diorite, and 291 ± 2 Ma and 277 ± 5 Ma with the emplacement of granite dykes **(Figs. 2.14B-D)**. In this context it is important to note that the older East dyke (WS15-001: ca. 291 Ma) preserves a ductile fabric suggesting it may be emplaced during the latest stages of D_3 or the earliest stages of D_4, whereas the younger Camp dyke (WS15-017: ca. 277 Ma) cuts-across all fabrics and is undeformed. The relationship between mineralized veins and the later 274 ± 6 Ma Koobaba Granite **(Figs. 2.2, 2.14I)** cannot be observed directly because the Koobaba Granite is 3 km to the northeast from Watershed, but the age constraints suggest that these granites are related to the intrusive events affecting the Watershed area. The granitic intrusive bodies do not show a conclusive genetic relationship with mineralization, and some (i.e. the diorite, **Figs. 2.3A, 2.5G**) predate mineralization considering that quartz-scheelite veinlets are developed in the diorite intrusion. This is also consistent with the widespread distribution of un-orientated andalusite grains in the area, which overgrow $S_{1\text{-}3}$ fabrics, but are cross-cut by mineralized veins. The ages for intrusive events coincide with a muscovite age of 276 ± 6 Ma **(Table 2.2)** obtained from the alteration halo assemblage of a mineralized vein. It would appear that the best age estimate for the second generation mineralization is ~275 Ma, immediately post-dating igneous activity in the Watershed area, with no direct evidence that the intrusive events provide a source for scheelite mineralization.

The kinematic setting of the late scheelite mineralization can be deduced from an orientation and kinematic analysis of the scheelite veins and associated D_4 shear zones **(Figs. 2.7-2.8)**. The larger north-northwest trending shear zones that transect the central parts of the deposit **(Fig. 2.7A)** are near vertical with steeply north or south pitching lineations recording a west-up movement sense, generally associated with a dextral component of shear. These shear zones control the distribution of scheelite-rich veins which show mostly east-west, north-northeast and northwest trending orientations (**Figs. 2.7-2.8**). Considering: (1) the spatial association between mineralized veins and shear zones; (2) the west-up sense of movement across the main north to north-northwest trending shears; (3) the great circle distribution of vein poles around a common direction of 103°/57° (**Fig. 2.7**) and (4) the normal sense of movement on most secondary structures (**Fig. 2.8**).

It is proposed that the scheelite-rich veins formed in a vertical deformation zone that trends 350° (i.e. approximately parallel to the trend of the principle D_4 shear zones and the older S_{1-2} fabric). This is in response to a west-up shear couple, resulting in a local orientation of σ_1 of ~100°/60° (i.e. the common lineation direction shared by the mineralized veins; **Fig. 2.7**), with σ_2 and σ_3 being equal, and the entire system being in extension to explain the rather homogenous great circle distribution of poles to veins in the ore zone. Such a model is similar to the emplacement of REE-U-enriched veins along a major fault described in the Mary Kathleen deposit in the Mt Isa Block of western Queensland (Oliver et al., 1999). More detailed observations on the distribution of scheelite in veins near D_4 shear zones (**Fig. 2.8**) indicate that veins are only mineralized where they occur in close proximity to the shear-zones; i.e. the shear-zones are the primary conduit systems for tungsten-bearing fluids, which deposit scheelite in veins hosted in skarn-altered conglomerate, which form in direct association with the shears. Thus, the late-stage tungsten mineralization formed at ~275 Ma during D_4 shearing and vein formation in a mechanism that is similar to that described for lode-gold deposits (e.g. Cox et al., 1995; Groves et al., 2003; Goldfarb et al., 2005; Dirks et al., 2013), in which the source of the fluids may be metamorphic, igneous or a mixture of both.

2.8.2 Garnet composition: magmatic vs non-magmatic origin

A way to test the igneous vs metamorphic origin of tungsten-bearing fluids contributing to scheelite mineralization in the Watershed area, is by assessing the chemical composition of garnet that formed during different stages of the metamorphic/metasomatic evolution of the area (**Table 2.1**), and by checking compositional trends towards a hypothetical intrusive source for the mineralizing fluids. Broadly speaking, garnets from mineralized skarn-altered conglomerate lenses in the Watershed area, which formed during prograde and peak metamorphism (i.e. D_{1-2}; **Table 2.1**) have similar compositions to those from strongly reduced tungsten skarns in western North America (Newberry, 1983) and Japan (Shimazaki, 1977). The scheelite-rich skarns in North America are described to be genetically linked to ilmenite series intrusive bodies and show an increase in almandine + spessartine mol% compositions towards a quartz-monzonite causative intrusion (Newberry, 1983). Similarly, at Watershed there is a potential link between the early scheelite-rich, monzonite dykes that were emplaced during D_{1-2} and peak-metamorphic spessartine + almandine rich-garnet that is intergrown with early-stage scheelite in skarn-altered conglomerate **(Figs. 2.9B, 2.10C)**. The observed garnet compositions confirm a possible link between scheelite mineralization and an igneous origin of the mineralizing fluids, which could have caused widespread tungsten enrichment of skarn-altered conglomerate (and to a lesser degree other rock types) in the area. However, due to the present dismembered nature of the skarn lenses, most likely a garnet and/or pyroxene mineral vector towards a monzonite causative source is obliterated, if there was any. Note, however, that a metamorphic origin for the D_{1-2} spessartine-almandine-rich garnets cannot be excluded, since their chemistry is consistent with garnets formed in greenschist facies metamorphic terranes (Atherton, 1964; Baxter et al., 2017).

2.8.3 Structural and lithological control on mineralization: A possibly metamorphic origin for Watershed

Scheelite-rich vein mineralization during D_4 displays strong lithological and structural controls. The majority of scheelite-rich veins are developed in skarn-altered conglomerate, lesser in psammite, associated with shear-zones, and they abruptly terminate where they encounter the less competent slaty units **(Figs. 2.6E, 2.9D)**. This selective development of veins occurred due to a rheology contrast between the more brittle, psammite and skarn-altered conglomerate units, and the far more ductile slaty units **(Fig. 2.8A)**. The distribution pattern of the vein systems may also reflect the tectonic setting in which the fluids originated. Examples of skarn hosted tungsten deposits that formed from fluids released by a causative underlying intrusion (e.g. Los Santos, Spain; Tornos et al., 2008), display widespread stockwork veining across all lithologies. In contrast, veins at Watershed are only developed in incompetent psammite and skarn-altered conglomerate, where they are distributed in a systematic manner **(Fig. 2.7)**. This systematic mechanical protolith control on scheelite-vein formation suggests a likely syn-tectonic and metamorphic origin for the Watershed deposit.

2.8.4 Calcium availability for scheelite formation and sodium availability for possible W transport and deposition mechanisms during D_4

Scheelite in skarn-altered conglomerate is temporal and spatially associated with widespread clinozoisite growth during Retrograde Stage 2. Clinozoisite pseudomorphing and partly replacing garnet **(Fig. 2.10G)** could play an important role in the nucleation of scheelite crystals, considering that clinozoisite contains less calcium than garnet. This retrograde reaction, therefore, will release calcium, which could seed scheelite growth.

The equilibrium between scheelite and sodium-rich plagioclase in the monzonite dykes and in the veins during Retrograde Stage 2 **(Figs. 2.11B, 2.11D; Table 2.1)** suggests that sodium played a role in the transport of tungsten to form the Watershed deposit. There is evidence that WO_4^{2-}, HWO_4^- and $H_2WO_4^0$ are the dominant aqueous species that carry tungsten in ore-forming processes (Wesolowski et al., 1984; Gibert et al., 1992; Wood and Samson, 2000) under hydrothermal conditions, and that tungsten solubility increases in the presence NaCl, NaOH, and KCl suggesting the presence of Na-tungstate and K-tungstate ion pairs like $NaHWO_4^0$ or $NaWO_4^-$ as critical carriers of tungsten (Wood and Vlassopoulos, 1989; Wood and Samson, 2000). The monzonite dykes could represent an initial source of enrichment for sodium and tungsten in the metasedimentary rocks at ca. 350 Ma. Later emplacement of tungsten-poor but sodium-rich granite dykes, provide a further source of sodium enrichment in the rocks, with sodium-rich fluids channelized through D_4 shear zones to be deposited in veins in the form of sodic plagioclase **(Figs. 2.7-2.8)**.

At Watershed, the shift in plagioclase compositions from an early calcium-rich core to later sodium-rich rims **(Figs. 2.11B, 2.11D-E)** may release calcium to combine with calcium released from garnet

replacement by clinozoisite **(Fig. 2.10G)**, to nucleate scheelite. At the same time, scheelite in equilibrium with Na-rich plagioclase suggests that tungsten has been transported as $Na_2WO_4^-$ or more likely $NaHWO_4^0$ (Wood and Vlassopoulos, 1989; Wood and Samson, 2000) since the latter is more stable in pH conditions between 4 and 6, which is a typical pH range of tungsten-mineralizing fluid (Wood and Samson, 2000). Consequently scheelite at Watershed most likely precipitated either by interaction of tungsten-rich fluids with the carbonate-rich ($CaCO_3$) conglomerate as a result of a pH shift that also involved an increase in the calcium activity, possibly in combination with decompression effects resulting from the formation of tension veins during extensional D_4 events.

2.9 Conclusions

1. At Watershed two stages of scheelite mineralization occurred: (a) an early stage at ca. 350 Ma, which occurred in association with monzonite dyke emplacement, when texturally early scheelite and garnet formed during D_{1-2}; and (b) a late stage during D_4 extensional deformation and veining at ca. 275 Ma, which cannot be linked directly to igneous events (in spite of the presence of contemporaneous intrusives), and that shows characteristics of metamorphic deposits similar to lode gold.
2. We propose that economic scheelite mineralization formed during D_4, and resulted from a hydrothermal up-grade of earlier (D_{1-2}) tungsten enrichment in the Watershed area.
3. The main controls on economic mineralization include: (a) D_4 shear-zones; (b) D_4 tension veins, especially those that opened up near shear zones; (c) skarn altered conglomerate units to provide calcium and chemical (pH-controlled) and physical (tension vein-controlled) traps for scheelite deposition; and (d) an extensional setting to allow fluid penetration.
4. Both stages of scheelite mineralization are associated with sodium-rich plagioclase, which suggests that tungsten was most likely transported as $NaHWO_4^0$. The source of Na-bearing fluids is possibly related to the ~350 Ma monzonite and the Permian granite intrusions.
5. Exploration should focus on the identification of ~350 Ma intrusions in association with skarn units, and younger (i.e. D_4) shear zones that formed in an extensional regime. The Permian Whypalla Supersuite possibly acted as a thermal trigger to help remobilize tungsten D_4 along shear-zones to be deposited in extensional veins.

Chapter 3 – Constraining scheelite mineralization with mineral chemistry: An example from the Watershed W deposit, northeast Queesnland, Australia

Abstract

The Watershed tungsten deposit (49.2 Mt averaging 0.14% WO_3) lies in the central part of the Mossman Orogen, which comprises multiply deformed Silurian-Ordovician metasedimentary rocks of the Hodgkinson Formation intruded by Carboniferous-Permian granites of the Kennedy Igneous Association. The Hodgkinson Formation, at Watershed, includes skarn-altered conglomerate, psammite and slate units, which record four deformation events evolving from ductile (D_{1-3}) to brittle ductile (D_4). Tungsten mineralization involved scheelite only, and occurs in several textural positions. Early scheelite is disseminated in D_{1-2} Carboniferous monzonite and in skarn-altered conglomerate, and scheelite grains are aligned within the S_{1-2} fabric. The economic mineralization is associated with late scheelite in skarn-altered conglomerate, and occurs in D_4 veins, vein haloes and associated D_4 shear zones. Whole-rock geochemistry in different rock types at Watershed coupled with trace element geochemistry in scheelite and associated skarn minerals from different deformational events provide information on the origin of the fluids and the redox conditions responsible for mineralization. It also provides information on the geochemical footprint, fingerprint, and element mobility of the Watershed deposit. The different types of mineralisation found at Watershed and associated scheelite compositions, can be differentiated on a ternary REE diagram. Early D_{1-2} scheelite in Carboniferous monzonite, not affected by later alteration, formed in response to magmatic processes and is characterised by enrichment in LREE. Texturally late D_4 scheelite in veins has compositions consistent with a hydrothermal origin characterised by more HREE and more variable REE compositions. The use of REE to differentiate between scheelite types can only be done if the mineral chemistry and interactions of scheelite with surrounding skarn minerals is fully understood. The Sr and Mo contents in scheelite provide additional means to illustrate compositional variability of texturally distinct scheelite grains. The Eu anomalies and Mo contents in scheelite from different textural positions, coupled with graphite inclusions and the presence of pyrrhotite and arsenopyrite, show that D_{1-2} scheelite precipitated from a relatively oxidized fluid, while scheelite in D_4 veins record a shift to more reduced conditions, which suggests an intimate relationship between mineralising fluids and the reduced host-rocks (i.e. carbonaceous shale). The geochemical fingerprint of Watershed is characterized by an enrichment of W-Be-B-Sc-Cu-Mo-Re. This element suite was probably introduced by the hydrothermal fluids. These fluids interacted with the skarn-altered conglomerate to leach REE, Y and Nb plus skarn-related elements (i.e., Ca, F, P, Fe and Sr) and add Rb, Cs and Li in vein haloes. Mineralising fluids promoted the precipitation of scheelite, plagioclase, fluorite, apatite and sulphides in veins and white mica in vein haloes. Based on psammite geochemistry, the regional footprint of the Watershed deposit is characterised by an enrichment in W-Cu-Mo-Ca-Fe-Mn-Li on approaching Watershed. REE geochemistry and enrichment in scheelite in the Carboniferous monzonite suggests that an early mineralisation event occurred at ca. 350 Ma. Our findings indicate that the bulk of the W mineralisation at Watershed was hydrothermal in nature, and formed

during D_4 around 275 Ma. This contrasts with previous models that link scheelite mineralization directly to the emplacement of Permian granites.

3.1 Introduction

The Watershed scheelite deposit is located in northeast Queensland, Australia (16.33°S – 144.86°W) **(Fig. 3.1)**, in a region that hosts significant tungsten and tin deposits (Chang et al., 2017) in addition to orogenic gold (Lisitsin et al., 2014) and placer gold deposits. Watershed has a JORC resource of 49.2 Mt grading at 0.14% WO_3 totaling 70,400 t of WO_3 (cut-off of 0.05% WO_3) (Vital Metals Inc., ASX announcements, 2018), which makes Watershed one of the biggest undeveloped tungsten deposits in the world outside of China. The tungsten deposits in this region have a variable origin and ore mineralogy, and include intrusion related deposits rich in wolframite with minor scheelite (e.g., Wolfram Camp (Plimer, 1974); **Fig. 3.1**), and deposits of metamorphic origin that are rich in both wolframite and scheelite (e.g. Mount Carbine (Cheng et al., 2018); **Fig. 3.1**). All W deposits are hosted by the Silurian-Devonian metasedimentary rock units of the intensely deformed Hodgkinson Formation (Henderson et al., 2013), which were intruded by S-type, granitic bodies of the Whypalla Supersuite (Champion and Bultitude, 2013).

Tungsten deposits can have variable origins. In some cases they originated from highly evolved intrusion-related systems, becoming economically significant when they are associated with greisen systems (quartz + muscovite with minor fluorite, topaz and tourmaline) and/or skarn alteration around S-type intrusions (Pirajno, 2009). Greisen systems are normally associated with enrichment in Sn, W, U, Mo, Be, Bi, Li and F. Tungsten deposits generally remain less significant if the style of mineralization is restricted to veins, replacement ore or breccia pipes (Pirajno, 2009). Tungsten-rich vein deposits associated with granitic rocks usually have a consistent mineral paragenesis (e.g. Wood and Samson, (2000), involving an early 'oxidized' phase rich in wolframite and scheelite (with wolframite >> scheelite) followed by a later sulphide stage or stages. The W-rich stage is usually accompanied by quartz, cassiterite, muscovite, molybdenite, and tourmaline. The later sulphide stage is accompanied by fluorite and carbonates. Usually the sulphides that characterize this stage are pyrrhotite, arsenopyrite and pyrite. Many of the tungsten deposits in north Queensland have been linked to intrusive rocks (Bateman, 1985; de Roo, 1988). Tungsten mineralization and specifically scheelite mineralization, is also common in association with orogenic gold deposits (Bell et al., 1989; Heinrich et al., 1996; Groves et al., 1998). Usually the ore elements in orogenic gold systems include Au, Ag, As, Sb, and W, accompanied with elevated values of B, Bi and Te, which accumulated under low to upper greenschist facies and less commonly lower amphibolite facies conditions (Goldfarb and Groves, 2015), with different element suites developed at different depths. This shows that Au and W can be mobilized together in active orogenic terrains. Some orogenic Au systems are enriched in scheelite to the extent that they have been mined for W, e.g. the Glenorchy deposit in the Otago schist belt in New Zealand (Henley et al., 1976). In north Queensland,

several Au-lode systems contain scheelite (Peters et al., 1990), indicating that here too scheelite has been mobilized by hydrothermal fluids during orogenic events.

Scheelite ($CaWO_4$) can incorporate many elements in trace levels. Rare earth elements (REE's) and large ion lithophile elements (LILE's: e.g., Sr, Pb, Ba) can enter the scheelite structure by replacing Ca, whilst Mo^{6+} and high field strength elements (HFSE's: e.g., Nb, Zr? Ta?) can replace W. Molybdenum as well as Fe-Mn can enter the scheelite structure in solid solution series with powellite ($CaMoO_4$), or wolframite ($(Mn, Fe)WO_4$) (Ghaderi et al., 1999). The elemental replacements can provide insights into the origin of the ore forming processes (Ghaderi et al., 1999; Song et al., 2014; Sun and Chen, 2017), and are dependent on the composition of the host-rock, metasomatic fluid, redox conditions and coexisting mineral phases (Guo et al., 2016). In particular REE's may record the chemistry of the mineralising fluid from which scheelite formed (Ghaderi et al., 1999). For instance it has been suggested that scheelite formed in granitic, skarn or orogenic environments preserve characteristic relative abundances of light (LREE), middle (MREE) and heavy (HREE) REE (Song et al., 2014; Fu et al., 2017). Song et al. (2014) and Fu et al. (2017) found that intrusion-related skarn and porphyry-related scheelite are enriched in LREE. In contrast, scheelite formed in association with Au-lode deposits show enrichment in MREE and HREE (Ghaderi et al., 1999; Roberts et al., 2006; Dostal et al., 2009; Hazarika et al., 2016; Raju et al., 2016; Cave et al., 2017).

The aim of this contribution is to describe the different scheelite types at Watershed, and use scheelite trace element geochemistry to investigate if scheelite grains that grew at different times and in different textural positions can be differentiated on the basis of REE and Mo content, or any other trace element discriminators. Whole-rock geochemistry from different rock-types and skarn minerals trace element geochemistry will be used to corroborate if scheelite originated from an externally derived hydrothermal fluid (fluid buffered) or from fluids generated locally by devolatilization (Phillips and Powell, 2010) of the surrounding host rock types (rock buffered). It will be shown that scheelite mineralization at Watershed has at least two different origins that may or may not be related: (1) early magmatic hydrothermal scheelite, which is overprinted by (2) hydrothermal scheelite with a metamorphic origin.

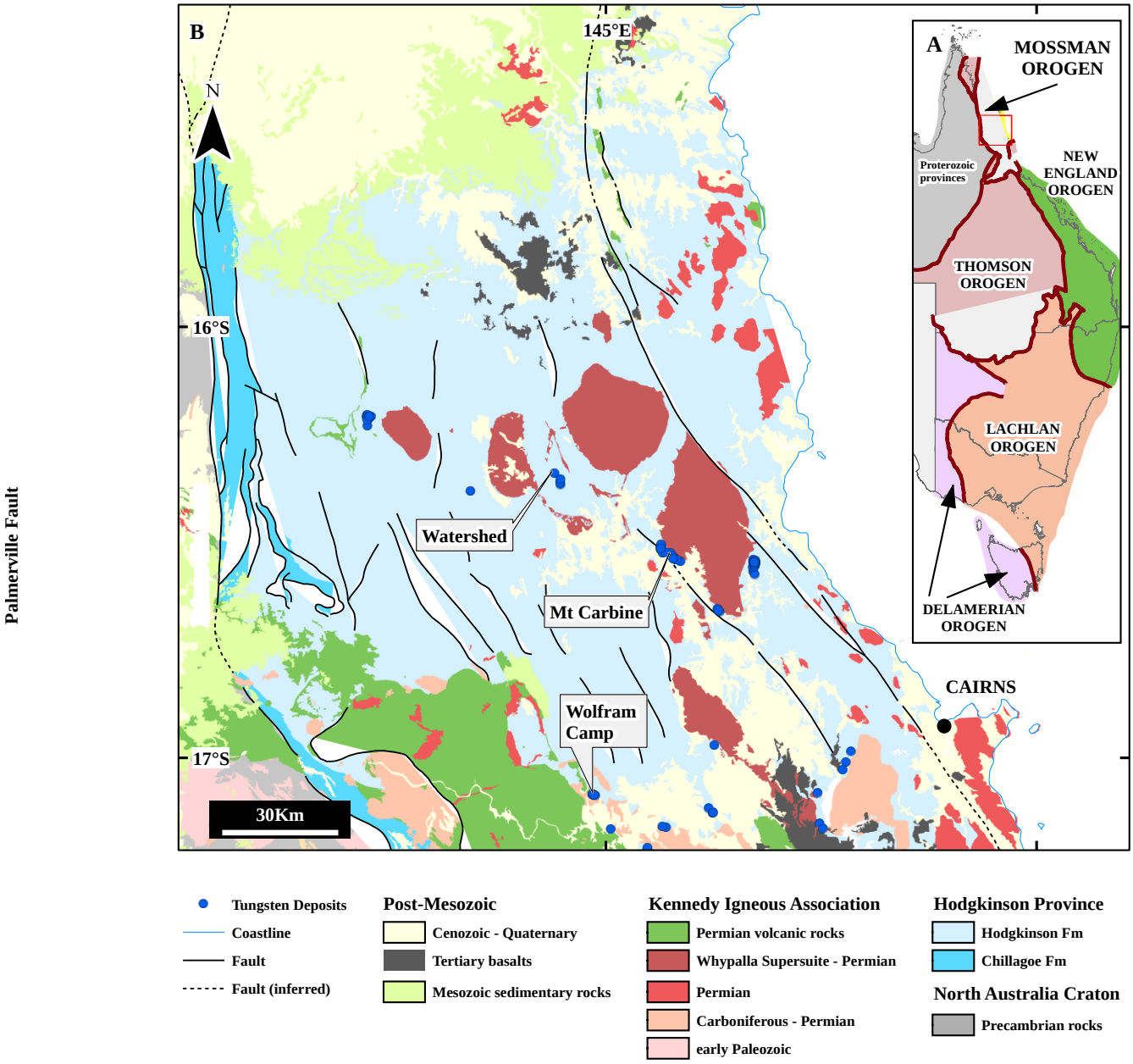

Figure 3.1 Regional geological setting of the Watershed deposit in northeast Queensland. **A.** Different orogens of eastern Australia. The red square is enlarged in **Figure 3.1B**. **B.** Geology of the Hodgkinson Province. The Permian volcanic rocks (green) and the Carboniferous-Permian (light orange) rocks of the Kennedy Igneous Province crop out to the south of the Hodgkinson Province. These rocks separates the Hodgkinson Province to the north from the Broken River Province to the south. Watershed is hosted by the Hodgkinson Formation and surrounded by S-type granites and syenogranites of the Permian Whypalla Supersuite (dark red). Other important tungsten deposits are shown in the map (blue dots), which are hosted by the Hodgkinson Formation.

3.2 Geological setting

3.2.1 Regional Setting

The Watershed deposit is located in the central part of the Mossman Orogen, which is a late-Paleozoic active margin system abutting the North Australian craton, from which it is separated by a major fault zone called the Palmerville Fault **(Figs. 3.1A-B)**. The Mossman Orogen comprises the Silurian and Devonian Hodgkinson and Broken River provinces, which form a belt 500 km long and up to 200 km wide, and are fault-bounded by the Thomson Orogen to the south and the New England Orogen to the southeast (Donchak et al., 2013; Fergusson and Henderson, 2013) **(Fig. 3.1A)**. The Mossman Orogen largely consists of multiply deformed sedimentary successions interpreted as turbiditic sequences with minor intercalations of mafic volcanic rocks and chert, deposited in a deep-marine environment (Henderson et al., 2013). The Hodgkinson and Broken River provinces are separated by Carboniferous to Permian granitoids of the Kennedy Igneous Association (Champion and Bultitude, 2013). Watershed is hosted by rocks of the Hodgkinson Province.

The northern portion of the Mossman Orogen comprises the Silurian to early Carboniferous Hodgkinson Formation (Adams et al., 2013; Kositcin et al., 2015), which comprise alternating sandstone-mudstone beds that are locally interbedded with greywacke units and rare intercalations of chert, volcanic rocks, limestone and polymictic conglomerate (Amos, 1968; de Keyser and Lucas, 1968). The Hodgkinson Formation is in contact to the west with the Silurian-Devonian Chillagoe Formation, which forms a narrow (2-5 km wide), north-south trending zone that runs for over ~250 km parallel to the Palmerville Fault **(Fig. 3.1B)**. The Chillagoe Formation comprises sandstone, limestone, chert, and mafic volcanic rocks, with minor mudstone, conglomerate and breccia, deposited in a shallow-marine shelf environment (Amos, 1968). Field relations and sedimentary characteristics indicate that the western and eastern portions of the Hodgkinson Formation represent the respective proximal and distal facies on a sub-marine fan delta system (Amos, 1968). The rocks of the Hodgkinson Formation are interpreted by Henderson (2013) to have formed in a fore-arc environment with rocks of the Pama Igneous Association (Withnall and Hutton, 2013) to the west representing a contemporary magmatic arc.

The Hodgkinson Formation has undergone intense deformation and regional metamorphism. On a regional scale, four deformation events, D_1 to D_4, have been recognized (Davis, 1993; Henderson et al., 2013). D_1 events are Devonian in age and coincided with peak metamorphism at low- to mid-greenschist facies in the southwest, grading to upper-greenschist facies in the northeast. D_1 is commonly represented by a bedding-parallel slaty cleavage and variably plunging, mesoscale isoclinal folds. D_2 is related to large-scale folds with wavelengths of several kilometers that formed during Devonian to early Carboniferous compressional events (Henderson et al., 2013). D_3 is represented by a penetrative crenulation cleavage best developed in aureole zones of Permian granitoids, and considered to have formed as a sub-horizontal cleavage during early Permian extension (Davis and Henderson, 1999). Structures assigned to D_4 are more localized and variable in nature,

and tend to be co-planar with D_2 structures making their recognition difficult. D_4 is linked to mesoscopic folds and associated with a north-south trending crenulation cleavage best developed near Permian granitoid plutons (Davis et al., 2002), and linked to compressional events during the late-Permian.

The rocks of the Hodgkinson Formation were intruded by late Carboniferous to Permian granites assigned to the Kennedy Igneous Association (Champion and Bultitude, 2013) **(Fig. 3.1B)**. In the northern portion of the Hodgkinson Province, these intrusions are represented by ~4,000 km^2 of outcrop of mainly Permian S-type and minor I-type granites assigned to the Daintree Sub-province (Mackenzie and Wellman, 1997). These intrusive rocks were emplaced along a northwest trend in the central part of the Hodgkinson Province, which coincides with a major crustal dislocation called the Desailly Structure (Davis et al., 1998). Intrusive rocks assigned to the Daintree Sub-province have been further subdivided based on geochemical characteristics (Bultitude and Champion, 1992). Thus, Watershed is surrounded by S-type granites assigned to the early Permian Whypalla Supersuite **(Fig. 3.1B)**, which were emplaced during D_4 (Davis, 1993) around 285-260 Ma (Champion and Bultitude, 2013). The granites of the Whypalla Supersuite are porphyritic to equigranular and include muscovite-biotite syenogranite and monzogranite with rare granodiorite (Bultitude and Champion, 1992).

3.2.2 Near mine Geology

The rocks around the Watershed deposit consist of metasedimentary units of the Hodgkinson Formation, and comprise psammite, polymict (skarn-altered) conglomerate, slate and slate-siltstone breccia units, with minor quartzite and rare chert **(Figs. 3.2-3.3)**. Psammite, with its minor variations, is the most common rock type within the Watershed deposit **(Fig. 3.3A)**. It is typically light to dark grey in colour and composed of small (<2 mm) angular to sub-rounded quartz grains (45 vol.%), euhedral to subhedral plagioclase grains (40 vol.%), and minor (5 vol.%) fine-grained biotite. Matrix grains consist of fine-grained quartz, plagioclase, biotite and muscovite. In some places, this rock type is strongly fractured and deformed, which is also evidenced by dynamic crystallization of framework grains. The polymictic skarn-altered conglomerate **(Fig. 3.2)** occurs interlayered with psammite, as isolated pod-like bodies and layer fragments, up to 15 m in width and tens of meters in length. This rock type includes pebbles that exhibit a skarn mineralogy **(Chapter 2, Fig. 3.3B)**. Clasts vary in size from 3 to 30 cm and are generally sub-rounded. They are fine- to medium-grained and contain variable amounts of carbonate, quartz, garnet, pyroxene and clinozoisite. The matrix surrounding the skarn-altered pebbles is green-grey and consists mainly of quartz, clinozoisite, garnet, minor pyroxene, feldspar and muscovite, with accessory carbonate, biotite, titanite, scheelite and pyrrhotite **(Table 3.1)**. The conglomerate unit is the main host for vein and disseminated scheelite mineralization **(Figs. 3.2B-C).** A few quartzite beds occur dispersed within the psammite unit **(Figs. 3.2B-C)**, and are composed of a medium-grained, dark grey

rock dominated by 2-5 mm large, sub-rounded quartz grains (>70 vol.%), with minor biotite and feldspar **(Fig. 3.3C)**.

Slate and slate-siltstone breccia units are widespread within the Watershed area **(Fig. 3.2A)**. Foliated slate occurs as massive units and interbedded with 0.5 to 20 cm thick siltstone layers **(Figs. 3.2B-C)**. The slate-silstone breccia is typically composed of isolated fragments (10-90 vol.%) of sandstone (psammite) **(Fig. 3.3D)** and siltstone that are 0.5 to 5 cm in size and set in a strongly foliated, dark grey matrix of mudstone (slate) defining an intense linear fabric **(Fig. 3.3D)**. Thinly banded, black to grey chert beds form a minor unit within the slate-siltstone breccia zones.

The sedimentary rocks at Watershed are strongly deformed with intense folding, and at least three penetrative foliations best developed in the slate and slate-siltstone breccia **(Figs. 3.2B-C)**. In psammite and conglomerate units the same deformation events caused extension along layering, resulting in isolated boudins, boudin trails and layer segments enveloped by slate and slate-siltstone breccia units **(Fig. 3.2A)**. Primary layering, S_0, is generally destroyed in fine-grained slate units and slate-siltstone breccia, but is locally preserved within boudins of psammite, or as layer segments of conglomerate. The semi-continuous boudin trails of skarn-altered conglomerate also provide evidence for primary layering **(Fig. 3.2A)**. D_1 and D_2 (D_{1-2}) events coincided with peak metamorphism **(Table 1)** and involved complete, and probably repeated, transposition of the primary layering associated with upright isoclinal folding, and the formation of a penetrative, steeply southwest dipping foliation, S_1/S_2 **(Chapter 2)**. D_3 deformation is represented by cm- to km-scale tight to open, upright folds, which fold the S_1/S_2 transposition fabric. D_3 folds are locally associated with a near-vertical, north-northwest-trending axial planar crenulation cleavage (S_3) **(Chapter 2)**. The S_3 foliation intensifies along a north-south trending D_3 high strain zone directly east of Watershed. D_4 events involved the formation of shear zones that cut and displace the dominant ductile D_1 to D_3 fabrics. The shear zones are generally narrow (< 10 cm) brittle-ductile shears, with a major D_4 shear zone occurring along the D_3 high strain zone east of Watershed, where it is associated with a steeply plunging, near down-dip lineation **(Fig. 3.2A)**. Around Watershed, the D_4 shear zones display a wide variety of orientations, but generally parallel the main north-northwest to north-south trending ductile S_{1-2} fabric. The larger (i.e. wider) shear zones are near vertical **(Figs. 3.2B-C)**, and generally record a dextral sense of movement. Numerous smaller fractures and shears that formed as secondary structures to major shears, display a greater variation of orientations; and a normal movement sense is common. The shear zones are spatially associated with the economic scheelite mineralization in D_4 veins and as alteration zones in places where they transect skarn-altered conglomerate **(Chapter 2)**.

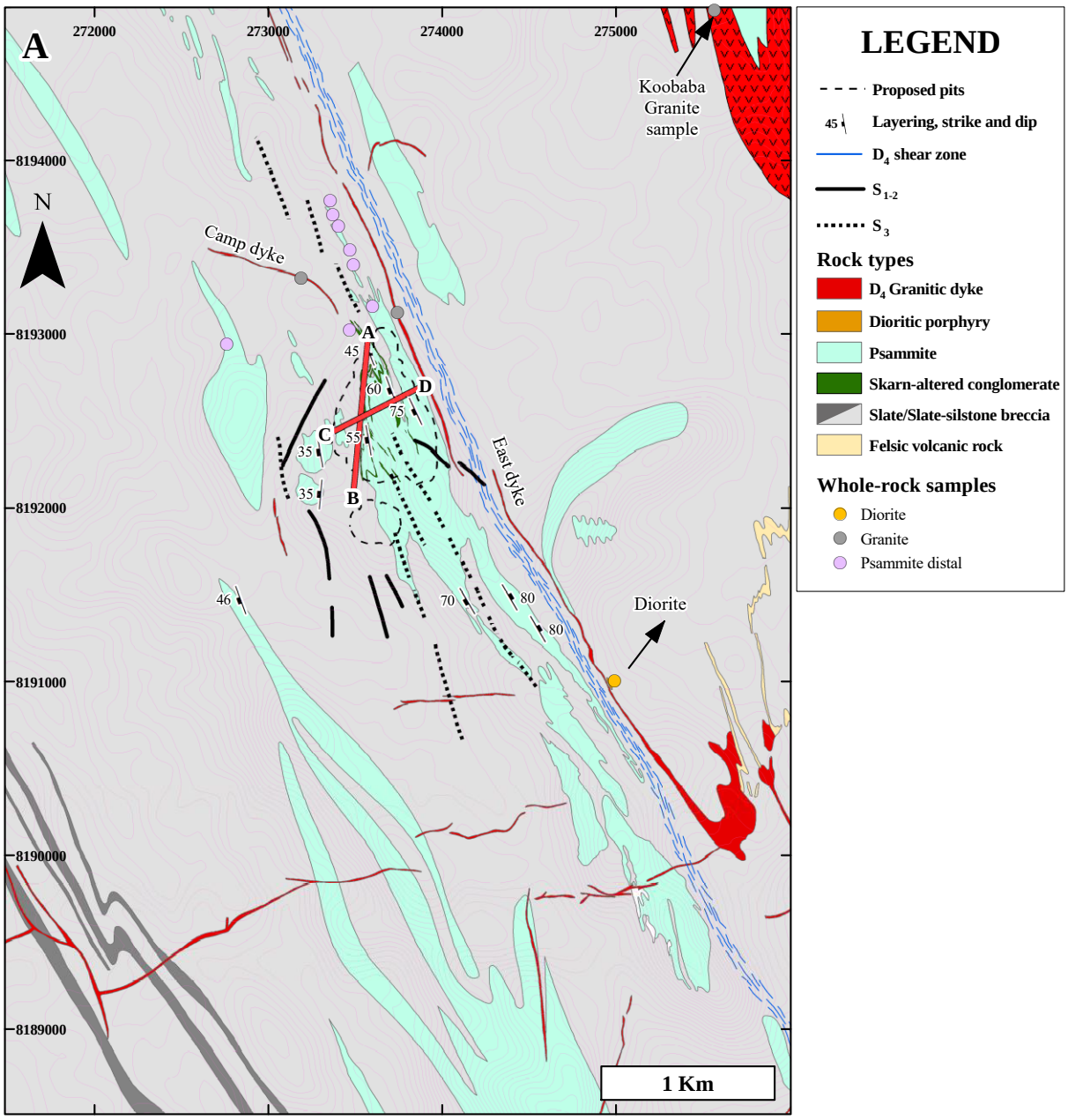

Figure 3.2 Generalized geologic map and cross-section of the Watershed deposit showing whole-rock geochemistry samples location. **A**. Generalized geological map of the Watershed deposit with surface sample location for whole-rock geochemistry. Base map from Skrzeczynski and Wood (1984). The red lines in the map denotes the long- and cross-sections, respectively, in **B** and **C.** The grid system is Geocentric Datum of Australia 1994 (GDA94), zone 55.

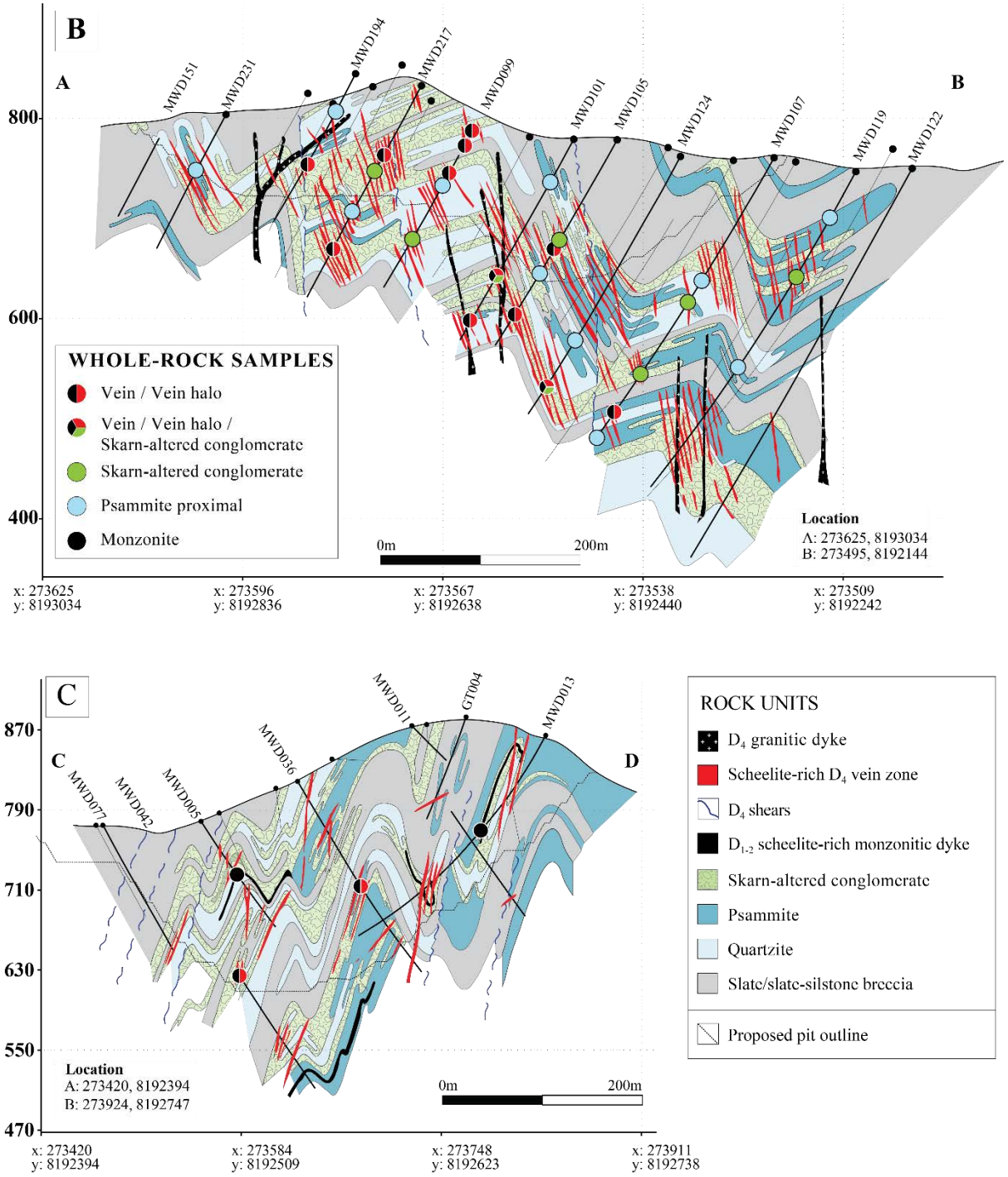

Figure 3.2 (cont) **B.** Long section (A-B in **Fig. 3.2A**) of the Watershed deposit with whole rock geochemistry samples. **C.** Cross section (C-D in **Fig. 3.2A**) of the Watershed deposit with whole rock geochemistry samples.

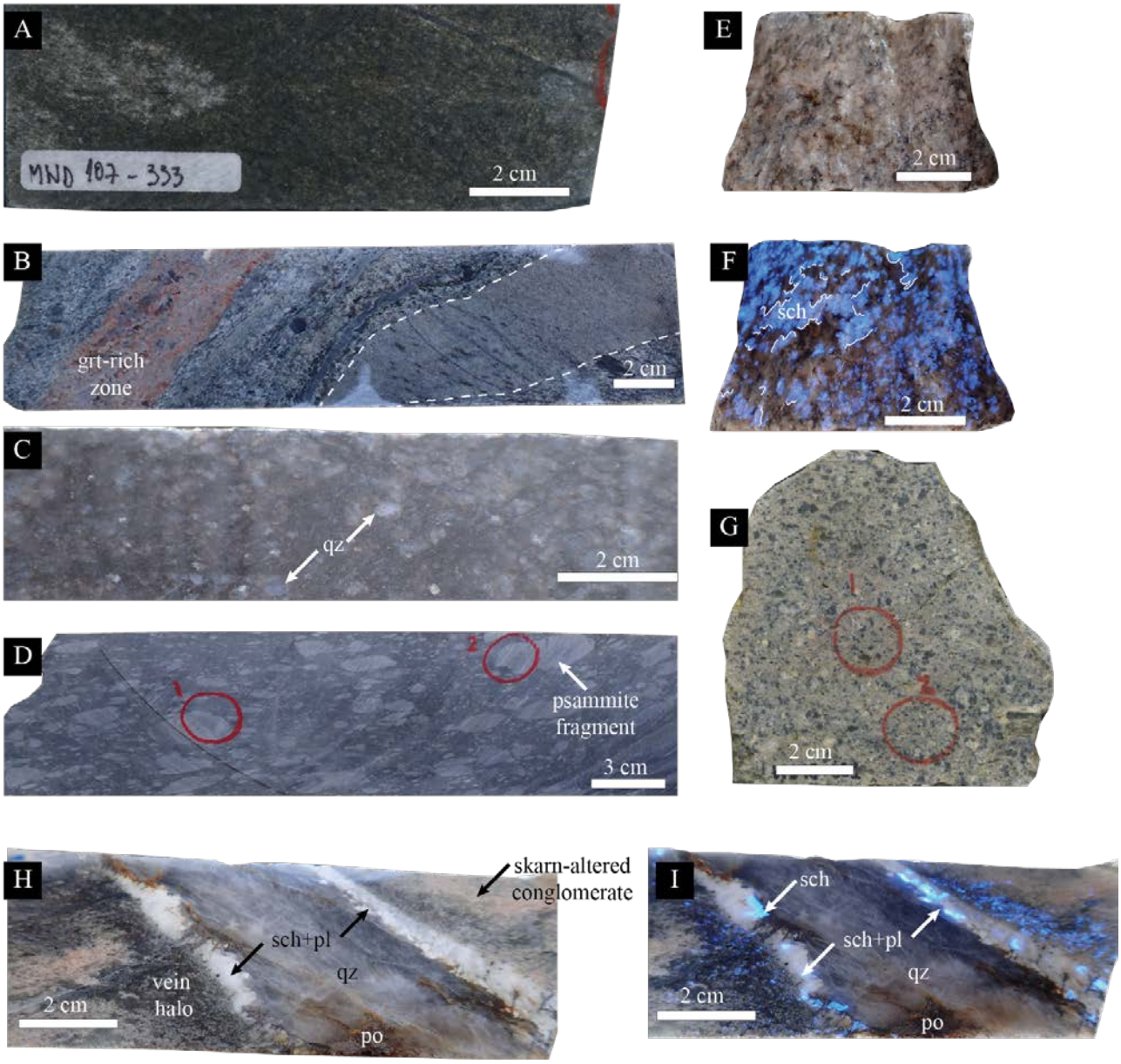

Figure 3.3 Hand specimens samples photographs of the different rock types at the Watershed deposit. Sample ID in parenthesis **(**for sample locations check **Figs. 2A-2C) A.** Psammite from hole **MWD107** at **333 m. B.** Skarn-altered conglomerate from hole **MWD107** at **256 m**. The reddish zone corresponds to garnet-rich (grt) zone and dashed line denotes a conglomerate clast. **C.** Quartzite from hole **MWD099** at **150** m, where quartz grains (qz) are indicated by the arrows. **D.** Slate/siltstone with fragments of psammite (arrow in image) from hole **MWD107** at **035** m. **E.** Carboniferous monzonite from hole **MWD013** at **99** m. **F.** Same Carboniferous monzonite from **Figure 3.3E** under ultra violet (UV) light showing blue fluorescent (Mo-poor) scheelite affected by $S_{1\text{-}2}$ fabric (few white traced lines for reference). **G.** Barren Permian granite. Sample taken from the East Dyke **(WS15-001, Fig. 3.2A)**. **H.** D_4 scheelite-rich quartz-plagioclase vein from hole **MWD107** at **259** m, with associated dark vein halo, cutting skarn-altered conglomerate. **I.** Same as **Figure 3.3H**, under UV light showing scheelite (sch) mineralization associated with plagioclase in vein margin (sch+pl) and in dark vein alteration halo, cutting reddish skarn-altered conglomerate. A late quartz (qz) vein is cutting the central part of the vein after extensional vein opening. Subsequent pyrrhotite (po) fracture-filling is cross-cutting the quartz vein **(Table 3.1)**. Mineral abbreviations after Whitney and Evans (2010).

Table 3.1 Mineral paragenesis table for the Watershed tungsten deposit. From **Chapter 2.**

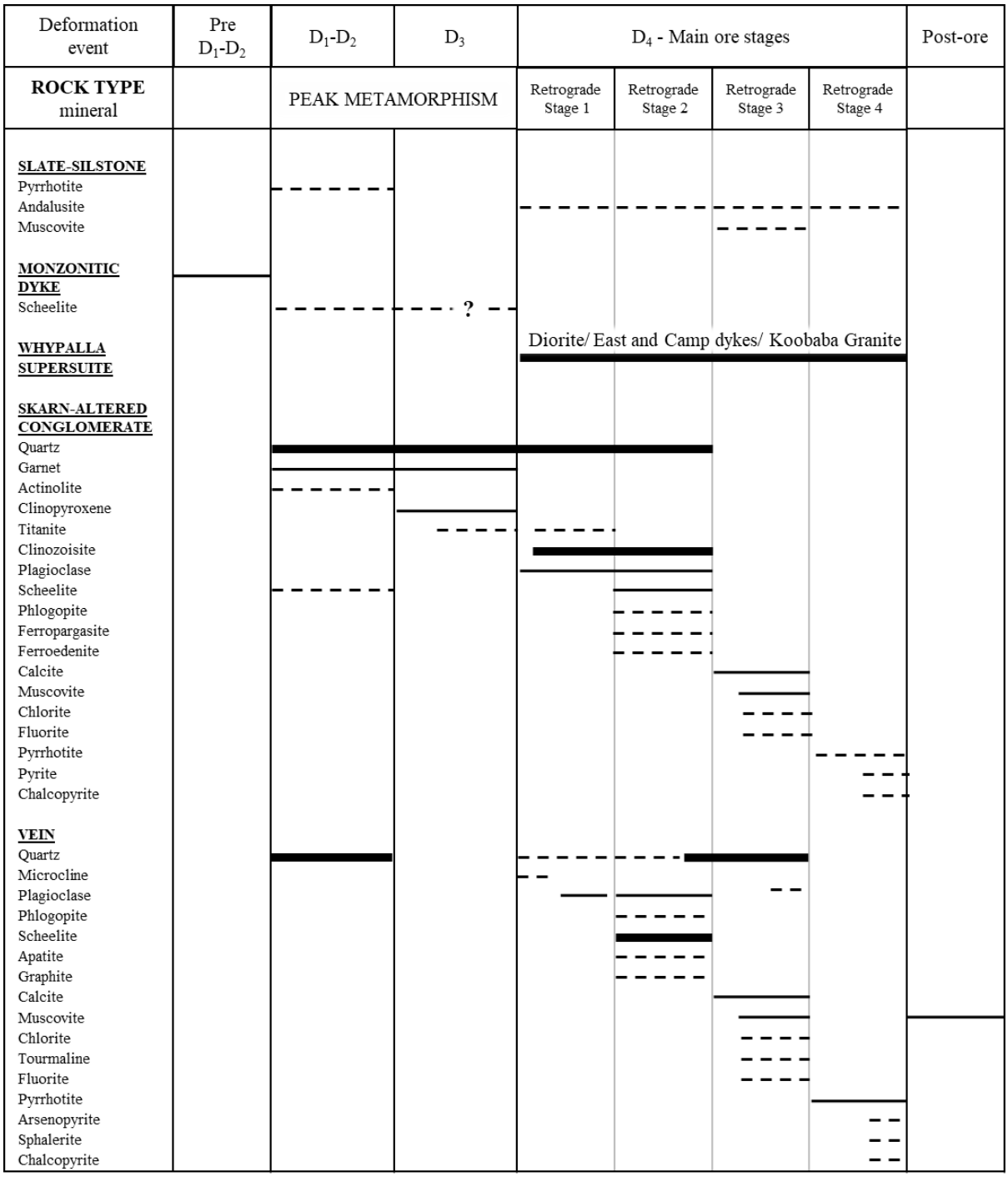

The metasedimentary rocks at Watershed were intruded by a series of Carboniferous and Permian dykes assigned to the Whypalla Supersuite **(Chapter 2)**. The oldest suite of dykes are Carboniferous (ca. 350 Ma) in age and monzonitic in composition **(Chapter 2)**. They have not been found on surface, but can be seen in drill core where they occur as narrow (<40 cm wide) dykes of dark to light grey color, which contain a foliation (S_{1-2}), indicating that they were emplaced early in the deformation history of the area **(Figs. 3.2C, 3.3E-F)**. The dykes are composed of 45 vol.% subhedral to euhedral plagioclase (<0.5 mm), 35 vol.% subhedral k-feldspar (< 0.5 mm) and ~5 vol.% anhedral quartz. Mafic minerals correspond to ~5 vol.% of the rock and consist entirely of subhedral biotite (<0.5 mm) **(Fig. 3.3E)**. These dyke segments are important for mineralization, because they contain 10-15 vol.% scheelite crystals, most of which are deformed, partly resorbed and strongly fractured **(Fig. 3.3F; see next section).** Younger, Permian dykes (ca. 291-277 Ma) are granitic in composition, and outcrop in the Watershed area **(Chapter 2, Figs. 3.2A-B)**. The older East dyke (ca. 291 Ma) preserves a ductile fabric suggesting it may be emplaced during the latest stages of D_3 or the earliest stages of D_4, whereas the younger Camp dyke (ca. 277 Ma) cuts-across all fabrics and is undeformed **(Chapter 2)**. The granite dykes vary in width from 0.5 m to several tens of meters, and can be traced along strike for hundreds of meters. They include coarse porphyritic **(Fig. 3.3G)** to fine-grained varieties. In the porphyritic dykes, the phenocrysts vary from 40 to 50 vol.%, with 45 vol. % k-feldspar, 45 vol.% quartz and 10 vol.% plagioclase. The groundmass is composed of equal amounts of fine-grained quartz, k-feldspar and muscovite. A small diorite body (ca. 281 Ma) **(Chapter 2)** occurs about 2 km southeast of Watershed, as an elongated body that parallels the East granitic dyke **(Fig. 3.2A)** over a short distance. The groundmass is dark grey and contains ~50 vol.% euhedral plagioclase (<2 mm) phenocrysts. Thin quartz with minor scheelite veinlets cross-cut this rock type.

3.2.3 Scheelite textures

Tungsten mineralization at Watershed consists of scheelite only. Scheelite occurs in several forms in variable textural positions associated with different rock types and veins **(Figs. 3.3F, 3.3H-I, 3.4A-D)**. Early scheelite crystals are found disseminated in Carboniferous monzonite dykes **(Fig. 3F)** and in skarn-altered conglomerate, and occur aligned within the S_{1-2} fabric **(Table 3.1; Fig. 3.4C)**. Most of the economic mineralization is associated with texturally late scheelite, which occurs in D_4 veins and vein haloes **(Figs. 3.3H-I)**, and in stringers associated with D_4 shears cutting across the skarn-altered conglomerate **(Table 3.1; Fig. 3.4D)**. Early and late scheelite grains show, in some cases, complex zoning patterns that can be recognized under cathodolumenescense (CL) **(Fig. 3.4A).**

3.2.3.1 Texturally early scheelite

Early scheelite, disseminated in the ca. 350 Ma monzonitic dyke includes deformed crystals, up to 1 cm in diameter **(Chapter 2, Figs. 3.3F, 3.4B)**. These scheelite crystals are aligned in S_{1-2} and are interpreted to have formed or recrystallized during D_{1-2} deformation events. Scheelite in monzonite has a broken appearance with

abundant internal fracturing. It is usually intergrown with oligoclase (sodium-rich plagioclase) **(Chapter 2, Fig. 3.4B; Table 3.1)**. Oligoclase also occurs between broken scheelite fragments.

Early scheelite grains in skarn-altered conglomerate have variable sizes (usually <5 mm), are aligned within the $S_{1\text{-}2}$ fabric, and are usually intergrown with $D_{1\text{-}2}$ garnet, which formed during peak metamorphism **(Table 3.1; Fig. 3.4C)**. In some places, they have a broken appearance with resorbed margins, and no particular CL patterns have been observed.

3.2.3.2 Texturally late scheelite

Texturally late scheelite was deposited at ca. 275 Ma in quartz-feldspar veins that are spatially associated with D_4 brittle-ductile shear zones **(Chapter 2, Figs. 3.3H-I)** during retrograde metamorphism **(Table 3.1)**. The formation of the major mineralized veins during D_4 involved at least four separate retrograde stages **(Table 3.1)**, with scheelite formation occurring mostly during Retrograde Stage 2 of vein opening, which coincided with deposition of sodium-rich plagioclase (oligoclase) **(Fig. 3.4D)**, minor quartz and phlogopite, and trace graphite and apatite **(Chapter 2, Table 3.1)**.

Late scheelite crystals in D_4 veins show variable textures and shapes, with grains generally <2 cm in length **(Fig. 3.3I)**. Larger scheelite crystals (up to 4 cm in length) locally occur in the central parts of the veins and are commonly fractured and boudinaged, with quartz filling the interstitial space between displaced scheelite fragments. The boudinaged shapes suggest that scheelite grew synchrounously with the deformational events that led to the formation of the tension veins at Watershed. Similarly to scheelite grains in monzonite dykes, some scheelite in veins shows textural variations under CL in which cores, growth zoning and later overgrowths can be observed; however not all scheelite grains in veins show zonation patterns.

Late D_4 scheelite mineralization also occurs along D_4 shears and in alteration haloes to both veins **(Figs. 3.3I, 3.4D)** and shears. This scheelite type varies in size from a few microns to ~1 mm in length. The late D_4 scheelite crystals from vein alteration haloes typically exhibit a broken appearance with boudinaged shapes intergrown with plagioclase **(Fig. 3.4D)**, phlogopite and minor quartz. It is also spatially associated with para-genetically later, fine-grained muscovite formed during Retrograde Stage 3 **(Table 3.1).** These types of scheelite grains commonly preserve complex textures and growth zoning under CL.

D_4 scheelite is also found in quartz-scheelite veinlets and stringers cutting skarn-altered conglomerate. This scheelite is finer grained than $D_{1\text{-}2}$ scheelite, and is constrained to the stringer margins. In some places D_4 scheelite in skarn-altered conglomerate is found as fracture fill in broken garnet grains associated with clinozoisite **(Fig. 3.4E; Table 3.1)**. Under CL no zoning was observed in D_4 scheelite hosted in skarn-altered conglomerate.

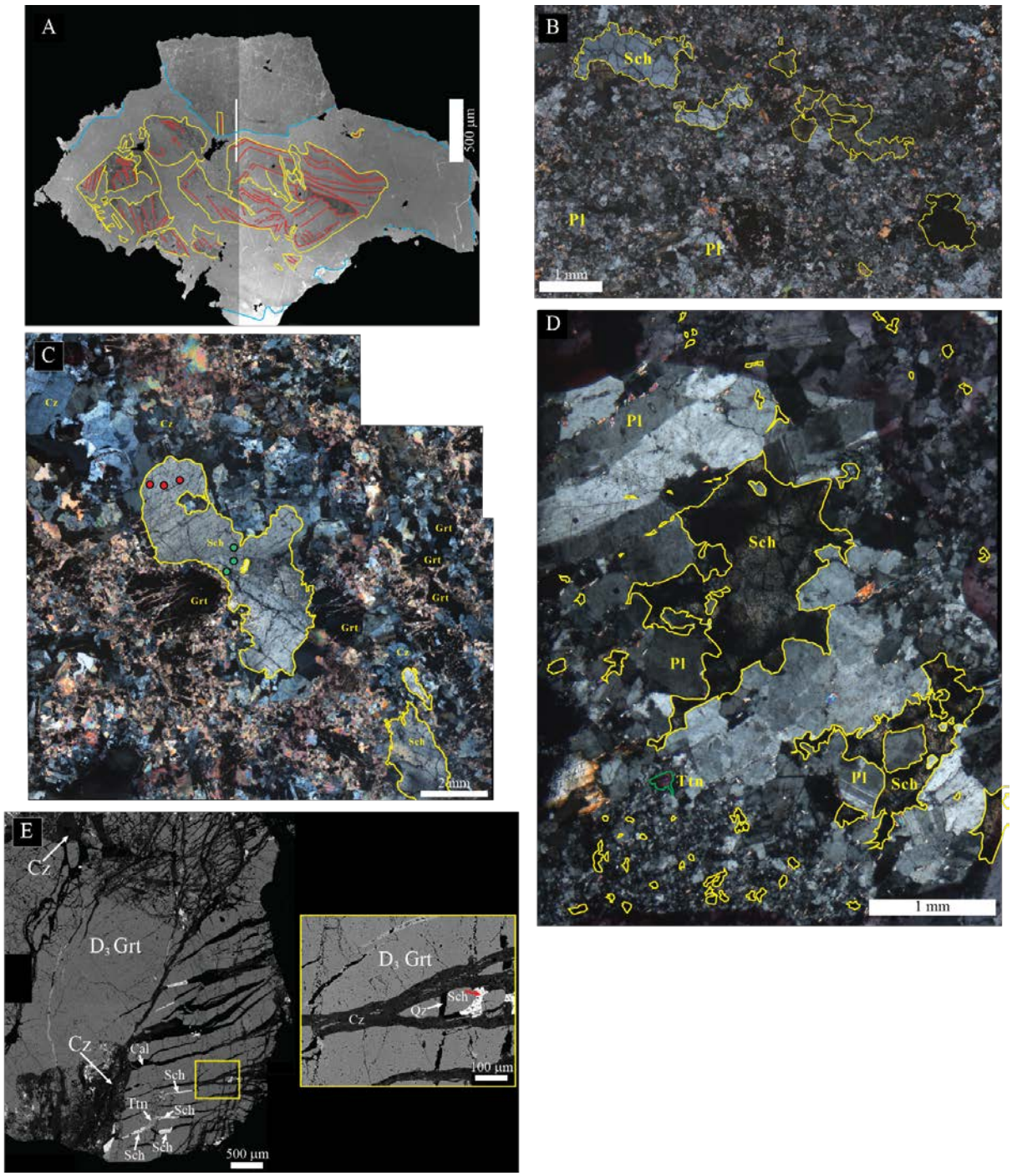

Figure 3.4 Cathodoluminesce (CL), microphotographs and back-scattered electron (BSE) images of the different timing and style of mineralization of scheelite at Watershed. See **Appendix 1.1** for samples location. **A.** Example of CL image of a scheelite crystal from sample mount **MWD099-163.5** showing a complex, multi-staged growth zoning and alternating grain fragmentation patterns. A broken core (yellow) with growing zones (red). Blue lines are limit of late growing zones (unstructured overgrowth). **B.** $D_{1\text{-}2}$ scheelite (Sch) in monzonitic dyke **(MWD013-099)**. Scheelite is surrounded by plagioclase (Pl). **C.** $D_{1\text{-}2}$ scheelite (Sch) in skarn altered conglomerate **(MWD011-147.5A)**, intergrown with $D_{1\text{-}2}$ garnet (Grt) and spatially associated with D_4 clinozoisite (Cz) after garnet. Minerals are aligned along the $S_{1\text{-}2}$ fabric. Green circles represents core spots and red circles are margin spots during LA-ICP-MS trace element analysis. **D.** D_4 scheelite (Sch) and plagioclase (Pl) in vein and vein haloes **(MWD122-289B)**. Minor titanite (Ttn) and muscovite are also noted in vein halo. **E.** Fractured D_3 garnet (Grt) cross-cut D_4 quartz (Qz), clinozoisite (Cz), scheelite (Sch), titanite (Ttn) and calcite (Cal) assemblage **(MWD042-197A)**. Detailed image on the top right corner corresponds to the yellow rectangle on the image on the left. This image illustrates the complex cross-cutting relationship in skarn altered conglomerate during D_4. Mineral abbreviations after Whitney and Evans (2010).

3.3 Sampling strategy and analytical methods

3.3.1 Sampling for whole-rock geochemistry

A total of sixty-two samples from monzonite and granite dykes, diorite porphyry, scheelite-bearing veins, alteration zones adjacent to veins (referred to as vein haloes or proximal skarn-altered conglomerate), skarn-altered conglomerate, and psammite **(Figs. 3.2A-C)** were analyzed for whole-rock geochemistry at Bureau Veritas Laboratories in Vancouver, Canada. Sample locations and full results are presented in **appendices 1.1 and 3.1**, respectively, with a summary of relevant statistical results provided in **Table 3.2**. Two samples of $D_{1\text{-}2}$ monzonite dykes from drill core **(Figs. 3.3E-F)**, three samples of $D_{3\text{-}4}$ granite **(Fig. 3.3G)** and one of D_4 diorite porphyry **(Fig. 3.2A)** were collected from outcrop. Fourteen samples of D_4 scheelite-rich quartz-plagioclase veins were taken from drill core and a further fourteen samples of vein halo were selected from the margins of the same veins. Since the D_4 scheelite-rich quartz-feldspar veins generally crosscut skarn-altered conglomerate, the vein halo samples represent altered or modified skarn-altered conglomerate **(Figs. 3.3H-I)**. In addition, eight samples of skarn-altered conglomerate away from mineralized veins were taken from drill core. In this context, the skarn-altered conglomerate samples are considered distal to mineralized veins, whereas the vein halo samples are considered proximal to vein mineralization. Twenty samples from psammite were collected at Watershed; nine samples from surface and eleven samples from drill core **(Figs. 3.2A-B)**. The samples taken from drill core were taken at different depths and have been grouped as 'psammite proximal'**.** The surface samples were taken along a 750 m long, N-S orientated transect, ~1 km north of Watershed; with each sample taken at approximately one hundred meter intervals. These psammite samples have been grouped as 'psammite distal'.

3.3.2 Procedures for whole-rock geochemistry

Prior to geochemical analysis the rock samples were crushed and finely milled to powders and then mixed with $LiBO_2$ / $Li_2B_4O_7$ flux and fused in a furnace. The cooled beads were dissolved in ACS grade nitric acid and analysed by ICP-OES and/or ICP-MS. For the analysis of ultra-trace elements, the prepared samples were digested with a modified Aqua Regia solution of equal parts concentrated HCl, HNO_3 and de-ionized H_2O for one hour in a heating block or hot water bath. The sample solution was then made up to volume with dilute HCl. Loss on ignition (LOI) was determined by heating a sample split, and then measuring the LOI.

FeO concentrations were determined by titration method. Samples were first digested with sulfuric acid (H_2SO_4), allowed to cool, and then digested with hydrofluoric acid. An indicator solution consisting of distilled water, sulfuric acid, phosphoric acid, boric acid and diphenylamine sulfonate was added to every sample solution. The solutions were then titrated using a standard dichromate ($K_2Cr_2O_7$) solution.

Table 3.2 Summary of whole-rock geochemistry results.

Rock type	Monzonitic dyke n = 2					Vein n = 14				
Element	**Average**	**Std Dev**	**Median**	**Min**	**Max**	**Average**	**Std Dev**	**Median**	**Min**	**Max**
SiO_2_%	44	8	44	36	52	81	17	86	49	99
Al_2O_3_%	18	2	18	16	20	3	4	2	0.09	12
Fe_2O_3_%	2	0.8	2	1	3	1	0.6	0.8	0.4	2
MgO_%	0.4	0.2	0.4	0.2	0.7	0.03	0.05	0.01	0.01	0.2
CaO_%	9	3	9	6	12	5	5	3	0.1	16
Na_2O_%	5	1	5	4	7	0.8	1	0.7	0.01	4
K_2O_%	1.1	0.5	1	0.6	2	0.1	0.2	0.05	0.01	0.7
TiO_2_%	0.3	0.01	0.3	0.3	0.3	0.01	0.01	0.01	0.01	0.04
P_2O_5_%	0.25	0.1	0.2	0.1	0.4	0.03	0.04	0.02	0.01	0.16
MnO_%	0.1	0.02	0.05	0.03	0.1	0.1	0.1	0.01	0.01	0.3
LOI_%	2	0.3	2	1.8	2.3	1.3	2	0.5	0.00	7
Ba_ppm	169	60	169	109	228	48	83	16	3	319
Sc_ppm	46	17	46	29	62	16	20	7	1	61
Cs_ppm	16	7	16	9	24	4	4	3	0.1	14
Hf_ppm	3.5	0	3.5	3.5	3.5	0.1	0.0	0.1	0.1	0.2
Nb_ppm	17	3	17	15	20	9	26	1	0.1	103
Rb_ppm	76	36	76	40	112	9	8	5	0.1	28
Sn_ppm	47	4	47	43	50	16	51	2	0.5	200
Sr_ppm	441	13	441	428	453	79	90	46	1.1	361
Th_ppm	12	1	12	11	13	0.3	0.2	0.2	0.1	0.9
U_ppm	3	0.3	3	3	4	0.1	0.01	0.05	0.05	0.1
V_ppm	15	11	15	4	25	6	7	4	4	33
W_ppm	129350	81830	129350	47520	211180	63270	94363	14095	153	278290
Zr_ppm	131	2	131	129	133	2.5	1.9	2	0.4	6
Y_ppm	22	3	22	20	25	33	78	6	0.1	306
La_ppm	29	1	29	28	30	3	5	1	0.3	19
Ce_ppm	54	0.1	54	54	54	8	15	1.7	0.2	57
Pr_ppm	6	0.01	6	6	6	1.2	2.2	0.2	0.03	8
Nd_ppm	23	1	23	23	24	5	10	1	0.2	33
Sm_ppm	4	0.1	4	4	4.1	2	3	0.2	0.03	10
Eu_ppm	0.9	0.2	0.9	0.7	1.1	0.5	0.9	0.1	0.01	3

Table 3.2. Summary of whole-rock geochemistry continued

Rock type	Monzonitic dyke n = 2					Vein n = 14				
Element	**Average**	**Std Dev**	**Median**	**Min**	**Max**	**Average**	**Std Dev**	**Median**	**Min**	**Max**
Gd_ppm	4	0.3	4	3.8	4.4	2	5	0.3	0.03	17
Tb_ppm	0.6	0.03	0.6	0.6	0.7	0.5	1.2	0.1	0.01	5
Dy_ppm	4	0.3	4	3.2	3.9	4	10	0.6	0.03	39
Ho_ppm	0.7	0.1	0.7	0.7	0.8	1.1	2.6	0.1	0.01	10
Er_ppm	2	0.1	2	2.3	2.4	3.5	9	0.5	0.02	34
Tm_ppm	0.3	0.04	0.3	0.3	0.4	0.5	1.2	0.1	0.01	5
Yb_ppm	2	0.4	2	1.8	2.6	3	7	0.7	0.03	27
Lu_ppm	0.4	0.1	0.4	0.3	0.5	0.4	0.8	0.1	0.01	3
Mo_ppm	3.1	1.2	3	1.9	4.3	1.1	0.3	1	0.7	1.7
Cu_ppm	86	39	86	47	126	25	21	20	3	75
Pb_ppm	4	0.5	4	4	5	8	15	2	0.1	54
Zn_ppm	41	8	41	33	49	45	134	6	2	509
Mn_ppm	281	120	281	161	400	341	541	76	32	1919
As_ppm	4	4	4	0.1	8	798	2645	2	0.4	9955
Au_ppb	2	1	2	1	3	11	31	1	0.1	117
Bi_ppm	0.1	0.04	0.1	0.1	0.1	5	16	0.3	0.01	62
B_ppm	3	0	3	3	3	9	15	4	0.5	59
Re_ppb	7	4	7	3	11	3	2	3	0.5	9
Be_ppm	11	6	11	4	17	2	4	2	0.2	15
Li_ppm	21	3	21	18	24	1	1	1	0.1	5
F_ppm	1121	145	1121	976	1265	576	1000	192	30	4020
LREE	113	1	113	111	114	17	32	4	1	116
MREE	14	1	14	13	15	10	22	1	0.1	84
HREE	5	0.6	5	5	6	7	17	1	0.1	69
REE_T	132	3	132	129	135	35	71	6	1.3	270
REE_T + Y	154	6	154	149	160	68	148	11	1.4	576
$(La/Sm)_N$	4.4	0.05	4	4	4	4.6	4	3	0.6	12
$(Gd/Yb)_N$	1.5	0.2	2	1	2	0.8	0.4	0.8	0.2	1
$(La/Yb)_N$	9	1	9	8	10	4	5	1	0.5	14
$Eu_{\_N}$	16	3	16	13	19	9	17	2	0.2	62
$Eu^*_{\_N}$	24	1	24	23	25	11	22	1.6	0.1	77
$(Eu/Eu^*)_N$	0.7	0.1	0.7	0.6	0.8	1.1	0.4	1	0.5	2.1

Table 3.2. Summary of whole-rock geochemistry continued

Rock type	Vein halo, proximal skarn n = 14					Skarn-altered conglomerate n = 8				
Element	**Average**	**Std Dev**	**Median**	**Min**	**Max**	**Average**	**Std Dev**	**Median**	**Min**	**Max**
SiO_2_%	68	5	68	56	76	63	13	68	34	77
Al_2O_3_%	13	3	11	9	20	11	1	10	9	13
Fe_2O_3_%	4.1	0.9	4.2	2.5	5.4	4.4	0.7	4.4	3.2	5.6
MgO_%	1.0	0.3	1	1	2	1	0.3	1	0.7	2
CaO_%	7	3	8	2	14	14	7	12	6	29
Na_2O_%	2.4	1	2	1	5.1	0.5	0.6	0.4	0.04	1.9
K_2O_%	1.2	1	1	0.2	4.8	0.2	0.2	0.2	0.02	1
TiO_2_%	0.4	0.1	0.4	0.3	1	0.4	0.1	0.4	0.3	0.5
P_2O_5_%	0.13	0.04	0.1	0.1	0.2	0.15	0.1	0.2	0.1	0.3
MnO_%	0.2	0.2	0.2	0.1	0.7	0.4	0.1	0.4	0.2	1
LOI_%	2	1.2	2	0.5	5	4	5	3	0.7	18
Ba_ppm	376	522	196	46	2135	75	81	43	20	282
Sc_ppm	11	3	10	6	17	7	2	8	4	10
Cs_ppm	42	22	35	11	101	9	10	4	0	30
Hf_ppm	5.0	1.4	4.6	3.0	8.1	3.9	1.0	3.8	2.8	5.7
Nb_ppm	12	5	11	6	23	9	2	9	6	13
Rb_ppm	99	57	89	26	259	20	21	12	1	68
Sn_ppm	107	76	78	24	322	207	208	120	16	560
Sr_ppm	281	85	247	180	468	262	110	249	74	453
Th_ppm	15	4	14	11	23	12	2	12	8	15
U_ppm	4	1	4	3	6	3	1	3	2	4
V_ppm	39	13	39	18	61	43	11	40	30	68
W_ppm	7017	7147	4982	282	25180	853	1125	269	10	3154
Zr_ppm	172	48	162	102	272	141	37	136	97	214
Y_ppm	26	7	24	16	38	24	4	25	16	30
La_ppm	32	8	31	21	46	25	6	27	13	37
Ce_ppm	62	15	59	41	92	50	12	53	27	71
Pr_ppm	7	2	7	5	10	6	1	6	3	8
Nd_ppm	26	5	24	18	38	22	5	23	11	30
Sm_ppm	5	1.1	4	4	7	4	1	4	3	6
Eu_ppm	0.8	0.2	1	0.5	1.3	0.8	0.2	0.8	0.5	1

Table 3.2. Summary of whole-rock geochemistry continued

Rock type	Vein halo, proximal skarn n = 14					Skarn-altered conglomerate n = 8				
Element	**Average**	**Std Dev**	**Median**	**Min**	**Max**	**Average**	**Std Dev**	**Median**	**Min**	**Max**
Gd_ppm	4	1.0	4	3	7	4	0.9	4	2	6
Tb_ppm	0.7	0.2	1	0.5	1.1	0.6	0.1	0.7	0.4	1
Dy_ppm	4	1.0	4	3	6	4	0.7	4	3	5
Ho_ppm	0.9	0.2	1	0.6	1.3	0.8	0.1	1	0.5	1
Er_ppm	3	1	2	2	4	2	0.4	3	2	3
Tm_ppm	0.4	0.1	0	0.2	0.6	0.4	0.1	0	0.3	0.5
Yb_ppm	3	1	2	1.5	4	2	0.3	2	2	3
Lu_ppm	0.4	0.1	0.4	0.2	0.6	0.4	0.05	0.4	0.3	0.4
Mo_ppm	2.3	3.3	1	0.6	13	0.4	0.3	0.2	0.1	1.2
Cu_ppm	139	80	105	55	309	16	11	19	2	36
Pb_ppm	6	6	3	3	24	3	1	3	2	5
Zn_ppm	64	27	53	30	142	46	23	41	22	94
Mn_ppm	868	392	795	431	1794	1253	637	1202	486	2155
As_ppm	561	1356	46	1	5354	13	11	11	2	41
Au_ppb	2	1	2	1	6	0.9	0.5	1	0.1	2
Bi_ppm	0.9	0.7	1	0.3	3	0.2	0.2	0.2	0.1	0.5
B_ppm	3	1	2	2	5	3	2	2	0.5	6
Re_ppb	9	4	8	5	19	2	1	0.8	0.5	4
Be_ppm	6	4	6	1	18	4	4	2	0.3	11
Li_ppm	58	27	54	21	135	11	13	5	0.7	40
F_ppm	2581	2008	2094	802	8458	2595	2673	1053	268	8050
LREE	127	29	121	85	184	103	26	109	54	146
MREE	16	4	14	12	24	14	3	14	9	19
HREE	6	2	6	4	9	6	0.8	6	4	7
REE_T	148	34	141	102	217	122	29	130	67	172
REE_T + Y	174	39	163	122	255	147	33	154	83	202
$(La/Sm)_N$	4.3	1	4	3	6	3.7	0.3	4	3	4
$(Gd/Yb)_N$	1.4	0.3	1	1	2	1.3	0.2	1	1	2
$(La/Yb)_N$	9	2	9	4	16	7	1	7	4	9
$Eu_{\_N}$	15	3	14	9	22	14	3	14	8	19
$Eu^*_{\_N}$	26	6	24	21	41	24	5	24	14	33
$(Eu/Eu^*)_N$	0.6	0.1	0.6	0.4	0.7	0.6	0.04	0.6	0.6	0.7

Table 3.2. Summary of whole-rock geochemistry continued

Rock type	Psammite proximal n = 11					Psammite distal n = 9				
Element	**Average**	**Std Dev**	**Median**	**Min**	**Max**	**Average**	**Std Dev**	**Median**	**Min**	**Max**
SiO_2_%	78	2	78	76	81	79	8	80	58	86
Al_2O_3_%	11	1	11	9	13	12	5	10	7	25
Fe_2O_3_%	3	1	3	2	4	2	0.7	2	1	3
MgO_%	0.7	0.2	0.7	0.5	1	0.6	0.5	0	0.1	2
CaO_%	2	1.1	2	1	4	0.8	0.7	1	0.2	3
Na_2O_%	3	0.6	3	2	4	3	0.7	3	1	4
K_2O_%	1.9	0.8	2	1	3	2.2	1.3	2	0.5	5
TiO_2_%	0.3	0.1	0.3	0.2	0.5	0.3	0.1	0.3	0.1	0.5
P_2O_5_%	0.07	0.04	0.06	0.04	0.2	0.04	0.01	0.05	0.03	0.1
MnO_%	0.1	0.02	0.05	0.02	0.1	0.03	0.02	0.03	0.01	0.1
LOI_%	0.8	0.5	0.6	0.3	2	1	0.9	0.8	0.3	3
Ba_ppm	378	179	327	150	738	573	360	488	109	1470
Sc_ppm	5	1	5	4	8	5	2	5	2	11
Cs_ppm	24	12	24	5	44	10	7	10	1	26
Hf_ppm	4.1	1.0	4.0	2.8	6.2	3.9	1.0	4.0	2.2	5.7
Nb_ppm	8	2	7	6	10	8	3	8	3	13
Rb_ppm	106	22	114	67	131	99	71	82	28	289
Sn_ppm	14	19	2	1	59	25	60	3	1	194
Sr_ppm	164	59	182	79	263	204	55	221	138	301
Th_ppm	14	2	14	10	16	13	4	13	6	20
U_ppm	3	1	3	2	4	3	1	3	1	5
V_ppm	38	8	38	27	56	39	25	31	17	105
W_ppm	181	477	18	3	1688	4	1	4	2	6
Zr_ppm	142	36	137	96	219	139	38	136	78	209
Y_ppm	20	3	19	15	24	27	15	21	8	58
La_ppm	32	4	32	26	38	39	14	39	13	70
Ce_ppm	62	7	65	51	75	69	25	64	27	125
Pr_ppm	7	1	7	6	9	8.8	3	8	3	15
Nd_ppm	25	3	26	20	31	32	13	30	10	54
Sm_ppm	4	0.7	4	3.5	5.8	5.6	2.3	5.1	2	9.4
Eu_ppm	0.8	0.1	0.8	0.7	1.0	0.9	0.4	0.8	0.4	2

Table 3.2. Summary of whole-rock geochemistry continued

Rock type	Psammite proximal n = 11					Psammite distal n = 9				
Element	**Average**	**Std Dev**	**Median**	**Min**	**Max**	**Average**	**Std Dev**	**Median**	**Min**	**Max**
Gd_ppm	4	0.6	4	3.0	4.9	5.0	2	4	2	9
Tb_ppm	0.6	0.1	0.6	0.5	0.8	0.8	0.4	0.7	0.2	1.5
Dy_ppm	4	0.6	3	2.7	4.5	4.5	2.3	3.7	1.4	9
Ho_ppm	0.7	0.1	0.7	0.5	0.9	0.9	0.5	0.8	0.3	2
Er_ppm	2	0.3	2	1.6	2.6	2.7	1.4	2.3	0.8	5
Tm_ppm	0.3	0.1	0.3	0.2	0.4	0.4	0.2	0.3	0.1	0.8
Yb_ppm	2	0.3	2	1.6	2.5	2.6	1.2	2.3	1.0	5
Lu_ppm	0.3	0.05	0.3	0.2	0.4	0.4	0.2	0.3	0.1	0.7
Mo_ppm	0.8	0.1	0.8	0.7	0.9	0.1	0.05	0	0.1	0.2
Cu_ppm	35	33	16	10	108	13	18	4	2	54
Pb_ppm	13	5	13	5	19	14	4	15	5	17
Zn_ppm	43	14	40	11	63	24	22	17	5	83
Mn_ppm	324	150	309	69	633	126	73	135	22	264
As_ppm	42	111	4	0	392	420	1169	1	0	3727
Au_ppb	0.2	0.3	0.1	0.1	0.9	3	4	2	1	15
Bi_ppm	0.3	0.2	0.3	0.1	0.7	0.6	1	0.2	0.1	4
B_ppm	1	0.8	0.5	0.5	3	1	2	0.5	0.5	6
Re_ppb	1.4	3	0.5	0.5	10	0.8	0.5	0.5	0.5	2
Be_ppm	0.6	0.7	0.2	0.05	2	0.5	0.6	0.3	0.05	2
Li_ppm	33	10	33	9	47	10	5	9	4	18
F_ppm	485	287	359	176	1049	334	492	168	66	1722
LREE	127	15	134	103	152	149	54	142	54	265
MREE	14	2	14	11	18	18	8	16	6	33
HREE	5	0.7	5	4	6	6	3	5	2	12
REE_T	146	18	156	118	176	172	64	159	62	303
REE_T + Y	166	20	176	136	200	199	76	178	70	340
$(La/Sm)_N$	5	0.4	5	4	5	4.5	0.5	5	3	5
$(Gd/Yb)_N$	1.6	0.1	1.6	1.4	2	1.6	0.2	1.5	1.3	2
$(La/Yb)_N$	11	1	11	9	13	11	3	11	7	18
$Eu_{\_N}$	14	2	14	12	18	17	7	14	8	29
$Eu^*_{\_N}$	24	4	24	19	31	31	13	28	11	54
$(Eu/Eu^*)_N$	0.6	0.1	0.6	0.5	0.7	0.6	0.1	0.5	0.5	0.7

Table 3.2. Summary of whole-rock geochemistry continued

Rock type	Granitic dyke n = 3					Diorite n = 1
Element	Average	Std Dev	Median	Min	Max	
SiO_2_%	76	2	75	73	79	63
Al_2O_3_%	14	0.5	14	13	14	15
Fe_2O_3_%	1.2	0.7	0.8	0.5	2	6
MgO_%	0.2	0.1	0.1	0.04	0.4	5
CaO_%	1	0.9	0.9	0.3	3	5
Na_2O_%	4	1	3	3	6	2
K_2O_%	3	2	4	0.3	5	2.3
TiO_2_%	0.1	0.1	0.03	0.01	0.3	0.6
P_2O_5_%	0.03	0.02	0.02	0.02	0.06	0.1
MnO_%	0.02	0.01	0.01	0.01	0.03	0.1
LOI_%	0.9	0.2	1	0.7	1.1	1
Ba_ppm	301	324	85	60	759	312
Sc_ppm	4	1	5	3	5	19
Cs_ppm	4	3	3	1	9	55
Hf_ppm	3.5	1.6	2.7	2.1	5.7	4
Nb_ppm	8	4	8	3	12	8
Rb_ppm	123	92	117	14	238	129
Sn_ppm	7	4	6	2	12	5
Sr_ppm	99	40	108	46	142	155
Th_ppm	14	5	11	10	20	10
U_ppm	4	1	4	3	5	2
V_ppm	10	5	9	4	17	113
W_ppm	8	5	6	5	15	1
Zr_ppm	91	74	52	26	195	133
Y_ppm	21	5	23	15	27	22
La_ppm	18	18	8	3	43	25
Ce_ppm	37	35	17	9	86	50
Pr_ppm	4.4	4	2.1	1.2	10	6
Nd_ppm	17	15	8	4	38	23
Sm_ppm	3.7	2.2	2.3	2	6.8	4
Eu_ppm	0.5	0.5	0.1	0.1	1.2	1

Table 3.2. Summary of whole-rock geochemistry continued

Rock type	Granitic dyke n = 3					Diorite n = 1
Element	Average	Std Dev	Median	Min	Max	
Gd_ppm	3.9	1.6	3.3	2.2	6.1	4.3
Tb_ppm	0.7	0.1	0.7	0.5	0.9	0.7
Dy_ppm	4.1	0.8	4.4	3.0	4.9	4.0
Ho_ppm	0.8	0.2	0.8	0.5	1.0	0.8
Er_ppm	2.0	0.8	2.2	1.0	2.9	2.4
Tm_ppm	0.3	0.1	0.3	0.2	0.4	0.3
Yb_ppm	1.8	0.7	1.9	0.9	2.6	2.1
Lu_ppm	0.2	0.1	0.3	0.1	0.4	0.3
Mo_ppm	0.7	0.5	1	0.2	1.4	0.6
Cu_ppm	9	5	12	1	13	26
Pb_ppm	6	3	6	3	10	7
Zn_ppm	17	18	5	3	42	56
Mn_ppm	84	84	35	14	202	453
As_ppm	7	5	4	3	15	2
Au_ppb	1.6	1.1	2	0.1	3	0.1
Bi_ppm	1.3	0.9	1.2	0.3	3	0.2
B_ppm	0.5	0	0.5	0.5	0.5	0.5
Re_ppb	0.5	0	0.5	0.5	0.5	1
Be_ppm	0.3	0.1	0.3	0.05	0.4	0.2
Li_ppm	7	7	4	0.3	17	88
F_ppm	118	79	123	19	212	592
LREE	76	71	35	18	176	104
MREE	14	5	12	8	21	15
HREE	4	2	5	2	6	5
REE_T	94	78	51	28	203	125
REE_T + Y	116	82	74	43	230	147
$(La/Sm)_N$	2.4	1.2	2	1	4	3.5
$(Gd/Yb)_N$	1.8	0.3	2	1	2	1.6
$(La/Yb)_N$	6	4	3	3	11	8
$Eu_{\_N}$	8	10	2	1	22	17
$Eu^*_{\_N}$	22	11	16	12	37	25
$(Eu/Eu^*)_N$	0.3	0.2	0.1	0.1	0.6	0.7

Fluorine concentrations were determined by decomposing the samples by fusion with sodium hydroxide, and then digesting the produced melt in water. The solution was acidified with citric acid and ultimately buffered with ammonium citrate solution. Fluoride was determined using an electrode composed of lanthanum fluoride crystal membrane that is an ionic conductor selective for un-complexed fluoride ions. The electrode was placed in the sample solution after the ion strength was adjusted to pH 6.5, and the potential was measured by an mV/pH meter. Fluorine concentrations were derived from a standard graph of potential vs. concentration of fluorine.

3.3.3 Data analysis

In analyzing the whole-rock data sample results were initially recalculated using a centered log ratio (CLR) transformation (Aitchison, 1982). This transformation sets the average value at zero with data values varying between $-\infty$ and $+\infty$, and is used to avoid the problem of closure or constant sum in whole-rock geochemistry. Following this, a Z-score transformation was applied to relate each element in a particular sample to all other samples by means of their standard deviation. Elements in a particular rock type that score above zero are considered relatively enriched in that element **(Fig. 3.5)**.

3.3.4 Mineral samples for trace element analyses

Scheelite, plagioclase and selected skarn minerals (garnet, titanite, clinozoisite, and apatite) from different rock types **(Table 3.1)** were analyzed for trace elements. Fourteen samples were selected, including polished thin sections and polished rock mounts. For samples location see **Appendix 1.1** and **Figure 3.2**, and for full results see **Appendix 3.2**. Elements selected for analysis include Na, Mn, Fe, Cu, Sr, Y, Nb, Mo, Sn, Ba, REE, Ta, Bi, Pb, Th, U **(Table 3.3)** for scheelite. The same suite of elements plus Sc, Ti, Zn, Rb, and W were analyzed for plagioclase and the skarn minerals **(Table 3.4)**.

Early $D_{1\text{-}2}$ scheelite was analyzed for monzonite dyke samples, including one mount (sample MWD013-099) **(Figs. 3.2C, 3.3E-F, 3.4B)** and one polished thin section (sample MWD005-067B) **(Fig. 3.2C)**. In addition, $D_{1\text{-}2}$ and D_4 scheelite and associated skarn minerals from two samples of skarn-altered conglomerate (sample MWD011-147.5A**; Figs. 3.2C and 3.4C,** and sample MWD042-197A**; Figs. 3.2C and 3.4E)** were chosen for trace element analysis. Sample MWD011-147.5A contains $D_{1\text{-}2}$ scheelite, $D_{1\text{-}2}$ garnet, D_3 garnet and D_4 clinozoisite and titanite, positioned along the $S_{1\text{-}2}$ fabric **(Fig. 3.4C)**. Sample MWD042-197A contains D_3 garnet that was fractured, with the fractures filled with D_4 scheelite and clinozoisite **(Fig. 3.4E)**. In both skarn-altered conglomerate samples clear cross-cutting relationships between different generations of minerals were observed.

Late D_4 scheelite and plagioclase crystals were analyzed from ten samples of retrograde D_4 veins and vein haloes. Four mounts from samples MWD099-054, MWD099-124, MWD099-163.5 and MWD101-149 were analyzed for D_4 scheelite **(Fig. 3.2B)**. In addition, five polished thin sections from vein samples MWD099-

165.5A, MWD101-159B, MWD107-259A **(Figs. 3.3H-I)**, MWD119-128A and MWD122-289B **(Figs. 3.2B-C)** were analyzed for D_4 scheelite and plagioclase. Late D_4 plagioclase in veins was analyzed for Retrograde Stages 1 and 2 **(Table 3.1)**. In addition, in sample MWD122-289B a D_4 apatite grain was analyzed that formed together with D_4 plagioclase within a vein. Finally, D_3 titanite and D_4 scheelite and plagioclase in a vein halo were analysed in a polished thin section from sample MWD122-289C **(Figs. 3.2B-C)**.

3.3.5 LA-ICP-MS trace elements analysis procedures

In situ trace element analyses were conducted by laser ablation ICP-MS using a Geolas Pro 193nm ArF excimer laser system coupled with a Bruker (formally Varian) 820–MS ICP-MS at the Advanced Analytical Centre, James Cook University. Ablation was conducted in a custom-build large volume cell (Fricker et al., 2011) (Fricker et al., 2011) using high-purity He as the carrier gas, which was subsequently mixed with Ar prior to introduction into the ICP-MS. The ICP-MS was tuned for maximum sensitivity under robust plasma conditions (Th/U sensitivity ratio ~1; see Pettke, 2008) and maintaining low oxide production rates (ThO/Th <0.4 %).

For spot analyses, the laser fluence was set to 6 J/cm^2 at the sample site with the laser repetition rate set to 10 Hz and the beam diameter to between 32 and 60 µm, respectively. The internal standard isotope used for data reduction was ^{43}Ca, based on Ca contents measured previously by WDS if available, or using the theoretical formula if WDS data was not available. NIST 610 was used as a bracketing external standard using the reference values of Spandler et al. (2011). We analysed NIST612 and GSD-1G glasses as secondary standards to evaluate accuracy.

3.3.6 Cathodoluminescence (CL) imaging

Cathodoluminescence (CL) imaging was carried out at the Advanced Analytical Centre, James Cook University on carbon-coated polished thin sections using a JEOL JSM5410LV SEM and a Robinson CL detector and photomultiplier. By covering the spectral range of 310 to 650 nm, the photomultiplier is more sensitive in gathering light in the blue to ultraviolet range than in the red to infrared range. Instrument operating conditions were set to an accelerating voltage of 20 kV and a beam current of ~10 nA.

Table 3.3 Summary of trace element distribution in scheelite

		Na23	**Mn55**	**Fe57**	**Cu65**	**Sr88**	**Y89**	**Nb93**	**Mo98**	**Sn118**	**Ba137**	**La139**	**Ce140**	**Pr141**	**Nd143**	**Sm147**	**Eu151**	**Gd157**	**Tb159**
ALL	*N*	*39*	*67*	*53*	*15*	*149*	*131*	*131*	*145*	*107*	*57*	*148*	*148*	*146*	*143*	*142*	*145*	*147*	*148*
scheelite	Min	5	4	50	0.1	4	0.04	2	2	0.09	0.03	0.01	0.01	0.001	0.02	0.01	0.01	0.06	0.01
	Max	701	11114	29208	1	247	720	421	98	175	445	99	223	33	165	52	18	62	10
	Average	88	193	792	0.2	104	118	55	22	2	23	14	42	7	33	10	4	12	2
	Std Dev	143	1345	4013	0.2	45	118	80	17	17	94	18	44	7	35	11	3	12	2
Monzonitic Dyke	*N*	*2*	*9*	*5*	*0*	*37*	*33*	*33*	*37*	*22*	*6*	*37*	*37*	*37*	*35*	*37*	*37*	*37*	*37*
$D_{1\text{-}2}$	Min	14	15	58	--	56	8	3	8	0.2	0.03	0.01	0.04	0.01	0.15	0.11	0.02	0.27	0.09
	Max	15	36	60	--	213	278	288	52	0.7	1.2	99	223	33	165	52	13	62	10
	Average	14	27	59	--	123	85	55	22	0.4	0.3	29.6	79.7	11.8	62	16.4	4.0	18.2	2.9
	Std Dev	1	6	1	--	40	68	70	11	0.1	0.4	26.6	55.3	8.0	41.7	14.3	3.1	17.4	2.8
Skarn-altered	*N*	*0*	*6*	*6*	*2*	*6*	*6*	*6*	*6*	*6*	*6*	*6*	*6*	*5*	*4*	*5*	*6*	*6*	*6*
conglomerate	Min	--	4	51	0.2	76	0	2	35	0.09	0.1	0.01	0.01	0	0.02	0.01	0.01	0.1	0.01
$D_{1\text{-}2}$	Max	--	8	63	0.3	192	6	4	98	0.15	0.3	0.4	0.8	0.1	0.8	0.3	0.08	0.4	0.2
	Average	--	6	54	0.3	155	2	3	69	0.11	0.1	0.1	0.2	0.04	0.3	0.1	0.04	0.2	0.0
	Std Dev	--	2	4	0.1	44	2	1	28	0.02	0.07	0.1	0.3	0.0	0.3	0.1	0.03	0.1	0.1
Vein	*N*	*34*	*45*	*35*	*13*	*99*	*89*	*89*	*99*	*73*	*38*	*98*	*98*	*98*	*98*	*96*	*99*	*99*	*99*
D_4	Min	5	5	52	0.1	20	10	2	2	0.1	0.05	0.03	0.16	0.02	0.08	0.08	0.03	0.06	0.04
	Max	701	62	87	1	202	720	421	58	1.1	1.1	50	152	22	97	28	18	38	7
	Average	73	25	57	0.2	91	138	59	18	0.4	0.3	9.2	32.0	5.2	26.0	8.5	4.0	11.5	2.3
	Std Dev	131	11	8	0.2	35	130	86	13	0.2	0.2	9.7	31.8	5.1	26.3	7.8	3.4	9.6	1.8
Vein Halo	*N*	*3*	*3*	*3*	*0*	*3*	*3*	*3*	*3*	*3*	*3*	*3*	*3*	*3*	*3*	*3*	*3*	*3*	*3*
D_4	Min	129	15	50	--	93	55	15	42	0.1	0.4	0.6	3.3	0.9	6.8	3.1	1.3	5.9	1.3
	Max	406	17	51	--	102	153	83	46	0.2	1.0	2	9	2	12	4	2	10	3
	Average	310	16	50	--	96	94	40	45	0.2	0.7	1	5	1	9	4	1	8	2
	Std Dev	128	1	0	--	4	43	31	2	0	0.2	0.5	2.7	0.5	2.2	0.6	0.1	1.8	0.8
Fracture filled	*N*	*0*	*4*	*4*	*0*	*4*	*0*	*0*	*0*	*3*	*4*	*4*	*4*	*3*	*3*	*1*	*0*	*2*	*3*
in D_3 garnet	Min	--	75	3170	--	4	--	--	--	3	9	0.3	1	1	5	1.5	--	1	0.1
skarn-altered	Max	--	11114	29208	--	247	--	--	--	175	445	9	16	2	7	1.5	--	1	0.2
conglomerate	Average	--	2866	9807	--	179	--	--	--	60	317	7	12	1	6	1.5	--	1	0.2
D_4	Std Dev	--	4762	11202	--	101	--	--	--	81	179	4	7	0.2	1	0	--	0	0

Table 3.3 Summary of trace element distribution in scheelite continued

		Dy163	**Ho165**	**Er167**	**Tm169**	**Yb171**	**Lu175**	**Ta181**	**Re185**	**Pb208**	**Bi209**	**Th232**	**U238**	**LREE**	**MREE**	**HREE**	**REE_T**
ALL	*N*	*148*	*146*	*146*	*143*	*143*	*143*	*74*	*95*	*149*	*122*	*65*	*138*	*148*	*148*	*146*	*149*
scheelite	Min	0.01	0.002	0.02	0.01	0.02	0.002	0.004	0	1	0.01	0.01	0.01	0.01	0.2	0.02	1
	Max	73	19	63	9	69	15	2	1	17	0.2	36	25	475	218	134	744
	Average	17	4	11	2	11	2	0	0	6.3	0.05	2	1	94	49	25	167
	Std Dev	16	3	10	2	11	2	0	0	2.5	0	6	3	98	44	23	143
Monzonitic Dyke	*N*	*37*	*37*	*37*	*37*	*37*	*37*	*25*	*31*	*37*	*30*	*29*	*35*	*37*	*37*	*37*	*37*
D_{1-2}	Min	0.90	0.25	0.88	0.13	0.50	0.05	0.00	0	2.6	0.01	0.01	0.02	0.06	1.63	2.03	4
	Max	68	12	32	4	31	5	1.8	1	14	0.1	36	10	475	218	68	744
	Average	18.9	3.7	10.0	1.3	9.2	1.5	0.2	0	6.3	0.04	3.7	1.9	179.8	64.2	22.0	266
	Std Dev	17.4	3.3	8.4	1.0	6.5	1.0	0.4	0	2.4	0.0	8.3	2.4	118.8	57.3	16.4	173
Skarn-altered	*N*	*6*	*5*	*4*	*3*	*3*	*3*	*0*	*0*	*6*	*6*	*0*	*6*	*6*	*6*	*4*	*6*
conglomerate	Min	0.01	0	0.02	0.01	0.02	0.002	--	--	1.7	0.05	--	0.02	0.0	0.2	0.0	0.6
D_{1-2}	Max	1.3	0.2	0.3	0.03	0.1	0.01	--	--	3.8	0.09	--	0.04	2.1	2.2	0.4	2.9
	Average	0.4	0.1	0.2	0.02	0.1	0.005	--	--	2.5	0.07	--	0.03	0.5	0.8	0.2	1.5
	Std Dev	0.5	0.1	0.1	0.01	0.03	0.002	--	--	0.7	0.0	--	0.005	0.8	0.6	0.1	0.9
Vein	*N*	*99*	*99*	*99*	*99*	*99*	*99*	*49*	*64*	*99*	*83*	*33*	*91*	*98*	*99*	*99*	*99*
D_4	Min	0.57	0.17	0.70	0.11	0.44	0.05	0.00	0	1.29	0.01	0.01	0.01	0.42	1.33	2	4.67
	Max	73	19	63	9	69	15	1	1	17	0.2	3	25	320	141	134	421
	Average	18.0	4.1	12.7	1.8	11.9	1.8	0.1	0	6.5	0.05	0.4	0.8	72.4	48.1	28.2	148.0
	Std Dev	14.8	3.4	11.1	1.7	12.4	2.1	0.2	0	2.4	0.0	0.7	2.8	70.0	36.8	25.4	113.2
Vein Halo	*N*	*3*	*3*	*3*	*3*	*3*	*3*	*0*	*0*	*3*	*3*	*0*	*3*	*3*	*3*	*3*	*3*
D_4	Min	10.2	2.4	6.8	0.8	3.9	0.5	--	--	5	0.05	--	0.1	12.4	24.5	12.5	49
	Max	30	8	22	3	14	2	--	--	7	0.07	--	0.1	25	57	40	123
	Average	18	4	12	1	7	1	--	--	6	0.06	--	0.1	17	38	22	77
	Std Dev	8.8	2.3	7.1	0.9	4.5	0.5	--	--	0.9	0.0	--	0.01	5.8	14.1	12.9	32.7
Fracture filled	*N*	*3*	*2*	*3*	*1*	*1*	*1*	*0*	*0*	*4*	*0*	*3*	*3*	*4*	*3*	*3*	*4*
in D_3 garnet	Min	1	0.2	0	0.3	2	0.3	--	--	1	--	2.4	0.8	1	2	0.4	4
skarn-altered	Max	1	0.4	1	0.3	2	0.3	--	--	9.1	--	3.1	1.0	32	3	3.4	35
conglomerate	Average	1	0.3	1	0.3	2	0.3	--	--	6.6	--	2.7	0.9	24	3	1.4	27
D_4	Std Dev	0.1	0.1	0.2	0	0	0	--	--	3.2	--	0.3	0.1	13	0.1	1.4	13

Table 3.3 Summary of trace element distribution in scheelite continued

		REE + Y	**$Eu_{\_N}$**	**$Eu^{*}_{\_N}$**	**$(Eu/Eu^{*})_N$**	**$(La/Sm)_N$**	**$(Gd/Yb)_N$**	**$(La/Yb)_N$**
ALL	*N*	*149*	*145*	*141*	*141*	*142*	*142*	*142*
scheelite	Min	1	0.2	0.2	0.3	0.04	0.004	0.02
	Max	1129	311	331	116	56	6	29
	Average	270	68	66	3	2	1	1
	Std Dev	223	60	66	10	5	1	3
Monzonitic Dyke	*N*	*37*	*37*	*37*	*37*	*37*	*37*	*37*
$D_{1\text{-}2}$	Min	11.61	0.34	1.01	0.3	0.04	0.21	0.02
	Max	1022	231	331	4.0	14	3	29
	Average	341.4	71.9	100.2	1.0	2.2	1.5	3.3
	Std Dev	219.2	54.4	91.9	0.8	3.2	0.9	5.5
Skarn-altered	*N*	*6*	*6*	*5*	*5*	*5*	*3*	*3*
conglomerate	Min	0.7	0.2	0.2	0.9	0.1	0.6	0.1
$D_{1\text{-}2}$	Max	8.5	1.5	1.6	1.5	0.9	6.2	0.3
	Average	3.5	0.7	0.7	1.3	0.4	4.1	0.1
	Std Dev	2.6	0.5	0.5	0.2	0.3	2.5	0.1
Vein	*N*	*99*	*99*	*96*	*96*	*96*	*99*	*98*
D_4	Min	13.55	0.49	1.17	0.35	0.04	0.00	0.03
	Max	1129	311	189	116	56	3	3
	Average	272.5	71.6	57.6	3.3	1.5	1.0	0.6
	Std Dev	218.5	61.2	49.0	11.8	5.7	0.7	0.6
Vein Halo	*N*	*3*	*3*	*3*	*3*	*3*	*3*	*3*
D_4	Min	104.7	22.8	24.8	0.6	0.1	0.6	0.1
	Max	276	28	40	1.1	0.2	1.6	0.2
	Average	170	26	31	0.9	0.2	1.1	0.1
	Std Dev	75.3	2.4	6.2	0.2	0.1	0.4	0.04
Fracture filled	*N*	*4*	*0*	*0*	*0*	*1*	*0*	*1*
in D_3 garnet	Min	4	--	--	--	3.8	--	0.1
skarn-altered	Max	35	--	--	--	3.8	--	0.1
conglomerate	Average	27	--	--	--	3.8	--	0.1
D_4	Std Dev	13	--	--	--	0	--	0

Table 3.4 Summary of trace element distribution in skarn minerals

Mineral/Rock-type		**Na23**	**Si29**	**Ca43**	**Sc45**	**Ti49**	**Mn55**	**Fe57**	**Zn66**	**Sr88**	**Y89**	**Nb93**	**Mo98**	**Sn118**	**Ba137**	**La139**	**Ce140**	**Pr141**	**Nd143**
Plagioclase	*N*	*2*	*3*	*3*	*2*	*0*	*1*	*2*	*2*	*3*	*1*	*0*	*0*	*2*	*3*	*3*	*3*	*1*	*1*
Monzonitic Dyke	Min	68278	268546	22870	6	--	31	14	1	524	0.1	--	--	0.3	20	0.004	0.003	0.1	0.2
D_{1-2}	Max	77956	355681	25728	7	--	31	35	3	735	0.1	--	--	0.9	29	0.4	0.7	0.1	0.2
	Average	73117	314241	24299	7	--	31	25	2	647	0.1	--	--	0.6	23	0.2	0.3	0.1	0.2
	Std Dev	4839	35700	1167	0	--	0	11	1	89	0	--	--	0	4	0.2	0	0	0
Garnet	*N*	*1*	*3*	*3*	*3*	*3*	*3*	*3*	*3*	*3*	*3*	*3*	*1*	*3*	*3*	*3*	*3*	*3*	*3*
Skarn-altered	Min	140	195002	171955	5	1464	54103	30700	29	1	10	1	0.4	18	0.4	0.1	0.1	0.01	0.05
conglomerate	Max	140	207504	177101	10	5458	59429	35745	52	9	60	67	0.4	144	0.9	0.3	0.6	0.1	0.1
D_{1-2}	Average	140	201074	174814	7	2856	56392	32929	39	5	32	23	0.4	102	0.7	0.2	0.3	0.02	0.1
	Std Dev	0	5110	2139	2	1841	2237	2101	10	3	21	31	--	59	0.2	0	0.2	0.02	0.0
Garnet	*N*	*0*	*3*	*3*	*2*	*3*	*3*	*3*	*3*	*2*	*2*	*2*	*1*	*3*	*1*	*0*	*2*	*2*	*2*
Skarn-altered	Min	--	201957	222055	5	1045	9818	19835	13	0.07	11	3	2	133	0.01	0	0.01	0.01	0.2
conglomerate	Max	--	205807	245283	5	2003	22600	75695	21	0.09	15	4	2	442	0.01	0	0.01	0.01	0.2
D_3	Average	--	203751	237445	5	1404	14851	38481	16	0.08	13	4	2	311	0.01	--	0.01	0.01	0.2
	Std Dev	--	1583	10883	0	426	5561	26314	4	0.01	2	0.2	--	130	0.0	--	0	0	0
Titanite	*N*	*2*	*2*	*2*	*2*	*2*	*2*	*2*	*2*	*2*	*2*	*2*	*2*	*2*	*2*	*2*	*2*	*2*	*2*
Vein halo	Min	35	155921	214408	87	231458	1243	1120	8.6	10.4	555	1889	0.2	3005	0.5	23	128	27	140
D_3	Max	96	157562	214408	131	233736	2298	1128	8.7	10.6	613	3549	0.3	3819	0.9	61	239	38	165
	Average	66	156741	214408	109	232597	1771	1124	8.7	10.5	584	2719	0.2	3412	0.7	42	183	32	152
	Std Dev	31	820	0	22	1139	527	4	0	0.1	29	830	0.1	407	0.2	19	55	6	12
Titanite	*N*	*2*	*2*	*2*	*2*	*2*	*2*	*2*	*2*	*2*	*2*	*2*	*2*	*2*	*2*	*2*	*1*	*1*	*1*
Skarn-altered	Min	85	162085	220125	4	175779	475	947	8	5.4	5	1494	0.1	202	0.5	0.002	0.6	0.1	0.2
conglomerate	Max	133	174059	220125	4	180389	604	1682	29	23	6	4167	0.2	253	2.8	0.3	0.6	0.1	0.2
D_4	Average	109	168072	220125	4	178084	540	1314	18	14	5	2831	0.1	228	1.6	0.1	0.6	0.1	0.2
	Std Dev	24	5987	0	0	2305	65	368	10	9	1	1337	0.0	26	1.2	0.1	0	0	0
Clinozoisite	*N*	*3*	*7*	*7*	*4*	*7*	*7*	*7*	*5*	*7*	*4*	*4*	*0*	*7*	*7*	*6*	*6*	*4*	*4*
Skarn-altered	Min	28	180604	175815	5	495	2102	21780	10	51	7	0.3	--	601	0.8	0.0	0.0	0.0	0.0
conglomerate	Max	46	234767	180103	12	3534	4368	78103	50	261	20	21	--	2326	7.1	1.1	1.2	0.2	0.9
D_4	Average	39	208952	178265	8	1604	2926	45250	33	153	16	7	--	1432	3.1	0.5	0.6	0.1	0.3
	Std Dev	8	15958	1702	3	926	831	25632	15	71	5	8	--	659	2	0	0	0	0

Table 3.4 Summary of trace element distribution in skarn minerals continued

Mineral/Rock-type		Sm147	Eu151	Gd157	Tb159	Dy163	Ho165	Er167	Tm169	Yb171	Lu175	W183	Pb208	Bi209	Th232	U238	LREE	MREE	HREE
Plagioclase	*N*	*1*	*2*	*0*	*0*	*0*	*0*	*0*	*1*	*0*	*0*	*3*	*3*	*0*	*1*	*1*	*3*	*2*	*1*
Monzonitic Dyke	Min	0.04	0.05	--	--	--	--	--	0.02	--	--	0.5	13	--	0.1	0.01	0.01	0.05	0.02
D_{1-2}	Max	0.04	0.1	--	--	--	--	--	0.02	--	--	7	16	--	0.1	0.01	1.4	0.10	0.02
	Average	0.04	0.1	--	--	--	--	--	0.02	--	--	5	15	--	0.12	0.01	0.6	0.07	0.02
	Std Dev	0	0	--	--	--	--	--	0	--	--	3	1	--	0	0.0	0.6	0	0
Garnet	*N*	*1*	*1*	*3*	*3*	*3*	*3*	*3*	*3*	*3*	*3*	*3*	*3*	*1*	*0*	*2*	*3*	*3*	*3*
Skarn-altered	Min	0.1	0.01	0.1	0.03	0.5	0.3	1	0.3	3	0.4	0.5	0.1	0.1	--	0.0	0.2	1	5
conglomerate	Max	0.1	0.0	0.2	0.2	5	2	6	1	6	0.8	35	0.9	0.1	--	0.0	1.1	7	14
D_{1-2}	Average	0.1	0.01	0.1	0.1	2	0.9	3	0.5	4	0.5	14	0.6	0.1	--	0.0	0.5	3	8
	Std Dev	0.0	0.0	0.1	0.1	2	1	2	0	2	0	15	0.4	0	--	0	0.4	2	4
Garnet	*N*	*2*	*3*	*2*	*3*	*3*	*3*	*3*	*3*	*3*	*3*	*3*	*1*	*0*	*0*	*2*	*2*	*3*	*3*
Skarn-altered	Min	0.2	0.1	0.5	0.1	1	0.3	1.2	0.2	1.5	0.3	1	0.1	--	--	0.09	0.21	2	3
conglomerate	Max	0.2	0.2	0.5	0.5	10	5	23	5	33	4	5	0.1	--	--	0.12	0.25	16	65
D_3	Average	0.2	0.2	0.5	0.2	4	2	9	2	12	2	3	0.1	--	--	0.10	0.23	7	24
	Std Dev	0	0	0	0	4	2	10	2	15	2	1	0.0	--	--	0.02	0.02	6	29
Titanite	*N*	*2*	*2*	*2*	*2*	*2*	*2*	*2*	*2*	*2*	*2*	*2*	*2*	*2*	*0*	*2*	*2*	*2*	*2*
Vein halo	Min	43	16	42	8	64	15	51	10	85	13	46	0.8	0.5	--	60	318	187	163
D_3	Max	45	21	47	9	71	16	55	10	88	14	114	2.2	0.7	--	131	502	208	164
	Average	44	18	44	9	67	15	53	10	87	13	80	1.5	0.6	--	96	410	198	163
	Std Dev	1	3	2	1	3	1	2	0	2	1	34	0.7	0	--	35	92	11	0
Titanite	*N*	*1*	*2*	*1*	*2*	*2*	*2*	*2*	*2*	*2*	*2*	*2*	*2*	*2*	*0*	*1*	*2*	*2*	*2*
Skarn-altered	Min	0.1	0.004	0.1	0.02	0.3	0.12	0.5	0.07	0.6	0.05	44	0.1	0.10	--	0.01	0.002	0.4	1.2
conglomerate	Max	0.1	0.01	0.1	0.03	0.5	0.14	0.6	0.10	0.7	0.07	156	1.0	0.14	--	0.01	1.1	0.8	1.5
D_4	Average	0.1	0.01	0.1	0.02	0.4	0.13	0.5	0.09	0.7	0.06	100	0.5	0.12	--	0.01	0.6	0.6	1.3
	Std Dev	0	0.004	0	0.01	0.1	0.01	0.1	0.01	0.1	0.01	56	0	0	--	0	1	0	0
Clinozoisite	*N*	*4*	*7*	*7*	*7*	*7*	*7*	*7*	*7*	*7*	*7*	*4*	*7*	*5*	*0*	*5*	*6*	*7*	*7*
Skarn-altered	Min	0.0	0.0	0.2	0.1	0.4	0.1	0.4	0.1	0.2	0.0	0.5	4	0.7	--	0.003	0.1	1.3	1.1
conglomerate	Max	0.5	0.6	1.3	0.3	2.5	0.8	2.3	0.4	2.8	0.4	1.9	14	2.5	--	0.31	3.4	5.4	5.9
D_4	Average	0.2	0.3	0.6	0.2	1.7	0.5	1.3	0.2	1.3	0.2	1	8	1.5	--	0.11	1.4	3.3	3
	Std Dev	0	0	0	0	1	0	1	0	1	0	0.5	3	1	--	0	1.1	1.2	2

Table 3.4 Summary of trace element distribution in skarn minerals continued

Mineral/Rock-type		**REE_T**	**REEY**	**$Eu_{\_N}$**	**$Eu^*_{\_N}$**	**$(Eu/Eu^*)_N$**	**$(La/Sm)_N$**	**$(Gd/Yb)_N$**	**$(La/Yb)_N$**
Plagioclase	*N*	*3*	*3*	*2*	*0*	*0*	*1*	*0*	*0*
Monzonitic Dyke	Min	0.1	0.1	1	--	--	7	--	--
D_{1-2}	Max	1.5	2	1	--	--	7	--	--
	Average	0.6	0.7	1.0	--	--	7	--	--
	Std Dev	1	1	0	--	--	0	--	--
Garnet	*N*	*3*	*3*	*1*	*1*	*1*	*1*	*3*	*3*
Skarn-altered	Min	6	16	0	0	0	4	0.02	0.0
conglomerate	Max	21	80	0	0	0	4	0.03	0.1
D_{1-2}	Average	12	44	0.2	0.4	0.4	4	0.02	0.0
	Std Dev	6	27	0	0	0	0	0.004	0.0
Garnet	*N*	*3*	*3*	*3*	*2*	*2*	*0*	*2*	*0*
Skarn-altered	Min	5	17	1	2	2	0	0.2	0.0
conglomerate	Max	81	81	4	2	2	0	0.3	0.0
D_3	Average	31	40	3	2	2	--	0.2	--
	Std Dev	35	29	1	0	0	--	0.0	--
Titanite	*N*	*2*	*2*	*2*	*2*	*2*	*2*	*2*	*2*
Vein halo	Min	689	1302	278	247	1.1	0.3	0.4	0.2
D_3	Max	853	1408	368	267	1.4	0.9	0.4	0.5
	Average	771	1355	323	257	1.3	0.6	0.4	0.3
	Std Dev	82	53	45	10	0	0	0.0	0.1
Titanite	*N*	*2*	*2*	*2*	*1*	*1*	*1*	*1*	*2*
Skarn-altered	Min	2	6	0.1	0.4	0.5	3	0.1	0.003
conglomerate	Max	3	10	0.2	0.4	0.5	3	0.1	0.3
D_4	Average	3	8	0.1	0.4	0.5	3	0.1	0.1
	Std Dev	1	2	0	0	0	0	0	0.1
Clinozoisite	*N*	*7*	*7*	*7*	*4*	*4*	*4*	*7*	*6*
Skarn-altered	Min	4	4	1	0.3	2	0	0.2	0.0
conglomerate	Max	12	32	10	4	7	5	1.4	0.5
D_4	Average	7	16	5	1.4	4	2	0.6	0.2
	Std Dev	4	9	4	1	2	2	0.4	0.2

Table 3.4 Summary of trace element distribution in skarn minerals continued

Mineral/Rock-type		**Na23**	**Si29**	**Ca43**	**Sc45**	**Ti49**	**Mn55**	**Fe57**	**Zn66**	**Sr88**	**Y89**	**Nb93**	**Mo98**	**Sn118**	**Ba137**	**La139**	**Ce140**	**Pr141**	**Nd143**
Apatite	*N*	*2*	*2*	*2*	*2*	*2*	*2*	*2*	*2*	*2*	*2*	*2*	*2*	*2*	*2*	*2*	*2*	*2*	*2*
Vein	Min	9420	2333218	397400	144	23134	36241	554927	1030	326	366	116	13	83	2258	85	219	45	194
D_4	Max	97964	2736199	397400	157	34687	38789	593248	1152	809	638	131	87	426	6019	176	418	58	288
	Average	53692	2534708	397400	151	28911	37515	574088	1091	567	502	124	50	255	4139	130	319	51	241
	Std Dev	44272	201490	0	6	5776	1274	19161	61	241	136	8	37	171	1880	45	100	7	47
Plagioclase	*N*	*8*	*11*	*11*	*7*	*4*	*4*	*7*	*6*	*11*	*6*	*2*	*2*	*7*	*11*	*7*	*7*	*4*	*2*
Retrograde Stage 1	Min	42284	253495	31447	6	1	6	29	3	121	0.01	0.03	0.04	0.2	27	0.01	0.02	0.003	0.04
Vein	Max	122966	645625	68611	10	238	15	673	12	1174	2.2	0.7	0.3	1.4	232	4.6	7.8	0.8	2.5
D_4	Average	67681	367700	54122	7	61	10	137	6	785	0.4	0.3	0.2	0.5	135	0.7	1.2	0.2	1.3
	Std Dev	22572	104606	11811	1	103	3	219	3	309	0.8	0.3	0.1	0.4	62	1.6	2.7	0.3	1.2
Plagioclase	*N*	*10*	*12*	*12*	*8*	*2*	*5*	*8*	*8*	*12*	*8*	*7*	*3*	*9*	*12*	*9*	*9*	*6*	*5*
Retrograde Stage 2	Min	3024	58050	16438	1	69	3	17	0.8	50	0.003	0.01	0.2	0.1	2	0.01	0.002	0.004	0.03
Vein	Max	89934	1038000	54317	8	145	60	494	55	1323	6.3	3.3	0.9	3.4	516	2.9	5.6	0.6	2.1
D_4	Average	47400	336789	31506	5	107	17	104	8	405	1.3	0.7	0.4	0.8	103	0.7	1.2	0.2	0.8
	Std Dev	28811	240368	10798	2	38	22	154	18	330	2.0	1.1	0.3	1.0	129	0.9	1.8	0.2	0.8
Plagioclase	*N*	*1*	*2*	*2*	*1*	*1*	*1*	*1*	*1*	*2*	*1*	*1*	*1*	*2*	*2*	*2*	*1*	*1*	*1*
Retrograde Stage 1	Min	55229	303887	48599	6	1.4	8	66	12	373	3.0	2.3	2.4	0.5	48	0.1	0.7	0.1	0.5
Vein halo	Max	55229	389799	58605	6	1.4	8	66	12	809	3.0	2.3	2.4	1.1	92	0.3	0.7	0.1	0.5
D_4	Average	55229	346843	53602	6	1.4	8	66	12	591	3.0	2.3	2.4	0.8	70	0.2	0.7	0.1	0.5
	Std Dev	0	42956	5003	0	0	0	0	0	218	0	0	0	0.3	22	0.1	0	0	0
Plagioclase	*N*	*1*	*1*	*1*	*1*	*1*	*0*	*1*	*1*	*1*	*1*	*1*	*1*	*1*	*1*	*1*	*1*	*1*	*1*
Retrograde Stage 2	Min	53548	284528	37878	6	2	0	38	6	470	0.2	0.1	0.2	0.4	59	0.03	0.05	0.01	0.03
Vein halo	Max	53548	284528	37878	6	2	0	38	6	470	0.2	0.1	0.2	0.4	59	0.03	0.05	0.01	0.03
D_4	Average	53548	284528	37878	6	2	--	38	6	470	0.2	0.1	0.2	0.4	59	0.03	0.05	0.01	0.03
	Std Dev	0	0	0	0	0	--	0	0	0	0	0	0	0	0	0	0	0	0

Table 3.4 Summary of trace element distribution in skarn minerals continued

Mineral/Rock-type		**Sm147**	**Eu151**	**Gd157**	**Tb159**	**Dy163**	**Ho165**	**Er167**	**Tm169**	**Yb171**	**Lu175**	**W183**	**Pb208**	**Bi209**	**Th232**	**U238**	**LREE**	**MREE**	**HREE**
Apatite	*N*	*2*	*2*	*2*	*2*	*2*	*2*	*2*	*2*	*2*	*2*	*1*	*2*	*0*	*0*	*2*	*2*	*2*	*2*
Vein	Min	50	5	46	6	31	6	22	3	20	3	374	81	--	--	6	543	144	49
D_4	Max	101	17	108	16	137	24	61	10	36	6	374	92	--	--	15	940	403	114
	Average	76	11	77	11	84	15	42	6	28	5	374	86	--	--	11	742	274	81
	Std Dev	26	6	31	5	53	9	20	3	8	2	0	6	--	--	4	198	129	32
Plagioclase	*N*	*1*	*7*	*1*	*2*	*1*	*1*	*1*	*1*	*1*	*1*	*6*	*11*	*0*	*0*	*2*	*7*	*7*	*1*
Retrograde Stage 1	Min	0.4	0.01	0.4	0.0	0.3	0.1	0.2	0.02	0.2	0.03	1	4	--	--	0.003	0.04	0.01	0.4
Vein	Max	0.4	0.2	0.4	0.1	0.3	0.1	0.2	0.02	0.2	0.03	527	28	--	--	0.4	16	1.3	0.4
D_4	Average	0.4	0.1	0.4	0.03	0.3	0.06	0.2	0.02	0.2	0.03	139	15	--	--	0.2	2	0.3	0.4
	Std Dev	0	0.1	0	0.03	0	0	0	0	0	0	183	5	--	--	0.2	5	0	0
Plagioclase	*N*	*4*	*8*	*4*	*5*	*4*	*4*	*5*	*4*	*4*	*4*	*10*	*12*	*2*	*0*	*4*	*10*	*9*	*5*
Retrograde Stage 2	Min	0.03	0.02	0.1	0.01	0.1	0.02	0.1	0.01	0.04	0.004	0.6	1	0.01	--	0.003	0.0	0.02	0.1
Vein	Max	0.5	0.1	0.5	0.23	1.0	0.28	2.0	0.11	0.6	0.08	174183	23	0.01	--	0.4	11	2.2	2.0
D_4	Average	0.3	0.04	0.2	0.09	0.4	0.10	0.7	0.04	0.3	0.04	36224	7	0.01	--	0.1	2	0.5	0.9
	Std Dev	0.2	0.0	0.2	0.08	0.4	0.10	0.7	0.04	0.2	0.03	63129	6	0.001	--	0.1	3	0.7	0.8
Plagioclase	*N*	*1*	*2*	*1*	*1*	*1*	*1*	*2*	*1*	*1*	*1*	*2*	*2*	*0*	*0*	*1*	*2*	*2*	*2*
Retrograde Stage 1	Min	0.1	0.1	0.3	0.06	0.5	0.14	0.1	0.04	0.3	0.03	2	13	--	--	0.04	0.1	0.4	0.1
Vein halo	Max	0.1	0.4	0.3	0.06	0.5	0.14	0.4	0.04	0.3	0.03	47963	21	--	--	0.04	1.6	1.2	0.8
D_4	Average	0.1	0.2	0.3	0.06	0.5	0.14	0.3	0.04	0.3	0.03	23983	17	--	--	0.04	0.9	0.8	0.4
	Std Dev	0	0.1	0	0	0	0	0.2	0	0	0	23981	4	--	--	0	1	0	0
Plagioclase	*N*	*0*	*1*	*0*	*1*	*1*	*1*	*1*	*1*	*1*	*1*	*1*	*1*	*0*	*0*	*0*	*1*	*1*	*1*
Retrograde Stage 2	Min	--	0.04	--	0.004	0.02	0.01	0.03	0.004	0.04	0.01	2778	15	--	--	--	0.1	0.1	0.1
Vein halo	Max	--	0.04	--	0.004	0.02	0.01	0.03	0.004	0.04	0.01	2778	15	--	--	--	0.1	0.1	0.1
D_4	Average	--	0.04	--	0.004	0.025	0.01	0.03	0.004	0.04	0.01	2778	15	--	--	--	0.1	0.1	0.1
	Std Dev	--	0	--	0	0	0	0	0	0	0	0	0	--	--	--	0	0	0

Table 3.4 Summary of trace element distribution in skarn minerals continued

Mineral/Rock-type		**REE_T**	**REEY**	**$Eu_{\_N}$**	**$Eu^*_{\_N}$**	**$(Eu/Eu^*)_N$**	**$(La/Sm)_N$**	**$(Gd/Yb)_N$**	**$(La/Yb)_N$**
Apatite	*N*	*2*	*2*	*2*	*2*	*2*	*2*	*2*	*2*
Vein	Min	737	1102	92	280	0.3	1.1	1.9	2.9
D_4	Max	1457	2095	309	609	0.5	1.1	2.4	3.3
	Average	1097	1599	201	444	0.4	1.1	2.1	3.1
	Std Dev	360	496	109	164	0.1	0	0.3	0.2
Plagioclase	*N*	*7*	*7*	*7*	*1*	*1*	*1*	*1*	*1*
Retrograde Stage 1	Min	0.1	0.1	0.2	2.3	1.1	8	2.03	19
Vein	Max	17	20	4	2.3	1.1	8	2.03	19
D_4	Average	3	3	2	2.3	1.1	8	2.03	19
	Std Dev	6	7	1	0	0.0	0	0.0	0.0
Plagioclase	*N*	*10*	*10*	*8*	*4*	*4*	*4*	*4*	*4*
Retrograde Stage 2	Min	0.03	0.03	0.4	0.2	0.2	0.8	0.5	0.3
Vein	Max	13	15	1.2	2	1.6	4.4	1.6	10.3
D_4	Average	3	4	0.6	1	0.8	2.4	1.0	4.4
	Std Dev	4	5	0.3	1	0.5	2	0.4	4.1
Plagioclase	*N*	*2*	*2*	*2*	*1*	*1*	*1*	*1*	*1*
Retrograde Stage 1	Min	0.6	0.6	1.5	1.1	1.3	1.4	0.9	0.8
Vein halo	Max	4	7	7	1.1	1.3	1.4	0.9	0.8
D_4	Average	2	4	4	1.1	1.3	1.4	0.9	0.8
	Std Dev	2	3	3	0	0	0	0	0.0
Plagioclase	*N*	*1*	*1*	*1*	*0*	*0*	*0*	*0*	*1*
Retrograde Stage 2	Min	0.3	0.5	0.8	--	--	--	--	0.4
Vein halo	Max	0.3	0.5	0.8	--	--	--	--	0.4
D_4	Average	0.3	0.5	0.8	--	--	--	--	0.4
	Std Dev	0	0	0	--	--	--	--	0

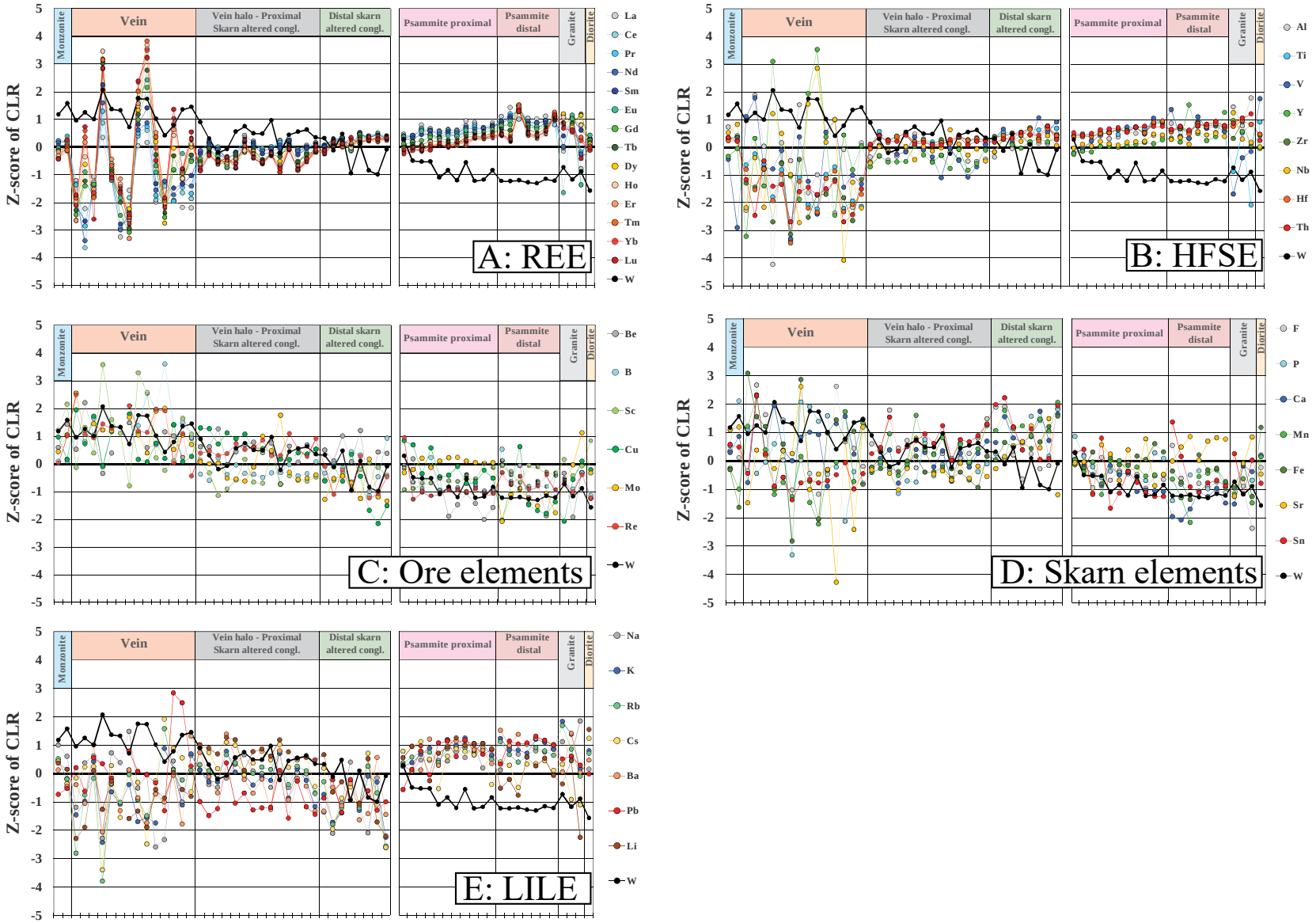

Figure 3.5 Spider plots diagrams separated by rock-type showing the whole-rock geochemistry results after applying the z-score centre log ratio (Z-score of CLR) transformation, represented in the Y-axis. The X-axis represents each sample, in the same order for the different diagrams. The samples that are above zero along the Y-axis are enriched in that particular element, and viceversa. The analyzed elements where grouped by similar enrichement pattern among the different rock types and compared with tungsten: **A.** REE. **B.** HFSE. **C.** W-related elements. **D.** Skarn related elements. **E.** LILE. **See text for explanations.**

3.4 Analytical results

3.4.1 Whole-rock geochemistry

After the geochemical data set was statistically treated, the different elements were grouped based on chemical similarities and similarities in distribution trends across the different rock types analyzed, i.e. intrusive rocks; veins; vein haloes (which equals proximal skarn-altered conglomerate); skarn-altered conglomerate distal to veins; proximal psammite; and distal psammite **(Fig. 3.5)**. The analyzed elements were grouped into five categories: (a) Rare Earth Elements (REE's) that show relative enrichment in veins **(Fig. 3.5A)**; (b) High Field Strength Elements (HFSE's) that show relative depletion in veins **(Fig. 3.5B)**; (c) elements with similar enrichment patterns to W **(Fig. 3.5C)**; (d) elements that are preferentially enriched in skarn-altered conglomerate **(Fig. 3.5D)**; and (e) Large Ion Lithophile Elements (LILE's), which are preferentially enriched in psammite **(Fig. 3.5E)**. Elemental enrichment trends for each rock type are discussed below and presented in **Figure 3.5**. Using the element groupings, we will examine the enrichment patterns among the different rock types to understand where elements are sourced from and how they were mobilised during deformation and mineralization.

3.4.1.1 Intrusive rocks

The early Carboniferous monzonite is enriched in Na_2O (4-7 wt.%) and Al_2O_3 (16-20 wt.%) and slightly enriched in CaO (6-12 wt.%) **(Figs. 3.5B, 3.5D-E)**. Trace elements are relatively enriched in HFSE's such as Sc (29-62 ppm) and Nb (15-20 ppm), as well as W (5-21 wt.%), Mo (2-4 ppm), Sr (428-453 ppm) and Be (4-17 ppm). The monzonite is depleted in Bi (<0.13 ppm) **(Table 3.2; Fig. 3.5)**. The monzonite REE_T are between 129-135 ppm, with $(La/Sm)_N$ and $(Gd/Yb)_N$ ratios higher than one, and $(Eu/Eu^*)_N$ values of 0.57-0.75 **(Table 3.2; Fig 3.6A)**.

The Permian diorite porphyry is enriched in Fe_2O_3 (6% wt.%), and TiO_2 (0.6 wt.%), with trace element enrichment in Cs (55 ppm), V (113 ppm) and Li (88 ppm), and depletion in W (1 ppm) **(Fig. 3.5)**. The REE_T of the diorite sample is 125 ppm **(Table 3.2)** with a $(Eu/Eu^*)_N$ value of 0.68 showing enrichment in LREE ($(La/Yb)_N = 8$) **(Fig. 3.6A)**

The Permian granitic dykes and Koobaba granite are enriched in K_2O (0.3-5 wt.%), Al_2O_3 (13-14 wt.%) and Na_2O (3-6 wt.%), and depleted in Fe_2O_3 (1-2 wt.%), MgO (0.1-0.4 wt.%) and CaO (0.3-2.5 wt.%) **(Table 3.2; Fig. 3.5)**. They also display trace element enrichment in LILE's (e.g. Rb at 14-238 ppm) **(Fig. 3.5E)** and HFSE such as Th (10-20 ppm), Hf (2-6 ppm) and Y (15-27 ppm) **(Fig. 3.5B)**. They are depleted in Sr (46-108 ppm), Sc (3-5 ppm), Li (0.3-4 ppm) and F (19-123 ppm). The REE_T concentrations range between 28-51 ppm **(Table 3.2)**, and the granites are slightly enriched in MREE. They yield the lowest $(La/Sm)_N$ and $(La/Yb)_N$, and highest $(Gd/Yb)_N$ ratios among the various intrusive rocks **(Fig. 3.6A)**.

3.4.1.2 Veins

Vein samples are enriched in CaO (0.1-16 wt.%), W (150 ppm to 28 wt.%) and Sc (0.5-61 ppm) **(Figs. 3.5C-D)**, and generally depleted in LILE, except for samples enriched in Pb, Rb and Cs **(Fig. 3.5E)**. Few samples are enriched in Nb (103 ppm), Sr (361 ppm), Y (306 ppm), B (59 ppm) and REE_T (270 ppm) **(Figs. 3.5A-D)**. Veins that show enrichment in REE's show corresponding enrichment in W. All vein samples tend to be more enriched in HREE's than LREE's **(Fig. 3.5A)**. The veins have the lowest concentrations of REE_T with an average value of 8 ppm and a range of 1-270 ppm (**Table 3.2**), with noticeable variable REE_N patterns **(Fig. 3.6B)**.

3.4.1.3 Vein haloes (skarn-altered conglomerate proximal to veins)

Vein haloes are slightly enriched in CaO (2-14 %.wt) and MnO (0.1-0.7 %.wt), and slightly depleted in Fe_2O_3 (2.5-5.4 %.wt) and K_2O (0.2-4.8 %.wt) **(Figs. 3.5D-E)**. Trace elements in vein haloes are enriched in some LILE, e.g. Li (21-135 ppm) and Cs (11-101 ppm) **(Fig. 3.5E)**, Sn (24-322 ppm), W (282-25180 ppm), Cu (55-309 ppm), Re (5-19 ppb), Be (1-18 ppm) and F (802-6110 ppm) **(Figs. 3.5C-D)**. In the studied samples, vein haloes contain relatively low concentrations of Pb (3-24 ppm), Ba (46-2135 ppm), Sr (180-468 ppm), Sc (6-17 ppm), V (18-61 ppm), Y (16-38 ppm) and $HREE_T$ (4-9 ppm) **(Fig. 3.5)**. The REE_T values are between 102-217 ppm, with $(Eu/Eu^*)_N$ between 0.4-0.6 **(Table 3.2)**, and relative enrichment in LREE ($(La/Yb)_N$ between 4-16) **(Fig. 3.6C)**.

3.4.1.4 Skarn-altered conglomerate (distal to veins)

Skarn-altered conglomerate is enriched in Fe_2O_3 (3-6 wt.%), CaO (6-29 wt.%) and MnO (0.2-0.7 wt.%) **(Fig. 3.5D)**, and depleted in Na_2O (0.04-1.91 wt.%) and K_2O (0.02-0.63 wt.%) **(Fig. 3.5E)**. The trace elements show strong enrichment in Sn (16-560 ppm), Sr (76-453 ppm) and F (268-8050 ppm) **(Fig. 3.5D)**, and depletions in LILE's such as Ba (20-282 ppm), Rb (1-68 ppm), Cs (0.4-30 ppm), Pb (2-5 ppm) and Li (1-40 ppm) **(Fig. 3.5E)**. The skarn-altered conglomerate is also depleted in Cu (2-36 ppm), Mo (0.1-1.2 ppm) and Sc (4-10 ppm) **(Fig. 3.5C)**. REE_T values range between 67-192 ppm **(Table 3.2)**, with slightly lower $(La/Yb)_N$ values (4-9) than other rock types, although the REE_N parameters are similar to other metasedimentary units **(Figs. 3.5A, 3.6C).**

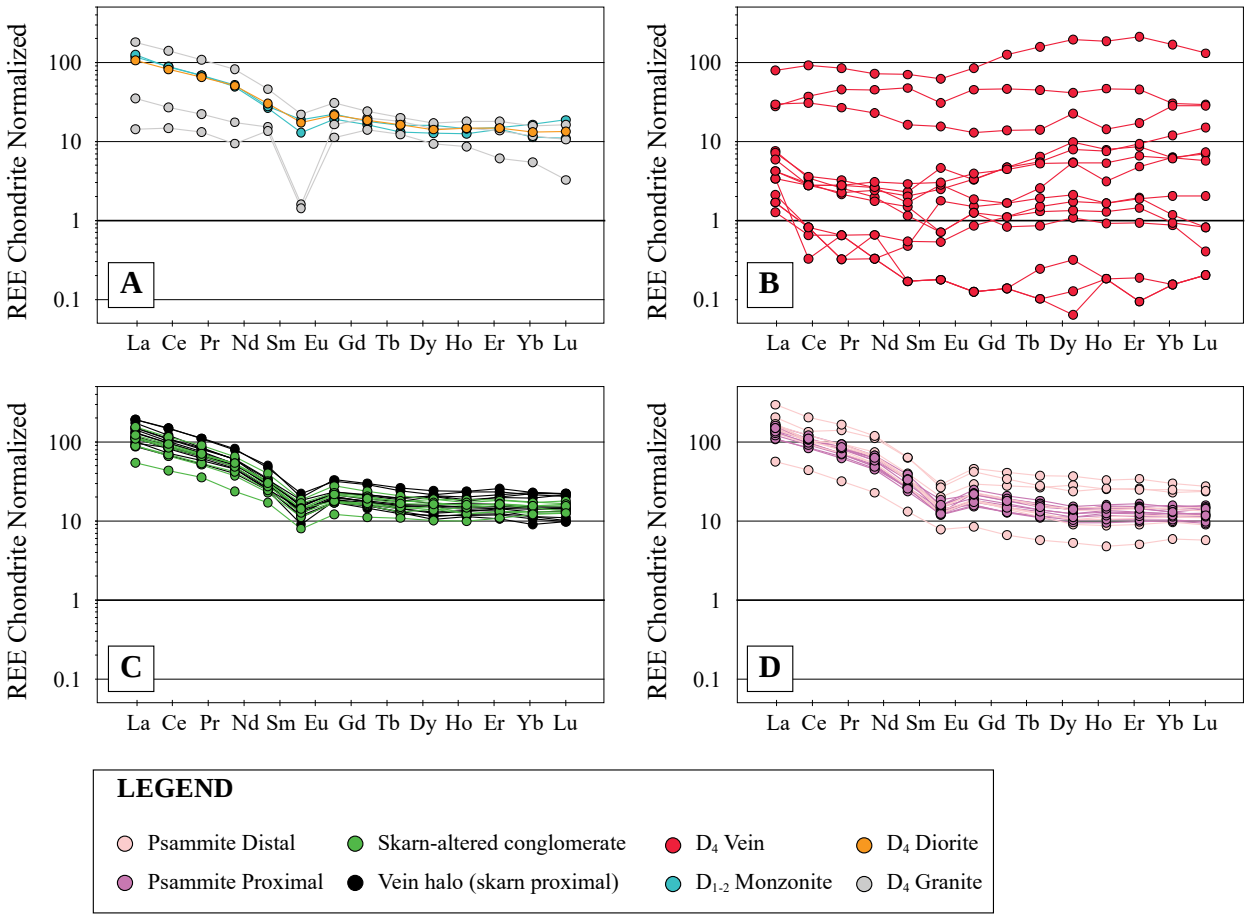

Figure 3.6 Chondrite (C1) normalized (McDonough and Sun, 1995) REE_N spider diagrams for the different rock types analyzed at the Watershed deposit. **A.** Mineralized Carboniferous D_{1-2} monzonite, barren Permian D_4 granite and diorite porphyry. **B.** D_4 veins show very different REE_N patterns among all the analyzed samples. **C.** Skarn-altered conglomerate and vein haloes show similar REE_N pattern. **D.** Distal and proximal psammite.

3.4.1.5 Psammite (distal and proximal)

Considering both distal and proximal psammite samples together, this rock type is enriched in K_2O (0.5-5.3 wt.%) and Na_2O (1.4-4.2 wt.%) **(Fig. 3.5E)**, and depleted in Fe_2O_3 (1-4 wt.%), CaO (0.2-4.5 wt.%) and MnO (<0.1 wt.%) **(Table 3.2; Fig. 3.5D)**. The trace elements show that psammite is enriched in LILE, e.g. Ba (109-1470 ppm), Rb (28-289 ppm), Pb (5-19 ppm) **(Fig. 3.5E)**, and in HFSE **(Fig. 3.5B)** except for Sc (2-11 ppm) and Nb (3-13 ppm). Psammite is depleted in Sn (1-194 ppm), W (2-1688 ppm), B (0.5-2 ppm), Re (0.5-2 ppb), Be (<2 ppm) and F (87-1049 ppm) **(Table 2; Figs. 3.5C-D)**. The REE_T values are the highest among the analyzed rock units, and vary between 118-302 ppm **(Table 3.2)**. Psammite has relatively high $(La/Yb)_N$ values (7 to 18), and $(Eu/Eu^*)_N$ is between 0.5 and 0.7 **(Fig. 3.6D)**.

When comparing distal psammite with proximal psammite, subtle enrichment and depletion patterns can be found. On approaching the Watershed deposit slight enrichment trends in CaO (0.8 wt.% [distal] vs 2 wt.% [proximal]), Fe_2O_3 (1.7 wt.% [distal] vs 2.7 wt.% [proximal]), MnO (0.03 wt.% [distal] vs 0.1 wt.% [proximal]); and subtle depletion trends in K_2O (2.2 wt.% [distal] vs 1.9 wt.% [proximal]) can be observed **(Table 3.2; Fig. 3.5)**. Trace elements show more significant changes on approaching the Watershed deposit, with most notable enrichment trends observed in Cs (10 ppm [distal] vs 24 ppm [proximal]), Li (10 ppm [distal] vs 33 ppm [proximal]), Cu (13 ppm [distal] vs 35 ppm [proximal]), Re (0.8 ppb [distal] vs 1.4 ppb [proximal]), Mo (0.1 ppm [distal] vs 0.8 ppm [proximal]), and W (4 ppm [distal] vs 181 ppm [proximal]). Noticeable depletion trends occur in Ba (573 ppm [distal] vs 378 ppm [proximal]), Sr (204 ppm [distal] vs 164 ppm [proximal]), As (420 ppm [distal] vs 42 ppm [proximal]), Au (3.2 ppb [distal] vs 0.2 ppb [proximal]), and REE_T (172 ppm [distal] vs 146 ppm [proximal]) **(Table 3.2; Fig. 3.5)**.

3.4.2 Mineral trace element geochemistry

Trace element geochemistry results for scheelite **(Table 3.3; Appendix 3.2)** plagioclase and selected skarn minerals including garnet, titanite and clinozoisite **(Table 3.4; Appendix 3.2)** are presented below. Results will focus on the distribution of REE and the elements that commonly substitute within the scheelite crystal lattice (i.e. Y, Nb, Mo, Na, Pb, Sr, Fe and Mn), or with the ability to provide a characteristic alteration signatures in plagioclase (e.g. W, Ba) and skarn minerals, (e.g. Zn, Sn, W). Some apatite from D_4 veins was also analyzed. The distribution of trace elements in the various minerals together with their textural position as a proxy for relative time of formation, will help constrain element mobility between minerals during progressive deformation, and determine what element suite was involved during mineralisation.

3.4.2.1 Scheelite

Scheelite trace element geochemistry results have been grouped into early D_{1-2} and late D_4 scheelite based on textural interpretations. All scheelite types share certain similarities across the different rock types, i.e. in general scheelite from Watershed contains relatively high total REE_T (1-744 ppm), Y (<720 ppm), Nb (2-421

ppm) and Sr (4-247 ppm) **(Table 3.3)**. Since Eu can enter into scheelite as Eu^{2+} or Eu^{3+}, relative enrichment in either has been used to assess the redox conditions of the ore fluids using a simple test relating Eu with Sm and Gd (Fig. 3.7A; Ghaderi et al., 1999). If Eu^{2+} has low concentrations in the hydrothermal fluid, then the Eu anomaly tends to be flat. This is represented as a positive array line of slope +1 in **Figure 3.7A**, because Eu will follow trivalent Sm and Gd. Inversely, if Eu^{2+} is present in high concentrations and REE has low concentrations in the fluid, then the Eu anomaly will tend to be positive plotting above the unity line in **Figure 3.7A.**

3.4.2.2.1. Early D_{1-2} scheelite in monzonite and skarn-altered conglomerate: Early D_{1-2} scheelite in monzonite contains the highest REE_T values between 4-744 ppm (average of 266 ppm). They are generally enriched in LREE (especially, Ce and Nd) and MREE, and preserve relatively high $(La/Yb)_N$ and $(La/Sm)_N$ ratios with relatively low Na content (14-15 ppm) and low $(Eu/Eu^*)_N$ ratios (0.3-4; average 0.8) **(Table 3.3; Figs. 3.7B-D, 3.8A)**.

The analyzed D_{1-2} scheelite in skarn-altered conglomerate is enriched in Mo (35-98 ppm), and depleted in Y (0.04-6 ppm), Nb (2-4 ppm) and Pb (1.7-3.8 ppm) **(Table 3.3; Figs. 3.7E-F)**. This scheelite also contains low REE_T (0.6-2.9 ppm), with $(La/Sm)_N$ values less than 1 and $(Gd/Yb)_N$ values higher than 1 **(Fig. 3.8B)**. From the six spots analyzed in this scheelite grain, three spots towards the margin show significant enrichments in $HREE_N$ ($(La/Yb)_N$ of 0.1-0.3) and Y (3-6 ppm), while three spots in the central part of the grain show preferential enrichment in $MREE_N$ ($(La/Sm)_N$ of 0.1-0.9) and Mo (95-98 ppm) **(Fig. 3.4C)**.

3.4.2.2.2. Late D_4 scheelite in veins, vein halo and fracture fill in skarn-altered conglomerate: The D_4 scheelite in veins shows enrichment in Y (385-4444 ppm), Nb (2-421 ppm) and Pb (2-17 ppm), and depletion in Mo (2-58 ppm) **(Figs. 3.7E-F)**. The REE_T values are between 5-421 ppm; the second highest recorded for D_4 minerals after D_4 apatite (**Tables 3.3-3.4)** with positive Eu anomalies ($(Eu/Eu^*)_N$ 0.35-116; average is 3) **(Fig. 3.7B)**. This type of scheelite is also enriched in $HREE_T$ (2-124 ppm) **(Fig. 3.8C)**.

The D_4 scheelite from vein haloes shows enrichment in Na (129-406 ppm), and depletion in Sr (93-102 ppm). The REE_T values are between 50-123 ppm with enrichment in $HREE_N$ ($(La/Yb)_N$ of 0.1-0.2) **(Fig. 3.8D)**. The scheelite from vein haloes also yields significant Y (55-153 ppm), Nb (15-83 ppm), Mo (42-46 ppm), Pb (5-7 ppm), Fe (50-51 ppm) and Mn (15-17 ppm). The D_4 scheelite in fracture fill within a D_3 garnet grain in skarn-altered conglomerate shows elevated Mn (75 ppm to ~1%), Fe (3170 ppm to ~3%) and Pb (1-9 ppm) **(Fig. 3.7E)**, and low REE_T (4-35 ppm), with values of $(La/Yb)_N$ of less than 0.1 **(Fig. 3.8E)**.

3.4.2.2 Plagioclase

D_{1-2} plagioclase in monzonite dykes contains elevated Sr (524-735 ppm), with low REE_T (0.05-1.5 ppm), consisting mostly of LREE at 0.01-1.4 ppm, Y (0.1 ppm), Fe (14-35 ppm) and Ba (20-29 ppm). This D_{1-2} plagioclase also contains W between 0.5-7 ppm, and Pb between 13-16 ppm (average 15 ppm) **(Table 3.4; Fig. 3.9A)**.

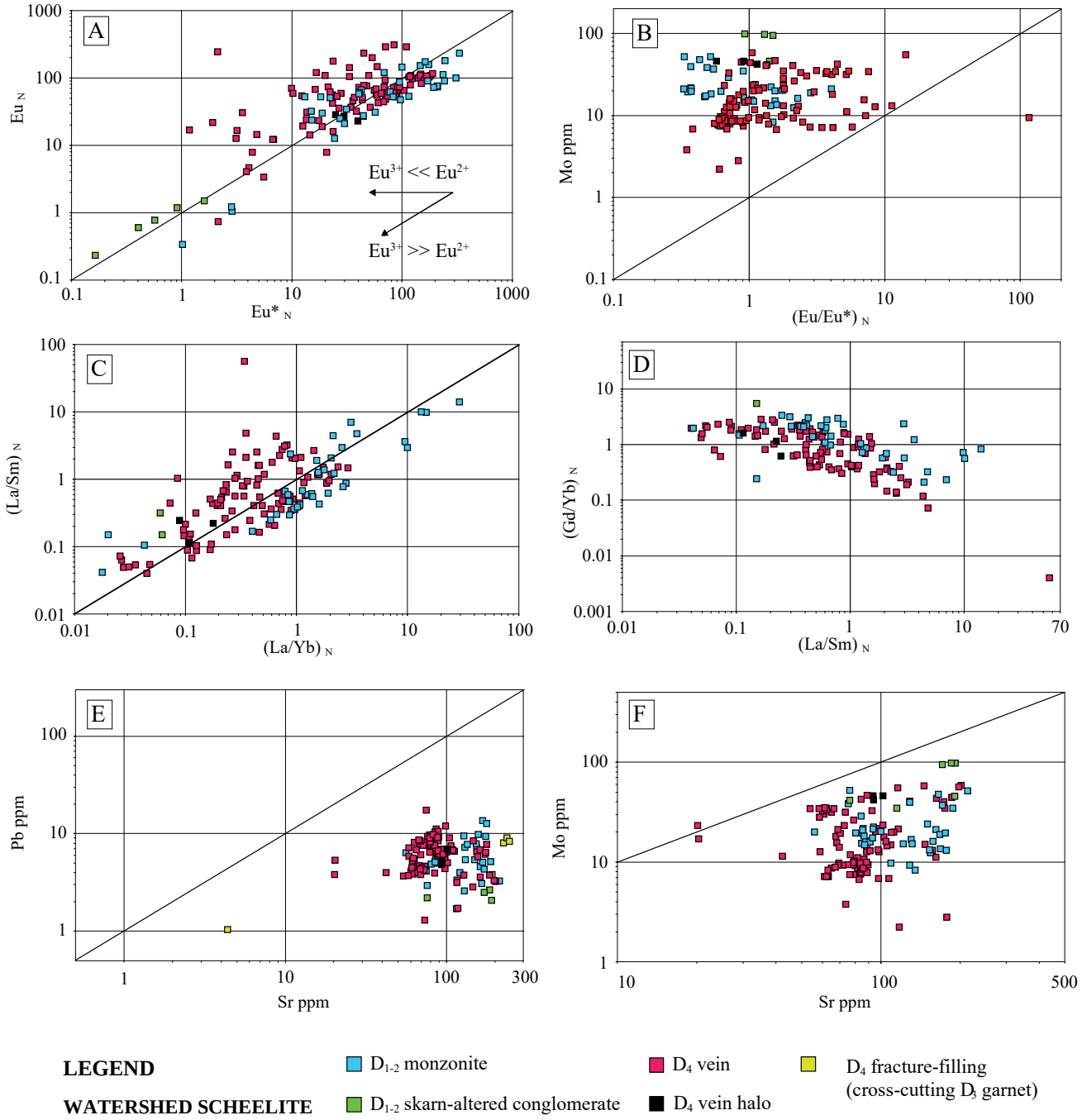

Figure 3.7 Scheelite trace element biplots **A.** Plot of calculated Eu^*_N values ($[Sm_N \times Gd_N]^{1/2}$) versus chondrite normalized Eu concentrations (Eu_N). Diagonal line shows Eu_N/Eu^*_N ratios of 1. High Eu_N/Eu^*_N ratios indicate scheelite crystallized from reduced fluids (vein and few spots in monzonite). **B.** Plot of $(Eu/Eu^*)_N$ ratio versus Mo. Vein D_4 scheelite shows predominantly ratio values higher than one with lower Mo contents, thus relative reduced conditions during precipitation. **C.** Plot of $(La/Yb)_N$ versus $(La/Sm)_N$ discriminates between early and late scheelite. **D.** Plot of $(La/Sm)_N$ versus $(Gd/Yb)_N$ differentiates between early and late scheelite. **E.** Plot of Sr versus Pb, where D_4 scheelite from veins shows relatively low Sr values, compared with $D_{1\text{-}2}$ scheelite from monzonite and $D_{1\text{-}2}$ and D_4 skarn-altered conglomerate. Lead values in scheelite are consistenly low (<12 ppm) **F.** Plot of Sr versus Mo. The low values of Mo (<100 ppm) in scheelite is consistent with scheelite precipitation in relatively reduced conditions and in lode-gold deposits (Song et al., 2014; Sun and Chen, 2017).

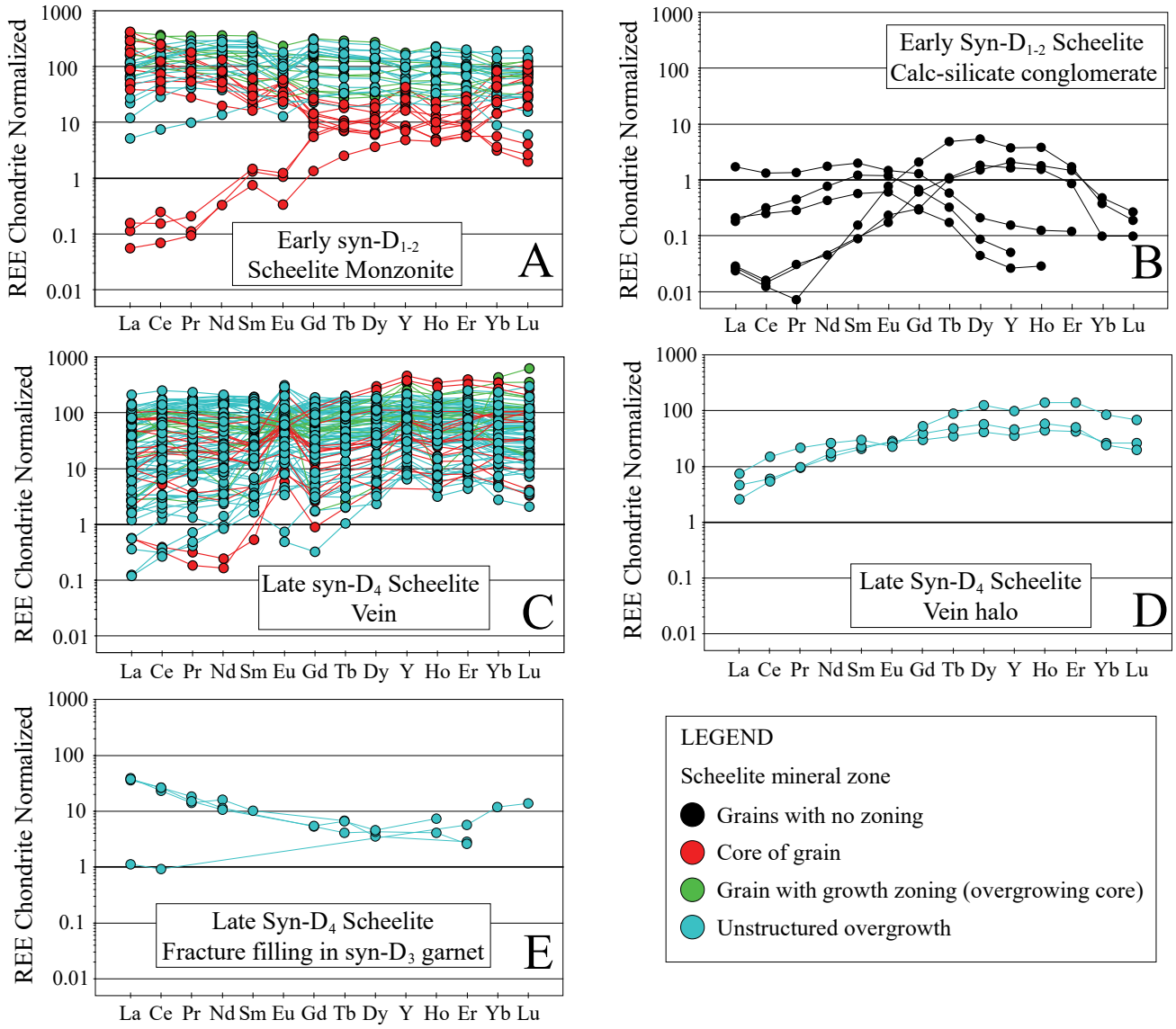

Figure 3.8 Chondrite normalized REE (McDonough and Sun, 1995) spider diagrams for scheelite by rock type and textural type (D_{1-2} vs D_4) at the Watershed deposit (see figure 3.4A for textural relationships). **A.** Early D_{1-2} scheelite in monzonite (MWD013-099 and MWD005-067A). **B.** Early D_{1-2} scheelite in skarn-altered conglomerate **(Figure 3.4C)** (MWD011-147.5A). Enriched $HREE_N$ patterns correspond to central parts of the crystal; and enriched $LREE_N$ patterns correspond to margins of scheelite crystal. **C.** Late D_4 scheelite in vein showing preferential $HREE_N$ enrichment. **D.** Late D_4 scheelite in vein halo. **E.** Late D_4 scheelite fracture fill in D_3 garnet in skarn-altered conglomerate.

D_4 plagioclase, from Retrograde Stages 1 and 2, formed in D_4 veins and associated vein haloes **(Table 3.1)**. Plagioclase that formed in D_4 veins during Retrograde Stage 1 **(Table 3.1)** shows elevated Sr (121-1174 ppm, average of 785 ppm), W (1-527 ppm), Fe (29-673 ppm) and Ba (27-232 ppm), and low Y (<2 ppm) and Nb (<0.7 ppm) values. The REE_T values are between 0.1-17 ppm and are enriched in LREE ($(La/Yb)_N$ = 19). Retrograde Stage 1 plagioclase also contains Pb between 4-28 ppm (average 15 ppm) **(Table 3.4)**. Plagioclase that formed in veins during Retrograde Stage 2, synchronous with scheelite **(Table 3.1)**, shows elevated W (1-17.4%) and Fe (17-494 ppm). This plagioclase shows low Y (<6 ppm), Nb (<3 ppm) and Sr (50-1323 ppm), Pb (1-23 ppm; average of 7 ppm) and Ba (2-516 ppm). Retrograde Stage 2 plagioclase in veins is depleted in HREE ($(La/Yb)_N$ between 0.3-10, with REE_T between 0.03-13 ppm **(Table 3.4; Fig. 3.9C-D)**.

The two analyzed spots for D_4 plagioclase (Retrograde Stage 1) from vein haloes show high Sr (373 and 809 ppm) and Pb (13 and 21 ppm, average of 17 ppm), consistent Ba (48 and 92 ppm) and contrasting W (2 ppm and 4.7%) values. They also show low REE_T (0.6 and 4 ppm), mostly as LREE. This Retrograde Stage 1 plagioclase also returned values for Fe (66 ppm), Y (3 ppm) and Nb (2.3 ppm). The single spot analyzed for Retrograde Stage 2 plagioclase in a vein halo shows elevated W (2778 ppm), Sr (470 ppm), Ba (59 ppm) and Pb (15 ppm), and low Fe (38 ppm), Nb (0.2 ppm) and Y (0.1 ppm). The REE_T are the lowest of the analyzed minerals at 0.5 ppm, with $(La/Yb)_N$ of 0.4 **(Table 3.4; Fig. 3.9C)**.

3.4.2.3 Skarn minerals

D_{1-2} garnet in skarn-altered conglomerate is enriched in Mn (5.4-5.9 wt.%), Fe (3-3.5 wt.%) and depleted in W (0.5-35 ppm), Pb (0.1-0.9 ppm), Sr (1-9 ppm). This garnet also contains Sn (18-144 ppm), Y (10-60 ppm), and Nb (0.1-67 ppm). The D_{1-2} garnet yields REE_T between 6-21 ppm, mostly as HREE (5-14 ppm) with $(La/Yb)_N$ ratios of less than 0.1 **(Table 3.4; Fig. 3.9A)**.

D_3 garnet in skarn-altered conglomerate is enriched in Fe (1.9-7.5 wt.%), low in Sr (<0.1 ppm), W (1-5 ppm), Pb (0.1 ppm) and depleted in Y (11-15 ppm) and Nb (3-4 ppm). It contains Sn (133-442 ppm), Mn (0.9-2.2 wt.%) and REE_T (5-81 ppm), with enrichments in $HREE_N$ ($(Gd/Yb)_N$ < 0.2). The D_3 titanite positioned in the vein halo contains elevated Y (555-613 ppm), Nb (1889-3459 ppm), Sn (3005-3819 ppm) and W (46-114 ppm). D_3 titanite also contains high REE_T (766 ppm), with slight $HREE_N$ enrichments with $(La/Yb)_N$ < 0.5 **(Fig. 3.9B)**. This D_3 titanite contains Mn (1243-2298 ppm), Fe (1120-1128 ppm) and low Sr (10 ppm), and Pb (0.8-2.2 ppm) **(Table 3.4)**.

D_4 clinozoisite in skarn-altered conglomerate shows elevated Sr (51-261 ppm), Ba (0.8-7 ppm) and Sn (600-2326 ppm), and enrichment in $HREE_N$, with $(La/Yb)_N$ <0.5, and low REE_T (4-12 ppm). This type of clinozoisite is depleted in W (0.5-1.9 ppm), Y (7-20 ppm), Nb (0.3-21 ppm), and contains Fe between 2.1-7.8 wt.%, and Mn between 2102-4368 ppm. The D_4 titanite in skarn-altered conglomerate shows elevated Nb (1494-4167 ppm), Sn (202-253 ppm) and W (44-156 ppm). This titanite shows low Sr (5-23 ppm), Pb (0.1-1 ppm), Y

(5-6 ppm), Mn (475-604 ppm) and Fe (947-1682 ppm).The REE_T are between 2-3 ppm, showing $(La/Yb)_N$ ratios of less than 0.3 **(Fig. 3.9C)**.

One grain of apatite that occurs together with plagioclase in a D_4 vein contains high values for most elements analyzed. The apatite gave a single elevated W value of 374 ppm. Apatite contains elevated Sr (326-809), Y (366-638 ppm), Nb (116-131 ppm), Sn (83-426 ppm), and Pb (81-92 ppm). The REE_T, with values between 737-1457 ppm, are also high with enrichment in LREE ($(La/Yb)_N$ of 2.9-3.3 **(Table 4; Fig. 3.9C)**.

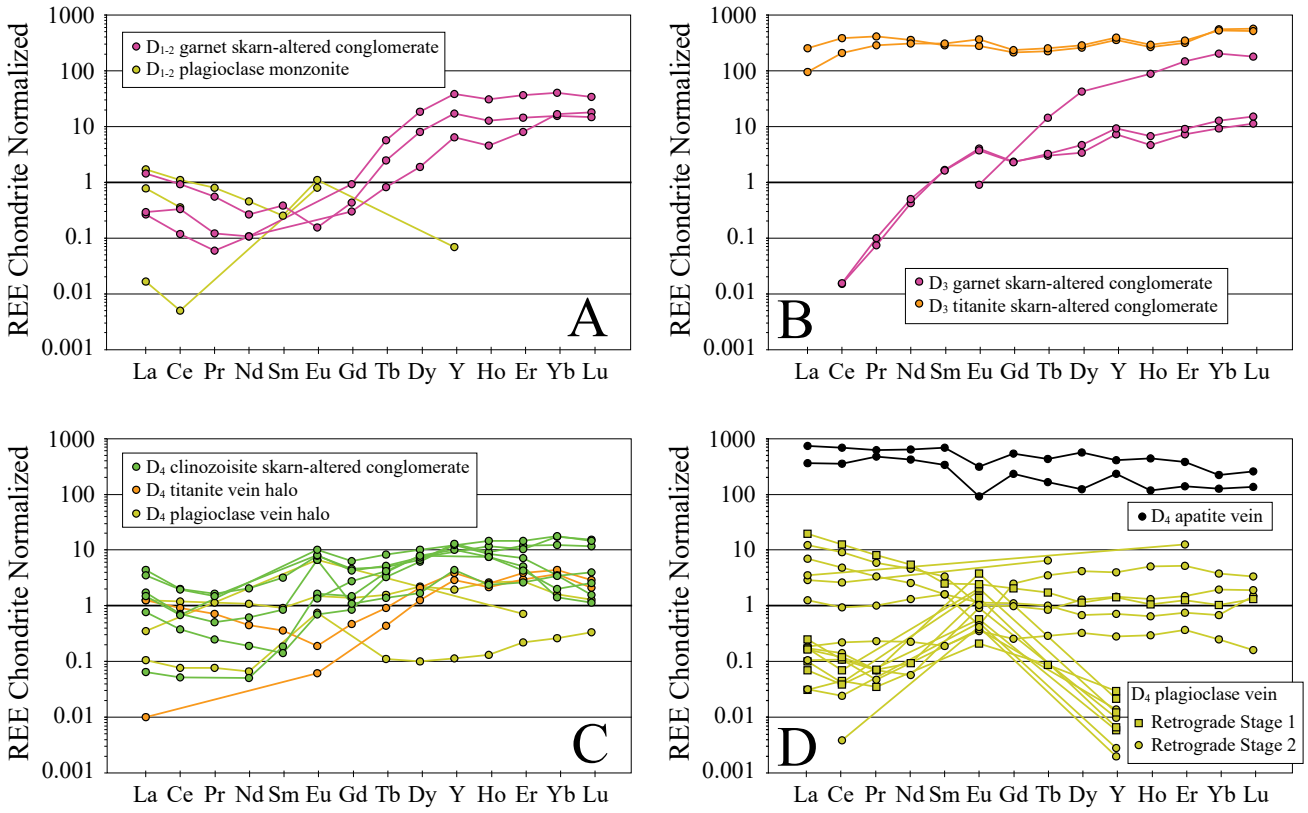

Figure 3.9 Chondrite normalized REE (McDonough and Sun, 1995) spider diagrams for minerals formed in skarn-altered conglomerate during D_{1-3} regional metamorphism and D_4 hydrothermal overprints at the Watershed deposit. **A.** D_{1-2} plagioclase from monzonite and D_{1-2} garnet from skarn-altered conglomerate. **B.** D_3 garnet and titanite from skarn-altered conglomerate. **C.** D_4 plagioclase and titanite from vein halo (i.e. proximal skarn-altered conglomerate) and D_4 clinozoisite from (distal) skarn-altered conglomerate. **D.** D_4 plagioclase (Retrogrades Stages 1 and 2) and apatite from vein.

3.5 Discussion

The fact that all W mineralization at Watershed occurs in the form of scheelite rather than wolframite, indicates that the availability of Ca was of primary importance in localizing the precipitation of W near skarn-altered conglomerate (Wood and Samson, 2000; Lecumberri-Sanchez et al., 2017); i.e. the Ca-enriched conglomerates preferentially trapped W from the mineralizing fluids. Information on the source of these fluids is less clear although a magmatic hydrothermal origin is generally assumed (e.g. Bain and Draper, 1997; Garrad and Bultitude, 1999). Similar to other scheelite deposits (Sylvester and Ghaderi, 1997; Ghaderi et al., 1999; Dostal et al., 2009; Song et al., 2014; Guo et al., 2016; Hazarika et al., 2016; Cave et al., 2017; Fu et al., 2017; Sun and Chen, 2017), constraints on the fluid composition that caused mineralization at Watershed have been obtained from trace element patterns in scheelite including REE, Y, Nb, Pb, Ba and Sr and Mo. Especially the relative abundance of LREE, MREE and HREE **(Fig. 3.10)** in scheelite provides a useful tool to assess the origin of W-bearing fluids (Song et al., 2014; Fu et al., 2017).

3.5.1 Magmatic versus hydrothermal scheelite

When scheelite compositions are plotted on a ternary LREE-MREE-HREE diagram, distinct fields can be defined for scheelite that formed in different environments, i.e. magmatic hydrothermal, skarn and hydrothermal metamorphic scheelite plot in different parts of the diagram (Raimbault et al., 1993; Ghaderi et al., 1999; Roberts et al., 2006; Dostal et al., 2009; Song et al., 2014; Guo et al., 2016; Hazarika et al., 2016; Raju et al., 2016; Cave et al., 2017; Fu et al., 2017; Orhan, 2017; Sun and Chen, 2017). When plotting the REE data from Watershed for texturally early (D_{1-2}) and texturally late (D_4) scheelite across different host rocks, the different scheelite types generally plot in distinct fields **(Fig. 3.10)**. D_{1-2} scheelite hosted in monzonite plots within the intrusion-related scheelite field and is enriched in LREE **(Fig. 3.8A)**, which is consistent with the whole-rock geochemistry for the Carboniferous monzonite **(Fig. 3.5A)**. It is common that intrusion-related scheelite mineralization is associated with evolved magmatism (Pirajno, 2009), and that scheelite replicates the REE patterns of the intrusive rocks to which it is related (Guo et al., 2016). However, not all scheelite grains in monzonite that were interpreted as being texturally early D_{1-2} plot onto the intrusion-related field **(Fig. 3.10)**. Those analyses that plot separately were affected by later alteration and will be discussed in more detail below.

Scheelite grains from skarn-altered conglomerate plot into two groups: (a) grains that plot near the field for skarn scheelite; and (b) grains that plot in the MREE-enriched field **(Fig. 3.10)**. Grains that plot near the skarn field include early D_{1-2} scheelite as well as grains that formed during D_4 along fractures within D_3 garnet. The scheelite grains that plot close to the MREE end member were affected by recrystallization and alteration processes and will be discussed in more detail below.

Scheelite grains that are texturally late and associated with the formation of D_4 veins and shears, preserve variable REE compositions that generally plot onto the field for scheelite associated with lode Au deposits **(Fig. 3.10)**, which suggests they grew from hydrothermal fluids of metamorphic origin (Goldfarb and Groves, 2015).

The D_4 scheelite in veins are either relatively enriched in LREE and/or MREE, and contain significant HREE **(Fig. 3.8**). They show flat REE_N patterns with slight LREE and MREE enrichment, typical for metamorphic scheelite (Ghaderi et al., 1999). The large variability in REE compositions may reflect variations in vein composition or timing (i.e. slight variations in fluid composition), or could have resulted from later recrystallization. Despite this variability, the overall pattern is clear and distinct from intrusion-related and skarn scheelite.

Thus, a ternary REE plot for scheelite compositions from Watershed appears to differentiate between the various scheelite types in a manner that is consistent with the literature (Song et al., 2014; Fu et al., 2017). The plot suggests that texturally early $D_{1\text{-}2}$ scheelite that was not affected by later alteration and that is hosted by monzonite intrusions and surrounding skarn-altered conglomerate, formed in response to magmatic hydrothermal processes. Similarly, texturally late D_4 scheelite that forms the bulk of the mineralization at Watershed, and that formed in late veins and faults, has compositions largely consistent with a hydrothermal origin **(Fig. 3.10)**. The difference in REE compositions between texturally early and texturally late scheelite can be further illustrated with La/Sm_N vs Gd/Yb_N and La/Yb_N vs La/Sm_N plots. These plots emphasis the relative enrichment of LREE and MREE in $D_{1\text{-}2}$ scheelite in monzonite **(Figs. 3.7C-D)**.

3.5.2 Trace element signatures in scheelite

The suggestion that most scheelite at Watershed was the result of hydrothermal-metamorphic processes during D_4 **(Fig. 3.10)** contrasts with earlier models for the deposit, which generally link scheelite mineralization to Permian granites (Bain and Draper, 1997; Garrad and Bultitude, 1999). To better assess whether the REE patterns in **Figure 3.10** truly reflect compositional variability in the formational fluids or whether they reflect host-rock and localized mineralogical controls (Guo et al., 2016), requires a closer inspection of reaction textures. Scheelite chondrite normalized REE patterns (REE_N) generally mimic the REE composition of the hydrothermal fluids (Ghaderi et al., 1999), but can be influenced by the mineralogy of the host rocks; e.g. mineral reactions that involved REE-enriched phases such as garnet and apatite can influence REE distribution trends in scheelite and other reaction products (Hermann and Rubatto, 2003), which explains some of the scatter in **Figure 3.10**. A good example of this is provided by the scheelite grains that formed during D_4 in skarn-altered conglomerate along fractures within D_3 garnet **(Fig. 3.4E)** that plot near the skarn field in **Figure 3.10**. The LREE enriched nature of these scheelite grains was probably strongly influenced by their close spatial association with HREE-enriched garnet **(Figs. 3.9A-B)**.

These competing influences on REE trends at Watershed are evident from variations in scheelite compositions in monzonite dykes. $D_{1\text{-}2}$ scheelite grains in monzonite preserve similar enrichment trends for $LREE_N$ as the monzonite itself **(Figs. 3.6A, 3.8A)**. However, not all of the analyzed grains show this trend **(Fig. 3.8A)**, with several scheelite grains yielding REE_N patterns that plot closer to the MREE end member (**Fig.**

3.10). These anomalous trends were derived from grains that are broken and partly resorbed, as a result of post-$D_{1\text{-}2}$ (i.e. D_4) hydrothermal alteration that must have remobilized the LREE.

Similar trends are visible in $D_{1\text{-}2}$ scheelite from skarn-altered conglomerate, which preserves two distinct types of REE_N patterns: one enriched in $LREE_N$ prevalent in central parts of crystals, and one enriched in $HREE_N$ towards the margins of the scheelite grain **(Figs. 3.4C, 3.8B)**. These trends have been interpreted to indicate that the core of the scheelite formed during $D_{1\text{-}2}$ together with garnet **(Fig. 3.9A)**, and the corresponding REE patterns reflect fluid conditions at this time, in part modified by the preferential fractionation of HREE into garnet resulting in relative enrichment of LREE in $D_{1\text{-}2}$ scheelite. The $HREE_N$–enriched marginal zones of the scheelite are interpreted to have formed during D_4 as overgrowths on (or recrystallization of) older grains **(Fig. 3.4C)**. Associated clinozoisite and titanite grains that replaced garnet during D_4 are similarly enriched in $HREE_N$ (**Figs. 3.4C, 3.9C).** This suggests that the hydrothermal replacement of regional metamorphic (i.e. $D_{1\text{-}2}$) garnet grains during D_4 could have resulted in localized enrichment in HREE in reaction products that formed after garnet. Thus, REE concentrations in garnet that formed early in the history of the skarn-altered conglomerate unit, controlled the availability of REE for scheelite and skarn minerals that formed during D_4. In other words, the REE concentration patterns in some $D_{1\text{-}2}$ scheelite grains **(**outlier skarn points in **Fig. 3.10)** in skarn-altered conglomerate, were modified during D_4 mineral reactions. This process affects the usefulness of the REE concentrations in determining the source fluids as presented in **Figure 3.10**, unless the geochemistry is underpinned by careful textural work.

Additional information on the mobility of REE between minerals in skarn-altered conglomerate can be gleaned from D_4 scheelite and clinozoisite that overprinted D_3 garnet **(Fig. 3.4E)**. The D_3 garnet is $HREE_N$ enriched, whilst D_4 scheelite and clinozoisite have $HREE_N$ values that are similar to D_3 garnet, but also show enrichment in $LREE_N$ **(Figs. 3.8E, 3.9B-C)**. This suggests that LREE's preferentially partitioned into clinozoisite and scheelite during D_4 **(Figs. 3.8E, 3.9C)**. Since there is a widespread replacement of $D_{1\text{-}3}$ garnet by D_4 clinozoisite **(Fig. 3.4C)**, enrichment of LREE in clinozoizite is consistent with the overall enrichment of skarn-altered conglomerate in LREE **(Fig. 3.6C).**

A partial host-rock control on the partitioning of REE's into scheelite can also be demonstrated for D_4 scheelite and adjacent plagioclase in veins and vein haloes. The precipitation of scheelite during Retrograde Stage 2 coincided with the growth of plagioclase that is relatively enriched in LREE **(Figs. 3.8C, 3.9D)**. This suggests that LREE preferentially partitioned into plagioclase, preventing the D_4 scheelite from veins to have a perfect flat REE_N pattern (Ghaderi et al., 1999) and making scheelite slightly enriched in $HREE_N$.

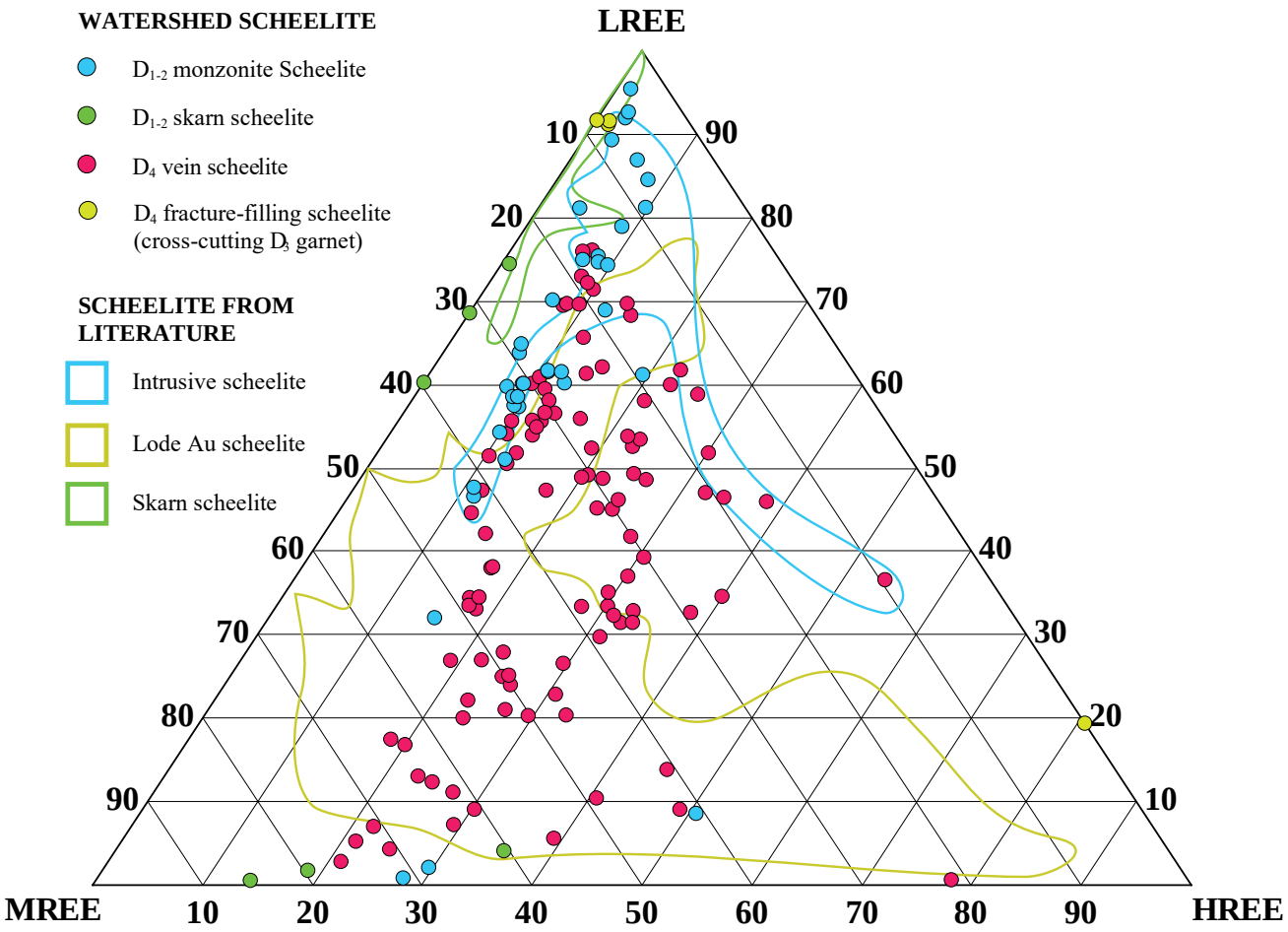

Figure 3.10 Ternary LREE-MREE-HREE diagram for analyzed scheelite from Watershed for trace elements geochemistry by LA-ICP-MS. Note how scheelite from D_4 veins from Watershed coincides with the field of scheelite associated with lode Au deposits. Fields were defined based on published data from: Raimbault et al. (1993); Song et al. (2014); Guo et al. (2016); Fu et al. (2017); Orhan et al. (2017) for intrusive related skarn; Sun et al. (2017) for granite related scheelite; and Ghaderi et al. (1999); Roberts et al. (2006); Dostal et al. (2009); Hazarika et al. (2016); Raju et al. (2016); Cave et al. (2017) for lode-Au deposits.

Similarly to the relationship between scheelite and plagioclase, scheelite and trace apatite also show preferential partitioning during Retrograde Stage 2 in D_4 veins. Apatite is the mineral phase that incorporate the most REE, with relative flat REE_N patterns or slight $LREE_N$ enriched **(Fig. 3.9D).** Apatite stability in D_4 veins is controlled by the availability of P, which shows similar enrichments with REE **(Figs. 3.5A, 3.5D)**. Then the scheelite REE signatures in D_4 veins, with slight $HREE_N$ enrichments, is controlled by the presence of trace apatite (i.e. presence of P).

Apart from the REE patterns, trace element signatures in scheelite more broadly can provide a means to illustrate the compositional variability of the different scheelite types, and constrain the formational setting of the deposit. The Pb content for all types of scheelite across all rock types is uniformly low, to reflect the low Pb content of the host lithologies **(Table 3.2; Fig. 3.7E)**. In contrast, the Ba content is highly variable (0.03 to 445 ppm) **(Table 3.3)**, indicating that Ba occurs within the system. It was locally incorporated into D_4 scheelite in skarn-altered conglomerate, but in D_4 veins Ba preferred to partition into apatite (<6019 ppm) and plagioclase (<516 ppm) **(Table 3.4)**. Generally, scheelite from Watershed contains significant Sr (**Table 3.3)**, interpreted to reflect a synchronous growth relationship between scheelite and Sr-enriched plagioclase (**Table 3.4**), which occurred in $D_{1\text{-}2}$ monzonite and D_4 veins. When Sr is plotted against Pb or Mo, early $D_{1\text{-}2}$ scheelite and late D_4 scheelite define overlapping, but distinct fields with early scheelite generally being more enriched in Sr and Mo **(Figs. 3.7E-F)**. The Mo content is generally low **(Table 3.3; Fig. 3.7F)**, and probably reflects a relatively reduced environment at Watershed, given that Mo is mobile under oxidizing conditions as Mo^{6+} (Song et al., 2014; Sun and Chen, 2017).

The redox conditions of the fluid during mineralization were further tested by comparing the Eu_N and Eu^*_N ($[Sm_N \times Gd_N]^{1/2}$) values in scheelite (Fig. 3.7A; Ghaderi et al., 1999). Eu for $D_{1\text{-}2}$ scheelite from monzonite plots along the x=y line suggesting it is dominated by Eu^{3+} (Fig. 3.7A; Ghaderi et al., 1999). This is consistent with the mostly negative Eu anomalies observed in the REE_N plots for monzonite samples **(Fig. 3.6A)**. Similarly, $D_{1\text{-}2}$ scheelite in skarn-altered conglomerate plots along the x=y line (**Fig. 3.7A)**. D_4 scheelite from veins, yield Eu compositions that either plot along or above the x=y line (**Fig. 3.7A)**, and indicate an increased presence of Eu^{2+} **(Figs. 3.7A-B)** interpreted to reflect a shift from relatively more oxidized to reduced conditions as D_4 progressed. This is consistent with the presence of graphite inclusions in D_4 scheelite in veins **(Table 3.1)** and the late-D_4 (i.e. Retrograde Stage 4; **Table 3.1**) precipitation of pyrrhotite and arsenopyrite. However, D_4 scheelite in vein haloes mostly plots along the x=y line, which may indicate that the skarn-altered lithologies buffer redox conditions.

3.5.3 Geochemical characterization of the Watershed deposit

The enrichment and depletion patterns observed in whole-rock geochemistry (**Fig. 3.5**) can be used to identify characteristic geochemical signatures for the Watershed deposit that may be of use in exploration. Such a signature also provides further constraints on the composition of the fluid responsible for mineralization

(Williams-Jones et al., 2012). Local (i.e. m-scale) element mobility associated with the emplacement of mineralized D_4 veins has been tested by comparing trace element patterns in D_4 veins, with skarn-altered conglomerate immediately adjacent to veins (i.e. vein haloes or proximal skarn-altered conglomerate, which occurs within cm's from vein margins), and skarn-altered conglomerate further away (i.e. >0.5 m) from D_4 veins, where alteration is less intense **(Fig. 3.3H)**. Regional (i.e. 100 m-scale) element mobility during mineralization has been tested by comparing element patterns in proximal (within the ore zone envelope) and distal (500-1500 m away from the ore envelope) psammite **(Fig. 3.2A-B)**. Skarn-altered conglomerate cannot be used for a regional alteration analysis for the simple reason that outcrops of this lithology are restricted to the immediate vicinity (within ~100m) of mineralization. The intrusive rocks around Watershed either constitute a source of W mineralization (the early W-enriched monzonites), or they could have overprinted the original geochemical footprint associated with mineralization (the late W-poor granite dykes).

3.5.3.1 Local element mobility: fingerprint the ore zone

The D_4 veins are strongly enriched in W as well as a series of other elements that have similar distribution patterns to W across the different rock types, and include Re, Mo, Cu, Sc, B and Be **(Fig. 3.5C)**. The abundance of this group of elements decreases when moving away from the vein via vein haloes to more distal skarn-altered conglomerate**.** Whilst vein haloes preserve similar enrichment patterns as the D_4 veins, though less intense and with depletions in Mo, B and Sc **(Fig. 3.5C)**, skarn-altered conglomerate is depleted in this element group. It is, therefore, likely that these elements were introduced during D_4 together with W by the same hydrothermal fluids. When viewed at the scale of individual minerals, Mo and Re were incorporated into scheelite, while Cu and Sc are enriched in trace apatite **(Tables 3.1, 3.4)**. Scandium and Be may also be present in phlogopite that formed during Retrograde Stage 2, and Cu is further concentrated in pyrrhotite that formed during Retrograde Stage 4 **(Table 3.1)**. Boron is concentrated in tourmaline in veins **(Table 3.1)**.

Compared to ore elements, the patterns are different for REE and HFSE, both of which are generally depleted in D_4 veins, and show an increase in concentration when moving away from the veins **(Figs 3.5A-B)**. However, these patterns are complex when viewed in detail. For the REE group, the most characteristic feature for the D_4 veins is their relative enrichment in HREE when compared to proximal vein haloes and distal skarn-altered conglomerate, which are relatively enriched in LREE **(Fig. 3.5A)**. The HREE enrichment in veins results from HREE-enriched scheelite **(see above)**. The D_4 vein haloes show slight depletion in both HREE and LREE when compared to distal skarn-altered conglomerate **(Figs. 3.4A, 3.5A)** suggesting that REE may have leached from the wall rock during vein formation and that REE were mobile in the mineralizing hydrothermal fluid.

The HFSE do not show clear enrichment trends away from the veins with the exception of Y and Nb, which also show localized enrichment in D_4 veins. This mimics the REE patterns and results from the presence of scheelite and apatite, which appear to have scavenged these elements from the wall rock **(Table 3.1)**. Thus, HREE, Y and Nb were mobile, at least locally, under the P-T conditions at which Watershed formed.

The group of elements enriched in skarn-altered conglomerate (i.e. F, P, Ca, Mn, Fe, Sr, and Sn) **(Fig. 3.5D)** are depleted in vein haloes and show highly variable, non-systematic distribution patterns in veins. This suggests that some of these elements were remobilized from the immediate wall rock to be incorporated in minerals like plagioclase (Ca, Sr), scheelite (Ca), apatite (P, F), fluorite (F), phlogopite (Fe) and Fe-sulphides in D_4 veins. The importance of this localized remobilization process is confirmed by the observation that almost all scheelite mineralization occurs in direct spatial association with Ca-bearing skarn-altered conglomerate, i.e. the localized availability of Ca was essential in the precipitation of scheelite from the hydrothermal fluid. When viewed at a grain scale, Mn, Ca, Fe, Sr and Sn enrichment in skarn-altered conglomerate is linked to metamorphic D_{1-3} garnet and D_4 clinozoisite **(Tables 3.1, 3.4)**; Sr and Sn are particularly enriched in D_4 clinozoisite where it replaced D_3 garnet **(Fig. 3.4C**). The enrichment of F in skarn-altered conglomerate and the presence of fluorite in veins suggests that the mobility of HREE, W and HFSE such as Y and Nb involved the formation of F complexes such as $HREEF^{2+}$ (Guo et al., 2016). The HREE can also bond to carbonate or phosphate complexes (Williams-Jones et al., 2012). During mineralization, the W, Y, Nb and REE were incorporated into D_4 scheelite and/or apatite, whereas F was incorporated into fluorite or apatite **(Table 3.1).**

The distribution pattern of the LILE's is somewhat distinct from the other element groups and shows enrichment in vein haloes (e.g. Rb, Cs, Li) compared to more distal skarn-altered conglomerate and D_4 veins **(Fig. 3.5E)**. This enrichment primarily results from the ubiquitous presence of white mica in the vein haloes **(Table 3.1)**, which formed as a proximal wall-rock alteration product of the mineralizing hydrothermal fluids. These elements were, therefore, mobile during D_4 and some may have been introduced by the mineralizing fluids **(Table 3.1; Fig. 3.4C)**.

In summary, the hydrothermal fluids responsible for W mineralization introduced Be, B, Sc, Cu, Mo and Re. These fluids interacted preferentially with the proximal skarn-altered conglomerate wall-rock from which they may have leached REE, Y and Nb, as well as Ca, F, P, Fe and Sr; adding Rb, Cs and Li in the vein haloes. This interaction promoted the precipitation of scheelite, plagioclase, fluorite, apatite and sulphides in veins and white mica in the vein haloes **(Table 3.1)**. Mobilization of REE, Y, Nb and W may have required F as a ligand (Guo et al., 2016), in addition W may have required Na **(Chapter 2)**. Thus, on 1-5 m scale ore zones are characterized by enrichments in W, Be, B, Sc in veins, and Ca, F, P, Mn, Fe and Sn in adjacent skarn-altered conglomerate.

3.5.3.2 Regional element mobility: the footprint of the ore zone

Whilst the veins and their immediate wall rocks show distinct element enrichment and depletion patterns, it is not clear if trends observed on m-scales persist over wider areas. To test the extent of the alteration system north of Watershed, samples of psammite were taken at regular intervals away from the deposit. Psammite in general is enriched in REE, HFSE**,** and LILE's and depleted in the ore and skarn element assemblages, with few clear enrichment or depletion trends when comparing proximal with distal psammite **(Fig. 3.5)**. However, some

trends do occur: e.g. proximal psammite is slightly depleted in REE's and HFSE, and slightly enriched in some elements associated with W such as Mo **(Fig. 3.5A-C)**. With regards the skarn-related elements and LILE's, subtle enrichment trends in Ca, Fe, Mn; and depletion trends in K and Na were observed when approaching mineralization **(Table 3.2; Figs. 3.5D-E)**. These trends probably result from stratigraphic compositional changes within the proximal psammite near skarn-altered conglomerate layers **(Figs. 3.2B-C)**, and cannot be linked conclusively to hydrothermal alteration effects.

The most notable enrichment trends towards mineralization occur in LILE's (Cs, Li) and in the ore element assemblage (Cu, Re, Mo, and W) **(Table 3.2; Fig. 3.5)**. It is expected that these elements are particularly enriched along the network of D_4 shears and associated joints, which acted as conduits for the mineralizing fluids **(Chapter 2)**. In addition, element depletion in proximal psammite can be observed for REE_T, Ba, and Sr **(Figs. 3.5)**, which suggests that these elements were mobilized into the fluid phase, to be incorporated into scheelite (REE's) and plagioclase (Ba, Sr) in D_4 veins.

Viewed together, the differences between proximal and distal psammite are subtle. However, some trends are real, and possibly of use in exploration. The proximal psammite enrichment in ore elements such as W and Cu, is in agreement with the historical stream sediments anomalies that led to the discovery of Watershed in the late 1970's (Meates, 1979). With the data presented, we are able to expand those anomalies to regional (i.e. 100 m scale) enrichment trends in Mo, Ca, Fe, Mn and Li on approaching Watershed.

3.5.3.3 Intrusive rocks

Carboniferous $D_{1\text{-}2}$ monzonite and Permian D_4 granite yield distinct geochemical enrichment and depletion trends. $D_{1\text{-}2}$ monzonite is generally enriched in LREE, HFSE, ore and skarn (except for Mn and Fe) related assemblages, as well as a few LILE's (e.g. Na and Li) **(Fig. 3.5)**. Enrichment in ore assemblage elements suggests an early mineralization event possibly associated with the emplacement of the monzonite at ~350 Ma **(Chapter 2)**, which is consistent with the $LREE_N$ enriched composition of $D_{1\text{-}2}$ scheelite in monzonite **(Figs. 3.8A, 3.10)**.

Published models for the Watershed deposit, suggest that scheelite mineralization resulted from the intrusion of Permian granites (Bain and Draper, 1997; Garrad and Bultitude, 1999). This is not apparent in the geochemistry of late-tectonic granite dykes in the region. Compared to the early monzonite, the late ~291-274 Ma granites intruding Watershed are depleted in ore and skarn related elements. However, they are generally enriched in REE, some HFSE (e.g. Al, Nb, Y) and LILE's (except for Li) **(Fig. 3.5)**. On geochemical grounds the Permian granites are unlikely to be the source of W mineralization, although their emplacement may have enhance element mobility along D_4 structures. Their enrichment in LILE and Al indicates the evolved nature of these granites, and possible interaction with Al-rich sediments of the Hodgkinson Formation.

3.6 Conclusions

A ternary REE plot for scheelite compositions from Watershed differentiates between the various scheelite types in a manner that is consistent with the literature (Song et al., 2014; Fu et al., 2017). Texturally early (D_{1-2}) scheelite, not affected by later alteration, has compositions consistent with magmatic hydrothermal processes. This scheelite is hosted in ~350Ma monzonite **(Chapter 2)** and surrounding skarn-altered conglomerate. Texturally late (D_4) scheelite has compositions consistent with a hydrothermal origin. This scheelite formed in late veins, associated faults and surrounding skarn-altered conglomerate and constitutes the bulk of mineralization at Watershed. Trace element signatures in scheelite more broadly and particularly the Sr and Mo content of texturally distinct scheelite grains provide an additional means to illustrate the compositional variability of different scheelite types.

When interpreting the data on a ternary REE plot, it is key to understand the influence of metamorphic/hydrothermal mineral reactions on local REE distribution gradients. Mineral reactions that involved REE-enriched phases such as garnet locally influenced REE distribution trends in scheelite from Watershed and explains some of the scatter in **Figure 3.10**.

The redox conditions of the mineralizing fluids were estimated from scheelite Eu anomalies and Mo content as well as the presence of texturally late graphite and sulphides. At Watershed, early D_{1-2} scheelite precipitated from relatively oxidized fluids, while D_4 veins record a shift to more reduced conditions as D_4 progressed, possibly as a result of the interaction of mineralizing fluids with reduced host rocks (i.e. carbonaceous slates; **Fig. 3.2)**.

The hydrothermal fluids that introduced W mineralization into the system also introduced Be, B, Sc, Cu, Mo and Re, thus providing a fingerprint for the deposit. These fluids interacted preferentially with the proximal skarn-altered conglomerate wall-rock from which they may have leached REE, Y and Nb, as well as Ca, F, P, Fe and Sr; adding Rb, Cs and Li in the vein haloes. This interaction promoted the precipitation of scheelite, plagioclase, fluorite, apatite and sulphides in veins and white mica in the vein haloes **(Table 3.1)**. Mobilization of REE, Y, Nb and W may have involved F and Na as ligands (Guo et al., 2016).

The deposit footprint of scheelite mineralization at Watershed as preserved in psammite is generally subtle. However, some trends are real, and of possible use to exploration. Deposit (i.e. 100 m scale) enrichment trends mimic trends observed in mineralized skarn-altered conglomerate and include W, Cu, Mo, Ca, Fe, Mn and Li on approaching Watershed. This is an expansion on the W, Cu stream sediments anomalies that were used in historical exploration (W and Cu; Meates, 1979).

REE geochemistry **(Fig. 3.10)** and enrichment in ore assemblage elements in ~350 Ma monzonite **(Chapter 2)** suggests that initial mineralization may have occurred during intrusive events in the Carboniferous. In contrast to earlier models for the deposit, which generally link scheelite mineralization to Permian granites (Bain and Draper, 1997; Garrad and Bultitude, 1999), no evidence has been found that supports a link between

Permian granites and mineralization. REE geochemistry and field relations indicate a metamorphic hydrothermal origin for most W mineralization. The depletion in the ore elements assemblage in Permian granites at Watershed indicate that they are unlikely to be the source of W mineralization, although their emplacement may have enhance element mobility along D_4 structures.

Chapter 4 – The Permian Watershed W deposit (northeast Queensland): fluid inclusion and stable isotope constraints

Abstract

The Watershed scheelite deposit is located in an extinct fore-arc basin in the Mossman Orogen. This fore-arc region comprises multiple deformed Silurian-Ordovician metasedimentary rocks of the Hodgkinson Formation and is intruded by Carboniferous-Permian granites of the Kennedy Igneous Association. At Watershed, the Hodgkinson Formation includes skarn-altered conglomerate, psammite and slate units, which record four deformation events evolving from ductile (D_{1-3}) to brittle ductile (D_4). Early D_{1-2} scheelite mineralization in Carboniferous monzonite and skarn-altered conglomerates occurred during prograde metamorphism, which reached upper greenschist to lower amphibolite facies conditions. Permian D_4 scheelite mineralization occurred in trans-tensional shear-related veins, vein haloes, and skarn-altered conglomerate during retrograde lower greenschist facies metamorphism. Four subsequent stages of retrograde metamorphism have been recognised (Retrograde Stages 1-4). Fluid inclusions in Retrograde Stage 2 D_4 vein scheelite and quartz are characterized by a low salinity H_2O-NaCl-CH_4 fluid (XCH_4 < 0.01, 0-9 wt.% NaCl). The fluid inclusions show evidence for fluid-fluid mixing between a low (close to 0 wt.% NaCl) and a medium (< 8 wt.% NaCl) saline fluid. Mineralization *P-T* conditions were determined to be ca. 300°C and 1-1.5 kbar (i.e. depths of 3.5-6 km), which are very similar to those recorded in lode-gold deposits in the Hodgkinson Gold Field and elsewhere. The mineralizing *P-T* conditions indicate a high geothermal gradient (50-100°C/km) associated with the Permian granitic intrusives. The presence of pyrrhotite and arsenopyrite in D_4 veins (Retrograde Stage 4), and graphite and methane in the fluid indicates reduced mineralization conditions, with the oxygen fugacity 0.6 to 0.8 $\log_{10}$ values below the Fayalite-Magnetite-Quartz buffer. Oxygen stable isotope ($\delta^{18}O_{VSMOW}$) from scheelite (+3.4 to +7.3‰), plagioclase (+7.0 to +11.8‰) and quartz (+12.6 to +15.5‰) from Retrograde Stage 2, and δD_{VSMOW} (−73.4 to −62.7‰) and $\delta^{18}O_{VSMOW}$ (+11.5 to +13.2‰) from muscovite from Retrograde Stage 3 indicate a metamorphic origin with a possible magmatic component for the mineralizing fluids. Sulphur isotope ($\delta^{34}S_{CDT}$) data from sulphides of Retrograde Stage 4 in veins indicates the presence of seawater sulphate (i.e., basinal brine). Metamorphic fluids probably originated from prograde devolatilization metamorphic reactions in the Hodgkinson Formation.

4.1 Introduction

The Watershed tungsten deposit is situated in central Mossman Orogen in northeast Queensland (Australia). The deposit occurs in strongly deformed Silurian-Devonian metasedimentary rocks (Henderson et al., 2013), which were intruded by Carboniferous-Permian S-type granites (Champion and Bultitude, 2013) **(Fig. 4.1)**. The Watershed deposit has a resource of 70,400 t of WO_3 (49.32 Mt @ 0.14% WO_3) (Vital Metals Inc., ASX announcement, 2018).

Tungsten mineralization, particularly scheelite, occurs in different styles of mineralization and can have contrasting origins. Scheelite occurs in granites (Wood and Samson, 2000), intrusive- and non-intrusive-related skarn (Newberry and Swanson, 1986; Meinert et al., 2005), and in lode veins **(Chapter 2)**. Scheelite is also a byproduct in several lode-gold deposits, where it is formed synchronous with gold (Henley et al., 1976; Peters et al., 1990; Groves, 1993; Goldfarb et al., 2005). Published data on fluid inclusions hosted in scheelite in tungsten deposits is scarce (So and Shelton, 1983; Cheilletz, 1984; Cattalani and Williams-Jones, 1991), i.e. most of the available data comes from minerals associated with scheelite. For instance in granites, aqueous fluid inclusions measured in quartz that formed coeval with scheelite, show salinities less than 15 wt.% NaCl, with trapping temperatures between 200-500°C and pressures between 0.2-1.7 kbar (Wood and Samson, 2000). In tungsten skarn deposits associated with granitoids, aqueous fluid inclusions with salinities between 26-61 wt.% NaCl in scheelite show trapping temperatures and pressures between 280-525°C, and 0.5-1.3 kbar, respectively (Kwak, 1986). In some cases, formation depths in excess of 8-10 km have been reported (e.g. Pine Creek skarn, California; Brown et al., 1985).

In scheelite-bearing lode-gold deposits, aqueous fluid inclusions are hosted in quartz and show homogenization temperatures (150-350°C) that are lower than those in granites and skarns. They have low salinities (<11 wt.% NaCl), and were formed over a wide range of crustal depths from 3 km to more than 10 km (Peters et al., 1990; Groves, 1993; Groves et al., 1998; Vos and Bierlein, 2006; Bodnar et al., 2014). Many fluid inclusions in lode-gold deposits hosted in metasedimentary rocks contain CH_4 and/or N_2, at concentrations similar to that of CO_2 (Bodnar et al., 2014). Additional information on the source of mineralizing fluids can be obtained from stable isotopes for ore and coexisting gangue minerals (Campbell and Larson, 1998; Shanks III, 2014).

Despite the large size of the Watershed deposit, the presence of good-quality rock exposures and the availability of detailed geological maps (Skrzeczynski and Wood, 1984), not much research has been performed to obtain a better understanding of the physico-chemical conditions of mineralization. This paper presents the results of a detailed fluid inclusions study from quartz and scheelite from mineralised veins that formed around ca. 275 Ma during the main Permian mineralizing event **(Chapter 2)**. In addition, a comprehensive set of oxygen, hydrogen and sulphur isotope data from scheelite and related quartz, plagioclase, muscovite, and sulphides has been collected. These data will allow us to (1) obtain a better understanding of the physico-chemical conditions during mineralization, and (2) identify the source(s) of the mineralizing fluid(s).

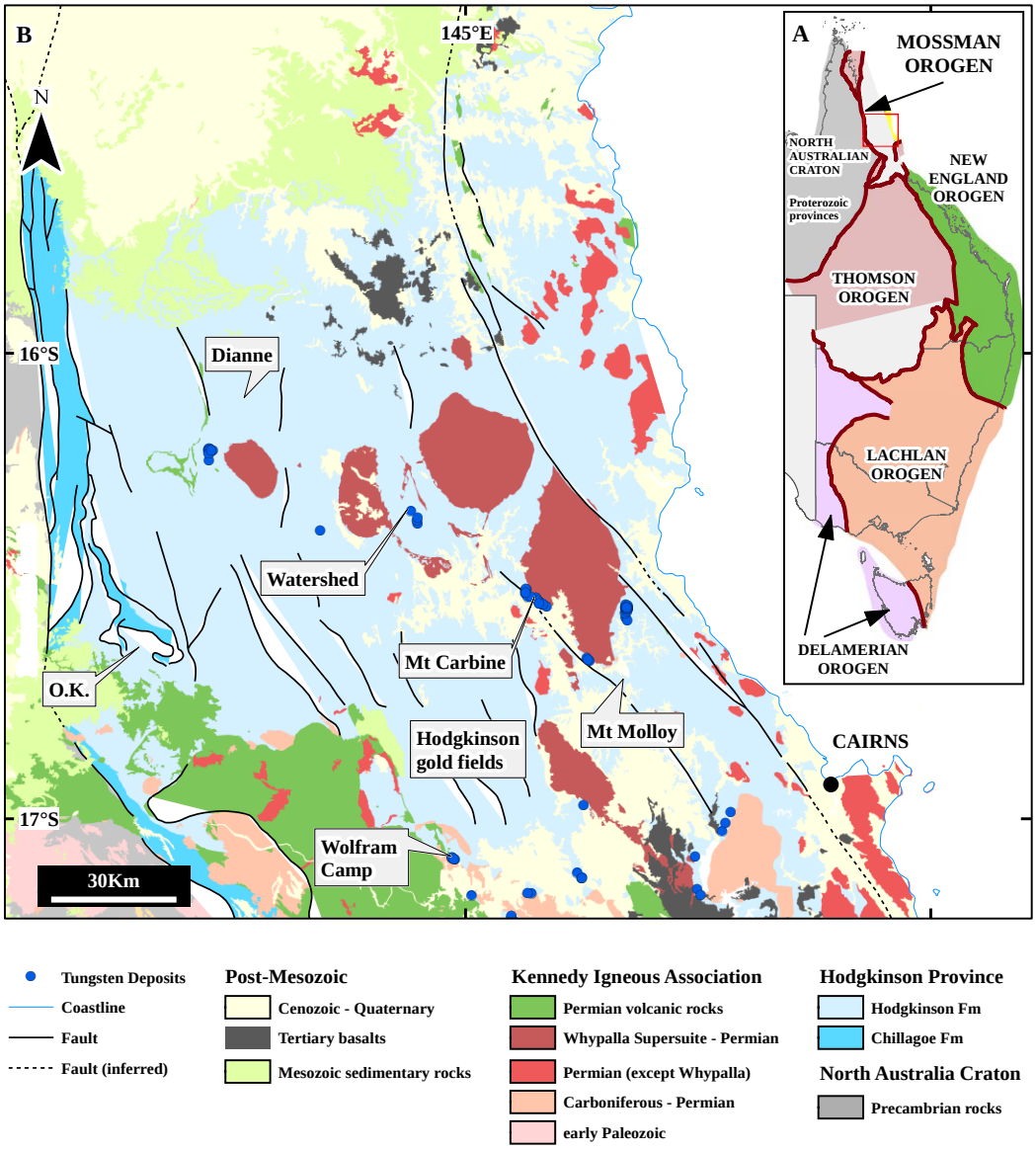

Figure 4.1 Regional geological setting of the Watershed deposit in northeast Queensland. **A.** Different orogens of eastern Australia and its relation with the Mossman Orogen. The red square is enlarged in **B**. **B.** Geology of the Hodgkinson Province. The Permian volcanic rocks (green) and the Carboniferous-Permian (light orange) rocks of the Kennedy Igneous Province crop out to the south of the Hodgkinson Province. These rocks separates the Hodgkinson Province to the north from the Broken River Province to the south. Watershed is hosted by the Hodgkinson Formation and surrounded by S-type granites and syenogranites of the Permian Whypalla Supersuite. Other important tungsten deposits and occurrences hosted by the Hodgkinson Formation are indicated in the map.

4.2 Regional Geology

The Watershed deposit is located in the central part of the Mossman Orogen, which is a late-Paleozoic active continental margin system abutting the North Australian craton, from which it is separated by a major fault zone (Palmerville Fault). The Mossman Orogen is composed of the Silurian and Devonian Hodgkinson and Broken River provinces, which form a belt 500 km long and up to 200 km wide. The Mossman Orogen is fault-bounded by the Thomson Orogen to the south and by the New England Orogen to the southeast (Donchak et al., 2013; Fergusson and Henderson, 2013) **(Fig. 4.1A)**. The Mossman Orogen largely consists of multiply deformed sedimentary successions interpreted as turbiditic sequences with minor intercalations of mafic volcanic rocks and chert, deposited in a deep-marine environment (Henderson et al., 2013). The Hodgkinson and Broken River provinces are separated from each other by Carboniferous to Permian granitoids of the Kennedy Igneous Association (Champion and Bultitude, 2013). The Watershed deposit is hosted by rocks of the Hodgkinson Province **(Fig. 4.1B)**.

The northern portion of the Mossman Orogen comprises the Silurian to early Carboniferous Hodgkinson Formation (Adams et al., 2013; Kositcin et al., 2015) **(Fig. 4.1B)**. The Hodgkinson Formation includes alternating sandstone-mudstone beds that are locally interbedded with greywacke and quartz-greywacke units and rare intercalations of chert, volcanic rocks, limestone and polymictic conglomerate (Amos, 1968; de Keyser and Lucas, 1968). The Hodgkinson Formation is bounded to the west by the Silurian-Devonian Chillagoe Formation, which forms a narrow (2-5 km), north-south trending zone that runs parallel to the Palmerville Fault for ca. 250 km **(Fig. 4.1B)**. The Chillagoe Formation comprises sandstone, limestone, chert, and mafic volcanic rocks with minor mudstone, conglomerate and breccia, which were deposited in a shallow-water marine shelf environment (Amos, 1968). Field relations and sedimentary textural characteristics indicate that the western and eastern portions of the Hodgkinson Formation represent the more proximal and distal facies, respectively, of a sub-marine fan delta system (Amos, 1968). The rocks of the Hodgkinson Formation are interpreted by Henderson et al (2013) to have formed in a fore-arc system with the rocks of the Pama Igneous Association (Withnall and Hutton, 2013), further west in the North Australia Craton **(Fig. 4.1A)**, representing a contemporary magmatic arc.

The Hodgkinson Formation has been affected by intense deformation with associated regional metamorphism. On a regional scale, four discrete deformation events, D_1 to D_4, have been recognized (Davis, 1993; Henderson et al., 2013). The first deformational event D_1 is Devonian in age and coincided with peak metamorphism at low- to mid-greenschist facies in the southwest, grading to upper-greenschist facies in the northeast of the Hodgkinson Formation. A bedding-parallel slaty cleavage and variably plunging, mesoscale isoclinal folds characterize D_1. The second deformational event D_2 is related to large scale folds with wavelengths of several kilometers, which formed during Devonian to early Carboniferous compressional events (Henderson et al., 2013). The third deformational event D_3 is represented by a penetrative crenulation cleavage best developed in aureole zones of Permian granitoids, and considered to have formed as a sub-horizontal

cleavage during early Permian extension (Davis and Henderson, 1999). Structures assigned to D_4 are more localized and variable in nature, and tend to be co-planar with D_2 structures making their recognition difficult. Deformation during D_4 is linked to mesoscopic folds and associated with a north-south trending crenulation cleavage best developed near Permian granitoid plutons (Davis et al., 2002), and linked to compressional events during the late-Permian.

The rocks of the Hodgkinson Formation were intruded by late Carboniferous to Permian granites assigned to the Kennedy Igneous Association (Champion and Bultitude, 2013) **(Fig. 4.1B)**. In the northern portion of the Hodgkinson Province, these intrusions are represented by ca. 4,000 km^2 of outcrop of mainly Permian S-type and minor I-type granites assigned to the Daintree Subprovince (Mackenzie and Wellman, 1997). The Daintree Subprovince has been further subdivided based on geochemical characteristics (Bultitude and Champion, 1992), thus Watershed is surrounded by S-type granites assigned to the early Permian Whypalla Supersuite **(Fig. 4.1B)**, which were emplaced during D_4 (Davis, 1993) around 285-260 Ma (Champion and Bultitude, 2013). The granites of the Whypalla Supersuite are porphyritic to equigranular and mainly consist of muscovite-biotite syenogranite and monzogranite with rare granodiorite (Bultitude and Champion, 1992).

4.3 Geology of the Watershed deposit

The rocks in the surroundings of Watershed consist of metasedimentary rock units assigned to the Hodgkinson Formation. The rock units at Watershed are psammite, polymict skarn-altered conglomerate, slate and slate-siltstone breccia, with minor quartzite and rare chert **(Figs. 4.2-4.3)**. Psammite is the most common rock type within Watershed **(Fig. 4.2)** and is light to dark grey, composed of fine- to medium-grained (less than 2 mm) angular to sub-rounded quartz grains (45 vol.%), euhedral to subhedral plagioclase grains (40 vol.%), and minor (5 vol.%) fine-grained biotite **(Fig. 4.4A)**. The matrix of the psammite consists of fine-grained quartz, plagioclase, biotite and muscovite. The polymict skarn-altered conglomerate occurs interlayered with the psammite **(Figs. 4.2-4.3)** as isolated pod-like bodies and layer fragments, up to 15 m wide and tens of meters in length. This rock type includes sub-rounded pebbles, 3-30 cm in diameter, that preserve a skarn mineralogy **(Chapter 2, Fig. 4.4B).** The polymict skarn-altered conglomerate unit is the main host for disseminated and vein-type scheelite mineralization **(Fig. 4.3)**. A few quartzite beds occur dispersed within the psammite unit **(Fig. 4.3)**, and are composed of a medium-grained, dark grey rock dominated by 2-5 mm large sub-rounded quartz grains (>70 vol. %), with minor biotite and feldspar **(Fig. 4.4C)**. Strongly deformed slate and slate-siltstone breccia units are widespread within Watershed and its immediate surroundings **(Figs. 4.2-4.3)**. Foliated slate occurs as massive units and are interbedded with 0.5 to 20 cm thick siltstone layers. The slate-siltstone breccia is typically composed of isolated fragments (10-90 vol.%) of sandstone **(Fig. 4.4D)** and siltstone that are 0.5 to 5 cm in size and set in a strongly foliated, dark grey matrix of mudstone (slate) defining an intense linear fabric. Thinly banded, black to grey chert beds form a minor unit within the slate-siltstone breccia.

The metasedimentary rocks at Watershed are strongly deformed and preserve evidence for intense folding, and at least three penetrative foliations that are best developed in the slate and slate-siltstone breccia units **(Fig. 4.4D)**. In psammite and polymict skarn-altered conglomerate the same deformation events resulted in extension along the layering and dominant mineral lineation, resulting in boudin trails and layer segments enveloped by slate and slate-siltstone breccia units **(Fig. 4.2)**. Primary layering is generally destroyed in fine-grained slate units and slate-siltstone breccia, but is locally preserved within psammite boudins, or as conglomerate layer segments. The semi-continuous boudin trails of skarn-altered conglomerate provide evidence for primary layering **(Fig. 4.2).** The first two deformational events, D_1 and D_2 ($D_{1\text{-}2}$), coincided with peak metamorphism **(Table 4.1)** and involved complete, and probably repeated, transposition of the primary layering associated with upright isoclinal folding, and the formation of a penetrative, steeply southwest dipping foliation, S_1/S_2 **(Chapter 2)**. The third deformational event D_3 is represented by cm- to km-scale tight to open, upright folds that fold the S_1/S_2 transposition fabric. D_3 folds are locally associated with a near vertical, north-northwest-trending axial planar crenulation cleavage (S_3) **(Chapter 2)**. Late, generally, brittle-ductile D_4 shear zones cut and displace D_1-D_3 fabrics. The shear zones are generally narrow (<10 cm wide) except for a major near-vertical D_4 shear zone with a steeply plunging, near down-dip lineation, which occurs along the eastern margin of Watershed **(Chapter 2, Fig. 4.2)**. Around Watershed, the narrow D_4 shear zones display a wide variety of orientations, but are generally parallel to the main north-northwest to north trending ductile $S_{1\text{-}2}$ fabric. The narrow D_4 shear zones are near vertical **(Fig. 4.3)** showing a dextral sense of movement **(Chapter 2)**. Numerous smaller fractures and shears, in the vicinity of major shears, display a greater variation of orientations and a normal movement sense is common. The shear zones are spatially associated with economic scheelite mineralization in veins and in alteration zones where they transect skarn-altered conglomerates **(Chapter 2)**.

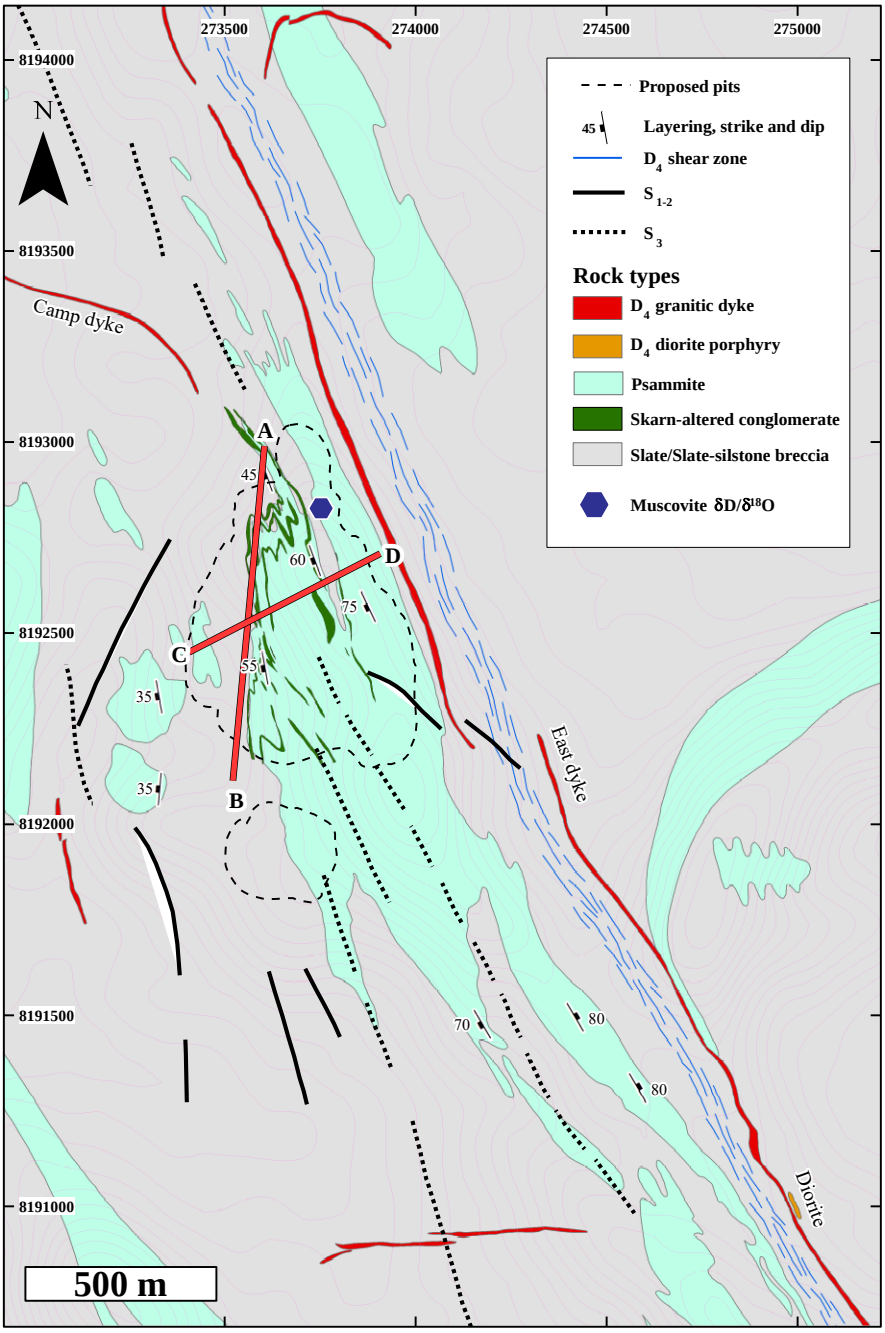

Figure 4.2 Generalized geological map of the Watershed deposit. Note that the skarn-altered conglomerates follow the regional fabric and show transposition. A-B and C-D refer to long- cross sections, respectively, shown in **Figure 4.3**. Base map from Skrzeczynski and Wood (1984). The grid system is Geocentric Datum of Australia 1994 (GDA94), zone 55.

Table 4.1 Mineral paragenesis table for the Watershed tungsten deposit. Modified from **Chapter 2**. Mineral abbreviations (Whitney and Evans, 2010) used in figures are indicated.

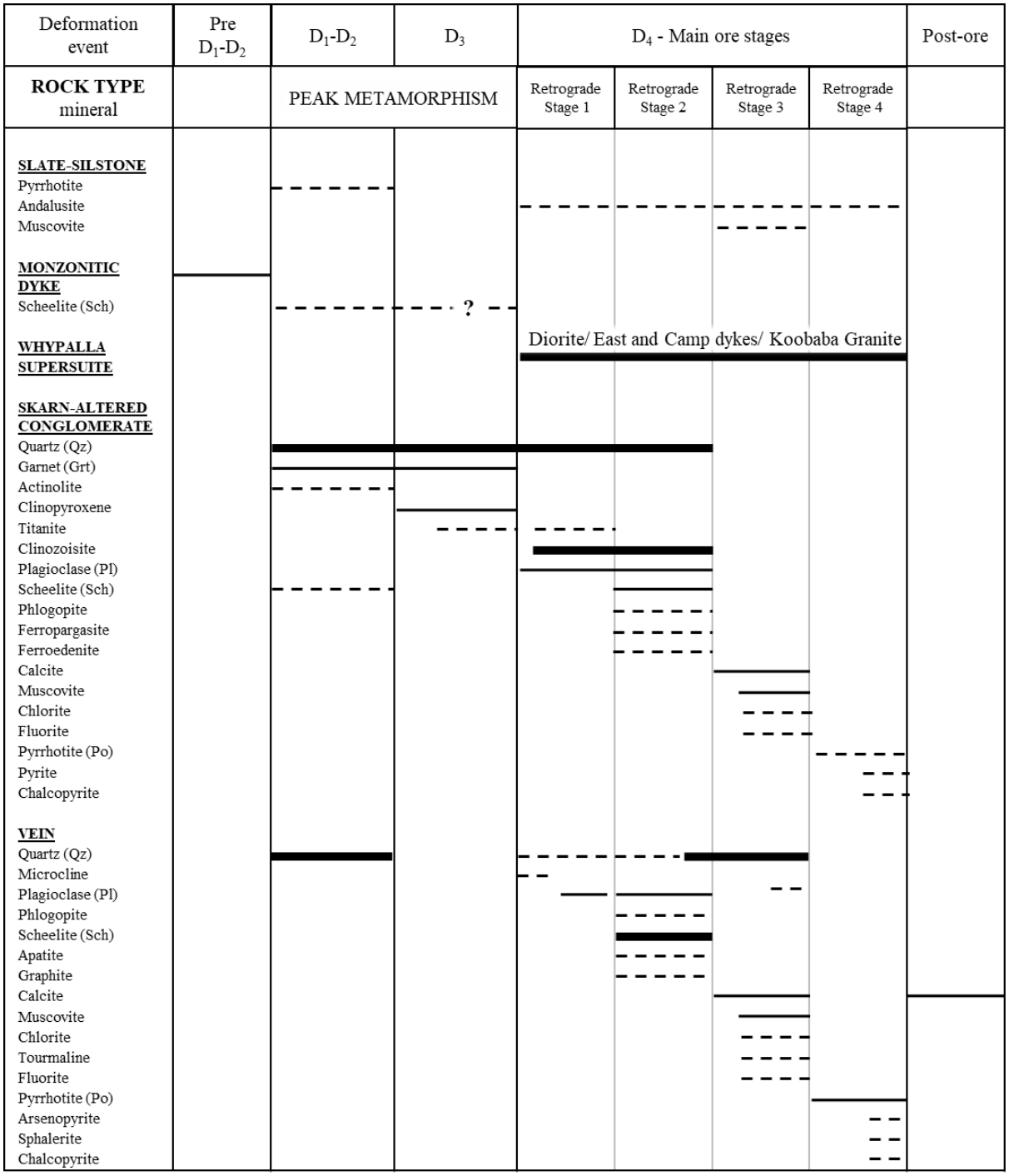

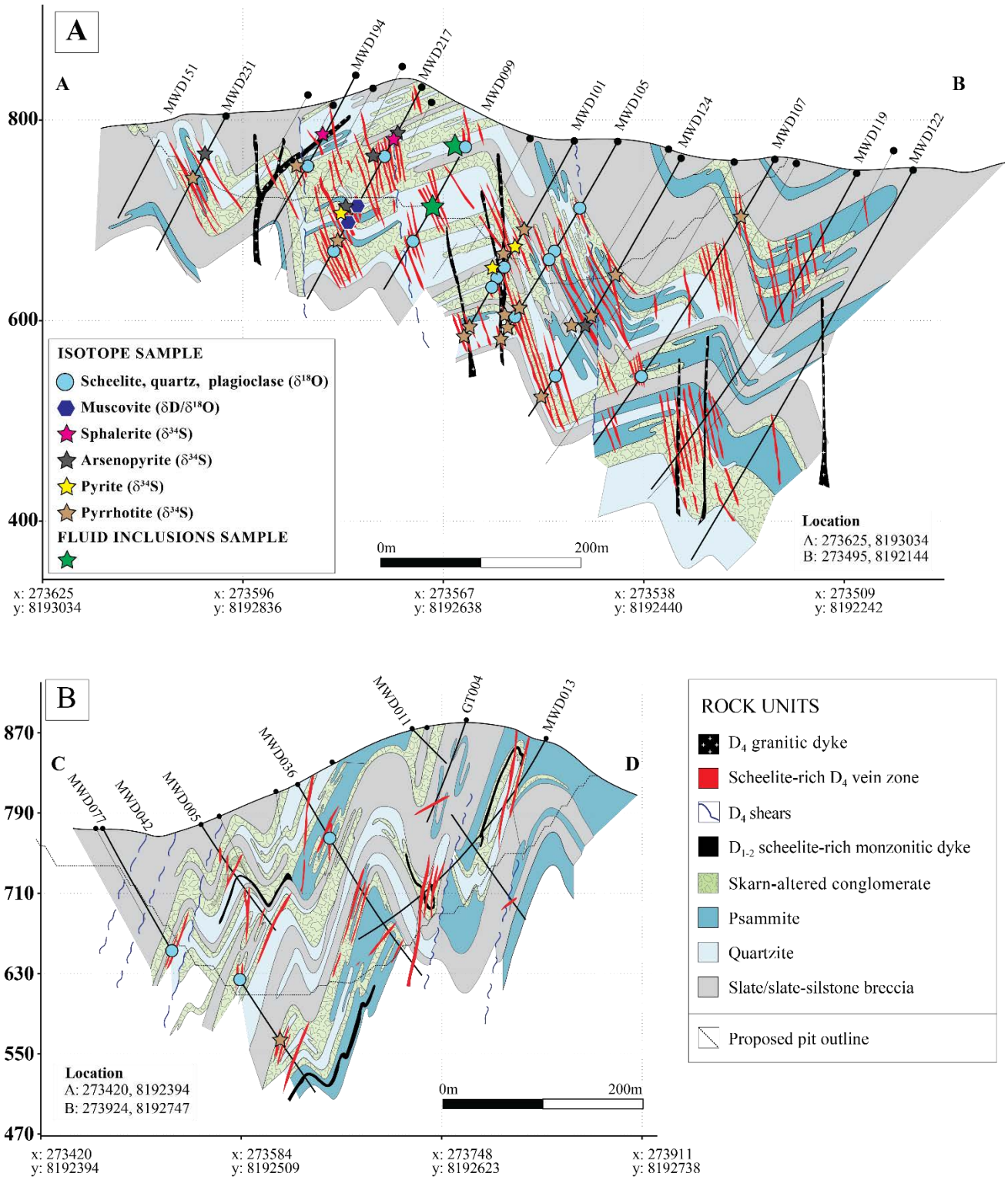

Figure 4.3 Generalized sections through the Watershed deposit showing chosen samples used for isotopes and fluid inclusions studies. **A.** North-northeast (008°section orientation) long section looking east. D_4 veins are visible in this section since the main orientation of these veins are east-west. **B.** Cross-section (055° section orientation) looking north. In the cross-section the early D_{1-2} and D_3 deformation events and related transposition are clearly visible since the σ_1 has a preferential east-west orientation. See **Figure 4.2** for the section locations. The grid system is Geocentric Datum of Australia 1994 (GDA94), zone 55.

The metasedimentary rocks at Watershed are intruded by a series of Carboniferous and Permian dykes assigned to the Whypalla Supersuite **(Chapter 2, Figs. 4.2-4.3)**. The Carboniferous dykes are ca. 350 Ma in age and monzonitic in composition **(Chapter 2)**. They have not been found on surface, but can be seen in drill core where they occur as less than 40 cm wide dykes of dark to light grey color, containing a foliation ($S_{1\text{-}2}$), indicating that they were emplaced and deformed early in the deformation history of the area **(Fig. 4.3B)**. Felsic minerals include 55 vol.% subhedral to euhedral plagioclase (<0.5 mm), 45 vol.% subhedral K-feldspar (< 0.5 mm) and ca. 5 vol.% anhedral quartz. Mafic minerals correspond to ca. 5 vol.% of the rock, and consist entirely of subhedral biotite (<0.5 mm) **(Fig. 4.4E)**. These dyke segments are important for mineralization, because they contain 10-15 vol.%, euhedral and partly resorbed to strongly fractured scheelite crystals **(Fig. 4.4F, see below)** that have been deformed and affected by recrystallization events following the formation of the $S_{1\text{-}2}$ fabric. This generation of scheelite occurs in close association with oligoclase **(Chapter 2, Table 4.1)**. Younger Permian dykes (ca. 291-277 Ma) are granitic in composition and occur on surface across the Watershed area **(Chapter 2, Fig. 4.2)**. The older East dyke (ca. 291 Ma) preserves a ductile fabric suggesting it may be emplaced during the latest stages of D_3 or the earliest stages of D_4, whereas the younger Camp dyke (ca. 277 Ma) cuts-across all fabrics and is undeformed **(Chapter 2).** The granitic dykes vary in width from 0.5 m to several tens of meters, and can be traced along strike for tens to hundreds of meters. They show varied textures, ranging from coarse porphyritic **(Fig. 4.4G)** to fine-grained varieties. The porphyritic dykes comprises phenocrysts of K-feldspar (20 vol.%) quartz (20 vol.%) and plagioclase (5 vol.%). The groundmass is composed of fine-grained quartz, K-feldspar and muscovite in approximately equal amounts.

4.3.1 Scheelite mineralization

Scheelite mineralization at Watershed is related to two events **(Chapters 2-3)**; an early Carboniferous intrusive-related event at ca. 350 Ma, which is overprinted by a later Permian hydrothermal metamorphic event at ca. 275 Ma. Early disseminated scheelite mineralization is aligned in $S_{1\text{-}2}$ and occurs in close spatial association with the ca. 350Ma monzonite dykes, while the bulk of the scheelite mineralization at Watershed occurs in D_4, trans-tensional quartz-plagioclase veins cutting skarn-altered conglomerate of the Hodgkinson Formation. Early $D_{1\text{-}2}$ scheelite mineralization is found disseminated in monzonite and in skarn-altered conglomerate and formed during prograde peak metamorphism **(Table 4.1; Figs. 4.4F, 4.4H)**. Late retrograde D_4 scheelite occurs as stringers in skarn-altered conglomerate, and along the margins and in alteration haloes of multi-staged quartz-plagioclase D_4 veins in skarn-altered conglomerate **(Fig. 4.4I)**. Based on cross-cutting relationships, the D_4 retrograde events have been sub-divided into four main retrograde stages **(Chapter 2, Table 4.1)**.

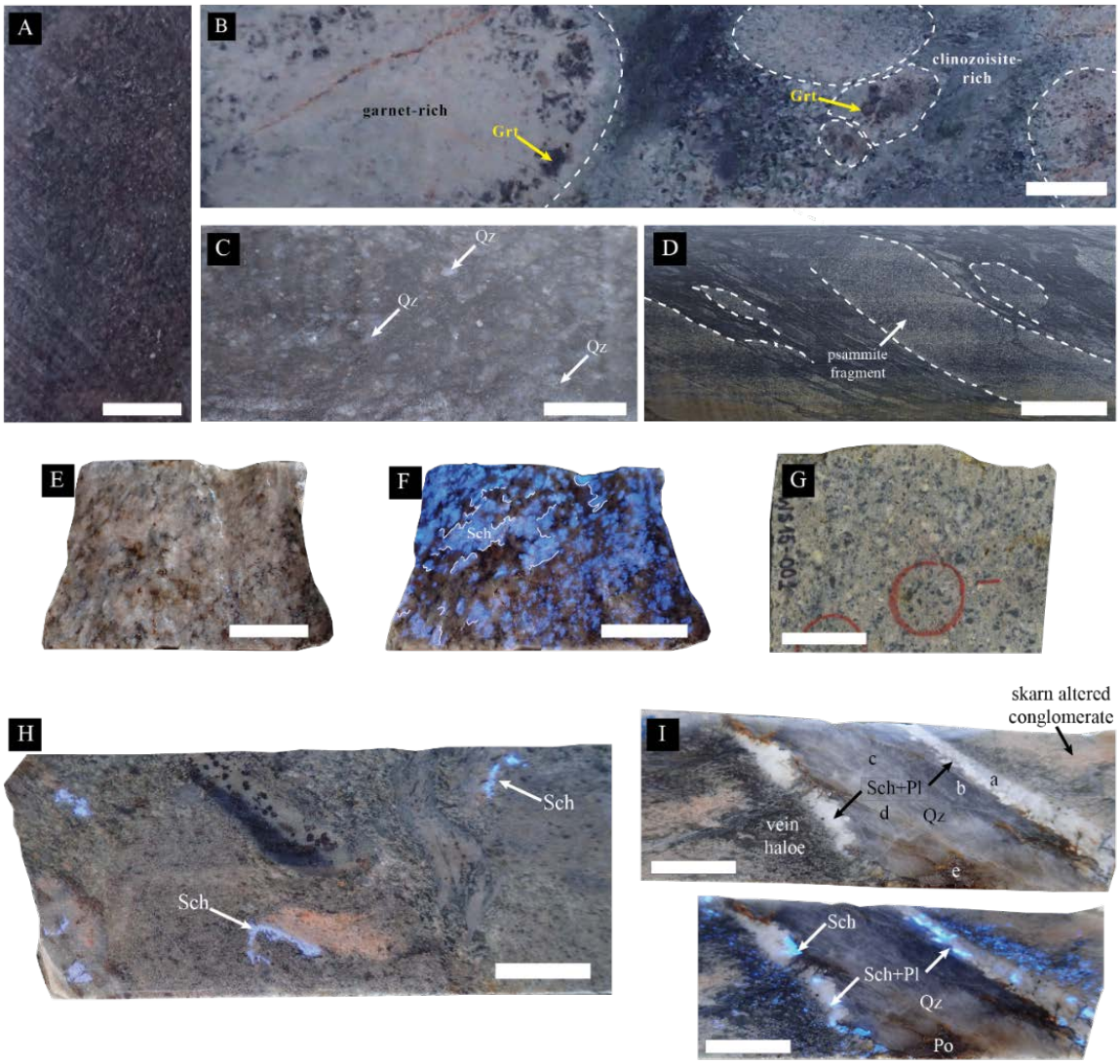

Figure 4.4 Hand specimens samples photographs of the different rock types at the Watershed deposit. For sample locations and mineral abbreviations, see **Figs. 4.2, 4.3A-B** and **Table 4.1**, respectively. White rectangles are 2 cm scale bars in each image. **A.** Psammite from drill core **MWD124 at 216 m**. **B.** Skarn-altered conglomerate from drill core **MWD101 at 159 m**. **C.** Quartzite from drill core **MWD099 at 150 m**. **D.** Slate-siltstone breccia from drill core **MWD119 at 20 m**. **E.** Monzonitic dyke from drill core **MWD013 at 99 m**. **F.** Scheelite mineralization (Sch) affected by the $S_{1\text{-}2}$ fabric (few white traced lines for reference) in $D_{1\text{-}2}$ monzonite (drill core **MWD013 at 99 m**) under UV light. **Figure 4.4E** shows the same sample without UV light. **G.** Granitic East dyke (WS15-001). **H.** Skarn-altered conglomerate (drill core **MWD011 at 147.5 m**) under UV light showing $D_{1\text{-}2}$ sigmoidal scheelite (Sch) mineralization along ductile $S_{1\text{-}2}$ fabric. **I.** Detailed images of a multi-stage scheelite-rich quartz plagioclase D_4 vein from drill core **MWD107 at 259 m** (note the blue color of scheelite under UV light in the bottom image). The letters in the image denotes different stages within the veins: **(a)** early plagioclase + scheelite (Sch + Pl) – quartz (Qz) assemblage as margins of veins (Retrograde Stages 1 and 2; **Table 4.1**); **(b)** grey quartz **(c)** white quartz veinlets **(d)** calcite stringers from Retrograde Stage 3 and **(e)** late pyrrhotite fracture filling from the late Retrograde Stage 4. Note the relation between the centimetric dark vein halo and the skarn-altered conglomerate on the top image.

4.3.1.1 Early D_{1-2} scheelite mineralization

D_{1-2} subhedral to euhedral scheelite crystals in monzonite dykes **(Fig. 4.4F)** are less than 2 mm in diameter and are generally strongly fractured. They have complex growth zoning, dissolution lamellae and resorbed boundaries, which suggest partial recrystallization during later deformation **(Chapter 3).** Scheelite also exhibits ductile deformational features such as sigmoidal shapes, boudin shapes, and in places scheelite trails were folded during D_3 **(Fig. 4.4F)** indicating that scheelite mineralization pre-dated D_3.

Disseminated D_{1-2} scheelite in polymict skarn-altered conglomerate occurs within the S_{1-2} foliation **(Fig. 4.4H)**. The foliation is characterized by quartz-rich patches, with scheelite coexisting with D_{1-2} Ca-rich garnet (Grs_{40-65}), actinolite, and plagioclase **(Table 4.1)**. The D_{1-2} quartz, plagioclase, actinolite and garnet assemblage formed during peak metamorphism **(Chapter 2)**.

4.3.1.2 Late D_4 scheelite mineralization associated with veining

The bulk of economic scheelite mineralization at Watershed occurs in veins associated with D_4 shear zones, and disseminations in vein haloes, within skarn-altered conglomerate **(Fig. 4.4I)**, where scheelite is intergrown with clinozoisite **(Chapter 2, Table 4.1; Fig. 4.4I).** The veins are of limited length (<30 m), vary in width from a few cm's to 3 m, and terminate abruptly in slate and/or slate-siltstone breccia. The widest veins are extensional in nature and generally trend east-west with a steep southerly dip **(Fig. 4.3A)**. Veins in all other directions are thinner (<10 cm) **(Chapter 2)**.

The D_4 veins opened in a number of distinct stages. The margins of the D_4 veins contain feldspar, scheelite and quartz **(Fig. 4.4I)**. This assemblage represents Retrograde Stages 1 and 2 **(Table 4.1)**. During Retrograde Stage 1 early sanidine (overgrown by plagioclase, An_{15-55}) formed with minor quartz in the vein margin **(Chapter 2)**. Retrograde Stage 2 is characterized by intergrown scheelite (containing graphite inclusions) and plagioclase (An_{3-43}) overgrowing early plagioclase, phlogopite and trace apatite **(Chapter 2)**. Further vein opening during Retrograde Stage 3 resulted in infilling of the central part of the vein by grey and white quartz, which is subsequently cross cut by muscovite and calcite **(Fig. 4.4I)** with minor chlorite, tourmaline and fluorite. Retrograde Stage 4 fractures cut the previous stages and contain pyrrhotite **(Fig. 4.4I)**, arsenopyrite with lesser pyrite, chalcopyrite, and sphalerite **(Table 4.1)**.

4.4 Sample selection

4.4.1 Fluid inclusion samples

Fluid inclusion studies were carried out on two drill core samples (MWD099-054B and MWD099-124B; **Fig. 4.3A; Appendix 1.1**) of coexisting scheelite and quartz (occurring as inclusions in scheelite), which formed during Retrograde Stage 2 in mineralized D_4 veins **(Table 4.1; Fig. 4.5A-B)**. Studying the fluid inclusions in these samples allows the identification of the mineralizing fluid and the physico-chemical conditions of ore formation during D_4 vein development.

4.4.2 Isotope samples

Oxygen ($\delta^{18}O$) isotope data were collected from D_4 scheelite, plagioclase, quartz, and muscovite **(Fig. 4.3; Appendix 1.1)** in veins and in vein haloes associated with the different Retrograde Stages. Scheelite, plagioclase and quartz were collected from veins associated with the Retrograde Stage 2 **(Table 4.1)**. Muscovite was collected from a vein-halo outcrop (WS16-006; **Fig. 4.2; Appendix 1.1**) of a mineralized D_4 vein, and from the muscovite centerlines in D_4 veins from drill-core associated with Retrograde Stage 3 **(Table 4.1; Fig. 4.3A, Appendix 1.1)**. The vein centerlines is a late post-ore event **(Table 4.1)** associated with the Hunter-Bowen Orogeny **(Chapter 2)** (Henderson et al., 2013). Sulphur isotopic compositions ($\delta^{34}S$) were collected from fracture filling Retrograde Stage 4 pyrrhotite, arsenopyrite, pyrite and sphalerite in D_4 veins **(Table 4.1; Fig. 4.3A, Appendix 1.1)**. The δD isotopic data were collected from muscovite in a D_4 vein-halo from a mineralized D_4 vein, and from muscovite centerlines in D_4 veins **(Table 4.1; Fig. 4.3A, Appendix 1.1)**.

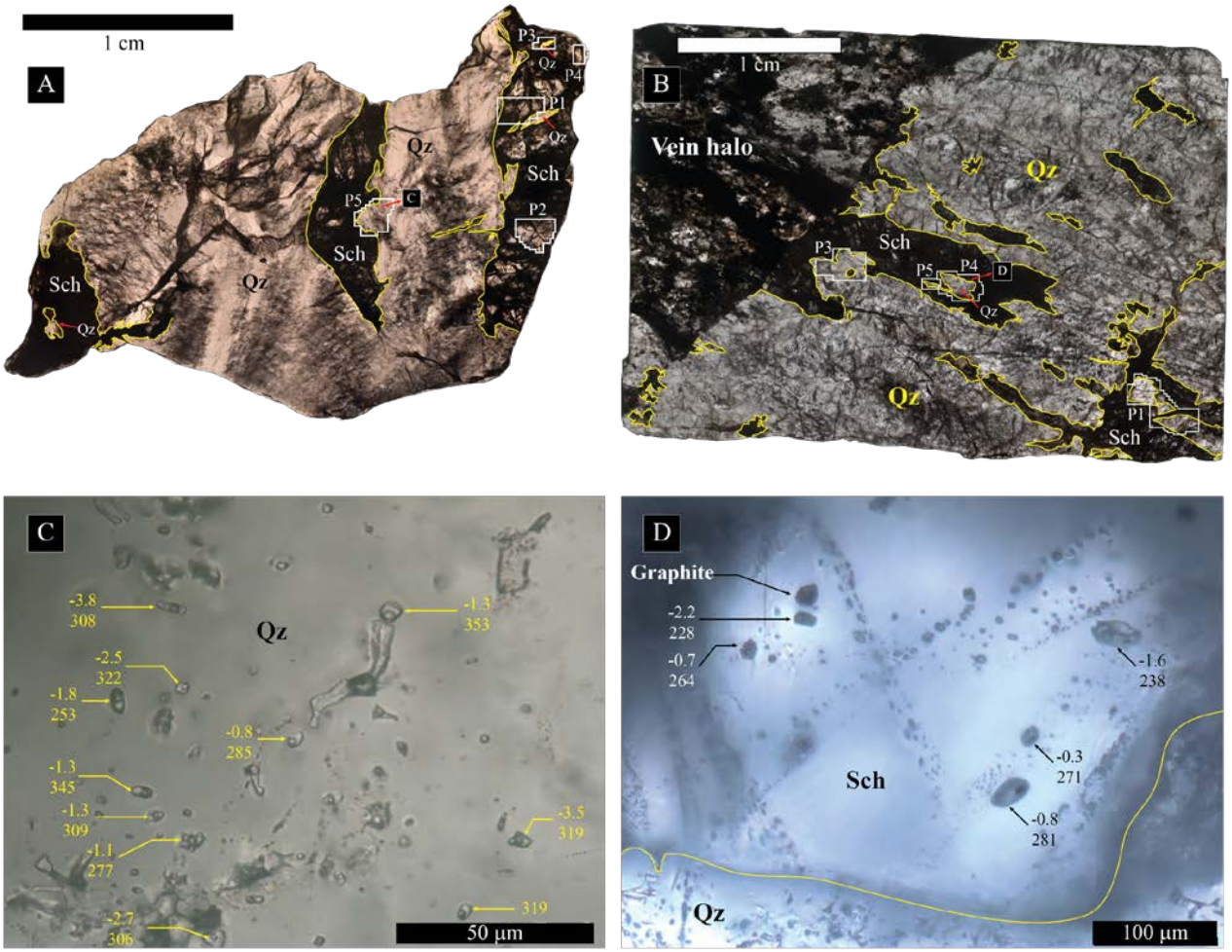

Figure 4.5 Microphotographs of analyzed samples for fluid inclusions. For sample locations and mineral abbreviations, see **Figs. 4.3A-B, Appendix 1.1** and **Table 4.1**, respectively. **A.** Stitched image of sample **MWD099-054B** where scheelite (Sch) is cut and intergrown with quartz (Qz). Yellow contours denotes scheelite (Sch) margins. Analyzed areas (P1 to P5) are shown. **B.** Stitched image of sample **MWD099-124B** where scheelite (Sch) is growing perpendicular to vein wall in a pure tension regime. Scheelite is intergrown and cross-cut by quartz (Qz). Yellow contours denotes scheelite (Sch) margins. Analyzed areas (P1, P3 to P5) are shown. **C.** Stitched microphotographs from different focus levels of a Qz grain in area P5 (P5-7, **Fig. 4.5A; Appendix 4.1)** from sample **MWD099-054B**. Final ice melting temperature (T_m) and homogenization temperatures (T_h) are indicated in °C. **D.** Stitched microphotographs from different focus levels of a scheelite (Sch) grain (P4-1, **Fig. 4.5B; Appendix 4.1)** from sample **MWD099-124B**. Final ice melting temperature (T_m) and homogenization temperatures (T_h) are indicated in °C. Note the graphite inclusion within scheelite (Sch).

4.5 Analytical techniques

4.5.1 Microthermometry

Twenty-four samples were inspected for their suitability for fluid inclusion study. Of those, two samples were selected for detailed study. Doubly polished sections (ca. 200 µm thick) were used for microthermometric measurements at James Cook University, Townsville, Australia. Fluid inclusion microthermometry was conducted using a Linkham MDS600 heating-freezing stage (temperature range between −196 and +600°C), attached to an Olympus BX51 microscope with 40 and 50× long-working distance objectives. The MDS600 heating-freezing stage is operated using Linksys 32 software. Samples were placed within the insulated stage on a 10 mm diameter quartz lens. Pure CO_2 and H_2O inclusions in quartz (supplied by FluidInc) were used for calibration at the triple points of CO_2 (−56.6°C) and H_2O (0.0°C). Critical homogenization temperatures of synthetic H_2O inclusions in quartz were used for calibration at 374°C. Phase transitions below room temperature have a precision of ±0.3°C; homogenization measurements of aqueous inclusions have a precision of ±5°C. The following phase transitions were systematically measured during the freezing and heating experiments:

1. Metastable freezing temperature (T_f) of the liquid phase in H_2O-rich fluid inclusions. The metastable freezing temperature is not an exact indicator of the salinity of the aqueous phase, but it is a good indication of the final ice melting temperatures (Wilkinson, 2017).
2. Initial melting (T_i) of the liquid phase in H_2O-rich fluid inclusions.
3. Final melting of ice (T_m) in H_2O-rich fluid inclusions.
4. Homogenization (T_h) of H_2O-rich fluid inclusions. Homogenization occurs by the disappearance of the bubble into the liquid phase.
5. Clathrate melting (T_{mcl}), which was occasionally observed in the larger H_2O-rich fluid inclusions

4.5.2 Raman microspectroscopy

Laser Raman spectroscopy analyses were conducted with a WITec Alpha300 Access Raman microspectrometer at the Advanced Analytical Centre of the James Cook University, Townsville, Australia. The WITec Alpha300 Access is equipped with a 532.1 nm UHTS 300 SMFC VIS-NIR laser source. Data processing was done with the WITec Project Data Analysis Software 4.1. The database compiled by Frezzotti et al. (2012) was used to identify fluid and solid phases

4.5.3 Stable isotopes analyses

Oxygen and hydrogen isotopes from plagioclase, quartz and scheelite were analysed at the Stable Isotope Laboratory at GNS Science (New Zealand). Oxygen was extracted from silicate and scheelite sample powders for isotope analyses using a CO_2-laser and BrF_5 (Sharp, 1990). Oxygen isotope values are reported in the $\delta^{18}O$ notation, relative to Vienna Standard Mean Ocean Water (VSMOW). Samples were normalized to the international quartz standard NBS-28 using a value of +9.6 per mil (‰). Values for four NBS-28 analyzed with the samples had values that varied by less than 0.15 ‰. Samples and standards were heated overnight to 200°C prior to loading into the vacuum extraction line. These were then evacuated for approximately 6 hours. Blank BrF_5 runs were done until yield was less than 0.2 µmoles oxygen. Oxygen yields were recorded and CO_2 gas analysed on a Geo 20-20 mass spectrometer. Muscovite hydrogen samples were analysed on a HEKAtech high temperature elemental analyser coupled with a GV Instruments IsoPrime mass spectrometer. Samples were pyrolyzed at 1450°C, in silver capsules. All samples were analysed in triplicate. All results are reported relative to VSMOW, normalized to international standards IAEA-CH-7, NBS30 and NBS22 (with reported values of −100‰, −66‰, and −118‰) and waters USGS46, 47, 48 and W62001 (with reported values of −235.8‰, −150.2‰, −2.0‰, −41.1‰). The external precision for these measurements is better than 2‰.

Sulphur ($\delta^{34}S$) isotope analyses of sulphide mineral phases were performed at the Central Science Laboratory of the University of Tasmania, Hobart, Australia using a NCS Combustion Mode coupled with an IsoPrime100 IRMS (Stable isotope ratio mass spectrometry) detector. Sulphide samples were drilled directly from the rock (10 mg), after which a small amount of powdered material (0.1 mg sulphur) was used for the analysis. Sulphides were combusted at a temperature of 1150°C in an O_2-enriched He atmosphere. After combustion, the bulk sample gas was stripped of H_2O in the water traps, and of SO_2 and CO_2 in the 'purge and traps' columns. The N_2 component gas is not trapped in a column and is the first to enter to the IRMS. The final gas to be released is SO_2, which occurs when the desorption column is heated to 220°C. The sample gas subsequently bypasses the CO_2 column, passes through a second water trap and enters the IRMS. Reference He, N_2, CO_2 and SO_2 are injected into the IsoPrime100 IRMS prior to each of the unknown measured components. The international reference standards and internal standards were repeatedly measured in between samples in order to control the analytical reproducibility. The precision was 0.2‰ for $\delta^{34}S$ and 0.25% for S-elemental analysis. All S isotope values are expressed as a delta notation in ‰ (per mil) relative to Cañón Diablo Troilite (CDT).

4.6 Results

4.6.1 Primary fluid inclusions in quartz

Isolated fluid inclusions and late fluid inclusion trails cutting grain boundaries were identified in quartz coexisting with scheelite. The late secondary fluid inclusions were excluded in this study, because they postdate the mineralization event. The isolated fluid inclusions (5-90 μm) in quartz are irregular in shape and in all cases contain a liquid phase and a bubble **(Fig. 4.5C)**. In some cases graphite, was identified by Raman microspectroscopy **(Fig. 4.6)** inside the fluid inclusions. The volume of the bubble in the fluid inclusions varies between 10-30%. Raman microspectroscopy indicates that the bubble comprises CH_4 **(Fig. 4.6A, 4.6C)**. Methane was occasionally also detected in the aqueous liquid phase **(Appendix 4.1)**. Cooling of larger fluid inclusions to temperatures of ca. −120°C (observations at lower temperature are difficult because of condensation) did not result in any change in the bubble (i.e., no liquid-vapour phase separation was observed). This indicates that the bubble comprises a CH_4 vapour with a density that is lower than 0.019 g/cm^3 or greater than 840 cm^3/mol (Setzmann and Wagner, 1991). Consequently, it is impossible to determine the exact fluid composition. The high molar volume of the CH_4 vapour phase indicates that the CH_4 content of the fluid must be less than 1 mol.% (i.e. < 0.6 mol/kg). Initial melting of the liquid phase occurred between −31 and −18°C, corresponding to the (meta) stable eutectic melting temperature of the H_2O-NaCl system (Goldstein and Reynolds, 1994). Final melting of ice occurred between −5.7 and −0.1°C **(Fig. 4.7A-C)** indicating a low salinity, which is in good agreement with freezing temperatures of the aqueous liquid phase between −35 and −50°C **(Fig. 4.7A)**. Homogenization into the liquid phase occurred between 171 and 386°C **(Figs. 4.7B, 4.7D)**. Clathrate melting was only observed in a few larger fluid inclusions at temperatures at ca. +10°C. Salinities of the aqueous liquid phase calculated using HokieFlincs (Steele-MacInnis et al., 2012) and the fluid inclusion densities vary between 0.2 and 8.8 wt.% NaCl and 0.66 and 0.92 g/cm^3, respectively **(Table 4.2)**. It must be noted that these salinities are probably slightly too high because the ice melting temperatures were measured in the presence of clathrates (e.g., Mao et al., 2013a).

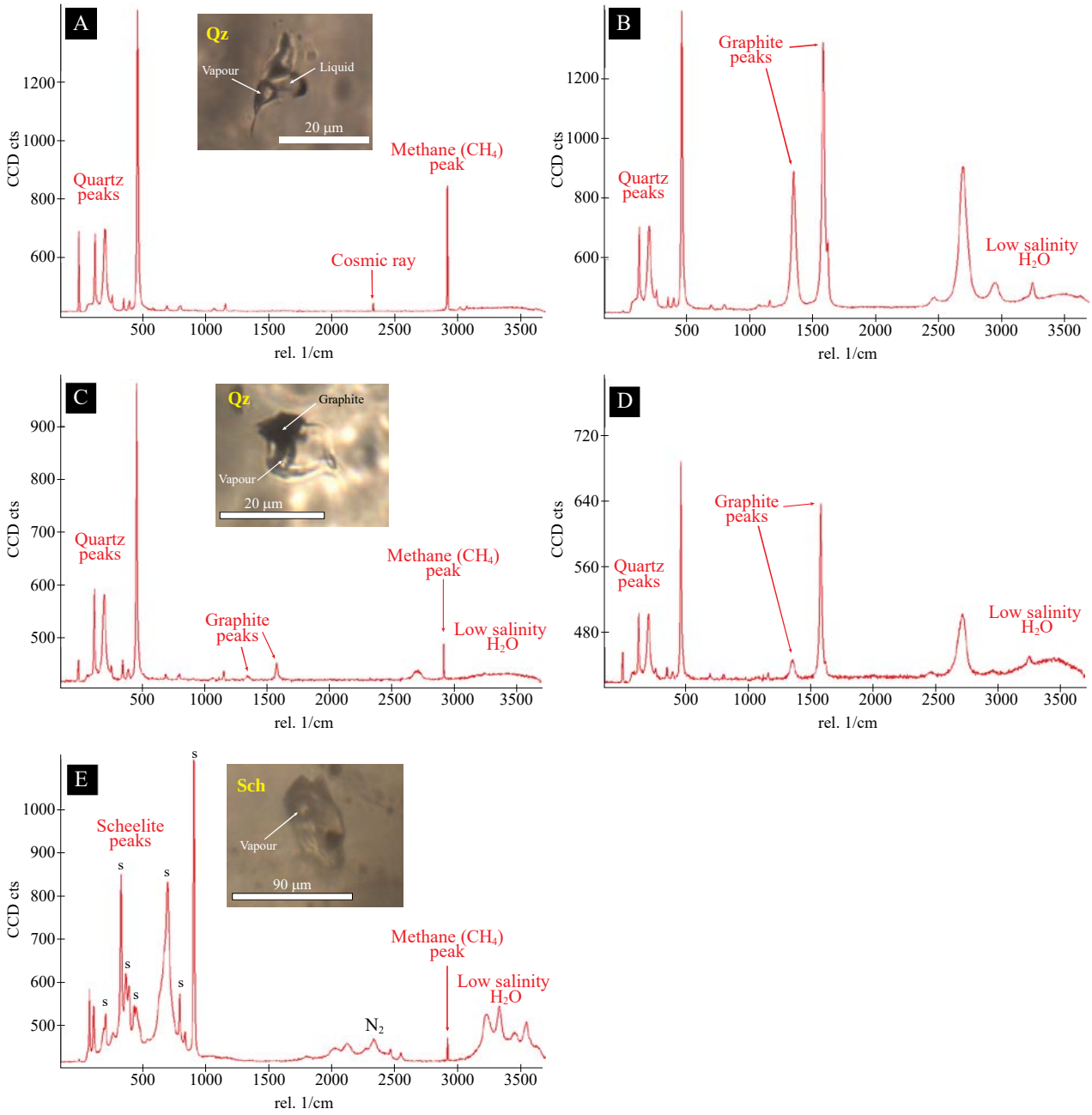

Figure 4.6 Example of Raman microspectroscopy analysis of fluid inclusions in quartz and scheelite in sample **MWD099-124B (Appendix 4.1)**. **A.** Vapour phase in fluid inclusion P4-2-3 in quartz **(Fig. 4.5B)**. Inset microphotograph shows fluid inclusion. **B.** Liquid phase in fluid inclusion P4-2-3 in quartz **(Fig. 4.5B)**. **C.** Vapour phase in fluid inclusion P4-1-1 in quartz **(Fig. 4.5B)**. Inset microphotograph shows fluid inclusion. **D.** Solid phase in fluid inclusion P4-2-3 in quartz **(Fig. 4.5B)**. **E.** Vapour phase in fluid inclusion P4-1-2 in scheelite **(Figs. 4.5B, 4.5D).** Inset microphotograph shows fluid inclusion.

4.6.2 Primary fluid inclusions in scheelite

Isolated fluid inclusions in scheelite (5-45 µm) are both irregular and regular in shape **(Fig. 4.5D)**. The fluid inclusions contain a liquid phase and a bubble. Graphite was detected in only one fluid inclusion **(Appendix 4.1)**. Similar to the fluid inclusions in quartz, the bubble size varies between 10 and 30 vol.%. Similar to the fluid inclusions in quartz, the bubble comprises a low-density CH_4 vapour **(Fig. 4.6E, Appendix 4.1)** indicating a density that is lower than 0.019 g/cm^3 or greater than 840 cm^3/mol (Setzmann and Wagner, 1991), i.e. the CH_4 content of the fluid must be less than 1 mol.% (i.e. < 0.6 mol/kg). Initial melting of the aqueous phase was observed between −33 and −21°C indicating the presence of NaCl, similar to primary fluid inclusions in quartz **(Appendix 4.1)**. Final melting of ice occurred between −5.1 and −0.3°C **(Fig. 4.7A-C)**, which is in good agreement with freezing temperatures of the aqueous liquid phase between −30 and −40°C **(Fig. 4.7A)**, and again similar to the primary fluid inclusions in quartz, homogenization into the liquid phase was observed at temperatures varying between 206-333°C **(Fig. 4.7B, 4.7D)**. Similar to the primary fluid inclusions in quartz, clathrate melting was observed for a few larger fluid inclusions at temperatures of ca. +10°C. Salinities of the aqueous liquid phase (Steele-MacInnis et al., 2012) and fluid inclusion densities vary between 0.5-8.0 wt.% NaCl and 0.68-0.91 g/cm^3, respectively **(Table 4.2)**. Similar to quartz, the calculated salinities are probably slightly too high because ice melting was measured in the presence of clathrates (e.g., Mao et al., 2013a).

Table 4.2 Characteristics of the measured fluid inclusions in D_4 veins from the Retrograde Stage 2

Mineral	D_4 quartz	D_4 scheelite
Composition	H_2O-NaCl-CH_4 0.2-8.8 wt% NaCl < 1 mol.% CH_4	H_2O-NaCl-CH_4 0.5-8 wt% NaCl < 1 mol.% CH_4
Density [g/cm^3]	0.54-0.92	0.68-0.92

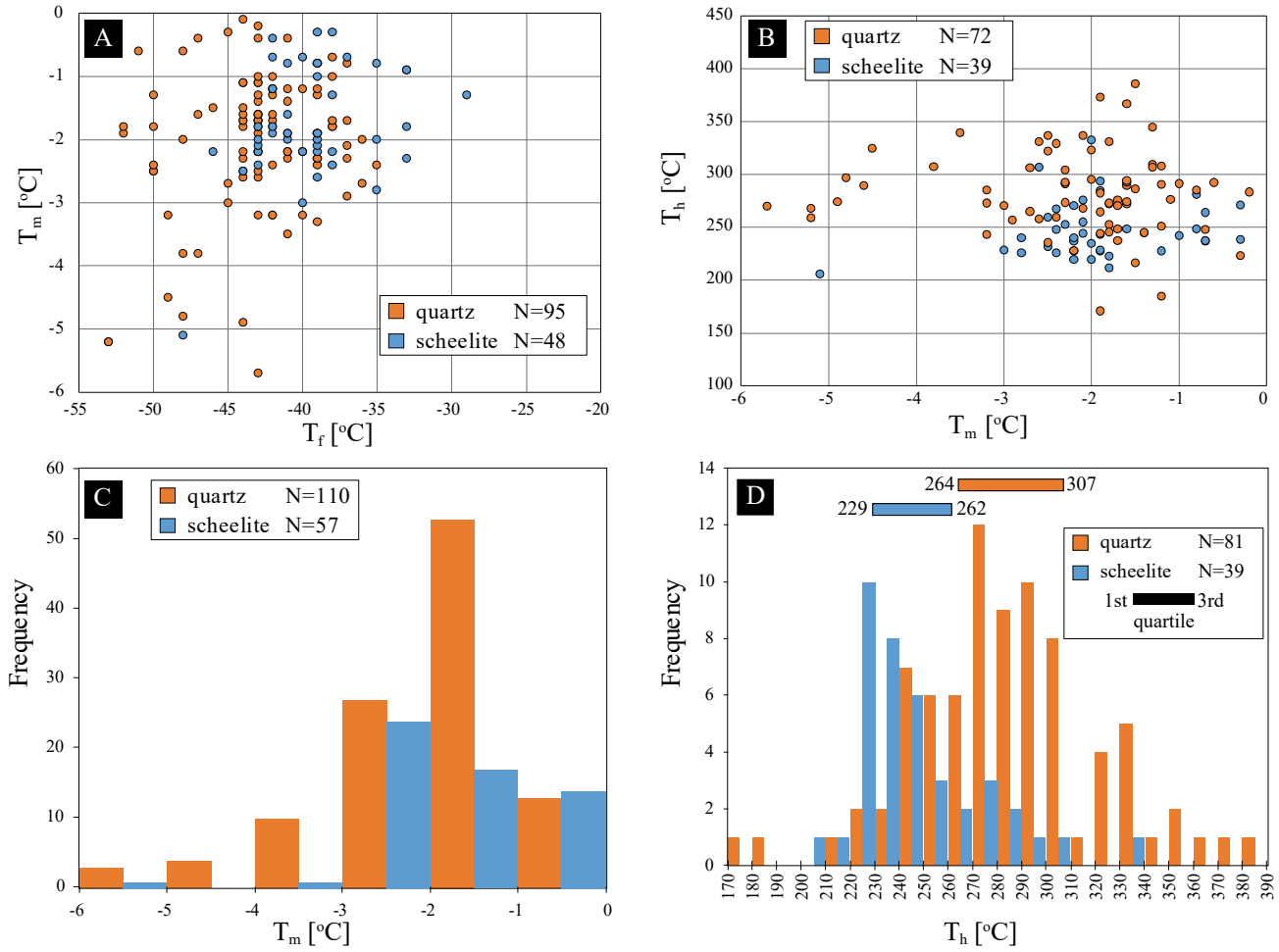

Figure 4.7 Fluid inclusions graphs from Watershed. **A.** Metastable freezing temperature (T_f) versus final ice-melting temperatures (T_m). **B.** Final ice-melting temperature (T_m) versus homogenization temperature (T_h). **C.** Frequency distribution for final ice-melting temperature (T_m). **D.** Frequency distribution for homogenization temperature (T_h).

4.6.3 Stable isotope geochemistry

4.6.3.1 Oxide and silicates

Scheelite grains from D_4 veins (Retrograde Stage 2, Table 1) were analyzed for oxygen isotopes ($\delta^{18}O_{VSMOW}$). The D_4 scheelite shows a large spread of values between +3.8 to +7.3‰ (n = 17) with an average value of +5.4±1.1‰ **(Table 4.3)**. Plagioclase grains coexisting with scheelite **(Table 4.1)** show $\delta^{18}O_{VSMOW}$ values ranging between +7.0 and +11.8‰ with an average value of +10.3±1.4‰ (n = 14) **(Table 4.3)**. Quartz formed in veins, together with or slightly post-dating scheelite and plagioclase **(Table 4.1)** shows $\delta^{18}O_{VSMOW}$ values ranging between +12.6 and +15.5‰ (n = 13) with an average value of +14.0±0.9‰ **(Table 4.3)**.

Three muscovite samples from Retrograde Stage 3 in D_4 veins and vein halo were analyzed for oxygen ($\delta^{18}O_{VSMOW}$) and hydrogen (δD_{VSMOW}) isotopes. The $\delta^{18}O_{VSMOW}$ values for muscovite along the centerlines are +11.5 and +12.4‰, and for muscovite from a vein halo +13.2‰. The δD_{VSMOW} values for the centerline muscovite grains are –73.4 and –62.7‰, and for the muscovite in the vein halo –63.3‰ **(Table 4.4)**.

4.6.3.2 Sulphides

Sulphur isotope data ($\delta^{34}S_{CDT}$) for pyrrhotite (n = 17), arsenopyrite (n = 5), pyrite (n = 3) and sphalerite (n = 2) in D_4 veins from Retrograde Stage 4 are shown in **Table 4.5**. In general, values for $\delta^{34}S_{CDT}$ for all sulphide minerals fall within a narrow range between –2.54 to +2.80‰ with an average of –0.06±1.31‰. Pyrrhotite shows the largest spread from –2.54 to +2.25‰ (average: –0.53±1.21‰); whereas arsenopyrite shows the highest values ranging from –0.19 to +2.80‰ (average: +1.43±0.97‰). Pyrite and sphalerite show values ranging from –0.50 to +1.25‰ (average: +0.10±0.82‰), and from –0.22 to +0.29‰ (two measurements only), respectively **(Fig. 4.8A)**.

Sulphur isotope data published for mineral deposits hosted in the Hodgkinson Formation near Watershed include results from the Dianne, Mt. Molloy, O.K. and Mt Carbine deposits, which are summarized for comparison. The sulphur isotope signatures for the D_4 sulphides in Watershed are similar to those reported for syn-mineralisation pyrite, sphalerite and chalcopyrite in the Dianne stratiform (situated 45 km northwest from Watershed) massive sulphide deposit (–2.5 to +2.6‰) **(Fig. 4.1B, 4.8B)**, which is hosted in shale, siltstone and greywacke. Diagenetic pyrite $\delta^{34}S_{CDT}$ values for the same deposit range from +3.8 to +11.8‰ (Gregory and Robinson, 1984). In addition, the $\delta^{34}S_{CDT}$ values in Watershed are somewhat lower than the values reported from the "ore zone" pyrite (+3.3 to +5.4‰) in the Mt. Molloy stratiform massive sulphide deposit (situated 65 km southeast from Watershed; **Fig. 4.1B**), which is hosted in shale, greywacke, basaltic-siltstone breccia and minor basalt. Diagenetic pyrite in Mt. Molloy has higher $\delta^{34}S_{CDT}$ values (+7.2 and +9.8‰). The O.K. stratiform massive sulphide mine, hosted in chert, spilite and flysch, 70 km to the west from Watershed **(Fig. 4.1B)**, yield pyrite "ore zone" $\delta^{34}S_{CDT}$ values between +2.5 and +3.6‰ (Gregory and Robinson, 1984). Cheng et al. (2017)

reported $\delta^{34}S_{CDT}$ values between −9.1and −6.0‰ for sulphide grains associated with vein-hosted tungsten mineralization in the Mt Carbine deposit **(Fig. 4.8B)** situated 30 km south of Watershed.

Table 4.3 Oxygen isotope data (‰ relative to VSMOW) of scheelite, plagioclase and quartz from D_4 veins

Sample No.	Deformation rock type	Scheelite	Plagioclase	Quartz	Δsch-ab ^{18}O [(a)]	T °C
MWD042-197	D_4 vein	+5.7		+12.8		
MWD101-159	D_4 vein	+6.3	+9.7			
MWD105-077	D_4 vein	+5.1	+11.7	+13.7	6.56	265
MWD105-135	D_4 vein	+6.7	+11.2	+13.9		
MWD036-075.5	D_4 vein	+4.1	+11.2	+13.7	7.15	234
MWD077-145	D_4 vein	+5.2	+11.8	+14.2	6.64	260
MWD099-054	D_4 vein	+3.7	+9.4		5.64	339
MWD099-163.5	D_4 vein	+7.2	+11.6	+13.2		
MWD101-149	D_4 vein	+7.3		+13.5		
MWD101-155	D_4 vein	+5.2	+10.4		5.15	409
MWD105-123.5	D_4 vein	+4.8	+10.9	+15.5	6.15	293
MWD105-206	D_4 vein	+4.8	+8.8			
MWD107-259	D_4 vein	+6.1	+11.5	+14.7	5.42	366
MWD124-240	D_4 vein	+6.0		+12.6		
MWD194-105.5	D_4 vein	+3.8	+10.1	+14.8	6.34	279
MWD217-078	D_4 vein	+5.6	+7.0	+14.8		
MWD217-189.5	D_4 vein	+4.4	+8.8	+15.1		
	Min				5.2	234
	Max				7.2	409
	Average				6.1	306
	Standard Deviation				0.6	56

(a) albite ⇔ H_2O; °C Zheng (1993a); scheelite ⇔ H_2O; 100-500°C Wesolowski and Ohmoto (1986)

Table 4.4 Oxygen and hydrogen isotope data of muscovite

Sample No.	Location	δD (‰) VSMOW	$\delta^{18}O$ (‰) VSMOW
MWD217-133A	Vein center line	−73.39	11.5
MWD217-149A	Vein center line	−62.72	12.4
WS16-006	Vein halo	−63.28	13.2

Table 4.5 Sulphur isotope data for D_4 sulphide minerals from the Retrograde Stage 4 in vein

Mineral	Sample No	$\delta^{34}S$ ‰ CDT
Arsenopyrite	MWD124-193.5B	−0.2
	MWD217-133A	+1.3
	MWD217-048.5A	+1.4
	MWD231-043A	+1.9
	MWD217-078A	+2.8
Pyrite	MWD217-142A	−0.5
	MWD101-149A	−0.4
	MWD101-119A	+1.3
Pyrrhotite	MWD105-206A	−2.5
	MWD105-215A	−2.2
	MWD107-062.5A	−1.7
	MWD124-180A	−1.5
	MWD217-181A	−1.3
	MWD124-280.5B	−1.2
	MWD101-222A	−0.9
	MWD124-193.5A	−0.9
	MWD105-234A	−0.8
	MWD231-068A	−0.7
	MWD124-130.5A	−0.5
	MWD042-269B	+0.2
	MWD101-211.5A	+0.2
	MWD194-105.5A	+0.5
	MWD101-104A	+0.8
	MWD101-121.5A	+1.1
	MWD105-200A	+2.2
Sphalerite	MWD194-065A	−0.2
	MWD217-056A	+0.3

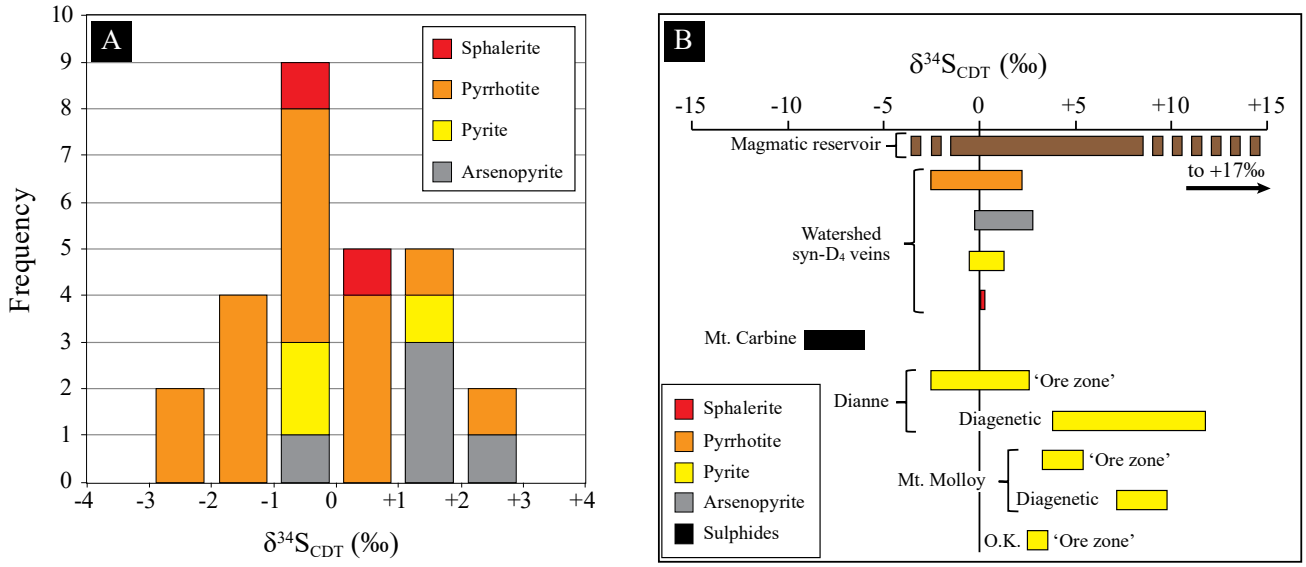

Figure 4.8 $\delta^{34}S_{CDT}$ values for sulfides from the Retrograde Stage 4 (sulfide stage) at Watershed. **A.** Frequency distribution showing the $\delta^{34}S_{CDT}$ for the different sulphide mineral phases. **B.** Watershed $\delta^{34}S_{CDT}$ data from this study shown together with those of unspecified sulphides from the Mt. Carbine tungsten deposit (Cheng et al., 2017) and pyrite from massive sulphide deposits hosted in the Hodgkinson Formation (Gregory and Robinson, 1984) **(Fig. 4.1B)**. The magmatic reservoir is from (Seal et al., 2000)

4.7 Discussion

4.7.1 Composition of fluids

Primary fluid inclusions in coexisting scheelite and quartz are identical in composition **(Figs. 4.7A-B)**, i.e. they consist of a low to medium salinity (0.2-9 wt.% NaCl) aqueous fluid containing less than 1 mol.% CH_4. The observed salinities are in agreement with those from other scheelite dominated deposits (Wood and Samson, 2000). The similarity in composition for fluid inclusions found in scheelite and quartz indicates that they formed from the same fluid. There is no evidence for fluid-fluid immiscibility as no fluid inclusions composed entirely of methane were found (e.g., Ramboz et al., 1982; Hurai, 2010). The presence of graphite in some of the fluid inclusions **(Figs. 4.5D, 4.6B-D)** indicates that the fluid was graphite saturated when it was trapped, and the graphite was trapped accidentally in some of the fluid inclusions. The fluid inclusions show a significant spread in salinities (between 0 and 9 wt.% NaCl), which is consistent with fluid-fluid mixing (Wilkinson, 2001) and, therefore, the presence of at least two fluid sources during mineralization (see below).

4.7.2 Temperature and pressure of mineralization

Isochores of primary fluid inclusions in scheelite and stable isotope geothermometry are used to constrain the temperature and pressure conditions of mineralization. Isochores for the H_2O-NaCl-CH_4 fluid inclusions can be used to constrain the pressure conditions of mineralization if the mineralization temperature can be established independently (e.g., Roedder and Bodnar, 1980). In this case, the mineralization temperature was calculated using the fractionation of oxygen isotope between coexisting scheelite and plagioclase (Wesolowski and Ohmoto, 1986; Zheng, 1993a), which yielded values between 234 and 409°C, with an average of 306±56°C **(Fig. 4.9)**. The average temperature of ca. 300°C is in good agreement with the observed CH_4 content of less than 1 mol.%, which will be discussed in more detail in the next section.

The calculation of the isochores for the H_2O-NaCl-CH_4 fluid inclusions includes some unavoidable inaccuracies. Firstly, the isochores were calculated following Lin and Bodnar (2010), in which NaCl is excluded as a component. Because most of the fluid inclusions have a salinity that is less than 5 wt.% NaCl ($T_m > -3$°C, see **Fig. 4.7C**) it is considered that the influence of NaCl on the position of the isochores is minor. Secondly, it is impossible to determine the exact fluid composition due to the uncertainty of the molar volume of CH_4. Therefore, isochores were constructed for 1 and 0.5 mol.% CH_4 (Lin and Bodnar, 2010). The isochores were calculated for the first (230°C) and third (260°C) quartile of the homogenization temperatures of fluid inclusions in scheelite **(Fig. 4.7D)**.

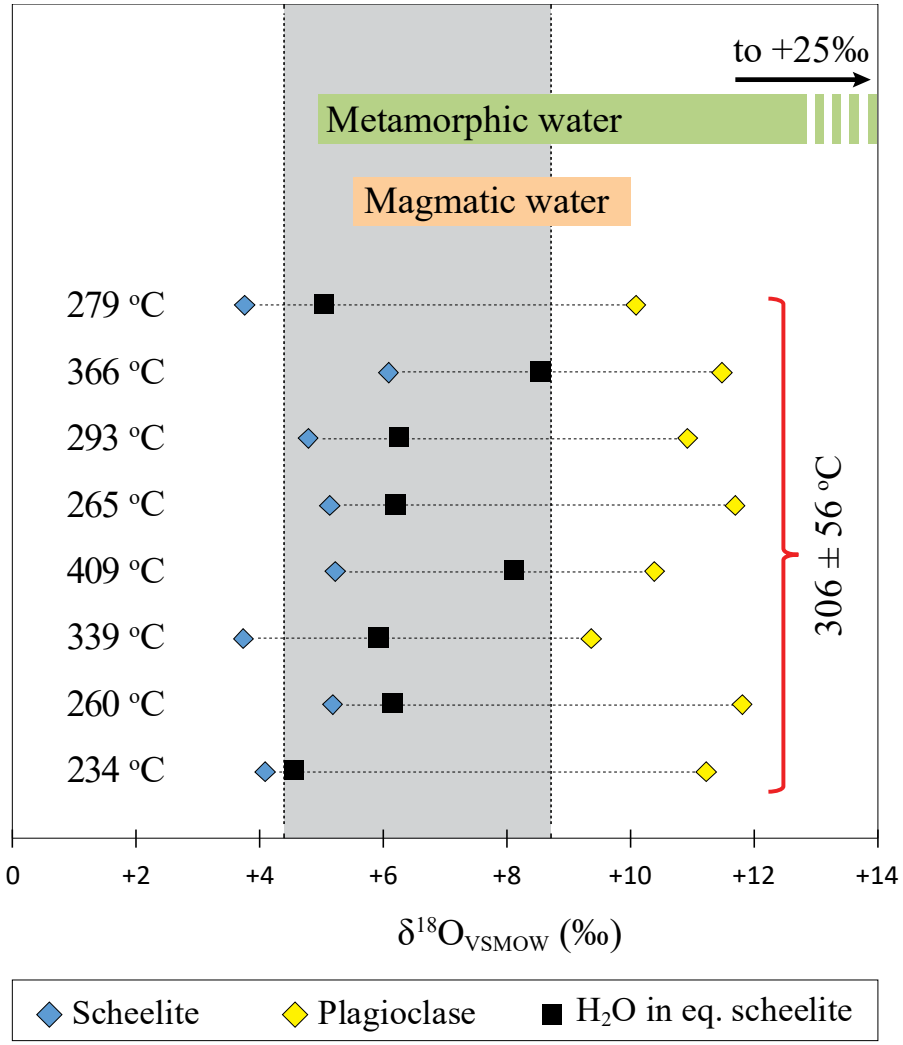

Figure 4.9 Oxygen isotopic composition for scheelite (blue rhomboids), plagioclase (yellow rhomboids) and water in equilibrium with the scheelite and plagioclase (black square) in D_4 veins. The fluid $\delta^{18}O_{VSMOW}$ compositions overlap with an igneous and a metamorphic fluid origin (Taylor, 1974). Also shown are the temperatures calculated using scheelite-plagioclase oxygen isotope fractionation (**Table 4.3)**.

Using the temperature range of 306±56°C obtained from the oxygen isotope thermometer together with the calculated isochores, the mineralization pressure can be constrained to 0.5-2.2 kbar and 0.7-2.6 kbar for 0.5 and 1 mol.% CH_4, respectively (**Figs. 4.10A-B)**. As will be explained in the next section, the CH_4 content constrains the mineralization temperature to ca. 300°C at a pressure of 1-1.5 kbar. Assuming a lithostatic fluid pressure and an average density of 2700 kg/m^3, these results indicate a depth of mineralization of 3-6 km and a corresponding elevated geothermal gradient of between 50 and 100 °C/km. It must be noted that the homogenization temperatures of the primary fluid inclusions in quartz are higher than those in scheelite **(Fig. 4.7D)**. This indicates that quartz precipitated at a higher temperature (320-460°C) than scheelite (at a pressure of 1-1.5 kbar, **Fig. 4.10C-D**), implying a higher geothermal gradient (50-150°C/km) at the time of quartz precipitation. These high gradients can be explained by the presence of Permian magmatism **(Fig. 4.1B)**.

4.7.3 Redox conditions during mineralization

Redox conditions of mineralization at Watershed can be estimated from the mineral phases that accompany scheelite mineralization. At Watershed, the mineralogy in skarn-altered conglomerate is characterized by garnet with low andradite content as well as pyrrhotite and arsenopyrite in D_4 veins **(Chapter 2, Table 1)**. This is indicative of reduced redox conditions, which is confirmed by the presence of CH_4 and graphite in the fluid inclusions **(Fig. 4.6A, 4.6C, 4.6E)** plus the presence of graphite inclusions in quartz and scheelite **(Fig. 4.5D)**. These findings are in agreement with the reduced conditions described for some tungsten skarn deposits (Shimazaki, 1980; Kwak, 1987).

The redox conditions of the fluid-rock system at Watershed, at known pressure and temperature, can be constrained in more detail by thermodynamic modelling of a carbon-saturated C-O-H fluid (French, 1966; Ohmoto and Kerrick, 1977; Huizenga, 2001). The fluid inclusion results in this study allow for these type of calculations since graphite is present (i.e., the fluid is carbon saturated) in the fluid inclusions and the pressure and temperature conditions can be constrained from fluid inclusion and stable isotope data (**Fig. 4.10A-B)**.

A carbon-saturated C-O-H fluid system has six compositional unknowns at a particular fluid pressure and temperature including the mole fractions of H_2O, CO_2, CH_4, H_2, and CO (denoted as XH_2O, XCO_2, XCH_4, XH_2, and XCO) and the fluid oxygen fugacity (fO_2). In order to calculate the fluid compositions, six equations are required. Four mass balance equations can be defined for a C-O-H fluid:

$$CO + ½O_2 \Leftrightarrow CO_2$$

$$H_2 + ½\ O_2 \Leftrightarrow H_2O$$

$$CH_4 + 2O_2 \Leftrightarrow CO_2 + 2H_2O$$

$$C + O_2 \Leftrightarrow CO_2.$$

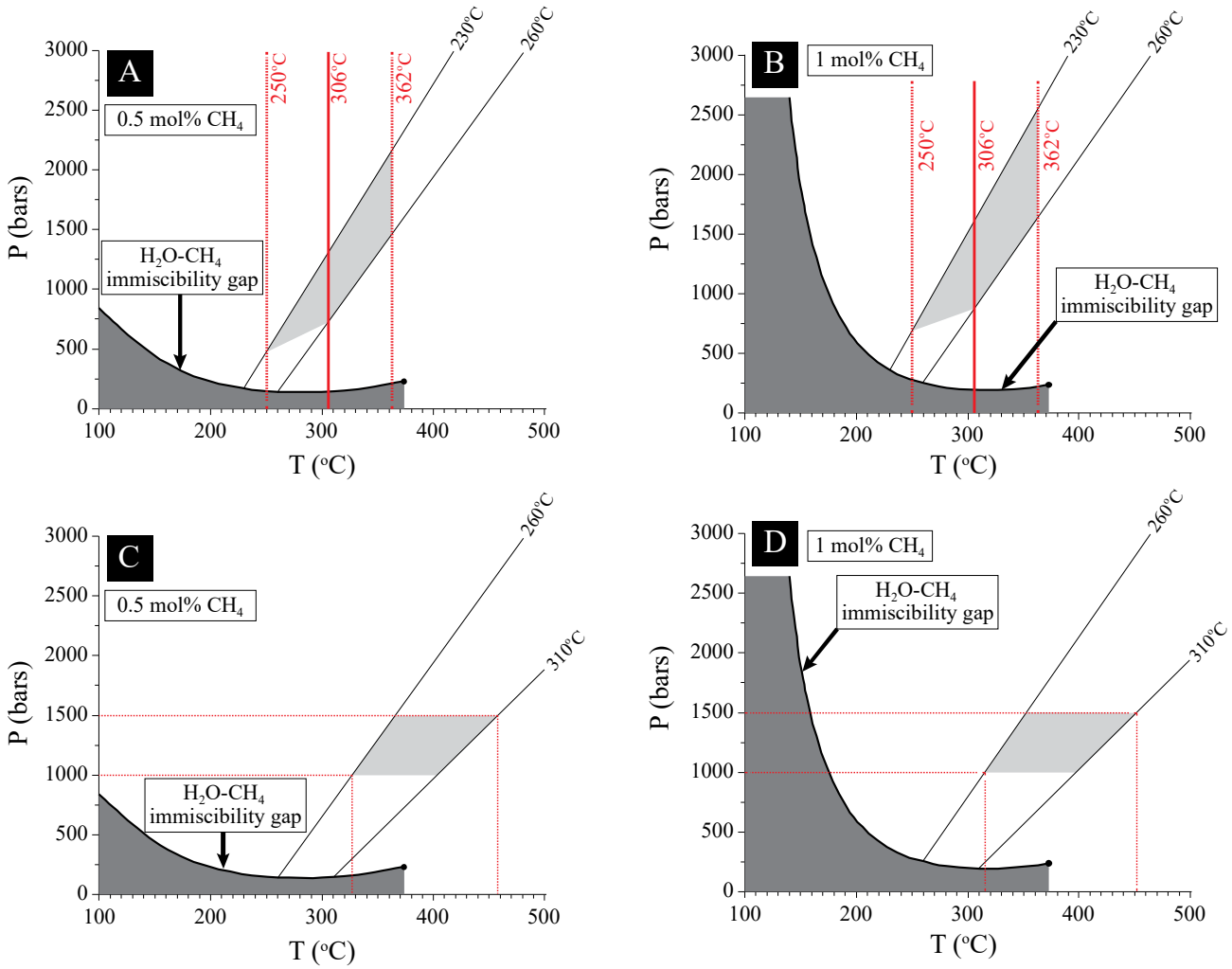

Figure 4.10 *P-T* diagrams for the H_2O-CH_4 system. The two upper diagrams **(A-B)** show the isochores for the first (230°C) and third (260°C) quartiles for the homogenization temperatures measured in scheelite for **A.** 0.5 mol% CH_4 and **B.** 1 mol% CH_4. The red lines in **A** and **B** represent the independent temperature constraints calculated using the oxygen fractionation between scheelite and plagioclase (306±56°C) (Wesolowski and Ohmoto, 1986; Zheng, 1993a). The grey areas in **A** and **B** represent the scheelite mineralization pressure-temperature conditions. The two bottom diagrams **(C-D)** show the isochores for the first (260°C) and third (310°C) quartiles for the homogenization temperatures measured in quartz for **C.** 0.5 mol% CH_4 and **D.** 1 mol% CH_4. The red lines in the Y axis of **C** and **D** represent the trapping pressures estimated from the C-O-H model calculations (1-1.5 kbar) intersected with the isochores (260 and 310°C) to calculate the range of trapping temperature of primary fluid inclusions in quartz (320-460°C), which is represented by the light grey areas. The black areas in all the *P-T* diagrams represent the H_2O-CH_4 immiscibility gap. Diagrams are modified after Lin and Bodnar (2010).

The equilibrium constants for these reactions were calculated using Holland and Powell's (2011) thermodynamic dataset. Note that the equilibrium constants are expressed in terms of fugacities (*f*) of the relevant fluid species. The fugacity (γ) and mole fraction of fluid species *i* is given by the relationship $f_i = \gamma_i X_i P$. The fugacity coefficients for the different fluid species are calculated using the equations of state by Zhang and Duan (2010) for non-ideal mixing. The fifth equation is given by the mass balance constraint, which is defined as follows (assuming that XO_2 is small):

$$XH_2O + XCO_2 + XCH_4 + XH_2 + XCO = 1$$

Considering that only five equations can be defined, one compositional variable needs to be specified in order to calculate the fluid composition at a specified pressure and temperature. In this case, the fact that CO_2 was not detected in the vapour phase of the fluid inclusions, indicates that $XCO_2/(XCO_2+XCH_4)$ should be less than 0.01. However, the exact $XCO_2/(XCO_2+XCH_4)$ value cannot be determined and the calculations were, therefore, performed for $XCO_2/(XCO_2+XCH_4)$ values of 0.01, 0.005 and 0.001. The five equations and the fixed value the $XCO_2/(XCO_2+XCH_4)$ ratio allows the fluid composition and oxygen fugacity to be calculated.

Calculations were performed for pressure and temperature conditions between 0.75-2.5 kbar and 300-350°C **(Fig. 4.10A-B)**, at a carbon activity (a_{carbon}) of 1.0 (i.e. graphite coexists with scheelite and quartz, (Huizenga, 2001), and $XCO_2/(XCO_2+XCH_4)$ ratios of 0.01, 0.005, and 0.001 as discussed. The calculations were done using the Excel spreadsheet program C-O-H (Huizenga, 2005) with results presented in **Table 4.6**. The validity of calculated results was evaluated by comparing the calculated fluid compositions with measured compositions obtained from fluid inclusions, i.e. calculated fluid compositions that resulted in XCH_4 values greater than 0.01 were discarded (shown in red in **Table 4.6**, the results shown in green are in agreement with the fluid composition obtained from fluid inclusions). From the calculations the following two conclusions can be drawn: (1) *P-T* conditions of mineralization can be constrained to 1-1.5 kbar and ca. 300°C; and (2) the calculated oxygen fugacity, expressed as $\log_{10}$ values relative to the Fayalite-Magnetite-Quartz buffer (O'Neill, 1987; Ballhaus et al., 1991) varies between FMQ–0.6 and FMQ–0.8.

4.7.4 Source of fluids

The origin of the mineralizing fluids can be constrained from isotope data for different mineral phases in D_4 veins. The $\delta^{18}O_{water}$ values can be calculated using the isotope fractionation equations for the scheelite-water system (Wesolowski and Ohmoto, 1986) combined with temperatures obtained for scheelite-plagioclase pairs **(Table 4.3)**, using the fractionation equations of Wesolowski and Ohmoto (1986) and Zheng (1993a). The obtained values range from +4.6 to +8.6‰, and are consistent with either a magmatic or a metamorphic source for the fluid, or a combined magmatic-metamorphic fluid (Taylor, 1974) from which D_4 scheelite precipitated **(Fig. 4.9)**.

Table 4.6 Thermodynamic calculations results of the C-O-H fluid compositions using an updated Excel spreadsheet from Huizenga (2005). Calculations are done for *P-T* conditions constrained by the fluid inclusion isochores **(Fig. 4.10)** for $XCO_2/(XCO_2+XCH_4)$ values of 0.01, 0.005, and 0.001. The XCH_4 values shown in red are incompatible with the observed fluid inclusion compositions, where the green ones are a good match. See text for further explanation.

$XCO_2/(XCO_2+XCH_4)$ 0.01					$XCO_2/(XCO_2+XCH_4)$ 0.005					$XCO_2/(XCO_2+XCH_4)$ 0.001				
Temperature (°C)	Pressure (kbar)	$\Delta\log_{10}fO_2$ (FMQ)	XH_2O	XCH_4	Temperature (°C)	Pressure (kbar)	$\Delta\log_{10}fO_2$ (FMQ)	XH_2O	XCH_4	Temperature (°C)	Pressure (kbar)	$\Delta\log_{10}fO_2$ (FMQ)	XH_2O	XCH_4
300	0.75	−0.6	0.985	0.015	300	0.75	−0.3	0.362	0.634	300	0.75	−0.9	0.148	0.850
300	1.00	**−0.6**	0.991	0.009	300	1.00	−0.7	0.984	0.015	300	1.00	−0.8	0.178	0.820
300	1.50	**−0.6**	0.996	0.004	300	1.50	**−0.8**	0.994	0.006	300	1.50	−0.7	0.260	0.739
325	0.75	−0.5	0.453	0.540	325	0.75	−0.7	0.301	0.694	325	0.75	−1.3	0.132	0.865
325	1.00	−0.8	0.962	0.038	325	1.00	−0.6	0.392	0.605	325	1.00	−1.2	0.155	0.842
325	1.50	−0.8	0.981	0.019	325	1.50	−0.9	0.968	0.032	325	1.50	−1.0	0.211	0.787
325	2.00	−0.8	0.989	0.011	325	2.00	−0.9	0.983	0.017	325	2.00	−0.9	0.294	0.705
350	1.50	−0.9	0.949	0.050	350	1.50	−0.9	0.709	0.289	350	1.50	−1.4	0.181	0.816
350	2.00	−0.9	0.970	0.029	350	2.00	−1.1	0.949	0.051	350	2.00	−1.3	0.236	0.762
350	2.50	−0.9	0.981	0.019	350	2.50	−1.1	0.969	0.031	350	2.50	−1.2	0.314	0.685

In a similar manner, the $\delta^{18}O_{water}$ values of the fluid involved in the formation of D_4 quartz can be calculated using the isotopic fractionation equation for quartz-water of Clayton et al. (1972). Considering the trapping temperatures of primary fluid inclusions in D_4 quartz (between 320-460°C; **Figs. 4.10C-D**), the obtained $\delta^{18}O_{water}$ for the aqueous fluid ranges from +6.7 to +12.6‰, which is slightly higher than the $\delta^{18}O_{water}$ value determined from coexisting scheelite and plagioclase during Retrograde Stage 2. The stable isotope results indicate that scheelite and quartz precipitated from the same fluid, which is in good agreement with the fluid inclusion results.

Muscovite occurs in D_4 vein haloes (ca. 275 Ma) and as centre lines in the D_4 veins (ca. 253 Ma) **(Chapter 2)**. The muscovite from vein halo postdates scheelite **(Table 4.1)**, indicating a muscovite formation temperature that is lower than that of scheelite, i.e. 250-300°C. Using the oxygen and hydrogen fractionation equations between muscovite and water (Zheng, 1993b; Vennemann and O'Neil, 1996), the $\delta^{18}O_{water}$ and δD_{water} values for the fluid that formed muscovite can be calculated to a range of +8.8 to +11.7‰, and −30.1 to −12.3‰, respectively. These values are indicative of a metamorphic fluid origin **(Fig. 4.11)** (Taylor, 1974) for the muscovite in the vein haloes and centre lines. The water composition of the late centre line muscovite plot slightly closer to a magmatic fluid field **(Fig. 4.11)**, suggesting that the ca. 253 Ma muscovite may have had additional input from a buried magmatic fluid source.

The $\delta^{34}S_{CDT}$ values for Retrograde Stage 4, D_4 vein sulphides are spread between −3 and +3‰ (average of −0.06 ± 1.3‰) **(Fig. 4.8A)**. These values are in good agreement with either a magmatic or a seawater sulphate source (Faure and Mensing, 2005) or both. Although a magmatic source cannot be excluded, it is more likely that the sulphur was derived from the reduction of seawater sulphate **(Fig. 4.12)**, indicating the presence of a basinal brine fluid. This is based on the fact that the sulphur isotope signature of the sulphide mineral phases overlaps with that of sea water sulfate (Fig. 4.12, modified after Chang et al., 2008), and scheelite has been found in metasedimentary rocks, which is an indication for seawater sulphate reduction (Goldfarb et al., 1997).

Based on fluid inclusion and stable isotope evidence, it is proposed that the mineralizing system involved at least two different fluids. The first fluid is a metamorphic fluid. Evidence for this is provided by $\delta^{18}O_{VSMOW}$ and $\delta^{18}D$ systematics of vein muscovite and quartz and the fact that the presence of metamorphic fluids cannot be denied. Peak metamorphic conditions of upper greenschist to lower amphibolite facies will result in devolatilization (Phillips and Powell, 2010) of metasedimentary rocks. The salinity of this metamorphic fluid would typically be between 0 and 5 wt.% NaCl.

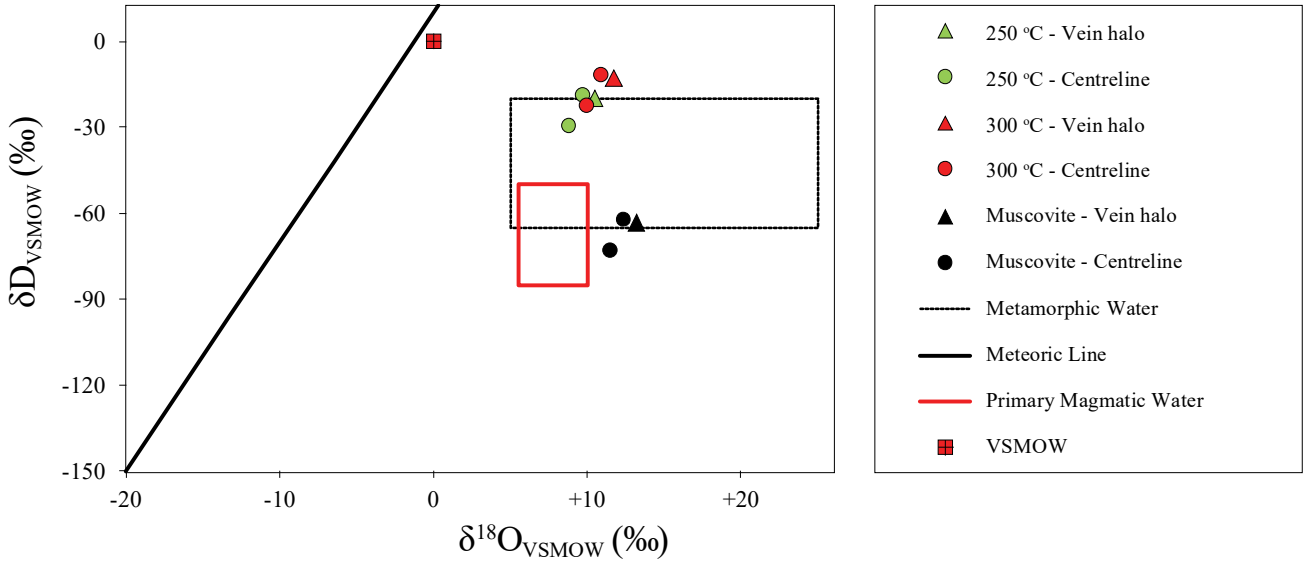

Figure 4.11 Muscovite δD and $\delta^{18}O_{VSMOW}$ isotopic values from muscovite at different temperatures at Watershed show a metamorphic origin for the muscovite formation. Black symbols are the isotopic composition of muscovite at Watershed. The magmatic and metamorphic water fields are from Taylor (1974), the meteoric line is from Craig (1961).

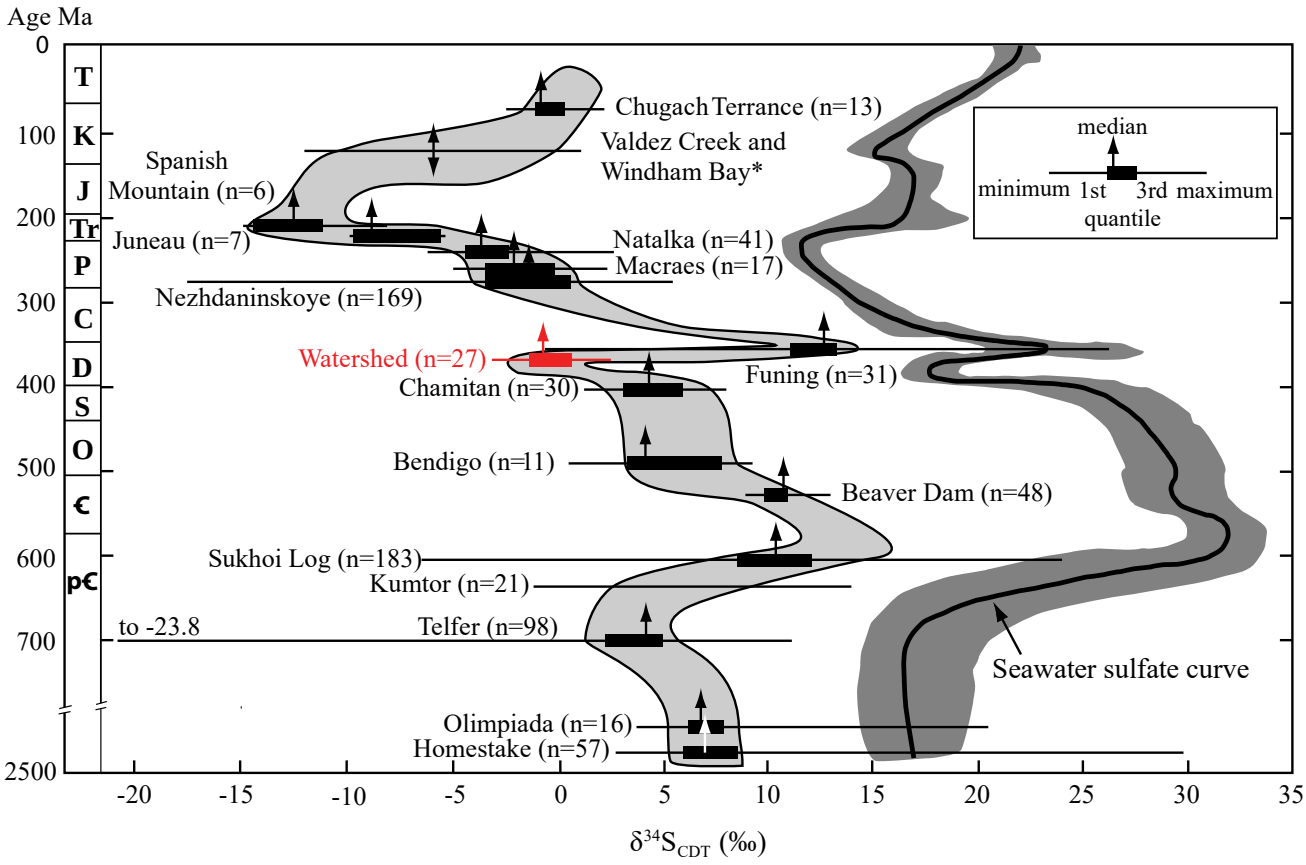

Figure 4.12 Historical distribution of $\delta^{34}S_{CDT}$ for sediment hosted orogenic gold deposits compared with the historical $\delta^{34}S_{CDT}$ of sea water sulfate (modified after Chang et al., 2008). Sulphur isotope data from Watershed (shown in red) falls in this trend implying that the sulfur that formed the sulfide minerals at Watershed during D_4 has its origin from the reduction of seawater sulphate.

The second fluid is a sulphate-bearing basinal brine based on the $\delta^{34}S_{CDT}$ of the sulphide mineral phases and the fact that the maximum salinity of the primary fluid inclusions in scheelite and quartz is ca. 9 wt.% NaCl without any Ca. This basinal brine can be characterised as a medium saline Cl-dominated halite-undersaturated aqueous fluid (Hanor, 1994). Similar to the metamorphic fluid, the presence of a basinal brine in the metasedimentary rocks is to be expected.

The presence of a magmatic fluid cannot be excluded, but there is no explicit evidence for it. Stable isotope and fluid inclusion data do not unequivocally indicate that a magmatic fluid was present. However, the high geotherm gradients obtained from the trapping *P-T* conditions for scheelite and quartz in D_4 veins, suggest that a magmatic intrusions were involved. These intrusions, upon crystallization, most likely acted as a heat source promoting metamorphic devolatilization reactions (Phillips and Powell, 2010) in the Hodgkinson Formation at ca. 275 Ma (i.e. the Whypalla Supersuite, **Fig. 4.1B**) **(Chapter 2)**, enhancing ore metal mobility. Likewise, the presence of low salinity meteoric water cannot be excluded. Typically, meteoric water has a very low salinity, i.e. fluid inclusions with salinities <1 wt.% NaCl could indicate the presence of meteoric water. However, these fluid inclusions could also represent a metamorphic fluid.

4.8 Conclusions

(1) The *P-T* conditions at which the D_4 vein scheelite was formed, i.e. ca. 300°C and 1-1.5 kbar, are similar to those of lode-gold deposits (Goldfarb and Groves, 2015), including the Hodgkinson Gold Field **(Fig. 4.1B)** to the south of Watershed (Peters et al., 1990; Vos and Bierlein, 2006), where mineralization occurred at *P-T* conditions of < 1.5 kbar and 150-400°C, respectively. These *P-T* condition indicate a high geothermal gradient (50-100°C/km), associated with Permian magmatic intrusions in the area.

(2) Scheelite mineralization occurred during retrograde metamorphism at lower greenschist facies conditions. Homogenization temperatures of primary fluid inclusions in quartz are higher compared to those in scheelite, indicating that quartz started to precipitate at higher temperatures and scheelite was formed during cooling.

(3) D_4 vein scheelite mineralization at Watershed is associated with a low salinity H_2O-NaCl-CH_4 fluid (XCH_4 < 0.01). There is no evidence for fluid-fluid immiscibility. Fluid inclusion data show evidence of fluid-fluid mixing indicating the presence of a low (close to 0 wt.% NaCl) and a medium saline fluid (8-9 wt.% NaCl). There is no evidence indicating which of those two fluids contained CH_4.

(4) The presence of sulphide mineral phases, graphite and CH_4 in the fluid indicates reduced mineralization conditions. The carbon-saturated H_2O-dominated fluid (XH_2O > 0.99, XCH_4 < 0.01) indicates a $\log_{10} f\,O_2$ below FMQ (FQM–0.6 to FMQ–0.8) at ca. 300°C and 1-1.5 kbar.

(5) Stable isotopes including calculated $\delta^{18}O_{water}$ (using scheelite, plagioclase, quartz, muscovite) and δD_{water} of muscovite indicate a metamorphic fluid origin. The sulphur isotopes from the sulphide mineral phases indicate the presence of seawater sulphate, i.e. the presence of a basinal brine. The metamorphic fluids were probably derived from prograde metamorphic devolatilization reactions (Phillips and Powell, 2010)

in the Hodgkinson Formation. In this scenario, the CH_4 would have been derived from the aqueous fluid interacting with carbonaceous slate/slate-siltstone breccia under reduced conditions. The presence of a magmatic and/or meteoric fluid cannot be excluded.

Chapter 5 – Conclusions and mineralization model

The aim of this PhD thesis is to document the geological characteristics of the Watershed tungsten deposit in the Mossman orogeny of northeast Queensland **(Fig. 1.3)**, including its geochemical and structural characteristics, timing and mineral paragenesis as well as the character of the mineralizing fluid. With this study of the Watershed deposit we hope to improve the understanding of tungsten deposits in northeast Queensland more broadly, and thus assist in future exploration and development of similar deposits in the area. The Watershed deposit was investigated using surface mapping and drill core logging, combined with various mineralogical, geochemical, isotopic and thermometric analytical methods. The results of this thesis include: a documentation of the geological characteristics and structural setting of the Watershed deposit; a geochemical characterization of the deposits that provides an improved understanding of its fingerprint and footprint with relevance to exploration techniques; and documentation of the origin and character of the fluids that formed the tungsten mineralization.

This PhD thesis is divided into an introduction (**Chapter 1**), three data chapters **(Chapters 2 to 4)** and the conclusions **(Chapter 5),** with all new information contained in the three data chapters, which have been prepared for publication. In **Chapter 2,** the metasedimentary and intrusive rocks that are spatially associated with the mineralization have been described, together with the veins that host the bulk of the scheelite mineralization. A detailed structural analysis of the deposit recognized four deformation events (D_{1-4}) and two mineralizing events. A first event of mineralization was associated with the emplacement of syn-tectonic (D_{1-2}) monzonite dykes dated by zircon U/Pb at ca. 350 Ma. A second and major event of mineralization occurred late (i.e. D_4) during the history of the area and was dated at ca. 275 Ma using ^{40}Ar-^{39}Ar techniques on muscovite from D_4 vein haloes. The second scheelite mineralization event is lithologically controlled by skarn-altered conglomerate that occur as tectonic lenses within the stratigraphy. There is also a strong structural control on mineralization exerted by D_4 tension veins and shear-zones characterized by normal faulting that provided trapping structures for mineralising fluids. By documenting the structural architecture of the host-conglomerates and scheelite-rich veins and shear zones, detailed sections for the deposit were constructed and constraints on mineralizing fluid pathways were defined **(Fig. 2.4)**.

In **Chapter 2**, we found that the Watershed tungsten deposit and especially the monzonite dykes that appear to control the early stages of mineralization is strongly modified by deformation and metamorphic events. The ca. 350 Ma, scheelite-rich monzonite dykes at Watershed were strongly deformed during the various overprinting deformation and metamorphic events. These events influenced the composition of hydrothermal/metamorphic minerals in the surrounding skarn-altered conglomerate making it difficult to assess and establish mineralogical vectors using mineral chemistry (i.e., garnet and pyroxene composition and relative abundances) towards a hypothetical igneous source (Meinert et al., 2005). The main exploration implications of the work presented in **Chapter 2** is the realization that the emplacement of Carboniferous (i.e. ~350 Ma)

intrusions played a role in the formation of early mineralization, which is associated with skarn-altered units of the Hodgkinson Formation, and that Permian shear zones and veins formed in an extensional regime were fundamental in upgrading the early mineralization to form the Watershed deposit.

The mineral and whole-rock geochemistry presented in **Chapter 3** provides insights into elements transfer processes between rock-types and minerals during deformation and mineralization, and investigates the interactions between mineralizing fluids and the host rocks. The mineralogical characteristics of scheelite and associated skarn minerals were documented, and redox conditions for mineralization determined. The relative REE abundance of scheelite was investigated to understand the origin of the texturally different scheelite grains (i.e., early D_{1-2} scheelite in monzonite and skarn-altered conglomerate versus late D_4 scheelite in veins and skarn-altered conglomerate) by utilizing a ternary LREE-MREE-HREE diagram **(Fig. 3.10)**. It was shown that with the use of this diagram it was possible to discriminate between magmatic-hydrothermal, metamorphic-hydrothermal and skarn scheelite. However, a detailed analysis of the mineral chemistry showed that REE compositions in scheelite were highly variable especially with respect metamorphic-hydrothermal scheelite in D_4 veins, and that hydrothermal-metamorphic processes at a grain scale could partly or totally destroy older REE signatures. This means that REE differentiation diagrams should be used with great care and only after detailed petrographic and mineral chemistry studies to understand the influence of metamorphic/hydrothermal mineral reactions on REE distribution patterns. As an example, some REE-rich mineral phases that accompany scheelite may explain outliers on the REE diagram, since these mineral phases will liberate REE into the system when they are replaced in (retrograde) metamorphic/hydrothermal reactions, e.g. HREE enriched scheelite formed when D_4 clinozoite replaced D_{1-3} garnet. In **Chapter 3,** the redox conditions of the mineralizing fluids at different stages were estimated from Eu anomalies and Mo content in scheelite **(Fig. 3.7)**. It was demonstrated that the Watershed system evolved from relatively oxidized conditions during D_{1-2} to more reduced conditions as D_4 progressed, indicating increased interaction with the reduced host-rock. (i.e., carbonaceous slate/slate-silstone breccia) consistent with a metamorphic/hydrothermal origin for the bulk of the mineralization. The redox conditions were determined in more detail in the fluid inclusion studies presented in **Chapter 4**.

The whole-rock geochemistry performed in **Chapter 3** resulted in a more detailed definition of the fingerprint and footprint of the Watershed deposit **(Fig. 3.5)**. The fingerprint of Watershed mineralization is characterized by enrichment of W, Be, B, Sc, Cu, Mo and Re, which were introduced by the hydrothermal fluids. These mineralizing fluids also leached REE, Y, Nb, Ca, F, P, Fe, and Sr from the skarn-altered conglomerate, which were incorporated into scheelite and related minerals in D_4 veins. The mobilization of W, REE, Y and Nb involved F and Na as ligands. Despite limited sampling, a regional footprint of the mineralization can be defined within the psammite units around Watershed. On approaching the Watershed deposit an increase in Mo, Ca, Fe, Mn and Li was noted in addition to the historical regional W and Cu stream sediment anomalies (Meates, 1979). These trends are real along the transect that was sampled (i.e. **Fig. 2.3A**), however, for future work it is recommended that a more systematic sampling approach is taken to investigate the extent of mineral anomalies around Watershed in all directions. The whole-rock and mineral geochemistry

performed in **Chapter 3** corroborate the occurrence of two stages of mineralization; an early intrusion-related scheelite mineralization event that occurred in association with monzonite during the Carboniferous (~350 Ma) and a later hydrothermal Permian (~275 Ma) mineralization event. All geochemical signatures for the later vein-related scheelite indicate a hydrothermal/metamorphic origin for this deposit, which contrasts with previous models for Watershed, which generally link scheelite mineralization to the emplacement of Permian granites (Bain and Draper, 1997; Garrad and Bultitude, 1999) of the Whypalla Supersuite.

The fluid inclusions and stable isotope studies performed in **Chapter 4** provide an understanding into the D_4 hydrothermal system at Watershed, and allow us to constrain the source(s) and *P-T* conditions of scheelite mineralization. The hydrothermal system during D_4 was characterized by a metamorphic-hydrothermal fluid with minor magmatic input that caused mineralization at 300°C and 1-1.5 kbar (<6 km depth). These conditions are similar to those recorded in lode-gold systems in northeast Queensland (Peters et al., 1990; Vos and Bierlein, 2006) and elsewhere (Groves, 1993; Groves et al., 1998; Bodnar et al., 2014). Thus, D_4 scheelite mineralization in the Watershed deposit is predominantly metamorphic in origin. Considering a continuum model (Groves, 1993) for this deposit type (i.e. possible mineralization could form between 2-20 km depth) it is feasible to consider the potential for mineralization at depth.

5.1 Mineralization model

Based on the conclusions of **Chapters 2 to 4**, a mineralization model is proposed for Watershed. This model will focus on the D_4 vein mineralization event, which forms the core of the scheelite mineralization at Watershed and overprints earlier D_{1-3} events.

During the Carboniferous (i.e., ca. 350 Ma, **Chapter 2)** the emplacement of the monzonitic dykes cutting the metasedimentary rocks of the Hodgkinson Formation occurred. These dykes carried an ore metals assemblage including W, Be, B, Sc, Cu, Mo and Re **(Fig. 2.5C)**, thereby enriching the Hodgkinson Formation in such elements. During this event, scheelite was preferentially deposited in monzonite and surrounding skarn-altered conglomerate **(Fig. 2.9)**. Following the emplacement of the monzonite dykes during the early stages of accretion (Davis, 1993; Henderson et al., 2013), east-west compression continued in a fore-arc basin environment where ductile deformation was accompanied by prograde metamorphism, reaching upper greenschist to lower amphibolite facies conditions **(Table 1.1)**. These deformation events, D_{1-3}, resulted in the formation of an intense linear fabric of the metasedimentary rock units i.e., transposition of the slaty units and the dismemberment of the skarn-altered conglomerate unit, which was boudinaged and deformed into semi-continuous elongated bodies **(Fig. 2.6)**. Minor scheelite was deposited along this linear fabric (S_{1-2}) during D_{1-2} in the skarn-altered conglomerate **(Figs. 2.9)**. The D_{1-3} events caused metamorphic devolatilization reactions to occur (Phillips and Powell, 2010) **(Chapter 3)** within the reduced carbonaceous sediments, thereby liberating C and forming CH_4 **(Chapter 4)** and increasing the ore metals assemblage solubility.

In proposing a model for the Permian (i.e., ca. 275 Ma) D_4 scheelite vein mineralization, some considerations have to be made regarding the nature of the fluid and possible ligands that can transport tungsten from the surrounding rocks towards the trapping sites in D_4 shears and veins near skarn-altered conglomerate. Few studies have discussed the physico-chemical transport and deposition mechanisms of tungsten in different environments (Wood and Samson, 2000). Pressure-temperature (*P-T*) conditions recorded in several scheelite dominated tungsten deposits are between 0.2-1.5 kbar and 200-500°C, respectively, with salinities <10 wt.% NaCl. Mineralizing fluids usually contain dissolved components such as Na^+ and Cl^- with minor Ca^{2+}, K^+, CO_3^{2-} and HCO^{3-}, and variable XCO_2 and XCH_4. Such fluids are generally moderately acidic (i.e., pH between 4 to 6) with oxygen fugacity between the QFM and HM buffers (Wood and Samson, 2000).

During the Permian at ca. 275 Ma, following the D_{1-3} devolatilization processes, retrograde metamorphism and formation of shear zones occurred **(Fig. 2.7-2.8)**. These shear zones acted as fluid pathways for tungsten. At Watershed, the retrograde *P-T* conditions of scheelite deposition in D_4 veins have been calculated at 1-1.5 kbar and 300 °C **(Chapter 4, Fig. 4.10)**. At these *P-T* conditions and considering fluid pH values between 4 and 6, the interaction of tungsten-rich fluids with carbonate-rich rocks (i.e., skarn-altered conglomerate), promotes a pH increase of the fluid, thereby diminishing the solubility of tungsten and promoting scheelite precipitation in D_4 veins. Additionally, the possible presence of basinal brines (i.e., mixing of fluids) may have resulted in fluid mixing causing further destabilisation of tungsten in the ore fluids **(Chapter 4, Fig. 4.12)**. The strong influence of carbonate-rich rock on buffering the ore fluids and causing the precipitation of scheelite is in agreement with the presence of generally narrow (i.e. <50 cm), scheelite-rich vein haloes **(Figs. 3.3H-I)**.

Several anionic complexes have been considered as efficient transport ligands for tungsten, e.g. solubilities of tungsten can reach 1000's ppm as alkali tungstate ($NaHWO_4^0$, KWO_4^-, etc) (Wood and Samson, 2000). Considering the calculated *P-T* conditions during scheelite deposition in D_4 veins (i.e. 300 ºC and 1-1.5 kbar) with pH values of the mineralizing fluid between 4 and 6, the most likely tungsten transport complexes are $NaWO_4^-$, HWO_4^- and WO_4^{2-} in which monzonite and granite were the most likely source for Na **(Fig. 2.5E).** These complexes can be destabilize by the interaction with more alkaline rocks such as the skarn-altered conglomerate, which is in agreement with the synchronous precipitation of scheelite and oligoclase (i.e., Na-rich plagioclase) during Retrograde Stage 2 **(Chapter 2, Fig. 2.11B)**.

Whilst scheelite may have been transported by Na-complexes, to form scheelite ($CaWO_4$) it is critical that Ca is available. This Ca was probably derived from the skarn-altered conglomerate lenses, given the close spatial association between mineralization and this rock type **(Chapter 2)**. In **Chapter 3** we recognized Ca depletion in vein haloes (i.e., proximal skarn-altered conglomerate) when compared to D_4 veins and skarn-altered conglomerate **(Fig. 2.5D)**. This indicates that Ca was scavenged from the host-rock to be incorporated into the D_4 veins and shears in part as scheelite. As demonstrated by Wood and Samson (2000), under the calculated *P-T* conditions at which D_4 veins were formed, Ca is soluble as Ca^{2+} and $CaCl^+$, thus facilitating Ca

mobility and scheelite precipitation. Additionally, as described in **Chapters 2 and 3**, Ca was liberated during metamorphic reactions i.e. during the replacement of garnet by clinoizoisite during D_4. Similar mechanisms have been described for other tungsten deposits (e.g., Panasqueiras, Lecumberri-Sanchez et al., 2017). At Watershed, the fact that Ca was not detected in fluid inclusions **(Chapter 4)** (Hanor, 1994) further supports the notion that Ca was sourced from the proximal skarn-altered conglomerate (i.e, vein haloes) to form scheelite ($CaWO_4$).

In summary, tungsten was sourced from Carboniferous monzonite that enriched the metasedimentary rock units of the Hodgkinson Formation. Further ductile deformation during $D_{1\text{-}3}$ promoted devolatilization (Phillips and Powell, 2010) and remobilization of tungsten. Later on during Permian D_4 brittle-ductile deformation, tungsten was channelized through shears and veins as $NaWO_4^-$, HWO_4^- and WO_4^{2-}, encountering the Ca-rich skarn-altered conglomerate levels destabilizing such ligands, increasing the fluid pH and co-precipitating the scheelite ($CaWO_4$) and oligoclase (Na-rich plagioclase) in D_4 veins and shears.

References

Adams, C. J., Wormald, R., and Henderson, R. A., 2013, Detrital zircons from the Hodgkinson Formation: constraints on its maximum depositional age and provenance, *in* Jell, P. A., ed., Geology of Queensland: State of Queensland, Geological Survey of Queensland, p. 239-241.

Aitchison, J., 1982, The Statistical Analysis of Compositional Data: Journal of the Royal Statistical Society. Series B *(Methodological)*, v. 44, p. 139-177.

Allmendinger, R. W., 2001, FaultKinWin, Version 1.1: a program for analyzing fault slip data for Windows™. (www.geo.cornell.edu/geology/faculty/RWA/programs.html).

Allmendinger, R. W., Cardozo, N., and Fisher, D., 2012, Structural geology algorithms: Vectors and tensors in structural geology, Cambridge University Press.

Alves Cruz, V. M., Bertolino, L. C., and Silva, F. J., 2016, Tungsten Mineralizations in High-Grade Terrains of Monumento/Cacaria, Rio de Janeiro: Anuário do Instituto de Geociências, v. 39, p. 89-97.

Amos, B. J., 1968, The structure of the Palaeozoic sediments of the Mossman and Cooktown areas, North Queensland: Journal of the Geological Society of Australia, v. 15, p. 195-208.

Angelier, J., 1994, Fault slip analysis and palaeostress reconstruction, in: Hancock, P.L. (Ed.), Continental Deformation: Oxford, Pergamon, Oxford, p. 101-120.

Angelier, J., and Mechler, P., 1977, Sur une méthode graphique de recherche des contraintes principales également utilisable en tectonique et en séismologie: la méthode des dièdres droits: Bulletin de la Société Géologique de France v. 7, p. 1309-1318.

Antipin, V. S., Andreeva, I. A., Kovalenko, V. I., and Kuznetsov, V. A., 2009, Geochemical specifics of ongonites in the Ary-Bulak Massif, eastern Transbaikalia: Petrology, v. 17, p. 558-569.

Antipin, V. S., Kovalenko, V. I., Kuznetsova, A. I., and Persikova, L. A., 1981, The Behaviour of Tin and Tungsten in Ore-bearing Acid Magmatic Rocks as Revealed by the Analysis of Distribution Coefficients: Geokhimiya, v. 2, p. 163-178.

Appel, P. W. U., 1986, Strata bound scheelite in the Archean Malene supracrustal belt, West Greenland: Mineralium Deposita, v. 21, p. 207-215.

Atherton, M. P., 1964, The garnet isograd in pelitic rocks and its relation to metamorphic facies: The American Mineralogist, v. 49, p. 1331-1349.

Bain, J. H. C., and Draper, J. J., 1997, North Queensland Geology, Australian Geological Survey Organisation Bulletin 240 and Queensland Department of Mines and Energy Queensland Geology 9, 676 p.

Ballhaus, C., Berry, R. F., and Gree, D. H., 1991, High pressure experimental calibration of the olivine-orthopyroxene-spinel oxygen barometer: implications for the oxidation state of the upper mantle: Contribution to Mineralogy and Petrology, v. 107, p. 27-40.

Barnes, R. G., 1983, Stratiform and stratabound tungsten mineralisation in the Broken Hill Block, N.S.W: Journal of the Geological Society of Australia, v. 30, p. 225-239.

Bateman, R., 1985, Aureole Deformation by Flattening around a Diapir during in Situ Ballooning: The Cannibal Creek Granite: The Journal of Geology, v. 93, p. 293-310.

Baxter, E. F., Caddick, M. J., and Dragovic, B., 2017, Garnet: A Rock-Forming Mineral Petrochronometer, *in* Kohn, M. J., Engi, M., and Lanari, P., eds., Petrochronology: Methods and Applications, 83. Reviews in Mineralogy and Geochemistry: Virginia, U.S.A., Mineralogical Society of America Geochemical Society, p. 469-533.

Bell, K., Anglin, C. D., and Franklin, J. M., 1989, Sm-Nd and Rb-Sr isotope systematics of scheelites: Possible implications for the age and genesis of vein-hosted gold deposits: Geology, v. 17, p. 500-504.

Beran, A., God, R., Gotzinger, M., and Zemann, J., 1985, A scheelite mineralization in calc-silicate rocks of the Moldanubicum (Bohemian Massif) in Austria: Mineralium Deposita, v. 20, p. 16-22.

Bevins, R. E., Kokelaar, B. P., and Dunkley, P. N., 1984, Petrology and geochemistry of lower to middle Ordovician igneous rocks in Wales: a volcanic arc to marginal basin transition: Proceedings of the Geologists' Association, v. 95, p. 337-347.

Black, L. P., Kamo, S. L., Allen, C. M., Aleinikoff, J. N., Davis, D. W., Korsch, R. J., and Foudoulis, C., 2003, TEMORA 1: a new zircon standard for Phanerozoic U–Pb geochronology: Chemical Geology, v. 200, p. 155-170.

Bodnar, R. J., Lecumberri-Sanchez, P., Moncada, D., and Steele-MacInnis, M., 2014, Fluid Inclusions in Hydrothermal Ore Deposits, Treatise on Geochemistry, p. 119-142.
Brown, P. E., Bowman, J. R., and Kelly, W. C., 1985, Petrologic and Stable Isotope Constraints on the Source and Evolution of Skarn-Forming Fluids at Pine Creek, California: Economic Geology, v. 80, p. 72-95.
Bultitude, R. J., and Champion, D. C., 1992, Granites of the Eatern Hodgkinson Province - Their field and petrographic characteristics, Department of Resource Industries, Record 1992/6.
Campbell, A. R., and Larson, P. B., 1998, Introduction to Stable Isotope Applications in Hydrothermal Systems, *in* Richards, J. P., and Larson, P. B., eds., Reviews in Economic Geology 10: Techniques in Hydrothermal Ore Deposits Geology, 10. Reviews in Economic Geology: Colorado US, Society of Economic Geologists, p. 173-193.
Cattalani, S., and Williams-Jones, A. E., 1991, C-O-H-N fluid evolution at Saint-Robert, Quebec: Implications for W-Bi-Ag mineral deposition: Canadian Mineralogist, v. 29, p. 435-452.
Cave, B. J., Pitcairn, I. K., Craw, D., Large, R. R., Thompson, J. M., and Johnson, S. C., 2017, A metamorphic mineral source for tungsten in the turbidite-hosted orogenic gold deposits of the Otago Schist, New Zealand: Mineralium Deposita, v. 52, p. 515-537.
Champion, D. C., and Bultitude, R. J., 2013, Kennedy Igneous Association, *in* Jell, P. A., ed., Geology of Queensland: State of Queensland, Geological Survey of Queensland, p. 473-514.
Chang, Z., Clarke, G., Cheng, Y., Poblete, J., and Liu, K., 2017, Sn-W-Mo mineralisation in north-east Queensland, *in* Phillips, G. N., ed., Australian Ore Deposits: Melbourne, Australia, The Australasian Institute of Mining and Metallurgy, p. 481-488.
Chang, Z., Large, R. R., and Maslennikov, V., 2008, Sulfur isotopes in sediment-hosted orogenic gold deposits: Evidence for an early timing and a seawater sulfur source: Geology, v. 36.
Cheilletz, A., 1984, Caractéristiques géochimiques et thermobarométriques des fluides associés à la scheelite et au quartz des minéralisations de tungstène du Jbel Aouam (Maroc Central): Bulletin de Minéralogie, v. 107, p. 255-272.
Cheng, Y., Chang, Z., and Huizenga, J. M., 2017, Geology and mineralization of the Mt Carbine Tungsten Deposit, Northern Queensland, Australia: FUTORES II Conference, Townsville, Australia, 2017, p. 18.
Cheng, Y., Chang, Z., and Poblete, J., 2015, Geology and Mineralization of the Mt Carbine Deposit, Northern QLD, Australia: SEG 2015: World-Class Ore Deposits: Discovery to Recovery, Hobart, TAS, Australia, 2015.
Cheng, Y., Chang, Z., and Poblete, J., 2016, Geology and Mineralization of the Mt Carbine Deposit, Northern QLD, Australia: Australian Earth Sciences Convention, Adelaide, SA, Australia, 2016.
Cheng, Y., Chang, Z., Poblete, J., Liu, K., Spandler, C., Clarke, G., and Dirks, P., 2018, Tin and tungsten deposits in northeast Queensland, Australia: Past, Present, and Prospectivity, 15th Quadrennial IAGOD Symposium: Salta, Argentina, p. 75-76.
Cladouhos, T. T., and Allmendinger, R. W., 1993, Finite strain and rotation from fault-slip data: Journal of Structural Geology, v. 15, p. 771-784.
Clayton, R. N., O'Neil, J. R., and Mayeda, T. K., 1972, Oxygen isotope exchange between quartz and water: Journal of Geophysical Research, v. 77, p. 3057-3067.
Cox, S. F., Sun, S.-S., Etheridge, M. A., Wall, V. J., and Potter, T. F., 1995, Structural and Geochemical Controls on the Development of Turbidite-Hosted Gold Quartz Vein Deposits, Wattle Gully Mine, Central Victoria, Australia: Economic Geology, v. 90, p. 1722-1746.
Craig, H., 1961, Isotopic Variations in Meteoric Waters: Science, v. 133, p. 1702-1703.
Davis, B. K., 1993, Mechanism of emplacement of the Cannibal Creek Granite with special reference to timing and deformation history of the aureole: Tectonophysics, v. 224, p. 337-362.
Davis, B. K., 1994, Synchronous syntectonic granite emplacement in the south palmer river region, Hodgkinson Province, Australia: Australian Journal of Earth Sciences, v. 41, p. 91-103.
Davis, B. K., Bell, C. C., Lindsay, M., and Henderson, R. A., 2002, A Single Late Orogenic Permian Episode of Gold mineralization in the Hodgkinson Province, North Queensland, Australia: Economic Geology, v. 97, p. 311-323.
Davis, B. K., and Forde, A., 1994, Regional slaty cleavage formation and fold axis rotation by re-use and reactivation of pre-existing foliations: the Fiery Creek Slate Belt, North Queensland: Tectonophysics, v. 230, p. 161-179.

Davis, B. K., and Henderson, R. A., 1999, Syn-orogenic extensional and contractional deformation related to granite emplacement in the northern Tasman Orogenic Zone, Australia: Tectonophysics, v. 305, p. 453-475.

Davis, B. K., Henderson, R. A., and Bultitude, R. J., 1998, Evidence for a major crustal dislocation in the Hodgkinson Province, North Queensland: Australian Journal of Earth Sciences, v. 45, p. 937-942.

de Keyser, F., 1961, Geology and Mineral Deposits of the Mossman 1:250,000 Sheet Area, North Queensland, Records 1961/110: Canberra, Department of National Development, Bureau of Mineral Resources, Geology and Geophysics, p. 1-48.

de Keyser, F., and Lucas, K. G., 1968, Geology of the Hodgkinson and Laura Basins, North Queensland, Bulletin 84: Canberra, Department of National Development, Bureau of Mineral Resources, Geology and Geophysics, p. 1-254.

de Roo, J. A., 1988, Structural Controls on the Emplacement of the Vein-type Tungsten-Tin Ore at Mount Carbine, Queensland, Australia: Economic Geology, v. 83, p. 1170-1180.

Delvaux, D., and Sperner, B., 2003, New aspects of tectonic stress inversion with reference to the TENSOR programme, in: Nieuwland, D.A. (Ed.), New insights into structural interpretation and modelling. : Geological Society of London, Special Publication, v. 212, p. 75-100.

Derre, C., Lecolle, M., and Roger, G., 1986, Les quartzites a silicates calciques et scheelite: Preconcentrations familieres ou pieges pour un tungstene etranger lie a l'hydrothermalisme perigranitique? Exemple du Nord-Est Transmontain (Portugal): Mineralium Deposita, v. 21, p. 164-168.

Dick, L. A., and Hodgson, C. J., 1982, The MacTung W-Cu(Zn) Contact Metasomatic and Related Deposits of the Northeastern Canadian Cordillera: Economic Geology, v. 77, p. 845-867.

Dirks, P. H. G. M., Charlesworth, E. G., and Munyai, M. R., 2009, Cratonic Extension and Archaean Gold Mineralisation in the Sheba-Fairview Mine, Barberton Greenstone Belt, South Africa: South African Journal of Geology, v. 112, p. 291-316.

Dirks, P. H. G. M., Charlesworth, E. G., Munyai, M. R., and Wormald, R., 2013, Stress analysis, post-orogenic extension and 3.01Ga gold mineralisation in the Barberton Greenstone Belt, South Africa: Precambrian Research, v. 226, p. 157-184.

Donchak, P. J. T., Purdy, D. J., Withnall, I. W., Blake, P. R., and Jell, P. A., 2013, New England Orogen, *in* Jell, P. A., ed., Geology of Queensland: State of Queensland, Geological Survey of Queensland, p. 305-472.

Dostal, J., Kontak, D. J., and Chatterjee, A. K., 2009, Trace element geochemistry of scheelite and rutile from metaturbidite-hosted quartz vein gold deposits, Meguma Terrane, Nova Scotia, Canada: genetic implications: Mineralogy and Petrology, v. 97, p. 95-109.

Einaudi, M. T., and Burt, D. M., 1982, Introduction--Terminology, Classification, and Composition of Skarn Deposits: Economic Geology, v. 77, p. 745-754.

Etchecopar, A., Vasseur, G., and Daignieres, M., 1981, An inverse problem in microtectonics for the determination of stress tensors from fault striation analysis: Journal of Structural Geology, v. 3, p. 51-65.

Faure, G., and Mensing, T. M., 2005, Isotopes: principles and applications: Hoboken, New Jersey, John Wiley & Sons, Inc.

Fergusson, C. L., and Henderson, R. A., 2013, Thomson Orogen, *in* Jell, P. A., ed., Geology of Queensland: State of Queensland, Geological Survey of Queensland, p. 113-224.

Fonteilles, M., Soler, P., Demange, M., Derre, C., Krier-Schellen, A. D., Guy, B., and Zahm, A., 1989, The Scheelite Skarn Deposit of Salau (Ariege, French Pyrenees): Economic Geology, v. 84, p. 1172-1209.

French, B. M., 1966, Some geological implications of equilibrium between graphite and a C-O-H gas at high temperatures and pressures: Reviews in Geophysics, v. 4, p. 223-254.

Frezzotti, M. L., Tecce, F., and Casagli, A., 2012, Raman spectroscopy for fluid inclusion analysis: Journal of Geochemical Exploration, v. 112, p. 1-20.

Fricker, M. B., Kutscher, D., Aeschlimann, B., Frommer, J., Dietiker, R., Bettmer, J., and Günther, D., 2011, High spatial resolution trace element analysis by LA-ICP-MS using a novel ablation cell for multiple or large samples: International Journal of Mass Spectrometry, v. 307, p. 39-45.

Fu, Y., Sun, X., Zhou, H., Lin, H., Jiang, L., and Yang, T., 2017, In-situ LA-ICP-MS trace elements analysis of scheelites from the giant Beiya gold–polymetallic deposit in Yunnan Province, Southwest China and its metallogenic implications: Ore Geology Reviews, v. 80, p. 828-837.

Fulp, M. S., and Renshaw, J. L., 1985, Volcanogenic-exhalative tungsten mineralization of Proterozoic age near Santa Fe, New Mexico, and implications for exploration: Geology, v. 13, p. 66-69.
Garrad, P. D., and Bultitude, R. J., 1999, Geology, mining history and mineralisation of the Hodgkinson and Kennedy Provinces, Cairns Region, North Queensland: Brisbane, Australia, Queensland Department of Mines and Energy.
Ghaderi, M., Palin, J. M., Campbell, I. H., and Sylvester, P. J., 1999, Rare Earth Element Systematics in Scheelite from Hydrothermal Gold Deposits in the Kalgoorlie-Norseman Region, Western Australia: Economic Geology, v. 94, p. 423-438.
Gibert, F., Moine, B., Schott, J., and Dandurand, J.-L., 1992, Modeling of the transport and deposition of tungsten in the scheelite-bearing calc-silicate gneisses of the Montagne Noire, France: Contribution to Mineralogy and Petrology, v. 112, p. 371-384.
Goldfarb, R. J., Baker, T., Dubé, B., Groves, D. I., Hart, C. J. R., and Gosselin, P., 2005, Distribution Character, and Genesis of Gold Deposits in Metamorphic Terranes: Economic Geology 100th Anniversary Volume, p. 407-450.
Goldfarb, R. J., and Groves, D. I., 2015, Orogenic gold: Common or evolving fluid and metal sources through time: Lithos, v. 233, p. 2-26.
Goldfarb, R. J., Miller, L. D., Leach, D. L., and Snee, L. W., 1997, Gold Deposits in Metamorphic Rocks of Alaska: Economic Geology Monograph, v. 9, p. 151-199.
Goldstein, R. H., and Reynolds, T. J., 1994, Systematics of fluid inclusions in diagenetic minerals.
Greenwood, M., 2017, Queensland Mineral Occurrence Data, *in* Greenwood, M., ed.: Brisbane, Queensland, Australia.
Gregory, P. W., and Robinson, B. W., 1984, Sulphur Isotope Studies of the Mt Molloy, Dianne and O.K. Stratiform Sulphide Deposits, Hodgkinson Province, North Queensland, Australia: Mineralium Deposita, v. 19, p. 36-43.
Groves, D. I., 1993, The crustal continuum model for late-Archean lode-gold deposits of the Yilgarn Block, Western Australia: Mineralium Deposita, v. 28, p. 366-374.
Groves, D. I., Goldfarb, R. J., Gebre-Mariam, M., Hageman, S. G., and Robert, F., 1998, Orogenic gold deposits: A proposed classification in the context of their crustal distribution and relationship to other gold deposit types: Ore Geology Reviews, v. 13, p. 7-27.
Groves, D. I., Goldfarb, R. J., Robert, F., and Hart, C. J. R., 2003, Gold Deposits in Metamorphic Belts : Overview of Current Understanding, Outstanding Problems, Future Research, and Exploration Significance: Economic Geology, v. 98, p. 1-29.
Guo, S., Chen, Y., Liu, C.-Z., Wang, J.-G., Su, B., Gao, Y.-J., Wu, F.-Y., Sein, K., Yang, Y.-H., and Mao, Q., 2016, Scheelite and coexisting F-rich zoned garnet, vesuvianite, fluorite, and apatite in calc-silicate rocks from the Mogok metamorphic belt, Myanmar: Implications for metasomatism in marble and the role of halogens in W mobilization and mineralization: Journal of Asian Earth Sciences, v. 117, p. 82-106.
Hanor, J. S., 1994, Origin of saline fluids in sedimentary basins, *in* Parnell, J., ed., Geofluids: Origin, Migration and Evolution of Fluids in Sedimentary Basins, 78, Geological Society Special Publication No. 78, p. 151-174.
Hazarika, P., Mishra, B., and Pruseth, K. L., 2016, Scheelite, apatite, calcite and tourmaline compositions from the late Archean Hutti orogenic gold deposit: Implications for analogous two stage ore fluids: Ore Geology Reviews, v. 72, p. 989-1003.
Heinrich, C. A., Walshe, J. L., and Harrold, B. P., 1996, Chemical mass transfer modelling of ore-forming hydrothermal systems: current practise and problems: Ore Geology Reviews, v. 10, p. 319-338.
Henderson, R. A., Donchak, P. J. T., and Withnall, I. W., 2013, Mossman Orogen, *in* Jell, P. A., ed., Geology of Queensland: State of Queensland, Geological Survey of Queensland, p. 225-304.
Henley, R. W., Norris, R. J., and Paterson, C. J., 1976, Multistage Ore Genesis in the New Zealand Geosyncline A history of Post-Metamorphic Lode Emplacement: Mineralium Deposita, v. 11, p. 180-196.
Hermann, J., and Rubatto, D., 2003, Relating zircon and monazite domains to garnet growth zones: age and duration of granulite facies metamorphism in the Val Malenco lower crust: Journal of Metamorphic Geology, v. 21, p. 833-852.
Holland, T. J. B., and Powell, R., 2011, An improved and extended internally consistent thermodynamic dataset for phases of petrological interest, involving a new equation of state for solids: Journal of Metamorphic Geology, v. 29, p. 333-383.

Huizenga, J.-M., 2001, Thermodynamic modelling of C-O-H fluids: Lithos, v. 55, p. 101-114.
Huizenga, J. M., 2005, COH, an Excel spreadsheet for composition calculations in the C–O–H fluid system: Computers & Geosciences, v. 31, p. 797-800.
Hurai, V., 2010, Fluid inclusion geobarometry: Pressure corrections for immiscible H2O–CH4 and H2O–CO2 fluids: Chemical Geology, v. 278, p. 201-211.
Ishihara, S., 1977, The Magnetite-series and Ilmenite-series Granitic Rocks: Mining Geology, v. 27, p. 293-305.
Ivanova, G. F., 1986, Geochemistry of tungsten, *in* Beus, A. A., ed., Geology of tungsten, 18: Paris, UNESCO, p. 11-43.
Jackson, S. E., Pearson, N. J., Griffin, W. L., and Belousova, E. A., 2004, The application of laser ablation-inductively coupled plasma-mass spectrometry to in situ U–Pb zircon geochronology: Chemical Geology, v. 211, p. 47-69.
Jiang, S. Y., Peng, N. J., Huang, L. C., Xu, Y. M., Zhan, G. L., and X.H., D., 2015, Geological characteristic and ore genesis of the giant tungsten deposits from the Dahutang ore-concentrated district in northern Jiangxi Province [in Chinese]: Acta Petrologica Sinica, v. 31, p. 639-655.
John, Y. W., 1963, Geology and origin of Sangdong tungsten mine, Republic of Korea: Economic Geology, v. 58, p. 1285-1300.
Kantor, J., 1974, Scheelite in the Male Karpaty Mts. Crystalline and its genetic relationship to basic volcanism: Geologica Carpathica, v. 25, p. 41-52.
Kim, O. J., 1971, Metallogenic Epochs and Provinces of South Korea: The Journal of the Geological Society of Korea, v. 7, p. 37-59.
Kositcin, N., Purdy, D. J., Brown, D. D., and Carr, P. A., 2015, Summary of results Joint GSQ–GA geochronology project: Thomson Orogen and Hodgkinson Province, 2012–2013. Queensland Geological Record 2015/02., *in* Queensland, G. S. o., ed.: Brisbane, Geological Survey of Queensland.
Kwak, T. A. P., 1986, Fluid inclusions in skarns (carbonate replacement deposits): Journal of Metamorphic Geology, v. 4, p. 363-384.
Kwak, T. A. P., 1987, W-Sn skarn deposits and related metamorphic skarns and granitoids: Amsterdam, Elsevier, 451 p.
Kwak, T. A. P., and Tan, T. H., 1981, The Geochemistry of Zoning in Skarn Minerals at the King Island (Dolphin) Mine: Economic Geology, v. 76, p. 468-497.
Lecumberri-Sanchez, P., Vieira, R., Heinrich, C. A., Pinto, F., and Wälle, M., 2017, Fluid-rock interaction is decisive for the formation of tungsten deposits: Geology, v. 45, p. 579-582.
Lin, F., and Bodnar, R. J., 2010, Synthetic fluid inclusions XVIII: Experimental determination of the PVTX properties of H2O–CH4 to 500°C, 3 kbar and XCH4 ⩽4 mol.%: Geochimica et Cosmochimica Acta, v. 74, p. 3260-3273.
Lisitsin, V. A., Dhnaram, C., Donchak, P., and Greenwood, M., 2014, Mossman orogenic gold province in north Queensland, Australia: regional metallogenic controls and undiscovered gold endowment: Mineralium Deposita, v. 49, p. 313-333.
Lisle, R. J., 1987, Principal stress orientations from faults: an additional constraint: Annales Tectonic v. 1, p. 155-158.
Ludwig, K. R., 2012, Isoplot 3.75 A Geochronological Toolkit for Microsof Excel: Berkeley Geochronology Center, Special Publication No. 5.
Mackenzie, D. E., and Wellman, P., 1997, Kennedy Province, *in* Bain, J. H. C., and Draper, J. J., eds., North Queensland Geology: Australia, Australian Geological Survey Organisation, Bulletin 240 and Queensland Department of Mines and Energy Queensland Geology 9, p. 488-500.
Mao, S., Hu, J., Zhang, D., and Li, Y., 2013a, Thermodynamic modeling of ternary CH_4 - H_2O - NaCl fluid inclusions: Chemical Geology, v. 335, p. 128-135.
Mao, Z., Cheng, Y., Liu, J., Yuan, S., Wu, S., Xiang, X., and Luo, X., 2013b, Geology and molybdenite Re–Os age of the Dahutang granite-related veinlets-disseminated tungsten ore field in the Jiangxin Province, China: Ore Geology Reviews, v. 53, p. 422-433.
Marrett, R., and Allmendinger, R. W., 1990, Kinematic analysis of fault-slip data: Journal of Structural Geology, v. 12, p. 973-986.
McDonough, W. F., and Sun, S.-S., 1995, The Composition of the Earth: Chemical Geology, v. 120, p. 223-253.

Meates, G. R., 1979, Annual Report to December 1978 on Authority to prospect 1877M, Maitland Dows Area, Queensland, Report No. 311, 1, p. 1-78.
Meinert, L. D., 1992, Skarns and Skarn Deposits: Geoscience Canada, v. 19, p. 145-162.
Meinert, L. D., 1995, Compositional variation of igneous rocks associated with skarn deposits - chemical evidence for a genetic connection between petrogenesis and mineralization, *in* Thompson, J. F. H., ed., Magmas, fluids, and ore deposits, 23, Mineralogical Association of Canada, p. 401-418.
Meinert, L. D., Dipple, G. M., and Nicolescu, S., 2005, World Skarn Deposits: Economic Geology 100th Anniversary Volume, p. 299-336.
Molnar, P., 1983, Average regional strain due to slip on numerous faults of different orientations: Journal of Geophysical Research v. 88, p. 6430-6432.
Murray, C. G., 1986, Metallogeny and tectonic development of the Tasman Fold Belt System in Queensland: Ore Geology Reviews, v. 1, p. 315-400.
Newberry, R. J., 1982, Tungsten-Bearing Skarns of the Sierra Nevada. I. The Pine Creek Mine, California: Economic Geology, v. 77, p. 823-844.
Newberry, R. J., 1983, The formation of subcalcic garnet in scheelite-bearing skarns: Canadian Mineralogist, v. 21, p. 529-544.
Newberry, R. J., and Swanson, S. E., 1986, Scheelite skarn granitoids: An evaluation of the roles of magmatic source and process: Ore Geology Reviews, v. 1, p. 57-81.
O'Neill, H. S. C., 1987, Quartz-fayalite-iron and quartz-fayalite-magnetite equilibria and the free energy formation of fayalite (Fe_2SiO_4) and magnetite (Fe_3O_4): American Mineralogist, v. 72, p. 67-75.
Ohmoto, H., and Kerrick, D., 1977, Devolatilization equilibria in graphitic systems: American Journal of Science, v. 277, p. 1013-1044.
Oliver, N. H. S., Pearson, P. J., Holcombe, R. J., and Ord, A., 1999, Mary Kathleen metamorphic-hydrothermal uranium — rare-earth element deposit: Ore genesis and numerical model of coupled deformation and fluid flow: Australian Journal of Earth Sciences, v. 46, p. 467-484.
Orhan, A., 2017, Evolution of the Mo-rich scheelite skarn mineralization at Kozbudaklar, Western Anatolia, Turkey: Evidence from mineral chemistry and fluid inclusions: Ore Geology Reviews, v. 80, p. 141-165.
Paton, C., Woodhead, J. D., Hellstrom, J. C., Hergt, J. M., Greig, A., and Maas, R., 2010, Improved laser ablation U-Pb zircon geochronology through robust downhole fractionation correction: Geochemistry, Geophysics, Geosystems, v. 11, p. n/a-n/a.
Pearce, J. A., Harris, N. B. W., and Tindle, A. G., 1984, Trace Element Discrimination Diagrams for the Tectonic Interpretation of Granitic Rocks: Journal of Petrology, v. 25, p. 956-983.
Peters, S. G., 1993, Polygenetic mélange in the Hodgkinson goldfield, Northern Tasman Orogenic Zone: Australian Journal of Earth Sciences, v. 40, p. 115-129.
Peters, S. G., Golding, S. D., and Dowling, K., 1990, Melange- and Sediment-Hosted Gold-Bearing Quartz Veins, Hodgkinson Gold Field, Queensland, Australia: Economic Geology, v. 85, p. 312-327.
Pettke, T., 2008, Analytical protocols for element concentration and Isotope ratio measurements in Fluid Inclusions by LA-(MC-)ICP-MS, *in* Sylvester, P., ed., Laser ablation ICP-MS in the Earth Sciences: Current practices and outstanding issues, 40: Vancouver, B.C., Mineralogical Association of Canada p. 189-217.
Phillips, G. N., and Powell, R., 2010, Formation of gold deposits: a metamorphic devolatilization model: Journal of Metamorphic Geology, v. 28, p. 689-718.
Pirajno, F., 2009, Hydrothermal Processes and Mineral Systems, Springer, 1273 p.
Pitcairn, I. K., Teagle, D. A. H., Craw, D., Olivo, G. R., Kerrich, R., and Brewer, T. S., 2006, Sources of Metals and Fluids in Orogenic Gold Deposits: Insights from the Otago and Alpine Schists, New Zealand: Economic Geology, v. 101, p. 1525-1546.
Plimer, I. R., 1974, Pipe-Like Molybdenite-Wolframite-Bismuth Deposits of Wolfram Camp, North Queensland, Australia: Mineralium Deposita, v. 9, p. 95-104.
Raimbault, L., Baumer, A., Dubru, M., Benkerrou, C., Croze, V., and Zahm, A., 1993, REE fractionation between scheelite and apatite in hydrothermal conditions: American Mineralogist, v. 78, p. 1275-1285.
Raith, J. G., 1991, Stratabound tungsten mineralization in regional metamorphic calc-silicate rocks from the Austroalpine Crystalline Complex, Austria: Mineralium Deposita, v. 26, p. 72-80.

Raju, P. V. S., Hart, C. J. R., and Sangurmath, P., 2016, Scheelite geochemical signatures by LA-ICP-MS and potential for rare earth elements from Hutti Gold Mines and fingerprinting ore deposits: Journal of African Earth Sciences, v. 114, p. 220-227.

Ramboz, C., Pichavant, M., and Weisbrod, A., 1982, Fluid immiscibility in natural processes: Use and misuse of fluid inclusion data: II. Interpretation of fluid inclusion data in terms of immiscibility: Chemical Geology, v. 37, p. 29-48.

Raymond, O. L., Totterdell, J. M., Stewart, A. J., and Woods, M. A., 2018, Australia Geological Provinces, 2018.01 edition [Digital Dataset], *in* Geoscience Australia, ed.: Canberra, Australia http://pid.geoscience.gov.au/dataset/ga/116269.

Roberts, S., Palmer, M. R., and Waller, L., 2006, Sm-Nd and REE Characteristics of Tourmaline and Scheelite from the Björkdal Gold Deposit, Northern Sweden: Evidence of an Intrusion-Related Gold Deposit?: Economic Geology, v. 101, p. 1415-1425.

Roedder, E., and Bodnar, R. J., 1980, Geologic pressure determinations from fluid inclusion studies: Annual Review of Earth and Planetary Sciences, v. 8, p. 263-301.

Rudnick, R. L., and Gao, S., 2014, Composition of the Continental Crust, Treatise on Geochemistry, p. 1-51.

Rundquist, D. V., and Denisenko, V. K., 1986, Classification of tungsten deposits, *in* Beus, A. A., ed., Geology of tungsten, 18: Paris, UNESCO, p. 59-77.

Sahlström, F., Dirks, P., Chang, Z., Arribas, A., Corral, I., Obiri-Yeboah, M., and Hall, C., 2018, The Paleozoic Mount Carlton Deposit, Bowen Basin, Northeast Australia: Shallow High-Sulfidation Epithermal Au-Ag-Cu Mineralization Formed During Rifting: Economic Geology, v. 113, p. 1733-1767.

Samson, S. D., and Alexander, E. C., 1987, Calibration of the interlaboratory 40Ar-39Ar Dating Standard, MMhb-1: Chemical Geology, v. 66, p. 27-34.

Sato, K., 1980, Tungsten Skarn Deposit of the Fujigatani Mine, Southwest Japan: Economic Geology, v. 75, p. 1066-1082.

Seal, R. R., Alpers, C. N., and Rye, R. O., 2000, Stable Isotope Systematics of Sulfate Minerals: Reviews in Mineralogy and Geochemistry, v. 40, p. 541-602.

Setzmann, U., and Wagner, W., 1991, A New Equation of State and Tables of Thermodynamic Properties for Methane Covering the Range from the Melting Line to 625 K at Pressures up to 100 MPa: Journal of Physical and Chemical Reference Data, v. 20, p. 1061-1155.

Shanks III, W. C. P., 2014, Stable Isotope Geochemistry of Mineral Deposits, *in* Holland, H. D., and Turekian, K. K., eds., Treatise on Geochemistry, Elsevier, p. 59-85.

Sharp, Z. D., 1990, A laser-based microanalytical method for the *in situ* determination of oxygen isotope ratios of silicates and oxides: Geochimica et Cosmochimica Acta, v. 54, p. 1353-1357.

Shedd, K. B., 2018, 2016 Minerals Yearbook TUNGSTEN [ADVANCE RELEASE], USGS, p. 21.

Shimazaki, H., 1977, Grossular-spessartine-almandine garnets from some Japanese scheelite skarns: Canadian Mineralogist, v. 15, p. 74-80.

Shimazaki, H., 1980, Characteristics of Skarn Deposits and Related Acid Magmatism in Japan: Economic Geology, v. 75, p. 173-183.

Skaarup, P., 1974, Strata-Bound Scheelite Mineralisation in Skarns and Gneisses from the Bindal Area, Northern Norway: Mineralium Deposita, v. 9, p. 299-308.

Skirrow, R. G., Huston, D. L., Mernagh, T. P., Thorne, J. P., Dulfer, H., and Senior, A. B., 2013, Critical commodities for a high-tech world: Australia's potenital to supply global demand. Geoscience Australia, Canberra., p. 1-126.

Skrzeczynski, R. H., and Wood, A. M., 1984, Annual Report for 1983 on Authority to prospect 3227M Maitland Dows Area North Queensland Report No. 391, 1984, p. 1-50.

So, C.-S., and Shelton, K. L., 1983, A sulfur isotopic and fluid inclusion study of the Cu-W-bearing tourmaline breccia pipe, Ilkwang Mine, Republic of Korea: Economic Geology, v. 78, p. 326-332.

So, C.-S., Shelton, K. L., Seidemann, D. E., and Skinner, B. J., 1983, The Dae Hwa Tungsten-MolybdenumM ine, Republic of Korea: A Geochemical Study: Economic Geology, v. 78, p. 920-930.

Solomon, M., 1981, An Introduction to the Geology and Metallic Ore Deposits of Tasmania: Economic Geology, v. 76, p. 194-208.

Song, G., Qin, K., Li, G., Evans, N. J., and Chen, L., 2014, Scheelite elemental and isotopic signatures: Implications for the genesis of skarn-type W-Mo deposits in the Chizhou Area, Anhui Province, Eastern China: American Mineralogist, v. 99, p. 303-317.

Song, W.-L., Yao, J.-M., Chen, H.-Y., Sun, W.-D., Ding, J.-Y., Xiang, X.-K., Zuo, Q.-S., and Lai, C.-K., 2018, Mineral paragenesis, fluid inclusions, H–O isotopes and ore-forming processes of the giant Dahutang W–Cu–Mo deposit, South China: Ore Geology Reviews, v. 99, p. 116-150.

Spandler, C., Pettke, T., and Rubatto, D., 2011, Internal and External Fluid Sources for Eclogite-faciesVeins in the Monviso Meta-ophiolite,Western Alps: Implications for Fluid Flow in Subduction Zones: Journal of Petrology, v. 52, p. 1207-1236.

Sperner, B., Müller, B., Heidbach, O., D., D., Reinecker, J., and Fuchs, K., 2003, Tectonic stress in the Earth's crust: advances in the world stress map project. in: Nieuwland, D.A. (Ed.), New insights into structural interpretation and modelling: Geological Society of London Special Publication, v. 212, p. 101-116.

Steele-MacInnis, M., Lecumberri-Sanchez, P., and Bodnar, R. J., 2012, HokieFlincs_H_2O-NaCl : A Microsoft Excel spreadsheet for interpreting microthermometric data from fluid inclusions based on the PVTX properties of H_2O–NaCl: Computers & Geosciences, v. 49, p. 334-337.

Strekopytov, S. V., 1998, Molybdenum and Tungsten in Oceanic Sediments and Nodules: Geochemistry International, v. 36, p. 838-845.

Sun, K., and Chen, B., 2017, Trace elements and Sr-Nd isotopes of scheelite: Implications for the W-Cu-Mo polymetallic mineralization of the Shimensi deposit, South China: American Mineralogist, v. 102, p. 1114-1128.

Sylvester, P. J., and Ghaderi, M., 1997, Trace element anaylisis of scheelite by excimer laser ablation-inductively coupled-plasma-mass spectrometry (ELA-ICP-MS) using a synthetic silicate glass standard: Chemical Geology, v. 141, p. 49-65.

Taylor, H. P. J., 1974, The Application of Oxygen and Hydrogen Isotope Studies to Problems of Hydrothermal Alteration and Ore Deposition: Economic Geology, v. 69, p. 843-883.

Thalhammer, O. A. R., Stumfl, E. F., and Jahoda, R., 1989, The Mittersill Scheelite Deposit, Austria: Economic Geology, v. 84, p. 1153-1171.

Tornos, F., Galindo, C., Crespo, J. L., and Spiro, B. F., 2008, Geochemistry and Origin of Calcic Tungsten-Bearing Skarns, Los Santos, Central Iberian Zone, Spain: The Canadian Mineralogist, v. 46, p. 87-109.

Tucker, R. T., Roberts, E. M., Hu, Y., Kemp, A. I. S., and Salisbury, S. W., 2013, Detrital zircon age constraints for the Winton Formation, Queensland: Contextualizing Australia's Late Cretaceous dinosaur faunas: Gondwana Research, v. 24, p. 767-779.

Tweto, O., 1960, Scheelite in the Precambrian gneisses of Colorado: Economic Geology, v. 55, p. 1406-1428.

Twiss, R. J., and Unruh, J. R., 1998, Analysis of fault slip inversions: Do they constrain stress or strain rate?: Journal of Geophysical Research v. 101, p. 8335-8361.

Vennemann, T. W., and O'Neil, J. R., 1996, Hydrogen isotope exchange reactions between hydrous minerals and molecular hydrogen: I. A new approach for the determination of hydrogen isotope fractionation at moderate temperatures: Geochimica et Cosmochimica Acta, v. 60, p. 2437-2451.

Vos, I. M. A., and Bierlein, F. P., 2006, Characteristics of orogenic-gold deposits in the Northcote district, Hodgkinson Province, north Queensland: implications for tectonic evolution: Australian Journal of Earth Sciences, v. 53, p. 469-484.

Werner, A. B. T., Sinclair, W. D., and Amey, E. B., 2014, International Strategic Mineral Issues Summary Report--Tungsten (ver. 1.1, November 2014): U.S. Geological Survey Circular 930-O: Washington, U.S., USGS, p. 74.

Wesolowski, D. J., Drummond, S. E., Mesmer, R. E., and Ohmoto, H., 1984, Hydrolysis Equilibria of Tungsten(VI) in Aqueous Sodium Chloride Solutions to 300C: Inorganic Chemistry, v. 23, p. 1120-1132.

Wesolowski, D. J., and Ohmoto, H., 1986, Calculated oxygen isotope fractionation factors between water and the minerals scheelite and powellite: Economic Geology, v. 81, p. 471-477.

Whitney, D. L., and Evans, B. W., 2010, Abbreviations for names of rock-forming minerals: American Mineralogist, v. 95, p. 185-187.

Wilkinson, J. J., 2001, Fluid inclusions in hydrothermal ore deposits: Lithos, v. 55, p. 229-272.

Wilkinson, J. J., 2017, Metastable freezing: A new method for the estimation of salinity in aqueous fluid inclusions: Economic Geology, v. 112, p. 185-193.

Williams-Jones, A. E., Migdisov, A. A., and Samson, I. M., 2012, Hydrothermal Mobilisation of the Rare Earth Elements - a Tale of "Ceria" and "Yttria": Elements, v. 8, p. 355-360.

Withnall, I. W., and Hutton, L. J., 2013, North Australian Craton, *in* Jell, P. A., ed., Geology of Queensland: State of Queensland, Geological Survey of Queensland, p. 23-112.

Wood, A. M., 1982, First Six Monthly Report on Authority to prospect 3250M Mailand Dows North Area, North Queensland, Report No. 382: Cairns, N.Q., p. 1-13.
Wood, S. A., and Samson, I. M., 2000, The Hydrothermal Geochemistry of Tungsten in Granitoid Environments: I. Relative Solubilities of Ferberite and Scheelite as a Function of T, P, pH, and mNaCl: Economic Geology, v. 95, p. 143-182.
Wood, S. A., and Vlassopoulos, D., 1989, Experimental determination of the hydrothermal solubility and speciationof tungsten at 500C and 1 kbar: Geochimica et Cosmochimica, v. 53, p. 303-312.
Xie, G., Mao, J., Li, W., Fu, B., and Zhang, Z., 2018, Granite-related Yangjiashan tungsten deposit, southern China: Mineralium Deposita.
Yingjun, L., and Dongsheng, M., 1993, Vein-type tungsten deposits of China and adjoining regions: Ore Geology Reviews, v. 8, p. 233-246.
Zhang, C., and Duan, Z., 2010, GFluid: An Excel spreadsheet for investigating C–O–H fluid composition under high temperatures and pressures: Computers & Geosciences, v. 36, p. 569-572.
Zheng, Y.-F., 1993a, Calculation of oxygen isotope fractionation in anhydrous silicate minerals: Geochimica et Cosmochimica Acta, v. 57, p. 1079-1091.
Zheng, Y.-F., 1993b, Calculation of oxygen isotope fractionation in hydroxyl-bearing silicates: Earth and Planetary Science Letters, v. 120, p. 247-263.
Zucchetto, R. G., Henderson, R. A., Davis, B. K., and Wysoczanski, R., 1999, Age constraints on deformation of the eastern Hodgkinson Province, north Queensland: New perspectives on the evolution of the northern Tasman Orogenic Zone: Australian Journal of Earth Sciences, v. 46, p. 105-114.

Appendices

Appendix 1: General information on samples used in this thesis

Appendix 1.1: Sample coordinates and performed analyses

					UTM GDA94 zone 55			Geochemistry			Dating			Stable isotopes				
Sample ID	Rock type[1]	Sample type	Drill core	Meter	Easting	Northing	Elevation m a.s.l.	W-R[2]	EPMA[2]	TE[2]	U/Pb Zrn[3]	^{40}Ar-^{39}Ar Ms[3]	Fluid Inclusions	δ^{34}S Sulph.[3]	δ^{18}O Sch[3]	δ^{18}O Pl[3]	δ^{18}O Qz[3]	δ^{18}O-δD Ms[3]
GT004-094	Ps	DDH	GT004	94	273741	8192620	795		✓									
MWD005-067	Mz - sk-alt cong	DDH	MWD005	67	273584	8192501	725	✓	✓	✓								
MWD005-128	Sk-alt cong	DDH	MWD005	128	273623	8192504	679		✓									
MWD011-147.5	Sk-alt cong	DDH	MWD011	147.5	273782	8192645	745		✓	✓								
MWD013-099	Mz	DDH	MWD013	99	273795	8192644	783	✓		✓	✓							
MWD036-075.5	Vn - sk-alt cong	DDH	MWD036	75.5	273658	8192567	756								✓	✓	✓	
MWD036-123	Vn - sk-alt cong	DDH	MWD036	123	273685	8192570	717	✓										
MWD042-197	Vn - sk-alt cong	DDH	MWD042	197	273570	8192534	618	✓	✓	✓					✓		✓	
MWD042-269	Sk-alt cong	DDH	MWD042	269	273617	8192530	564							✓				
MWD077-145	Vn - sk-alt cong	DDH	MWD077	145	273539	8192452	652								✓	✓	✓	
MWD099-034	Vn - sk-alt cong	DDH	MWD099	34	273606	8192603	789	✓										
MWD099-054	Vn - sk-alt cong	DDH	MWD099	54	273603	8192613	771	✓	✓	✓			✓		✓	✓		
MWD099-081	Sk-alt cong	DDH	MWD099	81	273599	8192626	748		✓									
MWD099-086	Vn - sk-alt cong	DDH	MWD099	86	273598	8192628	744	✓										
MWD099-102.5	Ps	DDH	MWD099	102.5	273596	8192636	730	✓										
MWD099-124	Vn - sk-alt cong	DDH	MWD099	124	273593	8192647	711		✓	✓			✓					
MWD099-163.5	Vn - sk-alt cong	DDH	MWD099	163.5	273589	8192667	678	✓	✓	✓					✓	✓	✓	
MWD101-046.5	Ps	DDH	MWD101	46.5	273539	8192533	739	✓										
MWD101-104	Vn - sk-alt cong	DDH	MWD101	104	273538	8192562	688							✓				
MWD101-119	Vn - qtz	DDH	MWD101	119	273538	8192569	676							✓				
MWD101-121.5	Vn - qtz	DDH	MWD101	121.5	273538	8192570	674							✓				
MWD101-149	Vn - sk-alt cong	DDH	MWD101	149	273538	8192584	650		✓	✓				✓	✓		✓	
MWD101-155	Vn - sk-alt cong	DDH	MWD101	155	273538	8192587	644	✓							✓	✓		
MWD101-159	Vn - sk-alt cong	DDH	MWD101	159	273538	8192589	641	✓	✓	✓					✓	✓		
MWD101-211.5	Vn - sk-alt cong	DDH	MWD101	211.5	273540	8192615	596	✓	✓					✓				
MWD101-222	Vn - qtz	DDH	MWD101	222	273540	8192621	586							✓				
MWD105-077	Vn - sk-alt cong	DDH	MWD105	77	273549	8192503	712								✓	✓	✓	
MWD105-115	Sk-alt cong	DDH	MWD105	115	273547	8192523	680	✓	✓									
MWD105-123.5	Vn - sk-alt cong	DDH	MWD105	123.5	273547	8192527	673	✓							✓	✓	✓	
MWD105-135	Vn - sk-alt cong	DDH	MWD105	135	273547	8192533	662								✓	✓	✓	
MWD105-165	Ps	DDH	MWD105	165	273546	8192549	637	✓										
MWD105-200	Vn - sk-alt cong	DDH	MWD105	200	273546	8192567	607							✓				

Appendix 1.1: Sample coordinates and performed analyses continued

					UTM GDA94 zone 55			Geochemistry			Dating			Stable isotopes				
Sample ID	Rock type[1]	Sample type	Drill core	Meter	Easting	Northing	Elevation m a.s.l.	W-R[2]	EPMA[2]	TE[2]	U/Pb Zrn[3]	^{40}Ar-^{39}Ar Ms[3]	Fluid Inclusions	δ^{34}S Sulph.[3]	δ^{18}O Sch[3]	δ^{18}O Pl[3]	δ^{18}O Qz[3]	δ^{18}O-δD Ms[3]
MWD105-206	Vn - sk-alt cong	DDH	MWD105	206	273546	8192571	602	✓	✓					✓	✓	✓		
MWD105-215	Vn - sk-alt cong	DDH	MWD105	215	273546	8192575	594							✓				
MWD105-234	Vn - sl	DDH	MWD105	234	273547	8192585	578							✓				
MWD107-062.5	Vn - sk-alt cong	DDH	MWD107	62.5	273546	8192338	707							✓				
MWD107-134	Ps	DDH	MWD107	134	273543	8192376	646	✓										
MWD107-172	Sk-alt cong	DDH	MWD107	172	273542	8192396	614	✓										
MWD107-259	Vn - sk-alt cong	DDH	MWD107	259	273543	8192444	542	✓	✓	✓					✓	✓	✓	
MWD107-310	Vn - sk-alt cong	DDH	MWD107	310	273546	8192473	500	✓										
MWD107-333	Ps	DDH	MWD107	333	273548	8192486	481	✓										
MWD119-050	Ps	DDH	MWD119	50	273505	8192255	703	✓										
MWD119-126	Sk-alt cong	DDH	MWD119	126	273501	8192294	638	✓	✓									
MWD119-128	Vn - sk-alt cong	DDH	MWD119	128	273501	8192295	636		✓	✓								
MWD119-246	Ps	DDH	MWD119	246	273501	8192360	538	✓										
MWD119-317	Sk-alt cong	DDH	MWD119	317	273503	8192401	480		✓									
MWD122-289	Vn - sk-alt cong	DDH	MWD122	289	273507	8192315	499		✓	✓								
MWD124-130.5	Sk-alt cong	DDH	MWD124	130.5	273520	8192470	649		✓					✓				
MWD124-180	Vn - ps	DDH	MWD124	180	273521	8192495	606							✓				
MWD124-193.5	Vn -ps	DDH	MWD124	193.5	273521	8192501	594							✓				
MWD124-216	Ps	DDH	MWD124	216	273522	8192513	575	✓										
MWD124-240	Vn - qtz	DDH	MWD124	240	273523	8192526	555								✓		✓	
MWD124-266	Vn - sk-alt cong	DDH	MWD124	266	273525	8192540	533	✓	✓									
MWD124-280.5	Qtz	DDH	MWD124	280.5	273526	8192548	521							✓				
MWD194-050	Ps	DDH	MWD194	50	273612	8192743	801	✓										
MWD194-065	Vn - qtz	DDH	MWD194	65	273610	8192750	788							✓				
MWD194-105.5	Vn - sk-alt cong	DDH	MWD194	105.5	273605	8192770	753	✓						✓	✓	✓	✓	
MWD217-048.5	Vn - qtz	DDH	MWD217	48.5	273570	8192683	791							✓				
MWD217-056	Vn - sk-alt cong	DDH	MWD217	56	273569	8192686	784					✓		✓				
MWD217-078	Vn - sk-alt cong	DDH	MWD217	78	273567	8192697	765	✓						✓	✓	✓	✓	
MWD217-098	Sk-alt cong	DDH	MWD217	98	273565	8192707	748	✓										
MWD217-133	Vn - qtz	DDH	MWD217	133	273561	8192724	717							✓				✓
MWD217-142	Sk-alt cong	DDH	MWD217	142	273561	8192729	710							✓				
MWD217-149	Vn - ps	DDH	MWD217	149	273560	8192732	704	✓										✓

Appendix 1.1: continued

Sample ID	Rock type[1]	Sample type	Drill core	Meter	UTM GDA94 zone 55		Elevation m a.s.l.	Geochemistry			Dating		Fluid Inclusions	Stable isotopes				
					Easting	Northing		W-R[2]	EPMA[2]	TE[2]	U/Pb Zrn[3]	^{40}Ar-^{39}Ar Ms[3]		δ^{34}S Sulph.[3]	δ^{18}O Sch[3]	δ^{18}O Pl[3]	δ^{18}O Qz[3]	δ^{18}O-δD Ms[3]
MWD217-181	Vn - sk-alt cong	DDH	MWD217	181	273558	8192748	676							✓				
MWD217-189.5	Vn - sk-alt cong	DDH	MWD217	189.5	273557	8192752	669	✓							✓	✓	✓	
MWD231-043	Vn - qtz	DDH	MWD231	43	273597	8192874	766							✓				
MWD231-068	Vn - ps	DDH	MWD231	68	273595	8192885	744	✓						✓				
WS15-001	Gr	Surface	--	--	273779	8193133	800	✓			✓							
WS15-003	Ps	Surface	--	--	272797	8192954	721	✓										
WS15-004	Ps	Surface	--	--	275468	8185155	655	✓										
WS15-005	Gr	Surface	--	--	275604	8194873	662	✓			✓							
WS15-006	Ps	Surface	--	--	273393	8193778	783	✓										
WS15-007	Ps	Surface	--	--	273407	8193699	793	✓										
WS15-008	Ps	Surface	--	--	273439	8193631	779	✓										
WS15-009	Ps	Surface	--	--	273505	8193493	762	✓										
WS15-010	Ps	Surface	--	--	273525	8193410	764	✓										
WS15-015	Ps	Surface	--	--	273503	8193035	838	✓										
WS15-016	Ps	Surface	--	--	273636	8193169	812	✓										
WS15-017	Gr	Surface	--	--	273225	8193331	744	✓			✓							
WS16-002	Di	Surface	--	--	275029	8191013	790	✓			✓							
WS16-006	Vn - sk-alt cong	Surface	--	--	273754	8192825	872					✓	✓					✓

[1]Rock types: Di: diorite, Gr: granite, Mz: monzonite, Ps: psammite, Qtz: quartzite, Sk-alt cong: skarn-altered conglomerate, Mz - sk-alt cong: monzonite cutting skarn altered conglomerate, Vn - ps: vein cutting psammite, Vn – qtz: vein cutting quartzite Vn - sl: vein cutting slate, Vn - sk-alt cong: vein cutting skarn-altered conglomerate,

[2]Abbreviations: EPMA: electron probe microanalyzer, TE: mineral trace element, W-R: whole-rock geochemistry

[3]Mineral abbreviations: Ms: muscovite, Pl: plagioclase, Qz: quartz, Sch: scheelite, Sulph: sulphides, Zrn: zircon. After Whitney and Evans (2010)

Appendix 2: Material linked to Chapter 2

Appendix 2.1: Fault kinematic analysis

Kinematic data from faults can be used to reconstruct palaeo-stress fields (Angelier and Mechler, 1977). To do this, information is required on the orientation of the fault plane, the slip direction visible as slickenlines, striations or gouge marks, and the sense of movement. Stress inversion techniques rely on the assumption that the slip direction coincides with the resolved shear stress on the fault plane, and that the set of faults used in the analysis, formed or were active in response to the same far field stress. Fault-slip data can be inverted to a reduced moment tensor with information on the direction of the principal stress axes and their relative size expressed as a stress ratio (Angelier, 1994; Delvaux and Sperner, 2003). This reduced stress tensor can be calculated using the P (principal compression) and T (principal tension) axes that bisect the fault plane and an auxiliary plane perpendicular to the fault, by using least-square minimization techniques of direction cosines (Marrett and Allmendinger, 1990) or iterative methods that test a variety of possible tensor solutions (Etchecopar et al., 1981). Stress axes can also be determined graphically using the right dihedron method (Lisle, 1987; Delvaux and Sperner, 2003), which constrains the orientation of principal stress axes by determining the area of maximum overlap of compressional and extensional quadrants for a suite of faults.

In analyzing the fault-slip data, we have used a linked Bingham distribution tensor calculated with the program FaultKinWin (Allmendinger, 2001) following methods described by Marrett and Allmendinger (1990) and Cladouhos and Allmendinger (1993). The FaultKinWin programme (Allmendinger, 2001) uses the distribution of P and T axes for a suite of faults (Angelier and Mechler, 1977) to calculate a Bingham axial distribution based on a least squares minimization technique for direction cosines. In this technique, the dihedral angle between the fault plane and an auxiliary plane is 90° and bisected by P and T axes. The eigenvectors for the calculated Bingham axial distribution provide average orientations for the maximum, minimum and intermediate concentration direction of the P and T axes, and the eigenvalues provide a measure of the relative concentration, or distribution of P and T axes. These eigenvalues vary between -0.5 and +0.5, with maximum values reached when P and T axes are perfectly concentrated. Variations in the eigenvalues (ev) can be linked to the stress regime using the relative size of the normalized eigenvalues expressed in a ratio, Rev, (with Rev = $[ev_2\text{-}ev_3]/[ev_1\text{-}ev_3]$) (constrictional stress: Rev = 1 with $ev_1 = ev_2$; plane stress: Rev = 0.5 with $ev_2 = 0$; flattening stress: Rev = 0 with $ev_2 = ev_3$). The FaultKinWin programme output is a plot of linked Bingham axes with eigenvalues and a related fault plane solution diagram displaying P and T quadrants in a manner similar to earthquake focal mechanisms **(Fig. 2.8C)**.

Although stress analysis from fault slip data is widely applied, debate continues whether the obtained solutions represent a stress field or provide a measure of strain and strain rate (Molnar, 1983; Twiss and Unruh, 1998). Marrett and Allmendinger (1990) and Allmendinger (2001), using FaultKinWin, prefer to interpret the fault plane solutions as an indicator of strain rather than stress.

Here, the linked Bigham fault plane solution through FaultKinWin has been interpreted as an indication of the paleo-stress field. In doing this we are aware of the various pitfalls. Faults, once formed, can interact in

complex ways in response to an imposed stress-field due to scale-dependent strain partitioning, complex fault interactions, block rotations, inhomogeneities in the rock mass etc. (Twiss and Unruh, 1998). In spite of such limitations, the paleo-stress analysis technique has been successfully applied in a wide variety of tectonic settings (Sperner et al., 2003; Dirks et al., 2009; Dirks et al., 2013), and we believe it provides valuable insights in the tectonic controls on scheelite mineralization at Watershed.

Misfits in collected datasets may have resulted from observational errors, the mixing of unrelated data points or limitations in the approach used. They can also be due to non-uniform stress fields as a result of fracture interactions, anisotropies in the rock mass, block rotations or slip partitioning. In near vertical shear fractures there is the added problem that a small rotation of the fracture plane around a horizontal axis can change it from a normal fracture compatible with the overall data set to a reverse fracture that is radically incompatible when using the computer programs. In calculating a Bingham tensor solution using FaultKinWin all data points were included. It is stressed that throughout the analyses of datasets, very few data points were incompatible with the final results, suggesting generally homogeneous data

As a general rule, the results from the paleo-stress analyses are best constrained for large data sets that combine fracture planes with different directions and movement sense. Thus, conjugate fracture sets, or Riedel, anti-Riedel and P-shear arrays provide good results more likely to be indicative of the regional paleo-stress field. Especially if the stress inversion is based on at least 15 fracture planes (Delvaux and Sperner, 2003; Sperner et al., 2003), whilst sites in which only few planes, or planes in a limited number of directions can be measured provide at best an indication only of the local paleo-stress field, which may or may not conform with the regional results.

Appendix 2.2: Methodology

Whole-rock geochemistry

Prior to geochemical analysis the rock samples were crushed and finely milled to powders and then mixed with $LiBO_2$ / $Li_2B_4O_7$ flux and fused in a furnace. The cooled bead was then dissolved in ACS grade nitric acid and analysed by ICP-OES and / or ICP-MS. For the analysis of ultra-trace elements, the prepared samples were digested with a modified Aqua Regia solution of equal parts concentrated HCl, HNO_3 and de-ionized H_2O for one hour in a heating block or hot water bath. The Sample solution was then made up to volume with dilute HCl. Loss on ignition (LOI) was determined by heating a sample split, and then measuring the LOI as follows: LOI % = (A - B) / C x 100 (A = mass of crucible + sample; B = mass of crucible + sample after ignition; C = mass of sample).

FeO concentrations were determined by titration method. Samples were first digested with sulfuric acid (H_2SO_4), then allowed to cool, and then digested with hydrofluoric acid. An indicator solution consisting of distilled water, sulfuric acid, phosphoric acid, boric acid and diphenylamine sulfonate was added to every sample solution. The solutions were then titrated using a standard dichromate ($K_2Cr_2O_7$) solution. The end point of the titration was determined when a purple colour persists in the sample solution for 30 seconds.

Fluorine concentrations were determined by decomposing the samples by fusion with sodium hydroxide, and then digesting the produced melt in water. The solution was acidified with citric acid and ultimately buffered with ammonium citrate solution. Fluoride was determined using an electrode composed of lanthanum fluoride crystal membrane that is an ionic conductor selective for un-complexed fluoride ions. The electrode was placed in the sample solution after the ion strength was adjusted to pH 6.5, and the potential was measured by an mV/pH meter. Fluorine concentrations were derived from a standard graph of potential vs. concentration of fluorine.

Muscovite ^{40}Ar-^{39}Ar geochronology

Muscovite separation was performed manually at James Cook University. The muscovite crystals were scratched off directly from the rock in a pergamyn paper envelope; and then place in a mortar where the muscovite grains were smashed by a pestle to separate single muscovite sheets. The resultant material was put into a plastic beaker with distilled water and an ultrasound bath was performed for one minute, with the aim of eliminating the attached material, e.g. quartz grains. After the ultrasonic bath, all the material was poured into a small glass beaker and sieved to obtain four different grain size fractions: <125, 125-250, 250-500 and >500 microns. Then, starting from the coarser grain fraction, the muscovite was placed on a glass plate under the binocular microscope and 30 mg of optically fresh muscovite grains were handpicked using fine tweezers.

Samples were wrapped in pure Al foil and irradiated for 90 MWhr hr at location 8C at the McMaster Nuclear Reactor at McMaster University in Hamilton, Ontario in irradiation package mc49 and mc55. Standard hornblende MMhb-1 was used as a neutron fluence monitor with an assumed age of 520.4 Ma (Samson and Alexander, 1987). All samples were incrementally heated with a Coherent Innova 5 W continuous argon-ion laser until complete fusion was achieved. Samples were loaded into 3 adjacent 2mm diameter wells and degassed each laser power setting for 30 seconds.

Argon isotopes were measured using a VG1200S mass spectrometer with a source operating at 150 µA total emission and equipped with a Daly detector operating in analog mode at the Argon Geochronology Laboratory (University of Michigan, U.S.A.). Mass discrimination was monitored daily using ~4x10-9 ccSTP of atmospheric Ar. Fusion system blanks were run every five fusion steps and blank levels from argon masses 36 through 40 (~2 x 10-14, ~3 x 10-14, ~1 x 10-14, ~3 x 10-14, and 2 x 10-12 ccSTP respectively) were subtracted from sample gas fractions. Corrections were also made for the decay of ^{37}Ar and ^{39}Ar, as well as interfering nucleogenic reactions from K, Ca and Cl as well as the production of ^{36}Ar from the decay of ^{36}Cl.

Silicate microprobe techniques

Quantitative major element analysis of all the silicates were carried out using a JEOL JXA 8200 superprobe in wavelength dispersive spectrometry (WDS) mode, with 15 [kV] acceleration voltage and a 5 [µm] beam with 20 [nA] beam current, at the Advanced Analytical Centre, James Cook University (JCU). Generally, counting times were 20 [s] on peak and 10 [s] on background for each element. The data were processed using the Armstrong/Love-Scott Phi-Rho-Z (φρz) method for matrix correction. Primary standards used are: albite for Na, orthoclase for K, forsterite for Mg, rutile for Ti, spessartine for Mn, wollastonite for Ca, synthetic SrO for F, and scapolite for Cl. The standards used for Al, Si and Fe will vary depending on the analyzed silicate.

Zircon cathodoluminescence (CL) imaging

Cathodoluminescence (CL) imaging was carried out at the Advanced Analytical Centre, James Cook University on carbon-coated polished mounts using a JEOL JSM5410LV SEM and a Robinson CL detector and photomultiplier. By covering the spectral range of 310 to 650 nm, the photomultiplier is more sensitive in gathering light in the blue to ultraviolet range than in the red to infrared range. Instrument operating conditions were set to an accelerating voltage of 20 kV and a beam current of ~10 nA.

In situ U/Pb dating of zircon by LA-ICP-MS

Uranium/Pb dating of zircon was conducted using laser ablation ICP-MS, using a Geolas Pro 193nm ArF excimer laser system coupled with a Bruker (formally Varian) 820–MS ICP-MS at the Advanced Analytical Centre, James Cook University. Ablation was conducted in a custom-build large volume cell (Fricker et al., 2011) using high-purity He as the carrier gas, which was subsequently mixed with Ar prior to introduction into

the ICP-MS. The ICP-MS was tuned for maximum sensitivity under robust plasma conditions (Th/U sensitivity ratio ~1; Pettke, 2008) and maintaining low oxide production rates (ThO/Th <0.4 %). Full analytical details are described in Tucker et al. (2013). Analytes collected were 29Si, 90Zr, 202Hg, 204Pb, 206Pb, 207Pb, 208Pb, 232Th, 235U, and 238U. The ICP-MS was tuned to ensure low oxide production levels (ThO/Th <0.5%) and approximately equal sensitivity of U, Th and Pb to minimize isotope fractionation due to matrix effects (Pettke, 2008). Fractionation and mass bias was corrected by using standard bracketing techniques with every ten zircon sample measurements bracketed by measurements of GJ1 (primary calibration standard; Jackson et al., 2004), and Temora 2 (Black et al., 2003). All zircons were analyzed with a beam spot diameter of 24 or 32 µm depending on the size of the zircon and selection of analytical sample spots was guided by CL images targeting external rims. Individual analyses consist of approximately 30 seconds of signal of the gas background followed by 30 seconds of signal collected during zircon ablation. Analysis of the NIST SRM 612 reference glass was conducted at the beginning, middle and end of every analytical session.

Data reduction was carried out using the Iolite software (Paton et al., 2010). All time-resolved single isotope signals from standards and samples were filtered for signal spikes or perturbations related to inclusions and fractures. Subsequently, the most stable and representative isotopic ratios were selected taking into account possible mixing of different age domains and zoning. Drift in instrumental measurements was corrected following analysis of drift trends in the raw data using measured values for the GJ1 primary zircon standard. Age calculations based on measured isotope ratios were completed using Isoplot/Ex version 4.15 (Ludwig, 2012). Analyses of the secondary zircon standards were used for verification of GJ1 following drift correction.

Appendix 2.3: Microprobe analytical data

Appendix 2.3.1: Garnet EPMA data from the Watershed tungsten deposit

		Major oxides, weight percent										Number of ions on the basis of 12 oxygen atoms									Garnet end-member[1]				
Sample	Spot	SiO_2	TiO_2	Al_2O_3	FeO	MnO	MgO	CaO	Na_2O	K_2O	Total	Si	Al	Ti	Fe^{3+}	Fe^{2+}	Mn	Mg	Ca	Total	Sps	Prp	Alm	Grs	Adr
MWD005-128A	005-128A-P1_1	37.5	0.1	21.3	8.9	12.8	0.2	19.1	0.0	0.0	99.9	2.95	1.98	0.01	0.06	0.52	0.86	0.03	1.61	8.02	28	1	17	50	3
MWD005-128A	005-128A-P1_2	38.0	0.0	21.1	9.4	12.1	0.2	19.3	0.0	0.0	100.2	2.98	1.95	0.00	0.06	0.56	0.81	0.02	1.62	8.01	27	1	19	51	3
MWD005-128A	005-128A-P1_3	37.9	0.4	20.5	16.3	9.1	0.4	16.3	0.0	0.0	100.8	2.98	1.90	0.02	0.10	0.97	0.61	0.05	1.37	8.00	20	2	32	41	5
MWD005-128A	005-128A-P1_4	38.2	0.3	20.4	16.4	8.7	0.4	16.1	0.0	0.0	100.5	3.01	1.90	0.02	0.08	1.00	0.58	0.05	1.36	7.99	19	2	34	41	4
MWD005-128A	005-128A-P1_5	37.8	0.1	20.9	10.4	10.6	0.2	20.3	0.0	0.0	100.3	2.97	1.93	0.01	0.10	0.58	0.71	0.02	1.70	8.01	23	1	19	52	5
MWD005-128A	005-128A-P1_6	38.0	0.1	20.9	11.0	7.2	0.2	23.0	0.0	0.0	100.4	2.96	1.92	0.01	0.12	0.60	0.47	0.03	1.92	8.02	16	1	20	58	6
MWD005-128A	005-128A-P1_7	37.9	0.2	20.7	10.2	7.0	0.2	23.4	0.0	0.0	99.4	2.97	1.91	0.01	0.11	0.56	0.46	0.02	1.96	8.01	15	1	19	60	6
MWD011-147	011-147-P1_1	38.0	0.1	20.9	5.6	8.9	0.1	26.0	0.0	0.0	99.4	2.97	1.92	0.00	0.11	0.25	0.58	0.01	2.17	8.01	19	0	8	66	6
MWD011-147	011-147-P1_10	37.3	0.1	20.8	7.1	7.4	0.2	26.5	0.0	0.0	99.3	2.92	1.92	0.01	0.16	0.31	0.49	0.02	2.22	8.04	16	1	10	65	8
MWD011-147	011-147-P1_11	37.9	0.1	21.1	11.2	8.2	0.3	21.9	0.0	0.0	100.6	2.95	1.94	0.01	0.10	0.63	0.54	0.03	1.83	8.02	18	1	21	55	5
MWD011-147	011-147-P1_12	37.5	0.1	21.1	6.8	7.4	0.2	26.4	0.0	0.0	99.5	2.93	1.94	0.01	0.13	0.31	0.49	0.03	2.20	8.03	16	1	10	66	7
MWD011-147	011-147-P1_16	38.3	0.4	20.2	8.3	5.4	0.1	27.7	0.0	0.0	100.4	2.96	1.84	0.02	0.18	0.36	0.35	0.01	2.29	8.01	12	0	12	67	9
MWD011-147	011-147-P1_17	38.4	0.3	20.6	7.8	6.1	0.1	27.1	0.0	0.0	100.5	2.96	1.87	0.02	0.15	0.36	0.40	0.01	2.24	8.01	13	0	12	67	7
MWD011-147	011-147-P1_18	38.5	0.6	19.9	7.2	5.1	0.1	29.1	0.0	0.0	100.5	2.96	1.80	0.04	0.20	0.26	0.33	0.01	2.40	8.00	11	0	9	70	10
MWD011-147	011-147-P1_19	38.1	0.2	20.1	12.8	6.6	0.2	22.5	0.0	0.0	100.4	2.98	1.85	0.01	0.16	0.67	0.43	0.02	1.88	8.01	14	1	22	54	8
MWD011-147	011-147-P1_2	38.0	0.1	20.9	5.1	9.8	0.1	25.2	0.0	0.0	99.3	2.97	1.92	0.01	0.10	0.24	0.65	0.01	2.11	8.01	22	0	8	65	5
MWD011-147	011-147-P1_20	38.0	0.3	20.1	7.9	3.8	0.1	29.8	0.0	0.0	99.9	2.94	1.83	0.02	0.21	0.29	0.25	0.01	2.47	8.02	8	0	10	71	11
MWD011-147	011-147-P1_21	38.3	0.3	20.2	6.9	6.4	0.1	28.5	0.0	0.0	100.6	2.95	1.83	0.02	0.20	0.24	0.42	0.01	2.35	8.02	14	0	8	68	10
MWD011-147	011-147-P1_22	38.1	0.5	19.8	7.9	5.6	0.1	28.1	0.0	0.0	100.0	2.95	1.81	0.03	0.21	0.30	0.37	0.01	2.34	8.01	12	0	10	67	11
MWD011-147	011-147-P1_23	38.5	0.5	20.0	7.4	5.1	0.1	28.8	0.0	0.0	100.2	2.97	1.81	0.03	0.19	0.28	0.33	0.01	2.38	8.00	11	0	9	70	10
MWD011-147	011-147-P1_24	38.0	0.3	19.9	8.2	5.6	0.1	27.6	0.0	0.0	99.7	2.96	1.82	0.02	0.20	0.33	0.37	0.01	2.30	8.01	12	0	11	66	10
MWD011-147	011-147-P1_25	38.1	0.6	19.8	9.2	6.8	0.1	25.6	0.0	0.0	100.0	2.97	1.81	0.03	0.19	0.41	0.45	0.01	2.13	8.00	15	0	14	61	10
MWD011-147	011-147-P1_26	38.0	0.4	19.9	13.1	6.8	0.2	22.0	0.0	0.0	100.3	2.97	1.84	0.02	0.17	0.69	0.45	0.02	1.84	8.00	15	1	23	53	9
MWD011-147	011-147-P1_27	37.5	0.2	20.5	8.1	5.1	0.1	28.0	0.0	0.0	99.5	2.92	1.89	0.01	0.18	0.35	0.34	0.01	2.33	8.03	11	0	11	68	9
MWD011-147	011-147-P1_3	37.8	0.2	20.6	9.4	7.2	0.2	23.8	0.0	0.0	99.3	2.97	1.91	0.01	0.11	0.50	0.48	0.02	2.00	8.01	16	1	17	61	6
MWD011-147	011-147-P1_31	37.3	0.2	20.7	10.3	6.5	0.2	24.1	0.0	0.0	99.3	2.93	1.92	0.01	0.14	0.54	0.43	0.02	2.03	8.03	14	1	18	60	7
MWD011-147	011-147-P1_32	37.6	0.2	20.8	11.4	7.5	0.2	22.5	0.0	0.0	100.0	2.95	1.92	0.01	0.13	0.62	0.49	0.03	1.88	8.02	16	1	20	56	6
MWD011-147	011-147-P1_33	37.6	0.1	20.7	10.9	7.2	0.2	23.1	0.0	0.0	99.9	2.95	1.91	0.01	0.13	0.58	0.48	0.03	1.94	8.02	16	1	19	57	7
MWD011-147	011-147-P1_34	37.5	0.1	20.7	4.7	10.3	0.1	25.4	0.0	0.0	98.9	2.95	1.92	0.01	0.12	0.19	0.69	0.01	2.14	8.02	23	0	6	65	6
MWD011-147	011-147-P1_35	37.6	0.2	19.5	7.4	2.5	0.0	31.7	0.0	0.0	99.1	2.93	1.79	0.01	0.27	0.21	0.17	0.00	2.64	8.03	6	0	7	74	13
MWD011-147	011-147-P1_36	37.3	0.2	20.6	10.5	7.8	0.2	22.5	0.0	0.0	99.2	2.94	1.91	0.01	0.13	0.56	0.52	0.03	1.91	8.02	17	1	19	56	7
MWD011-147	011-147-P1_37	37.1	0.2	20.3	9.7	6.5	0.2	24.5	0.0	0.0	98.6	2.94	1.90	0.01	0.15	0.48	0.43	0.03	2.08	8.03	14	1	16	61	8
MWD011-147	011-147-P1_38	37.4	0.2	20.6	9.0	7.0	0.2	24.8	0.0	0.0	99.2	2.94	1.91	0.01	0.14	0.45	0.47	0.02	2.09	8.02	15	1	15	62	7
MWD011-147	011-147-P1_4	37.6	0.3	20.4	8.8	7.3	0.2	24.6	0.0	0.0	99.2	2.95	1.89	0.02	0.14	0.43	0.49	0.02	2.07	8.02	16	1	14	61	7
MWD011-147	011-147-P1_5	37.2	0.3	20.6	9.9	5.7	0.1	25.9	0.0	0.0	99.7	2.91	1.90	0.02	0.17	0.47	0.38	0.02	2.17	8.04	13	1	16	63	9
MWD011-147	011-147-P1_6	37.6	0.3	20.6	8.3	5.3	0.1	27.4	0.0	0.0	99.7	2.93	1.89	0.02	0.16	0.38	0.35	0.01	2.28	8.03	12	0	12	67	8

Appendix 2.3.1: Garnet EPMA data from the Watershed tungsten deposit continued

		Major oxides, weight percent										Number of ions on the basis of 12 oxygen atoms									Garnet end-member[1]				
Sample	Spot	SiO_2	TiO_2	Al_2O_3	FeO	MnO	MgO	CaO	Na_2O	K_2O	Total	Si	Al	Ti	Fe^{3+}	Fe^{2+}	Mn	Mg	Ca	Total	Sps	Prp	Alm	Grs	Adr
MWD011-147	011-147-P1_7	37.7	0.2	20.5	7.9	4.1	0.1	28.9	0.0	0.0	99.5	2.93	1.88	0.01	0.18	0.33	0.27	0.01	2.40	8.03	9	0	11	70	9
MWD011-147	011-147-P1_8	37.5	0.3	20.9	8.8	7.3	0.2	24.7	0.0	0.0	99.6	2.93	1.93	0.02	0.12	0.45	0.48	0.02	2.07	8.02	16	1	15	62	6
MWD011-147	011-147-P1_9	37.7	0.3	20.5	9.1	6.6	0.2	25.2	0.0	0.0	99.6	2.95	1.89	0.01	0.15	0.45	0.43	0.02	2.11	8.02	14	1	15	62	7
MWD042-197A	042-197A-P1_1	38.0	0.2	20.4	5.3	1.2	0.1	34.3	0.0	0.0	99.6	2.92	1.85	0.01	0.22	0.12	0.08	0.01	2.82	8.03	3	0	4	82	11
MWD042-197A	042-197A-P1_2	38.2	0.1	20.5	5.2	1.3	0.1	34.3	0.0	0.0	99.6	2.93	1.85	0.01	0.21	0.12	0.08	0.01	2.82	8.03	3	0	4	82	11
MWD042-197A	042-197A-P1_6	38.1	0.2	20.2	5.2	1.2	0.0	35.0	0.0	0.0	99.9	2.92	1.82	0.01	0.25	0.08	0.08	0.01	2.87	8.03	3	0	3	82	13
MWD042-197A	042-197A-P1_7	38.3	0.2	20.5	5.2	1.4	0.0	34.1	0.0	0.0	99.7	2.94	1.85	0.01	0.21	0.13	0.09	0.00	2.80	8.03	3	0	4	82	10
MWD099-081B	099-081B-P1-01	38.1	0.1	19.7	9.6	3.9	0.1	26.5	0.0	0.0	97.9	3.01	1.83	0.00	0.15	0.48	0.26	0.01	2.25	7.99	9	0	16	67	8
MWD099-081B	099-081B-P1-02	38.1	0.1	19.9	9.3	3.9	0.1	26.5	0.0	0.0	97.9	3.01	1.85	0.00	0.13	0.48	0.26	0.01	2.24	7.99	9	0	16	68	7
MWD099-081B	099-081B-P1-07	38.0	0.1	19.9	9.3	3.6	0.1	26.6	0.0	0.0	97.5	3.01	1.86	0.00	0.13	0.48	0.24	0.01	2.26	7.99	8	0	16	69	7
MWD099-081B	099-081B-P2-01	38.2	0.1	19.7	11.1	7.2	0.2	21.8	0.0	0.0	98.2	3.04	1.84	0.00	0.11	0.62	0.48	0.02	1.85	7.98	16	1	21	56	6
MWD099-081B	099-081B-P2-02	40.4	0.0	20.1	11.7	6.4	0.1	18.9	0.0	1.3	99.1	3.17	1.86	0.00	0.00	0.77	0.43	0.02	1.59	7.83	15	1	27	57	0
MWD099-081B	099-081B-P2-03	38.3	0.0	20.1	11.1	6.1	0.1	22.9	0.0	0.0	98.5	3.02	1.87	0.00	0.10	0.63	0.41	0.01	1.94	7.99	14	0	21	60	5
MWD099-081B	099-081B-P2-04	38.7	0.1	20.0	9.9	5.5	0.1	24.2	0.0	0.0	98.6	3.04	1.86	0.01	0.10	0.55	0.37	0.02	2.04	7.98	12	1	19	64	5
MWD099-081B	099-081B-P2-05	38.7	0.1	19.5	8.1	3.0	0.1	28.9	0.0	0.0	98.4	3.03	1.80	0.01	0.17	0.36	0.20	0.01	2.42	7.98	7	0	12	73	8
MWD099-081B	099-081B-P2-06	38.1	0.1	19.8	10.0	4.0	0.1	26.6	0.0	0.0	98.7	2.99	1.83	0.00	0.17	0.48	0.27	0.01	2.24	8.00	9	0	16	66	9
MWD099-081B	099-081B-P2-07	38.5	0.2	19.9	13.0	7.2	0.2	19.9	0.0	0.0	98.8	3.05	1.86	0.01	0.08	0.77	0.48	0.03	1.69	7.97	16	1	26	52	4
MWD099-081B	099-081B-P2-08	38.3	0.1	19.8	11.7	7.0	0.1	21.1	0.0	0.0	98.0	3.05	1.86	0.00	0.09	0.69	0.47	0.02	1.80	7.97	16	1	23	56	5
MWD099-081B	099-081B-P2-09	38.8	0.1	19.3	8.1	2.8	0.1	29.1	0.0	0.0	98.3	3.03	1.78	0.01	0.18	0.35	0.18	0.01	2.43	7.98	6	0	12	73	9
MWD099-081B	099-081B-P2-10	38.5	0.1	20.2	9.8	4.2	0.1	25.7	0.0	0.0	98.5	3.02	1.87	0.01	0.10	0.54	0.28	0.01	2.16	7.98	9	0	18	67	5
MWD099-081B	099-081B-P2-11	38.3	0.1	20.2	10.6	4.3	0.1	25.1	0.0	0.0	98.7	3.01	1.87	0.00	0.12	0.58	0.29	0.01	2.12	7.99	10	0	19	65	6
MWD099-081B	099-081B-P2-12	37.2	0.0	20.1	11.2	6.7	0.2	21.8	0.0	0.0	97.2	2.99	1.91	0.00	0.10	0.65	0.46	0.02	1.88	8.00	15	1	22	57	5
MWD099-081B	099-081B-P3-04	38.0	0.1	18.7	5.3	0.5	0.0	35.2	0.0	0.0	97.8	2.97	1.72	0.00	0.31	0.03	0.04	0.00	2.94	8.01	1	0	1	82	16
MWD099-081B	099-081B-P3-05	38.2	0.1	18.8	5.8	3.7	0.0	30.2	0.0	0.0	96.7	3.03	1.75	0.00	0.22	0.17	0.25	0.00	2.57	7.98	8	0	6	75	11
MWD099-081B	099-081B-P3-06	37.6	0.2	20.0	5.2	1.1	0.1	33.4	0.0	0.0	97.6	2.95	1.84	0.01	0.20	0.14	0.07	0.01	2.80	8.02	2	0	5	83	10
MWD099-081B	099-081B-P3-07	38.2	0.3	19.7	5.2	1.0	0.1	33.3	0.0	0.0	97.7	2.98	1.81	0.02	0.19	0.15	0.07	0.01	2.78	8.00	2	0	5	83	10
MWD099-081B	099-081B-P4-01	37.7	0.0	19.9	10.0	3.9	0.1	25.5	0.0	0.0	97.1	3.01	1.87	0.00	0.13	0.54	0.26	0.01	2.18	8.00	9	0	18	66	6
MWD099-081B	099-081B-P4-02	37.9	0.1	19.8	9.7	4.0	0.1	26.0	0.0	0.0	97.6	3.01	1.85	0.01	0.14	0.51	0.27	0.01	2.21	7.99	9	0	17	67	7
MWD099-081B	099-081B-P4-03	38.0	0.0	19.9	8.1	4.2	0.1	26.4	0.0	0.0	96.7	3.03	1.87	0.00	0.10	0.44	0.28	0.01	2.25	7.98	9	0	15	70	5
MWD099-081B	099-081B-P4-07	38.9	0.0	19.9	7.6	4.2	0.1	27.7	0.0	0.0	98.4	3.04	1.83	0.00	0.13	0.37	0.28	0.01	2.32	7.98	9	0	12	71	7
MWD099-081B	099-081B-P4-08	38.7	0.0	19.7	7.4	3.8	0.1	27.6	0.0	0.0	97.3	3.05	1.83	0.00	0.11	0.38	0.25	0.01	2.33	7.97	9	0	13	73	6
MWD099-081B	099-081B-P4-09	39.3	0.1	19.7	8.8	4.7	0.1	25.7	0.0	0.0	98.3	3.08	1.81	0.00	0.10	0.48	0.31	0.01	2.15	7.96	11	0	16	68	5
MWD099-081B	099-081B-P4-10	39.2	0.1	20.3	9.0	4.8	0.1	25.0	0.1	0.0	98.6	3.07	1.87	0.00	0.06	0.53	0.32	0.01	2.10	7.95	11	0	18	68	3
MWD099-163.5C	099-163.5C-P1-01	38.8	0.3	19.4	5.4	0.7	0.1	33.9	0.0	0.0	98.6	3.00	1.77	0.02	0.21	0.13	0.05	0.01	2.80	7.99	2	0	4	83	11
MWD099-163.5C	099-163.5C-P1-02	38.9	0.3	19.4	5.4	0.8	0.0	33.7	0.0	0.0	98.5	3.01	1.77	0.02	0.20	0.15	0.05	0.00	2.79	7.99	2	0	5	83	10
MWD099-163.5C	099-163.5C-P1-03	39.3	0.3	19.5	5.2	0.8	0.1	33.9	0.0	0.0	99.0	3.02	1.77	0.02	0.20	0.14	0.05	0.01	2.79	7.98	2	0	5	83	10

Appendix 2.3.1: Garnet EPMA data from the Watershed tungsten deposit continued

		Major oxides, weight percent										Number of ions on the basis of 12 oxygen atoms									Garnet end-member[1]				
Sample	Spot	SiO_2	TiO_2	Al_2O_3	FeO	MnO	MgO	CaO	Na_2O	K_2O	Total	Si	Al	Ti	Fe^{3+}	Fe^{2+}	Mn	Mg	Ca	Total	Sps	Prp	Alm	Grs	Adr
MWD099-163.5C	099-163.5C-P1-04	39.1	0.3	19.5	5.2	0.7	0.0	33.4	0.0	0.0	98.2	3.03	1.78	0.02	0.18	0.16	0.04	0.00	2.77	7.98	1	0	5	84	9
MWD099-163.5C	099-163.5C-P1-06	38.8	0.3	19.5	5.4	0.7	0.0	33.6	0.0	0.0	98.2	3.01	1.78	0.01	0.20	0.15	0.05	0.01	2.79	7.99	2	0	5	83	10
MWD099-163.5C	099-163.5C-P3-01	38.3	0.2	20.5	15.8	10.0	0.4	15.0	0.0	0.0	100.1	3.03	1.91	0.01	0.05	0.99	0.67	0.04	1.27	7.98	22	1	33	40	3
MWD099-163.5C	099-163.5C-P3-02	38.4	0.0	20.5	15.5	9.8	0.4	15.3	0.0	0.0	99.8	3.04	1.91	0.00	0.04	0.98	0.66	0.04	1.30	7.98	22	1	33	41	2
MWD099-163.5C	099-163.5C-P3-03	38.8	0.1	20.4	9.3	8.9	0.1	22.2	0.0	0.0	99.8	3.03	1.87	0.00	0.09	0.52	0.59	0.02	1.86	7.98	20	1	17	58	5
MWD099-163.5C	099-163.5C-P3-04	38.7	0.0	20.4	8.3	9.2	0.1	22.7	0.0	0.0	99.4	3.03	1.88	0.00	0.09	0.45	0.61	0.01	1.91	7.98	20	0	15	59	5
MWD099-163.5C	099-163.5C-P3-05	39.1	0.1	19.9	5.8	1.0	0.1	33.4	0.0	0.0	99.3	3.00	1.80	0.01	0.20	0.17	0.06	0.01	2.75	8.00	2	0	6	82	10
MWD099-163.5C	099-163.5C-P3-06	39.0	0.1	19.8	5.5	0.9	0.0	33.5	0.0	0.0	98.9	3.01	1.79	0.01	0.19	0.16	0.06	0.01	2.76	7.99	2	0	5	83	10
MWD099-163.5C	099-163.5C-P3-07	39.0	0.2	20.0	9.1	9.8	0.1	21.3	0.0	0.0	99.5	3.05	1.85	0.01	0.09	0.51	0.65	0.01	1.79	7.97	22	0	17	56	5
MWD099-163.5C	099-163.5C-P3-08	38.4	0.1	20.0	11.8	10.9	0.2	17.8	0.0	0.0	99.2	3.04	1.87	0.01	0.08	0.70	0.73	0.03	1.51	7.98	25	1	24	47	4
MWD099-163.5C	099-163.5C-P3-09	38.9	0.1	20.3	9.2	9.1	0.1	22.2	0.0	0.0	99.9	3.03	1.87	0.00	0.10	0.51	0.60	0.01	1.86	7.98	20	0	17	57	5
MWD099-163.5C	099-163.5C-P3-10	38.8	0.0	20.2	8.5	8.8	0.1	23.2	0.0	0.0	99.6	3.03	1.86	0.00	0.11	0.45	0.58	0.01	1.94	7.98	20	0	15	59	6
MWD099-163.5C	099-163.5C-P3-11	38.8	0.2	20.1	5.6	1.0	0.1	33.1	0.0	0.0	98.8	2.99	1.83	0.01	0.17	0.19	0.06	0.01	2.74	8.00	2	0	6	83	9
MWD099-163.5C	099-163.5C-P3-12	39.1	0.2	19.7	5.7	0.9	0.1	33.6	0.0	0.0	99.4	3.00	1.78	0.01	0.21	0.16	0.06	0.01	2.76	7.99	2	0	5	82	10
MWD099-163.5C	099-163.5C-P4-00	38.9	0.4	19.7	4.2	0.8	0.0	34.1	0.0	0.0	98.2	3.01	1.79	0.02	0.17	0.10	0.05	0.00	2.82	7.98	2	0	3	86	9
MWD099-163.5C	099-163.5C-P4-01	38.9	0.3	19.7	5.5	0.9	0.1	33.6	0.0	0.0	98.9	3.00	1.79	0.02	0.20	0.15	0.06	0.01	2.78	7.99	2	0	5	83	10
MWD099-163.5C	099-163.5C-P4-02	39.1	0.3	19.8	5.4	0.9	0.0	33.6	0.0	0.0	99.1	3.00	1.79	0.02	0.19	0.16	0.06	0.00	2.76	7.99	2	0	5	83	9
MWD099-163.5C	099-163.5C-P4-03	39.2	0.3	19.5	5.3	0.8	0.0	33.9	0.0	0.0	98.9	3.02	1.77	0.02	0.20	0.14	0.05	0.01	2.79	7.98	2	0	5	83	10
MWD101-100A	101-100A-P2-01	38.2	0.2	19.3	5.9	1.0	0.0	32.3	0.0	0.0	96.9	3.01	1.79	0.01	0.19	0.19	0.07	0.00	2.73	7.99	2	0	6	81	10
MWD101-100A	101-100A-P2-02	38.2	0.2	19.2	5.8	0.9	0.1	33.0	0.0	0.0	97.3	2.99	1.77	0.01	0.22	0.16	0.06	0.01	2.77	8.00	2	0	5	81	11
MWD101-100A	101-100A-P3-01	38.4	0.0	20.0	9.2	2.9	0.1	27.9	0.0	0.0	98.5	3.00	1.84	0.00	0.15	0.45	0.19	0.01	2.34	8.00	6	0	15	71	8
MWD101-100A	101-100A-P3-02	39.0	0.1	19.8	8.3	3.9	0.1	27.7	0.0	0.0	98.7	3.04	1.81	0.01	0.14	0.40	0.25	0.01	2.31	7.98	9	0	14	71	7
MWD101-100A	101-100A-P3-03	38.2	0.0	20.0	9.2	4.3	0.1	26.3	0.0	0.0	98.2	3.01	1.86	0.00	0.13	0.48	0.29	0.01	2.22	7.99	10	0	16	67	7
MWD101-100A	101-100A-P3-04	38.5	0.1	20.0	9.0	4.2	0.1	26.7	0.0	0.0	98.6	3.02	1.85	0.00	0.13	0.46	0.28	0.01	2.24	7.99	9	0	15	68	7
MWD101-100A	101-100A-P3-05	38.6	0.0	20.0	8.3	5.3	0.1	26.3	0.0	0.0	98.6	3.03	1.85	0.00	0.13	0.41	0.35	0.01	2.21	7.99	12	0	14	67	7
MWD101-100A	101-100A-P3-06	38.6	0.1	19.9	8.1	5.6	0.1	26.3	0.0	0.0	98.5	3.03	1.84	0.00	0.13	0.39	0.37	0.01	2.21	7.98	12	0	13	67	7
MWD101-100A	101-100A-P3-07	39.1	0.2	19.4	5.9	0.9	0.0	32.7	0.0	0.0	98.3	3.03	1.77	0.01	0.18	0.20	0.06	0.00	2.71	7.98	2	0	7	82	9
MWD101-100A	101-100A-P3-08	38.9	0.2	19.7	6.4	1.0	0.1	32.4	0.0	0.0	98.7	3.01	1.79	0.01	0.19	0.23	0.07	0.01	2.69	7.99	2	0	8	81	9
MWD101-100A	101-100A-P3-09	38.9	0.1	19.4	7.0	1.5	0.0	31.3	0.0	0.0	98.4	3.03	1.78	0.01	0.18	0.27	0.10	0.00	2.61	7.98	3	0	9	78	9
MWD101-100A	101-100A-P3-10	39.0	0.1	19.6	8.5	1.9	0.1	29.7	0.0	0.0	98.8	3.03	1.80	0.00	0.17	0.38	0.12	0.01	2.47	7.98	4	0	13	74	9
MWD101-100A	101-100A-P3-11	38.2	0.2	19.0	6.4	5.0	0.0	29.6	0.0	0.0	98.5	2.99	1.75	0.01	0.24	0.18	0.33	0.00	2.49	8.00	11	0	6	71	12
MWD101-100A	101-100A-P3-12	38.5	0.1	18.9	6.3	4.6	0.0	29.9	0.0	0.0	98.2	3.01	1.74	0.00	0.24	0.18	0.30	0.00	2.51	7.99	10	0	6	72	12
MWD101-100A	101-100A-P3-13	37.9	0.1	20.3	10.6	4.5	0.1	24.9	0.0	0.0	98.5	2.99	1.89	0.01	0.11	0.58	0.30	0.02	2.10	8.00	10	1	19	64	6
MWD101-100A	101-100A-P3-14	38.4	0.2	20.3	10.1	4.5	0.2	25.2	0.0	0.0	98.7	3.01	1.87	0.01	0.11	0.56	0.30	0.02	2.12	7.99	10	1	19	65	5
MWD101-100A	101-100A-P4-06	39.3	0.1	20.3	4.4	0.4	0.1	34.2	0.0	0.0	98.7	3.02	1.84	0.00	0.14	0.14	0.03	0.01	2.82	7.99	1	0	5	87	7
MWD101-100A	101-100A-P4-07	39.4	0.1	20.2	4.3	0.4	0.1	34.4	0.0	0.0	98.8	3.02	1.82	0.01	0.15	0.12	0.03	0.01	2.83	7.99	1	0	4	87	8

Appendix 2.3.1: Garnet EPMA data from the Watershed tungsten deposit continued

		Major oxides, weight percent										Number of ions on the basis of 12 oxygen atoms									Garnet end-member[1]				
Sample	Spot	SiO_2	TiO_2	Al_2O_3	FeO	MnO	MgO	CaO	Na_2O	K_2O	Total	Si	Al	Ti	Fe^{3+}	Fe^{2+}	Mn	Mg	Ca	Total	Sps	Prp	Alm	Grs	Adr
MWD101-100A	101-100A-P4-08	37.8	0.0	20.0	6.6	1.3	0.1	32.2	0.0	0.0	98.0	2.95	1.85	0.00	0.20	0.23	0.09	0.01	2.70	8.02	3	0	8	79	10
MWD101-100A	101-100A-P4-09	39.1	0.1	20.2	4.1	0.4	0.1	34.7	0.0	0.0	98.6	3.01	1.83	0.00	0.16	0.10	0.02	0.01	2.86	7.99	1	0	3	87	8
MWD101-100A	101-100A-P4-13	39.2	0.2	20.1	4.3	0.3	0.0	35.0	0.0	0.0	99.1	3.00	1.82	0.01	0.18	0.10	0.02	0.00	2.87	8.00	1	0	3	87	9
MWD101-100A	101-100A-P4-14	39.3	0.1	20.1	4.2	0.4	0.0	34.7	0.0	0.0	98.8	3.01	1.82	0.00	0.16	0.11	0.02	0.00	2.86	7.99	1	0	4	87	8
MWD101-159A	101-159A-P1-01	39.5	0.7	20.1	5.2	1.0	0.1	34.6	0.0	0.0	101.0	2.98	1.78	0.04	0.20	0.12	0.06	0.01	2.80	7.99	2	0	4	83	10
MWD101-159A	101-159A-P1-02	39.5	0.7	19.9	5.2	1.0	0.0	34.6	0.0	0.0	100.9	2.98	1.77	0.04	0.21	0.12	0.06	0.00	2.80	7.99	2	0	4	83	11
MWD101-159A	101-159A-P1-03	39.1	0.5	20.3	5.1	1.0	0.1	34.7	0.0	0.0	100.7	2.96	1.81	0.03	0.20	0.12	0.07	0.01	2.81	8.01	2	0	4	83	10
MWD101-159A	101-159A-P3-01	39.4	0.7	19.9	5.3	1.0	0.1	34.5	0.0	0.0	100.9	2.98	1.77	0.04	0.21	0.12	0.06	0.01	2.79	7.99	2	0	4	83	11
MWD101-159A	101-159A-P3-02	39.4	0.7	20.3	5.4	1.0	0.0	34.7	0.0	0.0	101.5	2.96	1.80	0.04	0.20	0.14	0.07	0.00	2.79	8.00	2	0	5	83	10
MWD101-159A	101-159A-P3-03	39.5	0.7	20.3	5.4	1.0	0.1	34.5	0.0	0.0	101.4	2.97	1.80	0.04	0.20	0.15	0.06	0.01	2.78	8.00	2	0	5	83	10
MWD101-159A	101-159A-P3-05	39.5	0.7	19.8	5.2	1.0	0.1	34.6	0.0	0.0	100.9	2.98	1.76	0.04	0.21	0.12	0.06	0.01	2.80	7.99	2	0	4	83	11
MWD101-211.5A	101-211.5A-P3-01	37.1	0.2	20.9	6.5	5.4	0.1	28.2	0.0	0.0	98.5	2.91	1.93	0.01	0.14	0.29	0.36	0.02	2.37	8.04	12	1	9	71	7
MWD101-211.5A	101-211.5A-P3-03	37.0	0.6	19.9	3.6	0.9	0.1	35.7	0.0	0.0	97.6	2.89	1.83	0.03	0.23	0.00	0.06	0.01	2.99	8.04	2	0	0	86	12
MWD101-211.5A	101-211.5A-P3-05	37.7	0.2	20.0	7.8	2.9	0.1	29.3	0.0	0.0	97.9	2.96	1.86	0.01	0.17	0.34	0.19	0.01	2.47	8.01	6	0	11	73	9
MWD101-211.5A	101-211.5A-P3-06	37.3	0.2	20.2	7.5	2.5	0.1	30.4	0.0	0.0	98.2	2.93	1.87	0.01	0.19	0.30	0.16	0.01	2.56	8.03	5	0	10	75	10
MWD105-115A	105-115A-P1-01	38.8	0.1	20.0	12.1	8.1	0.2	20.5	0.0	0.0	99.7	3.04	1.85	0.01	0.09	0.70	0.54	0.02	1.72	7.97	18	1	23	53	5
MWD105-115A	105-115A-P1-02	38.6	0.2	19.9	10.4	7.5	0.1	22.2	0.0	0.0	98.9	3.04	1.85	0.01	0.10	0.59	0.50	0.01	1.87	7.98	17	0	20	58	5
MWD105-115A	105-115A-P1-03	39.1	0.2	19.6	6.5	4.9	0.0	28.0	0.0	0.0	98.4	3.05	1.80	0.01	0.13	0.29	0.32	0.01	2.34	7.96	11	0	10	72	7
MWD105-115A	105-115A-P1-04	39.0	0.2	19.6	7.3	4.9	0.1	28.0	0.0	0.0	99.1	3.03	1.79	0.01	0.16	0.31	0.32	0.01	2.33	7.98	11	0	11	70	8
MWD105-115A	105-115A-P1-05	39.1	0.0	20.0	10.5	6.8	0.1	23.2	0.0	0.0	99.8	3.05	1.84	0.00	0.11	0.57	0.45	0.02	1.93	7.97	15	1	19	59	6
MWD105-115A	105-115A-P1-06	39.2	0.1	20.0	9.6	6.3	0.1	24.6	0.0	0.0	99.9	3.04	1.83	0.00	0.12	0.50	0.42	0.01	2.05	7.98	14	0	17	63	6
MWD105-115A	105-115A-P1-07	39.5	0.2	19.5	5.3	2.2	0.1	32.4	0.0	0.0	99.1	3.04	1.77	0.01	0.18	0.16	0.14	0.01	2.67	7.97	5	0	5	80	9
MWD105-115A	105-115A-P1-08	39.4	0.3	19.7	5.4	2.4	0.1	32.1	0.0	0.0	99.3	3.03	1.79	0.02	0.17	0.18	0.16	0.01	2.64	7.98	5	0	6	80	9
MWD105-115A	105-115A-P1-09	39.5	0.2	20.1	8.0	5.6	0.1	26.9	0.0	0.0	100.3	3.04	1.82	0.01	0.13	0.39	0.36	0.01	2.21	7.97	12	0	13	68	7
MWD105-115A	105-115A-P1-10	39.2	0.1	19.9	7.7	5.3	0.0	27.1	0.0	0.0	99.3	3.04	1.82	0.01	0.13	0.37	0.35	0.00	2.25	7.97	12	0	12	69	7
MWD105-115A	105-115A-P3-01	40.0	0.3	19.5	4.7	1.1	0.1	34.2	0.0	0.0	99.9	3.04	1.75	0.02	0.19	0.11	0.07	0.01	2.78	7.97	2	0	4	84	10
MWD105-115A	105-115A-P3-02	39.2	0.3	19.7	4.7	1.1	0.1	33.7	0.0	0.0	98.7	3.02	1.78	0.02	0.18	0.13	0.07	0.01	2.78	7.98	2	0	4	84	9
MWD105-115A	105-115A-P3-03	39.8	0.3	19.7	4.8	1.1	0.1	34.0	0.0	0.0	99.7	3.03	1.77	0.02	0.18	0.12	0.07	0.01	2.78	7.98	2	0	4	84	9
MWD105-115A	105-115A-P3-04	39.7	0.3	19.5	4.9	1.2	0.1	33.4	0.0	0.0	99.2	3.04	1.76	0.02	0.17	0.14	0.08	0.01	2.74	7.97	3	0	5	83	9
MWD105-115A	105-115A-P3-05	39.8	0.3	19.7	5.0	1.2	0.1	33.6	0.0	0.0	99.7	3.03	1.77	0.02	0.18	0.14	0.08	0.01	2.74	7.97	3	0	5	83	9
MWD105-115A	105-115A-P3-06	39.4	0.3	19.7	4.8	1.1	0.1	34.0	0.0	0.0	99.4	3.02	1.78	0.02	0.19	0.12	0.07	0.01	2.78	7.98	2	0	4	84	9
MWD105-206B	105-206B-P2-01	38.2	0.2	20.6	9.2	3.4	0.1	28.4	0.0	0.0	100.2	2.95	1.88	0.01	0.16	0.44	0.22	0.01	2.35	8.02	7	0	14	70	8
MWD105-206B	105-206B-P2-02	38.9	0.3	20.2	6.1	2.3	0.1	32.7	0.0	0.0	100.5	2.97	1.81	0.02	0.20	0.19	0.15	0.01	2.67	8.01	5	0	6	79	10
MWD105-206B	105-206B-P2-03	38.3	0.2	20.7	9.2	3.3	0.1	28.2	0.0	0.0	100.0	2.96	1.89	0.01	0.14	0.45	0.21	0.01	2.34	8.01	7	0	15	70	7
MWD105-206B	105-206B-P2-04	39.2	0.3	20.3	5.6	1.7	0.1	33.8	0.0	0.0	100.9	2.97	1.81	0.02	0.21	0.15	0.11	0.01	2.74	8.01	4	0	5	81	10
MWD105-206B	105-206B-P2-06	39.2	0.6	19.9	5.9	2.3	0.0	32.7	0.0	0.0	100.7	2.98	1.78	0.04	0.20	0.17	0.15	0.00	2.66	7.99	5	0	6	79	10

Appendix 2.3.1: Garnet EPMA data from the Watershed tungsten deposit continued

		Major oxides, weight percent										Number of ions on the basis of 12 oxygen atoms									Garnet end-members[1]				
Sample	Spot	SiO_2	TiO_2	Al_2O_3	FeO	MnO	MgO	CaO	Na_2O	K_2O	Total	Si	Al	Ti	Fe^{3+}	Fe^{2+}	Mn	Mg	Ca	Total	Sps	Prp	Alm	Grs	Adr
MWD105-206B	105-206B-P2-07	39.1	0.7	20.4	5.7	2.0	0.1	33.0	0.0	0.0	100.9	2.96	1.82	0.04	0.17	0.19	0.13	0.01	2.68	8.00	4	0	6	81	9
MWD105-206B	105-206B-P3-01	39.5	0.2	21.0	4.1	1.0	0.1	35.0	0.0	0.0	100.9	2.98	1.86	0.01	0.15	0.11	0.06	0.01	2.83	8.01	2	0	4	87	8
MWD105-206B	105-206B-P3-05	38.5	0.2	20.3	9.0	3.7	0.1	28.1	0.0	0.0	99.8	2.98	1.85	0.01	0.16	0.42	0.24	0.01	2.33	8.00	8	0	14	70	8
MWD107-259B	107-259B-P1-02	38.1	0.3	20.0	6.5	2.4	0.1	32.5	0.0	0.0	99.9	2.93	1.82	0.02	0.23	0.19	0.15	0.01	2.68	8.02	5	0	6	77	12
MWD107-259B	107-259B-P1-03	38.2	0.3	20.1	5.7	1.7	0.0	33.1	0.0	0.0	99.2	2.95	1.83	0.02	0.21	0.16	0.11	0.00	2.74	8.02	4	0	5	80	10
MWD107-259B	107-259B-P1-04	37.7	0.2	20.2	6.5	2.2	0.1	31.9	0.0	0.0	98.8	2.93	1.85	0.01	0.21	0.21	0.15	0.01	2.66	8.03	5	0	7	78	10
MWD107-259B	107-259B-P1-05	37.3	0.4	20.3	4.6	0.8	0.1	35.2	0.0	0.0	98.6	2.89	1.85	0.02	0.23	0.06	0.05	0.01	2.92	8.04	2	0	2	84	12
MWD107-259B	107-259B-P1-07	38.0	0.2	20.7	7.0	3.3	0.1	30.4	0.0	0.0	99.8	2.93	1.89	0.01	0.17	0.28	0.22	0.01	2.52	8.03	7	0	9	75	9
MWD107-259B	107-259B-P1-08	37.9	0.2	20.1	6.1	1.7	0.1	33.2	0.0	0.0	99.4	2.93	1.83	0.01	0.23	0.16	0.11	0.01	2.75	8.03	4	0	5	79	12
MWD107-259B	107-259B-P1-09	37.7	0.2	20.2	6.4	2.0	0.1	32.4	0.0	0.0	98.9	2.93	1.84	0.01	0.21	0.20	0.13	0.01	2.69	8.03	4	0	7	78	11
MWD107-259B	107-259B-P1-10	37.8	0.2	20.3	9.1	3.8	0.1	28.0	0.0	0.0	99.3	2.95	1.87	0.01	0.17	0.42	0.25	0.01	2.34	8.02	8	0	14	69	9
MWD107-259B	107-259B-P2-01	38.0	0.2	20.1	6.1	1.6	0.1	33.2	0.0	0.0	99.3	2.94	1.82	0.01	0.23	0.16	0.10	0.01	2.75	8.03	3	0	5	79	12
MWD107-259B	107-259B-P2-03	37.6	0.3	20.2	5.8	1.3	0.1	33.9	0.0	0.0	99.1	2.90	1.84	0.02	0.24	0.13	0.09	0.01	2.81	8.04	3	0	4	80	12
MWD107-259B	107-259B-P4-02	38.7	0.5	19.8	4.4	0.9	0.0	34.9	0.0	0.0	99.3	2.96	1.79	0.03	0.22	0.07	0.06	0.01	2.87	8.00	2	0	2	85	11
MWD119-126A	119-126A-P1-01	38.5	0.3	20.2	14.6	8.6	0.3	17.0	0.0	0.0	99.4	3.04	1.89	0.02	0.05	0.91	0.58	0.04	1.44	7.97	19	1	31	46	3
MWD119-126A	119-126A-P1-02	38.3	0.2	20.8	9.2	11.9	0.2	19.5	0.0	0.0	100.1	3.01	1.93	0.01	0.06	0.54	0.79	0.02	1.64	7.99	26	1	18	52	3
MWD119-126A	119-126A-P1-03	38.5	0.1	20.5	16.7	8.2	0.4	16.1	0.0	0.0	100.5	3.03	1.91	0.01	0.06	1.04	0.55	0.04	1.36	7.98	18	1	35	42	3
MWD119-126A	119-126A-P1-04	38.4	0.3	20.3	16.4	7.9	0.3	16.9	0.0	0.0	100.4	3.02	1.88	0.02	0.08	1.00	0.52	0.04	1.42	7.98	18	1	33	44	4
MWD119-126A	119-126A-P1-07	38.3	0.0	21.0	10.2	9.1	0.2	21.3	0.0	0.0	100.0	3.00	1.93	0.00	0.07	0.60	0.60	0.02	1.78	8.00	20	1	20	56	4
MWD119-126A	119-126A-P3-01	38.7	0.3	20.6	15.3	7.8	0.3	18.2	0.0	0.0	101.1	3.02	1.89	0.02	0.07	0.92	0.51	0.03	1.52	7.98	17	1	31	47	4
MWD119-126A	119-126A-P3-02	38.1	0.5	20.2	15.7	8.8	0.3	16.5	0.0	0.0	100.0	3.01	1.88	0.03	0.08	0.96	0.59	0.04	1.40	7.98	20	1	32	43	4
MWD119-126A	119-126A-P3-03	38.9	0.1	20.7	16.2	6.8	0.2	18.4	0.0	0.0	101.1	3.03	1.90	0.00	0.07	0.98	0.45	0.02	1.53	7.98	15	1	33	48	4
MWD124-130.5A	124-130.5A-P1-01	37.7	0.4	20.1	15.4	7.8	0.3	17.5	0.0	0.0	99.1	3.00	1.88	0.02	0.09	0.94	0.52	0.03	1.49	7.99	18	1	31	45	5
MWD124-130.5A	124-130.5A-P1-03	37.5	0.3	20.0	14.5	7.5	0.2	18.1	0.0	0.0	98.1	3.01	1.89	0.02	0.08	0.90	0.51	0.03	1.55	7.98	17	1	30	48	4
MWD124-130.5A	124-130.5A-P2-01	38.2	0.6	20.0	13.8	6.4	0.1	20.9	0.0	0.0	100.0	3.00	1.85	0.04	0.12	0.79	0.42	0.01	1.76	7.98	14	0	26	53	6
MWD124-130.5A	124-130.5A-P2-02	38.1	0.4	20.0	14.2	7.0	0.2	20.0	0.0	0.0	99.8	3.00	1.86	0.02	0.12	0.82	0.46	0.02	1.69	7.99	16	1	27	50	6
MWD124-130.5A	124-130.5A-P2-03	37.7	0.4	19.9	14.3	6.8	0.2	19.1	0.0	0.0	98.4	3.01	1.87	0.02	0.10	0.86	0.46	0.02	1.64	7.98	15	1	29	50	5
MWD124-130.5A	124-130.5A-P3-01	38.1	0.3	20.0	14.8	7.4	0.3	18.4	0.0	0.0	99.2	3.02	1.87	0.02	0.09	0.89	0.49	0.03	1.57	7.98	17	1	30	48	5
MWD124-130.5A	124-130.5A-P3-02	38.2	0.3	20.1	14.4	7.1	0.2	19.2	0.0	0.0	99.4	3.02	1.87	0.02	0.09	0.86	0.47	0.02	1.62	7.98	16	1	29	50	5
MWD124-130.5A	124-130.5A-P3-05	37.8	0.3	20.1	14.3	6.8	0.2	19.1	0.0	0.0	98.8	3.01	1.89	0.02	0.08	0.87	0.46	0.03	1.63	7.98	15	1	29	50	4

[1] Garnet end-members: Sps: spessartine, Prp: pyrope, Alm: almandine, Grs: grossular, Adr: andradite. After Whitney and Evans (2010)

Appendix 2.3.2: Clinopyroxene EPMA data from the Watershed tungsten deposit

		Major oxides, weight percent										Number of ions on the basis of 6 oxygen atoms										Cpx end-members[1]		
Sample	Spot	SiO_2	TiO_2	Al_2O_3	FeO	MnO	MgO	CaO	Na_2O	K_2O	Total	Si	Ti	Al	Fe^{2+}	Mn	Mg	Ca	Na	K	Total	Di	Hd	Jhn
MWD099-163.5C	099-163.5C-P1-05	52.2	0.0	0.2	15.7	0.9	8.1	23.8	0.1	0.0	101.0	2.00	0.00	0.01	0.50	0.03	0.46	0.98	0.01	0.00	3.99	46	51	3
MWD099-163.5C	099-163.5C-P1-07	52.0	0.0	0.1	15.1	0.9	7.9	23.9	0.0	0.0	100.0	2.01	0.00	0.01	0.49	0.03	0.46	0.99	0.00	0.00	3.99	47	51	3
MWD099-163.5C	099-163.5C-P1-08	51.8	0.0	0.3	15.4	0.7	8.1	23.7	0.1	0.0	100.1	2.00	0.00	0.01	0.50	0.02	0.47	0.98	0.00	0.00	3.99	47	51	2
MWD099-163.5C	099-163.5C-P1-09	51.7	0.0	0.2	17.8	0.5	6.8	23.4	0.1	0.0	100.5	2.01	0.00	0.01	0.58	0.02	0.39	0.98	0.01	0.00	3.99	40	59	2
MWD099-163.5C	099-163.5C-P3-13	52.1	0.0	0.2	16.6	0.6	7.4	24.0	0.1	0.0	101.1	2.00	0.00	0.01	0.54	0.02	0.43	0.99	0.01	0.00	3.99	43	55	2
MWD099-163.5C	099-163.5C-P3-14	51.7	0.0	0.2	16.4	0.5	7.5	24.2	0.1	0.0	100.6	2.00	0.00	0.01	0.53	0.02	0.43	1.00	0.01	0.00	4.00	44	55	2
MWD099-163.5C	099-163.5C-P4-07	52.0	0.0	0.2	16.1	0.5	7.8	23.8	0.1	0.0	100.6	2.01	0.00	0.01	0.52	0.01	0.45	0.98	0.01	0.00	3.99	45	53	1
MWD099-163.5C	099-163.5C-P4-08	51.4	0.0	0.2	16.6	0.6	7.5	23.6	0.1	0.0	100.0	2.00	0.00	0.01	0.54	0.02	0.44	0.99	0.00	0.00	4.00	43	55	2
MWD099-163.5C	099-163.5C-P4-09	52.0	0.0	0.2	17.4	0.6	7.0	23.4	0.1	0.0	100.6	2.01	0.00	0.01	0.56	0.02	0.40	0.97	0.01	0.00	3.98	41	57	2
MWD099-081B	099-081B-P2-13	50.5	0.0	0.3	18.5	0.8	6.2	23.2	0.1	0.0	99.5	1.99	0.00	0.02	0.61	0.03	0.37	0.98	0.01	0.00	4.00	36	61	2
MWD099-081B	099-081B-P2-14	50.7	0.0	0.3	17.3	0.8	6.4	23.2	0.1	0.0	98.6	2.01	0.00	0.01	0.57	0.03	0.38	0.98	0.00	0.00	3.99	38	59	3
MWD099-081B	099-081B-P2-15	52.5	0.0	0.2	13.0	1.0	9.6	23.7	0.1	0.0	99.9	2.01	0.00	0.01	0.41	0.03	0.55	0.97	0.01	0.00	3.99	55	42	3
MWD099-081B	099-081B-P2-19	51.9	0.0	0.1	14.4	0.7	8.8	23.9	0.0	0.0	99.7	2.00	0.00	0.00	0.46	0.02	0.51	0.99	0.00	0.00	3.99	51	47	2
MWD099-081B	099-081B-P2-21	51.8	0.0	0.2	15.4	0.6	8.1	23.6	0.0	0.0	99.6	2.01	0.00	0.01	0.50	0.02	0.47	0.98	0.00	0.00	3.99	47	51	2
MWD099-081B	099-081B-P3-01	51.6	0.0	0.2	15.6	1.1	7.5	23.4	0.1	0.0	99.4	2.01	0.00	0.01	0.51	0.04	0.43	0.98	0.00	0.00	3.98	44	52	4
MWD099-081B	099-081B-P3-12	51.5	0.0	0.1	16.5	0.9	7.3	23.4	0.1	0.0	99.8	2.01	0.00	0.01	0.54	0.03	0.42	0.98	0.00	0.00	3.99	42	55	3
MWD099-081B	099-081B-P3-02	51.1	0.0	0.2	17.6	0.9	6.2	23.5	0.1	0.0	99.6	2.01	0.00	0.01	0.58	0.03	0.36	0.99	0.00	0.00	3.99	37	60	3
MWD099-081B	099-081B-P3-03	51.4	0.0	0.1	16.3	1.4	7.0	23.7	0.0	0.0	99.9	2.01	0.00	0.00	0.53	0.05	0.41	0.99	0.00	0.00	3.99	41	54	5
MWD099-081B	099-081B-P3-09	51.1	0.0	0.2	17.4	0.8	6.5	23.1	0.1	0.0	99.2	2.01	0.00	0.01	0.57	0.03	0.38	0.97	0.01	0.00	3.99	39	59	3
MWD101-100A	101-100A-P4-12	51.6	0.0	0.3	18.4	0.4	6.8	23.5	0.1	0.0	100.9	2.00	0.00	0.01	0.60	0.01	0.39	0.98	0.01	0.00	4.00	39	60	1
MWD101-159A	101-159A-P1-04	52.5	0.0	0.2	16.5	0.5	7.7	24.5	0.1	0.0	102.1	2.00	0.00	0.01	0.53	0.02	0.44	1.00	0.01	0.00	4.00	44	54	2
MWD101-211.5A	101-211.5A-P3-07	51.1	0.0	0.2	16.6	0.7	7.2	23.8	0.1	0.0	99.8	2.00	0.00	0.01	0.54	0.02	0.42	1.00	0.01	0.00	4.00	42	55	2
MWD105-206B	105-206B-P1-01	52.4	0.0	0.2	15.3	0.5	8.8	24.6	0.1	0.0	101.9	1.99	0.00	0.01	0.48	0.02	0.50	1.00	0.01	0.00	4.01	50	49	2
MWD105-206B	105-206B-P1-03	52.6	0.0	0.2	15.4	0.5	8.7	24.5	0.1	0.0	102.0	2.00	0.00	0.01	0.49	0.02	0.49	1.00	0.00	0.00	4.00	49	49	2
MWD105-206B	105-206B-P3-04	50.5	0.0	5.0	17.0	0.5	11.9	12.4	0.6	0.3	98.1	1.94	0.00	0.23	0.55	0.02	0.68	0.51	0.04	0.02	3.98	48	51	1
MWD105-206B	105-206B-P3-06	53.8	0.1	2.5	14.0	0.6	14.8	12.8	0.3	0.1	98.9	2.01	0.00	0.11	0.44	0.02	0.82	0.51	0.02	0.01	3.95	59	39	1
MWD107-259B	107-259B-P3-01	51.8	0.0	0.2	15.2	0.6	8.4	24.6	0.1	0.0	100.8	1.99	0.00	0.01	0.49	0.02	0.48	1.01	0.01	0.00	4.01	49	49	2
MWD107-259B	107-259B-P3-02	52.1	0.1	0.2	14.2	0.4	9.4	24.7	0.1	0.0	101.1	1.99	0.00	0.01	0.45	0.01	0.53	1.01	0.01	0.00	4.01	54	45	1
MWD107-259B	107-259B-P3-04	52.1	0.0	0.2	14.4	0.4	9.5	24.8	0.0	0.0	101.3	1.98	0.00	0.01	0.46	0.01	0.54	1.01	0.00	0.00	4.01	54	45	1
MWD107-259B	107-259B-P3-05	52.0	0.1	0.3	15.4	0.7	8.3	24.4	0.1	0.0	101.3	1.99	0.00	0.01	0.49	0.02	0.48	1.00	0.01	0.00	4.00	48	50	2

Appendix 2.3.2: Clinopyroxene EPMA data from the Watershed tungsten deposit continued

		Major oxides, weight percent										Number of ions on the basis of 6 oxygen atoms										Cpx end-members[1]		
Sample	Spot	SiO_2	TiO_2	Al_2O_3	FeO	MnO	MgO	CaO	Na_2O	K_2O	Total	Si	Ti	Al	Fe^{2+}	Mn	Mg	Ca	Na	K	Total	Di	Hd	Jhn
MWD005-128A	005-128A-P1-10	43.5	0.1	11.5	22.5	0.9	5.9	12.2	0.9	1.2	98.7	1.73	0.00	0.54	0.75	0.03	0.35	0.52	0.07	0.06	4.06	25	72	2
MWD005-128A	005-128A-P1-13	42.0	0.1	12.8	22.1	0.7	5.9	12.2	1.2	1.2	98.2	1.68	0.00	0.61	0.74	0.02	0.35	0.52	0.09	0.06	4.09	26	73	2
MWD119-317A	119-317A-P1-01	51.4	0.0	0.2	15.3	0.6	8.3	24.5	0.1	0.0	100.5	1.99	0.00	0.01	0.49	0.02	0.48	1.02	0.00	0.00	4.01	49	49	2
MWD119-317A	119-317A-P1-02	50.9	0.0	0.2	16.5	1.0	7.0	24.4	0.1	0.0	100.2	1.99	0.00	0.01	0.54	0.03	0.41	1.02	0.01	0.00	4.01	42	55	3
MWD119-317A	119-317A-P1-03	51.3	0.0	0.2	15.4	0.7	8.4	24.7	0.1	0.0	100.8	1.98	0.00	0.01	0.50	0.02	0.48	1.02	0.01	0.00	4.02	49	48	2

[1] Clinopyroxene (Cpx) end-members: Di: diopside, Hd: hedenbergite, Jhn: johannsenite. After Whitney and Evans (2010)

Appendix 2.3.3: Feldspar EPMA data from the Watershed tungsten deposit

		Major oxides, weight percent										Number of ions on the basis of 8 oxygen atoms										Feldspar end-members[1]		
Sample	Spot	SiO_2	TiO_2	Al_2O_3	FeO	MnO	MgO	CaO	Na_2O	K_2O	Total	Si	Ti	Al	Fe^{2+}	Mn	Mg	Ca	Na	K	Total	Or	Ab	An
MWD099-163.5A	099-163.5A-P1-1	65.0	0.0	21.6	0.0	0.0	0.0	3.2	10.2	0.1	100.1	2.86	0.00	1.12	0.00	0.00	0.00	0.15	0.87	0.00	5.01	0	85	15
MWD099-163.5A	099-163.5A-P1-2	67.4	0.0	20.8	0.0	0.0	0.0	2.3	10.9	0.1	101.5	2.92	0.00	1.06	0.00	0.00	0.00	0.11	0.92	0.00	5.01	0	89	10
MWD099-163.5A	099-163.5A-P1-3	67.6	0.0	21.1	0.0	0.0	0.0	3.0	10.3	0.1	102.1	2.91	0.00	1.07	0.00	0.00	0.00	0.14	0.86	0.01	4.98	1	86	14
MWD099-163.5A	099-163.5A-P2-1	62.3	0.0	23.4	0.0	0.0	0.0	5.5	9.1	0.1	100.3	2.76	0.00	1.22	0.00	0.00	0.00	0.26	0.78	0.01	5.03	1	75	25
MWD099-163.5A	099-163.5A-P2-2	61.1	0.0	24.3	0.0	0.0	0.0	6.4	8.7	0.1	100.6	2.71	0.00	1.27	0.00	0.00	0.00	0.30	0.75	0.00	5.03	0	71	29
MWD101-159B	101-159B-P1-1	66.8	0.1	22.1	0.0	0.0	0.0	3.5	10.2	0.1	102.7	2.87	0.00	1.12	0.00	0.00	0.00	0.16	0.85	0.00	5.00	0	84	16
MWD101-159B	101-159B-P1-2	62.3	0.0	24.3	0.0	0.0	0.0	6.0	8.8	0.1	101.6	2.73	0.00	1.25	0.00	0.00	0.00	0.28	0.75	0.01	5.02	1	72	27
MWD101-159B	101-159B-P1-3	65.7	0.1	22.9	0.0	0.0	0.0	4.4	9.0	0.1	102.2	2.83	0.00	1.17	0.00	0.00	0.00	0.20	0.75	0.00	4.96	0	78	21
MWD101-159B	101-159B-P1-4	66.2	0.0	22.2	0.0	0.0	0.0	3.3	10.6	0.1	102.3	2.86	0.00	1.13	0.00	0.00	0.00	0.15	0.89	0.00	5.03	0	85	15
MWD101-159B	101-159B-P1-5	66.3	0.0	22.4	0.0	0.0	0.0	3.6	9.9	0.1	102.2	2.86	0.00	1.14	0.00	0.00	0.00	0.17	0.83	0.00	4.99	0	83	17
MWD101-159B	101-159B-P1-6	64.5	0.0	22.8	0.0	0.0	0.0	4.7	7.1	3.0	102.1	2.82	0.00	1.17	0.00	0.00	0.00	0.22	0.60	0.17	4.98	17	61	22
MWD101-159B	101-159B-P2-1	62.1	0.0	24.2	0.0	0.0	0.0	6.3	8.9	0.1	101.6	2.72	0.00	1.25	0.00	0.00	0.00	0.29	0.76	0.01	5.03	1	72	28
MWD101-159B	101-159B-P2-2	65.5	0.0	22.4	0.0	0.0	0.0	3.8	10.3	0.1	102.0	2.84	0.00	1.14	0.00	0.00	0.00	0.18	0.86	0.00	5.02	0	83	17
MWD101-159B	101-159B-P2-3	64.6	0.0	22.5	0.0	0.0	0.0	3.7	10.3	0.1	101.2	2.82	0.00	1.16	0.00	0.00	0.00	0.17	0.87	0.01	5.04	0	83	17
MWD101-159B	101-159B-P2-4	62.7	0.0	23.7	0.0	0.0	0.0	5.7	9.2	0.1	101.5	2.75	0.00	1.23	0.00	0.00	0.00	0.27	0.79	0.01	5.03	1	74	25
MWD101-159B	101-159B-P2-5	65.9	0.0	22.0	0.0	0.0	0.0	3.3	10.6	0.1	101.8	2.86	0.00	1.12	0.00	0.00	0.00	0.15	0.89	0.00	5.03	0	85	15
MWD101-159B	101-159B-P2-6	62.7	0.0	23.9	0.0	0.0	0.0	5.8	9.0	0.1	101.5	2.75	0.00	1.23	0.00	0.00	0.00	0.27	0.76	0.00	5.02	0	73	26
MWD107-259A	107-259A-P1-1	67.2	0.0	21.7	0.0	0.0	0.0	3.5	9.8	0.1	102.3	2.89	0.00	1.10	0.00	0.00	0.00	0.16	0.82	0.00	4.97	0	83	16
MWD107-259A	107-259A-P1-2	66.1	0.0	21.7	0.0	0.0	0.0	3.3	10.2	0.0	101.4	2.87	0.00	1.11	0.00	0.00	0.00	0.15	0.86	0.00	5.00	0	85	15
MWD107-259A	107-259A-P1-3	66.7	0.0	21.2	0.0	0.0	0.0	2.8	10.7	0.1	101.4	2.89	0.00	1.08	0.00	0.00	0.00	0.13	0.90	0.00	5.01	0	87	13
MWD107-259A	107-259A-P1-4	65.3	0.0	22.0	0.0	0.0	0.0	3.8	10.4	0.1	101.6	2.84	0.00	1.13	0.00	0.00	0.00	0.18	0.88	0.00	5.03	0	83	17
MWD107-259A	107-259A-P2-1	65.9	0.0	21.9	0.0	0.0	0.0	3.7	10.1	0.1	101.7	2.86	0.00	1.12	0.00	0.00	0.00	0.17	0.85	0.01	5.01	1	83	17
MWD107-259A	107-259A-P3-1	71.8	0.0	19.6	0.0	0.0	0.0	0.6	11.9	0.1	103.9	3.02	0.00	0.97	0.00	0.00	0.00	0.03	0.97	0.00	4.98	0	97	3
MWD107-259A	107-259A-P3-2	65.9	0.0	20.9	0.0	0.0	0.0	2.9	9.2	0.1	99.1	2.91	0.00	1.09	0.00	0.00	0.00	0.14	0.79	0.00	4.94	0	84	15
MWD107-259A	107-259A-P3-3	64.6	0.0	18.1	0.0	0.0	0.0	0.0	0.7	14.8	98.1	3.02	0.00	1.00	0.00	0.00	0.00	0.00	0.06	0.88	4.96	94	6	0
MWD107-259A	107-259A-P3-4	64.8	0.0	18.2	0.0	0.0	0.0	0.0	0.7	14.8	98.6	3.01	0.00	1.00	0.00	0.00	0.00	0.00	0.07	0.88	4.96	93	7	0
MWD107-259A	107-259A-P4-1	66.4	0.0	21.9	0.0	0.0	0.0	3.8	10.4	0.1	102.5	2.86	0.00	1.11	0.00	0.00	0.00	0.17	0.87	0.00	5.02	0	83	17
MWD107-259A	107-259A-P4-2	64.9	0.0	18.4	0.0	0.0	0.0	0.0	0.6	15.1	99.0	3.01	0.00	1.00	0.00	0.00	0.00	0.00	0.05	0.89	4.96	94	6	0
MWD119-128A	119-128A-P1-1	58.1	0.0	26.2	0.0	0.0	0.0	8.9	6.8	0.1	100.2	2.60	0.00	1.38	0.00	0.00	0.00	0.43	0.59	0.01	5.01	1	58	42
MWD119-128A	119-128A-P1-2	64.4	0.0	23.1	0.0	0.0	0.0	5.0	8.5	0.0	101.1	2.81	0.00	1.19	0.00	0.00	0.00	0.24	0.72	0.00	4.96	0	75	25
MWD119-128A	119-128A-P1-4	58.3	0.0	25.6	0.0	0.0	0.0	8.5	7.0	0.1	99.6	2.62	0.00	1.36	0.00	0.00	0.00	0.41	0.61	0.00	5.01	0	60	40
MWD119-128A	119-128A-P1-5	58.2	0.0	25.7	0.0	0.0	0.0	8.7	6.9	0.1	99.6	2.62	0.00	1.36	0.00	0.00	0.00	0.42	0.60	0.00	5.01	0	59	41
MWD119-128A	119-128A-P1-6	60.1	0.0	24.4	0.0	0.0	0.0	7.3	7.5	0.1	99.3	2.69	0.00	1.29	0.00	0.00	0.00	0.35	0.65	0.00	4.99	0	65	35
MWD119-128A	119-128A-P1-7	60.3	0.0	24.4	0.0	0.0	0.0	7.0	7.7	0.1	99.5	2.70	0.00	1.29	0.00	0.00	0.00	0.33	0.67	0.01	4.99	1	66	33
MWD119-128A	119-128A-P1-8	57.8	0.0	26.0	0.1	0.0	0.0	8.8	6.7	0.0	99.3	2.60	0.00	1.38	0.00	0.00	0.00	0.42	0.58	0.00	5.00	0	58	42
MWD119-128A	119-128A-P1-9	62.1	0.0	23.6	0.0	0.0	0.0	5.7	8.4	0.0	99.9	2.76	0.00	1.23	0.00	0.00	0.00	0.27	0.72	0.00	4.99	0	72	27

Appendix 2.3.3: Feldspar EPMA data from the Watershed tungsten deposit continued

		Major oxides, weight percent										Number of ions on the basis of 8 oxygen atoms										Feldspar end-members[1]		
Sample	Spot	SiO_2	TiO_2	Al_2O_3	FeO	MnO	MgO	CaO	Na_2O	K_2O	Total	Si	Ti	Al	Fe^{2+}	Mn	Mg	Ca	Na	K	Total	Or	Ab	An
MWD119-128A	119-128A-P1-10	63.7	0.0	22.5	0.0	0.0	0.0	4.7	9.0	0.1	99.9	2.82	0.00	1.17	0.00	0.00	0.00	0.22	0.77	0.00	4.98	0	77	22
MWD119-128A	119-128A-P2-1	60.8	0.0	24.5	0.0	0.0	0.0	7.0	7.7	0.1	100.2	2.70	0.00	1.28	0.00	0.00	0.00	0.33	0.67	0.01	4.99	1	66	33
MWD119-128A	119-128A-P2-2	63.6	0.0	22.8	0.0	0.0	0.0	5.0	8.9	0.0	100.4	2.80	0.00	1.18	0.00	0.00	0.00	0.24	0.76	0.00	4.99	0	76	24
MWD119-128A	119-128A-P2-3	57.2	0.0	26.7	0.1	0.0	0.0	9.4	6.4	0.1	99.9	2.57	0.00	1.41	0.00	0.00	0.00	0.45	0.56	0.00	5.01	0	55	45
MWD119-128A	119-128A-P2-4	57.1	0.0	26.8	0.0	0.0	0.0	9.6	6.1	0.1	99.7	2.57	0.00	1.42	0.00	0.00	0.00	0.46	0.53	0.00	4.99	0	53	46
MWD119-128A	119-128A-P2-5	57.2	0.0	26.7	0.0	0.0	0.0	9.5	6.4	0.0	99.9	2.57	0.00	1.41	0.00	0.00	0.00	0.46	0.56	0.00	5.00	0	55	45
MWD119-128A	119-128A-P2-6	58.8	0.0	25.0	0.0	0.0	0.0	7.9	7.2	0.0	98.9	2.65	0.00	1.33	0.00	0.00	0.00	0.38	0.63	0.00	5.00	0	62	38
MWD119-128A	119-128A-P2-7	57.5	0.0	25.6	0.0	0.0	0.0	8.6	6.8	0.0	98.6	2.61	0.00	1.37	0.00	0.00	0.00	0.42	0.60	0.00	5.00	0	58	41
MWD119-128A	119-128A-P2-8	57.7	0.0	25.8	0.0	0.0	0.0	8.8	6.6	0.1	99.0	2.61	0.00	1.37	0.00	0.00	0.00	0.43	0.58	0.00	4.99	0	57	42
MWD119-128A	119-128A-P2-9	55.6	0.0	27.3	0.0	0.0	0.0	10.4	5.8	0.1	99.2	2.52	0.00	1.46	0.00	0.00	0.00	0.50	0.51	0.00	5.00	0	50	50
MWD119-128A	119-128A-P3-1	57.9	0.0	25.4	0.0	0.0	0.0	8.3	6.9	0.0	98.6	2.63	0.00	1.36	0.00	0.00	0.00	0.40	0.61	0.00	5.00	0	60	40
MWD119-128A	119-128A-P3-2	53.9	0.0	27.9	0.0	0.0	0.0	11.3	5.2	0.0	98.2	2.48	0.00	1.51	0.00	0.00	0.00	0.55	0.46	0.00	5.00	0	45	55
MWD119-128A	119-128A-P3-3	56.0	0.0	26.5	0.0	0.0	0.0	9.6	6.1	0.0	98.3	2.56	0.00	1.43	0.00	0.00	0.00	0.47	0.54	0.00	5.00	0	53	47
MWD119-128A	119-128A-P3-4	57.6	0.0	25.8	0.0	0.0	0.0	8.6	6.9	0.1	98.9	2.61	0.00	1.38	0.00	0.00	0.00	0.42	0.60	0.00	5.01	0	59	41
MWD119-128A	119-128A-P3-6	62.9	0.0	22.5	0.0	0.0	0.0	4.6	8.9	0.0	99.0	2.81	0.00	1.18	0.00	0.00	0.00	0.22	0.77	0.00	4.99	0	77	22
MWD119-128A	119-128A-P3-7	63.4	0.0	22.0	0.0	0.0	0.0	4.1	9.3	0.0	98.9	2.83	0.00	1.16	0.00	0.00	0.00	0.19	0.81	0.00	5.00	0	80	20
MWD119-128A	119-128A-P3-8	55.5	0.0	27.0	0.0	0.0	0.0	10.1	5.7	0.0	98.4	2.53	0.00	1.45	0.00	0.00	0.00	0.49	0.51	0.00	4.99	0	51	49
MWD119-128A	119-128A-P3-8A	56.9	0.0	26.3	0.0	0.0	0.0	9.2	6.2	0.1	98.6	2.58	0.00	1.41	0.00	0.00	0.00	0.45	0.54	0.00	4.99	0	55	45
MWD119-128A	119-128A-P3-9	62.7	0.0	22.4	0.0	0.0	0.0	4.5	9.3	0.1	99.0	2.80	0.00	1.18	0.00	0.00	0.00	0.21	0.81	0.00	5.01	0	79	21
MWD119-128A	119-128A-P3-10	56.0	0.0	26.5	0.0	0.0	0.0	9.7	6.0	0.0	98.3	2.56	0.00	1.43	0.00	0.00	0.00	0.47	0.53	0.00	4.99	0	53	47
MWD119-128A	119-128A-P3-11	57.2	0.0	25.9	0.0	0.0	0.0	8.9	6.3	0.1	98.3	2.60	0.00	1.39	0.00	0.00	0.00	0.43	0.55	0.00	4.98	0	56	44
MWD119-128A	119-128A-P4-1	66.4	0.0	20.1	0.0	0.0	0.0	2.0	10.1	0.1	98.6	2.95	0.00	1.05	0.00	0.00	0.00	0.09	0.87	0.01	4.97	1	90	10
MWD119-128A	119-128A-P4-2	63.0	0.0	22.1	0.0	0.0	0.0	4.2	8.9	0.0	98.4	2.82	0.00	1.17	0.00	0.00	0.00	0.20	0.78	0.00	4.98	0	79	21
MWD119-128A	119-128A-P4-3	64.0	0.0	21.7	0.0	0.0	0.0	3.7	9.3	0.0	98.8	2.85	0.00	1.14	0.00	0.00	0.00	0.18	0.81	0.00	4.98	0	82	18
MWD119-128A	119-128A-P4-4	66.9	0.0	20.4	0.1	0.0	0.0	1.9	10.1	0.2	99.5	2.94	0.00	1.06	0.00	0.00	0.00	0.09	0.86	0.01	4.96	1	89	10
MWD119-128A	119-128A-P4-5	61.0	0.0	23.2	0.0	0.0	0.0	6.1	8.1	0.0	98.5	2.75	0.00	1.23	0.00	0.00	0.00	0.30	0.71	0.00	4.99	0	70	30
MWD119-128A	119-128A-P4-6	61.0	0.0	23.8	0.0	0.0	0.0	6.0	8.2	0.1	99.1	2.73	0.00	1.26	0.00	0.00	0.00	0.29	0.71	0.00	4.99	0	71	29
MWD119-128A	119-128A-P4-7	60.8	0.0	23.6	0.0	0.0	0.0	6.1	8.3	0.0	98.8	2.73	0.00	1.25	0.00	0.00	0.00	0.29	0.72	0.00	5.00	0	71	29
GT004-094A	004-094A-P1_3	64.6	0.0	22.1	0.0	0.0	0.0	3.6	10.4	0.1	100.9	2.84	0.00	1.14	0.00	0.00	0.00	0.17	0.88	0.01	5.04	1	83	16
GT004-094A	004-094A-P1_5	61.7	0.0	23.6	0.0	0.0	0.0	5.6	9.1	0.2	100.1	2.74	0.00	1.24	0.00	0.00	0.00	0.26	0.79	0.01	5.04	1	74	25
GT004-094A	004-094A-P1_6	63.8	0.0	22.3	0.0	0.0	0.0	4.2	9.9	0.1	100.4	2.82	0.00	1.16	0.00	0.00	0.00	0.20	0.85	0.01	5.03	1	81	19
GT004-094A	004-094A-P2_1	51.8	0.0	30.1	0.0	0.0	0.0	14.0	3.9	0.1	99.9	2.36	0.00	1.61	0.00	0.00	0.00	0.68	0.34	0.01	5.01	1	33	66
GT004-094A	004-094A-P2_2	59.7	0.0	24.6	0.0	0.0	0.0	7.5	7.9	0.1	99.8	2.67	0.00	1.30	0.00	0.00	0.00	0.36	0.69	0.01	5.02	1	65	34
GT004-094A	004-094A-P2_3	57.1	0.0	26.0	0.0	0.0	0.0	8.8	6.8	0.1	98.8	2.59	0.00	1.39	0.00	0.00	0.00	0.43	0.60	0.00	5.01	0	58	42
GT004-094A	004-094A-P2_4	55.8	0.0	27.3	0.0	0.0	0.0	10.6	6.1	0.1	100.0	2.52	0.00	1.45	0.00	0.00	0.00	0.51	0.53	0.01	5.02	1	51	49
MWD005-067B	005-067B-P1_1	65.8	0.0	21.3	0.0	0.0	0.0	2.7	10.9	0.1	100.8	2.88	0.00	1.10	0.00	0.00	0.00	0.13	0.92	0.00	5.03	0	87	12

Appendix 2.3.3: Feldspar EPMA data from the Watershed tungsten deposit continued

		Major oxides, weight percent										Number of ions on the basis of 8 oxygen atoms										Feldspar end-members[1]		
Sample	Spot	SiO_2	TiO_2	Al_2O_3	FeO	MnO	MgO	CaO	Na_2O	K_2O	Total	Si	Ti	Al	Fe^{2+}	Mn	Mg	Ca	Na	K	Total	Or	Ab	An
MWD005-067B	005-067B-P1_2	64.0	0.0	22.6	0.0	0.0	0.0	4.2	10.1	0.1	100.8	2.81	0.00	1.17	0.00	0.00	0.00	0.20	0.86	0.00	5.04	0	81	19
MWD005-067B	005-067B-P1_3	65.7	0.0	21.1	0.0	0.0	0.0	2.7	10.7	0.1	100.4	2.89	0.00	1.09	0.00	0.00	0.00	0.13	0.91	0.00	5.03	0	87	12
MWD005-067B	005-067B-P2_1	64.6	0.0	21.8	0.0	0.0	0.0	3.6	10.4	0.1	100.5	2.84	0.00	1.13	0.00	0.00	0.00	0.17	0.89	0.00	5.04	0	84	16
MWD005-067B	005-067B-P2_2	64.8	0.0	21.5	0.0	0.0	0.0	3.2	10.3	0.1	99.9	2.86	0.00	1.12	0.00	0.00	0.00	0.15	0.88	0.01	5.02	1	84	15
MWD099-054C	099-054C-P2_1	52.2	0.1	30.1	0.2	0.0	0.0	13.7	4.3	0.0	100.6	2.36	0.00	1.61	0.01	0.00	0.00	0.66	0.38	0.00	5.02	0	36	64
MWD099-054C	099-054C-P2_2	62.8	0.0	23.5	0.1	0.0	0.0	5.4	9.4	0.1	101.2	2.76	0.00	1.22	0.00	0.00	0.00	0.25	0.80	0.00	5.04	0	76	24
MWD099-054C	099-054C-P3_6	54.4	0.0	28.8	0.0	0.0	0.0	12.1	5.3	0.0	100.6	2.45	0.00	1.53	0.00	0.00	0.00	0.58	0.46	0.00	5.02	0	44	56
MWD099-054C	099-054C-P3_7	50.4	0.0	31.2	0.1	0.0	0.0	15.0	3.5	0.0	100.1	2.30	0.00	1.68	0.00	0.00	0.00	0.73	0.30	0.00	5.02	0	29	71
MWD099-054C	099-054C-P3_8	50.6	0.0	31.0	0.1	0.0	0.0	15.1	3.3	0.0	100.2	2.31	0.00	1.67	0.00	0.00	0.00	0.74	0.29	0.00	5.01	0	28	72
MWD099-054C	099-054C-P3_9	53.2	0.0	29.3	0.1	0.0	0.0	12.7	4.5	0.0	99.9	2.41	0.00	1.57	0.01	0.00	0.00	0.62	0.39	0.00	5.00	0	39	61
MWD099-124C	099-124C-P2_2	61.1	0.0	24.0	0.0	0.0	0.0	6.4	8.5	0.1	100.2	2.72	0.00	1.26	0.00	0.00	0.00	0.30	0.73	0.01	5.02	0	70	29
MWD099-124C	099-124C-P2_3	60.8	0.0	24.8	0.0	0.0	0.0	7.0	8.2	0.2	101.0	2.69	0.00	1.29	0.00	0.00	0.00	0.33	0.70	0.01	5.02	1	67	32
MWD099-124C	099-124C-P2_4	60.5	0.0	24.7	0.1	0.0	0.0	7.0	8.1	0.2	100.5	2.69	0.00	1.29	0.00	0.00	0.00	0.33	0.70	0.01	5.02	1	67	32
MWD101-149C	101-149C-P1_3	62.5	0.0	23.6	0.0	0.0	0.0	5.6	9.0	0.1	100.9	2.75	0.00	1.23	0.00	0.00	0.00	0.27	0.77	0.01	5.02	1	74	25
MWD122-289B	122-289B-P1_1	59.6	0.0	25.1	0.0	0.0	0.0	7.6	7.9	0.1	100.2	2.66	0.00	1.32	0.00	0.00	0.00	0.36	0.68	0.00	5.03	0	65	35
MWD122-289B	122-289B-P1_2	54.6	0.0	28.1	0.0	0.0	0.0	11.5	5.5	0.1	99.8	2.47	0.00	1.50	0.00	0.00	0.00	0.56	0.48	0.00	5.02	0	46	53
MWD122-289B	122-289B-P1_3	59.2	0.0	24.8	0.1	0.0	0.0	6.6	8.0	0.1	98.9	2.67	0.00	1.32	0.00	0.00	0.00	0.32	0.70	0.01	5.02	1	68	31
MWD122-289B	122-289B-P1_4	57.6	0.1	26.6	0.1	0.0	0.0	9.3	6.9	0.1	100.5	2.57	0.00	1.40	0.00	0.00	0.00	0.44	0.60	0.00	5.02	0	57	43
MWD122-289B	122-289B-P1_8	62.5	0.0	23.7	0.1	0.0	0.0	5.2	9.0	0.1	100.7	2.76	0.00	1.23	0.00	0.00	0.00	0.25	0.77	0.00	5.01	0	75	25
MWD122-289B	122-289B-P2_1	64.3	0.0	22.6	0.0	0.0	0.0	4.9	10.0	0.1	101.9	2.80	0.00	1.16	0.00	0.00	0.00	0.23	0.85	0.00	5.04	0	78	21
MWD122-289B	122-289B-P2_10	58.4	0.0	26.2	0.0	0.0	0.0	9.0	7.2	0.1	100.7	2.60	0.00	1.37	0.00	0.00	0.00	0.43	0.62	0.00	5.03	0	59	41
MWD122-289B	122-289B-P2_11	64.6	0.0	22.5	0.0	0.0	0.0	4.2	10.0	0.1	101.3	2.82	0.00	1.16	0.00	0.00	0.00	0.19	0.85	0.00	5.03	0	81	19
MWD122-289B	122-289B-P2_12	57.8	0.0	26.2	0.0	0.0	0.0	8.8	7.2	0.1	100.2	2.59	0.00	1.38	0.00	0.00	0.00	0.42	0.63	0.01	5.03	0	59	40
MWD122-289B	122-289B-P2_13	62.9	0.0	23.1	0.0	0.0	0.0	5.0	9.5	0.1	100.6	2.78	0.00	1.20	0.00	0.00	0.00	0.23	0.81	0.00	5.03	0	77	23
MWD122-289B	122-289B-P2_14	63.0	0.0	22.9	0.0	0.0	0.0	4.7	9.1	0.1	99.8	2.79	0.00	1.20	0.00	0.00	0.00	0.22	0.79	0.00	5.00	0	77	22
MWD122-289B	122-289B-P2_16	60.4	0.0	23.9	0.0	0.0	0.0	5.2	8.7	0.1	98.2	2.73	0.00	1.27	0.00	0.00	0.00	0.25	0.76	0.00	5.02	0	75	25
MWD122-289B	122-289B-P2_17	59.1	0.0	25.2	0.0	0.0	0.0	7.6	7.7	0.2	99.8	2.65	0.00	1.33	0.00	0.00	0.00	0.37	0.67	0.01	5.03	1	64	35
MWD122-289B	122-289B-P2_18	57.3	0.0	26.4	0.0	0.0	0.0	9.4	6.8	0.1	100.1	2.57	0.00	1.40	0.00	0.00	0.00	0.45	0.60	0.01	5.03	1	57	43
MWD122-289B	122-289B-P2_19	58.7	0.0	25.8	0.0	0.0	0.0	8.3	7.6	0.1	100.5	2.62	0.00	1.36	0.00	0.00	0.00	0.40	0.66	0.00	5.03	0	62	38
MWD122-289B	122-289B-P2_2	59.3	0.1	25.2	0.0	0.0	0.0	7.6	7.8	0.1	100.0	2.65	0.00	1.33	0.00	0.00	0.00	0.37	0.68	0.00	5.02	0	65	35
MWD122-289B	122-289B-P2_20	57.5	0.0	26.5	0.0	0.0	0.0	9.4	6.7	0.1	100.2	2.58	0.00	1.40	0.00	0.00	0.00	0.45	0.58	0.01	5.02	1	56	43
MWD122-289B	122-289B-P2_21	58.5	0.0	25.8	0.0	0.0	0.0	8.6	7.5	0.1	100.5	2.61	0.00	1.36	0.00	0.00	0.00	0.41	0.65	0.01	5.03	1	61	39
MWD122-289B	122-289B-P2_3	58.9	0.0	25.5	0.0	0.0	0.0	8.3	7.5	0.0	100.4	2.63	0.00	1.34	0.00	0.00	0.00	0.40	0.65	0.00	5.02	0	62	38
MWD122-289B	122-289B-P2_4	63.6	0.0	22.8	0.0	0.0	0.0	4.7	9.8	0.0	100.9	2.79	0.00	1.18	0.00	0.00	0.00	0.22	0.83	0.00	5.03	0	79	21
MWD122-289B	122-289B-P2_5	59.0	0.0	25.7	0.0	0.0	0.0	8.3	7.5	0.1	100.5	2.63	0.00	1.35	0.00	0.00	0.00	0.40	0.65	0.00	5.02	0	62	38
MWD122-289B	122-289B-P2_6	62.6	0.0	23.8	0.0	0.0	0.0	6.2	9.2	0.1	101.9	2.74	0.00	1.23	0.00	0.00	0.00	0.29	0.78	0.00	5.04	0	73	27

Appendix 2.3.3: Feldspar EPMA data from the Watershed tungsten deposit continued

		Major oxides, weight percent										Number of ions on the basis of 8 oxygen atoms										Feldspar end-members[1]		
Sample	Spot	SiO_2	TiO_2	Al_2O_3	FeO	MnO	MgO	CaO	Na_2O	K_2O	Total	Si	Ti	Al	Fe^{2+}	Mn	Mg	Ca	Na	K	Total	Or	Ab	An
MWD122-289B	122-289B-P2_7	61.0	0.0	24.6	0.0	0.0	0.0	7.2	8.3	0.0	101.2	2.69	0.00	1.28	0.00	0.00	0.00	0.34	0.71	0.00	5.02	0	67	32
MWD122-289B	122-289B-P2_8	59.8	0.0	24.9	0.0	0.0	0.0	7.7	7.8	0.1	100.3	2.66	0.00	1.31	0.00	0.00	0.00	0.37	0.68	0.00	5.02	0	64	35
MWD122-289B	122-289B-P2_9	62.4	0.0	23.7	0.0	0.0	0.0	6.1	9.2	0.1	101.4	2.74	0.00	1.23	0.00	0.00	0.00	0.29	0.78	0.00	5.04	0	73	27
MWD122-289B	122-289B-P3_1	62.5	0.0	23.1	0.1	0.0	0.1	4.8	9.4	0.1	100.1	2.77	0.00	1.21	0.01	0.00	0.01	0.23	0.81	0.00	5.03	0	77	23
MWD122-289B	122-289B-P3_11	61.5	0.0	24.2	0.0	0.0	0.0	6.1	8.6	0.1	100.6	2.72	0.00	1.26	0.00	0.00	0.00	0.29	0.74	0.00	5.02	0	71	28
MWD122-289B	122-289B-P3_12	63.9	0.0	22.6	0.0	0.0	0.0	4.6	9.6	0.1	100.8	2.81	0.00	1.17	0.00	0.00	0.00	0.22	0.82	0.00	5.02	0	79	21
MWD122-289B	122-289B-P3_13	62.5	0.0	23.8	0.0	0.0	0.0	5.8	8.7	0.1	100.9	2.75	0.00	1.24	0.00	0.00	0.00	0.27	0.74	0.00	5.01	0	73	27
MWD122-289B	122-289B-P3_14	62.6	0.0	23.6	0.0	0.0	0.0	5.4	9.3	0.1	101.0	2.75	0.00	1.22	0.00	0.00	0.00	0.26	0.79	0.00	5.03	0	75	24
MWD122-289B	122-289B-P3_2	63.0	0.0	23.5	0.0	0.0	0.0	5.2	9.1	0.1	101.0	2.77	0.00	1.22	0.00	0.00	0.00	0.25	0.78	0.01	5.02	1	76	24
MWD122-289B	122-289B-P3_3	62.9	0.1	23.1	0.1	0.0	0.1	4.7	9.5	0.1	100.5	2.78	0.00	1.20	0.00	0.00	0.01	0.22	0.81	0.00	5.03	0	77	22
MWD122-289B	122-289B-P3_5	57.5	0.0	26.6	0.0	0.0	0.0	9.5	6.8	0.1	100.7	2.57	0.00	1.40	0.00	0.00	0.00	0.46	0.59	0.01	5.03	1	56	43
MWD122-289B	122-289B-P3_6	61.5	0.0	24.3	0.0	0.0	0.0	6.5	8.7	0.1	101.1	2.71	0.00	1.26	0.00	0.00	0.00	0.31	0.75	0.01	5.03	1	71	29
MWD122-289B	122-289B-P3_7	62.0	0.0	24.4	0.0	0.0	0.0	6.7	8.5	0.1	101.7	2.71	0.00	1.26	0.00	0.00	0.00	0.31	0.73	0.00	5.02	0	70	30
MWD122-289B	122-289B-P3_8	61.2	0.1	24.1	0.0	0.0	0.0	6.4	8.7	0.1	100.6	2.71	0.00	1.26	0.00	0.00	0.00	0.30	0.75	0.00	5.03	0	71	29
MWD122-289B	122-289B-P3_9	64.5	0.0	22.6	0.0	0.0	0.0	3.8	10.1	0.1	101.1	2.82	0.00	1.16	0.00	0.00	0.00	0.18	0.85	0.01	5.02	1	82	17
MWD122-289C	122-289C-P1_1	59.2	0.0	25.2	0.0	0.0	0.0	7.7	7.4	0.1	99.5	2.65	0.00	1.33	0.00	0.00	0.00	0.37	0.64	0.00	5.00	0	63	37
MWD122-289C	122-289C-P1_2	58.9	0.0	25.4	0.0	0.0	0.0	8.2	7.6	0.1	100.2	2.63	0.00	1.34	0.00	0.00	0.00	0.39	0.66	0.00	5.03	0	62	37
MWD122-289C	122-289C-P1_8	57.7	0.0	26.1	0.0	0.0	0.0	9.4	6.8	0.0	100.0	2.59	0.00	1.38	0.00	0.00	0.00	0.45	0.59	0.00	5.02	0	57	43
MWD122-289C	122-289C-P2-1	62.8	0.0	22.9	0.0	0.0	0.0	4.8	9.5	0.1	100.1	2.78	0.00	1.20	0.00	0.00	0.00	0.23	0.81	0.00	5.03	0	78	22
MWD122-289C	122-289C-P2-10	63.8	0.0	22.9	0.0	0.0	0.0	4.5	9.8	0.1	101.1	2.80	0.00	1.18	0.00	0.00	0.00	0.21	0.83	0.01	5.03	1	79	20
MWD122-289C	122-289C-P2-11	62.6	0.0	23.2	0.0	0.0	0.0	5.5	9.2	0.1	100.5	2.77	0.00	1.21	0.00	0.00	0.00	0.26	0.79	0.00	5.03	0	75	25
MWD122-289C	122-289C-P2-12	61.8	0.1	23.8	0.0	0.0	0.0	5.7	9.0	0.1	100.5	2.74	0.00	1.24	0.00	0.00	0.00	0.27	0.77	0.01	5.03	1	74	26
MWD122-289C	122-289C-P2-2	58.1	0.0	25.6	0.0	0.0	0.0	8.6	7.2	0.1	99.6	2.62	0.00	1.36	0.00	0.00	0.00	0.41	0.63	0.00	5.02	0	60	40
MWD122-289C	122-289C-P2-3	63.2	0.1	22.7	0.0	0.0	0.0	4.8	9.8	0.1	100.8	2.79	0.00	1.18	0.00	0.00	0.00	0.23	0.84	0.00	5.04	0	78	21
MWD122-289C	122-289C-P2-4	63.3	0.0	22.7	0.0	0.0	0.0	4.5	9.6	0.1	100.2	2.80	0.00	1.18	0.00	0.00	0.00	0.21	0.82	0.01	5.02	0	79	21
MWD122-289C	122-289C-P2-5	58.6	0.0	23.9	0.0	0.0	0.0	4.7	8.2	0.1	95.5	2.72	0.00	1.31	0.00	0.00	0.00	0.23	0.74	0.01	5.00	1	76	24
MWD122-289C	122-289C-P2-6	65.0	0.0	22.0	0.0	0.0	0.0	3.6	10.2	0.1	100.9	2.84	0.00	1.14	0.00	0.00	0.00	0.17	0.87	0.00	5.02	0	83	16
MWD122-289C	122-289C-P2-7	57.9	0.1	26.4	0.0	0.0	0.0	9.2	6.7	0.1	100.4	2.59	0.00	1.39	0.00	0.00	0.00	0.44	0.58	0.01	5.01	1	57	43
MWD122-289C	122-289C-P2-8	63.3	0.0	23.1	0.0	0.0	0.0	5.0	9.5	0.1	100.9	2.78	0.00	1.20	0.00	0.00	0.00	0.23	0.81	0.00	5.03	0	77	22
MWD122-289C	122-289C-P2-9	62.2	0.1	23.7	0.0	0.0	0.0	5.7	9.0	0.1	100.8	2.74	0.00	1.23	0.00	0.00	0.00	0.27	0.77	0.01	5.03	1	74	26
MWD122-289C	122-289C-P3-1	62.0	0.0	24.0	0.0	0.0	0.0	5.9	8.7	0.1	100.6	2.74	0.00	1.25	0.00	0.00	0.00	0.28	0.75	0.00	5.01	0	72	27
MWD122-289C	122-289C-P3-13	58.0	0.1	26.7	0.0	0.0	0.0	9.2	6.9	0.1	101.0	2.58	0.00	1.40	0.00	0.00	0.00	0.44	0.60	0.01	5.02	1	57	42
MWD122-289C	122-289C-P3-14	60.8	0.0	24.7	0.1	0.0	0.0	6.9	7.9	0.1	100.5	2.69	0.00	1.29	0.00	0.00	0.00	0.33	0.68	0.01	5.00	1	67	32
MWD122-289C	122-289C-P3-15	61.1	0.0	24.8	0.1	0.0	0.0	7.0	8.6	0.1	101.8	2.68	0.00	1.29	0.00	0.00	0.00	0.33	0.73	0.01	5.04	1	68	31
MWD122-289C	122-289C-P3-2	60.3	0.0	24.5	0.1	0.0	0.0	6.7	8.3	0.1	100.0	2.69	0.00	1.29	0.00	0.00	0.00	0.32	0.72	0.00	5.02	0	69	31
MWD122-289C	122-289C-P3-3	63.8	0.0	22.6	0.0	0.0	0.0	4.7	10.0	0.0	101.1	2.80	0.00	1.17	0.00	0.00	0.00	0.22	0.85	0.00	5.04	0	79	21

Appendix 2.3.3: Feldspar EPMA data from the Watershed tungsten deposit continued

		Major oxides, weight percent										Number of ions on the basis of 8 oxygen atoms										Feldspar end-members[1]		
Sample	Spot	SiO_2	TiO_2	Al_2O_3	FeO	MnO	MgO	CaO	Na_2O	K_2O	Total	Si	Ti	Al	Fe^{2+}	Mn	Mg	Ca	Na	K	Total	Or	Ab	An
MWD122-289C	122-289C-P3-5	65.3	0.0	18.2	0.0	0.0	0.0	0.0	0.0	16.2	99.8	3.02	0.00	0.99	0.00	0.00	0.00	0.00	0.00	0.96	4.97	99	0	0
MWD122-289C	122-289C-P3-6	57.8	0.0	26.4	0.0	0.0	0.0	8.9	7.1	0.1	100.3	2.58	0.00	1.39	0.00	0.00	0.00	0.43	0.62	0.01	5.03	0	59	41
MWD122-289C	122-289C-P3-7	62.1	0.0	24.0	0.0	0.0	0.0	6.0	9.0	0.1	101.1	2.73	0.00	1.25	0.00	0.00	0.00	0.28	0.77	0.00	5.03	0	73	27
MWD122-289C	122-289C-P4-1	61.1	0.0	24.5	0.1	0.0	0.0	6.8	8.2	0.2	100.9	2.70	0.00	1.28	0.00	0.00	0.00	0.32	0.70	0.01	5.02	1	68	31
MWD122-289C	122-289C-P4-2	62.5	0.0	23.4	0.0	0.0	0.0	5.3	9.0	0.1	100.3	2.77	0.00	1.22	0.00	0.00	0.00	0.25	0.77	0.00	5.01	0	75	25
MWD122-289C	122-289C-P4-3	58.6	0.0	24.8	0.0	0.0	0.0	6.1	6.7	1.6	97.9	2.68	0.00	1.34	0.00	0.00	0.00	0.30	0.59	0.09	5.00	10	60	31
MWD122-289C	122-289C-P4-4	59.4	0.0	25.7	0.0	0.0	0.0	8.2	7.6	0.1	101.0	2.63	0.00	1.34	0.00	0.00	0.00	0.39	0.65	0.00	5.02	0	62	37
MWD122-289C	122-289C-P4-5	61.4	0.0	24.4	0.0	0.0	0.0	6.6	8.3	0.1	100.7	2.71	0.00	1.27	0.00	0.00	0.00	0.31	0.71	0.00	5.01	0	69	30
MWD122-289C	122-289C-P4-6	59.1	0.0	26.0	0.0	0.0	0.0	8.6	7.4	0.1	101.3	2.62	0.00	1.35	0.00	0.00	0.00	0.41	0.64	0.01	5.03	1	60	39

[1] Plagioclase end-members: Or: orthoclase, Ab: albite, An: anorthite. After Whitney and Evans (2010)

Appendix 2.3.4: Clinozoisite EPMA data from the Watershed tungsten deposit

		Major oxides, weight percent											Number of ions on the basis of 12.5 oxygen atoms										
Sample	Spot	SiO_2	TiO_2	Al_2O_3	FeO	MnO	MgO	CaO	Na_2O	K_2O	F	Cl	Total	Si	Ti	Al	Fe^{2+}	Fe^{3+}	Mn	Mg	Ca	Na	K	Total
MWD099-081B	099-081B-P1-3	38.5	0.0	26.2	6.1	0.1	0.0	23.3	0.0	0.0	--	--	94.2	3.09	0.00	2.47	0.00	0.41	0.00	0.00	2.00	0.00	0.00	7.98
MWD099-081B	099-081B-P1-4	39.1	0.1	26.2	6.9	0.2	0.1	23.5	0.0	0.0	--	--	96.1	3.08	0.01	2.43	0.00	0.45	0.01	0.01	1.98	0.00	0.00	7.98
MWD099-081B	099-081B-P1-5	38.6	0.0	26.8	6.0	0.2	0.1	23.6	0.0	0.0	--	--	95.3	3.06	0.00	2.51	0.00	0.39	0.01	0.01	2.00	0.00	0.00	7.99
MWD099-081B	099-081B-P2-16	38.4	0.2	26.0	6.9	0.3	0.1	23.0	0.0	0.0	--	--	94.9	3.07	0.01	2.44	0.00	0.46	0.02	0.01	1.96	0.00	0.00	7.97
MWD099-081B	099-081B-P2-18	38.2	0.1	25.8	7.6	0.2	0.0	23.3	0.0	0.0	--	--	95.2	3.04	0.01	2.42	0.00	0.51	0.01	0.00	1.99	0.00	0.00	7.99
MWD099-081B	099-081B-P2-20	38.4	0.1	26.2	6.7	0.1	0.0	23.3	0.0	0.0	--	--	94.9	3.06	0.00	2.46	0.00	0.45	0.01	0.00	1.99	0.00	0.00	7.98
MWD099-081B	099-081B-P2-22	38.5	0.1	26.8	5.6	0.0	0.0	23.1	0.0	0.0	--	--	94.2	3.08	0.00	2.53	0.00	0.38	0.00	0.00	1.98	0.00	0.00	7.97
MWD099-081B	099-081B-P3-10	38.5	0.1	27.5	4.8	0.0	0.0	23.7	0.0	0.0	--	--	94.6	3.06	0.00	2.58	0.00	0.32	0.00	0.00	2.02	0.00	0.00	7.99
MWD099-081B	099-081B-P3-11	38.1	0.1	25.6	7.2	0.1	0.0	23.4	0.0	0.0	--	--	94.4	3.06	0.01	2.42	0.00	0.48	0.01	0.00	2.01	0.00	0.00	7.99
MWD099-081B	099-081B-P4-11	38.7	0.1	26.4	6.8	0.2	0.0	23.7	0.0	0.0	--	--	95.8	3.06	0.00	2.46	0.00	0.45	0.01	0.00	2.01	0.00	0.00	7.99
MWD099-081B	099-081B-P4-4	38.8	0.0	26.8	6.2	0.1	0.0	23.5	0.0	0.0	--	--	95.5	3.07	0.00	2.50	0.00	0.41	0.01	0.00	1.99	0.00	0.00	7.98
MWD099-124A	099-124A-P2-2	38.8	0.1	26.4	6.2	0.4	0.0	23.0	0.0	0.0	--	--	94.9	3.08	0.01	2.47	0.00	0.41	0.02	0.01	1.96	0.00	0.00	7.97
MWD099-124A	099-124A-P2-4	38.2	0.0	27.6	6.5	0.3	0.0	23.4	0.0	0.0	--	--	96.0	3.01	0.00	2.56	0.00	0.43	0.02	0.00	1.98	0.00	0.00	8.00
MWD099-163.5C	099-163.5C-P4-4	38.8	0.1	27.1	6.1	0.2	0.1	23.5	0.2	0.0	--	--	96.1	3.05	0.01	2.51	0.00	0.40	0.01	0.01	1.98	0.02	0.00	8.00
MWD099-163.5C	099-163.5C-P4-5	39.4	0.0	28.0	2.8	0.1	0.1	24.0	0.0	0.0	--	--	94.4	3.12	0.00	2.62	0.00	0.19	0.01	0.01	2.04	0.00	0.00	7.98
MWD099-163.5C	099-163.5C-P4-6	38.9	0.1	26.6	6.8	0.2	0.1	23.8	0.0	0.0	--	--	96.4	3.06	0.00	2.46	0.00	0.45	0.01	0.01	2.00	0.00	0.00	7.99
MWD101-100A	101-100A-P2-6	39.1	0.1	28.0	4.5	0.1	0.0	23.6	0.0	0.0	--	--	95.5	3.08	0.01	2.60	0.00	0.29	0.01	0.00	1.99	0.00	0.00	7.97
MWD101-100A	101-100A-P2-7	39.0	0.1	28.3	4.6	0.2	0.0	23.4	0.0	0.0	--	--	95.5	3.06	0.00	2.62	0.00	0.30	0.01	0.00	1.97	0.00	0.00	7.97
MWD101-100A	101-100A-P2-8	38.6	0.0	27.1	5.9	0.2	0.1	23.4	0.0	0.0	--	--	95.2	3.06	0.00	2.53	0.00	0.39	0.01	0.01	1.98	0.00	0.00	7.98
MWD101-100A	101-100A-P4-10	39.0	0.0	27.1	6.3	0.1	0.0	23.7	0.0	0.0	--	--	96.2	3.06	0.00	2.51	0.00	0.41	0.01	0.00	1.99	0.00	0.00	7.98
MWD101-100A	101-100A-P4-11	39.1	0.1	27.3	6.0	0.2	0.0	23.6	0.0	0.0	--	--	96.3	3.07	0.01	2.52	0.00	0.39	0.01	0.00	1.98	0.00	0.00	7.98
MWD101-100A	101-100A-P4-2	38.6	0.0	25.8	7.9	0.2	0.0	23.3	0.0	0.0	--	--	95.8	3.05	0.00	2.41	0.00	0.52	0.01	0.00	1.98	0.00	0.00	7.98
MWD101-100A	101-100A-P4-3	39.0	0.0	25.4	8.5	0.1	0.0	23.4	0.0	0.0	--	--	96.4	3.07	0.00	2.36	0.00	0.56	0.01	0.00	1.97	0.00	0.00	7.97
MWD101-159A	101-159A-P3-4	39.4	0.1	28.2	5.3	0.2	0.1	24.9	0.0	0.0	--	--	98.1	3.03	0.01	2.56	0.00	0.34	0.01	0.01	2.05	0.00	0.00	8.01
MWD101-159A	101-159A-P3-6	39.1	0.1	27.5	6.4	0.1	0.0	24.6	0.0	0.0	--	--	97.9	3.03	0.01	2.51	0.00	0.41	0.01	0.00	2.04	0.00	0.00	8.01
MWD101-159A	101-159A-P3-7	39.3	0.0	27.7	6.9	0.1	0.0	24.7	0.0	0.0	--	--	98.8	3.02	0.00	2.51	0.00	0.44	0.01	0.00	2.03	0.00	0.00	8.01
MWD101-211.5A	101-211.5A-P1-4	38.3	0.1	27.2	5.9	0.1	0.0	24.0	0.0	0.0	--	--	95.6	3.03	0.00	2.53	0.00	0.39	0.01	0.00	2.03	0.00	0.00	8.00
MWD101-211.5A	101-211.5A-P1-6	38.6	0.0	27.8	5.7	0.2	0.0	23.9	0.0	0.0	--	--	96.1	3.03	0.00	2.57	0.00	0.37	0.01	0.00	2.01	0.00	0.00	8.00
MWD101-211.5A	101-211.5A-P3-2	37.8	0.0	28.2	5.9	0.5	0.0	23.3	0.0	0.0	--	--	95.9	2.98	0.00	2.63	0.00	0.39	0.03	0.00	1.97	0.00	0.00	8.01
MWD101-211.5A	101-211.5A-P3-4	38.6	0.1	27.6	4.9	0.3	0.1	24.4	0.0	0.0	--	--	95.9	3.04	0.00	2.56	0.00	0.32	0.02	0.01	2.06	0.00	0.00	8.01
MWD105-115A	105-115A-P1-12	39.4	0.1	26.8	6.9	0.3	0.0	23.6	0.0	0.0	--	--	97.2	3.07	0.00	2.46	0.00	0.45	0.02	0.01	1.97	0.00	0.00	7.98
MWD105-115A	105-115A-P1-13	39.6	0.0	28.1	5.7	0.2	0.0	23.8	0.0	0.0	--	--	97.4	3.06	0.00	2.56	0.00	0.37	0.01	0.00	1.97	0.00	0.00	7.98
MWD105-115A	105-115A-P2-1	39.5	0.0	27.5	6.0	0.3	0.0	23.2	0.0	0.0	--	--	96.5	3.08	0.00	2.53	0.00	0.39	0.02	0.00	1.94	0.00	0.00	7.96
MWD105-115A	105-115A-P2-2	39.3	0.0	27.1	6.4	0.2	0.0	23.7	0.0	0.0	--	--	96.7	3.07	0.00	2.49	0.00	0.42	0.01	0.00	1.98	0.00	0.00	7.98
MWD105-115A	105-115A-P2-3	39.6	0.0	28.0	5.8	0.2	0.0	23.9	0.0	0.0	--	--	97.6	3.06	0.00	2.55	0.00	0.38	0.01	0.00	1.98	0.00	0.00	7.98
MWD105-115A	105-115A-P2-4	39.2	0.0	29.0	4.5	0.2	0.0	24.0	0.0	0.0	--	--	96.9	3.04	0.00	2.65	0.00	0.29	0.01	0.00	1.99	0.01	0.00	7.99

Appendix 2.3.4: Clinozoisite EPMA data from the Watershed tungsten deposit continued

		Major oxides, weight percent											Number of ions on the basis of 12.5 oxygen atoms									
Sample	Spot	SiO_2	TiO_2	Al_2O_3	FeO	MnO	MgO	CaO	Na_2O	K_2O	F	Cl	Total	Si	Ti	Al	Fe^{2+}	Fe^{3+}	Mn	Mg	Ca	Na	K	Total
MWD105-206B	105-206B-P1-4	39.4	0.1	28.0	6.3	0.1	0.0	24.6	0.0	0.0	--	--	98.5	3.02	0.01	2.54	0.00	0.40	0.01	0.00	2.02	0.00	0.00	8.00
MWD105-206B	105-206B-P2-5	39.3	0.1	27.6	5.6	0.2	0.1	24.3	0.0	0.0	--	--	97.2	3.05	0.01	2.53	0.00	0.36	0.01	0.01	2.03	0.00	0.00	8.00
MWD105-206B	105-206B-P3-2	39.7	0.3	28.7	4.8	0.2	0.1	24.6	0.0	0.0	--	--	98.4	3.04	0.02	2.59	0.00	0.30	0.01	0.01	2.02	0.00	0.00	8.00
MWD105-206B	105-206B-P3-3	39.3	0.2	27.4	6.3	0.2	0.1	24.7	0.0	0.0	--	--	98.1	3.03	0.01	2.50	0.00	0.41	0.01	0.01	2.04	0.00	0.00	8.01
MWD107-259B	107-259B-P1-6	39.0	0.1	28.1	5.6	0.2	0.1	24.6	0.0	0.0	--	--	97.6	3.02	0.00	2.57	0.00	0.36	0.01	0.01	2.04	0.00	0.00	8.02
MWD107-259B	107-259B-P2-2	38.8	0.1	27.1	6.3	0.2	0.1	24.6	0.0	0.0	--	--	97.1	3.03	0.01	2.49	0.00	0.41	0.01	0.01	2.05	0.00	0.00	8.01
MWD107-259B	107-259B-P3-3	38.9	0.3	27.7	5.7	0.2	0.1	24.4	0.0	0.0	--	--	97.1	3.03	0.01	2.54	0.00	0.37	0.01	0.01	2.03	0.00	0.00	8.01
MWD107-259B	107-259B-P4-1	39.0	0.1	27.8	5.3	0.2	0.1	24.6	0.0	0.0	--	--	97.1	3.04	0.01	2.55	0.00	0.34	0.01	0.01	2.05	0.00	0.00	8.01
MWD119-126A	119-126A-P3-4	39.0	0.1	26.6	7.3	0.3	0.0	23.8	0.0	0.0	--	--	97.0	3.05	0.00	2.45	0.00	0.48	0.02	0.00	1.99	0.00	0.00	7.99
MWD119-126A	119-126A-P3-8	39.2	0.0	26.7	7.3	0.3	0.0	23.8	0.0	0.0	--	--	97.4	3.05	0.00	2.45	0.00	0.48	0.02	0.00	1.98	0.00	0.00	7.99
MWD005-128A	005-128A-P1_12	38.7	0.1	26.8	7.4	0.2	0.0	24.5	0.0	0.0	0.2	0.0	98.1	3.01	0.01	2.46	0.00	0.48	0.02	0.00	2.04	0.00	0.00	8.02
MWD005-128A	005-128A-P1_9	38.6	0.1	27.5	6.6	0.2	0.0	24.8	0.0	0.0	0.1	0.0	97.9	3.00	0.01	2.51	0.00	0.43	0.01	0.00	2.07	0.00	0.00	8.03
MWD011-147	011-147-P1_13	38.5	0.0	28.1	5.6	0.3	0.1	24.9	0.0	0.0	0.0	0.0	97.5	2.99	0.00	2.58	0.00	0.36	0.02	0.01	2.07	0.00	0.00	8.03
MWD011-147	011-147-P1_14	38.4	0.2	27.2	6.7	0.2	0.1	24.8	0.0	0.0	0.1	0.0	97.7	2.99	0.01	2.49	0.00	0.44	0.01	0.01	2.07	0.00	0.00	8.03
MWD011-147	011-147-P1_15	38.2	0.1	27.3	6.0	0.1	0.0	24.9	0.0	0.0	0.5	0.0	97.0	3.00	0.01	2.53	0.00	0.39	0.01	0.01	2.10	0.00	0.00	8.03
MWD011-147	011-147-P1_28	38.3	0.1	28.0	5.2	0.3	0.1	24.7	0.0	0.0	0.0	0.0	96.8	2.99	0.01	2.59	0.00	0.34	0.02	0.01	2.07	0.00	0.00	8.04
MWD011-147	011-147-P1_29	38.4	0.2	28.0	6.0	0.3	0.1	24.8	0.0	0.0	0.0	0.0	97.6	2.98	0.01	2.56	0.00	0.39	0.02	0.01	2.07	0.00	0.00	8.04
MWD011-147	011-147-P1_30	38.2	0.1	27.7	5.8	0.3	0.0	24.9	0.0	0.0	0.5	0.0	97.4	2.99	0.01	2.55	0.00	0.38	0.02	0.01	2.09	0.01	0.00	8.04
MWD011-147	011-147-P1_39	38.0	0.1	26.8	6.8	0.2	0.1	24.8	0.0	0.0	0.3	0.0	97.1	2.99	0.01	2.48	0.00	0.45	0.01	0.01	2.09	0.00	0.00	8.04
MWD011-147	011-147-P1_40	38.4	0.1	27.7	5.5	0.3	0.1	24.6	0.0	0.0	0.3	0.0	96.9	3.01	0.01	2.56	0.00	0.36	0.02	0.01	2.06	0.00	0.00	8.02
MWD011-147	011-147-P1_41	38.0	0.1	27.3	6.5	0.3	0.1	24.7	0.0	0.0	0.4	0.0	97.3	2.98	0.01	2.52	0.00	0.43	0.02	0.01	2.07	0.00	0.00	8.04
MWD042-197A	042-197A-P1_3	38.2	0.0	27.8	5.6	0.3	0.0	24.9	0.0	0.0	0.1	0.0	97.1	2.99	0.00	2.57	0.00	0.37	0.02	0.00	2.09	0.00	0.00	8.04
MWD042-197A	042-197A-P1_4	38.2	0.2	27.0	6.7	0.2	0.0	25.2	0.0	0.0	0.0	0.0	97.4	2.98	0.01	2.49	0.00	0.43	0.01	0.01	2.11	0.00	0.00	8.04
MWD042-197A	042-197A-P1_8	38.1	0.3	26.9	6.6	0.3	0.1	24.6	0.0	0.0	0.0	0.0	97.1	2.99	0.02	2.49	0.00	0.44	0.02	0.01	2.07	0.00	0.00	8.03
MWD099-054C	099-054C-P3_1	38.7	0.0	27.9	6.3	0.2	0.0	24.8	0.0	0.0	0.1	0.0	98.0	3.00	0.00	2.54	0.00	0.41	0.02	0.00	2.06	0.00	0.00	8.03
MWD099-054C	099-054C-P3_10	38.5	0.0	28.0	6.1	0.2	0.0	24.9	0.0	0.0	0.3	0.0	98.0	2.99	0.00	2.56	0.00	0.39	0.01	0.01	2.07	0.00	0.00	8.03
MWD099-054C	099-054C-P3_11	39.6	0.0	29.8	3.7	0.2	0.0	24.6	0.1	0.0	0.6	0.0	98.7	3.03	0.00	2.69	0.00	0.23	0.01	0.00	2.02	0.01	0.00	8.01
MWD099-054C	099-054C-P3_13	38.2	0.1	27.0	6.7	0.1	0.0	24.4	0.0	0.0	0.0	0.0	96.6	3.00	0.01	2.50	0.00	0.44	0.01	0.00	2.05	0.00	0.00	8.02
MWD099-054C	099-054C-P3_2	38.8	0.0	28.4	5.8	0.1	0.0	24.9	0.0	0.0	0.4	0.0	98.3	2.99	0.00	2.58	0.00	0.37	0.01	0.00	2.06	0.00	0.00	8.03
MWD099-054C	099-054C-P3_3	38.6	0.0	27.6	6.5	0.2	0.0	24.4	0.0	0.0	0.0	0.0	97.4	3.00	0.00	2.53	0.00	0.42	0.01	0.00	2.03	0.00	0.00	8.02
MWD099-054C	099-054C-P3_4	39.2	0.1	30.1	3.6	0.2	0.0	25.1	0.0	0.0	0.0	0.0	98.2	3.00	0.00	2.72	0.00	0.23	0.01	0.00	2.06	0.00	0.00	8.02
MWD101-149C	101-149C-P1_4	39.1	0.1	27.7	6.2	0.2	0.0	24.7	0.0	0.0	0.2	0.0	98.1	3.02	0.00	2.53	0.00	0.40	0.02	0.00	2.05	0.00	0.00	8.01

Appendix 2.3.5: Mica EPMA data from the Watershed tungsten deposit

			Major oxides, weight percent											Number of ions on the basis of 20 oxygen atoms										
Sample	Spot	Mica group[1]	SiO_2	TiO_2	Al_2O_3	FeO	MnO	MgO	CaO	Na_2O	K_2O	F	Cl	Total	T-Si	T-Al	M-Al	M-Ti	M-Fe	M-Mn	M-Mg	I-Ca	I-Na	I-K	Fe/(Fe+Mg)
MWD099-124A	099-124A-P2-005	Ms-AlCel	48.9	0.1	29.8	2.5	0.1	2.7	0.0	0.2	9.9	--	--	94.1	6.58	1.42	3.32	0.01	0.28	0.01	0.54	0.00	0.06	1.69	0.34
MWD099-124A	099-124A-P2-006	Ms-AlCel	50.6	0.1	30.6	2.4	0.1	2.7	0.0	0.1	8.1	--	--	94.6	6.67	1.33	3.43	0.01	0.27	0.01	0.53	0.00	0.03	1.36	0.34
MWD099-124A	099-124A-P2-007	Ms-AlCel	49.1	0.2	29.4	2.7	0.1	2.7	0.0	0.2	9.6	--	--	93.9	6.62	1.38	3.30	0.02	0.30	0.01	0.54	0.00	0.04	1.65	0.36
MWD099-124A	099-124A-P2-008	Ms-AlCel	48.9	0.5	29.8	2.2	0.1	2.4	0.0	0.1	9.1	--	--	93.1	6.61	1.39	3.36	0.05	0.24	0.01	0.49	0.00	0.04	1.56	0.33
MWD099-124A	099-124A-P2-009	Ms-AlCel	49.3	0.0	30.1	2.0	0.1	2.5	0.0	0.2	9.6	--	--	93.7	6.64	1.36	3.40	0.00	0.22	0.01	0.49	0.00	0.05	1.65	0.31
MWD099-124A	099-124A-P2-010	Ms-AlCel	49.1	0.2	29.3	2.6	0.1	2.8	0.0	0.2	9.6	--	--	93.8	6.63	1.37	3.29	0.02	0.29	0.01	0.56	0.00	0.05	1.65	0.34
MWD099-124A	099-124A-P2-011	Ms-AlCel	49.5	0.1	29.4	2.6	0.1	2.7	0.0	0.2	9.4	--	--	94.1	6.65	1.35	3.32	0.01	0.29	0.01	0.54	0.00	0.06	1.61	0.35
MWD119-128A	119-128A-P5-001	Phl-Ann	40.3	0.1	14.9	15.3	0.3	14.5	0.0	0.1	9.0	--	--	94.4	6.01	1.99	0.63	0.01	1.91	0.04	3.21	0.00	0.03	1.70	0.37
MWD119-128A	119-128A-P5-002	Phl-Ann	40.9	0.1	14.3	14.3	0.4	14.2	0.1	0.1	8.9	--	--	93.2	6.15	1.85	0.68	0.01	1.80	0.05	3.17	0.01	0.03	1.70	0.36
MWD119-128A	119-128A-P5-003	Phl-Ann	37.9	0.1	17.2	15.9	0.4	13.6	0.0	0.1	8.7	--	--	93.8	5.72	2.28	0.78	0.01	2.01	0.05	3.05	0.01	0.02	1.67	0.40
MWD119-128A	119-128A-P5-004	Phl-Ann	40.5	0.1	14.7	14.2	0.3	14.2	0.0	0.1	9.0	--	--	93.2	6.08	1.92	0.69	0.01	1.79	0.04	3.19	0.00	0.02	1.73	0.36
MWD119-128A	119-128A-P5-005	Phl-Ann	40.9	0.1	13.8	14.5	0.4	14.1	0.0	0.1	9.0	--	--	92.9	6.18	1.82	0.63	0.01	1.83	0.05	3.18	0.00	0.02	1.74	0.37
MWD124-130.5A	124-130-5A-P1-4	Ms-AlCel	49.5	0.0	30.8	1.0	0.1	2.2	0.0	0.2	8.8	--	--	92.5	6.66	1.34	3.55	0.00	0.11	0.01	0.43	0.01	0.05	1.52	0.21
MWD124-130.5A	124-130-5A-P3-3	Ms-AlCel	48.7	0.0	33.5	0.7	0.0	1.4	0.1	0.3	8.7	--	--	93.4	6.48	1.52	3.74	0.00	0.08	0.00	0.28	0.01	0.08	1.48	0.21
MWD124-130.5A	124-130-5A-P3-4	Ms-AlCel	49.0	0.0	31.3	1.8	0.1	1.6	0.0	0.3	8.9	--	--	92.9	6.60	1.40	3.57	0.00	0.20	0.01	0.33	0.01	0.07	1.52	0.38
MWD124-266A	124-266A-P2-005	Phl-Ann	37.7	0.4	15.2	16.8	0.5	12.8	0.1	0.0	6.9	--	--	90.5	5.88	2.12	0.68	0.05	2.19	0.07	2.97	0.02	0.01	1.38	0.42
GT004-094A	004-094A-P1_1	Phl-Ann	39.6	0.6	16.2	15.9	0.4	12.4	0.0	0.1	8.8	1.2	0.0	95.2	5.95	2.05	0.81	0.07	1.99	0.05	2.77	0.00	0.02	1.68	0.42
GT004-094A	004-094A-P1_2	Phl-Ann	38.7	0.8	15.7	16.8	0.4	12.5	0.0	0.1	9.5	1.2	0.0	95.8	5.84	2.16	0.64	0.09	2.13	0.05	2.82	0.00	0.02	1.84	0.43
GT004-094A	004-094A-P2_6	Phl-Ann	38.7	0.9	15.6	16.5	0.4	12.9	0.0	0.1	9.5	1.4	0.0	96.0	5.84	2.16	0.61	0.11	2.09	0.05	2.89	0.00	0.02	1.83	0.42
MWD005-067B	005-067B-P2_3	Ms-AlCel	47.7	0.3	30.3	2.6	0.1	2.6	0.0	0.3	10.6	0.4	0.0	94.8	6.46	1.54	3.30	0.03	0.29	0.01	0.51	0.00	0.08	1.83	0.36
MWD005-067B	005-067B-P2_4	Phl-Ann	37.5	0.3	16.2	17.3	0.6	13.4	0.0	0.1	8.9	1.5	0.0	95.8	5.70	2.30	0.60	0.04	2.19	0.08	3.02	0.01	0.02	1.72	0.42
MWD099-054C	099-054C-P1_1	Phl-Ann	40.4	0.6	14.7	12.4	0.6	16.8	0.1	0.1	9.8	2.7	0.0	98.1	5.93	2.07	0.47	0.07	1.52	0.07	3.67	0.01	0.02	1.84	0.29
MWD099-054C	099-054C-P1_3	Phl-Ann	40.2	0.7	14.5	13.0	0.5	15.2	0.0	0.0	9.7	2.9	0.0	96.7	6.01	1.99	0.55	0.07	1.62	0.07	3.39	0.00	0.01	1.85	0.32
MWD099-054C	099-054C-P2_5	Phl-Ann	40.9	0.3	14.2	14.0	0.4	15.5	0.0	0.0	9.4	2.3	0.0	97.1	6.06	1.94	0.54	0.04	1.73	0.05	3.42	0.01	0.01	1.77	0.34
MWD122-289B	122-289B-P1_5	Phl-Ann	37.7	0.3	16.3	16.3	0.5	13.3	0.0	0.1	9.5	1.4	0.0	95.2	5.73	2.27	0.66	0.03	2.07	0.06	3.01	0.00	0.02	1.85	0.41
MWD122-289B	122-289B-P1_6	Phl-Ann	40.0	0.5	14.6	14.3	0.4	14.5	0.1	0.1	9.4	2.1	0.0	95.9	6.00	2.00	0.59	0.05	1.79	0.05	3.25	0.01	0.02	1.80	0.35
MWD122-289B	122-289B-P1_7	Phl-Ann	38.3	0.5	16.6	16.9	0.5	12.4	0.1	0.1	9.5	0.8	0.0	95.7	5.77	2.23	0.73	0.06	2.12	0.06	2.78	0.02	0.02	1.82	0.43
MWD122-289B	122-289B-P3_4		36.6	0.3	31.1	8.4	0.1	7.0	1.1	2.2	0.0	0.0	0.0	86.8	5.39	2.61	2.78	0.03	1.03	0.02	1.54	0.18	0.61	0.00	0.40
MWD122-289C	122-289C-P1_3	Phl-Ann	39.6	0.7	14.8	16.7	0.5	13.1	0.1	0.0	9.4	2.1	0.0	96.8	5.95	2.05	0.57	0.08	2.10	0.06	2.93	0.01	0.01	1.81	0.42
MWD122-289C	122-289C-P1_4	Phl-Ann	35.6	0.5	15.6	20.0	0.6	12.9	0.2	0.0	6.8	1.1	0.0	93.3	5.57	2.43	0.45	0.06	2.62	0.08	3.01	0.04	0.00	1.36	0.46
MWD122-289C	122-289C-P1_7	Phl-Ann	39.4	0.6	15.0	17.0	0.4	13.0	0.1	0.1	9.3	2.1	0.0	97.1	5.92	2.08	0.58	0.07	2.14	0.06	2.92	0.01	0.02	1.79	0.42
MWD122-289C	22-289C-P3-11	Phl-Ann	38.1	0.5	15.4	15.7	0.5	14.7	0.2	0.1	7.7	1.6	0.0	94.3	5.79	2.21	0.55	0.05	2.00	0.06	3.33	0.03	0.02	1.50	0.38

Appendix 2.3.5: Mica EPMA data from the Watershed tungsten deposit continued

			Major oxides, weight percent											Number of ions on the basis of 20 oxygen atoms										
Sample	Spot	Mica group[1]	SiO_2	TiO_2	Al_2O_3	FeO	MnO	MgO	CaO	Na_2O	K_2O	F	Cl	Total	T-Si	T-Al	M-Al	M-Ti	M-Fe	M-Mn	M-Mg	I-Ca	I-Na	I-K	Fe/(Fe+Mg)
MWD122-289C	122-289C-P3-9	Phl-Ann	40.9	0.6	15.4	14.5	0.4	13.6	0.0	0.1	9.4	1.0	0.0	95.9	6.06	1.94	0.73	0.07	1.80	0.05	2.99	0.01	0.03	1.77	0.38
GT004-094A	004-094A-P1_4	Ms-AlCel	47.5	0.0	33.7	1.5	0.0	0.7	0.0	0.3	10.7	0.2	0.0	94.7	6.38	1.62	3.70	0.00	0.16	0.00	0.14	0.00	0.08	1.84	0.54
GT004-094A	004-094A-P2_5	Ms-AlCel	47.4	0.0	35.2	1.2	0.1	0.3	0.0	0.4	10.2	0.4	0.0	95.1	6.30	1.70	3.82	0.00	0.13	0.01	0.07	0.00	0.09	1.73	0.66
MWD005-067B	005-067B-P1_4	Ms-AlCel	49.2	0.1	30.1	1.7	0.0	2.5	0.0	0.2	10.7	0.5	0.0	95.0	6.60	1.40	3.37	0.01	0.19	0.00	0.49	0.00	0.06	1.83	0.28
MWD005-067B	005-067B-P2_5	Phl-Ann	37.7	1.1	16.1	16.8	0.6	12.0	0.0	0.1	9.1	1.4	0.0	95.0	5.76	2.24	0.66	0.13	2.15	0.07	2.74	0.01	0.03	1.78	0.44
MWD099-054C	099-054C-P1_2	Ms-AlCel	48.6	0.1	30.3	2.1	0.0	2.6	0.0	0.2	10.8	0.5	0.0	95.3	6.53	1.47	3.33	0.01	0.24	0.00	0.52	0.00	0.04	1.86	0.31
MWD099-054C	099-054C-P2_3	Ms-AlCel	48.9	0.0	30.4	1.8	0.1	2.6	0.0	0.2	10.9	0.5	0.0	95.4	6.55	1.45	3.35	0.00	0.20	0.01	0.53	0.00	0.05	1.86	0.28
MWD099-054C	099-054C-P3_12	Ms-AlCel	49.9	0.0	29.9	1.0	0.0	3.1	0.0	0.1	10.8	0.9	0.0	95.7	6.64	1.36	3.35	0.00	0.11	0.00	0.61	0.00	0.04	1.83	0.15
MWD099-054C	099-054C-P3_5	Ms-AlCel	50.6	0.0	29.6	1.0	0.0	2.7	0.4	1.0	10.5	0.5	0.0	96.4	6.68	1.32	3.29	0.00	0.11	0.01	0.52	0.06	0.27	1.76	0.17
MWD099-124C	099-124C-P1_1	Ms-AlCel	48.0	0.2	30.8	2.5	0.1	2.2	0.0	0.2	10.5	0.0	0.0	94.5	6.48	1.52	3.37	0.02	0.28	0.01	0.44	0.00	0.06	1.81	0.39
MWD099-124C	099-124C-P1_2	Ms-AlCel	46.6	0.2	29.9	3.6	0.1	2.7	0.0	0.3	10.4	0.0	0.0	93.7	6.40	1.60	3.23	0.02	0.41	0.01	0.54	0.00	0.07	1.83	0.43
MWD099-124C	099-124C-P1_3	Ms-AlCel	48.2	0.2	29.9	2.6	0.1	2.6	0.0	0.2	10.7	0.5	0.0	94.9	6.52	1.48	3.28	0.02	0.29	0.01	0.53	0.00	0.05	1.84	0.35
MWD099-124C	099-124C-P2_1	Ms-AlCel	47.1	0.2	30.3	3.2	0.1	2.4	0.0	0.2	10.6	0.6	0.0	94.8	6.42	1.58	3.29	0.02	0.36	0.02	0.49	0.00	0.05	1.83	0.43
MWD101-149C	101-149C-P1_1	Phl-Ann	41.6	0.3	14.4	13.2	0.4	15.3	0.0	0.1	9.4	2.1	0.0	96.6	6.14	1.86	0.63	0.03	1.63	0.05	3.36	0.01	0.01	1.77	0.33
MWD101-149C	101-149C-P1_2	Ms-AlCel	48.5	0.1	29.6	2.7	0.1	2.8	0.0	0.2	10.2	0.8	0.0	94.9	6.56	1.44	3.28	0.01	0.30	0.01	0.57	0.00	0.06	1.76	0.35
MWD122-289B	122-289B-P2_15	Ms-AlCel	48.5	0.0	30.0	2.2	0.0	1.8	0.3	0.6	9.8	0.5	0.0	93.8	6.59	1.41	3.40	0.00	0.25	0.01	0.37	0.04	0.16	1.71	0.40
MWD122-289B	122-289B-P2_22	Ms-AlCel	48.8	0.0	30.9	2.1	0.1	2.0	0.1	0.2	10.8	0.1	0.0	95.1	6.53	1.47	3.41	0.00	0.24	0.01	0.41	0.01	0.06	1.84	0.37
MWD122-289C	122-289C-P2-13	Ms-AlCel	48.6	0.0	30.9	2.5	0.0	2.2	0.0	0.2	10.6	0.7	0.0	95.8	6.51	1.49	3.39	0.00	0.28	0.00	0.44	0.01	0.05	1.81	0.39
MWD122-289C	122-289C-P2-14	Ms-AlCel	48.4	0.0	30.0	2.8	0.1	2.2	0.0	0.2	10.2	0.6	0.0	94.4	6.57	1.43	3.37	0.00	0.31	0.01	0.44	0.00	0.05	1.76	0.42
MWD122-289C	122-289C-P3-10	Ms-AlCel	48.8	0.4	30.4	2.3	0.1	2.3	0.0	0.2	10.2	0.4	0.0	94.9	6.54	1.46	3.35	0.04	0.26	0.01	0.45	0.00	0.04	1.74	0.36
MWD122-289C	122-289C-P3-12	Ms-AlCel	47.8	0.2	31.0	2.7	0.1	2.2	0.0	0.2	10.1	0.2	0.0	94.4	6.45	1.55	3.39	0.02	0.30	0.01	0.44	0.00	0.05	1.73	0.41
MWD122-289C	122-289C-P3-4	Ms-AlCel	49.4	0.0	30.2	1.9	0.1	1.8	0.0	0.2	10.2	0.2	0.0	94.1	6.65	1.35	3.45	0.00	0.21	0.01	0.37	0.00	0.05	1.75	0.36
MWD122-289C	122-289C-P3-8	Ms-AlCel	48.8	0.0	30.8	1.9	0.0	2.1	0.0	0.2	10.2	0.6	0.0	94.7	6.56	1.44	3.44	0.00	0.21	0.00	0.43	0.01	0.05	1.74	0.33

[1]Mineral abbreviations: AlCel: aluminoceladonite, Ann: annite, Ms: muscovite, Phl: phlogopite. After Whitney and Evans (2010)

Appendix 2.3.6: Amphibole EPMA data from the Watershed tungsten deposit

Spot	Amp group[1]	Def. event	Major oxides, weight percent										Number of ions on the basis of 23 oxygen atoms												Mg / (Mg+Fe)
			SiO_2	TiO_2	Al_2O_3	FeO	MnO	MgO	CaO	Na_2O	K_2O	Total	T-Si	T-Al	C-Al	C-Ti	C-Fe^{3+}	C-Mg	C-Fe^{2+}	C-Mn	B-Ca	B-Na	A-Na	A-K	Total	
Sample MWD099-081B																									
099-81B-P1-8	Act	D_{1-2}	51.5	0.0	4.1	15.5	0.7	12.7	12.2	0.4	0.3	97.4	7.54	0.46	0.24	0.00	0.19	2.77	1.71	0.08	1.92	0.08	0.04	0.05	15.09	0.62
099-81B-P2-17	Act	D_{1-2}	51.8	0.0	3.4	16.8	0.7	11.5	12.1	0.4	0.2	96.7	7.69	0.31	0.28	0.00	0.04	2.55	2.04	0.09	1.92	0.08	0.03	0.04	15.06	0.56
099-81B-P4-5	Act	D_{1-2}	52.1	0.0	2.9	13.8	0.7	13.9	12.5	0.4	0.2	96.5	7.67	0.33	0.17	0.00	0.09	3.04	1.60	0.09	1.96	0.04	0.07	0.03	15.10	0.65
099-81B-P4-6	Act	D_{1-2}	51.5	0.0	4.7	15.1	0.8	12.2	12.3	0.6	0.3	97.4	7.56	0.44	0.38	0.00	0.00	2.67	1.86	0.09	1.93	0.07	0.09	0.06	15.14	0.59
099-81B-P5-2	Mhb	D_{1-2}	49.1	0.0	6.3	17.0	0.7	11.1	12.4	0.7	0.5	97.8	7.27	0.73	0.36	0.00	0.15	2.45	1.95	0.09	1.97	0.03	0.16	0.09	15.25	0.56
099-81B-P5-3	Act	D_{1-2}	54.0	0.0	2.1	16.0	0.8	12.9	12.5	0.3	0.1	98.8	7.82	0.18	0.18	0.00	0.01	2.79	1.93	0.09	1.94	0.06	0.03	0.02	15.05	0.59
099-81B-P5-4	Act	D_{1-2}	52.2	0.0	3.4	14.8	0.7	13.7	12.6	0.4	0.2	98.2	7.57	0.43	0.15	0.00	0.18	2.96	1.62	0.09	1.96	0.04	0.08	0.04	15.13	0.65
099-81B-P5-5	Act	D_{1-2}	53.5	0.0	2.9	13.5	0.7	13.9	12.4	0.4	0.2	97.5	7.76	0.24	0.26	0.00	0.00	3.00	1.63	0.09	1.93	0.07	0.04	0.04	15.06	0.65
Sample MWD101-100A																									
101-100A-P4-1	Act	D_4	52.4	0.0	3.1	18.1	0.5	11.7	12.2	0.3	0.1	98.4	7.65	0.35	0.18	0.00	0.23	2.56	1.98	0.06	1.92	0.08	0.01	0.02	15.03	0.56
101-100A-P4-4	Act	D_4	52.5	0.0	3.1	18.2	0.5	11.0	12.2	0.3	0.1	97.8	7.74	0.26	0.28	0.00	0.03	2.42	2.21	0.06	1.93	0.07	0.01	0.02	15.03	0.52
101-100A-P4-5	Fac	D_4	51.0	0.0	3.4	20.0	0.8	10.1	12.4	0.3	0.2	98.2	7.59	0.41	0.19	0.00	0.14	2.23	2.34	0.10	1.98	0.02	0.07	0.03	15.10	0.49
Sample MWD101-159A																									
101-159A-P2-1	Act	D_{1-2}	54.5	0.0	3.0	10.6	0.8	16.6	13.1	0.4	0.2	99.1	7.67	0.33	0.17	0.00	0.06	3.49	1.19	0.10	1.98	0.02	0.09	0.03	15.12	0.74
101-159A-P2-2	Act	D_{1-2}	54.3	0.0	2.7	11.9	0.7	16.0	13.2	0.4	0.2	99.3	7.69	0.31	0.13	0.00	0.05	3.37	1.36	0.09	2.00	0.00	0.10	0.03	15.12	0.71
Sample MWD101-211.5A																									
101-211.5A-P1-3	Act	D_{1-2}	51.9	0.0	4.0	11.8	0.8	14.3	12.5	0.6	0.2	96.1	7.61	0.39	0.30	0.00	0.00	3.13	1.44	0.10	1.96	0.04	0.12	0.04	15.14	0.68
101-211.5A-P1-5	Act	D_{1-2}	52.6	0.1	3.5	11.1	0.7	15.4	12.9	0.4	0.2	96.9	7.62	0.38	0.22	0.01	0.00	3.34	1.35	0.09	1.99	0.01	0.12	0.04	15.15	0.71
101-211.5A-P2-1	Act	D_{1-2}	53.5	0.0	2.1	12.4	0.9	15.0	12.7	0.3	0.1	97.1	7.77	0.23	0.13	0.00	0.03	3.25	1.48	0.12	1.98	0.02	0.07	0.02	15.09	0.69
Sample MWD105-115A																									
105-115A-P1-11	Act	D_{1-2}	53.0	0.0	3.1	15.9	0.9	12.3	12.3	0.3	0.1	97.9	7.74	0.26	0.27	0.00	0.02	2.68	1.91	0.11	1.92	0.08	0.01	0.02	15.03	0.58
Sample MWD105-206B																									
105-206B-P1-2	Act	D_{1-2}	53.7	0.0	2.0	18.2	0.8	12.0	12.9	0.2	0.1	99.7	7.78	0.22	0.12	0.00	0.02	2.58	2.19	0.09	2.00	0.00	0.06	0.03	15.09	0.54
Sample MWD119-126A																									
119-126A-P1-5	Act	D_{1-2}	52.4	0.0	2.9	15.8	1.0	12.9	11.8	0.2	0.1	97.2	7.64	0.36	0.15	0.00	0.43	2.80	1.50	0.12	1.84	0.06	0.00	0.02	14.93	0.65
119-126A-P1-6	Act	D_{1-2}	52.4	0.0	2.6	16.9	1.1	11.8	12.5	0.3	0.2	97.6	7.74	0.26	0.18	0.00	0.01	2.60	2.08	0.13	1.98	0.02	0.06	0.03	15.09	0.56
119-126A-P2-1	Fts	D_4	43.3	0.2	12.8	19.6	0.9	7.5	12.1	1.1	1.3	98.7	6.48	1.52	0.74	0.02	0.30	1.68	2.14	0.11	1.94	0.06	0.25	0.25	15.49	0.44
119-126A-P2-2	Fed	D_4	42.8	0.3	12.2	20.0	0.7	6.8	11.6	1.2	1.3	96.8	6.56	1.44	0.76	0.04	0.20	1.56	2.36	0.09	1.90	0.10	0.26	0.24	15.51	0.40

Appendix 2.3.6: Amphibole EPMA data from the Watershed tungsten deposit continued

Spot	Amp group[1]	Def. event	Major oxides, weight percent										Number of ions on the basis of 23 oxygen atoms												Mg / (Mg+Fe)
			SiO_2	TiO_2	Al_2O_3	FeO	MnO	MgO	CaO	Na_2O	K_2O	Total	T-Si	T-Al	C-Al	C-Ti	C-Fe^{3+}	C-Mg	C-Fe^{2+}	C-Mn	B-Ca	B-Na	A-Na	A-K	Total	
Sample MWD119-126A continued																									
119-126A-P2-3	Mhb	D_4	50.7	0.1	5.8	17.4	1.0	11.3	12.3	0.7	0.4	99.5	7.34	0.66	0.32	0.01	0.27	2.44	1.84	0.12	1.90	0.10	0.09	0.07	15.16	0.57
119-126A-P2-4	Fprg	D_4	42.5	0.1	12.7	21.1	0.7	6.3	11.5	1.4	1.3	97.6	6.50	1.50	0.77	0.01	0.28	1.43	2.42	0.09	1.87	0.13	0.30	0.26	15.56	0.37
119-126A-P3-5	Act	D_{1-2}	52.4	0.0	2.8	18.5	1.3	10.8	12.3	0.3	0.1	98.5	7.71	0.29	0.19	0.00	0.10	2.37	2.17	0.16	1.94	0.06	0.03	0.02	15.05	0.52
119-126A-P3-6	Fts	D_{1-2}	43.1	0.0	13.2	20.2	1.0	7.0	11.3	0.9	0.8	97.5	6.44	1.56	0.77	0.00	0.76	1.56	1.77	0.13	1.80	0.20	0.06	0.15	15.21	0.47
119-126A-P3-7	Act	D_{1-2}	54.0	0.0	1.8	16.8	1.1	12.6	12.5	0.1	0.1	99.1	7.80	0.20	0.11	0.01	0.15	2.72	1.87	0.14	1.93	0.04	0.00	0.02	14.99	0.59
119-126A-P4-1	Fe-Hbl	D_4	44.8	0.1	10.1	20.0	0.6	7.5	11.9	1.0	1.1	97.0	6.84	1.16	0.65	0.01	0.10	1.71	2.46	0.07	1.94	0.06	0.23	0.21	15.45	0.41
119-126A-P4-2	Fprg	D_4	41.3	0.4	13.2	22.8	0.5	5.1	11.5	1.1	1.9	97.7	6.37	1.63	0.77	0.04	0.28	1.18	2.67	0.07	1.91	0.09	0.23	0.36	15.59	0.31
119-126A-P4-3	Fprg	D_4	41.1	0.2	13.2	21.8	0.7	5.2	11.9	1.2	1.8	97.1	6.40	1.60	0.82	0.02	0.05	1.22	2.79	0.10	1.98	0.02	0.35	0.35	15.70	0.30
119-126A-P4-4	Fed	D_4	42.5	0.2	11.9	23.0	0.5	5.1	11.9	1.2	1.4	97.7	6.58	1.42	0.75	0.02	0.07	1.18	2.91	0.07	1.97	0.03	0.31	0.28	15.59	0.29
119-126A-P4-5	Fprg	D_4	41.8	0.1	12.8	23.4	0.5	5.1	12.0	1.2	1.4	98.3	6.43	1.57	0.75	0.01	0.19	1.16	2.82	0.07	1.98	0.02	0.35	0.28	15.63	0.29
119-126A-P4-6	Fe-Hbl	D_4	46.2	0.1	8.7	20.1	0.6	8.5	12.1	0.9	1.2	98.3	6.94	1.06	0.48	0.01	0.18	1.91	2.34	0.07	1.95	0.05	0.21	0.22	15.43	0.45
Sample MWD124-130.5A																									
124-130.5A-P3-7A	Mhb	D_4	50.4	0.1	5.2	15.1	1.1	11.9	12.3	0.4	0.3	96.7	7.45	0.55	0.36	0.01	0.12	2.62	1.75	0.14	1.95	0.05	0.05	0.05	15.11	0.60
124-130.5A-P3-7B	Act	D_4	52.0	0.1	2.9	15.9	1.4	12.3	12.1	0.2	0.3	97.1	7.66	0.34	0.16	0.01	0.23	2.70	1.72	0.17	1.90	0.07	0.00	0.05	15.02	0.61
124-130.5A-P3-8	Mhb	D_4	51.5	0.0	4.5	12.9	0.9	14.3	12.6	0.4	0.2	97.3	7.46	0.54	0.23	0.00	0.22	3.09	1.35	0.11	1.96	0.04	0.08	0.03	15.12	0.70
Sample MWD005-128A																									
005-128A-P1_11	Fac	D_4	53.1	0.0	1.2	20.5	1.1	10.2	12.6	0.1	0.1	99.9	7.86	0.14	0.07	0.00	0.03	2.26	2.51	0.14	1.99	0.01	0.04	0.01	15.05	0.47

[1]Mineral abbreviations: Amp: amphibole, Act: actinolite, Fac: ferro-actinolite, Fed: ferro-edenite, Fe-Hbl: ferrohornblende, Fprg: ferropargasite, Fts: ferrotschermakite, Mhb: magnesiohornblende. After Whitney and Evans (2010)

Appendix 2.4: Whole-rock geochemistry of intrusive rocks

Sample_ID	WS16-002	MWD005-067	MWD013-099	WS15-001	WS15-005	WS15-017
Rock_type	Diorite	Monzonitic dyke	Monzonitic dyke	Granitic dyke	Koobaba granite	Granitic dyke
Type	Rock	Drill Core	Drill Core	Rock	Rock	Rock
SiO2_%	62.9	52.06	35.62	75.37	73.2	78.58
Al2O3_%	14.51	20.21	15.67	14.4	13.72	13.24
Fe2O3_%	6.19	2.95	1.37	0.83	2.23	0.5
MgO_%	4.97	0.67	0.19	0.08	0.35	0.04
CaO_%	5.15	6.44	12.08	0.34	2.5	0.88
Na2O_%	1.96	6.55	3.98	3.15	2.57	5.75
K2O_%	2.28	1.56	0.62	4.65	3.94	0.3
TiO2_%	0.57	0.32	0.33	0.03	0.26	<0.01
P2O5_%	0.1	0.14	0.35	0.02	0.06	0.02
MnO_%	0.1	0.07	0.03	0.01	0.03	<0.01
Cr2O3_%	0.045	0.004	0.002	<0.002	<0.002	<0.002
Sum_%	99.83	93.32	72	99.97	99.92	100
Ba_ppm	312	228	109	85	759	60
Sc_ppm	19	29	62	5	5	3
Cs_ppm	55.4	23.6	9.1	8.5	3.1	1.1
Ga_ppm	15.8	21.2	14	21	15.4	13.1
Hf_ppm	4.1	3.5	3.5	2.7	5.7	2.1
Nb_ppm	7.8	14.6	19.7	12.2	7.6	3
Rb_ppm	129.3	111.5	40.1	237.8	116.8	13.5
Sn_ppm	5	50	43	12	2	6
Sr_ppm	155.4	428.1	453.2	45.8	141.7	108.1
Ta_ppm	0.7	1.1	0.7	1.9	0.5	1.5
Th_ppm	10	12.8	10.8	9.9	19.9	10.8
U_ppm	1.9	2.9	3.5	4.1	2.6	4.5
V_ppm	113	25	<8	<8	17	9
W_ppm	1.4	>10000	>10000	14.8	4.6	6
Zr_ppm	132.8	129.2	132.5	52.2	195.4	26.4
Y_ppm	22.2	19.9	25	22.8	26.7	14.6
La_ppm	25.2	27.8	29.8	8.3	42.9	3.4
Ce_ppm	50	54.3	54	16.5	85.8	9
Pr_ppm	6.09	6.39	6.36	2.07	10.03	1.22
Nd_ppm	23.2	22.6	23.8	8	37.6	4.3
Sm_ppm	4.48	3.95	4.14	2.27	6.8	2
Eu_ppm	0.97	0.73	1.06	0.09	1.24	0.08
Gd_ppm	4.27	3.78	4.42	3.26	6.09	2.24
Tb_ppm	0.67	0.59	0.65	0.71	0.87	0.51
Dy_ppm	3.99	3.24	3.93	4.4	4.91	3.01
Ho_ppm	0.8	0.68	0.79	0.81	0.98	0.47
Er_ppm	2.35	2.28	2.39	2.19	2.86	0.98
Tm_ppm	0.32	0.29	0.36	0.3	0.39	0.15
Yb_ppm	2.11	1.82	2.64	1.88	2.55	0.88
Lu_ppm	0.33	0.27	0.46	0.26	0.4	0.08
Ni_ppm	34	<10	<10	<10	<10	<10
LOI_%	1	2.3	1.8	1.1	1	0.7
TOT/C_%	0.02	0.33	0.14	0.03	0.14	0.05
TOT/S_%	0.09	0.88	0.23	<0.01	<0.01	<0.01
Mo_ppm	0.6	1.91	4.34	0.18	0.66	1.4
Cu_ppm	26.1	125.55	46.64	1.2	12.44	12.56
Pb_ppm	7.32	3.93	4.87	5.81	10.31	3.33
Zn_ppm	56.4	49.4	32.7	2.7	41.7	5.3
Ag_ppb	53	114	39	86	36	391
Ni_ppm	32.9	7.3	6.2	0.5	3.2	0.8
Co_ppm	18.1	3.2	4.7	<0.1	3.6	0.3
Mn_ppm	453	400	161	35	202	14

Appendix 2.4: Whole-rock geochemistry of intrusive rocks continued

Sample_ID	WS16-002	MWD005-067	MWD013-099	WS15-001	WS15-005	WS15-017
Rock_type	Diorite	Monzonitic dyke	Monzonitic dyke	Granitic dyke	Koobaba granite	Granitic dyke
Type	Rock	Drill Core	Drill Core	Rock	Rock	Rock
As_ppm	1.7	0.1	8.3	14.7	3.7	3.1
Au_ppb	<0.2	0.5	2.6	2.1	<0.2	2.7
Cd_ppm	0.04	0.64	0.26	0.02	0.06	<0.01
Sb_ppm	0.02	<0.02	<0.02	0.06	0.09	<0.02
Bi_ppm	0.19	0.13	0.05	1.23	0.27	2.52
Cr_ppm	235.8	10.4	12.3	1.8	5.3	2
B_ppm	<1	3	3	<1	<1	<1
Tl_ppm	0.66	0.14	0.13	0.09	0.22	<0.02
Hg_ppb	<5	<5	*	<5	<5	<5
Se_ppm	<0.1	<0.1	<0.1	<0.1	<0.1	0.9
Te_ppm	<0.02	<0.02	<0.02	0.05	<0.02	0.05
Ge_ppm	0.1	<0.1	<0.1	<0.1	<0.1	<0.1
In_ppm	<0.02	<0.02	<0.02	<0.02	0.02	<0.02
Re_ppb	<1	3	11	<1	<1	<1
Be_ppm	0.2	4.4	16.9	0.4	<0.1	0.3
Li_ppm	87.7	23.9	18.3	4	17.4	0.3
Pd_ppb	<10	<10	<10	<10	<10	<10
Pt_ppb	<2	<2	<2	<2	<2	<2
F_ppm	592	1265	976	123	212	19
FeO_%	5.14	2.52	1.03	0.45	1.61	0.29
W_%	N.A.	4.752	21.118	N.A.	N.A.	N.A.

Appendix 2.5: LA-ICP-MS U/Pb zircon dating data and CL imaging

	Age estimates with 2 sigma uncertainty (Ma)								Isotopic Ratios with absolute errors								Concentrations ppm		
	$^{207}Pb/^{206}Pb$		$^{207}Pb/^{235}U$		$^{206}Pb/^{238}U$		Preferred Age		$^{207}Pb/^{206}Pb$		$^{207}Pb/^{235}U$		$^{206}Pb/^{238}U$			U/Th			
Analysis	Ma	± 2s Error	Ma	± 2s Error	Ma	± 2s Error	Ma *	± 2s Error	Ratio	± 1s Error	Ratio	± 1s Error	Ratio	± 1s Error	rho	Ratio	U	Th	Pb
WS15-001 - East Dyke																			
1	721.7	66.9	282.7	9.2	237.5	5.0	233.8	5.0	0.06340	0.00100	0.32100	0.00600	0.03753	0.00040	0.57	0.84	604	860	448
2	320.2	86.1	283.4	9.2	290.5	4.6	290.2	4.6	0.05280	0.00100	0.32200	0.00600	0.04609	0.00037	0.43	1.04	320	310	229
3	358.5	197.5	264.8	18.6	285.0	8.0	284.4	8.2	0.05370	0.00235	0.29800	0.01200	0.04520	0.00065	0.36	1.09	124.6	115.6	83.4
4	440.4	99.9	304.0	12.7	320.0	6.7	318.9	6.9	0.05570	0.00125	0.34900	0.00850	0.05090	0.00055	0.44	1.43	346	241	233
5	320.2	107.6	253.0	10.2	292.4	6.8	292.2	6.9	0.05280	0.00125	0.28300	0.00650	0.04640	0.00055	0.52	1.12	249	227	183
6	337.3	93.7	241.1	8.8	278.3	5.8	277.9	5.9	0.05320	0.00110	0.26800	0.00550	0.04412	0.00047	0.52	0.73	373	522	389
7	412.2	174.8	246.7	15.8	274.5	6.8	273.4	7.0	0.05500	0.00215	0.27500	0.01000	0.04350	0.00055	0.35	1.10	200	195	142
8	420.3	186.1	245.9	20.5	270.2	8.6	269.0	8.8	0.05520	0.00230	0.27400	0.01300	0.04280	0.00070	0.34	0.92	231	252	186
9	311.6	164.4	246.7	16.6	289.9	8.6	289.7	8.8	0.05260	0.00190	0.27500	0.01050	0.04600	0.00070	0.40	1.02	138.6	137.8	114.3
10	416.3	129.8	249.9	11.1	274.5	8.0	273.4	8.1	0.05510	0.00160	0.27900	0.00700	0.04350	0.00065	0.60	1.17	257	223	139
11	320.2	94.7	264.1	8.6	288.5	4.9	288.2	5.0	0.05280	0.00110	0.29700	0.00550	0.04577	0.00040	0.47	1.03	222	227	175.1
12	311.6	90.9	277.3	10.0	292.9	3.6	292.8	3.7	0.05260	0.00105	0.31400	0.00650	0.04649	0.00029	0.30	1.16	212.6	188.3	157.1
13	302.9	108.8	319.7	14.0	297.0	4.1	297.0	4.2	0.05240	0.00125	0.37000	0.00950	0.04715	0.00033	0.27	1.17	180.4	154.4	128.5
14	320.2	86.1	283.4	9.2	266.5	8.0	266.1	8.1	0.05280	0.00100	0.32200	0.00600	0.04220	0.00065	0.83	0.88	195.5	228	138
15	333.1	170.8	307.7	20.0	282.2	5.8	281.8	6.0	0.05310	0.00200	0.35400	0.01350	0.04475	0.00047	0.28	1.00	181	181	131
16	395.9	69.8	291.9	9.9	286.8	7.4	285.9	7.5	0.05460	0.00085	0.33300	0.00650	0.04550	0.00060	0.68	0.79	429	680	389
17	333.1	93.9	277.3	10.0	279.1	4.7	278.6	4.8	0.05310	0.00110	0.31400	0.00650	0.04424	0.00038	0.41	0.83	160	195	116.2
18	518.4	68.5	289.6	8.4	275.9	5.4	273.9	5.4	0.05770	0.00090	0.33000	0.00550	0.04373	0.00044	0.60	1.45	703	499	150
19	328.8	209.8	262.5	19.4	275.7	8.0	275.3	8.2	0.05300	0.00245	0.29500	0.01250	0.04370	0.00065	0.35	0.95	82.4	87.2	57.3
20	375.2	191.3	278.0	19.9	297.3	9.2	296.6	9.4	0.05410	0.00230	0.31500	0.01300	0.04720	0.00075	0.39	0.69	62.3	90.8	68.7
21	452.4	107.0	285.0	11.4	298.6	4.2	297.2	4.4	0.05600	0.00135	0.32400	0.00750	0.04741	0.00035	0.31	1.01	201.8	198.2	131.8
22	328.8	89.9	254.6	8.7	280.9	4.3	280.5	4.4	0.05300	0.00105	0.28500	0.00550	0.04453	0.00035	0.41	0.86	303	354	239
23	424.4	108.9	269.5	10.8	286.8	4.4	285.7	4.6	0.05530	0.00135	0.30400	0.00700	0.04550	0.00036	0.34	0.90	263	321	219
24	592.7	105.3	271.9	11.6	277.0	6.8	274.3	6.9	0.05970	0.00145	0.30700	0.00750	0.04390	0.00055	0.51	0.74	199	285	197

Appendix 2.5: LA-ICP-MS U/Pb zircon dating data and CL imaging continued

	Age estimates with 2 sigma uncertainty (Ma)								Isotopic Ratios with absolute errors								Concentrations ppm		
	$^{207}Pb/^{206}Pb$	$^{207}Pb/^{206}Pb$	$^{207}Pb/^{235}U$	$^{207}Pb/^{235}U$	$^{206}Pb/^{238}U$	$^{206}Pb/^{238}U$	Preferred Age		$^{207}Pb/^{206}Pb$	$^{207}Pb/^{206}Pb$	$^{207}Pb/^{235}U$	$^{207}Pb/^{235}U$	$^{206}Pb/^{238}U$	$^{206}Pb/^{238}U$		U/Th			
Analysis	Ma	± 2s Error	Ma	± 2s Error	Ma	± 2s Error	Ma *	± 2s Error	Ratio	± 1s Error	Ratio	± 1s Error	Ratio	± 1s Error	rho	Ratio	U	Th	Pb
WS15-017 - Camp Dyke																			
1	404.1	216.5	264.8	19.4	257.8	7.4	256.7	7.6	0.05480	0.00265	0.29800	0.01250	0.04080	0.00060	0.35	1.21	212	125.9	147
2	337.3	174.6	273.4	16.2	271.4	8.0	270.9	8.2	0.05320	0.00205	0.30900	0.01050	0.04300	0.00065	0.44	0.82	657	583	538
3	371.0	125.1	280.4	12.3	273.9	4.5	273.1	4.6	0.05400	0.00150	0.31800	0.00800	0.04340	0.00037	0.33	1.17	306	202	215
4	456.3	87.0	300.2	8.3	285.0	6.8	283.5	6.8	0.05610	0.00110	0.34400	0.00550	0.04520	0.00055	0.76	2.26	2970	1036	1063
5	298.5	135.2	274.2	13.9	275.1	6.8	274.9	6.9	0.05230	0.00155	0.31000	0.00900	0.04360	0.00055	0.43	1.37	511	312.1	296
6	341.6	165.6	278.8	16.8	274.5	7.4	274.0	7.6	0.05330	0.00195	0.31600	0.01100	0.04350	0.00060	0.40	1.21	673	687	444
7	350.1	202.8	284.2	23.5	277.6	8.6	277.0	8.8	0.05350	0.00240	0.32300	0.01550	0.04400	0.00070	0.33	1.59	563	444	255
8	610.8	172.3	321.9	18.3	284.4	8.0	281.5	8.2	0.06020	0.00240	0.37300	0.01250	0.04510	0.00065	0.43	1.48	292	255	210
9	2189.6	152.3	733.8	66.8	340.3	21.4	305.4	20.4	0.13700	0.00600	1.06000	0.07000	0.05420	0.00175	0.49	1.78	287	200	510
10	412.2	207.3	297.2	21.7	286.2	7.4	285.2	7.6	0.05500	0.00255	0.34000	0.01450	0.04540	0.00060	0.31	1.19	213.5	210.5	158.5
11	320.2	129.1	278.8	12.3	274.1	4.8	273.8	4.9	0.05280	0.00150	0.31600	0.00800	0.04344	0.00039	0.35	1.10	491	528	320
12	320.2	94.7	291.9	10.6	286.8	4.3	286.6	4.4	0.05280	0.00110	0.33300	0.00700	0.04550	0.00035	0.36	1.59	428	289	232
13	350.1	101.4	277.3	10.0	270.2	4.1	269.6	4.2	0.05350	0.00120	0.31400	0.00650	0.04281	0.00033	0.37	1.75	419	266	193.6
14	592.7	130.7	290.3	17.4	249.1	11.2	246.5	11.2	0.05970	0.00180	0.33100	0.01150	0.03940	0.00090	0.66	2.36	647	291	224
15	404.1	200.2	289.6	21.2	282.5	8.6	281.5	8.8	0.05480	0.00245	0.33000	0.01400	0.04480	0.00070	0.37	2.48	353	139	111
16	452.4	436.1	291.1	48.4	272.0	11.7	270.6	12.3	0.05600	0.00550	0.33200	0.03250	0.04310	0.00095	0.23	0.81	139.6	166.2	178
17	379.4	157.7	302.5	17.2	296.7	12.3	296.0	12.5	0.05420	0.00190	0.34700	0.01150	0.04710	0.00100	0.64	3.42	466	127	125
18	341.6	182.6	278.0	18.4	268.9	8.0	268.4	8.2	0.05330	0.00215	0.31500	0.01200	0.04260	0.00065	0.40	0.85	237	265	223
19	366.9	125.4	277.3	12.3	268.4	4.1	267.7	4.3	0.05390	0.00150	0.31400	0.00800	0.04252	0.00034	0.31	1.82	293	158	129
20	383.5	177.9	294.1	19.6	282.5	6.8	281.7	7.0	0.05430	0.00215	0.33600	0.01300	0.04480	0.00055	0.32	0.95	209.9	209.6	192.3
21	289.8	96.5	270.3	9.3	266.3	4.1	266.2	4.2	0.05210	0.00110	0.30500	0.00600	0.04218	0.00033	0.40	1.63	689	375	191
22	420.3	178.0	279.6	16.8	271.4	6.8	270.2	7.0	0.05520	0.00220	0.31700	0.01100	0.04300	0.00055	0.37	1.39	167	120	105
23	495.4	193.0	289.6	21.9	268.9	6.8	267.1	7.0	0.05710	0.00250	0.33000	0.01450	0.04260	0.00055	0.29	1.12	90.3	80.2	68.6
24	302.9	87.0	300.2	9.0	300.4	6.8	300.4	6.9	0.05240	0.00100	0.34400	0.00600	0.04770	0.00055	0.66	3.34	876	242.4	235
25	358.5	126.1	296.4	12.8	291.4	5.5	290.8	5.7	0.05370	0.00150	0.33900	0.00850	0.04624	0.00045	0.39	1.09	261	257	157
26	302.9	82.7	280.4	9.2	277.6	6.2	277.4	6.3	0.05240	0.00095	0.31800	0.00600	0.04400	0.00050	0.60	6.90	2360	388	295
27	350.1	122.5	284.2	11.4	283.0	4.7	282.5	4.9	0.05350	0.00145	0.32300	0.00750	0.04488	0.00039	0.37	1.75	290	182.3	125.1
28	311.6	138.5	279.6	14.5	277.0	7.4	276.7	7.5	0.05260	0.00160	0.31700	0.00950	0.04390	0.00060	0.46	2.10	428	226.6	151.1
29	104.2	373.5	263.3	33.9	281.9	12.3	283.2	12.8	0.04810	0.00380	0.29600	0.02200	0.04470	0.00100	0.30	1.09	84.1	86.7	57.9
30	324.5	81.6	301.0	9.0	297.4	4.6	297.2	4.7	0.05290	0.00095	0.34500	0.00600	0.04722	0.00038	0.46	2.03	938	527	399
31	371.0	150.1	288.0	15.2	283.3	5.5	282.6	5.7	0.05400	0.00180	0.32800	0.01000	0.04493	0.00045	0.32	1.68	314	205.9	129.8
32	354.3	160.1	297.2	17.3	291.8	6.8	291.2	7.0	0.05360	0.00190	0.34000	0.01150	0.04630	0.00055	0.35	1.49	207	164	112
33	324.5	154.5	286.5	16.0	283.3	5.6	283.0	5.8	0.05290	0.00180	0.32600	0.01050	0.04493	0.00046	0.31	0.94	278	336	237

Appendix 2.5: LA-ICP-MS U/Pb zircon dating and CL imaging data continued

	Age estimates with 2 sigma uncertainty (Ma)								Isotopic Ratios with absolute errors								Concentrations ppm		
	^{207}Pb / ^{206}Pb		^{207}Pb / ^{235}U		^{206}Pb / ^{238}U		Preferred Age		^{207}Pb / ^{206}Pb		^{207}Pb / ^{235}U		^{206}Pb / ^{238}U			U / Th			
Analysis	Ma	± 2s Error	Ma	± 2s Error	Ma	± 2s Error	Ma *	± 2s Error	Ratio	± 1s Error	Ratio	± 1s Error	Ratio	± 1s Error	rho	Ratio	U	Th	Pb
WS15-005 - Koobaba Granite																			
1	320.2	73.2	284.2	7.6	279.3	3.3	279.0	3.4	0.05280	0.00085	0.32300	0.00500	0.04428	0.00027	0.39	1.48	200.9	166	117.6
2	322.4	38.7	288.0	4.8	279.4	3.1	279.1	3.2	0.05285	0.00045	0.32790	0.00315	0.04430	0.00026	0.60	3.37	1114	412	307.4
3	236.3	68.0	272.0	6.7	273.5	3.3	273.8	3.3	0.05090	0.00075	0.30720	0.00435	0.04334	0.00027	0.43	2.86	550	259	176.1
4	320.2	68.9	291.3	7.4	287.4	4.1	287.1	4.1	0.05280	0.00080	0.33230	0.00490	0.04559	0.00033	0.49	2.34	348	182	118.5
5	1822.4	84.7	528.6	17.9	272.6	6.8	252.6	6.9	0.11140	0.00260	0.68300	0.01500	0.04320	0.00055	0.58	2.93	269	115	195
6	366.9	71.1	297.3	7.2	291.6	5.4	291.0	5.4	0.05390	0.00085	0.34020	0.00480	0.04628	0.00044	0.67	2.53	554	275	197.7
7	245.3	49.6	276.4	5.1	280.5	2.7	280.8	2.8	0.05110	0.00055	0.31290	0.00330	0.04447	0.00022	0.47	2.13	429	260	179
8	328.8	85.6	295.7	9.8	290.7	4.0	290.4	4.1	0.05300	0.00100	0.33800	0.00650	0.04613	0.00033	0.37	2.82	367	158.7	127.5
9	307.2	73.8	277.3	7.7	269.0	3.6	268.7	3.7	0.05250	0.00085	0.31400	0.00500	0.04261	0.00029	0.43	2.08	399	227	150.2
10	330.9	41.9	295.7	5.5	291.1	3.1	290.8	3.1	0.05305	0.00049	0.33810	0.00365	0.04619	0.00025	0.50	2.30	723	318	215.4
11	429.2	30.6	301.6	4.2	286.2	3.1	285.0	3.2	0.05542	0.00038	0.34580	0.00280	0.04539	0.00026	0.69	3.71	1440	315	290
12	311.6	103.8	289.6	10.6	286.6	4.9	286.4	5.0	0.05260	0.00120	0.33000	0.00700	0.04546	0.00040	0.41	1.74	209.9	97.1	91.6
13	302.9	60.9	280.4	6.4	281.0	3.2	280.8	3.3	0.05240	0.00070	0.31800	0.00415	0.04455	0.00026	0.45	1.98	300	124.3	104.9
14	328.8	68.5	288.8	8.4	286.1	4.1	285.7	4.1	0.05300	0.00080	0.32900	0.00550	0.04538	0.00033	0.43	1.83	257	105	91.9
15	341.6	106.2	287.3	10.7	282.0	3.9	281.5	4.0	0.05330	0.00125	0.32700	0.00700	0.04472	0.00032	0.33	1.99	187.5	72.9	57.4
16	362.7	117.4	282.7	13.0	275.2	3.8	274.5	4.0	0.05380	0.00140	0.32100	0.00850	0.04361	0.00031	0.27	1.16	377	270	203
17	395.9	201.2	276.5	21.4	267.9	5.5	267.0	5.8	0.05460	0.00245	0.31300	0.01400	0.04244	0.00045	0.23	1.18	156	103.4	77.2
18	819.0	44.0	359.8	7.0	294.0	3.7	288.9	3.7	0.06640	0.00070	0.42520	0.00495	0.04666	0.00030	0.55	2.82	918	260	310.7
19	311.6	77.9	294.1	9.1	291.3	3.7	291.2	3.8	0.05260	0.00090	0.33600	0.00600	0.04623	0.00030	0.36	2.04	390	142	109.5
20	289.8	122.8	289.6	12.9	291.1	6.8	291.2	6.9	0.05210	0.00140	0.33000	0.00850	0.04620	0.00055	0.46	1.34	224.7	142	108
21	307.2	99.8	265.6	10.1	275.7	6.2	275.5	6.3	0.05250	0.00115	0.29900	0.00650	0.04370	0.00050	0.53	2.56	944	439	262
22	307.2	78.1	281.1	8.4	280.3	3.6	280.1	3.7	0.05250	0.00090	0.31900	0.00550	0.04444	0.00030	0.39	2.20	343	207	128.6
23	311.6	82.2	288.8	9.9	286.3	3.8	286.1	3.8	0.05260	0.00095	0.32900	0.00650	0.04542	0.00031	0.34	1.43	233	217	133
24	267.7	71.1	275.8	7.4	277.3	3.6	277.3	3.7	0.05160	0.00080	0.31210	0.00480	0.04395	0.00030	0.44	1.63	503	403	238
25	302.9	65.3	291.1	7.4	288.9	4.4	288.8	4.4	0.05240	0.00075	0.33200	0.00490	0.04584	0.00036	0.52	2.73	462	218	140
26	289.8	74.6	271.9	8.5	272.2	4.4	272.1	4.5	0.05210	0.00085	0.30700	0.00550	0.04313	0.00036	0.46	1.76	641	470	264.3
27	337.3	144.8	306.2	15.7	298.5	6.8	298.2	6.9	0.05320	0.00170	0.35200	0.01050	0.04740	0.00055	0.39	1.91	188	105	70
28	294.2	74.4	267.2	8.5	272.6	6.8	272.5	6.9	0.05220	0.00085	0.30100	0.00550	0.04320	0.00055	0.70	3.35	1272	465	268
29	302.9	56.6	276.2	6.2	273.7	2.8	273.5	2.8	0.05240	0.00065	0.31260	0.00400	0.04337	0.00023	0.41	2.01	373	217.1	133.4
30	578.1	124.6	310.0	14.9	276.5	5.2	274.0	5.4	0.05930	0.00170	0.35700	0.01000	0.04383	0.00043	0.35	1.79	150	91.9	67.2
31	320.2	81.8	288.0	9.1	283.1	3.3	282.8	3.4	0.05280	0.00095	0.32800	0.00600	0.04490	0.00027	0.32	1.38	291	183.9	150.6
32	350.1	80.3	288.0	8.4	280.9	3.9	280.3	4.0	0.05350	0.00095	0.32800	0.00550	0.04453	0.00032	0.43	1.95	320	133	102.9
33	294.2	83.1	281.1	9.2	272.5	3.8	272.3	3.8	0.05220	0.00095	0.31900	0.00600	0.04317	0.00031	0.38	2.25	274	109.4	85.1
34	302.9	82.7	291.1	9.1	286.4	3.7	286.3	3.8	0.05240	0.00095	0.33200	0.00600	0.04543	0.00030	0.37	1.82	197.2	102.6	80.7

Appendix 2.5: LA-ICP-MS U/Pb zircon dating data and CL imaging continued

	Age estimates with 2 sigma uncertainty (Ma)								Isotopic Ratios with absolute errors								Concentrations ppm		
	$^{207}Pb/^{206}Pb$		$^{207}Pb/^{235}U$		$^{206}Pb/^{238}U$		Preferred Age		$^{207}Pb/^{206}Pb$		$^{207}Pb/^{235}U$		$^{206}Pb/^{238}U$			U/Th			
Analysis	Ma	± 2s Error	Ma	± 2s Error	Ma	± 2s Error	Ma *	± 2s Error	Ratio	± 1s Error	Ratio	± 1s Error	Ratio	± 1s Error	rho	Ratio	U	Th	Pb
WS15-005 - Koobaba Granite continued																			
35	311.6	77.9	285.0	8.4	282.3	3.9	282.0	4.0	0.05260	0.00090	0.32400	0.00550	0.04476	0.00032	0.42	1.46	362	257	180
36	276.6	92.8	280.4	9.2	277.9	5.1	278.0	5.2	0.05180	0.00105	0.31800	0.00600	0.04406	0.00041	0.49	1.88	413	220.1	150.7
37	328.8	132.7	281.9	14.5	278.8	6.2	278.4	6.3	0.05300	0.00155	0.32000	0.00950	0.04420	0.00050	0.38	1.84	257	148	94.4
38	302.9	113.1	280.4	11.5	272.1	4.5	271.8	4.6	0.05240	0.00130	0.31800	0.00750	0.04311	0.00037	0.36	1.70	311	205	131
39	311.6	64.9	282.7	8.4	276.8	3.9	276.5	3.9	0.05260	0.00075	0.32100	0.00550	0.04387	0.00032	0.42	1.03	394	522	315
40	1539.9	63.0	368.1	9.1	212.2	4.4	200.3	4.5	0.09560	0.00160	0.43700	0.00650	0.03347	0.00036	0.71	1.11	527	532	323
41	294.2	61.2	280.0	7.0	277.6	4.1	277.5	4.1	0.05220	0.00070	0.31750	0.00455	0.04400	0.00033	0.52	2.96	969	313	242
42	307.2	65.1	276.9	6.6	271.2	3.2	270.9	3.3	0.05250	0.00075	0.31350	0.00430	0.04297	0.00026	0.44	2.15	463.2	201	173
43	311.6	69.2	285.7	7.6	280.8	3.6	280.5	3.7	0.05260	0.00080	0.32500	0.00500	0.04452	0.00030	0.43	1.75	357	183	158.2
44	218.1	68.8	276.9	7.5	280.5	4.2	281.0	4.3	0.05050	0.00075	0.31350	0.00490	0.04448	0.00034	0.49	2.00	403	177	142.8
45	195.0	93.0	262.5	8.6	269.9	4.3	270.4	4.4	0.05000	0.00100	0.29500	0.00550	0.04275	0.00035	0.43	1.42	268.4	178.1	141.1
46	302.9	65.3	284.0	6.5	279.2	3.2	279.0	3.3	0.05240	0.00075	0.32270	0.00425	0.04426	0.00026	0.45	1.43	361	239	189.2
47	350.1	84.5	343.1	10.8	340.0	5.4	339.9	5.5	0.05350	0.00100	0.40200	0.00750	0.05415	0.00044	0.44	1.09	251	229	220.3
48	195.0	130.2	266.4	13.2	274.7	5.2	275.3	5.3	0.05000	0.00140	0.30000	0.00850	0.04354	0.00042	0.34	0.91	177.6	198.2	151.4
49	834.7	149.5	315.9	17.7	266.5	7.4	261.4	7.5	0.06690	0.00240	0.36500	0.01200	0.04220	0.00060	0.43	0.88	412	464	312
50	307.2	60.7	274.9	6.8	270.5	4.1	270.2	4.1	0.05250	0.00070	0.31090	0.00440	0.04285	0.00033	0.54	2.02	660	327.8	244.8

Appendix 2.5: LA-ICP-MS U/Pb zircon dating data and CL imaging continued

	Age estimates with 2 sigma uncertainty (Ma)								Isotopic Ratios with absolute errors								Concentrations ppm		
	^{207}Pb / ^{206}Pb		^{207}Pb / ^{235}U		^{206}Pb / ^{238}U		Preferred Age		^{207}Pb / ^{206}Pb		^{207}Pb / ^{235}U		^{206}Pb / ^{238}U			U / Th			
Analysis	Ma	± 2s Error	Ma	± 2s Error	Ma	± 2s Error	Ma *	± 2s Error	Ratio	± 1s Error	Ratio	± 1s Error	Ratio	± 1s Error	rho	Ratio	U	Th	Pb
WS16-002 - Dioritic body																			
1	302.9	47.9	259.2	5.9	255.7	3.8	255.3	3.9	0.05240	0.00055	0.29080	0.00375	0.04046	0.00031	0.59	1.69	2770	1456	1038
2	320.2	111.9	276.5	11.5	273.3	6.1	272.9	6.2	0.05280	0.00130	0.31300	0.00750	0.04330	0.00050	0.48	1.90	832	390	298
4	1518.1	22.0	1489.1	10.5	1467.3	14.4	1463.2	15.6	0.09450	0.00055	3.33400	0.02250	0.25560	0.00140	0.81	12.83	1950	135.1	586
5	292.0	34.6	285.1	5.7	281.1	3.3	281.0	3.4	0.05215	0.00040	0.32420	0.00370	0.04457	0.00027	0.53	1.24	6420	4670	3430
6	298.5	74.2	266.4	7.8	266.4	4.6	266.2	4.6	0.05230	0.00085	0.30000	0.00500	0.04219	0.00037	0.53	1.24	3080	2270	1710
7	646.3	122.9	469.0	20.9	436.2	7.2	433.2	7.5	0.06120	0.00175	0.58700	0.01650	0.07000	0.00060	0.30	1.12	267	199	256
8	1815.9	37.6	1693.9	16.9	1606.0	20.6	1584.4	22.8	0.11100	0.00115	4.30300	0.04450	0.28290	0.00205	0.70	0.86	577	579	2694
9	366.9	71.1	273.4	7.7	265.0	4.4	264.3	4.4	0.05390	0.00085	0.30900	0.00500	0.04197	0.00036	0.52	0.94	1657	1543	1146
10	1118.6	38.9	1095.0	13.7	1087.7	10.9	1086.2	11.5	0.07690	0.00075	1.94000	0.02000	0.18380	0.00100	0.53	2.21	697	271	816
11	294.2	65.6	262.8	7.0	260.0	3.7	259.8	3.7	0.05220	0.00075	0.29540	0.00450	0.04116	0.00030	0.47	1.48	1990	1179	845
12	302.9	69.6	282.7	7.7	280.4	3.7	280.2	3.8	0.05240	0.00080	0.32100	0.00500	0.04446	0.00030	0.43	1.70	1526	817	641
13	1629.7	33.4	1517.9	17.4	1433.8	23.2	1417.8	25.0	0.10030	0.00090	3.45900	0.03850	0.24910	0.00225	0.81	0.97	827	769	3008
14	1214.1	65.8	312.2	8.9	205.6	2.8	197.8	2.9	0.08070	0.00135	0.36000	0.00600	0.03240	0.00023	0.42	1.09	1052	906	600
15	298.5	82.9	288.0	8.4	278.8	3.5	278.6	3.5	0.05230	0.00095	0.32800	0.00550	0.04419	0.00028	0.38	1.41	698	463	376
17	698.1	231.0	156.8	16.4	128.3	4.6	126.0	4.7	0.06270	0.00340	0.16700	0.00950	0.02010	0.00037	0.32	0.82	525	758	211
18	345.8	97.4	292.6	9.8	285.2	4.1	284.7	4.2	0.05340	0.00115	0.33400	0.00650	0.04524	0.00034	0.38	1.76	304	227	134
19	366.9	154.7	276.5	15.3	265.8	9.9	265.1	10.0	0.05390	0.00185	0.31300	0.01000	0.04210	0.00080	0.59	3.84	357.3	128.1	81
20	452.4	79.3	451.5	11.6	451.8	6.6	451.8	6.8	0.05600	0.00100	0.56000	0.00900	0.07260	0.00055	0.47	0.74	236	460	413
21	589.1	251.1	425.2	38.0	415.0	16.9	412.8	17.4	0.05960	0.00345	0.52000	0.02900	0.06650	0.00140	0.38	0.84	140.2	208.5	148
22	320.2	90.4	285.0	12.2	284.4	4.9	284.1	5.0	0.05280	0.00105	0.32400	0.00800	0.04511	0.00040	0.36	2.22	1023	566	297
23	298.5	61.1	286.7	6.5	283.1	3.0	282.9	3.0	0.05230	0.00070	0.32620	0.00425	0.04489	0.00024	0.41	2.50	1370	740	390
24	391.8	53.5	346.7	7.9	337.1	3.4	336.5	3.4	0.05450	0.00065	0.40700	0.00550	0.05368	0.00028	0.38	1.81	1106	746	522
25	341.6	140.2	141.0	8.8	131.1	3.5	130.4	3.5	0.05330	0.00165	0.14900	0.00500	0.02055	0.00028	0.40	4.24	1290	508	128
26	315.9	99.3	285.7	11.4	280.7	5.6	280.4	5.7	0.05270	0.00115	0.32500	0.00750	0.04451	0.00046	0.44	1.50	712	418	386
27	428.4	128.8	346.0	15.8	345.1	8.5	344.3	8.7	0.05540	0.00160	0.40600	0.01100	0.05500	0.00070	0.47	1.45	592	382	423
28	1551.7	25.4	1454.5	19.0	1423.0	26.8	1412.8	28.8	0.09620	0.00065	3.18900	0.03950	0.24700	0.00260	0.85	23.50	3560	147	443
29	320.2	81.8	278.8	8.5	272.3	3.3	271.9	3.4	0.05280	0.00095	0.31600	0.00550	0.04314	0.00027	0.36	2.04	415	180	168.5
30	181.0	103.2	156.6	6.4	152.1	2.3	152.0	2.3	0.04970	0.00110	0.16670	0.00370	0.02388	0.00018	0.34	1.83	515	265	135.9
31	298.5	52.3	286.3	6.0	280.9	3.0	280.7	3.0	0.05230	0.00060	0.32570	0.00390	0.04453	0.00024	0.45	2.14	1510	693	610
32	1498.0	26.3	1469.7	17.3	1456.5	18.5	1453.2	20.0	0.09350	0.00065	3.25200	0.03650	0.25350	0.00180	0.63	2.91	1019	338	1450
33	670.7	176.3	160.3	11.2	127.0	3.9	124.9	4.0	0.06190	0.00255	0.17100	0.00650	0.01990	0.00031	0.41	2.47	215	87.2	38.2
34	1594.0	68.3	1553.9	28.2	1514.9	23.4	1507.9	26.1	0.09840	0.00180	3.62000	0.06500	0.26490	0.00230	0.48	2.02	73.8	36	155.5

Appendix 2.5: LA-ICP-MS U/Pb zircon dating data and CL imaging continued

	Age estimates with 2 sigma uncertainty (Ma)								Isotopic Ratios with absolute errors								Concentrations ppm		
	^{207}Pb / ^{206}Pb		^{207}Pb / ^{235}U		^{206}Pb / ^{238}U		Preferred Age		^{207}Pb / ^{206}Pb		^{207}Pb / ^{235}U		^{206}Pb / ^{238}U			U / Th			
Analysis	Ma	± 2s Error	Ma	± 2s Error	Ma	± 2s Error	Ma *	± 2s Error	Ratio	± 1s Error	Ratio	± 1s Error	Ratio	± 1s Error	rho	Ratio	U	Th	Pb
MWD013-099 - Monzonitic dyke																			
1	1526.1	29.8	1615.8	15.8	1685.4	24.3	1701.4	27.4	0.09490	0.00075	3.91000	0.03850	0.29880	0.00245	0.83	2.04	553	249.8	1158
2	2123.4	35.9	1562.7	36.4	1173.7	38.0	1102.9	38.8	0.13190	0.00135	3.66000	0.08500	0.19970	0.00355	0.77	2.62	948	354	1647
3	1541.9	25.5	1522.9	15.3	1499.6	16.8	1496.0	18.4	0.09570	0.00065	3.48100	0.03400	0.26190	0.00165	0.65	4.63	3520	706	2540
4	1620.4	57.8	1636.2	24.0	1646.5	35.9	1649.1	40.1	0.09980	0.00155	4.01000	0.06000	0.29100	0.00360	0.83	0.46	512	1680	4130
5	1555.6	29.2	1405.6	19.9	1306.7	32.0	1289.2	33.8	0.09640	0.00075	2.99200	0.03950	0.22470	0.00305	1.03	1.01	3710	3620	2450
6	1745.5	30.9	1774.2	17.0	1796.1	26.3	1802.1	29.9	0.10680	0.00090	4.73900	0.04850	0.32130	0.00270	0.82	7.45	1534	204.2	836
7	362.7	41.9	352.2	6.0	350.3	4.6	350.2	4.6	0.05380	0.00050	0.41460	0.00420	0.05585	0.00038	0.66	1.44	1390	1240	838
8	315.9	129.5	357.5	16.3	364.7	7.9	365.2	8.1	0.05270	0.00150	0.42200	0.01150	0.05820	0.00065	0.41	2.39	814	355	302
9	1557.5	29.2	1509.0	14.6	1470.9	24.6	1463.7	26.6	0.09650	0.00075	3.42000	0.03200	0.25630	0.00240	1.00	1.18	1630	1430	5000
10	362.7	67.1	353.9	9.3	350.6	4.3	350.5	4.4	0.05380	0.00080	0.41700	0.00650	0.05590	0.00036	0.41	2.19	939	452	414
11	1473.6	20.6	1512.9	11.4	1536.7	17.8	1542.2	19.5	0.09230	0.00050	3.43700	0.02500	0.26920	0.00175	0.89	2.50	2110	936	3500
12	366.9	87.8	387.7	11.0	392.0	6.7	392.3	6.8	0.05390	0.00105	0.46500	0.00800	0.06270	0.00055	0.51	1.72	665	432	412
13	366.9	50.2	358.3	6.2	356.7	3.9	356.6	4.0	0.05390	0.00060	0.42320	0.00435	0.05689	0.00032	0.55	2.07	687	377	343
14	1149.4	83.9	1112.1	40.0	1088.8	39.1	1085.9	41.1	0.07810	0.00165	1.99000	0.06000	0.18400	0.00360	0.65	2.33	734	377	1090
15	1559.5	31.1	1587.2	17.1	1606.0	26.6	1610.3	29.4	0.09660	0.00080	3.77400	0.04050	0.28290	0.00265	0.87	2.18	632	330	1302
16	856.3	153.6	428.5	25.0	354.9	12.2	348.9	12.3	0.06760	0.00250	0.52500	0.01900	0.05660	0.00100	0.49	1.37	294	249	234
17	328.8	77.1	354.6	10.0	360.0	5.3	360.4	5.4	0.05300	0.00090	0.41800	0.00700	0.05744	0.00044	0.45	1.23	775	718	652
18	1036.0	38.3	1081.4	13.2	1101.3	14.1	1104.4	15.0	0.07380	0.00070	1.90100	0.01900	0.18630	0.00130	0.70	5.01	759	184	451
19	379.4	70.5	363.2	9.9	358.6	6.1	358.4	6.2	0.05420	0.00085	0.43000	0.00700	0.05720	0.00050	0.54	1.38	1200	1140	990
20	954.5	69.2	414.4	16.7	321.9	8.0	314.8	8.0	0.07090	0.00120	0.50400	0.01250	0.05120	0.00065	0.51	0.92	2980	3710	3090
21	1771.0	62.4	1738.3	21.8	1721.0	34.0	1715.4	38.4	0.10830	0.00185	4.54000	0.06000	0.30600	0.00345	0.85	1.21	258	221.6	998
22	1561.4	69.8	1492.8	27.6	1434.3	30.9	1424.2	33.6	0.09670	0.00180	3.35000	0.06000	0.24920	0.00300	0.67	1.99	1589	831	2830
23	358.5	84.1	421.8	13.3	430.1	7.2	431.0	7.4	0.05370	0.00100	0.51500	0.01000	0.06900	0.00060	0.45	1.05	430	429	466
24	506.9	88.1	372.4	16.1	348.2	7.9	346.5	8.0	0.05740	0.00115	0.44300	0.01150	0.05550	0.00065	0.45	3.23	1820	680	567
25	529.8	75.5	361.8	12.0	334.1	8.0	332.1	8.0	0.05800	0.00100	0.42800	0.00850	0.05320	0.00065	0.62	0.93	1413	1572	1154
26	2193.4	54.4	1497.4	36.5	1047.8	26.2	971.7	27.4	0.13730	0.00215	3.37000	0.08000	0.17650	0.00240	0.57	20.41	935	46.6	174

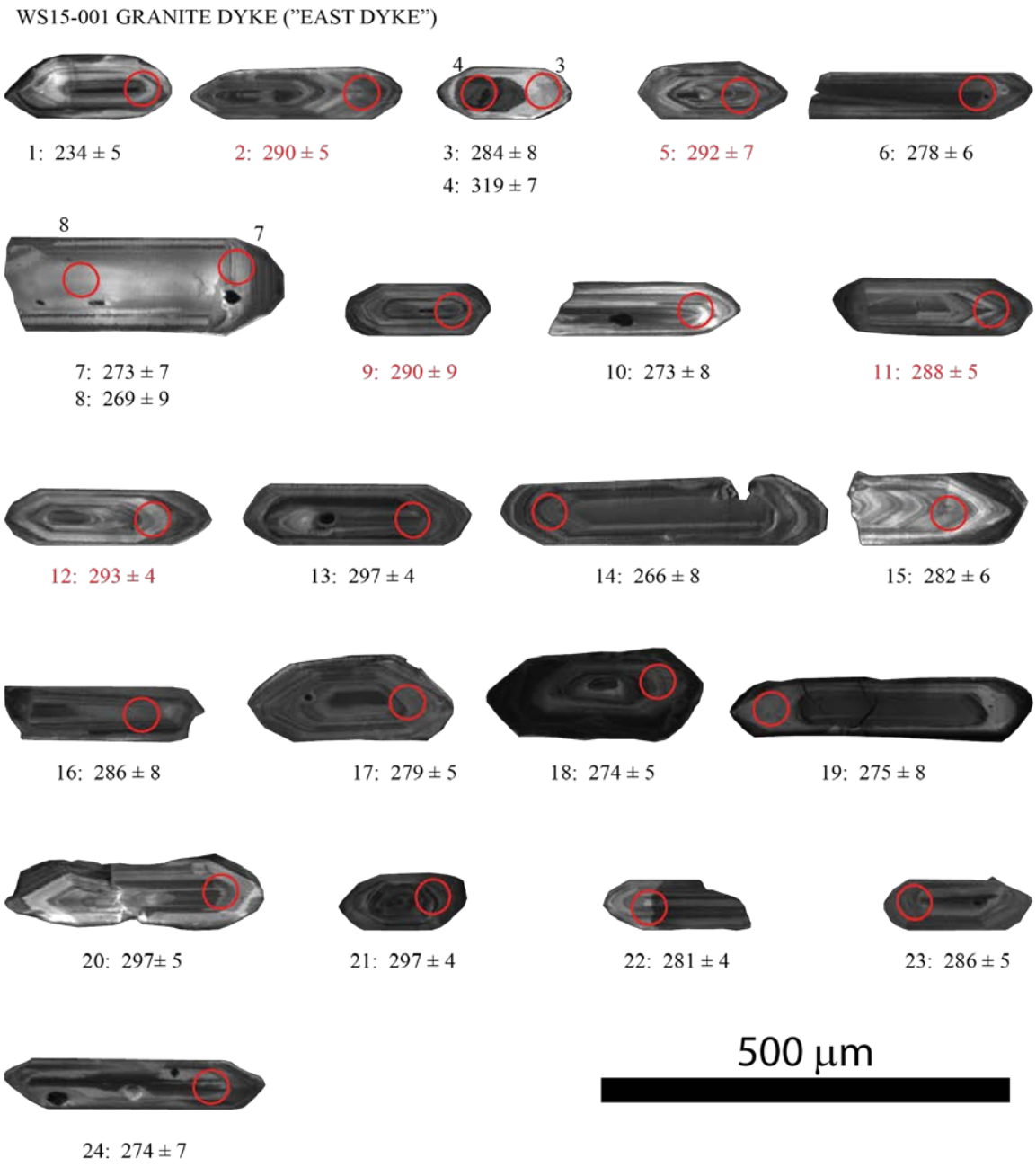

Cathodoluminiscence (CL) images of analyzed zircon grains from sample WS15-001, red circles denote the analyzed laser spot and the ages in red are those used to calculate the preferred weighted average age

Cathodoluminiscence (CL) images of analyzed zircon grains from sample WS15-017, red circles denote the analyzed laser spot and the ages in red are those used to calculate the preferred weighted average age

Cathodoluminiscence (CL) images of analyzed zircon grains from sample WS15-005, red circles denote the analyzed laser spot and the ages in red are those used to calculate the preferred weighted average age

Appendix 2.5: LA-ICP-MS U/Pb zircon dating data and CL imaging continued

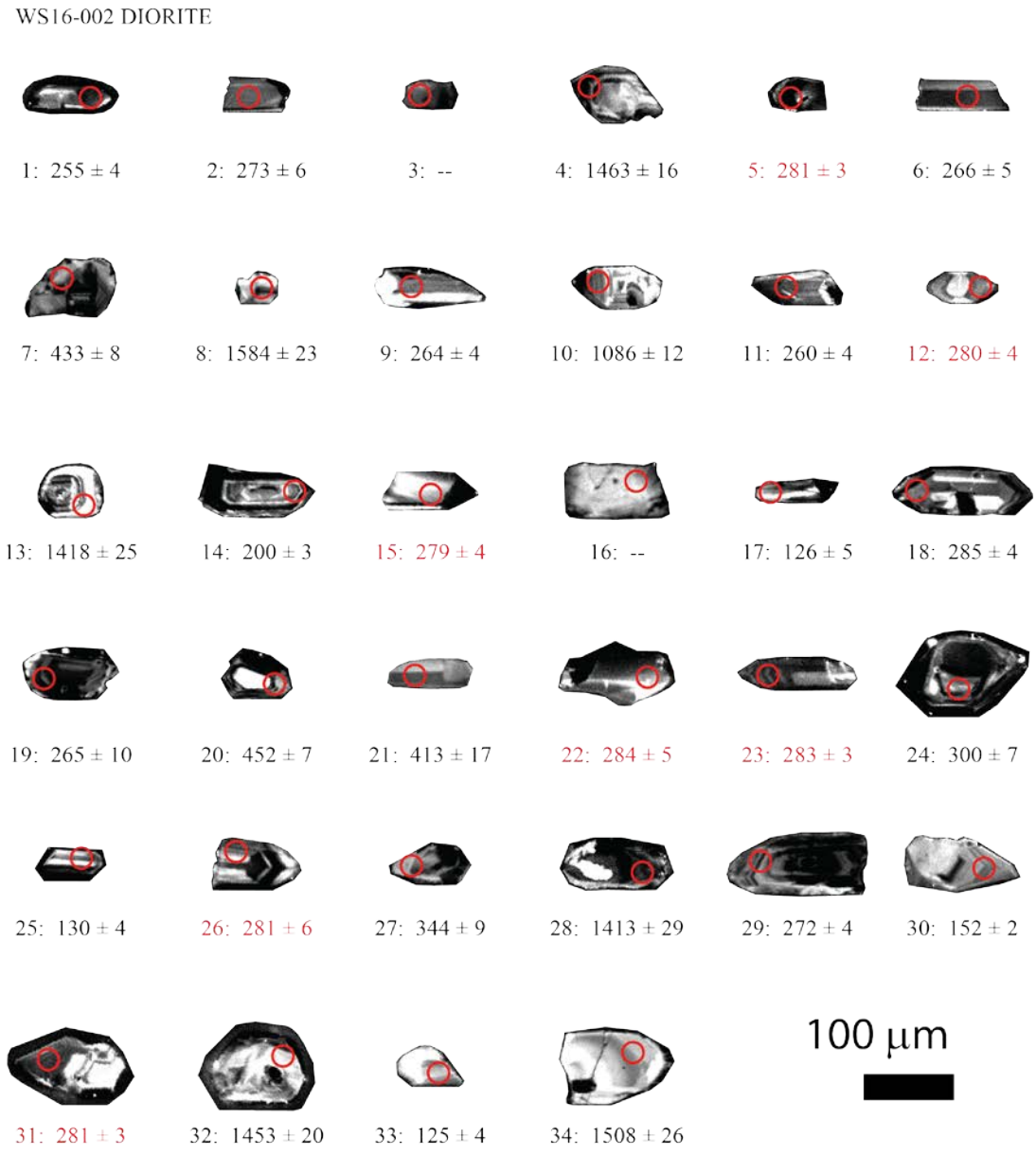

Cathodoluminiscence (CL) images of analyzed zircon grains from sample WS16-002, red circles denote the analyzed laser spot and the ages in red are those used to calculate the preferred weighted average age

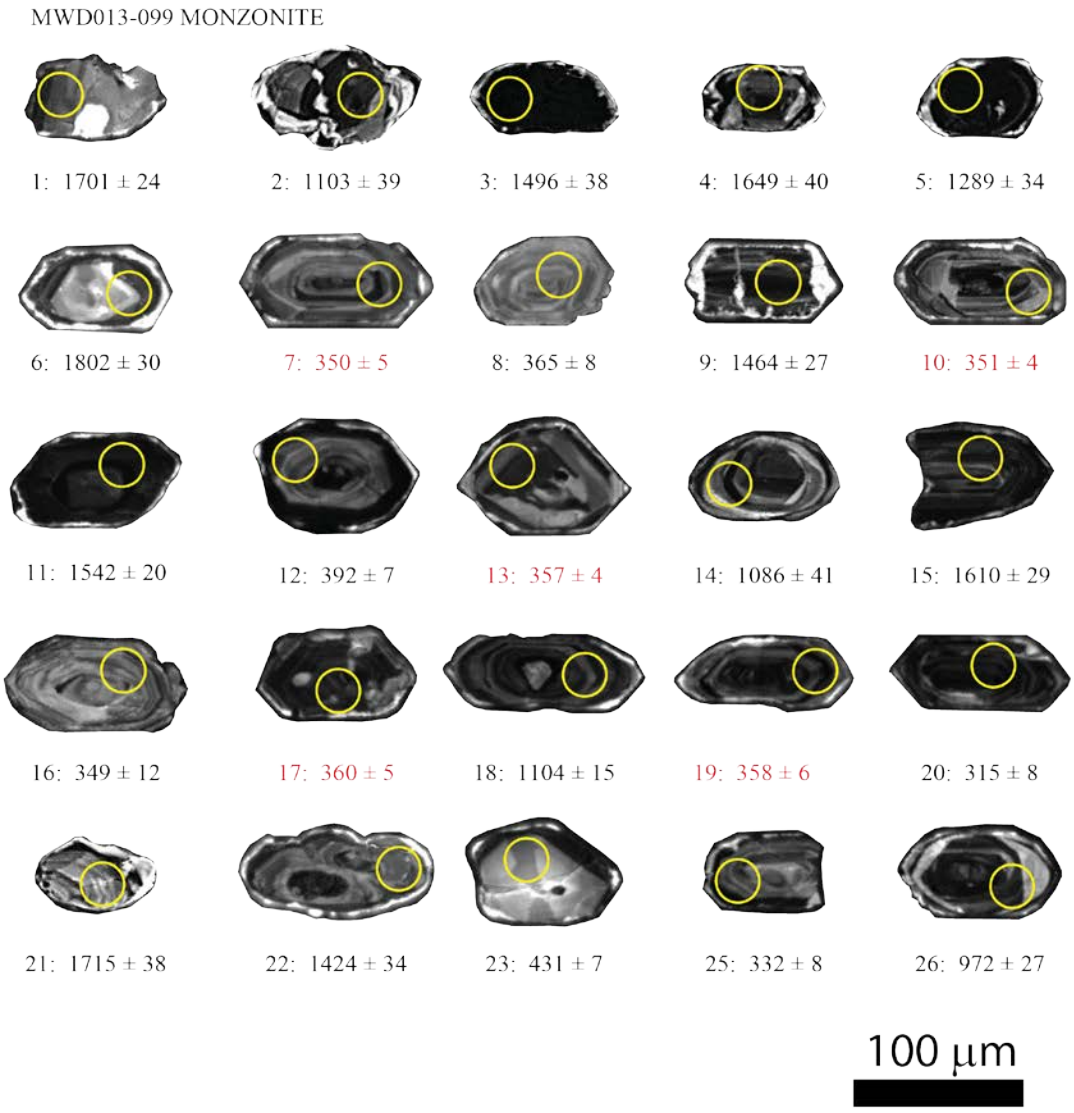

Cathodoluminiscence (CL) images of analyzed zircon grains from sample MWD013-099, yellow circles denote the analyzed laser spot and the ages in red are those used to calculate the preferred weighted average age

Appendix 2.6: ^{40}Ar-^{39}Ar muscovite dating data

MWD217-056: muscovite (run mc49-b8a)

Laser Power	Isotopic values						Age ± 1σ
(mW)	^{36}Ar ± 1σ	^{37}Ar ± 1σ	^{38}Ar ± 1σ	^{39}Ar ± 1σ	^{40}Ar ± 1σ	Cumulative ^{39}Ar	(Ma)
100	0.01051 ± 0.0026	0.00974 ± 0.0045	0.00408 ± 0.0016	0.009 ± 0.0020	2.81 ± 0.0084	0.0006	-126.67 ± 341.65
200	0.00129 ± 0.0014	0.00922 ± 0.0059	0.00017 ± 0.0017	0.004 ± 0.0029	0.43 ± 0.0071	0.0009	688.27 ± 548.45
300	0.00020 ± 0.0014	0.00207 ± 0.0064	0.00012 ± 0.0016	0.016 ± 0.0039	1.27 ± 0.0086	0.0020	288.54 ± 104.76
400	0.00433 ± 0.0017	0.00058 ± 0.0066	0.00199 ± 0.0016	0.061 ± 0.0036	4.90 ± 0.0318	0.0062	206.84 ± 29.81
600	0.00418 ± 0.0017	0.01473 ± 0.0073	0.00571 ± 0.0012	2.594 ± 0.0140	191.78 ± 0.8837	0.1877	251.36 ± 1.78
800	0.00208 ± 0.0013	0.00866 ± 0.0082	0.00302 ± 0.0019	4.680 ± 0.0189	345.95 ± 1.5693	0.5151	252.44 ± 1.46
1000	0.00285 ± 0.0017	0.03408 ± 0.0067	0.00066 ± 0.0041	1.598 ± 0.0076	119.66 ± 0.5721	0.6269	254.20 ± 1.89
1200	0.00584 ± 0.0016	0.03141 ± 0.0071	0.00489 ± 0.0015	2.561 ± 0.0121	191.04 ± 0.8895	0.8061	252.85 ± 1.68
1400	0.00193 ± 0.0018	0.01597 ± 0.0068	0.00034 ± 0.0020	1.589 ± 0.0118	118.27 ± 0.5153	0.9173	255.57 ± 2.3
1600	0.00031 ± 0.0016	0.01188 ± 0.0066	0.00239 ± 0.0023	0.374 ± 0.0051	27.96 ± 0.1243	0.9435	256.04 ± 5.37
1800	0.00128 ± 0.0017	0.00068 ± 0.0074	0.00126 ± 0.0016	0.268 ± 0.0025	20.30 ± 0.0838	0.9623	253.80 ± 6.58
2000	0.00074 ± 0.0016	0.00620 ± 0.0072	0.00041 ± 0.0016	0.184 ± 0.0022	13.63 ± 0.0639	0.9751	257.08 ± 8.95
2400	0.00151 ± 0.0018	0.00915 ± 0.0076	0.00085 ± 0.0021	0.179 ± 0.0023	12.67 ± 0.0638	0.9877	234.68 ± 10.25
2800	0.00123 ± 0.0013	0.01040 ± 0.0079	0.00146 ± 0.0014	0.064 ± 0.0034	4.74 ± 0.0232	0.9921	272.59 ± 23.46
3200	0.00310 ± 0.0018	0.00391 ± 0.0042	0.00201 ± 0.0012	0.062 ± 0.0018	4.65 ± 0.0236	0.9964	304.23 ± 27.76
4000	0.00368 ± 0.0010	0.00849 ± 0.0050	0.00199 ± 0.0013	0.051 ± 0.0033	4.15 ± 0.1634	1	341.92 ± 28.91

J = 0.00203517 ± 0.00000934035 Total gas age = 253.22 ± 1.37 Ma Plateau age = 252.98 ± 1.33 Ma

Red color denotes values <0

Appendix 2.6: ^{40}Ar-^{39}Ar muscovite dating data continued

MWD217-056: muscovite (run mc49-b8b)

Laser Power	Isotopic values						Age ± 1σ
(mW)	^{36}Ar ± 1σ	^{37}Ar ± 1σ	^{38}Ar ± 1σ	^{39}Ar ± 1σ	^{40}Ar ± 1σ	Cumulative ^{39}Ar	(Ma)
100	0.00464 ± 0.0016	0.00668 ± 0.0098	0.00250 ± 0.0017	0.036 ± 0.0036	4.01 ± 0.0262	0.0010	251.48 ± 48.51
200	0.00007 ± 0.0012	0.00944 ± 0.0083	0.00738 ± 0.0015	0.053 ± 0.0029	4.30 ± 0.0280	0.0024	276.92 ± 25.72
300	0.00466 ± 0.0010	0.01623 ± 0.0075	0.00304 ± 0.0017	0.144 ± 0.0040	11.73 ± 0.0570	0.0063	245.93 ± 9.34
400	0.00327 ± 0.0016	0.01105 ± 0.0080	0.00315 ± 0.0014	1.129 ± 0.0104	83.17 ± 0.3677	0.0371	249.28 ± 2.74
600	0.01188 ± 0.0014	0.00797 ± 0.0081	0.00884 ± 0.0019	5.934 ± 0.0294	443.20 ± 2.3276	0.1989	253.41 ± 1.73
800	0.00914 ± 0.0015	0.02175 ± 0.0044	0.01042 ± 0.0016	9.843 ± 0.0563	728.28 ± 3.2934	0.4672	252.17 ± 1.73
1000	0.00613 ± 0.0014	0.02092 ± 0.0048	0.00719 ± 0.0018	5.918 ± 0.0218	440.04 ± 1.9608	0.6285	253.23 ± 1.39
1200	0.00352 ± 0.0017	0.00712 ± 0.0054	0.00489 ± 0.0015	3.049 ± 0.0181	223.86 ± 0.9905	0.7116	250.15 ± 1.81
1400	0.00877 ± 0.0016	0.01045 ± 0.0062	0.00476 ± 0.0026	2.218 ± 0.0141	165.49 ± 0.6968	0.7721	251.29 ± 1.93
1600	0.02087 ± 0.0015	0.02000 ± 0.0054	0.01177 ± 0.0022	6.148 ± 0.0346	459.15 ± 2.0270	0.9397	252.08 ± 1.71
1800	0.00144 ± 0.0015	0.00927 ± 0.0073	0.00195 ± 0.0020	1.298 ± 0.0066	97.74 ± 0.4225	0.9751	256.20 ± 1.94
2000	0.00134 ± 0.0019	0.00271 ± 0.0072	0.00125 ± 0.0016	0.567 ± 0.0055	43.57 ± 0.2034	0.9905	264.18 ± 4.18
2400	0.00187 ± 0.0015	0.01485 ± 0.0091	0.00121 ± 0.0018	0.283 ± 0.0028	21.31 ± 0.0991	0.9982	263.67 ± 5.61
2800	0.00167 ± 0.0015	0.00038 ± 0.0058	0.00420 ± 0.0015	0.053 ± 0.0026	4.12 ± 0.0229	0.9997	293.73 ± 28.96
3200	0.00217 ± 0.0015	0.00447 ± 0.0056	0.00046 ± 0.0018	0.005 ± 0.0027	0.61 ± 0.0090	0.9998	706.47 ± 360.58
4000	0.00071 ± 0.0013	0.00182 ± 0.0052	0.00105 ± 0.0015	0.006 ± 0.0029	0.81 ± 0.0185	1	510.33 ± 262.21

J = 0.00203517 ± 0.00000934035 Total gas age = 252.83 ± 1.29 Ma Plateau age = 252.46 ± 1.25 Ma

Red color denotes values <0

Appendix 2.6: ^{40}Ar-^{39}Ar muscovite dating data continued

WS16-006: muscovite (run mc55-s13a)

Laser Power	**Isotopic values**						**Age ± 1σ**
(mW)	^{36}Ar ± 1σ	^{37}Ar ± 1σ	^{38}Ar ± 1σ	^{39}Ar ± 1σ	^{40}Ar ± 1σ	**Cumulative ^{39}Ar**	(Ma)
100	0.02768 ± 0.0024	0.00946 ± 0.0139	0.01158 ± 0.0029	0.150 ± 0.0018	20.15 ± 0.0730	0.0088	274.98 ± 15.72
200	0.01260 ± 0.0025	0.00861 ± 0.0078	0.00072 ± 0.0019	0.613 ± 0.0033	54.74 ± 0.1890	0.0451	285.23 ± 4.13
300	0.00590 ± 0.0016	0.00257 ± 0.0098	0.00294 ± 0.0021	2.059 ± 0.0127	168.96 ± 0.6170	0.1669	278.67 ± 1.99
400	0.00095 ± 0.0018	0.00069 ± 0.0106	0.00169 ± 0.0020	2.551 ± 0.0130	205.27 ± 0.7012	0.3177	275.98 ± 1.70
600	0.00742 ± 0.0019	0.00189 ± 0.0086	0.00448 ± 0.0019	3.495 ± 0.0123	283.88 ± 1.0399	0.5245	276.68 ± 1.41
800	0.00289 ± 0.0015	0.00405 ± 0.0033	0.00457 ± 0.0012	1.529 ± 0.0089	123.45 ± 0.4654	0.6149	275.47 ± 1.99
1000	0.00244 ± 0.0015	0.00052 ± 0.0058	0.00048 ± 0.0015	1.456 ± 0.0070	116.79 ± 0.4212	0.7010	273.96 ± 1.80
1200	0.00056 ± 0.0015	0.00412 ± 0.0049	0.00190 ± 0.0018	2.612 ± 0.0126	211.49 ± 0.7789	0.8555	277.66 ± 1.66
1400	0.00179 ± 0.0011	0.00642 ± 0.0046	0.00152 ± 0.0018	0.464 ± 0.0036	37.91 ± 0.1247	0.8830	276.42 ± 3.12
1600	0.00129 ± 0.0027	0.00480 ± 0.0055	0.00031 ± 0.0017	0.369 ± 0.0027	29.87 ± 0.1084	0.9048	274.86 ± 7.17
1800	0.00126 ± 0.0021	0.00480 ± 0.0070	0.00263 ± 0.0014	1.096 ± 0.0047	89.01 ± 0.3503	0.9696	277.56 ± 2.37
2000	0.00100 ± 0.0018	0.00609 ± 0.0060	0.00233 ± 0.0023	0.194 ± 0.0044	15.83 ± 0.0617	0.9811	275.48 ± 10.68
2400	0.00155 ± 0.0019	0.00284 ± 0.0063	0.00169 ± 0.0015	0.103 ± 0.0040	8.63 ± 0.0361	0.9872	273.24 ± 19.92
2800	0.00081 ± 0.0018	0.00617 ± 0.0075	0.00273 ± 0.0025	0.191 ± 0.0042	15.58 ± 0.0547	0.9985	283.96 ± 10.58
3200	0.00082 ± 0.0018	0.01445 ± 0.0060	0.00106 ± 0.0018	0.020 ± 0.0025	1.77 ± 0.0148	0.9996	339.68 ± 88.74
4000	0.00044 ± 0.0021	0.01509 ± 0.0074	0.00002 ± 0.0017	0.006 ± 0.0026	0.47 ± 0.0143	1	197.21 ± 343.24

J = 0.00205681 ± 0.00000940214 Total gas age = 277.03 ± 1.37 Ma Plateau age = 276.72 ± 1.34 Ma

Red color denotes values <0

Appendix 2.6: ^{40}Ar-^{39}Ar muscovite dating data continued

WS16-006: muscovite (run mc55-s13b)

Laser Power	Isotopic values						Age ± 1σ
(mW)	^{36}Ar ± 1σ	^{37}Ar ± 1σ	^{38}Ar ± 1σ	^{39}Ar ± 1σ	^{40}Ar ± 1σ	Cumulative ^{39}Ar	(Ma)
100	0.03751 ± 0.0020	0.01813 ± 0.0073	0.008 ± 0.0019	0.142 ± 0.0025	22.40 ± 0.0687	0.0104	272.17 ± 13.69
200	0.00959 ± 0.0015	0.01040 ± 0.0062	0.003 ± 0.0015	0.635 ± 0.0037	54.73 ± 0.2083	0.0569	278.58 ± 2.90
300	0.00853 ± 0.0021	0.00439 ± 0.0091	0.002 ± 0.0015	1.520 ± 0.0086	124.47 ± 0.4727	0.1683	273.73 ± 2.16
400	0.00343 ± 0.0016	0.00507 ± 0.0105	0.001 ± 0.0018	1.796 ± 0.0087	147.08 ± 0.5738	0.2998	277.30 ± 1.81
600	0.00422 ± 0.0019	0.00544 ± 0.0068	0.001 ± 0.0018	2.377 ± 0.0121	193.31 ± 0.7164	0.4739	275.63 ± 1.77
800	0.00370 ± 0.0016	0.00911 ± 0.0036	0.001 ± 0.0027	1.490 ± 0.0101	121.25 ± 0.4812	0.5830	275.08 ± 2.26
1000	0.00028 ± 0.0013	0.00582 ± 0.0037	0.000 ± 0.0019	1.108 ± 0.0062	89.20 ± 0.3262	0.6642	274.42 ± 2.01
1200	0.00311 ± 0.0017	0.00032 ± 0.0072	0.000 ± 0.0017	3.812 ± 0.0203	308.49 ± 1.1443	0.9434	275.20 ± 1.71
1400	0.00007 ± 0.0017	0.00521 ± 0.0056	0.001 ± 0.0012	0.312 ± 0.0025	25.18 ± 0.1058	0.9663	275.11 ± 5.46
1600	0.00130 ± 0.0010	0.01241 ± 0.0061	0.000 ± 0.0013	0.156 ± 0.0019	12.52 ± 0.0381	0.9778	265.42 ± 6.80
1800	0.00287 ± 0.0012	0.01465 ± 0.0071	0.004 ± 0.0020	0.206 ± 0.0023	16.82 ± 0.0532	0.9929	265.22 ± 6.29
2000	0.00224 ± 0.0010	0.01291 ± 0.0101	0.005 ± 0.0022	0.047 ± 0.0017	3.99 ± 0.0152	0.9963	242.66 ± 21.45
2400	0.00148 ± 0.0013	0.00421 ± 0.0063	0.005 ± 0.0023	0.015 ± 0.0023	1.19 ± 0.0106	0.9975	173.88 ± 85.94
2800	0.00489 ± 0.0021	0.02059 ± 0.0075	0.007 ± 0.0018	0.016 ± 0.0016	1.13 ± 0.0119	0.9987	-71.92 ± 147.98
3200	0.00225 ± 0.0014	0.00238 ± 0.0055	0.000 ± 0.0013	0.013 ± 0.0030	1.07 ± 0.0097	0.9996	421.58 ± 121.26
4000	0.00063 ± 0.0015	0.00646 ± 0.0074	0.000 ± 0.0016	0.005 ± 0.0031	0.52 ± 0.0116	1	460.59 ± 367.03

J = 0.00204262 ± 0.0000100141 Total gas age = 274.79 ± 1.49 Ma Plateau age = 275.24 ± 1.45 Ma

Red color denotes values <0

Appendix 2.6: ^{40}Ar-^{39}Ar muscovite dating data continued

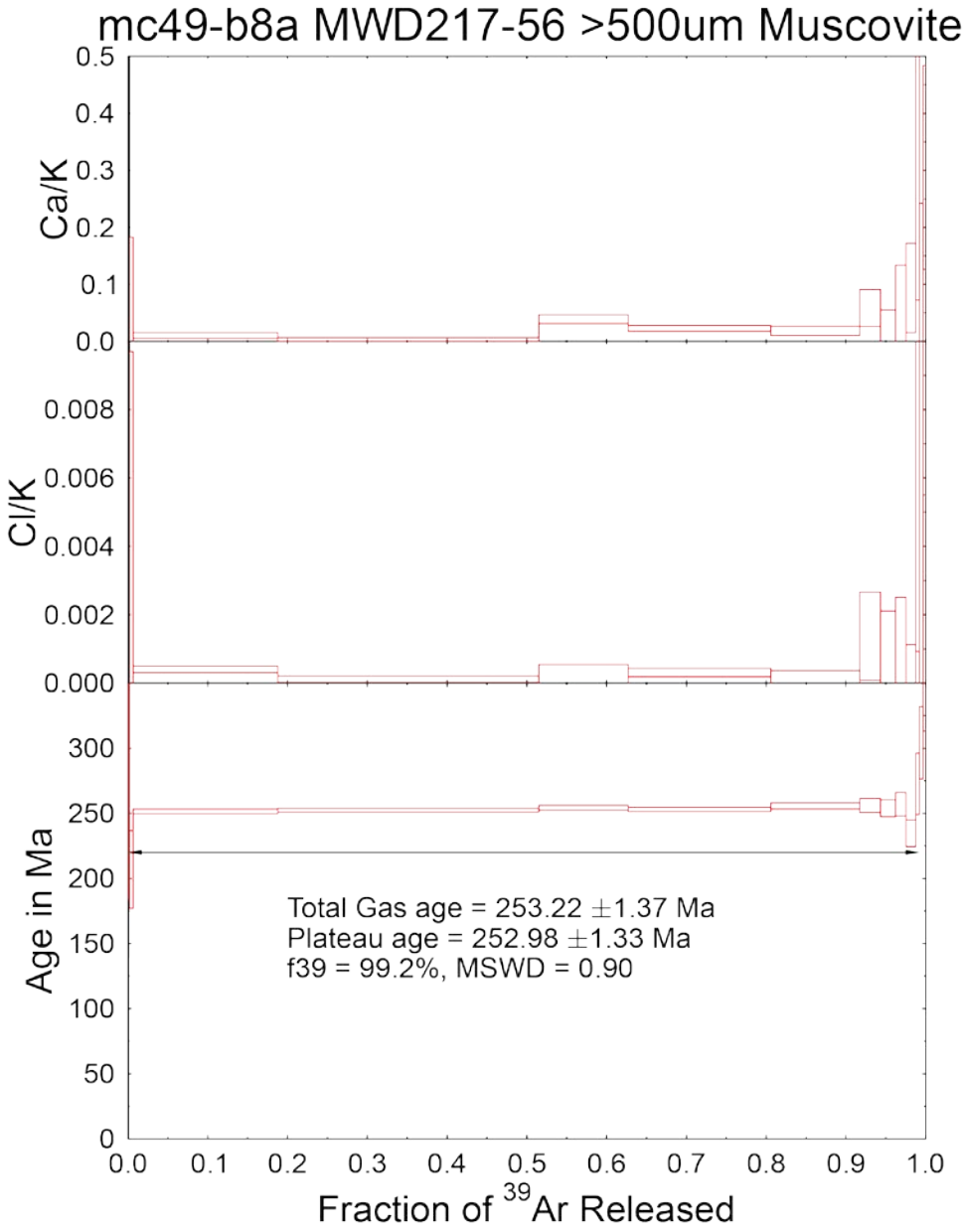

Plateau diagrams for sample MWD217-056, first run

Appendix 2.6: ^{40}Ar-^{39}Ar muscovite dating data continued

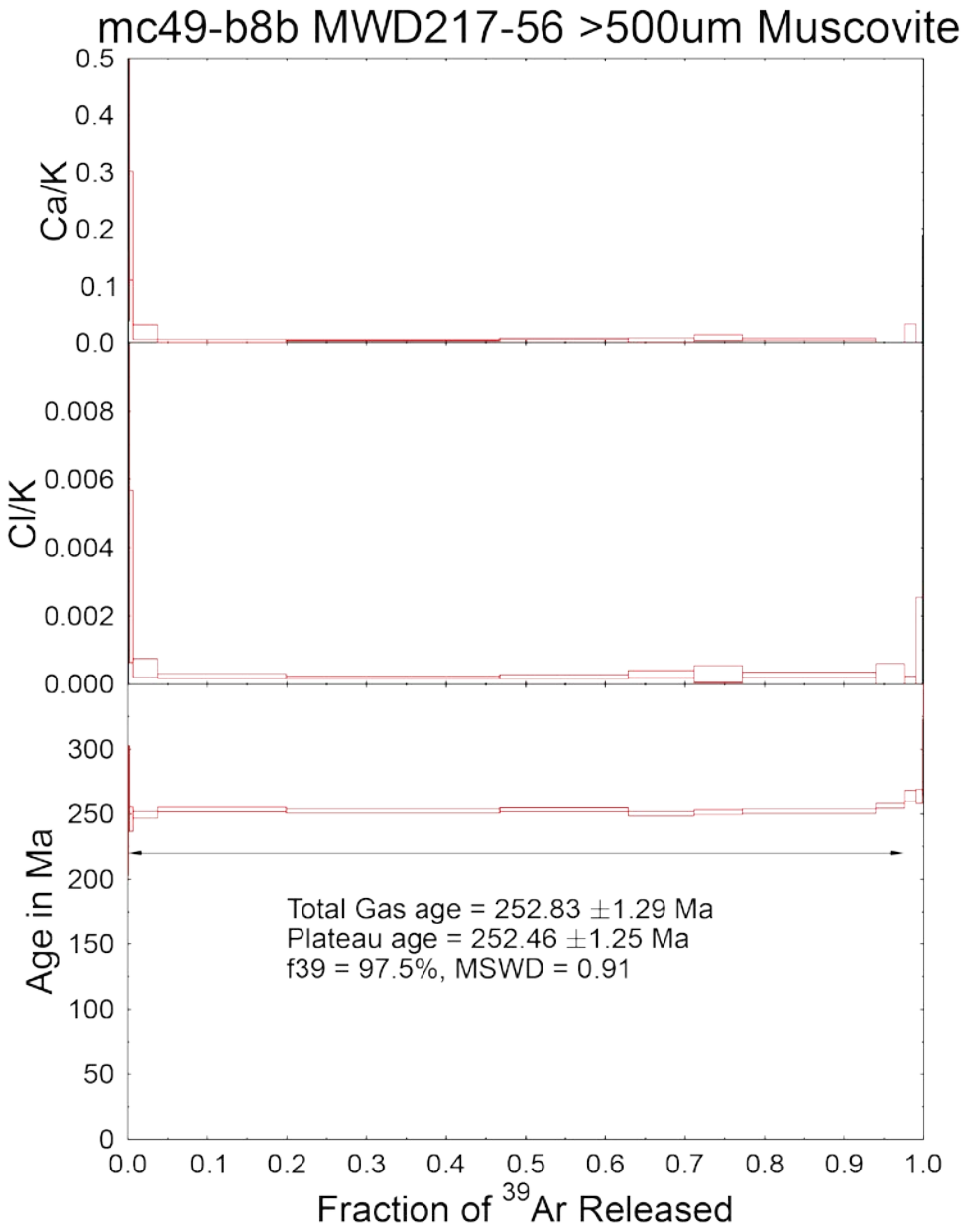

Plateau diagrams for sample MWD217-056, second run

Appendix 2.6: ^{40}Ar-^{39}Ar muscovite dating data continued

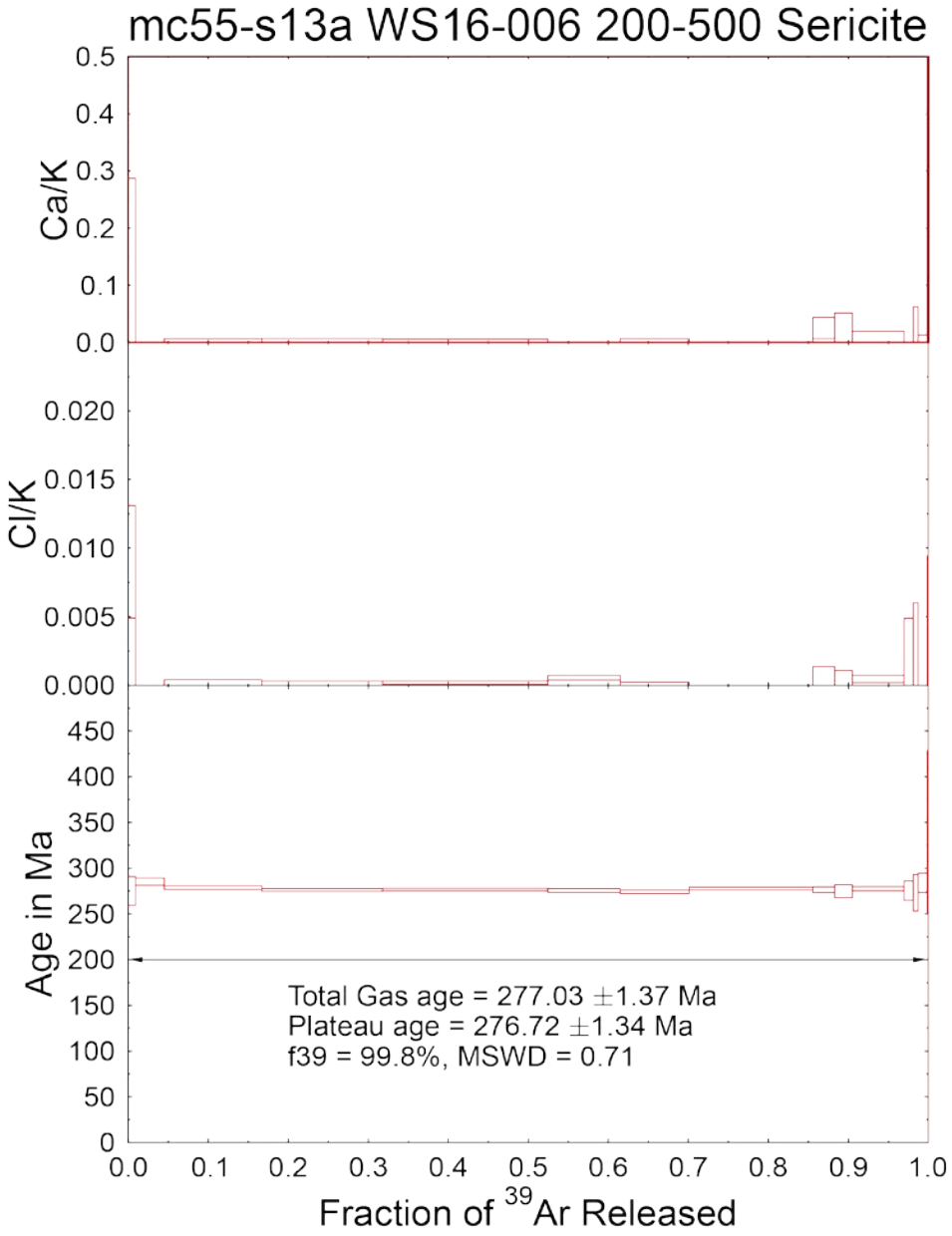

Plateau diagrams for sample WS16-006, first run

Appendix 2.6: ^{40}Ar-^{39}Ar muscovite dating data continued

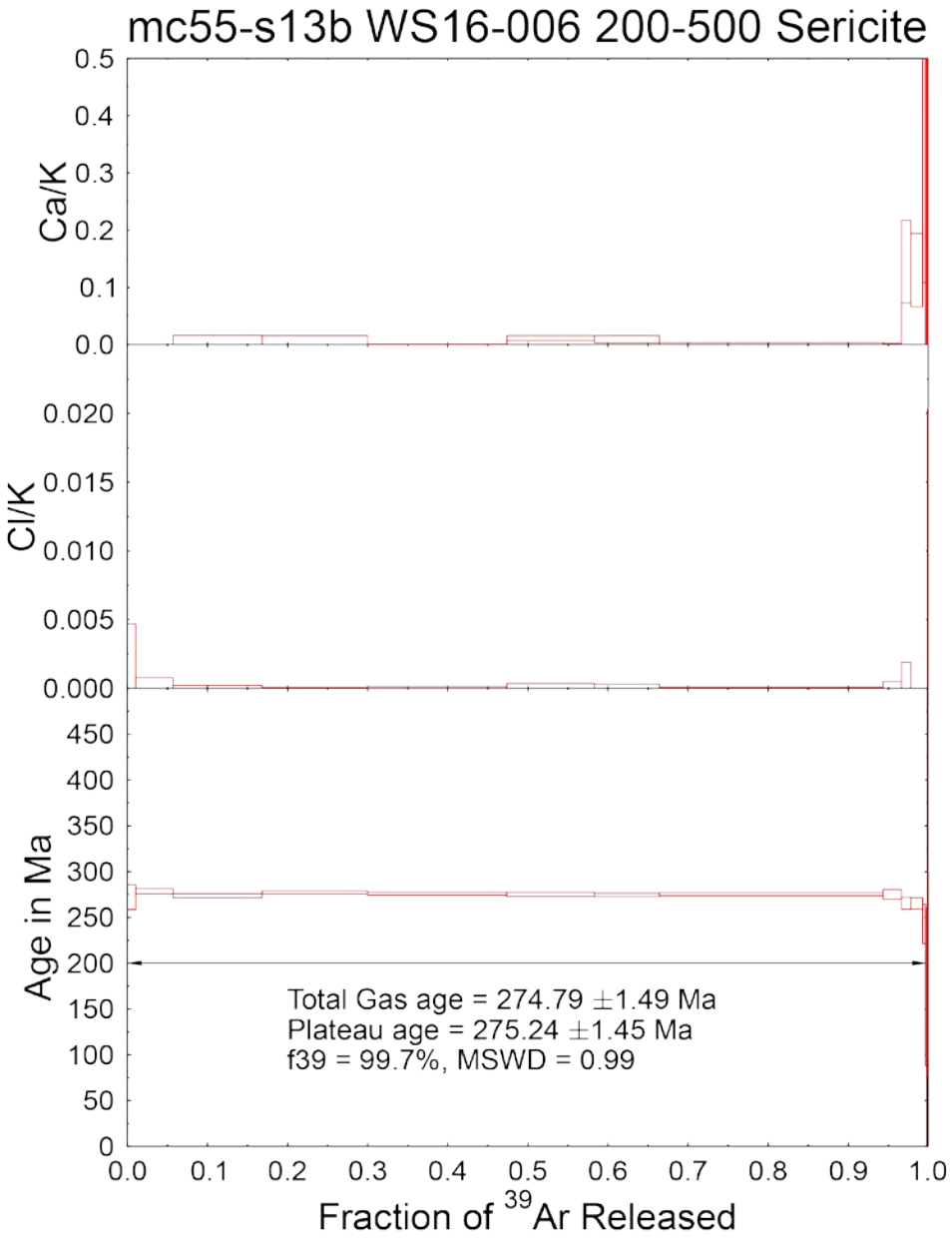

Plateau diagrams for sample MWD217-056, second run

Appendix 3: Material linked to Chapter 3

Appendix 3.1: Whole-rock geochemistry data

Sample	MWD013-099	MWD005-067	MWD036-123V	MWD042-197V	MWD099-034V	MWD099-054V	MWD099-086V	MWD101-155V	MWD101-211.5V	MWD105-123.5V
Rock type[1]	Mz	Mz	Vn	Vn	Vn	Vn	Vn	Vn	Vn	Vn
Type	Drill Core	Drill Core	Drill Core	Drill Core	Drill Core	Drill Core	Drill Core	Drill Core	Drill Core	Drill Core
SiO2_%	35.62	52.06	98.47	63.31	92.48	55.39	94.5	62.17	92.46	78.41
Al2O3_%	15.67	20.21	0.1	12.39	2.36	0.09	1.64	10.69	3.28	0.92
Fe2O3_%	1.37	2.95	1.07	2.19	1.43	0.41	0.63	0.94	1.61	0.67
MgO_%	0.19	0.67	0.01	0.06	0.05	<0.01	0.02	<0.01	<0.01	<0.01
CaO_%	12.08	6.44	0.1	15.96	1.16	8.49	0.89	6.28	1.03	4.13
Na2O_%	3.98	6.55	0.02	0.75	0.81	0.02	0.59	4.04	1.07	0.27
K2O_%	0.62	1.56	<0.01	0.05	0.3	<0.01	0.04	0.23	0.04	0.02
TiO2_%	0.33	0.32	<0.01	0.04	0.02	<0.01	0.01	<0.01	<0.01	<0.01
P2O5_%	0.35	0.14	0.01	0.02	0.02	0.03	0.03	0.02	0.03	0.09
MnO_%	0.03	0.07	0.02	0.34	0.03	<0.01	<0.01	0.03	0.01	<0.01
Cr2O3_%	0.002	0.004	<0.002	<0.002	<0.002	<0.002	<0.002	<0.002	<0.002	<0.002
Sum_%	72	93.32	99.89	98.18	99.36	64.48	98.47	85.56	99.84	84.73
Ba_ppm	109	228	6	13	141	3	16	50	20	19
Sc_ppm	62	29	<1	8	3	41	5	36	<1	45
Cs_ppm	9.1	23.6	0.6	4.7	3.8	<0.1	2.5	3	1.4	2.8
Ga_ppm	14	21.2	0.7	17.3	1.1	<0.5	2.8	6.7	0.6	<0.5
Hf_ppm	3.5	3.5	<0.1	0.1	0.2	<0.1	0.1	<0.1	<0.1	<0.1
Nb_ppm	19.7	14.6	<0.1	1.5	0.2	6	1.8	4.4	<0.1	11.8
Rb_ppm	40.1	111.5	<0.1	4.6	8.4	<0.1	3.9	16.8	4.4	4.1
Sn_ppm	43	50	<1	200	6	1	1	3	<1	2
Sr_ppm	453.2	428.1	5	72.1	51.8	40.5	35.5	360.6	89.6	36.9
Ta_ppm	0.7	1.1	<0.1	0.1	<0.1	<0.1	<0.1	<0.1	<0.1	0.2
Th_ppm	10.8	12.8	<0.2	<0.2	0.9	0.3	0.2	0.4	<0.2	0.4
U_ppm	3.5	2.9	<0.1	<0.1	<0.1	<0.1	<0.1	<0.1	<0.1	<0.1
V_ppm	<8	25	<8	33	<8	<8	<8	<8	<8	<8
W_ppm	>10000	>10000	1072.3	>10000	5006.3	>10000	>10000	>10000	728.8	>10000
Zr_ppm	132.5	129.2	0.7	2.8	5.5	0.4	4.6	1.4	3.9	0.7
Y_ppm	25	19.9	0.1	8.5	1.7	64.7	2.1	15.3	0.5	35.4
La_ppm	29.8	27.8	0.4	0.8	1.8	6.6	1	1.7	0.5	7
Ce_ppm	54	54.3	0.5	0.2	2.1	22.8	1.8	2.2	0.5	18.8
Pr_ppm	6.36	6.39	0.06	0.06	0.24	4.23	0.2	0.3	0.03	2.49
Nd_ppm	23.8	22.6	<0.3	<0.3	0.9	20.6	0.8	1.2	<0.3	10.5
Sm_ppm	4.14	3.95	<0.05	0.07	0.17	7.03	0.22	0.34	<0.05	2.42
Eu_ppm	1.06	0.73	<0.02	0.1	0.04	1.73	0.04	0.26	<0.02	0.87
Gd_ppm	4.42	3.78	<0.05	0.3	0.25	9	0.25	0.65	<0.05	2.58
Tb_ppm	0.65	0.59	<0.01	0.06	0.03	1.67	0.04	0.17	<0.01	0.5
Dy_ppm	3.93	3.24	<0.05	0.63	0.21	10.96	0.32	1.58	0.06	3.47
Ho_ppm	0.79	0.68	<0.02	0.17	0.05	2.55	0.07	0.43	<0.02	0.78
Er_ppm	2.39	2.28	<0.03	0.77	0.15	7.27	0.23	1.38	<0.03	2.74
Tm_ppm	0.36	0.29	<0.01	0.13	0.02	0.88	0.03	0.18	<0.01	0.52
Yb_ppm	2.64	1.82	<0.05	1.02	0.14	4.91	0.15	1	<0.05	4.55
Lu_ppm	0.46	0.27	<0.01	0.17	0.01	0.72	0.02	0.14	<0.01	0.7
Ni_ppm	<10	<10	<10	<10	<10	<10	<10	<10	<10	<10
LOI_%	1.8	2.3	0.1	3.1	0.7	0.1	0.1	1.2	0.3	0.3
TOT/C_%	0.14	0.33	0.04	0.78	0.2	0.07	0.04	0.27	0.09	0.03
TOT/S_%	0.23	0.88	0.09	0.08	0.27	0.02	0.09	0.12	0.51	0.05
Mo_ppm	4.34	1.91	1.7	1.36	1.51	1.13	0.67	I.S.	0.89	1.25
Cu_ppm	46.64	125.55	21.63	23.84	64.22	7.02	20.33	I.S.	30.82	13.43
Pb_ppm	4.87	3.93	0.53	1.12	3.01	2.49	0.9	I.S.	1.66	2.62
Zn_ppm	32.7	49.4	8.5	10.1	6.5	4.4	5.1	I.S.	5.6	2.9
Ag_ppb	39	114	25	16	94	15	19	I.S.	77	26
Ni_ppm	6.2	7.3	2.1	1.1	2.8	1.1	1	I.S.	5.2	1.5
Co_ppm	4.7	3.2	1.3	1	1.6	0.5	0.8	I.S.	2.6	0.6
Mn_ppm	161	400	135	693	201	64	42	I.S.	76	60
As_ppm	8.3	0.1	1	0.7	6.9	1.5	0.8	I.S.	0.7	2.1

Appendix 3.1: Whole-rock geochemistry data continued

Sample	MWD013-099	MWD005-067	MWD036-123V	MWD042-197V	MWD099-034V	MWD099-054V	MWD099-086V	MWD101-155V	MWD101-211.5V	MWD105-123.5V
Rock type[1]	Mz	Mz	Vn	Vn	Vn	Vn	Vn	Vn	Vn	Vn
Type	Drill Core	Drill Core	Drill Core	Drill Core	Drill Core	Drill Core	Drill Core	Drill Core	Drill Core	Drill Core
Au_ppb	2.6	0.5	2.1	1.3	1.4	1.7	1.1	I.S.	2.6	1.1
Cd_ppm	0.26	0.64	0.02	0.44	0.1	0.08	0.01	I.S.	0.01	0.07
Sb_ppm	<0.02	<0.02	0.03	0.03	0.04	<0.02	<0.02	I.S.	<0.02	<0.02
Bi_ppm	0.05	0.13	<0.02	0.06	0.26	0.04	0.03	I.S.	0.85	0.27
Cr_ppm	12.3	10.4	4.4	1.4	4.3	1.8	1.8	I.S.	2	2.3
B_ppm	3	3	<1	2	5	<1	2	I.S.	4	5
Tl_ppm	0.13	0.14	0.02	<0.02	0.02	<0.02	0.02	I.S.	<0.02	0.03
Hg_ppb	*	<5	*	<5	<5	<5	<5	I.S.	*	*
Se_ppm	<0.1	<0.1	<0.1	<0.1	<0.1	<0.1	<0.1	I.S.	<0.1	<0.1
Te_ppm	<0.02	<0.02	<0.02	<0.02	<0.02	<0.02	<0.02	I.S.	<0.02	0.03
Ge_ppm	<0.1	<0.1	<0.1	1	<0.1	<0.1	<0.1	I.S.	0.1	<0.1
In_ppm	<0.02	<0.02	<0.02	<0.02	<0.02	<0.02	<0.02	I.S.	<0.02	<0.02
Re_ppb	11	3	4	3	2	4	2	I.S.	4	4
Be_ppm	16.9	4.4	0.2	14.9	1.8	0.2	0.4	I.S.	1.6	3
Li_ppm	18.3	23.9	<0.1	0.4	3.5	0.7	1.4	I.S.	0.2	0.9
Pd_ppb	<10	<10	<10	<10	<10	<10	<10	I.S.	<10	<10
Pt_ppb	<2	<2	2	<2	<2	2	<2	I.S.	4	2
F_ppm	976	1265	30	4020	1015	65	113	382	78	154
FeO_%	1.03	2.52	0.94	1.09	1.09	0.51	0.51	0.87	1.45	0.59
W_%	21.118	4.752	N.A.	1.599	N.A.	27.829	1.22	11.2	N.A.	11.865
As_%	N.A.	N.A.	N.A.	N.A.	N.A.	N.A.	N.A.	N.A.	N.A.	N.A.

[1] Rock type abbreviations: Mz: monzonite, Vn: vein

Appendix 3.1: Whole-rock geochemistry data continued

Sample	MWD105-206V	MWD107-310V	MWD124-266V	MWD194-105.5V	MWD217-078V	MWD217-189.5V	MWD036-123H	MWD042-197H	MWD099-034H	MWD099-054H
Rock type[1]	Vn	Vn	Vn	Vn	Vn	Vn	V-H	V-H	V-H	V-H
Type	Drill Core	Drill Core	Drill Core	Drill Core	Drill Core	Drill Core	Drill Core	Drill Core	Drill Core	Drill Core
SiO2_%	49.13	98.78	97.58	76.38	92.38	78.76	72.38	64.3	67.27	59.4
Al2O3_%	3.69	0.26	0.1	3.63	0.52	4.02	10.83	14.91	11.11	17.03
Fe2O3_%	0.75	0.48	0.45	1.84	1.57	0.68	3.47	5.06	4.36	5.43
MgO_%	<0.01	0.01	<0.01	0.19	0.02	0.03	0.99	1.58	0.75	1.6
CaO_%	9.09	0.13	1.11	9.11	1.47	7.47	4.48	8.5	9.93	3.66
Na2O_%	1.22	<0.01	<0.01	1.08	0.12	1.29	2.64	1.85	1.35	2.81
K2O_%	0.06	<0.01	0.16	0.34	0.04	0.68	1.21	0.9	0.73	4.8
TiO2_%	0.01	<0.01	<0.01	<0.01	<0.01	<0.01	0.28	0.7	0.41	0.66
P2O5_%	0.16	0.02	<0.01	0.01	0.02	0.02	0.11	0.16	0.12	0.1
MnO_%	<0.01	<0.01	<0.01	0.24	0.01	0.14	0.09	0.15	0.4	0.1
Cr2O3_%	<0.002	<0.002	<0.002	<0.002	<0.002	<0.002	0.002	0.006	0.004	0.006
Sum_%	64.23	99.69	100	99.44	97.26	97.54	97.67	99.39	99.79	99.67
Ba_ppm	15	6	3	61	5	319	613	281	115	2135
Sc_ppm	61	1	<1	4	10	8	15	14	6	10
Cs_ppm	0.5	0.8	7.8	14	6.7	2	51.9	57.5	24.3	101.3
Ga_ppm	<0.5	<0.5	1.4	2	<0.5	2.1	13.8	15.8	16.2	15.8
Hf_ppm	0.1	<0.1	<0.1	<0.1	<0.1	0.1	3	7.4	4.5	8.1
Nb_ppm	102.9	0.8	1.3	<0.1	0.6	0.3	6.1	15	10.5	22.9
Rb_ppm	4.4	1.5	27.8	21.6	9.3	19.4	102.3	102.1	56.8	258.6
Sn_ppm	4	<1	<1	6	1	3	37	71	322	65
Sr_ppm	121.6	14.9	1.1	119.4	14	141	237.7	468.2	249.5	244.4
Ta_ppm	1.1	<0.1	<0.1	<0.1	<0.1	<0.1	0.6	1.3	0.9	1.5
Th_ppm	0.7	<0.2	<0.2	<0.2	<0.2	0.4	11.9	23.1	15.5	20.7
U_ppm	0.1	<0.1	<0.1	<0.1	<0.1	<0.1	2.9	5.8	3.4	4.5
V_ppm	<8	<8	<8	<8	<8	<8	29	61	44	55
W_ppm	>10000	2006.6	153.2	3703.6	>10000	>10000	>10000	3033.8	380.3	838.6
Zr_ppm	5.2	0.6	0.9	2.2	0.5	5.1	102.3	253.4	164.4	272.3
Y_ppm	306	2.7	0.2	12.5	3.3	8.4	18.3	34	23.5	32.5
La_ppm	18.8	0.3	0.4	1.4	0.8	1	24	45.5	31.2	22.8
Ce_ppm	56.7	0.4	0.5	1.7	1.7	1.7	43.9	90.4	59.2	51.7
Pr_ppm	7.82	0.06	0.03	0.21	0.26	0.26	5.41	10.32	6.68	6.2
Nd_ppm	33	0.3	0.3	1.1	1.2	1.4	20.8	37.6	24.6	23.6
Sm_ppm	10.42	0.08	<0.05	0.3	0.25	0.43	3.67	7.01	4.2	4.68
Eu_ppm	3.49	0.03	<0.02	0.14	0.16	0.17	0.66	1.25	0.76	0.87
Gd_ppm	16.89	0.17	<0.05	0.66	0.37	0.78	3.38	6.34	4.08	4.42
Tb_ppm	4.55	0.04	<0.01	0.17	0.06	0.16	0.52	1.04	0.63	0.77
Dy_ppm	38.77	0.37	<0.05	1.35	0.47	1.29	3.04	5.92	3.87	4.82
Ho_ppm	10.17	0.09	<0.02	0.41	0.09	0.29	0.64	1.28	0.77	1.1
Er_ppm	33.87	0.31	0.03	1.49	0.3	1.05	1.92	3.71	2.31	3.43
Tm_ppm	4.92	0.04	<0.01	0.25	0.05	0.15	0.26	0.55	0.34	0.52
Yb_ppm	27.08	0.19	<0.05	1.93	0.33	0.98	1.71	3.48	2.27	3.67
Lu_ppm	3.22	0.02	<0.01	0.37	0.05	0.18	0.24	0.5	0.35	0.54
Ni_ppm	<10	<10	<10	<10	<10	<10	<10	15	<10	16
LOI_%	0.2	0	0.6	6.6	1.1	4.4	1.1	1.2	3.3	3.8
TOT/C_%	0.02	0.03	0.02	2.77	0.14	1.85	0.2	0.11	0.71	2.51
TOT/S_%	0.17	<0.01	0.01	0.77	0.56	0.14	0.93	1.02	0.67	1.34
Mo_ppm	1.24	1.07	0.88	0.72	1.06	0.85	1.44	1.77	1.53	1
Cu_ppm	28.87	7.45	2.7	74.63	10.29	16.5	235.76	309.32	129.23	291.77
Pb_ppm	5.56	0.46	0.12	53.6	27.12	3.42	3.74	3.04	3.25	23.58
Zn_ppm	3.4	4.2	1.5	17.4	7	508.7	79.6	71.8	49.5	141.5
Ag_ppb	63	12	11	1768	1808	39	204	353	213	414
Ni_ppm	1.1	0.9	0.7	3.2	1	0.8	13.1	20.7	9.4	18.4
Co_ppm	2.1	0.5	0.4	1	0.6	0.7	7.2	10	5.6	8.8
Mn_ppm	54	44	32	1919	81	1031	525	488	1553	633
As_ppm	321.5	2.1	0.4	69.6	9954.5	15.1	59.9	1.4	14.5	455.1

Appendix 3.1: Whole-rock geochemistry data continued

Sample	MWD105-206V	MWD107-310V	MWD124-266V	MWD194-105.5V	MWD217-078V	MWD217-189.5V	MWD036-123H	MWD042-197H	MWD099-034H	MWD099-054H
Rock type[1]	Vn	Vn	Vn	Vn	Vn	Vn	V-H	V-H	V-H	V-H
Type	Drill Core	Drill Core	Drill Core	Drill Core	Drill Core	Drill Core	Drill Core	Drill Core	Drill Core	Drill Core
Au_ppb	5.9	1.1	0.4	<0.2	117.3	0.7	1.9	3	3	1.6
Cd_ppm	0.19	<0.01	<0.01	1.15	0.35	48.91	0.66	0.39	1.18	2.46
Sb_ppm	<0.02	0.03	<0.02	<0.02	0.22	<0.02	0.04	0.03	0.12	0.17
Bi_ppm	2.66	0.05	0.07	4.33	61.68	0.27	0.31	0.67	0.35	1.22
Cr_ppm	1.6	2.3	1.8	1.8	2.1	2	16.3	25	15.6	31.6
B_ppm	59	3	20	6	5	3	2	2	5	3
Tl_ppm	<0.02	<0.02	<0.02	0.06	0.02	<0.02	0.65	0.7	0.27	1.03
Hg_ppb	*	<5	<5	<5	*	<5	*	*	*	*
Se_ppm	0.4	<0.1	<0.1	<0.1	<0.1	<0.1	0.3	0.6	<0.1	0.2
Te_ppm	0.04	<0.02	0.03	<0.02	0.61	<0.02	<0.02	0.03	0.04	0.02
Ge_ppm	0.1	<0.1	<0.1	0.1	0.1	<0.1	0.3	0.3	1.3	0.3
In_ppm	<0.02	<0.02	<0.02	<0.02	0.02	0.23	0.02	0.03	0.08	0.03
Re_ppb	9	3	2	1	3	<1	6	9	6	9
Be_ppm	3	0.4	0.6	2.9	0.6	2.3	5.6	7.7	18	3.1
Li_ppm	1.1	0.6	0.3	5.4	1.9	1.8	64.4	74.7	48.8	135.2
Pd_ppb	<10	<10	<10	<10	<10	<10	<10	<10	<10	<10
Pt_ppb	<2	4	<2	<2	<2	<2	<2	<2	<2	<2
F_ppm	167	40	833	608	341	216	2050	2187	8458	2693
FeO_%	0.65	0.47	0.44	1.76	0.43	0.65	2.76	4.1	2.53	4.48
W_%	27.197	N.A.	N.A.	N.A.	2.274	4.127	2.073	N.A.	N.A.	N.A.
As_%	N.A.	N.A.	N.A.	N.A.	N.A.	N.A.	N.A.	N.A.	N.A.	N.A.

[1] Rock type abbreviations: Vn: vein, V-H: vein halo (proximal skarn-altered conglomerate)

Appendix 3.1: Whole-rock geochemistry data continued

Sample	MWD099-086H	MWD101-155H	MWD101-211.5H	MWD105-123.5H	MWD105-206H	MWD107-310H	MWD124-266H	MWD194-105.5H	MWD217-078H	MWD217-189.5H
Rock type[1]	V-H	V-H	V-H	V-H	V-H	V-H	V-H	V-H	V-H	V-H
Type	Drill Core	Drill Core	Drill Core	Drill Core	Drill Core	Drill Core	Drill Core	Drill Core	Drill Core	Drill Core
SiO2_%	71.25	56.04	67.08	70.49	69.34	76.28	65.89	72.55	71.07	61.77
Al2O3_%	12.34	19.97	13.4	11.38	10.66	11.53	12.63	10.43	9.41	11.14
Fe2O3_%	4.17	4.7	3.53	4.13	3.66	2.89	4.38	3.22	2.51	5.25
MgO_%	1.17	0.5	0.91	1.11	0.75	0.82	1.25	0.77	0.74	0.85
CaO_%	4.27	8.75	8.1	5.33	8.04	2.39	9.77	4.84	7.58	13.61
Na2O_%	3.26	5.14	2.56	2.69	1.14	2.27	1.51	2.58	2.21	1.02
K2O_%	1.02	0.94	0.56	1.02	0.67	2.59	0.36	1.38	0.7	0.2
TiO2_%	0.45	0.28	0.38	0.39	0.31	0.3	0.51	0.38	0.34	0.33
P2O5_%	0.08	0.08	0.2	0.11	0.11	0.12	0.23	0.13	0.1	0.13
MnO_%	0.1	0.74	0.19	0.18	0.29	0.08	0.29	0.12	0.19	0.55
Cr2O3_%	0.004	0.003	0.002	0.003	0.003	<0.002	0.002	0.003	0.003	0.003
Sum_%	99.15	98.52	99.2	99.16	96.96	99.82	99.17	99.07	98.89	99.46
Ba_ppm	464	180	102	220	46	620	94	212	135	49
Sc_ppm	8	15	8	9	17	7	12	9	8	10
Cs_ppm	55.1	15.9	27.7	53.3	29.4	55.6	28.7	34	35.6	11
Ga_ppm	11.5	22.9	14.8	10.8	14	13.1	14.6	10.5	9.7	18
Hf_ppm	5.6	4	4.5	4.1	3.8	3.6	6.6	4.8	4.6	4.8
Nb_ppm	10.5	6.7	11.2	11.1	10	18.7	15.1	8.8	9.9	7.1
Rb_ppm	106.4	72.7	66.8	106.3	76.3	183.8	47.7	103	73.9	26.2
Sn_ppm	52	75	113	77	168	24	102	78	99	211
Sr_ppm	232.4	437	380.2	256.6	219.9	179.7	339.8	217.2	250.8	226.2
Ta_ppm	0.9	0.5	0.9	0.9	0.8	5.9	1.3	0.8	0.8	0.6
Th_ppm	16.9	11.5	12.9	13.6	10.8	13.6	20.6	12.5	13.3	15.1
U_ppm	3.8	2.9	4.3	3.5	2.9	3.1	5.3	3.6	3.3	4
V_ppm	36	55	41	39	18	39	38	21	25	50
W_ppm	5494.8	>10000	4614.9	5196.8	>10000	281.5	4766.8	6108.8	7398.1	2847.7
Zr_ppm	198	130	149.9	142.6	142.3	128.6	236.5	161.7	161.8	162.2
Y_ppm	20.3	32.3	26.1	24.6	24.3	16.3	37.9	17.9	19.8	32.4
La_ppm	20.6	41.5	35.4	30.9	26.4	33.8	45.7	26.3	27.8	36.3
Ce_ppm	41.1	74.2	66.6	59.1	50.3	62.4	91.7	51.8	54.7	67.9
Pr_ppm	4.89	7.9	7.54	6.64	5.73	7.03	10.29	6.03	6.27	7.68
Nd_ppm	18.3	27.3	28.1	24.2	21.1	24	36.4	22.3	23.4	27.5
Sm_ppm	3.6	4.58	5.12	4.36	3.74	4.25	7.4	3.87	4.38	4.96
Eu_ppm	0.51	0.92	0.84	0.73	0.79	0.78	1.12	0.63	0.69	1.03
Gd_ppm	3.55	4.25	4.65	3.86	3.69	3.77	6.6	3.39	4	4.62
Tb_ppm	0.58	0.68	0.75	0.65	0.62	0.57	1.08	0.56	0.64	0.77
Dy_ppm	3.51	4.36	4.54	4.02	3.73	3.14	6.48	3.22	3.54	4.71
Ho_ppm	0.74	0.96	0.9	0.82	0.81	0.62	1.3	0.66	0.72	1.02
Er_ppm	2.13	3.24	2.59	2.42	2.43	1.71	4.09	1.97	2.29	3.17
Tm_ppm	0.3	0.49	0.37	0.36	0.37	0.23	0.59	0.28	0.32	0.47
Yb_ppm	1.84	3.57	2.32	2.35	2.45	1.46	3.69	1.83	2.08	3.16
Lu_ppm	0.25	0.55	0.35	0.36	0.37	0.24	0.55	0.27	0.33	0.53
Ni_ppm	<10	<10	<10	<10	<10	<10	14	13	<10	<10
LOI_%	1	1.4	2.3	2.3	2	0.5	2.3	2.7	4	4.6
TOT/C_%	0.23	0.62	0.51	0.52	0.36	0.05	0.68	0.96	1.46	1.68
TOT/S_%	1.05	1.17	0.61	0.76	0.46	0.14	0.55	1.11	0.62	1.01
Mo_ppm	0.59	0.55	1.13	5.94	2.34	13.14	1.08	0.66	0.64	0.83
Cu_ppm	137.78	174.54	99.31	110.35	76.77	54.57	71.95	84	72.33	100.11
Pb_ppm	3.37	4.97	2.79	3.52	2.89	10.91	2.57	8.64	3.05	2.57
Zn_ppm	49.1	30.3	53.6	50.2	52.9	93.5	84.9	40.3	51.9	52.3
Ag_ppb	147	228	311	177	94	155	149	315	86	97
Ni_ppm	11.3	3.4	10.9	10.1	9.6	7.1	11.7	11.3	8.7	8.4
Co_ppm	6.1	3.4	5.2	6.2	6.1	4.1	7.1	7	4.9	5.6
Mn_ppm	431	1263	806	826	787	566	803	684	988	1794
As_ppm	24.4	32.1	15.6	917.3	20.1	1.7	148.2	5354.3	602.6	199.8

Appendix 3.1: Whole-rock geochemistry data continued

Sample	MWD099-086H	MWD101-155H	MWD101-211.5H	MWD105-123.5H	MWD105-206H	MWD107-310H	MWD124-266H	MWD194-105.5H	MWD217-078H	MWD217-189.5H
Rock type[1]	V-H	V-H	V-H	V-H	V-H	V-H	V-H	V-H	V-H	V-H
Type	Drill Core	Drill Core	Drill Core	Drill Core	Drill Core	Drill Core	Drill Core	Drill Core	Drill Core	Drill Core
Au_ppb	1.4	0.9	1.5	5.6	1.3	2.1	2.7	1.2	0.7	0.7
Cd_ppm	0.34	0.54	0.37	0.88	0.74	0.21	1.08	1.22	2.12	2.35
Sb_ppm	0.04	0.03	0.03	0.06	0.03	0.04	0.06	0.24	0.08	0.08
Bi_ppm	0.33	0.31	0.39	2.55	0.66	2.5	0.36	1.35	0.54	0.54
Cr_ppm	19.1	6.9	15.4	18.6	13.6	15.7	14.4	11.8	14.2	12.2
B_ppm	3	2	2	2	2	2	4	2	2	4
Tl_ppm	0.68	0.12	0.34	0.54	0.38	0.99	0.3	0.36	0.33	0.17
Hg_ppb	*	*	*	*	*	*	*	*	*	*
Se_ppm	<0.1	<0.1	<0.1	<0.1	<0.1	<0.1	<0.1	0.1	<0.1	<0.1
Te_ppm	<0.02	<0.02	<0.02	<0.02	<0.02	<0.02	<0.02	0.06	<0.02	<0.02
Ge_ppm	0.2	0.2	0.4	0.3	0.4	0.3	0.4	<0.1	0.5	1.8
In_ppm	0.02	<0.02	0.03	<0.02	0.02	0.05	0.05	0.04	0.02	0.05
Re_ppb	9	7	8	13	5	5	19	8	5	13
Be_ppm	4	6.2	7.5	4.8	6.6	0.6	7.4	2.5	6.2	5.3
Li_ppm	75.7	21.2	48.7	63	37.4	73.3	59.8	39.3	37.1	36.8
Pd_ppb	<10	<10	<10	<10	<10	<10	<10	<10	<10	<10
Pt_ppb	<2	2	<2	3	<2	4	2	2	<2	<2
F_ppm	2218	802	2138	1644	1343	1104	1493	1541	2546	5911
FeO_%	3.8	4.04	2.96	3.54	2.75	2.49	2.9	2.53	2.2	4
W_%	N.A.	1.137	N.A.	N.A.	2.518	N.A.	N.A.	N.A.	N.A.	N.A.
As_%	N.A.	N.A.	N.A.	N.A.	N.A.	N.A.	N.A.	N.A.	N.A.	N.A.

[1] Rock type abbreviations: V-H: vein halo (proximal skarn-altered conglomerate)

Appendix 3.1: Whole-rock geochemistry data continued

Sample	MWD099-163.5	MWD101-159	MWD105-115	MWD107-172	MWD107-259	MWD119-126	MWD124-266	MWD217-098	MWD105-165	MWD099-102.5
Rock type[1]	sk-alt cong	sk-alt cong	sk-alt cong	sk-alt cong	sk-alt cong	sk-alt cong	sk-alt cong	sk-alt cong	ps prox	ps prox
Type	Drill Core	Drill Core	Drill Core	Drill Core	Drill Core	Drill Core	Drill Core	Drill Core	Drill Core	Drill Core
SiO2_%	59.83	66.99	33.52	68.27	57.84	73.42	69.58	76.54	80.91	77.41
Al2O3_%	10.61	11.48	11.4	10.33	12.5	9.05	10.17	9.86	9.18	11.45
Fe2O3_%	5.63	4.41	4.62	4.3	3.82	5.04	4.39	3.19	2.8	2.64
MgO_%	0.79	1.26	1.66	0.87	0.65	1	1.06	0.72	0.69	0.66
CaO_%	18.88	11.78	29.16	11.25	19.78	7.34	10.58	6.13	1.77	0.93
Na2O_%	0.04	0.37	0.11	0.37	0.09	1.06	0.44	1.91	2.23	2.56
K2O_%	0.02	0.12	0.63	0.33	0.05	0.37	0.1	0.34	1.42	3.35
TiO2_%	0.31	0.47	0.4	0.35	0.31	0.38	0.36	0.25	0.23	0.35
P2O5_%	0.19	0.25	0.21	0.14	0.08	0.08	0.19	0.08	0.06	0.05
MnO_%	0.67	0.26	0.47	0.39	0.56	0.23	0.33	0.25	0.06	0.05
Cr2O3_%	0.002	0.004	0.005	0.004	<0.002	0.004	0.003	0.003	0.003	0.004
Sum_%	99.87	99.73	99.88	99.54	99.82	99.86	99.46	99.93	99.94	99.91
Ba_ppm	20	24	29	43	78	282	43	77	150	562
Sc_ppm	5	9	10	8	5	7	8	4	4	5
Cs_ppm	0.4	3.6	29.7	21	1	2.7	4.6	5	36.2	24.4
Ga_ppm	18.1	14.5	20.4	26.1	19.3	8.9	14.3	10.8	9.1	11
Hf_ppm	2.8	5.7	3.1	4.6	3.3	4.3	4.4	2.8	2.8	4.4
Nb_ppm	5.9	13	10.2	8.7	9	9.3	10.8	6.7	6	7.2
Rb_ppm	0.9	9.3	67.5	41.4	3.1	14.2	8.8	17.9	104.3	130.3
Sn_ppm	283	116	19	560	516	16	124	23	2	4
Sr_ppm	74.4	452.6	265.6	231.6	186.1	382.8	288.2	211.2	79.2	112.2
Ta_ppm	0.6	1.2	0.8	0.8	0.5	0.8	0.8	0.6	0.6	0.6
Th_ppm	7.5	14.4	12.7	12.3	9	15.2	11.7	10.1	10.2	13.9
U_ppm	2.1	4.3	3.5	3	2.3	3.1	3.2	2.2	1.9	2.8
V_ppm	44	37	68	52	42	37	37	30	27	40
W_ppm	264.6	811.3	21.4	2280.4	273	10	3154.4	10.2	52.6	48
Zr_ppm	96.7	213.7	116.8	167.4	110.8	162	155.2	108.7	96	151.5
Y_ppm	21.9	29.7	29.6	26.8	24.1	21.6	25.7	15.9	15	19.2
La_ppm	21.5	36.8	26.9	27.1	21.2	26.1	29	12.9	31.8	37.4
Ce_ppm	40.5	71.1	54.3	54.4	42.5	51.8	57.7	26.7	59.2	66.8
Pr_ppm	4.78	8.42	6.36	6.49	4.98	6.11	6.61	3.29	6.72	7.44
Nd_ppm	17.2	30	24.4	24.1	19.2	22.3	24.7	10.8	23.3	26.4
Sm_ppm	3.37	5.93	4.75	4.58	3.62	4.08	4.46	2.52	3.9	4.35
Eu_ppm	0.63	1.05	0.95	0.8	0.72	0.82	0.8	0.45	0.81	0.85
Gd_ppm	3.38	5.51	4.51	4.23	3.48	3.54	4.31	2.4	3.17	3.88
Tb_ppm	0.57	0.86	0.74	0.71	0.59	0.61	0.69	0.4	0.46	0.6
Dy_ppm	3.21	5.09	4.3	4.41	3.51	3.71	4.1	2.68	2.72	3.38
Ho_ppm	0.67	1.01	0.93	0.85	0.67	0.81	0.87	0.54	0.52	0.71
Er_ppm	2.11	2.97	2.9	2.65	2.11	2.54	2.61	1.74	1.57	2.03
Tm_ppm	0.32	0.46	0.43	0.39	0.32	0.32	0.36	0.27	0.23	0.28
Yb_ppm	2.02	2.8	2.74	2.48	2.12	2.38	2.51	1.96	1.61	1.99
Lu_ppm	0.31	0.41	0.44	0.4	0.32	0.33	0.38	0.31	0.23	0.31
Ni_ppm	<10	13	13	<10	<10	12	<10	<10	<10	<10
LOI_%	2.9	2.3	17.7	2.9	4.1	1.9	2.3	0.7	0.6	0.4
TOT/C_%	0.72	0.34	5.31	0.36	1	0.27	0.35	0.1	0.13	0.03
TOT/S_%	0.04	0.23	0.01	0.22	0.01	0.49	0.16	0.18	0.12	0.14
Mo_ppm	0.11	0.19	1.18	0.22	0.38	0.15	0.54	0.26	0.92	0.81
Cu_ppm	3.78	21.31	4.28	20.95	25.72	1.9	16.35	36.31	16.32	10.8
Pb_ppm	1.93	2.77	3.99	4.07	4.98	1.57	1.89	4.21	12.61	19.41
Zn_ppm	21.8	68.3	37.6	53.4	26.4	44	93.9	23.9	43.9	40.3
Ag_ppb	33	62	8	68	139	32	54	38	69	73
Ni_ppm	3.5	9.6	10.3	8.6	12.6	3.4	8.2	5.3	7.4	5.2
Co_ppm	2.7	6	5	5.2	6	3.2	4.9	2.9	4.5	3.9
Mn_ppm	2095	644	2155	1555	635	1605	849	486	427	309
As_ppm	11	40.9	11.5	19.6	2.2	6.9	10	4.8	4.2	0.1

Appendix 3.1: Whole-rock geochemistry data continued

Sample	MWD099-163.5	MWD101-159	MWD105-115	MWD107-172	MWD107-259	MWD119-126	MWD124-266	MWD217-098	MWD105-165	MWD099-102.5
Rock type[1]	sk-alt cong	sk-alt cong	sk-alt cong	sk-alt cong	sk-alt cong	sk-alt cong	sk-alt cong	sk-alt cong	ps prox	ps prox
Type	Drill Core	Drill Core	Drill Core	Drill Core	Drill Core	Drill Core	Drill Core	Drill Core	Drill Core	Drill Core
Au_ppb	1	<0.2	0.5	0.8	1.7	0.8	1	1.4	0.7	<0.2
Cd_ppm	1.25	1.22	0.51	1.76	0.15	1.69	1.93	0.29	0.04	0.04
Sb_ppm	0.09	0.05	0.06	0.06	0.06	0.08	0.04	0.04	0.04	0.04
Bi_ppm	0.09	0.12	0.54	0.32	0.18	0.08	0.06	0.24	0.48	0.17
Cr_ppm	8.9	10.9	15.9	12.5	14.5	5.4	9.2	8.1	14.1	12
B_ppm	6	4	<1	2	2	1	2	3	<1	1
Tl_ppm	<0.02	0.03	0.41	0.26	0.07	<0.02	0.04	0.09	0.64	0.52
Hg_ppb	*	<5	<5	<5	<5	*	*	<5	<5	<5
Se_ppm	<0.1	<0.1	<0.1	<0.1	<0.1	<0.1	<0.1	0.1	<0.1	<0.1
Te_ppm	0.05	<0.02	<0.02	<0.02	<0.02	<0.02	<0.02	<0.02	<0.02	<0.02
Ge_ppm	2.5	0.8	0.3	2.8	0.3	2.5	0.7	0.3	<0.1	<0.1
In_ppm	<0.02	<0.02	0.07	0.04	0.03	0.05	0.02	<0.02	<0.02	<0.02
Re_ppb	1	4	<1	3	<1	<1	2	<1	<1	<1
Be_ppm	2	11.4	0.3	4.5	1.5	2.4	7.9	1.2	0.2	0.2
Li_ppm	0.7	4.1	25.6	40.3	5.2	1.4	10	3.2	32.9	34.2
Pd_ppb	<10	<10	<10	<10	<10	<10	<10	<10	<10	<10
Pt_ppb	<2	<2	<2	<2	<2	<2	<2	<2	<2	<2
F_ppm	4138	1100	566	8050	5119	510	1005	268	203	347
FeO_%	N.A.	N.A.	N.A.	N.A.	N.A.	N.A.	N.A.	N.A.	N.A.	N.A.
W_%	N.A.	N.A.	N.A.	N.A.	N.A.	N.A.	N.A.	N.A.	N.A.	N.A.
As_%	N.A.	N.A.	N.A.	N.A.	N.A.	N.A.	N.A.	N.A.	N.A.	N.A.

[1] Rock type abbreviations: ps prox: psammite proximal, sk-alt cong: skarn-altered conglomerate

Appendix 3.1: Whole-rock geochemistry data continued

Sample	MWD101-46.5	MWD107-134	MWD107-333	MWD119-050	MWD119-246	MWD124-216	MWD194-050	MWD217-149	MWD231-068	WS15-003
Rock type[1]	ps prox	ps prox	ps prox	ps prox	ps prox	ps prox	ps prox	ps prox	ps prox	ps dist
Type	Drill Core	Drill Core	Drill Core	Drill Core	Drill Core	Drill Core	Drill Core	Drill Core	Drill Core	Surface
SiO2_%	78.15	80.6	78.25	79	75.96	79.11	76.18	75.5	76.18	80.12
Al2O3_%	11.08	9.48	11.28	10.5	11.88	10.81	10.93	9.43	13.03	10.27
Fe2O3_%	3.15	2.03	2.05	2.72	3.73	2.13	2.99	3.27	1.84	1.98
MgO_%	0.82	0.58	0.52	0.75	1.06	0.47	0.85	0.6	0.49	0.46
CaO_%	1.01	1.66	1.84	2.75	1.05	0.85	3.73	4.46	1.43	2.75
Na2O_%	2.95	1.99	3.1	2.37	1.74	4.13	1.97	2.56	2.73	2.61
K2O_%	1.53	2.82	2.13	0.9	2.74	1.48	1.37	1.17	2.42	0.46
TiO2_%	0.49	0.23	0.29	0.3	0.47	0.28	0.37	0.35	0.34	0.34
P2O5_%	0.08	0.05	0.05	0.06	0.09	0.04	0.11	0.17	0.06	0.06
MnO_%	0.04	0.06	0.04	0.07	0.04	0.03	0.06	0.1	0.02	0.06
Cr2O3_%	0.005	0.003	0.003	0.003	0.005	0.002	0.003	0.004	0.003	<0.002
Sum_%	99.91	99.94	99.93	99.92	99.9	99.94	99.88	99.68	99.89	99.89
Ba_ppm	224	531	523	203	408	327	211	286	738	109
Sc_ppm	7	4	4	5	8	4	5	5	5	5
Cs_ppm	6.6	18.4	25.5	5.4	30.7	18.3	43.8	36.3	21.4	2
Ga_ppm	10.8	8.7	11.1	11	13.2	10.1	10.9	7.9	12.7	8.7
Hf_ppm	6.2	3.7	3.4	3.6	5.9	2.9	4.1	4.1	4	4.6
Nb_ppm	10	5.8	6.6	7.1	10.3	6.3	9.4	8.4	8.8	7.6
Rb_ppm	79.4	114.1	125.2	67.1	130.6	79.6	117.9	89.9	127.2	28.2
Sn_ppm	2	2	7	1	2	2	37	32	59	3
Sr_ppm	129.9	96.2	181.5	190	103.3	209.9	219.1	221.1	262.8	300.9
Ta_ppm	0.9	0.6	0.6	0.9	1	0.7	0.8	0.7	0.8	0.6
Th_ppm	15.7	12.4	10.3	13.7	15.7	12.5	14	16	15.1	13.1
U_ppm	3.5	2.5	2.4	3.1	3.6	2.6	3.4	3.4	3.5	2.7
V_ppm	49	35	38	38	56	29	32	30	40	31
W_ppm	18	15.1	3.9	6.7	5.1	3.4	88.3	1687.6	66.4	6.3
Zr_ppm	218.5	122.2	121	122.8	197.3	102.7	143.7	147.5	137.1	163.2
Y_ppm	23.9	16.2	17.5	19.4	21.4	17.5	22.6	21.7	22.1	16.2
La_ppm	38.2	25.8	25.9	28.7	33.2	30.5	32.4	35.6	35.5	34.1
Ce_ppm	74.6	52.2	50.7	56.2	67.2	59.9	65.4	66.3	67.9	64.1
Pr_ppm	8.67	6.07	5.78	6.48	7.68	6.57	7.67	7.76	8	7.25
Nd_ppm	30.8	21.2	20.4	22.7	28.4	22.1	28.8	26.7	28.8	24.7
Sm_ppm	5.75	3.84	3.51	3.89	4.86	3.78	5.04	4.91	4.93	4.07
Eu_ppm	0.88	0.67	0.68	0.73	0.72	0.69	0.89	1.04	0.9	0.69
Gd_ppm	4.94	3.01	3.15	3.66	4.47	3.44	4.44	4.29	4.37	3.6
Tb_ppm	0.75	0.47	0.47	0.57	0.68	0.53	0.69	0.65	0.65	0.54
Dy_ppm	4.45	2.8	2.78	3.42	4.1	3.25	4.05	3.9	3.7	3.06
Ho_ppm	0.87	0.57	0.64	0.74	0.84	0.68	0.81	0.78	0.83	0.62
Er_ppm	2.63	1.64	1.83	2.06	2.45	1.98	2.39	2.33	2.29	1.88
Tm_ppm	0.39	0.24	0.26	0.31	0.36	0.29	0.38	0.33	0.35	0.28
Yb_ppm	2.42	1.67	1.81	1.97	2.52	1.9	2.22	2.08	2.1	1.89
Lu_ppm	0.39	0.24	0.28	0.3	0.37	0.29	0.36	0.35	0.29	0.29
Ni_ppm	11	<10	<10	<10	16	<10	<10	<10	<10	<10
LOI_%	0.6	0.4	0.3	0.5	1.1	0.6	1.3	2	1.2	0.8
TOT/C_%	0.08	0.07	0.02	0.09	0.1	0.06	0.23	0.57	0.09	0.11
TOT/S_%	0.08	0.11	0.05	0.08	0.21	0.23	0.67	0.94	0.48	0.38
Mo_ppm	0.83	0.89	0.92	0.88	0.8	0.66	0.78	0.69	0.73	0.18
Cu_ppm	15.11	14.39	21.63	15.57	21.44	9.76	87.43	107.5	64.49	35.25
Pb_ppm	14.87	17.04	9.87	18.6	12.64	14.19	9.56	4.69	6.65	4.68
Zn_ppm	55	39.5	38	57.3	57.5	34.3	63	37.5	11.4	83.3
Ag_ppb	92	81	37	62	50	78	219	183	185	126
Ni_ppm	12.3	6	5.3	9.7	15.1	4.9	9.1	7.9	6.6	4
Co_ppm	6.7	4	4.1	6.5	7.7	3.9	5.7	5.7	3.7	4.5
Mn_ppm	195	379	249	462	234	196	414	633	69	264
As_ppm	2.4	2.6	1.7	8.9	1.3	5.2	33.3	9.7	392.3	0.9

Appendix 3.1: Whole-rock geochemistry data continued

Sample	MWD101-46.5	MWD107-134	MWD107-333	MWD119-050	MWD119-246	MWD124-216	MWD194-050	MWD217-149	MWD231-068	WS15-003
Rock type[1]	ps prox	ps prox	ps prox	ps prox	ps prox	ps prox	ps prox	ps prox	ps prox	ps dist
Type	Drill Core	Drill Core	Drill Core	Drill Core	Drill Core	Drill Core	Drill Core	Drill Core	Drill Core	Surface
Au_ppb	<0.2	<0.2	<0.2	0.9	<0.2	<0.2	<0.2	<0.2	<0.2	15.2
Cd_ppm	0.05	0.04	0.05	0.05	0.04	0.05	0.4	0.42	0.05	7.5
Sb_ppm	0.05	0.04	0.04	0.22	0.03	0.03	0.06	0.03	0.05	0.03
Bi_ppm	0.31	0.23	0.11	0.14	0.26	0.13	0.61	0.46	0.68	3.54
Cr_ppm	20.9	15	14.2	20.6	18.3	12.6	16.9	12.7	6.3	12.8
B_ppm	<1	<1	<1	<1	<1	<1	1	2	3	<1
Tl_ppm	0.38	0.53	0.61	0.47	0.56	0.44	0.54	0.41	0.07	0.2
Hg_ppb	<5	<5	<5	<5	<5	<5	<5	<5	<5	<5
Se_ppm	<0.1	<0.1	<0.1	<0.1	<0.1	<0.1	<0.1	<0.1	<0.1	0.1
Te_ppm	<0.02	<0.02	<0.02	<0.02	<0.02	<0.02	<0.02	<0.02	<0.02	0.1
Ge_ppm	<0.1	<0.1	<0.1	0.1	<0.1	<0.1	<0.1	<0.1	<0.1	0.1
In_ppm	<0.02	<0.02	0.02	<0.02	0.02	<0.02	<0.02	<0.02	<0.02	0.11
Re_ppb	<1	<1	<1	<1	<1	<1	<1	10	<1	<1
Be_ppm	0.1	<0.1	0.1	0.5	<0.1	0.1	2.2	1.4	1.2	<0.1
Li_ppm	32.7	29.5	44.2	26.1	40.7	32.2	46.9	30.2	9.3	10.5
Pd_ppb	<10	<10	<10	<10	<10	<10	<10	<10	<10	<10
Pt_ppb	<2	<2	<2	<2	<2	<2	<2	<2	<2	<2
F_ppm	314	365	490	297	359	176	1049	926	812	145
FeO_%	N.A.	N.A.	N.A.	N.A.	N.A.	N.A.	N.A.	N.A.	N.A.	N.A.
W_%	N.A.	N.A.	N.A.	N.A.	N.A.	N.A.	N.A.	N.A.	N.A.	N.A.
As_%	N.A.	N.A.	N.A.	N.A.	N.A.	N.A.	N.A.	N.A.	N.A.	N.A.

[1] Rock type abbreviations: ps dist: psammite distal, ps prox: psammite proximal

Appendix 3.1: Whole-rock geochemistry data continued

Sample	WS15-004	WS15-006	WS15-007	WS15-008	WS15-009	WS15-010	WS15-015	WS15-016	WS15-001	WS15-005	WS15-017	WS16-002
Rock type[1]	ps dist	ps dist	ps dist	ps dist	ps dist	ps dist	ps dist	ps dist	gr	gr	gr	di
Type	Surface	Surface	Surface	Surface	Surface	Surface	Surface	Surface	Surface	Surface	Surface	Surface
SiO2_%	85.66	79.62	79.72	81	77.17	82.87	57.71	84.69	75.37	73.2	78.58	62.9
Al2O3_%	7.34	11.14	10.48	10.09	12.29	9.53	24.67	9.01	14.4	13.72	13.24	14.51
Fe2O3_%	1.22	1.44	1.83	1.53	2.39	1.05	3.17	1.08	0.83	2.23	0.5	6.19
MgO_%	0.25	0.39	0.5	0.44	0.52	0.13	2.04	0.23	0.08	0.35	0.04	4.97
CaO_%	0.41	0.54	0.94	0.58	0.83	0.45	0.56	0.21	0.34	2.5	0.88	5.15
Na2O_%	1.44	3.5	2.92	2.65	4.23	2.85	2.37	2.86	3.15	2.57	5.75	1.96
K2O_%	2.96	1.7	2.39	2.39	1.37	1.74	5.28	1.26	4.65	3.94	0.3	2.28
TiO2_%	0.14	0.34	0.39	0.28	0.38	0.28	0.49	0.23	0.03	0.26	<0.01	0.57
P2O5_%	0.05	0.04	0.04	0.03	0.05	0.05	0.05	0.03	0.02	0.06	0.02	0.1
MnO_%	0.03	0.02	0.04	0.03	0.03	<0.01	0.05	0.01	0.01	0.03	<0.01	0.1
Cr2O3_%	<0.002	0.002	0.003	0.002	0.002	<0.002	0.004	<0.002	<0.002	<0.002	<0.002	0.045
Sum_%	99.9	99.87	99.86	99.89	99.88	99.84	99.65	99.92	99.97	99.92	100	99.83
Ba_ppm	670	436	512	488	423	725	1470	322	85	759	60	312
Sc_ppm	2	5	5	5	6	4	11	4	5	5	3	19
Cs_ppm	1.4	10	14.6	11.1	12.7	5.1	25.5	9.5	8.5	3.1	1.1	55.4
Ga_ppm	6	11.1	10.7	10	13.8	8.7	37.1	8.5	21	15.4	13.1	15.8
Hf_ppm	2.2	4	4.5	3.4	4.5	3.1	5.7	3.1	2.7	5.7	2.1	4.1
Nb_ppm	2.8	7.9	8.6	7	9.1	6.3	12.6	5.8	12.2	7.6	3	7.8
Rb_ppm	88	82.4	99.5	100.9	72.9	61.2	289.1	64.6	237.8	116.8	13.5	129.3
Sn_ppm	<1	3	4	3	2	3	194	12	12	2	6	5
Sr_ppm	137.8	221	221	176.9	138.6	244	252	142.7	45.8	141.7	108.1	155.4
Ta_ppm	0.3	0.7	0.7	0.7	0.7	0.7	0.9	0.6	1.9	0.5	1.5	0.7
Th_ppm	6.3	13.6	15.9	12.1	13.1	11.6	20.4	9.9	9.9	19.9	10.8	10
U_ppm	0.9	3.1	3.2	2.6	3.5	2.8	5.2	2.2	4.1	2.6	4.5	1.9
V_ppm	17	33	37	30	47	29	105	22	<8	17	9	113
W_ppm	5.5	3.7	4.6	2.2	2.9	4.1	6.4	2.7	14.8	4.6	6	1.4
Zr_ppm	77.7	136.1	159.9	124.6	166.2	111.5	209.1	101.1	52.2	195.4	26.4	132.8
Y_ppm	8.3	44.4	21.3	16.4	23.1	57.8	37.2	14.2	22.8	26.7	14.6	22.2
La_ppm	13.4	38.7	38.9	30.7	36	48.7	70.2	40.3	8.3	42.9	3.4	25.2
Ce_ppm	26.9	63.5	73.9	57.7	60	82.8	125	64.2	16.5	85.8	9	50
Pr_ppm	2.96	8.77	8.49	6.67	8.01	13.1	15.43	8.75	2.07	10.03	1.22	6.09
Nd_ppm	10.4	34.1	30.8	24.6	30.1	51.4	54.3	28.9	8	37.6	4.3	23.2
Sm_ppm	1.95	5.9	5.26	3.97	5.13	9.29	9.43	4.97	2.27	6.8	2	4.48
Eu_ppm	0.44	1.13	0.85	0.72	0.81	1.62	1.5	0.76	0.09	1.24	0.08	0.97
Gd_ppm	1.68	5.85	4.41	3.5	4.59	9.15	8.33	3.67	3.26	6.09	2.24	4.27
Tb_ppm	0.24	1	0.68	0.52	0.69	1.48	1.23	0.51	0.71	0.87	0.51	0.67
Dy_ppm	1.41	6.52	3.98	3.04	3.69	9.18	6.87	2.78	4.4	4.91	3.01	3.99
Ho_ppm	0.26	1.38	0.75	0.57	0.81	1.79	1.4	0.48	0.81	0.98	0.47	0.8
Er_ppm	0.81	4.14	2.3	1.73	2.37	5.47	4	1.44	2.19	2.86	0.98	2.35
Tm_ppm	0.13	0.63	0.36	0.27	0.32	0.77	0.64	0.22	0.3	0.39	0.15	0.32
Yb_ppm	0.95	3.69	2.36	1.81	2.27	4.82	3.99	1.56	1.88	2.55	0.88	2.11
Lu_ppm	0.14	0.58	0.36	0.27	0.33	0.68	0.59	0.22	0.26	0.4	0.08	0.33
Ni_ppm	<10	<10	<10	<10	<10	<10	<10	<10	<10	<10	<10	34
LOI_%	0.4	1.1	0.6	0.9	0.6	0.9	3.3	0.3	1.1	1	0.7	1
TOT/C_%	0.02	0.04	0.06	0.02	0.07	0.05	0.15	0.04	0.03	0.14	0.05	0.02
TOT/S_%	<0.01	<0.01	0.03	0.02	<0.01	0.08	0.01	0.02	<0.01	<0.01	<0.01	0.09
Mo_ppm	0.12	0.06	0.15	0.07	0.12	0.2	0.07	0.11	0.18	0.66	1.4	0.6
Cu_ppm	2.75	4.36	2.53	2.47	3.68	53.69	3.43	6.82	1.2	12.44	12.56	26.1
Pb_ppm	12	14.54	17.14	17.09	15.44	16.09	13.21	12.93	5.81	10.31	3.33	7.32
Zn_ppm	13.6	21.9	24.5	17.3	34.8	12.2	5.1	7.6	2.7	41.7	5.3	56.4
Ag_ppb	25	35	87	64	19	117	325	29	86	36	391	53
Ni_ppm	3.3	1.9	1.3	1.3	5.1	2	0.7	0.7	0.5	3.2	0.8	32.9
Co_ppm	1.8	1.7	1.1	1.2	2.6	2.7	0.6	0.4	<0.1	3.6	0.3	18.1
Mn_ppm	126	135	182	139	172	40	22	58	35	202	14	453
As_ppm	0.6	1.7	0.2	0.8	4.6	1.1	3726.7	44	14.7	3.7	3.1	1.7

Appendix 3.1: Whole-rock geochemistry data continued

Sample	WS15-004	WS15-006	WS15-007	WS15-008	WS15-009	WS15-010	WS15-015	WS15-016	WS15-001	WS15-005	WS15-017	WS16-002
Rock type[1]	ps dist	ps dist	ps dist	ps dist	ps dist	ps dist	ps dist	ps dist	gr	gr	gr	di
Type	Surface	Surface	Surface	Surface	Surface	Surface	Surface	Surface	Surface	Surface	Surface	Surface
Au_ppb	2.1	2	1.6	2	1.1	1.7	1.8	1	2.1	<0.2	2.7	<0.2
Cd_ppm	0.02	0.04	0.03	0.03	0.01	0.3	0.05	0.02	0.02	0.06	<0.01	0.04
Sb_ppm	0.14	0.02	<0.02	<0.02	<0.02	0.02	0.11	0.03	0.06	0.09	<0.02	0.02
Bi_ppm	0.09	0.15	0.16	0.11	0.12	0.11	1.13	0.43	1.23	0.27	2.52	0.19
Cr_ppm	5.5	9.1	12.4	7.4	10.3	6.4	1.3	4.6	1.8	5.3	2	235.8
B_ppm	<1	1	<1	<1	<1	<1	6	<1	<1	<1	<1	<1
Tl_ppm	0.19	0.29	0.43	0.35	0.38	0.13	0.07	0.16	0.09	0.22	<0.02	0.66
Hg_ppb	<5	<5	<5	<5	<5	<5	<5	<5	<5	<5	<5	<5
Se_ppm	<0.1	<0.1	<0.1	0.2	0.2	0.1	0.2	<0.1	<0.1	<0.1	0.9	<0.1
Te_ppm	<0.02	<0.02	0.03	<0.02	<0.02	<0.02	0.06	<0.02	0.05	<0.02	0.05	<0.02
Ge_ppm	<0.1	<0.1	<0.1	<0.1	<0.1	<0.1	<0.1	<0.1	<0.1	<0.1	<0.1	0.1
In_ppm	<0.02	<0.02	0.02	<0.02	<0.02	<0.02	<0.02	<0.02	<0.02	0.02	<0.02	<0.02
Re_ppb	<1	<1	1	<1	<1	1	2	<1	<1	<1	<1	<1
Be_ppm	0.2	0.5	<0.1	0.3	0.1	1	2.1	0.4	0.4	<0.1	0.3	0.2
Li_ppm	3.9	8.8	17.6	11	18.4	4	9.1	5.6	4	17.4	0.3	87.7
Pd_ppb	<10	<10	<10	<10	<10	<10	<10	<10	<10	<10	<10	<10
Pt_ppb	<2	<2	<2	<2	<2	<2	<2	<2	<2	<2	<2	<2
F_ppm	66	159	168	168	217	153	1722	209	123	212	19	592
FeO_%	N.A.	N.A.	N.A.	N.A.	N.A.	N.A.	N.A.	N.A.	0.45	1.61	0.29	5.14
W_%	N.A.	N.A.	N.A.	N.A.	N.A.	N.A.	N.A.	N.A.	N.A.	N.A.	N.A.	N.A.
As_%	N.A.	N.A.	N.A.	N.A.	N.A.	N.A.	N.A.	N.A.	N.A.	N.A.	N.A.	N.A.

[1] Rock type abbreviations: di: diorite, gr: granite, ps dist: psammite distal

Appendix 3.2: LA-ICP-MS trace element data

Appendix 3.2.1: LA-ICP-MS scheelite geochemistry data

Spot	Rock type[1]	Mineral zone[2]	Def event	Na23	P31	Ca43	Mn55	Fe57	Cu65	Sr88	Y89	Nb93	Mo98	Sn118	Ba137	La139	Ce140	Pr141	Nd143	Sm147	Eu151	Gd157
MWD005-067B																						
2-4	mz	GZ	D_{1-2}			138007	33			86			18	0.6		30	103	17	87	27	5	31
2-5	mz	UO	D_{1-2}			139200	15	59		76	29	13	52	0.2	0.1	1	5	1	6	3	1	6
2-1	mz	UO	D_{1-2}			138007	26			85			19	0.4		20	86	17	102	34	4	38
2-2	mz	UO	D_{1-2}			138007	26			86			22	0.3	0.1	22	90	18	108	33	4	38
2-3	mz	UO	D_{1-2}	15		139200	25	58		93	155	46	21	0.3	1.2	20	86	17	101	32	4	35
2-6	mz	UO	D_{1-2}			138007	23			93			17	0.6		38	151	27	134	39	6	41
2-7	mz	UO	D_{1-2}			139200	26	60		75	86	32	38	0.2	0.05	6	30	6	35	14	3	20
2-8	mz	UO	D_{1-2}			139200	30	59		80	154	56	20	0.3	0.04	28	121	24	138	40	5	44
2-9	mz	UO	D_{1-2}	14		139200	36	60		85	255	61	21	0.3	0.03	22	98	20	126	46	6	60
MWD013-099																						
3-3	mz	CG	D_{1-2}			139222				56	62	251	20			9	23	3	9	2	1	3
4-1	mz	CG	D_{1-2}			139222				213	8	4	52			0.03	0.2	0.01	0.2	0.1	0.02	0.3
4-2	mz	CG	D_{1-2}			139222				129	12	3	40	0.3		0.01	0.0	0.01		0.2	0.1	1
4-3	mz	CG	D_{1-2}			139222				166	11	5	48			0.04	0.1	0.02		0.2	0.1	1
1-2	mz	CG	D_{1-2}			139222				155	14	12	12	0.3		50	72	7	22	3	2	2
1-3	mz	CG	D_{1-2}			139222				162	36	7	21			21	45	5	19	3	3	2
1-5	mz	CG	D_{1-2}			139222				168	41	10	19			42	76	8	26	4	3	3
2-4	mz	CG	D_{1-2}			139222				158	27	14	16	0.5		81	133	12	36	5	3	3
2-5	mz	CG	D_{1-2}			139222				150	25	11	24			12	34	5	24	6	2	5
2-6	mz	CG	D_{1-2}			139222				168	14	129	14	0.5		99	157	13	37	4	2	2
5-1	mz	CG	D_{1-2}			139222				178	68	170	13	0.5		69	153	17	61	9	3	5
1-4	mz	GZ	D_{1-2}			139222				122	79	9	15	0.3		23	56	7	33	7	4	7
2-7	mz	GZ	D_{1-2}			139222				176	67	190	20	0.4		39	89	10	42	8	2	7
3-1	mz	GZ	D_{1-2}			139222				131	87	65	15			79	146	17	76	17	5	16
3-7	mz	GZ	D_{1-2}			139222				153	49	22	13	0.4		97	223	26	100	17	4	11
4-4	mz	GZ	D_{1-2}			139222				135	56	27	8	0.7		16	55	9	42	8	3	6
4-5	mz	GZ	D_{1-2}			139222				129	148	288	9	0.5		49	132	16	63	15	3	14
2-2	mz	GZ	D_{1-2}			139222				85	141	78	15			22	72	12	68	23	9	27
5-3	mz	GZ	D_{1-2}			139222				87	152	42	15	0.4		23	85	14	78	26	10	30
5-4	mz	GZ	D_{1-2}			139222				109	278	80	10	0.7		65	213	33	165	52	13	62

Appendix 3.2.1: LA-ICP-MS scheelite geochemistry data continued

Spot	Rock type[1]	Mineral zone[2]	Def event	Tb159	Dy163	Ho165	Er167	Tm169	Yb171	Lu175	Ta181	Pb208	Bi209	Th232	U238
MWD005-067B															
2-4	mz	GZ	D_{1-2}	5	31	6	17	2.4	18	3.0		9	0.06	0.82	3.79
2-5	mz	UO	D_{1-2}	1	9	2	4	0.4	1	0.1		3	0.07		0.03
2-1	mz	UO	D_{1-2}	6	35	7	18	2.3	14	2.1		5		0.05	0.38
2-2	mz	UO	D_{1-2}	5	34	7	18	2.3	14	2.1		5	0.04	0.06	0.32
2-3	mz	UO	D_{1-2}	5	32	6	16	2.1	13	2.0		5	0.08		0.41
2-6	mz	UO	D_{1-2}	7	47	10	28	4.3	31	4.7		7		0.84	4.24
2-7	mz	UO	D_{1-2}	3	23	5	11	1.1	5	0.6		4	0.08		0.08
2-8	mz	UO	D_{1-2}	6	35	6	16	1.9	12	1.8		5	0.07		0.46
2-9	mz	UO	D_{1-2}	9	60	12	32	4.0	23	3.5		5	0.07		0.43
MWD013-099															
3-3	mz	CG	D_{1-2}	1	5	1	5	0.8	7	1.4	0.19	6	0.04	0.19	1.84
4-1	mz	CG	D_{1-2}	0.1	1	0.2	0.9	0.1	0.9	0.1	0.01	3	0.01		0.05
4-2	mz	CG	D_{1-2}	0.3	3	1	1.5	0.1	0.5	0.05		3	0.01	0.01	
4-3	mz	CG	D_{1-2}	0.3	3	1	1.4	0.1	0.6	0.1		3	0.02		
1-2	mz	CG	D_{1-2}	0.3	1	0.3	1.0	0.2	2	0.5	0.01	7	0.06	4.50	1.74
1-3	mz	CG	D_{1-2}	0.3	2	0.4	1.9	0.6	7	1.6	0.00	5	0.05	0.62	1.13
1-5	mz	CG	D_{1-2}	0.4	3	1	2.7	0.7	9	2.2	0.01	5	0.03	0.72	1.35
2-4	mz	CG	D_{1-2}	0.4	2	0.4	1.4	0.4	4	0.9	0.01	10	0.07	8.21	3.22
2-5	mz	CG	D_{1-2}	1	4	1	2.3	0.4	4	0.7	0.01	5	0.01	0.17	0.18
2-6	mz	CG	D_{1-2}	0.3	2	0.3	0.9	0.2	2	0.5	0.12	14	0.06	35.92	7.84
5-1	mz	CG	D_{1-2}	0.8	5	1	4	1.0	13	2.7	1.83	13		25.61	10.23
1-4	mz	GZ	D_{1-2}	1.2	11	2	8	1.2	10	1.8		4	0.03	0.21	0.41
2-7	mz	GZ	D_{1-2}	1.1	8	2	7	1.2	10	1.8	0.53	9	0.02	2.05	1.41
3-1	mz	GZ	D_{1-2}	2	16	3	8	0.9	5	0.8	0.04	5		19	8.14
3-7	mz	GZ	D_{1-2}	1	7	1	4	0.7	7	1.3	0.03	8	0.04	1.51	0.94
4-4	mz	GZ	D_{1-2}	1	7	2	5	0.9	7	1.3	0.03	8		1.18	1.36
4-5	mz	GZ	D_{1-2}	3	18	4	13	2.0	16	3.1	0.42	9		5	2.60
2-2	mz	GZ	D_{1-2}	5	30	6	15	1.8	12	2.0	0.09	8	0.05	0.70	4.63
5-3	mz	GZ	D_{1-2}	5	34	6	16	1.9	11	1.6	0.06	6	0.11	0.07	0.82
5-4	mz	GZ	D_{1-2}	10	68	12	29	3.3	17	2.3	0.15	7	0.03	0.24	1.99

Appendix 3.2.1: LA-ICP-MS scheelite geochemistry data continued

Spot	Rock type[1]	Mineral zone[2]	Def event	Na23	P31	Ca43	Mn55	Fe57	Cu65	Sr88	Y89	Nb93	Mo98	Sn118	Ba137	La139	Ce140	Pr141	Nd143	Sm147	Eu151	Gd157
MWD013-099 cont																						
1-1	mz	UO	D_{1-2}			139222				188	36	8	35			11	38	6	26	5	1	4
2-1	mz	UO	D_{1-2}			139222				84	59	20	29			5	25	4	17	5	1	5
2-3	mz	UO	D_{1-2}			139222				130	104	47	17			15	64	12	70	19	3	20
3-2	mz	UO	D_{1-2}			139222				94	97	21	22			15	54	9	50	16	8	19
3-4	mz	UO	D_{1-2}			139222				100	75	23	20			3	18	4	31	10	7	13
3-5	mz	UO	D_{1-2}			139222				88	135	32	16			27	83	14	85	27	9	33
3-6	mz	UO	D_{1-2}			139222				91	191	43	16	0.3		24	88	17	111	37	10	47
5-2	mz	UO	D_{1-2}			139222				171	44	8	37			14	46	8	40	10	2	10
MWD011-147.5A																						
1-1	sk-alt cong	NZ	D_{1-2}			138150	7	54		115	3	2.0	35	0.1	0.1	0.01	0.01				0.01	0.12
1-2	sk-alt cong	NZ	D_{1-2}			138150	6	51		191	3	2.6	46	0.1	0.1	0.01	0.01	0.00	0.02	0.01	0.01	0.06
1-3	sk-alt cong	NZ	D_{1-2}			138150	8	51		76	6	2.1	42	0.1	0.1	0.01	0.01	0.00		0.02	0.04	0.41
1-4	sk-alt cong	NZ	D_{1-2}			138150	5	63	0.3	192	0	3.3	98	0.1	0.3	0.40	0.82	0.13	0.79	0.29	0.08	0.26
1-5	sk-alt cong	NZ	D_{1-2}			138150	4	56	0.2	185	0	3.1	98	0.1	0.1	0.04	0.20	0.04	0.35	0.18	0.07	0.14
1-6	sk-alt cong	NZ	D_{1-2}			138150	6	52		171	0	3.8	95	0.1	0.1	0.05	0.15	0.03	0.20	0.08	0.03	0.06
MWD099-054																						
1-1	vn	UO	D_4			139222				82	125	16	11	0.3		4	21	5	29	12	3	19
3-5	vn	UO	D_4			139222				86	131	19	11	0.3		2	16	4	28	13	4	21
3-6	vn	UO	D_4			139222				76	57	9	7			1	5	1	11	6	2	10
4-3	vn	UO	D_4			139222				102	46	9	23			2	11	2	11	5	2	7
4-4	vn	UO	D_4			139222				89	78	16	14	0.3		3	13	3	17	7	2	11
1-2	vn	UO	D_4			139222				88	85	11	13			1	11	3	21	10	3	15
1-3	vn	UO	D_4			139222				80	143	19	9	0.5		8	39	9	60	22	6	29
1-4	vn	UO	D_4			139222				85	115	28	8	0.5		11	45	9	59	20	5	23
1-5	vn	UO	D_4			139222				80	112	24	10	0.3		8	40	10	66	23	5	28
2-1	vn	UO	D_4			139222				82	124	33	8			14	56	11	72	24	6	26
2-2	vn	UO	D_4			139222				82	131	36	8	0.4		17	76	14	75	23	6	25
2-3	vn	UO	D_4			139222				82	124	35	9			17	68	12	64	19	6	21
2-4	vn	UO	D_4			139222				81	185	41	7	0.3		18	73	13	65	19	6	22
2-5	vn	UO	D_4			139222				84	173	40	8			20	87	16	81	24	6	26

Appendix 3.2.1: LA-ICP-MS scheelite geochemistry data continued

Spot	Rock type[1]	Mineral zone[2]	Def event	Tb159	Dy163	Ho165	Er167	Tm169	Yb171	Lu175	Ta181	Pb208	Bi209	Th232	U238
MWD013-099 cont															
1-1	mz	UO	D_{1-2}	1	5	1	3	0.5	4	0.7	0.01	5	0.02	0.16	0.45
2-1	mz	UO	D_{1-2}	1	9	2	5	0.7	5	0.7	0.02	5	0.03		0.02
2-3	mz	UO	D_{1-2}	3	22	4	12	1.8	12	1.9	0.33	7	0.02	0.19	0.30
3-2	mz	UO	D_{1-2}	3	23	4	11	1.3	8	1.2	0.02	5	0.02	0.11	1.82
3-4	mz	UO	D_{1-2}	2	15	3	7	0.9	5	0.8	0.01	6	0.03	0.10	1.95
3-5	mz	UO	D_{1-2}	5	33	6	15	1.8	10	1.5	0.03	6	0.04	0.12	1.55
3-6	mz	UO	D_{1-2}	7	48	9	23	2.7	15	2.4	0.03	6	0.03	0.13	1.29
5-2	mz	UO	D_{1-2}	2	10	2	6	0.7	3	0.4	0.01	4		0.03	0.08
MWD011-147.5A															
1-1	sk-alt cong	NZ	D_{1-2}	0.04	0.45	0.09	0.1	0.01	0.02	0.0		2	0.07		0.02
1-2	sk-alt cong	NZ	D_{1-2}	0.04	0.37	0.10	0.2	0.03	0.08	0.0		2	0.06		0.02
1-3	sk-alt cong	NZ	D_{1-2}	0.18	1.34	0.21	0.3	0.02	0.06	0.0		2	0.09		0.02
1-4	sk-alt cong	NZ	D_{1-2}	0.02	0.05	0.01	0.02					4	0.06		0.04
1-5	sk-alt cong	NZ	D_{1-2}	0.01	0.02							3	0.06		0.03
1-6	sk-alt cong	NZ	D_{1-2}	0.01	0.01	0.002						3	0.05		0.03
MWD099-054															
1-1	vn	UO	D_4	3	25	5	15	1.7	9	1.3	0.02	7			0.02
3-5	vn	UO	D_4	4	28	6	16	1.8	9	1.3	0.02	7	0.02		0.05
3-6	vn	UO	D_4	2	13	3	7	0.8	4	0.5	0.01	8			
4-3	vn	UO	D_4	1	9	2	5	0.6	3	0.5	0.01	5	0.02		0.02
4-4	vn	UO	D_4	2	15	3	9	1.0	5	0.8	0.03	6	0.02		0.01
1-2	vn	UO	D_4	3	17	4	10	1.1	6	0.8	0.00	6			0.02
1-3	vn	UO	D_4	5	31	6	16	1.8	9	1.2	0.01	7	0.02		0.10
1-4	vn	UO	D_4	4	24	5	13	1.6	8	1.2	0.03	6		0.03	0.09
1-5	vn	UO	D_4	4	26	5	14	1.5	8	1.2	0.02	8	0.01		0.07
2-1	vn	UO	D_4	4	28	6	16	1.8	9	1.4	0.04	7		0.03	0.09
2-2	vn	UO	D_4	4	27	6	16	1.9	10	1.6	0.05	8	0.02	0.06	0.16
2-3	vn	UO	D_4	3	23	5	14	1.8	10	1.5	0.05	8	0.02	0.04	0.18
2-4	vn	UO	D_4	4	31	7	20	2.8	16	2.3	0.11	8	0.02	0.14	0.21
2-5	vn	UO	D_4	4	31	7	20	2.6	14	2.2	0.07	8	0.02	0.07	0.19

Appendix 3.2.1: LA-ICP-MS scheelite geochemistry data continued

Spot	Rock type[1]	Mineral zone[2]	Def event	Na23	P31	Ca43	Mn55	Fe57	Cu65	Sr88	Y89	Nb93	Mo98	Sn118	Ba137	La139	Ce140	Pr141	Nd143	Sm147	Eu151	Gd157
MWD099-054 cont																						
3-1	vn	UO	D_4			139222				87	161	52	8			14	71	13	67	20	6	21
3-2	vn	UO	D_4			139222				83	209	54	8	0.3		19	81	14	77	25	5	31
3-3	vn	UO	D_4			139222				85	242	56	8	0.5		22	95	17	92	28	6	34
3-4	vn	UO	D_4			139222				89	234	58	8	0.5		25	100	17	88	28	6	33
3-7	vn	UO	D_4			139222				83	173	27	10	0.5		7	46	11	69	28	7	38
3-8	vn	UO	D_4			139222				84	195	42	8	0.3		20	82	15	81	26	6	32
4-1	vn	UO	D_4			139222				98	46	9	22			1	6	1	10	5	3	8
4-2	vn	UO	D_4			139222				84	149	45	8			13	53	10	65	23	5	28
MWD099-124																						
2-2	vn	CG	D_4			139222				68	67	21	16	0.4		12	24	3	8	2	4	2
1-1	vn	GZ	D_4			139222				178	90	9	3			0.7	4	1	9	5	2	10
2-1	vn	GZ	D_4			139222				99	139	347	13	0.4		25	71	10	45	12	3	14
3-2	vn	GZ	D_4			139222				89	99	103	8	0.8		21	62	8	28	6	3	6
3-4	vn	GZ	D_4			139222				83	150	61	7			10	37	6	28	8	4	9
3-3	vn	GZ	D_4			139222				86	77	35	9	0.8		19	61	9	41	10	4	10
1-2	vn	UO	D_4			139222				79	85	34	10	0.5		7	36	6	29	7	4	7
1-3	vn	UO	D_4			139222				87	121	162	9	0.4		20	74	11	47	12	4	12
1-4	vn	UO	D_4			139222				79	71	54	9	0.4		14	56	9	43	10	3	10
1-5	vn	UO	D_4			139222				87	106	150	9			24	89	14	63	15	4	16
1-6	vn	UO	D_4			139222				85	121	182	8	0.3		28	108	16	68	15	4	14
1-7	vn	UO	D_4			139222				76	64	45	12	0.4		18	50	7	34	7	3	8
1-8	vn	UO	D_4			139222				79	118	36	10	0.3		31	103	15	64	13	5	11
3-1	vn	UO	D_4			139222				89	78	32	9	0.6		19	71	10	45	10	4	9
MWD099-163.5																						
4-1	vn	CG	D_4	50		138222	37	54		69	720	421	9	0.8	0.3	24	66	9	36	13	4	25
4-2	vn	CG	D_4	51		138222	35	54	0.1	67	589	392	9	0.8	0.3	18	52	7	28	11	3	22
1-1	vn	CG	D_4			138222	48			58			28	0.6		2	4	0.3	2	1	0.4	0.8
1-3	vn	CG	D_4			138222	30			20			17	0.5	0.2	2	3	0.3	1		0.5	0.5
1-2	vn	GZ	D_4	34		138222	62	52	1	75	240	257	9	1.1	0.4	35	24	1	2	0.4	14	0.3
1-3	vn	GZ	D_4	43		138222	41	54	0.1	72	534	217	9	0.6	0.2	15	37	4	13	4	3	6

Appendix 3.2.1: LA-ICP-MS scheelite geochemistry data continued

Spot	Rock type[1]	Mineral zone[2]	Def event	Tb159	Dy163	Ho165	Er167	Tm169	Yb171	Lu175	Ta181	Pb208	Bi209	Th232	U238
MWD099-054 cont															
3-1	vn	UO	D_4	4	27	6	18	2.3	13	2.0	0.15	9	0.02	0.09	0.26
3-2	vn	UO	D_4	6	41	9	24	3.1	16	2.2	0.17	8	0.01	0.04	0.14
3-3	vn	UO	D_4	6	44	9	27	3.5	20	2.8	0.19	8	0.03	0.14	0.36
3-4	vn	UO	D_4	6	43	9	26	3.5	19	2.7	0.27	8	0.04	0.15	0.25
3-7	vn	UO	D_4	6	42	9	22	2.3	11	1.6	0.03	7	0.01		0.14
3-8	vn	UO	D_4	5	37	8	23	2.9	15	2.3	0.09	8	0.03	0.08	0.18
4-1	vn	UO	D_4	1	10	2	6	0.6	3	0.5	0.02	5	0.01		0.02
4-2	vn	UO	D_4	4	30	6	18	2.2	12	1.9	0.10	8	0.01	0.04	0.11
MWD099-124															
2-2	vn	CG	D_4	0.4	4	1	5	1.1	12	2.6		8	0.11	3	4.20
1-1	vn	GZ	D_4	2	20	5	12	1.2	4	0.4	0.01	8			
2-1	vn	GZ	D_4	3	19	5	16	2.5	16	2.8	0.48	12	0.03	2	2.92
3-2	vn	GZ	D_4	1	10	2	8	1.6	13	2.3	0.78	11	0.04	0.69	0.61
3-4	vn	GZ	D_4	2	16	4	15	2.8	20	3.1	0.45	10	0.02	0.21	0.18
3-3	vn	GZ	D_4	2	11	2	7	1.1	8	1.4	0.09	10	0.02	0.20	0.15
1-2	vn	UO	D_4	1	10	2	8	1.2	7	1.3	0.12	8		0.09	0.15
1-3	vn	UO	D_4	2	18	4	13	1.8	11	1.7	0.58	11	0.02	0.55	1.00
1-4	vn	UO	D_4	2	11	3	7	0.9	5	0.7	0.09	10		0.05	0.07
1-5	vn	UO	D_4	3	18	4	11	1.6	8	1.3	0.15	11	0.01	0.80	0.88
1-6	vn	UO	D_4	2	18	4	12	1.5	9	1.4	0.38	10	0.03	0.76	0.94
1-7	vn	UO	D_4	1	8	2	6	1.0	7	1.1	0.04	9		0.31	0.19
1-8	vn	UO	D_4	2	12	3	9	1.3	9	1.4	0.02	9	0.02	0.09	0.05
3-1	vn	UO	D_4	2	11	2	7	1.1	8	1.4	0.06	9	0.03	0.11	0.10
MWD099-163.5															
4-1	vn	CG	D_4	7	73	19	63	9	55	6.6		8	0.07		0.40
4-2	vn	CG	D_4	6	63	16	52	7	42	5.1		9	0.07		0.25
1-1	vn	CG	D_4	0.3	3	0.4	1.3	0.3	2	0.2		7	0.19	0.42	0.91
1-3	vn	CG	D_4	0.3	1	0.2	1.3	0.2	3	0.3		5	0.19	0.68	0.82
1-2	vn	GZ	D_4	0.1	1	0.4	4	3	69	15.2		17	0.09		24.65
1-3	vn	GZ	D_4	2	28	8	31	6	38	4.6		8	0.06		0.14

Appendix 3.2.1: LA-ICP-MS scheelite geochemistry data continued

Spot	Rock type[1]	Mineral zone[2]	Def event	Na23	P31	Ca43	Mn55	Fe57	Cu65	Sr88	Y89	Nb93	Mo98	Sn118	Ba137	La139	Ce140	Pr141	Nd143	Sm147	Eu151	Gd157
MWD099-163.5 cont																						
1-7	vn	GZ	D_4	75		138222	25	56		63	581	296	8	1.0	0.2	20	49	6	23	8	8	14
1-1	vn	UO	D_4	13		138222	33	54		91	91	30	13	0.5	0.1	7	18	2	7	2	2	3
1-4	vn	UO	D_4	9		138222	41	53		69	155	38	10	0.4	0.4	33	86	11	36	8	4	8
1-8	vn	UO	D_4	16		138222	41	53		88	188	62	10	0.8	0.2	19	32	3	11	2	7	3
1-9	vn	UO	D_4	11		138222	35	54		98	57	31	13	0.4	0.1	6	14	2	6	2	1	3
4-3	vn	UO	D_4	13		138222	22	53		68	20	6	18	0.3	0.1	2	6	0.7	2	0.5	0.7	0.6
4-4	vn	UO	D_4	7		138222	20	55		70	28	10	19	0.2	0.1	2	5	0.7	3	0.7	0.8	1
4-5	vn	UO	D_4			138222	21	53		73	37	12	23	0.3	0.0	1	6	0.9	3	0.9	0.7	1.5
4-6	vn	UO	D_4	11		138222	21	55		69	40	11	21	0.3	0.1	3	9	1	4	1.0	0.7	1.3
1-5	vn	UO	D_4	9		138222	44	55	0.2	65	132	43	9	0.4	0.6	50	152	22	97	21	4	20
1-6	vn	UO	D_4	39		138222	26	54		59	123	31	13	0.4	0.2	8	42	8	46	14	4	17
1-2	vn	UO	D_4			138222	34			20			23	0.6		5	17	2	13	8	2	16
1-4	vn	UO	D_4			138222	13			70			14	0.3		3	11	2	12	4	2	5
MWD101-149																						
1-3	vn	CG	D_4			139222				116	30	4	55			0.1	0.2	0.03	0.1	0.1	0.9	0.5
1-5	vn	CG	D_4			139222				146	17	3	58			0.1	0.2	0.02	0.1		0.3	0.2
2-2	vn	CG	D_4			139222				65	173	29	32			0.5	3	0.8	5	5	13	12
3-1	vn	GZ	D_4			139222				79	201	253	26			4	12	2	10	6	6	13
3-4	vn	GZ	D_4			139222				61	107	80	35	0.3		1	2	0	2	3	6	10
1-1	vn	UO	D_4			139222				117	11	4	21			0.03	0.2	0.1	0.7	0.5	0.3	1.1
1-2	vn	UO	D_4			139222				61	304	31	30			3	11	2	9	11	16	32
1-4	vn	UO	D_4			139222				129	55	5	41			0.13	1	0	2	2	1	5
1-7	vn	UO	D_4			139222				60	341	31	32	0.3		3	9	1	7	8	18	25
2-3	vn	UO	D_4			139222				84	45	11	42	0.3		0.1	0	0	0	1	3	4
2-4	vn	UO	D_4			139222				62	106	96	35	0.3		3	7	1	4	2	6	5
2-5	vn	UO	D_4			139222				73	338	29	31			4	17	3	16	8	16	18
3-2	vn	UO	D_4			139222				62	48	25	33	0.3		0.4	2	1	4	3	3	6
3-3	vn	UO	D_4			139222				66	87	22	34			1	4	1	4	2	10	7
3-5	vn	UO	D_4			139222				54	95	21	34	0.4		0.3	1	0	1	3	8	10
3-6	vn	UO	D_4			139222				58	216	22	34			0.4	2	0	2	5	11	17

Appendix 3.2.1: LA-ICP-MS scheelite geochemistry data continued

Spot	Rock type[1]	Mineral zone[2]	Def event	Tb159	Dy163	Ho165	Er167	Tm169	Yb171	Lu175	Ta181	Pb208	Bi209	Th232	U238
MWD099-163.5 cont															
1-7	vn	GZ	D_4	4	43	11	43	7	56	8.7		8	0.14		6.17
1-1	vn	UO	D_4	1	7	2	6	1.0	7	1.0		6	0.05		0.06
1-4	vn	UO	D_4	2	14	3	12	2	16	2.5		6	0.06		0.30
1-8	vn	UO	D_4	1	7	2	8	2	37	7.3		9	0.10		2.46
1-9	vn	UO	D_4	1	6	2	5	0.6	4	0.6		6	0.05		0.09
4-3	vn	UO	D_4	0.2	2	0.4	1.4	0.2	2	0.3		5	0.06		0.08
4-4	vn	UO	D_4	0.2	2	0.6	2	0.4	3	0.5		4	0.06		0.06
4-5	vn	UO	D_4	0.4	4	0.9	3	0.5	3	0.4		4	0.06		0.04
4-6	vn	UO	D_4	0.3	3	0.8	3	0.5	3	0.5		4	0.06		0.08
1-5	vn	UO	D_4	3	21	4	12	2	12	1.9		7	0.06		0.42
1-6	vn	UO	D_4	3	19	4	12	2	10	1.4		6	0.06		0.18
1-2	vn	UO	D_4	3	18	4	10	1.3	8	0.9		4		2	2.80
1-4	vn	UO	D_4	1	7	2	5	0.6	4	0.6		4		0.14	0.38
MWD101-149															
1-3	vn	CG	D_4	0.2	3	0.7	2	0.3	1	0.1		3	0.04		0.09
1-5	vn	CG	D_4	0.1	1	0.3	1	0.2	1	0.1	0.01	3	0.05		0.03
2-2	vn	CG	D_4	3	27	6	17	2	13	1.6	0.02	4	0.02		0.55
3-1	vn	GZ	D_4	4	33	7	19	2	13	1.6	0.28	6	0.02		0.99
3-4	vn	GZ	D_4	2	18	3	8	0.9	4	0.4	0.08	4	0.02		1.21
1-1	vn	UO	D_4	0.3	2	1	1	0.1	0.4	0.1	0.01	3	0.02		
1-2	vn	UO	D_4	7	48	8	21	3	18	2.5	0.06	4	0.03		1.53
1-4	vn	UO	D_4	1	13	3	8	0.7	3	0.3	0.01	4	0.03	0.01	
1-7	vn	UO	D_4	6	43	8	22	3	20	2.6	0.02	4	0.03		1.10
2-3	vn	UO	D_4	1	9	2	3	0.3	2	0.2	0.02	4	0.05		0.26
2-4	vn	UO	D_4	1	11	2	7	1.0	6	0.8	0.22	4	0.05	0.02	7.68
2-5	vn	UO	D_4	5	44	10	29	4	23	3.1	0.02	5	0.04		1.20
3-2	vn	UO	D_4	1	10	2	5	0.5	2	0.2	0.02	4	0.02		0.07
3-3	vn	UO	D_4	2	13	3	7	0.8	4	0.4	0.02	4	0.02		0.37
3-5	vn	UO	D_4	2	16	3	7	0.7	4	0.4		4	0.05		0.99
3-6	vn	UO	D_4	4	31	6	15	2	9	0.9	0.01	4	0.05		1.05

Appendix 3.2.1: LA-ICP-MS scheelite geochemistry data continued

Spot	Rock type[1]	Mineral zone[2]	Def event	Na23	P31	Ca43	Mn55	Fe57	Cu65	Sr88	Y89	Nb93	Mo98	Sn118	Ba137	La139	Ce140	Pr141	Nd143	Sm147	Eu151	Gd157
MWD101-149 cont																						
1-6	vn	UO	D_4			139222				202	16	2	58			1	1	0.1	0.4	0.4	0.2	1.1
2-1	vn	UO	D_4			139222				198	12	7	56								0.03	0.06
MWD101-159B																						
2-5	vn	CG	D_4	46		138222	24	59		89	40	13	47	0.2	0.5	4	11	2	7	2	1	2
2-2	vn	GZ	D_4	121		138222	26	53		109	392	197	15	0.7	0.2	9	40	7	36	13	4	21
2-3	vn	GZ	D_4	77		138222	26	55		106	286	124	15	0.5	0.2	9	34	5	25	8	3	12
2-7	vn	GZ	D_4	38		138222	26	60		96	202	74	20	0.5	0.3	7	26	4	21	6	3	9
1-1	vn	UO	D_4			138222	21			107			7		0.3	2	6	1	4	2	0	5
1-2	vn	UO	D_4			138222	19			103			18	0.5		9	40	7	38	11	4	15
1-3	vn	UO	D_4			138222	18			112			20	0.5		10	41	8	38	11	4	13
1-4	vn	UO	D_4			138222	5			118			2	0.4		0.4	1	0.2	1	1	0	2
2-1	vn	UO	D_4	256		138222	18	55		93	196	82	33	0.5	0.4	5	22	4	21	8	2	14
2-4	vn	UO	D_4	48		138222	24	55		110	240	102	20	0.5	0.2	6	26	5	26	9	3	14
2-6	vn	UO	D_4	16		138222	22	55	0.1	98	79	25	7	0.2	0.1	1	4	1	6	3	1	6
2-8	vn	UO	D_4			138222	20			104			16	0.9		9	37	6	32	11	3	18
MWD107-259A																						
1-3	vn	CG	D_4	14		138222	12	54	0.1	63	76	9	7	0.2	0.2	5	16	2	8	2	3	2
1-4	vn	CG	D_4	17		138222	25	60		63	111	10	7	0.2	0.2	11	29	4	13	3	4	3
1-5	vn	CG	D_4	14		138222	25	86	0.1	61	120	10	7	0.3	0.3	18	46	5	18	3	4	4
1-6	vn	CG	D_4	15		138222	24	87	0.3	62	111	10	7	0.2	0.3	19	48	6	19	4	4	4
1-1	vn	CG	D_4	12		138222	14	52		42	52	5	11	0.2	0.1	4	12	2	9	3	3	5
1-2	vn	UO	D_4	5		138222	8	52	0.1	73	10	3	4	0.1	0.05	0.03	0.2	0.04	0.4	0.2	0.04	0.6
MWD119-128A																						
2-1	vn	UO	D_4	8		138222	14	57		154	24	3	13	0.1	0.3	0.7	2	0.3	2	0.5	2	0.7
2-2	vn	UO	D_4	12		138222	16	53	0.1	157	14	3	13	0.1	0.3	0.8	2	0.3	1	0.3	1.2	0.3
2-3	vn	UO	D_4	250		138222	16	54		162	13	4	11	0.2	0.9	0.8	2	0.3	2	0.5	0.9	0.6
MWD122-289B																						
2-1	vn	CG	D_4	58		138222	21	55		174	55	19	40	0.1	0.8	4	18	3	17	4	3	5
2-2	vn	CG	D_4	701		138222	17	56	0.1	175	52	20	35	0.1	1.1	2	12	3	14	4	2	4
2-3	vn	UO	D_4			138222	15			147			15		0.7	1	5	1	5	2	1	4

Appendix 3.2.1: LA-ICP-MS scheelite geochemistry data continued

Spot	Rock type[1]	Mineral zone[2]	Def event	Tb159	Dy163	Ho165	Er167	Tm169	Yb171	Lu175	Ta181	Pb208	Bi209	Th232	U238
MWD101-149 cont															
1-6	vn	UO	D_4	0.2	2	0.3	1	0.1	0.8	0.1		3	0.05		
2-1	vn	UO	D_4	0.04	1	0.4	2	0.4	2	0.3		3	0.02		
MWD101-159B															
2-5	vn	CG	D_4	0.5	4	1	3	0.6	5	0.8		7	0.06		0.08
2-2	vn	GZ	D_4	5	45	11	37	6	35	4.5		7	0.05		0.23
2-3	vn	GZ	D_4	3	30	8	27	4	25	3.3		7	0.05		0.18
2-7	vn	GZ	D_4	2	19	5	18	3	21	3.0		6	0.06		0.31
1-1	vn	UO	D_4	1	10	2	7	1	5	0.8		8			
1-2	vn	UO	D_4	3	28	7	26	4	29	4.0		7		0.12	0.18
1-3	vn	UO	D_4	3	22	5	19	3	19	2.6		7			0.15
1-4	vn	UO	D_4	0.5	4	1	5	0.8	4	0.4		2	0.05		
2-1	vn	UO	D_4	3	27	6	21	3	17	2.2		7	0.05		0.13
2-4	vn	UO	D_4	3	27	7	24	4	22	3.0		7	0.05		0.21
2-6	vn	UO	D_4	1	11	3	9	1.1	6	0.7		4	0.05		0.05
2-8	vn	UO	D_4	5	44	11	40	6	38	4.7		9		0.12	0.13
MWD107-259A															
1-3	vn	CG	D_4	0.4	5	2	7	1.5	11	1.7		5	0.05		0.27
1-4	vn	CG	D_4	0.7	7	2	11	2	17	2.7		5	0.05		0.23
1-5	vn	CG	D_4	0.9	10	3	13	2	15	2.2		5	0.06		0.14
1-6	vn	CG	D_4	0.9	8	3	12	2	17	2.6		6	0.06		0.19
1-1	vn	CG	D_4	1.0	7	1	3	0.4	3	0.3		4	0.06		0.18
1-2	vn	UO	D_4	0.2	1.5	0.4	1	0.2	0.7	0.1		1	0.04		0.03
MWD119-128A															
2-1	vn	UO	D_4	0.2	1.4	0.4	2	0.3	2	0.3		6	0.07		0.38
2-2	vn	UO	D_4	0.1	0.6	0.2	1	0.2	1.2	0.2		6	0.09		0.74
2-3	vn	UO	D_4	0.1	0.9	0.2	1	0.2	1.2	0.2		7	0.07		0.37
MWD122-289B															
2-1	vn	CG	D_4	0.8	7	2	5	0.8	5	0.8		6	0.05		0.06
2-2	vn	CG	D_4	0.8	7	2	6	0.9	5	0.8		6	0.06		0.04
2-3	vn	UO	D_4	0.7	7	2	6	0.8	5	0.7		8			0.05

Appendix 3.2.1: LA-ICP-MS scheelite geochemistry data continued

Spot	Rock type[1]	Mineral zone[2]	Def event	Na23	P31	Ca43	Mn55	Fe57	Cu65	Sr88	Y89	Nb93	Mo98	Sn118	Ba137	La139	Ce140	Pr141	Nd143	Sm147	Eu151	Gd157
MWD122-289B cont																						
2-4	vn	UO	D_4	300		138222	15	56	0.1	162	36	15	44	0.1	0.6	1	4	1	5	2	1	5
2-5	vn	UO	D_4	97		138222	16	57	0.1	186	48	12	45	0.2	0.7	1	4	1	7	4	1	7
MWD122-289C																						
4-1	V-H	UO	D_4	396		138150	16	51		94	55	15	42	0.2	1.0	1	4	1	7	3	2	6
4-2	V-H	UO	D_4	406		138150	15	50		102	73	22	46	0.1	0.7	1	3	1	8	3	2	8
4-3	V-H	UO	D_4	129		138150	17	50		93	153	83	46	0.2	0.4	2	9	2	12	4	1	10
MWD042-197A																						
1-3	sk-alt cong	UO	D_4			138222	11114	29208		4				175	9.2	0	1					
1-1	sk-alt cong	UO	D_4			138222	191	3271		226				2.9	383	9	14	1	7	1		
1-2	sk-alt cong	UO	D_4			138222	75	3170		238				2.9	431	9	16	2	5			1
1-4	sk-alt cong	UO	D_4			138222	84	3579		247					445	9	16	1	5			1

Appendix 3.2.1: LA-ICP-MS scheelite geochemistry data continued

Spot	Rock type[1]	Mineral zone[2]	Def event	Tb159	Dy163	Ho165	Er167	Tm169	Yb171	Lu175	Ta181	Pb208	Bi209	Th232	U238
MWD122-289B cont															
2-4	vn	UO	D_4	0.9	7	2	5	0.6	3	0.4		4	0.05		0.03
2-5	vn	UO	D_4	1.3	10	2	6	0.7	3	0.4		4	0.06		0.04
MWD122-289C															
4-1	V-H	UO	D_4	1.3	10	2	7	0.8	4	0.6		5	0.05		0.06
4-2	V-H	UO	D_4	2	14	3	8	0.9	4	0.5		7	0.07		0.07
4-3	V-H	UO	D_4	3	30	8	22	3	14	1.7		5	0.05		0.05
MWD042-197A															
1-3	sk-alt cong	UO	D_4				1	0.3	2	0.3		1			
1-1	sk-alt cong	UO	D_4	0.2	0.9		0.5					8		2	0.75
1-2	sk-alt cong	UO	D_4	0.1	1.1	0.2	0.4					9		3	1.05
1-4	sk-alt cong	UO	D_4	0.2	1.1	0.4						8		3	0.87

[1]Rock type: mz: monzonite, sk-alt-cong: skarn-altered conglomerate, vn: vein, V-H: vein halo

[2]Mineral zone: CG: core of grain, GZ: grain with growth zoning (overgrowing core), NZ: grain with no zoning, UO: unstructured overgrowth

Appendix 3.2.2: LA-ICP-MS skarn minerals and plagioclase data

Sample MWD	Spot	Rock type[1]	Mineral[2]	Retrograde Stage[3]	Def event	Na23	Ca43	Sc45	Ti49	Mn55	Fe57	Cu65	Zn66	Rb85	Sr88	Y89	Nb93	Mo98	Sn118	Ba137	La139	Ce140	Pr141	Nd143
005-067B	2-1	mz	Pl	N/A	D_{1-2}	68278	22870	6		31	14		0.9		524				0.3	20	0.004	0.003		
005-067B	2-2	mz	Pl	N/A	D_{1-2}	77956	25728	7			35		3	0.6	735	0.1			0.9	29	0.4	0.7	0.07	0.21
005-067B	2-3	mz	Pl	N/A	D_{1-2}		24300								681					21	0.2	0.2		
011-147.5A	1-2	sk-alt cong	Grt	N/A	D_{1-2}	140	177101	10	1647	55645	30700		29	0.9	5	60	0.7		144	0.9	0.1	0.1	0.01	0.05
011-147.5A	1-3	sk-alt cong	Grt	N/A	D_{1-2}		171955	5	5458	59429	35745	0.6	35		1	10	67	0.4	18	0.4	0.1	0.2	0.01	0.05
011-147.5A	1-1	sk-alt cong	Grt	N/A	D_{1-2}		175386	7	1464	54103	32343	0.7	52		9	27	0.5		143	0.8	0.3	0.6	0.05	0.12
011-147.5A	1-4	sk-alt cong	Grt	N/A	D_3		222055		2003	22600	75695		21					2	133					
042-197A	1-1	sk-alt cong	Grt	N/A	D_3		245283	5	1165	9818	19914		13		0	11	4		357			0.01	0.01	0.2
042-197A	1-2	sk-alt cong	Grt	N/A	D_3		244997	5	1045	12134	19835		15		0	15	3		442	0.01		0.01	0.01	0.2
122-289C	1-1	sk-alt cong	Ttn	N/A	D_3	96	214408	87	233736	2298	1128	8	9	0.1	11	555	3549	0.2	3005	0.9	61	239	38	165
122-289C	1-2	sk-alt cong	Ttn	N/A	D_3	35	214408	131	231458	1243	1120	8	9		10	613	1889	0.3	3819	0.5	23	128	27	140
011-147.5A	1-1	sk-alt cong	Ttn	RS1	D_4	85	220125	4	175779	475	947	6	8	0.3	5	5	4167	0.2	253	0.5	0.002			
011-147.5A	1-2	sk-alt cong	Ttn	RS1	D_4	133	220125	4	180389	604	1682	7	29	0.7	23	6	1494	0.1	202	3	0.3	0.6	0.1	0.2
011-147.5A	1-1	sk-alt cong	Czo	?	D_4		177244		774	2184	69275		35		202				601	0.8				
011-147.5A	1-2	sk-alt cong	Czo	?	D_4		176529	12	1395	2998	26835	0.4	50		171	16	6		628	2	0.02	0.03		0.02
011-147.5A	1-3	sk-alt cong	Czo	?	D_4	42	175815	8	3534	3948	22259		47	0.2	197	19	21		919	7	0.2	0.2	0.02	0.09
042-197A	1-1	sk-alt cong	Czo	?	D_4	28	177959	5	495	4368	21939		10		261	7	0.3		2326	4	0.4	0.4	0.05	0.3
042-197A	1-2	sk-alt cong	Czo	?	D_4	46	180103	6	1402	2497	21780		20	0.8	51	20	1		1606	3	1	1	0.2	1

Appendix 3.2.2: LA-ICP-MS skarn minerals and plagioclase data continued

Sample MWD	Spot	Rock type[1]	Mineral[2]	Retrograde Stage[3]	Def event	Sm147	Eu151	Gd157	Tb159	Dy163	Ho165	Er167	Tm169	Yb171	Lu175	Ta181	W183	Pb208	Bi209	Th232	U238
005-067B	2-1	mz	Pl	N/A	D_{1-2}		0.05										0.5	13			
005-067B	2-2	mz	Pl	N/A	D_{1-2}	0.04	0.06										7	16			0.01
005-067B	2-3	mz	Pl	N/A	D_{1-2}								0				7	16		0.1	
011-147.5A	1-2	sk-alt cong	Grt	N/A	D_{1-2}			0.2	0.2	5	2	6	0.9	6	0.8		0.5	0.1			0.01
011-147.5A	1-3	sk-alt cong	Grt	N/A	D_{1-2}			0.06	0.03	0.5	0.3	1	0.3	3	0.4		35	0.8			
011-147.5A	1-1	sk-alt cong	Grt	N/A	D_{1-2}	0.06	0.01	0.09	0.09	2	0.7	2	0.4	3	0.4		7	0.9	0.07		0.01
011-147.5A	1-4	sk-alt cong	Grt	N/A	D_3		0.05		0.5	10	5	23	5	33	4		1	0.1			
042-197A	1-1	sk-alt cong	Grt	N/A	D_3	0.2	0.2	0.5	0.1	0.8	0.3	1.2	0.2	1	0.3		2				0.12
042-197A	1-2	sk-alt cong	Grt	N/A	D_3	0.2	0.2	0.5	0.1	1.1	0.4	1.5	0.3	2	0.4		5				0.09
122-289C	1-1	sk-alt cong	Ttn	N/A	D_3	43	16	42	8	64	15	51	10	88	14		114	2	0.71		131.0
122-289C	1-2	sk-alt cong	Ttn	N/A	D_3	45	21	47	9	71	16	55	10	85	13		46	0.8	0.46		60.5
011-147.5A	1-1	sk-alt cong	Ttn	RS1	D_4		0.004		0.02	0.3	0.1	0.5	0.1	0.6	0.1		156	0.1	0.10		
011-147.5A	1-2	sk-alt cong	Ttn	RS1	D_4	0.1	0.0	0.1	0.0	0.5	0.1	0.6	0.1	0.7	0.1		44	1	0.14		0.01
011-147.5A	1-1	sk-alt cong	Czo	?	D_4		0.08	0.6	0.2	1.9	0.4	0.7	0.1	0.3	0.1			9	1.78		
011-147.5A	1-2	sk-alt cong	Czo	?	D_4	0.03	0.09	0.3	0.1	2.0	0.4	0.8	0.1	0.2	0.03		0.7	10	2.46		0.003
011-147.5A	1-3	sk-alt cong	Czo	?	D_4	0.02	0.04	0.2	0.1	1.5	0.5	1.1	0.1	0.6	0.04		2	14	1.80		0.004
042-197A	1-1	sk-alt cong	Czo	?	D_4	0.1	0.4	0.2	0.1	0.4	0.1	0.4	0.1	0.6	0.1		0.9	7	0.70		0.05
042-197A	1-2	sk-alt cong	Czo	?	D_4	0.5	0.4	0.9	0.2	2	0.5	2	0.3	2	0.3		0.5	8	0.90		0.2

Appendix 3.2.2: LA-ICP-MS skarn minerals and plagioclase data continued

Sample MWD	Spot	Rock type[1]	Mineral[2]	Retrograde Stage[3]	Def event	Na23	Ca43	Sc45	Ti49	Mn55	Fe57	Cu65	Zn66	Rb85	Sr88	Y89	Nb93	Mo98	Sn118	Ba137	La139	Ce140	Pr141	Nd143
042-197A	1-2B	sk-alt cong	Czo	?	D_4		180103		2123	2102	78103				63				1863	2	0.8	1	0.1	
042-197A	1-3	sk-alt cong	Czo	?	D_4		180103		1502	2382	76562				127				2081	3	0.4	0.4		
122-289B	1-1	vn	Ap	RS2	D_4	97964	397400	144	23134	38789	593248		1030	14973	809	638	116	13	83	2258	176	418	58	288
122-289B	1-2	vn	Ap	RS2	D_4	9420	397400	157	34687	36241	554927	219	1152	15069	326	366	131	87	426	6019	85	219	45	194
107-259A	1-3	vn	Pl	?	D_4	61313	20012	6			13	0.3	1	3	323	0.01			0.3	80	0.01	0.02	0.004	
107-259A	1-4	vn	Pl	?	D_4	84442	27159	8		11	26	0.7	2	75	455	0.02			0.5	354	0.1	0.15	0.01	0.02
122-289B	2-4	vn	Pl	?	D_4		41452								875					44				
101-159B	2-1	vn	Pl	RS1	D_4	63849	45026	6	1	8	29		3	0.4	506				0.5	37	0.02	0.03		
101-159B	2-4	vn	Pl	RS1	D_4	66051	40738	7			31		3	2	605	0.05	0.03	0.04	0.3	27	0.01	0.03	0.003	
101-159B	1-2	vn	Pl	RS1	D_4		42882			15					1007					232				
101-159B	1-3	vn	Pl	RS1	D_4		31447			10				5	733					194				
119-128A	2-3	vn	Pl	RS1	D_4	42284	67182								540					119				
119-128A	2-4	vn	Pl	RS1	D_4	53664	68611	7		6	65		12	2	1174	0.01			0.3	168	0.02	0.02		
122-289B	2-1	vn	Pl	RS1	D_4	57807	54317	7	2		66		7	1	1058	0.02			0.4	121	0.04	0.04		
122-289B	2-2	vn	Pl	RS1	D_4	73034	59320	8	1		57		8	1	1148	0.03			0.4	118	0.06	0.07	0.01	
122-289B	2-19	vn	Pl	RS1	D_4	61794	59320	7			41		3	6	783	0.01			0.2	111	0.04	0.07	0.01	0.04
122-289B	2-18	vn	Pl	RS1	D_4	122966	67182	10	238		673	2		8	121	2	0.7	0.3	1	204	5	8	1	2

Appendix 3.2.2: LA-ICP-MS skarn minerals and plagioclase data continued

Sample MWD	Spot	Rock type[1]	Mineral[2]	Retrograde Stage[3]	Def event	Sm147	Eu151	Gd157	Tb159	Dy163	Ho165	Er167	Tm169	Yb171	Lu175	Ta181	W183	Pb208	Bi209	Th232	U238
042-197A	1-2B	sk-alt cong	Czo	?	D_4		0.5	0.9	0.2	2	0.6	2	0.3	3	0.4			4			
042-197A	1-3	sk-alt cong	Czo	?	D_4		0.6	1	0.3	3	0.8	2	0.4	3	0.4			4			0.3
122-289B	1-1	vn	Ap	RS2	D_4	101	17	108	16	137	24	61	10	36	6			81			15
122-289B	1-2	vn	Ap	RS2	D_4	50	5	46	6	31	6	22	3	20	3		374	92			6.3
107-259A	1-3	vn	Pl	?	D_4		0.01										6	3			
107-259A	1-4	vn	Pl	?	D_4		0.1										5	4			
122-289B	2-4	vn	Pl	?	D_4												306	8			
101-159B	2-1	vn	Pl	RS1	D_4		0.1											28			
101-159B	2-4	vn	Pl	RS1	D_4		0.01		0.003								527	17			
101-159B	1-2	vn	Pl	RS1	D_4													13			
101-159B	1-3	vn	Pl	RS1	D_4												127	10			
119-128A	2-3	vn	Pl	RS1	D_4													17			
119-128A	2-4	vn	Pl	RS1	D_4		0.03											13			0.003
122-289B	2-1	vn	Pl	RS1	D_4		0.1										22	14			
122-289B	2-2	vn	Pl	RS1	D_4		0.2										153	16			
122-289B	2-19	vn	Pl	RS1	D_4		0.1											16			
122-289B	2-18	vn	Pl	RS1	D_4	0.4	0.1	0.4	0.06	0.3	0.06	0.20	0.02	0.2	0.03		3	4			0.4

Appendix 3.2.2: LA-ICP-MS skarn minerals and plagioclase data continued

Sample MWD	Spot	Rock type[1]	Mineral[2]	Retrograde Stage[3]	Def event	Na23	Ca43	Sc45	Ti49	Mn55	Fe57	Cu65	Zn66	Rb85	Sr88	Y89	Nb93	Mo98	Sn118	Ba137	La139	Ce140	Pr141	Nd143
122-289B	2-5	vn	Pl	RS1	D_4		59320								959					157				
099-163.5A	1-1	vn	Pl	RS2	D_4		16438							546	243				3	516	0.7	2		
101-159B	2-2	vn	Pl	RS2	D_4	44465	27158	5			21		1.4	9	413	0.02			0.3	58	0.04	0.09	0.01	0.03
101-159B	2-5	vn	Pl	RS2	D_4	37878	23585	4			17		1.2	2	369	0.004	0.01		0.2	69	0.01	0.01		
101-159B	2-3	vn	Pl	RS2	D_4	51630	26444	4	69	11	159	2	1.2	3	50	1	0.3	0.2	1	90	2	3	0.3	1
101-159B	1-1	vn	Pl	RS2	D_4		25014								1323					43				
107-259A	1-2	vn	Pl	RS2	D_4	88865	23585	8			46		1.5	4	410	0.02	0.01		0.4	84	0.03	0.1	0.004	
107-259A	1-1	vn	Pl	RS2	D_4	76800	25014	7		4	46	0.4	1.1	7	364	0.4	0.1	0.2	0.4	69	0.04	0.1	0.02	0.1
119-128A	2-1	vn	Pl	RS2	D_4	46146	50029								701					83				
119-128A	2-2	vn	Pl	RS2	D_4	22496	35735	3		6	33		5	0.7	543	0.003			0.2	68		0.002		
122-289B	2-16	vn	Pl	RS2	D_4	3024	37164						55		185		3			2	0.8			
122-289B	2-3	vn	Pl	RS2	D_4	12765	33591	1		3	17		1	0.1	132	6	0.7	0.9	0.1	13	0.3	0.6	0.1	0.6
122-289B	2-17	vn	Pl	RS2	D_4	89934	54317	8	145	60	494			6	124	2	0.8		1	146	3	6	0.6	2
122-289C	4-1	V-H	Pl	?	D_4	55229	48599	6	1	8	66		12	0.5	373	3	2	2	0.5	48	0.3	0.7	0.1	0.5
122-289C	4-3	V-H	Pl	?	D_4		58605								809				1	92	0.1			
122-289C	4-2	V-H	Pl	?	D_4	53548	37878	6	2		38		6	0.5	470	0.2	0.1	0.2	0.4	59	0.03	0.05	0.01	0.03

Appendix 3.2.2: LA-ICP-MS skarn minerals and plagioclase data continued

Sample MWD	Spot	Rock type[1]	Mineral[2]	Retrograde Stage[3]	Def event	Sm147	Eu151	Gd157	Tb159	Dy163	Ho165	Er167	Tm169	Yb171	Lu175	Ta181	W183	Pb208	Bi209	Th232	U238
122-289B	2-5	vn	Pl	RS1	D_4												1	12			
099-163.5A	1-1	vn	Pl	RS2	D_4				0.2								249	1			
101-159B	2-2	vn	Pl	RS2	D_4		0.05										0.8	12			
101-159B	2-5	vn	Pl	RS2	D_4		0.03										0.6	9			
101-159B	2-3	vn	Pl	RS2	D_4	0.2	0.06	0.2	0.04	0.2	0.04	0.1	0.02	0.1	0.04		2	2	0.01		0.2
101-159B	1-1	vn	Pl	RS2	D_4												1	23			
107-259A	1-2	vn	Pl	RS2	D_4		0.02										3	4			
107-259A	1-1	vn	Pl	RS2	D_4	0.03	0.02	0.05	0.01	0.08	0.02	0.06	0.01	0.04	0.004		26395	5			0.003
119-128A	2-1	vn	Pl	RS2	D_4													14			
119-128A	2-2	vn	Pl	RS2	D_4		0.02											6			
122-289B	2-16	vn	Pl	RS2	D_4							2					174183	4			
122-289B	2-3	vn	Pl	RS2	D_4	0.2	0.03	0.5	0.13	1	0.3	0.8	0.1	0.6	0.1		147458	3	0.01		0.02
122-289B	2-17	vn	Pl	RS2	D_4	0.5	0.06	0.2	0.03	0.3	0.07	0.2	0.03	0.3	0.05		13945	5			0.4
122-289C	4-1	V-H	Pl	?	D_4	0.1	0.08	0.3	0.06	0.5	0.14	0.4	0.04	0.3	0.03		47963	13			0.04
122-289C	4-3	V-H	Pl	?	D_4		0.4					0.1					2	21			
122-289C	4-2	V-H	Pl	?	D_4		0.04		0.004	0.02	0.01	0.03	0.004	0.04	0.01		2778	15			

[1]Rock type: mz: monzonite, sk-alt-cong: skarn-altered conglomerate, vn: vein, V-H: vein halo

[2]Mineral: Ap: apatite, Czo: clinozoisite, Grt: garnet, Pl: plagioclase, Ttn: titanite. After Whitney and Evans (2010)

[3]Retrograde Stage: RS1: Retrograde Stage 1, RS2: Retrograde Stage 2, ?: unkwnown, N/A.: not applicable

Appendix 4: Material linked to Chapter 4

Appendix 4.1: Fluid inclusions data

Inclusion ID	Tf °C*	Ti °C*	Tm °C*	Th °C*	$Tmcl_i$ °C*	$Tmcl_f$ °C*	NaCl wt.%	Inclusion shape[1]	Inclusion length um	Bubble area um^2	Bubble diameter um	Inclusion area um^2	Bubble/ Inclusion	ρ_{BULK} g/cm^3	Note	Raman Vapor	Raman Liquid	Raman Solid
MWD099-054B - Quartz																		
P3-2-01	--	--	--	--	--	--	--	irre	14	7	3	30	0.23	--	Nothing happened when Tm	--	--	--
P3-2-02	–37	–28	–2.9	257	–8.3	--	4.80	ir	24	17	5	75	0.22	0.83	--	--	--	--
P3-2-03	–38	–21	–1.8	272	–8	--	3.06	irre	21	8	3	68	0.12	0.79	--	--	--	--
P3-2-04	–35	--	–2.4	--	–11	--	4.03	irre	53	85	10	298	0.29	--	Not possible to see Th	--	--	--
P5-1-01	-48	–28	–2.0	323	--	--	3.39	irre	7	2	2	14	0.17	0.70	--	H_2O	H_2O	--
P5-1-02	--	–22	–2.1	337	--	--	3.55	irre	7	5	2	13	0.36	0.67	--	H_2O	H_2O	--
P5-1-03	--	--	--	--	--	--	--	irre	5	2	2	8	0.29	--	Too small and blurry fluid inclusion	H_2O	H_2O	--
P5-1-04	–52	–31	–1.9	--	–9	--	3.23	ie	14	5	2	19	0.24	--	Bubble dissapeared prior to Th	--	--	--
P5-1-05	–41	–24	–2.2	228	--	--	3.71	ib	10	2	2	22	0.08	0.86	--	--	--	--
P5-2-01	–42	–23	–2.4	260	--	11	4.03	io	13	14	4	78	0.18	0.82	--	H_2O	H_2O	--
P5-2-02	–37	–25	–2.1	268	--	--	3.55	irre	7	5	2	19	0.26	0.80	--	H_2O	H_2O	--
P5-3-01	--	–23	–1.6	367	--	--	2.74	ir	10	9	3	25	0.37	0.59	--	--	--	--
P5-4-01	–43	–32	–5.7	270	--	--	8.81	ir	16	3	2	24	0.14	0.85	--	--	--	--
P5-4-02	–39	–24	–2.3	292	--	--	3.87	it	19	4	2	23	0.18	0.76	--	--	--	--
P5-5-01	–40	--	–3.2	243	--	--	5.26	irre	12	7	3	42	0.16	0.85	--	--	--	--
P5-5-02	–45	–31	–3.0	271	--	--	4.96	ie	17	4	2	26	0.14	0.81	--	--	--	--
P5-5-03	–38	–23	–0.7	248	--	--	1.22	ib	4	3	2	12	0.22	0.81	--	--	--	--
P5-5-04	–43	–28	–1.1	--	--	--	1.91	ir	9	5	2	21	0.23	--	Not clear FI for Th	--	--	--
P5-6-01	–43	--	–0.4	--	--	--	0.70	ie	13	3	2	11	0.30	--	Bubble dissapeared prior to Th	--	--	--
P5-6-02	–50	–26	–2.5	337	--	10	4.18	io	7	5	3	27	0.20	0.68	--	--	--	--
P5-6-03	–48	–29	–4.8	297	–6	--	7.59	is	5	4	2	16	0.24	0.80	--	--	--	--

Appendix 4.1: Fluid inclusions data continued

Inclusion ID	Tf °C*	Ti °C*	Tm °C*	Th °C*	$Tmcl_i$ °C*	$Tmcl_f$ °C*	NaCl wt.%	Inclusion shape[1]	Inclusion length um	Bubble area um^2	Bubble diameter um	Inclusion area um^2	Bubble/ Inclusion	ρ_{BULK} g/cm^3	Note	Raman Vapor	Raman Liquid	Raman Solid
MWD099-054B - Quartz continued																		
P5-6-04	–50	–24	–2.4	329	–4	--	4.03	it	16	6	3	57	0.11	0.70	--	--	--	--
P5-6-05	–53	–25	–5.2	268	--	--	8.14	io	4	2	1	11	0.14	0.84	--	--	--	--
P5-6-06	--	–30	–4.6	289	--	--	7.31	io	6	7	3	23	0.29	0.81	Th as double bubble formation	--	--	--
P5-6-07	–49	–25	–4.5	325	–11	--	7.17	ir	10	10	4	37	0.28	0.75	Triple bubble formation when Th	--	--	--
P5-6-08	–47	–25	–3.8	--	--	--	6.16	irre	13	12	4	70	0.18	--	Bubble dissapeared prior to Th	--	--	--
P5-7-01	–48	–26	–3.8	308	–8	--	6.16	rec	8	6	3	23	0.25	0.76	--	--	--	--
P5-7-02	–50	–25	–2.5	322	–8	--	4.18	io	4	3	2	10	0.26	0.71	Triple bubble formation when Th	--	--	--
P5-7-03	–36	–24	–2.7	306	--	--	4.49	io	4	3	2	14	0.23	0.75	--	--	--	--
P5-7-04	–50	–30	–1.3	309	–7	--	2.24	irre	5	1	1	10	0.10	0.71	--	--	--	--
P5-7-05	–44	–27	–1.1	277	--	--	1.91	irre	6	5	3	20	0.25	0.77	--	--	--	--
P5-7-06	--	–21	–1.3	345	--	--	2.24	io	5	4	2	12	0.37	0.64	--	--	--	--
P5-7-07	–50	–24	–1.8	253	–8	--	3.06	ib	6	3	2	13	0.22	0.82	--	--	--	--
P5-7-08	–52	–28	--	353	–10	4.3	--	io	5	7	3	22	0.35	--	--	--	--	--
P5-7-09	–37	–28	–0.8	285	--	--	1.40	io	5	3	2	14	0.23	0.75	--	--	--	--
P5-7-10	–41	–28	--	--	–7.8	--	--	io	5	3	2	14	0.23	--	--	--	--	--
P5-7-11	–42	–25	--	319	--	--	--	io	4	2	2	10	0.24	--	--	--	--	--
P5-7-12	–41	–26	–3.5	340	--	6	5.71	it	6	4	2	15	0.29	0.70	--	--	--	--
P5-8-01	–44	–25	–4.9	275	--	--	7.73	irre	4	2	1	8	0.19	0.83	Th as double bubble formation	--	--	--
P5-8-02	–37	–25	–1.7	276	--	--	2.90	ir	5	2	2	10	0.19	0.78	--	--	--	--
P5-8-03	–52	–23	--	285	--	--	--	ib	6	3	2	13	0.20	--	--	--	--	--
P5-8-04	--	--	--	--	--	--	--	it	5	2	2	7	0.29	--	Nothing happened when Tm	--	--	--

Appendix 4.1: Fluid inclusions data continued

Inclusion ID	Tf °C*	Ti °C*	Tm °C*	Th °C*	$Tmcl_i$ °C*	$Tmcl_f$ °C*	NaCl wt.%	Inclusion shape[1]	Inclusion length um	Bubble area um^2	Bubble diameter um	Inclusion area um^2	Bubble/ Inclusion	ρ_{BULK} g/cm^3	Note	Raman Vapor	Raman Liquid	Raman Solid
MWD099-124B - Quartz																		
P1-1-01	–39	--	–2.3	304	--	--	3.87	is	42	36	7	182	0.20	0.74	Contains solid	$C + CH_4$	H_2O	Graphite
P1-1-02	–39	–29	–2.4	--	--	8	4.03	it	48	31	6	359	0.09	--	Contains solid; decrepitated at 309.3°C	CH_4	H_2O	Graphite
P1-14-1	–47	–23	–1.6	294	–11	--	2.74	ir	42	29	6	121	0.24	0.75	--	--	--	--
P1-15-01	–43	–23	–1.3	--	--	--	2.24	irre	71	50	8	503	0.10	--	Apparently decrepitated with P1-1-02	--	--	--
P1-15-02	–42	–19	–1.8	246	--	--	3.06	is	19	5	2	46	0.11	0.83	--	--	--	--
P1-15-03	–42	–23	–1.2		–10	--	2.07	ir	29	25	6	88	0.29		--	--	--	--
P1-16-01	–39	--	–1.2	308	–4.4	0.6	2.07	io	25	22	5	83	0.26	0.71	--	CH_4	H_2O	--
P1-16-02	–41	--	–0.4	--	–17	--	0.70	ir	19	12	4	41	0.29	--	Turned black, not possible to heat for Th	H_2O	H_2O	--
P1-16-03	--	–27	–2.2	--	--	--	3.71	ir	47	20	5	66	0.30	--	Bubble dissapeared prior to Th	CH_4	--	--
P1-16-04	–46	–23	–1.5	386	–16	--	2.57	rr	24	9	3	39	0.22	0.54	--	CH_4	H_2O	--
P1-16-05	–44	–28	–2.3	274	–12	--	3.87	it	25	16	5	78	0.21	0.79	--	--	--	--
P1-16-06	–44	–22	–2.6	331	--	--	4.34	it	32	29	6	128	0.22	0.70	--	CH_4	--	--
P1-2-01	–41	--	–2.2	--	--	--	3.71	irre	61	57	9	252	0.23	--	Turned black, not possible to heat for Th	--	--	--
P1-3-01	--	--	--	--	--	--	--	irre	39	38	7	150	0.25	--	Nothing happened when Tm and Th	--	--	--
P1-3-02	–43	–24	–1.7	271	--	--	2.90	io	28	24	6	128	0.19	0.79	--	--	--	--
P1-3-03	–52	--	–1.8	331	--	--	3.06	irre	30	14	4	100	0.14	0.68	--	--	--	--
P1-3-04	–41	–21	–2.3	291	--	--	3.87	bi	24	8	3	46	0.18	0.76	--	--	--	--
P1-4-01	–41	–24	–1.4	245	--	--	2.41	io	25	9	3	88	0.10	0.82	--	--	--	--
P1-4-02	–39	--	–1.9	283	--	--	3.23	irre	18	6	3	44	0.14	0.77	--	--	--	--
P1-5-01	–43	--	–1.6	290	–10	2	2.74	ie	73	20	5	151	0.13	0.75	--	$CH_4 + H_2O$	H_2O	--

Appendix 4.1: Fluid inclusions data continued

Inclusion ID	Tf °C*	Ti °C*	Tm °C*	Th °C*	$Tmcl_i$ °C*	$Tmcl_f$ °C*	NaCl wt.%	Inclusion shape[1]	Inclusion length um	Bubble area um^2	Bubble diameter um	Inclusion area um^2	Bubble/ Inclusion	ρ_{BULK} g/cm^3	Note	Raman Vapor	Raman Liquid	Raman Solid
MWD099-124B - Quartz continued																		
P1-5-02	–40	–22	–2.2	--	--	--	3.71	ir	67	51	8	137	0.37	--	Strong CH_4 peak	CH_4	H_2O	--
P1-6-01	–40	–22	–1.2	291	--	--	2.07	ib	30	9	3	76	0.11	0.74	--	--	--	--
P1-6-02	–38	–30	–1.8	273	–13	13	3.06	ie	28	6	3	52	0.11	0.79	--	--	--	--
P1-6-03	--	–23	–0.5	--	--	--	0.88	is	23	10	4	44	0.22	--	--	--	--	--
P1-6-04	–39	–25	–3.3	--	–9	--	5.41	it	10	6	3	21	0.31	--	--	--	--	--
P1-6-05	--	--	–1.5	216	--	--	2.57	irre	11	3	2	19	0.16	0.87	--	--	--	--
P3-2-01	–79	–27	–0.8	--	--	--	1.40	irre	49	--	--	--	--	--	Decrepitated when heating	--	--	--
P3-2-02	–42	–24	–3.2	--	--	4.9	5.26	ov	27	--	--	--	--	--	Decrepitated when heating	--	--	--
P3-2-03	–43	–25	–1.6	--	--	--	2.74	it	51	--	--	--	--	--	Decrepitated when heating	CH_4	--	--
P3-2-04	–31	–26	--	--	--	--	--	irre	48	--	--	--	--	--	Decrepitated when heating	--	--	--
P3-3-01	–44	–25	–1.1	--	10.2	11.9	1.91	irre	40	--	--	--	--	--	Decrepitated when heating	CH_4	H_2O	--
P3-3-02	–43	–27	–1.0	--	--	--	1.74	it	33	--	--	--	--	--	Decrepitated when heating	--	H_2O	--
P3-3-03	–42	–25	–1.3	--	13.3	14.2	2.24	ir	49	--	--	--	--	--	Decrepitated when heating	CH_4	H_2O	--
P3-3-04	–42	–24	–1.0	--	--	--	1.74	ia	30	--	--	--	--	--	Decrepitated when heating	--	--	--
P3-3-05	–49	–26	–3.2	--	--	-10.0	5.26	is	31	--	--	--	--	--	Decrepitated when heating	$CaCO_3 + H_2O$	$CaCO_3$ + H_2O	--
P3-3-06	–43	–23	–1.1	--	--	--	1.91	it	17	--	--	--	--	--	Decrepitated when heating	H_2O	H_2O	--
P3-4-01	–44	--	–0.1	--	--	--	0.18	bi	46	--	--	--	--	--	Decrepitated when heating	CH_4	H_2O	--
P3-4-02	–44	–26	–1.7	--	10.0	11.0	2.90	irre	38	--	--	--	--	--	Decrepitated when heating	--	--	--
P3-4-03	–44	–21	–1.6	--	--	15.2	2.74	irre	31	--	--	--	--	--	Decrepitated when heating	CH_4	CH_4	--
P3-4-04	–43	–28	–1.8	--	--	5.5	3.06	bi	25	--	--	--	--	--	Muscovite liquid (3621)? decrepitated when heating	CH_4	Ms	--

Appendix 4.1: Fluid inclusions data continued

Inclusion ID	Tf °C*	Ti °C*	Tm °C*	Th °C*	$Tmcl_i$ °C*	$Tmcl_f$ °C*	NaCl wt.%	Inclusion shape[1]	Inclusion length um	Bubble area um^2	Bubble diameter um	Inclusion area um^2	Bubble/ Inclusion	ρ_{BULK} g/cm^3	Note	Raman Vapor	Raman Liquid	Raman Solid
MWD099-124B - Quartz continued																		
P3-5-01	–44	–26	–2.2	--	--	--	3.71	tri	20	--	--	--	--	--	Decrepitated when heating	H_2O	--	--
P3-5-02	–48	–25	–0.6	--	--	8.8	1.05	irre	28	--	--	--	--	--	Decrepitated when heating	CH_4	H_2O	--
P3-5-03	–45	–27	–0.3	--	--	--	0.53	irre	22	--	--	--	--	--	Decrepitated when heating	CH_4	H_2O	--
P3-5-04	--	–27	--	--	--	--	--	irre	36	--	--	--	--	--	Decrepitated when heating	CH_4	--	--
P3-5-05	–47	–26	–0.4	--	–8.6	15.1	0.70	irre	12	--	--	--	--	--	Decrepitated when heating	--	--	--
P4-2-01	–43	--	–1.7	--	3.5	8.1	2.90	irre	10	18	5	53	0.33	--	FI turned black and bubble dissapeared	C + CH_4	H_2O + CH_4	--
P4-2-02	–37	--	–2.3	293	--	10.2	3.87	rec	7	4	2	21	0.18	0.76	Borate in V; CH_4 lquid (2914)	--	CH_4	--
P4-2-03	–45	–25	--	351	--	7.2	--	it	12	16	5	59	0.28	--	N_2 in vapor (2326)?	CH_4	C + H_2O	--
P4-2-04	--	--	--	346	--	--	--	irre	6	8	3	20	0.38	--	--	--	--	--
P4-2-05	–42	–26	–3.2	273	--	--	5.26	it	8	11	4	38	0.27	0.81	--	--	--	--
P4-2-06	–53	--	–5.2	259	--	--	8.14	irre	14	12	4	119	0.10	0.86	--	--	--	--
P4-2-07	–51	–25	–0.6	293	--	--	1.05	irre	4	3	2	15	0.22	0.73	--	--	--	--
P4-2-08	–43	--	–3.2	286	--	--	5.26	it	6	7	3	26	0.27	0.79	--	--	--	--
P4-2-09	–42	--	–1.6	293	--	--	2.74	irh	7	4	2	20	0.18	0.75	Elongated vapour bubble	--	--	--
P4-3-01	–38	–25	–1.7	238	–2.4	13.8	2.90	ir	28	12	4	77	0.15	0.84	--	--	--	--
P4-3-02	--	--	–1.9	244	–5.4	--	3.23	ib	38	18	5	111	0.16	0.83	--	--	--	--
P4-3-03	–42	–27	–1.2	185	–3.3	13.6	2.07	io	17	13	4	49	0.27	0.90	--	--	--	--
P4-3-04	–57	–19	--	280	--	--	--	irre	45	35	7	235	0.15	--	--	--	--	--
P4-3-05	--	–25	–1.6	275	–3.4	--	2.74	io	14	5	2	18	0.26	0.78	--	--	--	--
P4-3-06	–45	–27	--	264	--	--	--	io	25	10	3	73	0.13	--	--	--	--	--

Appendix 4.1: Fluid inclusions data continued

Inclusion ID	Tf °C*	Ti °C*	Tm °C*	Th °C*	$Tmcl_i$ °C*	$Tmcl_f$ °C*	NaCl wt.%	Inclusion shape[1]	Inclusion length um	Bubble area um^2	Bubble diameter um	Inclusion area um^2	Bubble/ Inclusion	ρ_{BULK} g/cm^3	Note	Raman Vapor	Raman Liquid	Raman Solid
MWD099-124B - Quartz continued																		
P4-3-07	--	--	–1.2	251	--	11.6	2.07	irre	25	8	3	48	0.16	0.81	--	--	--	--
P4-4-01	–36	–24	–2.0	296	–3.3	--	3.39	irre	51	56	8	284	0.20	0.75	--	--	--	--
P4-4-02	--	–28	–1.6	272	–3	--	2.74	rec	15	6	3	27	0.23	0.78	--	--	--	--
P4-4-03	–45	–22	–2.7	265	--	--	4.49	irre	56	74	10	314	0.24	0.81	--	--	--	--
P4-5-01	–42	--	--	308	–9.7	15.2	--	irre	59	72	10	326	0.22	--	--	--	--	--
P4–5–02	--	--	--	--	--	--	--	rec	29	5	3	130	0.04	--	--	--	--	--
P4–5–03	--	-24	--	--	--	--	--	irre	35	--	--	--	--	--	--	--	--	--
P4–5–04	--	--	–0.3	224	--	--	0.53	it	21	7	3	50	0.15	0.84	--	--	--	--
P4–5–05	–42	–21	–1.7	––	--	--	2.90	irre	--	--	--	--	--		--	--	--	--
P4–6–01	–41	--	–1.2	––	--	5.5	2.07	irre	89	136	13	639	0.21	--	CH_4 vapor (2914)	CH_4	H_2O	––
P4–6–02	–43	--	–2.6	258	--	7.6	4.34	tri	39	21	5	160	0.13	0.82	--	H_2O	H_2O	Graphite (Paragonite?)
P4–6–03	–44	--	––	301	--	--	--	it	18	12	4	53	0.23	--	--	H_2O	H_2O	--
P4–6–04	–43	--	–2.2	--	2.1	--	3.71	ir	83	--	--	--	--	--	CH_4 vapor (2914) $MgSO_4 \cdot H_2O$ (3295)	CH_4	H_2O	--
P4–7–01	–43	--	–1.9	171	–8.7	--	3.23	ib	33	19	5	78	0.24	0.92	--	H_2O	H_2O	--
P4–7–02	–43	--	–1.4	245	–3.3	16	2.41	it	17	7	3	28	0.24	0.82	CH_4 vapor (2909)	$H_2O + CH_4$	--	--
P4–7–03	–43	--	–2.5	236	--	--	4.18	irre	38	29	6	147	0.19	0.85	CH_4 vapour (2914–3019) N_2 (2327) CH_4 liquid (2910)	CH_4	$H_2O + CH_4$	--
P4–7–04	--	--	–1.9	373	--	--	3.23	it	16	7	3	26	0.26	0.59	CH_4 vapor (2915)	$H_2O + CH_4$	H_2O	--

Appendix 4.1: Fluid inclusions data continued

Inclusion ID	Tf °C*	Ti °C*	Tm °C*	Th °C*	$Tmcl_i$ °C*	$Tmcl_f$ °C*	NaCl wt.%	Inclusion shape[1]	Inclusion length um	Bubble area um^2	Bubble diameter um	Inclusion area um^2	Bubble/ Inclusion	ρ_{BULK} g/cm^3	Note	Raman Vapor	Raman Liquid	Raman Solid
MWD099-124B - Quartz continued																		
P4-7-05	–43	–23	–1.6	--	--	--	2.74	irre	34	7	3	97	0.07	--	CH_4 vapor (2915) Borate liquid (950-964)	$H_2O + CH_4$	H_2O + Borate	--
P4-7-06	–43	–28	–0.2	284	2.3	--	0.35	irre	49	17	5	129	0.13	0.74	CH_4 vapor (2914) CH_4 liquid (2914)	$H_2O + CH_4$	$H_2O + CH_4$	--
P4-7-07	--	–27	–1.9	265	--	10.1	3.23	rec	21	13	4	56	0.24	0.80	CH_4 vapor (2914)	$H_2O + CH_4$	--	--
P4-7-08	–44	–29	–1.7	--	–3.3	--	2.90	irre	18	7	3	28	0.27	--	No bubble at 25°C to heat	--	--	--
P4-7-09	–43	–29	–1.7	249	--	15	2.90	ie	36	10	4	65	0.16	0.82	--	H_2O	--	--
P4-7-10	–44	–28	–1.8	--	--	16.1	3.06	it	16	6	3	23	0.26	--	No bubble at 25°C to heat	--	--	--
P4-7-11	–44	–18	–1.5	287	4.4	--	2.57	is	17	5	2	40	0.12	0.76	--	H_2O	--	--
P4-7-12	–38	--	–1.0	292	--	--	1.74	irre	81	56	8	477	0.12	0.74	CH_4 vapor (2915)	CH_4	H_2O	--
P4-7-13	–39	–23	–1.3	307	--	--	2.24	irre	26	14	4	78	0.18	0.72	--	--	--	--
P4-7-14	–43	–23	--	264	–16	2.6	--	irre	49	51	8	202	0.25	--	--	--	--	--

Appendix 4.1: Fluid inclusions data continued

Inclusion ID	Tf °C*	Ti °C*	Tm °C*	Th °C*	$Tmcl_i$ °C*	$Tmcl_f$ °C*	NaCl wt.%	Inclusion shape[1]	Inclusion length um	Bubble area um^2	Bubble diameter um	Inclusion area um^2	Bubble/ Inclusion	ρ_{BULK} g/cm^3	Note	Raman Vapor	Raman Liquid	Raman Solid
MWD099-054B - Scheelite																--	--	--
P1-1-01	–46	–30	–2.2	--	--	8	3.71	bi	29	20	5	61	0.33	--	Turned black, not possible to heat for Th	$H_2O + CH_4$	H_2O	--
P1-1-02	--	–26	–2.8	226	–11	15	4.65	ov	16	2	2	31	0.07	0.87	--	H_2O	H_2O	--
P1-1-03	–43	–33	–2.2	220	--	--	3.71	sq	10	6	3	70	0.08	0.87	--	H_2O	H_2O	--
P1-1-04	--	–30	–1.6	249	--	14	2.74	rho	12	15	4	80	0.18	0.82	--	H_2O	H_2O	--
P1-1-05	--	–28	–0.3	239	--	0.7	0.53	tri	19	20	5	110	0.18	0.82	--	H_2O	H_2O	--
P1-1-06	–37	–24	–0.7	237	--	--	1.22	rec	23	29	6	176	0.16	0.82	--	$H_2O + CH_4$	H_2O	--
P1-1-07	–44	–28	–2.5	232	–3.9	--	4.18	ip	10	8	3	60	0.13	0.86	--	H_2O	H_2O	--
P1-1-08	--	–27	–1.3	--	–11	--	2.24	rho	11	8	3	64	0.13	--	Turned black, not possible to heat for Th	--	--	--
P1-2-01	–39	–28	–2.6	307	–3.5	--	4.34	ib	20	36	7	186	0.20	0.74	--	H_2O	$H_2O + CH_4$	--
P1-2-02	–41	–28	–2.0	--	–5.7	--	3.39	rho	14	15	4	139	0.11	--	Turned black, not possible to heat for Th	H_2O	H_2O	--
P1-2-03	–39	–31	–2.1	255	–8.7	--	3.55	rho	25	36	7	328	0.11	0.82	--	H_2O	H_2O	--
P1-2-04	–43	–32	–2.4	248	–3.1	--	4.03	irh	36	62	9	407	0.15	0.83	--	H_2O	H_2O	--
P1-2-05	–43	–31	–2.2	237	–11	--	3.71	rho	18	15	4	241	0.06	0.85	--	H_2O	H_2O	--
P1-2-06	–39	–28	–2.2	271	–13.5	--	3.71	rec	22	31	6	235	0.13	0.80	--	H_2O	--	--
P1-3-01	--	–29	–1.9	285	–9.7	13.4	3.23	rho	17	13	4	172	0.07	0.77	--	H_2O	H_2O	--
P1-3-02	–38	–27	–2.2	240	–7.5	--	3.71	ip	15	9	3	112	0.08	0.84	--	H_2O	H_2O	--
P1-3-03	–42	–28	–1.8	--	–12.5	--	3.06	ip	15	24	6	122	0.20	--	Turned black, not possible to heat for Th	H_2O	H_2O	--
P1-3-04	–42	–22	–1.9	--	–6.8	16.5	3.23	irre	19	11	4	150	0.07	--	Th: heated to 300°C but likely crepitated with P1-3-10	H_2O	H_2O	--
P1-3-05	–39	–32	–2.0	333	–10	--	3.39	ir	16	15	4	128	0.12	0.68	--	--	--	--
P1-3-06	–41	–26	–1.9	243	–18	--	3.23	ir	12	14	4	89	0.16	0.83	--	--	--	--

Appendix 4.1: Fluid inclusions data continued

Inclusion ID	Tf °C*	Ti °C*	Tm °C*	Th °C*	$Tmcl_i$ °C*	$Tmcl_f$ °C*	NaCl wt.%	Inclusion shape[1]	Inclusion length um	Bubble area um^2	Bubble diameter um	Inclusion area um^2	Bubble/ Inclusion	ρ_{BULK} g/cm^3	Note	Raman Vapor	Raman Liquid	Raman Solid
MWD099-054B - Scheelite continued																--	--	--
P1-3-07	–43	–28	–1.8	223	–8.1	7	3.06	it	13	7	3	90	0.08	0.86	--	--	--	--
P1-3-08	–43	–31	–2.0	220	–8	--	3.39	ir	18	12	4	182	0.07	0.87	--	--	--	--
P1-3-09	--	–28	–2.1	244	–9.8	--	3.55	irh	42	36	7	509	0.07	0.84	--	--	--	--
P1-3-10	–41	–26	–1.6	--	--	--	2.74	irh	20	9	3	198	0.04	--	Decrepitated at 273°C	--	--	--
P1-3-11	–39	–30	–1.9	229	–9.4	--	3.23	irh	--	--	--	--	0.16	0.85	--	--	--	--
P1-3-12	--	–25	–2.4	226	–6	12	4.03	irh	14	6	3	116	0.05	0.86	Th: stopped moving around meniscus	--	--	--
P1-3-13	–43	–30	–2.1	276	--	--	3.55	irh	17	19	5	141	0.13	0.79	--	--	--	--
P1-3-14	–40	–29	–3.0	229	--	--	4.96	ir	18	15	4	195	0.08	0.87	--	--	--	--
P1-4-01	--	–27	–2.3	--	–9	--	3.87	ir	5	7	3	64	0.11	--	Turned black, not possible to heat for Th	--	--	--
P1-4-02	--	–30	–1.7	--	–11	--	2.90	irre	5	15	4	80	0.18	--	Turned black, not possible to heat for Th	--	--	--
P1-4-03	–41	–29	–1.9	228	--	--	3.23	irh	7	12	4	139	0.08	0.86	--	--	--	--
P1-4-04	–41	–24	–0.8	249	--	--	1.40	it	6	12	4	98	0.12	0.81	--	--	--	--
P1-4-05	–42	–26	–1.2	228	--	--	2.07	irre	8	9	3	128	0.07	0.85	--	--	--	--
P3-1-01	--	–26	--	--	–7.5	--	--	irre	12	8	3	47	0.16	--	No Th measured since no Tmice possible to measure	--	--	--
P3-1-02	–48	–28	–5.1	206	–13	--	8.00	el	18	3	2	36	0.08	0.92	--	H_2O	H_2O	--
P4-1-01	--	--	--	--	--	--	--	irre	19	14	4	111	0.12	--	Turned black, not possible to heat for Th	--	--	--
P4-1-02	–39	–29	–1.0	242	--	--	1.74	ir	8	5	3	26	0.21	0.82	--	--	--	--
P4-1-03	–35	–28	–2.8	240	–8	--	4.65	ir	24	13	4	149	0.09	0.85	--	--	--	--
P4-1-04	–38	–24	–2.4	267	–5.3	--	4.03	irre	14	6	3	54	0.12	0.81	--	--	--	--
P4-1-05	–35	–28	–2.0	235	–11	--	3.39	ir	19	6	3	58	0.10	0.85	--	--	--	--

Appendix 4.1: Fluid inclusions data continued

Inclusion ID	Tf °C*	Ti °C*	Tm °C*	Th °C*	$Tmcl_i$ °C*	$Tmcl_f$ °C*	NaCl wt.%	Inclusion shape[1]	Inclusion length um	Bubble area um^2	Bubble diameter um	Inclusion area um^2	Bubble/ Inclusion	ρ_{BULK} g/cm^3	Note	Raman Vapor	Raman Liquid	Raman Solid
MWD099-054B - Scheelite continued																--	--	--
P4-1-06	–40	–29	–2.2	--	–7.6	--	3.71	oe	24	16	4	83	0.19	--	No bubble at 25°C to heat, possible decrepitation	--	--	--
P4-1-07	–33	–28	–1.8	212	--	--	3.06	ir	21	15	4	115	0.13	0.87	--	--	--	--
P4-2-01	–39	–31	–1.9	294	–6.5	--	3.23	irh	14	10	4	91	0.11	0.75	--	--	--	--
P4-2-02	–33	–32	–2.3	253	--	--	3.87	irre	30	53	8	322	0.16	0.83	--	--	--	--
P4-2-03	–44	–29	–2.5	260	–9	--	4.18	ib	17	24	5	140	0.17	0.82	Good FI	--	--	--
MWD099-124B - Scheelite																--	--	--
P3-1-01	–35	–24	–0.8	--	--	11.1	1.40	bi	44	--	--	--	--	--	Decrepitated during heating	--	--	--
P3-1-02	–39	–21	–0.8	--	--	--	1.40	rec	27	--	--	--	--	--	Decrepitated during heating	--	--	--
P3-1-03	–29	–22	–1.3	--	9.7	15.4	2.24	bi	38	--	--	--	--	--	Decrepitated during heating	CH_4	--	--
P3-1-04	–39	–25	–0.3	--	--	--	0.53	is	19	--	--	--	--	--	Decrepitated during heating	--	--	--
P3-1-05	–33	--	–0.9	--	--	--	1.57	rho	23	--	--	--	--	--	Decrepitated during heating	CO_2	--	--
P3-1-06	–46	–23	--	--	--	--	--	bi	21	--	--	--	--	--	Decrepitated during heating	--	--	--
P3-1-07	–38	–23	–1.3	--	--	--	2.24	bi	19	--	--	--	--	--	Decrepitated during heating	$C + CH_4$	--	--
P3-1-08	–42	--	–0.4	--	--	--	0.70	tri	23	--	--	--	--	--	Decrepitated when heating	--	--	--
P3-1-09	–37	–24	--	--	--	8.1	--	ov	18	--	--	--	--	--	Decrepitated when heating	C	--	--
P3-1-10	–39	–31	–0.8	--	--	--	1.40	ov	42	--	--	--	--	--	Decrepitated during heating	CH_4	--	--
P3-1-11	–33	--	–0.9	--	--	--	1.57	bi	13	--	--	--	--	--	Decrepitated during heating	C	--	--
P4-1-01	–38	–21	–0.3	271	--	0.3	0.53	ov	17	5	3	45	0.12	0.76	--	C		
P4-1-02	–40	--	–0.7	238	--	--	1.22	irre	41	25	6	157	0.16	0.82	--	CH_4	--	Graphite
P4-1-03	–39	--	–0.8	281	--	--	1.40	ir	34	13	4	130	0.10	0.75	--	--	--	--
P4-1-04	–43	–26	–2.2	228	--	8.5	3.71	rec	17	4	2	38	0.11	0.86	--	--	--	
P4-1-05	–42	–25	–0.7	264	--	--	1.22	ir	14	6	3	39	0.15	0.78	--	--		

[1]Inclusion shape: bi: bipyramidal, el: elongated, irre: irregular, ia: irregular angular, ib: irregular bipyramidal, ie: irregular elongated, io: irregular oval, ip: irregular pyramidal, ir: irregular rectangular, irh: irregular rhomboid, is: irregular square, it: irregular triangular, ov: oval, oe: oval elongated, rec: rectangular, rho: rhomboid, rr: round rectangular, sq: squared, tri: triangular

*Temperature abbreviations: Tf: metastable freezing temperature, Ti: initial melting, Tm: final metling of ice, Th: Homogenization of H_2O-rich fluid inclusions, $Tmcl_i$: initial clathrate melting, $Tmcl_f$: final clathrate melting

Appendix 5: Other contributions during the time of this project

Appendix 5.1: Society of Economic Geologists 2015 Conference Abstract

Scheelite vein mineralization at the Watershed tungsten deposit, Northeast Queensland, Australia

Jaime Poblete,[1*] Zhaoshan Chang,[1] Yanbo Cheng,[1] Martin Griessmann,[2] Jamie Williamson,[2] and Isaac Corral[1]

[1]Economic Geology Research Centre, College of Science, Technology and Engineering, James Cook University, 34 James Cook Drive, Townsville, QLD Australia

[2]Vital Metals Ltd., 1/91 Hay Street, Subiaco WA Australia

The Watershed tungsten deposit is located in far north Queensland, about 100 km northwest of Cairns. It has a combined JORC resource of 49.32 Mt @ 0.14% WO_3 totaling 70,400 tonnes of contained WO_3. Watershed lies within the Mossman Orogen, in the northernmost part of the Tasman Fold Belt of eastern Australia. The Mossman Orogen comprises a folded sequence of Ordovician-Devonian metasediments, intruded by Carboniferous-Permian granites of the Kennedy Province. The Watershed deposit is hosted in a sequence of folded slates and, locally calcareous, psammites of the Hodgkinson Formation which form a NNW striking and NNW-plunging anticline. In addition, multiple felsic dykes occur cutting the metasediments that might be part of the Permian S-type Whypalla Supersuite granites that crop out to the west and east from Watershed.

Mineralization is mainly restricted to altered psammites units with blue-fluorescing (Mo-poor) scheelite being the sole ore mineral at Watershed. Scheelite mineralization mainly occurs in centimetric vein halos, within veins and is scarcely disseminated at locations away from veins. Widespread Fe-poor red-green calc-silicate alteration (garnet-clinozoisite) is spatially related to mineralization.

At least three major veining events (Stages I, II and III) have been recognized in drill core. The earliest mineralization event is hosted in quartzite and in fine-grained psammite as (I) sinuous and/or deformed quartz + feldspar + biotite ± scheelite ± pyrrhotite veinlets and veins. The main alteration mineral associated with this event is biotite, and scheelite mineralization is not of economic significance in this stage.

Post-dating Stage I, the most extensive scheelite mineralization occurs in centimetric halos of quartz – feldspar – scheelite - pyrrhotite and minor arsenopyrite veins from Stage II. This vein set, with <50 cm wide sinuous to planar E-W striking veins, mostly cuts green and red calc-silicate altered psammite breccia, minor quartzite, and granitic dykes. Additionally, minor scheelite occurs

disseminated in calc-silicate altered psammite, and coarse-grained in granitic dykes. Generally, at least six mineral sub-stages are recognized in Stage II: (IIa) early quartz + feldspar – scheelite assemblage as margins of veins (<3 cm wide); (IIb) grey quartz, locally with up to 3 cm scheelite, occupying the centre of the veins. Stage IIc are white quartz veinlets, which cut across previous veins, locally cut by calcite stringers of Stage IId. Stage IIe corresponds to muscovite-sericite veins with minor siderite center line and Stage IIf corresponds to fracture-filling pyrrhotite and /or arsenopyrite veins, locally with up to 5 cm arsenopyrite mega crystals, post-dating all the above events.

The latest scheelite mineralization occurred in Stage III as quartz-feldspar-scheelite-minor pyrrhotite veins/veinlets with 'ladder' texture. They are <3 cm wide, planar or rarely sinuous. Such veins are typically high-grade.

Different veining events associated with scheelite may reflect different mineralization pulses in the Watershed deposit. The formation temperature, pressure and depth will be constrained by fluid inclusion and stable isotope studies. Fluid source will be inferred and the potential for more and/or higher-grade mineralization at depth will be assessed.

Appendix 5.2: Australian Earth Sciences Convention 2016 Abstract

The Watershed tungsten deposit (NE Queensland, Australia): Scheelite vein mineralization, alteration and mineral chemistry

Poblete, Jaime[1]; Chang, Zhaoshan[1]; Cheng, Yanbo[1]

[1]*Economic Geology Research Centre and Earth and Oceans Academic Group, College of Science, Technology and Engineering, James Cook University, Townsville, Australia*

The Watershed deposit is located in far north Queensland, about 100 km northwest of Cairns. It has a combined JORC resource of 49.32 Mt @ 0.14% WO_3 totalling 70,400 tonnes of WO_3. Watershed lies within the Mossman Orogen, which comprises a folded sequence of Ordovician-Devonian metasediments intruded by Carboniferous-Permian granites of the Kennedy Province. Mineralization is hosted by a sequence of folded slates and, locally calcareous, psammites of the Hodgkinson Formation. In addition, multiple felsic dykes of the Permian S-type Whypalla Supersuite granites occur cutting the metasediments.

Veining, alteration and mineralization occur in mainly five stages. Stage 0 corresponds to strongly deformed quartz-calcite-mica veins cutting slate units. Stage 1 is a widespread red-green prograde skarn in psammitic units. It is comprise mainly of grossular-spessartine-almandine garnets of up to 2 mm and hedengbergitic-diopsidic pyroxene, and is overprinted by clinozoisite, actinolite-ferroactinolite-magnesiohornblende-tourmaline-biotite-scheelite-calcite retrograde alteration.

The first mineralization event occurred in Stage 2. Mineralisation is hosted in quartzite and fine-grained psammite as sinuous and/or deformed quartz+feldspar+biotite±scheelite±pyrrhotite veins and veinlets. In this stage, scheelite mineralization is not of economic significance. The main alteration mineral in the halo of such veins is biotite.

The most extensive scheelite mineralization occurred in Stage 3, in centimetric halos of quartz–feldspar–scheelite-pyrrhotite and minor arsenopyrite veins. This vein set, with <50 cm wide sinuous to planar E-W striking, S dipping veins, mostly cuts skarn altered psammite breccia, minor quartzite, and granitic dykes (LA-ICP-MS U-Pb zircon age of 300 ± 4 Ma). Additionally, in this stage minor scheelite occurs disseminated in skarn and as coarse grains in granitic dykes. At least six sub-stages are recognized in Stage 3: (3a) early quartz+oligoclase–scheelite assemblage as vein margins (<3 cm wide); (3b) grey quartz-scheelite occupying the centre of the veins. Stage 3c are white quartz veinlets, which cut across previous veins. It is locally cut by calcite stringers of Stage 3d. Stage 3e is defined by muscovite-sericite veins (muscovite $^{40}Ar/^{39}Ar$ age of 252.9 ± 1.3 Ma) with minor siderite center line. Stage 3f post-dates all previous events, and corresponds to fracture-filling pyrrhotite-arsenopyrite veins.

The latest scheelite mineralization occurred in Stage 4 as quartz-oligoclase-scheelite-minor pyrrhotite veins/veinlets with 'ladder' texture. They are <3 cm wide, planar or rarely sinuous. Such veins are typically high-grade. New short-wavelength infra-red (SWIR) spectroscopy shows locally illite crystallinity values up to 8, incidating temperatures of ~350° - 420°C.

The new pre-mineral dyke age of ca. 300 Ma is somewhat 35 Ma older than reported ages for intrusions of the Whypalla Supersuite. Mineralization occurred close to ca. 253 Ma. Garnet compositions confirm the reduced nature of the alteration fluids, and together with the crystal size suggests a hydrothermal origin for the skarn. The illite crystallinity values suggest that high-grade greisen/skarn may be present below the current drilling levels at Watershed.

Appendix 5.3: FUTORESII 2017 Conference Abstract

The Watershed scheelite skarn deposit, Far North Queensland, Australia

J.A. Poblete[1], Z. Chang[2]

[1] Economic Geology Research Centre (EGRU), James Cook University, Townsville QLD 4811, Jaime.PobleteAlvarado@my.jcu.edu.au

[2] Economic Geology Research Centre (EGRU), James Cook University, Townsville QLD 4811, Zhaoshan.Chang@jcu.edu.au

Watershed (JORC 70,400 tonnes of WO_3) lies within the Mossman Orogen comprising Ordovician-Devonian metasediments intruded by Carboniferous-Permian granites of the Kennedy Igneous Association. Mineralization is hosted in a sequence of folded slates and, locally calcareous, psammites of the Hodgkinson Formation. In addition, multiple felsic dykes of the Permian S-type Whypalla Supersuite cut across the metasedimentary rocks. Two pre-mineral dykes have been dated at 354 ± 5 Ma and 300 ± 4 Ma (LA-ICP-MS zircon U-Pb) in this study.

Alteration and mineralization is strongly lithological controlled in psammitic units and have occurred in at least seven stages: starting with a pre-skarn event, followed by a prograde skarn event, subsequently four retrograde skarn stages occurred with a late fracture filling sulphide event (Figure 1). Scheelite occurs in veins, and is disseminated in vein halos, granitic dykes, and to a lesser extent in skarn replacing psammite in the first retrograde stage. REE patterns of scheelite (LA-ICP-MS) are consistently flat with slightly negative Eu anomaly and enriched with respect to chondrite in veins and in a granitic dyke. In contrast, scheelite from another granitic dyke is bell-shaped enriched in HREE and depleted in LREE, with consistent positive Eu anomaly. The mineralization age is constrained by a retrograde 3 stage muscovite age of 252.98 ± 2.66 Ma ($^{40}Ar/^{39}Ar$ and 2σ error). The isotopic values for hydrothermal calcite from Watershed (-7 to -19 $\delta^{13}C$‰ VPDB and 14 to 22 $\delta^{18}O$ ‰VSMOW) are similar to that of calcite from other W skarns.

	Pre skarn	Prograde	Retrograde 1	Retrograde 2	Retrograde 3	Retrograde 4	Sulphide
Wall rock	Grs < 80 Qz	Grs > 70 Di 31-61 Titanite	Czo X^{Fe3+}<0.38 Qz Scheelite An > 15	Phlogopite (Na)-Amp An < 25	Chlorite Muscovite Calcite Fluorite	Aerinite	Po
Vein			Qz Or > 93 An > 15 Scheelite	Qz An 3-33	Muscovite Biotite Calcite Chlorite	Laumontite Prehnite	Po Apy Sp Ccp

Fig. 1 Watershed paragenesis table based on sample descriptions, petrography and subsequent EPMA analysis. Amp: amphibole; An: anortite; Apy: arsenopyrite; Ccp: chalcopyrite; Di: diopside; Czo: clinozoisite; Grs: grossular; Or: orthoclase; Po: phyrrhotite; Qz: quartz; Sp: sphalerite

Appendix 5.4: Society of Economic Geologists 2017 Conference Abstract

SEG 2017 Conference

The Watershed scheelite skarn deposit, Far North Queensland, Australia

Jaime A Poblete*, Zhaoshan Chang

*EGRU - JCU, Townsville, Australia, Queensland, Email: japoblet@gmail.com

Appendix 5.5: Society of Economic Geologists 2018 Conference Abstract

The Watershed shear-vein tungsten deposit, Far North Queensland, Australia: A metamorphic fluid origin

J.A. Poblete[1†], Z. Chang[1], Paul Dirks[1], Jan M. Huizenga[1]

[1] Economic Geology Research Centre (EGRU), James Cook University, Townsville, Queensland 4811, Australia [†]Jaime.PobleteAlvarado@my.jcu.edu.au

The Watershed tungsten deposit (49.2 Mt averaging 0.14% WO_3) lies within the Mossman Orogen, which comprises deformed Silurian-Ordovician metasedimentary rocks of the Hodgkinson Formation intruded by Carboniferous-Permian granites of the Kennedy Igneous Association. The Hodgkinson Formation at the Watershed area comprises calc-silicate conglomerate, psammite and slate units, which record at least four events of coaxial deformation evolving from ductile isoclinal folding and transposition (D_1 to D_3) to brittle ductile shear zones (D_4). Calc-silicate mineralogy, formed during ductile deformation, comprises garnet ($gr_{40-87}al_{0-35}sp_{1-25}ad_{0-16}$), actinolite, quartz, clinopyroxene ($di_{36-59}hd_{39-61}jo_{1-5}$) and titanite (U/Pb ages of 321±11 Ma, 306±18 Ma and 301±13 Ma). Multiple felsic dykes cut across the metasedimentary rocks at Watershed, including a deformed Carboniferous monzonitic dyke (zircon U/Pb of 350±3 Ma) and granitic dykes assigned to D_4 (zircon U/Pb of 276±2 Ma and 275±2 Ma). A first mineralization event corresponds to scheelite dissemination in monzonitic dyke (D_3?) and in calc-silicate during ductile deformation (D_3). The bulk of the scheelite mineralization occurs in a second event in shear-related quartz-plagioclase veins and vein halos which were emplaced during D_4 (muscovite ^{40}Ar-^{39}Ar 276±6 Ma). Such veins are developed in calc-silicate units, terminating abruptly when they encounter slaty units. Calc-silicate mineralogy associated with D_4 comprises mainly clinozoisite and quartz, accompanied by plagioclase, scheelite, phlogopite, Na-rich amphibole, minor muscovite, calcite and titanite (U/Pb ages of 271±8 Ma, 263±8 Ma and 254±9 Ma). Fluid inclusions in quartz and scheelite from veins are CH_4-H_2O-rich and contain graphite, with Th between 170° to 307°C and %NaCl values between 0.5 to 8.1%, suggesting fluid mixing. The Th are in agreement with the scheelite-albite $\Delta^{18}O$ geothermometer results of 306±56 °C, in addition muscovite δD (-66‰ VSMOW) and $\delta^{18}O$ (12‰ VSMOW) values show a metamorphic origin for the mineralizing fluids, which is in agreement with the fluid inclusions compositions and the geological field observations.

Appendix 5.6: Society of Economic Geologists 2015 Conference Abstract (Cheng et al.)

Geology and Mineralization of the Mt Carbine Deposit, Northern QLD, Australia

Yanbo Cheng, Zhaoshan Chang, and Jaime Poblete

Economic Geology Research Center, College of Science, Technology and Engineering, James Cook University, Townsville, 4811, Australia

The Mt Carbine wolframite-scheelite sheeted vein deposit is located ~80 km NW of Cairns, Northern Queensland. It was the largest vein type W deposit in Australia and accounted for 43% of Australia's annual W production in 1986, prior to closure because of international Sn-W market crash. The hard rock resources at Mt Carbine at last review were Indicated Mineral Resource 18Mt at 0.14% WO_3, Inferred Mineral Resource 29.3Mt at 0.12% WO_3 (Carbine Tungsten Limited Annual Report 2014). The vein system in Mt Carbine is hosted in Ordovician to Devonian Hodgkinson Formation metasedimentary rocks, which include turbiditic meta-sediments composed mainly of greywacke, siltstone-shale, slate, basalts, conglomerates and chert. There are at least 3 types of felsic igneous rocks in the mining district, including porphyritic biotite granite, equigranular coarse-grained biotite granite and fine-grained felsic dyke (which cuts the ore body). There is no contact between equigranular coarse-grained biotite granite and the mineralized vein system, thus their relationship is unclear. Mineralized quartz veins and chlorite alteration occur in the porphyritic biotite granite, whereas no quartz vein and alteration are present in the fine-grained felsic dyke, indicating that the porphyritic biotite granite was earlier than mineralization and the felsic dyke later than mineralization.

There are four 30-40 m wide vein zones in the open pit with different orientations, with Zones 1 - 3 being ~300°/80° (strike/dip), and Zone 4 is 270°/65°. Based on drill core logging and open pit inspection, 6 types of veins including 3 types of quartz-dominant veins have been identified. They are Type 1 curved and discontinuous quartz-dominant vein in Hodgkinson Formation meta-sediment; Type 2 continuous quartz-dominant vein with irregular and curved margins; Type 3 straight & continuous quartz-dominant veins with sharp boundaries; Type 4 calcite vein; Type 5 feldspar vein, and Type 6 fluorite-feldspar vein. The W mineralization is mostly in quartz veins (Types 1-3), with no mineralization in the other 3 types of veins. Ore minerals are wolframite and scheelite. Wolframite is typically euhedral and occurs in quartz veins, while the occurrences of scheelite are: (1) filling the intersticies between wolframite grains, (2) pseudomorphing wolframite grains or cutting across wolframite grains as veinlets, and (3) as scheelite clots in Hodgkinson Formation meta-sediments. Scheelite was later than wolframite. The gangue minerals include muscovite, chlorite, fluorite, albite/feldspar, biotite and calcite, and sulphides include arsenopyrite, pyrrhotite, chalcopyrite, sphalerite and minor molybdenite. The paragenesis study is currently underway.

Appendix 5.7: Australian Earth Sciences Convention 2016 Abstract (Cheng et al.)

Geology and Mineralization of the Mt Carbine Deposit, Northern QLD, Australia

Yanbo Cheng[1], Zhaoshan Chang[1], Jaime Poblete[1]

1 Economic Geology Research Center (EGRU), College of Science, Technology and Engineering (CEST), James Cook University, Townsville, 4811, Australia

The Mt Carbine quartz-wolframite-scheelite sheeted vein deposit is located ~80 km NW of Cairns, Northern Queensland. It was the largest vein type W deposit in Australia and accounted for 43% of Australia's annual W production in 1986, prior to closure because of international Sn-W market crash. The hard rock resources at Mt Carbine at last review include indicated resources of 18 Mt at 0.14% WO_3 and inferred resource of 29.3 Mt at 0.12% WO_3 (Carbine Tungsten Limited Annual Report 2014). The vein system in Mt Carbine is hosted in Ordovician to Devonian Hodgkinson Formation metasedimentary rocks, which include turbiditic meta-sediments composed mainly of greywacke, siltstone-shale, slate, basalt, conglomerates and chert. There are at least 3 types of felsic igneous rocks in the mining district, including porphyritic biotite granite, equigranular coarse-grained biotite granite and fine-grained felsic dyke that cuts across the ore body. There is no observable contact between granite and the W veins, thus their relationship is unclear. Mineralized quartz veins and chlorite alteration occur in the porphyritic biotite granite, whereas no quartz vein and alteration are present in the fine-grained felsic dyke, indicating that the porphyritic biotite granite was earlier than mineralization and the felsic dyke later than mineralization. This observation is consistent with the latest dating results: the LA-ICP-MS zircon U/Pb age of the porphyritic biotite granite is 298 ± 3 Ma and the felsic dyke 261 ± 7 Ma, whereas the molybdenite Re-Os age from the mineralized quartz vein is 284 ± 1 Ma, and the muscovite ^{40}Ar-^{39}Ar ages are 282-277 (± 1-2) Ma. There is no overlap between the 2 muscovite ^{40}Ar-^{39}Ar ages, probably indicates there was some post-mineralization tectono-thermal activities.

There are four 30-40 m wide vein zones in the open pit with different orientations, with Zones 1 - 3 being ~300°/80° (strike/dip), and Zone 4 270°/65°. Based on drill core logging and open pit observation, the paragenesis sequence has been established. Stage 0 is represented by the deformed curvy and discontinuous quartz-dominant vein with minor to none W mineralization. Stage I continuous quartz-dominant veins have straight and continuous margin, and are composed of wolframite ± scheelite ± K-feldspar ± biotite ± tourmailine ± apatite. Stage II veins are straight & continuous, quartz-dominant with sharp boundaries, and contain chlorite ± scheelite ± wolframite ± cassiterite ± muscovite. Stage III is represented by undeformed straight and continuous quartz ± chlorite ± muscovite ± molybdenite ± arsenopyrite ± chalcopyrite ± pyrite ± pyrrhotite ± sphalerite veins, without W mineralization. Stage IV veins are featured by the undeformed straight and continuous shape and quartz ± calcite ± fluorite mineralogy without any W mineralization. The W mineralization is mostly in stage II quartz veins, with less economic W mineralization in the other 3 stages of veins. Ore minerals are wolframite and scheelite. Wolframite is typically euhedral and occurs in quartz veins, while the occurrences of scheelite are: (1) euhedral grains in quartz vein and, (2) pseudomorphing wolframite grains or cutting across wolframite grains as veinlets.

Appendix 5.8: 15th Quadrennial IAGOD 2018 Conference Abstract (Cheng et al.)

TIN AND TUNGSTEN DEPOSITS IN NORTHEAST QUEENSLAND, AUSTRALIA: PAST, PRESENT, AND PROSPECTIVITY

Yanbo Cheng[1], Zhaoshan Chang, Jaime Poblete, Kairan Liu, Carl Spandler, Gavin Clarke, Paul Dirks

[1]*Economic Geology Research Centre (EGRU) and Department of Geoscience, James Cook University, 1 James Cook Dr, Douglas, QLD 4811, Australia - yanbo.cheng1@jcu.edu.au*

Northeast Queensland of Australia is an important Sn-W-Mo-Au mineralized province in Australia, particularly for Sn and W, which includes ~10% of Australia's Economic Demonstrated Resources (EDR) of Sn and ~13% of the country's EDR of tungsten (Chang et al, 2017). Sn-dominant deposits mainly occur in three districts: the Kangaroo Hills, Herberton and Cooktown districts. The W-dominant deposits occur only in the northeast Mt Carbine-Watershed area. W-Mo deposits have been found in both the Herberton (e.g., Wolfram Camp) and Kangaroo Hill districts.

To discern differences between "fertile" and "non-fertile" igneous rocks associated with Sn- W-Mo mineralization and reveal the genetic links between coeval intrusive and extrusive rocks, we integrate whole rock geochemistry, geochronology and Hf isotope signatures of igneous zircons from contemporaneous plutonic and volcanic rocks from the Herberton Sn and W-Mo mineral field. The 310-300 Ma intrusive rocks and associated intra-plutonic W-Mo mineralization formed from relatively oxidized magmas after moderate degrees of crystal fractionation. The geochemical and isotopic features of the coeval volcanic succession are best reconciled utilizing the widely-accepted volcanic-plutonic connection model, whereby the volcanic rocks represent fractionated derivatives of the intrusive rocks. The volcanic rocks of 335-310 Ma (Sn formation stage) are compositionally less evolved than the coeval intrusive rocks. In this case, we propose that the most fractionated magmas were not lost to volcanism, but instead were effectively retained at the plutonic level, which allowed further localized build-up of volatiles and lithophile metals in the plutonic environment. Given the common occurrence of volcanic and plutonic rocks associated with Sn-W-Mo mineralization worldwide, we suggest that a proper understanding of plutonic-volcanic connections can assist in assessment of regional-scale mineralization potential, which in turn can aid strategies for future ore deposit exploration.

The Wolfram Camp Mine deposit is a greisen type W-Mo deposit. The host rock of the deposit is Late Carboniferous James Creek granite and which has locally intruded Hodgkinson Formation sandstone. The orebodies contain wolframite and molybdenite occur as pipe-like bodies of quartz in the roof zone of the intrusion. Alteration associated with the Wolfram Camp mineralization is mainly greisen type. The alteration can be divided into quartz-rich greisen zones, muscovite-rich greisen zones and greisenized granite zones with decreasing alteration levels. The mineralization in the study area are closely related to post- intrusive hydrothermal events and can be divided into several stages. The major ore minerals, wolframite and molybdenite, formed during the greisen stage, and base metal sulphide minerals and scheelite formed in later sulphide and calcite stages. Fluid inclusion studies was conducted on the ore bearing quartz crystals in the pipes. The homogenization temperatures of the fluid inclusions quartz containing wolframite are about 410 °C. Results from a stable isotope study suggest that the source of the hydrothermal fluid related to the formation of the wolframite, molybdenite and base metal sulphides is purely magmatic. However, the fluid responsible for the introduction of the calcite is a combination of magmatic water and meteoric water.

The Mt Carbine quartz-wolframite-scheelite sheeted vein deposit is hosted in Ordovician to Devonian Hodgkinson Formation metasedimentary rocks. Field observation and drill core logging have provided evidence for a five stage paragenetic sequence of mineralization and veining, with two of the stages having significant W mineralization. Wolframite is typically euhedral and occurs in quartz veins, while scheelite occurs as (1) euhedral grains in quartz vein and, (2) pseudomorphing wolframite grains or cutting across wolframite grains as veinlets. This observation is consistent with the scheelite CL images and in-situ composition variation. The LA-ICP-MS zircon U-Pb dating results reveal the magmatic activities occurred during 300-265 Ma. Molybdenite Re-Os age and muscovite 40Ar-39Ar ages are between 285-275 Ma. Fluid inclusion studies reveal that most of the inclusion are primary and distributed in assemblages or isolated, with homogenization temperatures ranging from 290 to 210 °C. Laser Raman analysis identified CH_4 in vapour bubbles. Together with H-O-S isotopic compositions, our data indicate that both magmatic fluid and metamorphic water contributed the formation of Mt Carbine W deposit.

The Watershed scheelite deposit lies within the Mossman Orogen, which comprises deformed Silurian-Ordovician metasedimentary rocks of the Hodgkinson Formation by Carboniferous and Permian granites of the Kennedy Igneous Association. Multiple felsic dykes cut cross the metasedimentary rocks at Watershed including: (a) monzonite dyke (~350 Ma); and (b) dioritic, granitic plutons and dykes (281-271 Ma). A first non-economic

mineralization event corresponds to the crystallization of disseminated scheelite in monzonite dykes. The bulk of the scheelite mineralization formed during a second event in shear-related quartz multi-staged veins and vein halos. The vein stages occurred synchronously with three retrograde stages in calc-silicate conglomerate. The retrograde minerals in calc-silicate comprises clinozoisite after garnet, quartz, plagioclase, scheelite and phlogopite with minor sodium-rich amphibole. The principal control on scheelite mineralization at Watershed are: (a) early monzonite dykes enriched in scheelite (W source); (b) shear zone that acted as fluid conduits transporting tungsten; (c) calc-silicate conglomerate that provide a source for calcium to form scheelite; and (d) an extensional depositional environment characterized by vein formation and normal faulting, which provide trapping structures for fluids, with fluid decompression being a likely control on scheelite deposition.

Based on metal commodities, the mineral deposits of the northeast Queensland Sn-W-Mo-Au province can be classified into five types: Sn-dominant, W-dominant, W-Mo, porphyry-skarn Au-Cu and the traditionally recognized intrusion related gold deposits (IRGDs). Based on geological characteristics and our high precision geochronological results, Sn-dominant deposits and associated igneous rocks in northeast Queensland formed in three episodes: ~265 Ma, 330-310 Ma and ~345 Ma. The W-dominant mineralization only formed during 285-250 Ma, and W-Mo mineralization occurred during 310-300 Ma and 345-335 Ma. The porphyry-skarn type Au-Cu deposits in Chillagoe District formed during 335-295 Ma, and the Au-dominant deposits in Georgetown and Cape York Peninsula formed in two episodes: 350-335 Ma and 285-280 Ma. Overall, the combined results from dating both magmatic and hydrothermal activities show a younging trend from southwest to northeast in the northeast Queensland Sn-W-Mo-Au province.

REFERENCE

Chang, Z., Clarke, G., Cheng, Y., Poblete, J., Liu, K. 2017. Sn-W-Mo mineralization in north- east Queensland. In: Phillips, G N (ed) Australian Ore Deposits, The Australasian Institute of Mining and Metallurgy: Melbourne, pp. 681-688.

Appendix 5.9: AusIMM 2017 Monograph (Chang et al.)

Phillips, G N (ed), 2017. *Australian Ore Deposits*, 864 p (The Australasian Institute of Mining and Metallurgy: Melbourne).

Sn-W-Mo mineralisation in north-east Queensland

Z Chang[1], G Clarke[2], Y Cheng[3], J Poblete[3] and K Liu[3]

1. MAusIMM, Economic Geology Research Centre (EGRU) and Academic Group of Geosciences, James Cook University, Townsville Qld, zhaoshan.chang@jcu.edu.au; **2.** MAusIMM, EGRU and Academic Group of Geosciences, James Cook University, Townsville Qld; **3.** EGRU and Academic Group of Geosciences, James Cook University, Townsville Qld.

Content has been removed
due to copyright restrictions

Content has been removed
due to copyright restrictions

Content has been removed
due to copyright restrictions

Content has been removed
due to copyright restrictions